An Experimental Investigation of Multiphase Gas-Liquid Pipe Flow at Low Liquid Loading

by

Gaël Chupin

A Thesis Submitted for the Degree

of

Doktor Ingeniør

Norwegian University of Science and Technology
Department of Energy and Process Technology

Trondheim,
September 2003

URN:NBN:no-7245

URN:NBN:no-7245

Abstract

In this thesis, the co-current flow of gas, oil and water in pipes has been studied at low input liquid loading. Despite the frequent occurrence of low liquid loaded gas flow in pipes involved in the production of gas fields, the basic flow mechanisms are not accurately accounted for by current multiphase flow models. This is partly due to a lack of experimental data, especially in three-phase gas-liquid-liquid flow.

In this thesis, new laboratory pipe flow measurements at low liquid loading have been performed in an atmospheric multiphase flow loop with air, water and oil. The initial motivation for the experiments was to test the influence of pipe material on wall wetting. Two types of experiments have been carried out: steady-state flow tests in near horizontal pipes of different material (acrylic, steel and epoxy coated steel) and transient flow tests in horizontal and vertical gas pipes of gradually changing liquid wetting. In both cases, accurate measurements of the pressure drop and phase fractions have been performed.

The wall material was found to influence the steady-state pressure drop and phase fractions in three-phase flow. Hydrophillic walls delayed the formation of dispersions in the liquid phase but also affected the distribution of droplets on the upper-pipe wall in atomization flow. It has been possible to alter the water affinity of the acrylic pipe wall by either contaminating or cleaning the wall surface, resulting in fairly different flow measurements. In vertical pipes, the presence of a thin liquid film at the wall did not result in drag reduction as was expected theoretically. Despite the low liquid holdup at the wall, the frictional pressure drop was significantly higher than for single phase gas flow. For very thin films, the friction factor approached that of a rough pipe with an hydraulic roughness scaling with the average equivalent film thickness.

Predictions from one-dimensional multiphase pipe flow models have been compared with the experimental measurements at low liquid loading and severe discrepancies were observed. For steady gas-liquid flow in slightly inclined pipes, the Modified Apparent Rough Surface model by Grolman (1994) compared best with the experimental data. For both gas-liquid and gas-oil-water flow, the commercial simulator PETRA was relatively close to the measured data. However, when local separation of oil and water occurred in the pipe, the holdup was under predicted. For atomization flow and upper pipe wall wetting, the pressure drop was also under predicted by PETRA.

A steady-state three-phase stratified flow model has been derived in this thesis to incorporate the prediction of interfacial curvature depending on the preferred wetting of the pipe wall by either one of the liquid phases. The model gave predictions in closer agreement with measurements than three-layer models assuming flat interfaces.

URN:NBN:no-7245

URN:NBN:no-7245

Preface

The work presented in this dissertation has been performed at the Norwegian University of Science and Technology (NTNU) between August 2000 and August 2003. It is part of a Joint Industry Project (JIP) headed by Institut Français du Pétrole (IFP) and NTNU. I am indebted to the sponsors of this JIP, BP, Enagas, Gas-de-France, Statoil, Total and the Research Council of Norway, for financing the three years of this doctoral work.

My supervisor throughout this thesis has been Professor Ole-Jørgen Nydal whom I thank for his advice and for giving me the opportunity and motivation to undertake this work. No less important was the support from my co-supervisor Professor Jon-Steinar Gudmundsson and the other members of the JIP-NTNU team, Professor Helge Andersson, André Strupstad and Stian Solbakken.

I would like to express special thanks to the Research Centre of Statoil for taking interest in this thesis, allowing me to use some of their high pressure data and financing project students who assisted me with the experimental work. The students who contributed to this research are: Sébastien Labesques (ENSAIS Strasbourg) for the flow loop setup and instrument calibrations, Patrick Laux (ENSAM Bordeaux) for the steel pipe measurements, François Motard (ENSAM Paris) for the construction of the epoxy coating, Yoong Hsiang See Toh (Imperial College, London) for the vertical film thinning experiments and Nicolas François (ENSEEIHT Toulouse) for the experiments in the acrylic pipe. I express them my warmest thanks for their patience and the quality of their work.

In the laboratory at NTNU, I would like to thank Knut Glasø and Erling Mikkelsen who have skilfully participated to the construction and maintenance of the multiphase flow rig. I am also grateful to my fellow doctoral students at the Energy and Process Technology Department for the nice atmosphere, the suggestions and the help they provided me during the thesis period.

The results discussed in this dissertation have been, so far, partially presented at the following conferences:

- Chupin G., Nydal O.J., 2003, *An Experimental Study of Air/Oil/Water Pipe Flow at Low Liquid Loading,* 11th International Conference on Multiphase Flow, Multiphase 03, San Remo, Italy, 11-13 June 2003

- Chupin G., Nydal O.J., 2003, *Stratified Gas/Liquid Flow at Low Liquid Loading,* 2nd International Conference on Heat Transfer, Fluid Mechanics and Thermodynamics, Livingstone, Zambia, 23-26 June 2003

New publications incorporating later results are expected to be released during the year 2004 depending on acceptance from conference and journal peer-review comities.

URN:NBN:no-7245

Contents

Nomenclature

Roman symbols:

Symbol	Unit	Denotes
A	m^2	pipe cross sectional area
A	-	universal constant, A = 8.5 (in Chapter 5)
A_L	m^2	liquid cross sectional area
A_O	m^2	oil cross sectional area
A_W	m^2	water cross sectional area
B	-	universal constant, B = 5 (in Chapter 5)
B_o	-	Bond number
c_O	-	gas-oil interface curvature index
c_W	-	oil-water interface curvature index
C_a	-	capillary number (defined in Biberg 1999)
C_D	kg/m^3	droplet concentration in the gas stream, Equation [3.72]
D	m	pipe internal diameter
D_G	m	gas phase hydraulic diameter
D_i	m	diameter of the oil-water interfacial arc
D_j	m	diameter of the gas-oil interfacial arc
D_L	m	liquid phase hydraulic diameter
D_O	m	oil phase hydraulic diameter
D_W	m	water phase hydraulic diameter
EF	-	droplet entrained fraction, $EF = U_{SLE}/U_{SL}$
f_k	-	Fanning friction factor, $f_k = \lambda_k/4$
F	N	force (in Chapter 4)
F_f	-	drag factor
F_G	N/m	gas momentum or scaled gas momentum, $F_G = \tau_G S_G$ (in Chapter 6, Chapter 7, Appendix D and Appendix E)
F_j	Pa/m	gas-liquid frictional pressure drop, $F_j = \tau_j S_j/A$ (in Chapter 5)
F_j	N/m	gas-liquid interfacial momentum or scaled interfacial momentum, $F_j = \tau_j S_j$ (in Chapter 6, Chapter 7, Appendix D and Appendix E)
F_L	Pa/m	liquid-wall frictional pressure drop, $F_L = \tau_L S_L/A$ (in Chapter 5)

Symbol	Unit	Denotes
F_L	N/m	liquid momentum or scaled liquid momentum, $F_L = \tau_L S_L$ (in Chapter 6, Chapter 7, Appendix D and Appendix E)
F_n	-	friction number (defined in Grolman et al. 1997)
Fr_G	-	gas phase Froude number, Equation [3.38]
Fr_L	-	liquid phase Froude number, Equation [3.35] or Equation [3.45]
Fr_O	-	oil phase Froude number, Equation [3.120]
g	m/s^2	acceleration of gravity $g = 9.81\ m/s^2$
h_L	m	average liquid film height at the pipe center line
H, H_L, H_{tot}	-	liquid holdup
H_O	-	oil holdup
H_W	-	water holdup
k	m^{-1}	wave number ($k = 2\pi/\lambda$), Equation [3.76]
k_e	m	effective roughness
k_S	m	equivalent sand grain roughness
K	-	empirical constant, $K \cong 750$ (defined in Biberg 1999)
L	m	length scale
m	m	average radial film thickness
m_G^+	-	dimensionless film thickness (defined in Asali et al. 1985)
M	kg	mass
n	-	number of measurements
P	Pa	pressure
dP/dx	Pa/m	pressure drop
QCV	-	in-situ water fraction, $QCV = H_W/H_{tot}$
Q_G	m^3/s	gas volumetric flow rate
Q_L	m^3/s	liquid volumetric flow rate
Q_O	m^3/s	oil volumetric flow rate
Q_W	m^3/s	water volumetric flow rate
r	m	radial coordinate
r_G	m	radial coordinate at the gas-liquid interface
r_{10}	m	gas viscous sub-layer thickness
R	m	pipe radius
R_a	m	arithmetical mean roughness, Equation [4.2]
R_D	kg/m^2s	droplet deposition rate, Equation [3.71]
Re_G	-	gas phase Reynolds number, $Re_G = \rho_G U_G D_G/\mu_G$

Symbol	Unit	Denotes
Re_{SG}	-	gas phase Reynolds number based on the superficial gas velocity, $Re_{SG} = \rho_G U_{SG} D/\mu_G$
Re_L	-	liquid phase Reynolds number, $Re_L = \rho_L U_L D_L/\mu_L$
Re_{SL}	-	liquid phase Reynolds number based on the superficial liquid velocity, $Re_{SL} = \rho_L U_{SL} D/\mu_L$
Re_O	-	oil phase Reynolds number, $Re_O = \rho_O U_O D_O/\mu_O$
Re_W	-	water phase Reynolds number, $Re_W = \rho_W U_W D_W/\mu_W$
Re_τ	-	Reynold number based on the friction velocity, $Re_\tau = Ru_\tau/\nu_G$
R_q	m	root-mean-square roughness, Equation [4.3]
R_z	m	mean peak-to-valley height, Equation [4.4]
R_y	m	maximum profile height, Equation [4.5]
S	m	pipe perimeter
Sec	m^2	section
S_G	m	gas wetted perimeter
S_i	m	oil-water interfacial perimeter
S_j	m	gas-oil interfacial perimeter
S_L	m	liquid wetted perimeter
S_O	m	oil wetted perimeter
S_W	m	water wetted perimeter
t	s	time
T	^oC, ^oK	temperature
u_G	m/s	gas local velocity
u_j	m/s	gas-liquid interfacial local velocity
u_{jG}^*	m/s	gas frictional velocity at the gas-liquid interface, $u_{jG}^* = \sqrt{\tau_j/\rho_G}$
u_{jL}^*	m/s	liquid frictional velocity at the gas-liquid interface, $u_{jL}^* = \sqrt{\tau_j/\rho_L}$
u_L	m/s	liquid local velocity
u_L^*	m/s	liquid frictional velocity at the wall, $u_L^* = \sqrt{\tau_L/\rho_L}$
u_τ	m/s	friction velocity, $u_\tau = \sqrt{\tau_k/\rho_k}$
U_G	m/s	gas average velocity
U_i	m/s	boundary velocity (oil-water flow)
U_j	m/s	boundary velocity (gas-liquid flow)
U_{KH}	m/s	gas velocity at inception of KH waves, Equation [3.77]
U_L	m/s	liquid average velocity

Symbol	Unit	Denotes
U_L^*	m/s	interfacial velocity, Equation [3.66]
U_O	m/s	oil average velocity
U_r	m/s	relative or slip velocity, $U_r = U_1 - U_2$
U_W	m/s	water average velocity
U_{SG}	m/s	gas superficial velocity
U_{SL}	m/s	liquid superficial velocity
U_{SLE}	m/s	entrained liquid droplet superficial velocity
U_{SO}	m/s	oil superficial velocity
U_{SW}	m/s	water superficial velocity
V	m^3	volume
V_k	m^3	volume of phase k
V_{tot}	m^3	volume of the quick closed section
w_i	rad	view angle at interfacial arc intersection, Equation [C.31] or Equation [C.32]
w_j	rad	view angle at interfacial arc intersection, Equation [C.31] or Equation [C.32]
We	-	Weber number, Equation [3.79]
We_L	-	Weber number based on the actual liquid velocity, Equation [5.58]
We_{SL}	-	Weber number based on the liquid superficial velocity, Equation [3.37]
WF	-	input water fraction, $WF = U_{SW}/U_{SL}$
x, z	m	longitudinal (axial) coordinate
X	-	Martinelli parameter, Equation [D.21]
y	m	vertical coordinate
Y	-	inclination parameter, Equation [D.22]
y_i	na	measured value
$\widehat{y_o}$, $\widehat{y_i}$	na	interpolation value
z	m	surface profile elevation

Greek symbols:

Symbol	Unit	Denotes
α	-	gas phase fraction, $\alpha = A_G/A$
∂	m	gas viscous sub-layer thickness, Equation [5.49]
δ	rad	wetted half-angle
δ_i	rad	view angle of the oil-water interfacial arc

Symbol	Unit	Denotes
δ_j	rad	view angle of the gas-oil interfacial arc
δ_j^*	rad	view angle of the gas-oil interfacial arc in the critical case
δ_L	rad	liquid wetted half-angle
δ_O	rad	oil wetted half-angle
δ^P	rad	wetted half-angle for a plane interface
$\delta_O{}^P$	rad	oil wetted half-angle for a plane gas-liquid interface
$\delta_W{}^P$	rad	water wetted half-angle for a plane gas-oil interface
δ_W	rad	water wetted half-angle
δ	-	dimensionless wetted half-angle, $\delta = \delta/\pi$
$\tilde{\delta}_0$	-	dimensionless wetted half-angle for a plane gas-liquid interface, $\tilde{\delta}_0 = \delta^P/\pi$
Δ	rad	contact angle hysteresis, $\Delta = \xi_A - \xi_R$
Δ	rad	circular triangle area (Appendix C)
ΔE	J	total energy difference, Equation [8.3]
Δh	m	mean wave height
ε	m	hydraulic roughness
ε_i	m	oil-water interfacial roughness
ε_j	m	gas-oil interfacial roughness
ε_v	-	Eötvos number, Equation [8.1]
ε_{vi}	m	oil-water Eötvos number
ε_{vj}	m	gas-oil Eötvos number
φ	-	volume fraction of the dispersed phase
Φ_i	rad	oil-water interfacial curvature
Φ_i^*	rad	optimal oil-water interfacial curvature
Φ_j	rad	gas-oil interfacial curvature
Φ_j^*	rad	optimal gas-oil interfacial curvature
γ	-	viscosity ratio $\gamma = \mu_W/\mu_O$
κ	-	Von-Karman constant, $\kappa = 0.41$
λ	m	wave length
λ_k	-	Moody friction factor
λ_G	-	gas-wall friction factor
λ_L	-	liquid-wall friction factor
λ_i	-	oil-water interfacial friction factor
λ_j	-	gas-oil interfacial friction factor
λ_O	-	oil-wall friction factor
λ_{TP}	-	gas friction factor, Equation [3.82]

Symbol	Unit	Denotes
λ_W	-	water-wall friction factor
μ_G	Pa.s	gas dynamic viscosity
μ_L	Pa.s	liquid dynamic viscosity
μ_m	Pa.s	mixture dynamic viscosity
μ_O	Pa.s	oil dynamic viscosity
μ_W	Pa.s	water dynamic viscosity
ν_G	m^2/s	gas kinematic viscosity
ν_L	m^2/s	liquid kinematic viscosity
ρ_G	kg/m^3	gas density
ρ_i	kg/m^3	oil-water interfacial density
ρ_j	kg/m^3	gas-oil interfacial density
ρ_L	kg/m^3	liquid density
ρ_m	kg/m^3	mixture density
ρ_O	kg/m^3	oil density
ρ_W	kg/m^3	water density
σ	N/m	gas-liquid surface tension
τ_G	Pa	gas-wall shear stress
τ_i	Pa	oil-water interfacial shear stress
τ_j	Pa	gas-oil interfacial shear stress
τ_k	Pa	wall shear stress
τ_L	Pa	liquid-wall shear stress
τ_O	Pa	oil-wall shear stress
τ_w	Pa	total shear stress
τ_W	Pa	water-wall shear stress
θ	rad	pipe inclination
Θ	-	Taylor dimensionless group, Equation [3.75]
Θ_W	-	Taylor dimensionless group for water
ξ	rad	equilibrium contact angle
ξ_A	rad	advancing contact angle
ξ_e	rad	equilibrium contact angle
ξ_i	rad	oil/water/solid equilibrium contact angle
ξ_j	rad	gas/oil/solid equilibrium contact angle
ξ_R	rad	receding contact angle

Subscripts:

Subscript	Denotes
1	index 1 (upper, lighter phase)
12	relative to 1 and 2
2	index 2 (lower, denser phase)
crit	critical
C	circle
eq.	equivalent
fric	frictional
init	initial
k	phase or interface k
K	in ^{o}K
LF	Laminar Film
meas	measured
SLF	Static Liquid Film

Abbreviations:

Abbreviation	Denotes
AGA	American Gas Association
atm	atmospheric
ARS	Apparent Rough Surface
calc.	calculation
cont	continuous
dble	double
deg.	degree
DRA	drag reducing agent
elmag	electro-magnetic flow meter
eq.	equation
exp.	experiment
dp, DP	differential pressure
err	error
gamma	gamma-densitometer
GPIB	General Purpose Interface Bus
i.d.	internal diameter (m)
i.e.	"id est", that is

Abbreviation	Denotes
incl	inclination
Int.	international
J.	journal
KH	Kelvin-Helmoltz
liq.	liquid
LES	Large Eddy Simulation
LGR	liquid-to-gas ratio (m^3/Sm^3 or %)
MARS	Modified Apparent Rough Surface
na	not available, or, not adequate
No.	number
p., pp.	page, pages
PC	personal computer
pdf	probability density function
plexi	plexiglass (acrylic) pipe
PLR	Pressure Loss Reduction
PVC	poly vinyl chloride
QCV	quick-closing valve
r.m.s	root-mean-square
RANS	Reynold Average Navier Stockes
Ref.	Reference
S	Standard
std	standard deviation
Vol.	volume
wat.	water
wt.	weight
μ	mean
σ	standard deviation
#	number

Chapter 1 Introduction

1.1 Background

The research performed in this thesis has been motivated by the need to improve transport capacity of existing and future gas pipelines. Gas production is planned to increase in the next decade due to fast growing demand in the OECD countries, especially for power generation purposes. New technologies are needed in order to transport larger volumes of gas in existing pipelines. In addition, the response time of distribution networks must be shortened to tackle rapid variations of the demand in future deregulated gas markets.

In this context, a Joint Industry Project (JIP) was initiated in 1999 by research institutions, gas producing companies and gas network operators to screen and develop methods for reducing the pressure drop in gas pipelines. Existing and new technologies were considered, including frictional coatings, advanced surface structures and drag reducing chemicals. This part of the project was assigned the task to study the pressure loss in presence of small amounts of liquid flowing together with the gas.

A critical complication, with respect to the design of gas pipelines, is due to the fact that production or condensation of liquids almost invariably takes place. Retrograde condensation of heavy hydrocarbon fractions and water leads to liquid dropout as pressure and temperature decrease along the line. In smaller quantities, liquid-based chemicals can also be added to the gas in the form of hydrate inhibitors or corrosion inhibitors. The presence of liquid in the pipeline leads to enhanced pressure drop and causes liquid management problems. A small liquid flowrate can accumulate to large liquid volumes with the associated risk of unstable flow (slugging, operational transients).

New gas production pipelines being planned for transport of gas from North Sea fields to shore will require pressure boosting during the lifetime of the field. Pressure Loss Reduction methods (PLR) are therefore important, not only for dry gas lines but also for gas/condensate pipelines. One objective of this work was to study two- and three-phase flow at low liquid loading as background for evaluation whether PLR technology for dry gas systems can be beneficial for multiphase gas-condensate systems.

Despite the frequent occurrence of low liquid loaded gas flow, the basic flow mechanisms have been little studied in the past, especially in the case of three-phase gas-oil-water flow, which results in pressure drop and holdup not being accurately predicted by standard multiphase flow models. The important issues are the prediction of the pressure drop, itself related to the degree of wetting of the pipe wall, and of the phase fractions at low gas velocity when local separation of oil and water may occur in the pipeline.

1.2 Scope of the thesis

In this thesis, gas pipe flow at low liquid loading has been studied experimentally. This work's contributions include:

- The acquisition of new experimental data on gas flow at low liquid loading in two-phase gas-liquid and three-phase gas-oil-water flow in near horizontal pipes.
- The experimental investigation of possible drag reduction in gas pipes with a liquid film between the turbulent gas core and the wall.
- The review and testing of one-dimensional prediction models for gas-liquid two- and three-phase flow at low liquid loading.

A main challenge is due to surface (interfacial) effects being particularly important to consider at low liquid loading due to the high surface-to-volume ratio at low liquid holdups. Figure 1–1 shows how this ratio increases with decreasing values of the liquid wetted angle. Surface tension effects influence the liquid wetting of the pipe wall and therefore has an impact on the pressure drop and the in-situ phase fractions. In this thesis, the effect of changing pipe wall material in two- and three-phase flow has been investigated as well as ways to relate this sensitivity to measurements of contact angles.

1.3 Definitions

In this dissertation, the notions of condensate, wet gas pipeline, low liquid loading and liquid-to-gas ratio have been used. These terms are defined below.

- The word "condensate" is used in this thesis to refer to a liquid, hydrocarbon or water, in thermodynamic equilibrium with a gas.
- The expression "liquid-to-gas ratio" (LGR) is used for the ratio of the gas volumetric flow rate to the liquid volumetric flow rate at standard conditions of pressure and temperature (in m^3/Sm^3 or vol. %).
- It is called "wet gas pipeline", pipelines characterized by a LGR smaller or equal to 0.1%. Wet gas pipelines include gas transport trunk lines, gas gathering pipelines, gas field producing flowlines and distribution network pipelines. Wet-gas pipelines encompass a great diversity of pipeline systems as shown in Table 1–1: pipeline diameters can range from 0.1 to 1.0 m, pipeline lengths from 2 to 330 km, operational pressures from 20 to 140 barg and internal temperatures from 2 to 40 ^oC. In general, pipeline routes are chosen to achieve pipe inclinations smaller than +/- 1 deg. but in some regions, the seabed is uneven and larger slopes, up to +/- 15 deg. are current.
- The expression "low liquid loading" is used for volumetric flow rate conditions characterized by an input LGR smaller or equal to 1%. It can be seen from Table 1–1 that in-field gas pipelines have LGR well below this value. In reservoir engineering, gas field

production include retrograde gas, wet gas and dry gas reservoirs. From such reservoirs, the produced liquid-to-gas ratio is typically smaller than 0.2% according to McCain (1989). After processing and liquid removal, the gas LGR usually drops even further.

1.4 Organization of the dissertation

This dissertation is divided into nine chapters and five appendices. The content of each chapter is summarized below.

Chapter 1 Introduction. The background and scope of the thesis are defined.

Chapter 2 Literature review. This part reviews laboratory studies of stratified gas-liquid flow and stratified gas-oil-water flow with focus on gas dominated flows.

Chapter 3 Modelling. Steady, one-dimensional models for stratified gas-liquid and gas-oil-water flow are reviewed. Specific models for gas-liquid flow at low liquid loading and three-layer gas-oil-water flow models are derived, including hydraulic models and friction laws.

Chapter 4 Flow facility. The multiphase flow loop used in this thesis is relatively new and has not been previously described. This chapter contains a detailed description of the infrastructure, instrumentation and data acquisition together with characterizations of the test sections and an evaluation of the measuring accuracy.

Chapter 5 Gas flow with wet walls. This is a chapter devoted to transient film thinning experiments conducted to investigate the frictional pressure drop in presence of liquid films or droplets at the wall.

Chapter 6 Two-phase gas-liquid flow at low liquid loading. Steady-state two-phase gas-liquid flow experiments at low liquid loading are described. The data is presented in form of plots of pressure drop and holdup versus operational conditions. The two-phase measurements are compared with predictions from one-dimensional models.

Chapter 7 Three-phase gas-oil-water flow at low liquid loading. Three-phase gas-oil-water flow experiments are described, as a continuation of the two-phase gas-liquid experiments described in Chapter 6. Phenomena related to the presence of water and the influence of wall material are discussed. The data is compared to predictions from one-dimensional three-layer models and the multiphase pipe flow simulator PETRA.

Chapter 8 A three-layer model with curved interfaces. A three-layer model is derived to include the prediction of gas-liquid and oil-water interfacial curvature. The model is tested against some of the three-phase experimental data acquired in Chapter 7.

Chapter 9 Conclusions. This final chapter summarizes the thesis and presents the final conclusions.

Appendix A Tabulated experimental data. The experimental measurements corresponding to Chapter 5, Chapter 6 and Chapter 7 are tabulated.

Appendix B Details of the flow facility. Additional information is given on the multiphase flow rig.

Appendix C Details of the Three-Circle model. Specific derivations related to the three-layer model described in Chapter 8 are given.

Appendix D Terms of the pressure drop and holdup equations. This appendix contains a stand-alone study of the relative importance of the contributions to the pressure drop and holdup for two-phase stratified flow data at low liquid loading.

Appendix E Test of two-phase gas-liquid flow models at low liquid loading on an experimental data bank. This is also a stand-alone study devoted to the comparison of two-phase flow model predictions with data from an experimental data bank composed of low and high pressure measurements at low liquid loading.

Table 1–1: Operational data for gas-condensate pipelines from the specialized literature

Source	Pipeline	i.d. (m)	length (km)	Liquids	P (bara)[a]	T (^oC)[a]	LGR (m^3/Sm^3)[b]
Furukawa et al. (1987)	export line	0.337	52	condensate	53	40	$10 \cdot 10^{-6}$
Oliemans (1987)	export lines	0.5-0.9	33-117	condensate	50-110	-	$3\text{-}390 \cdot 10^{-6}$
Baker et al. (1988)	export line	0.794	330	condensate	50-140	-	$6 \cdot 10^{-6}$
	export line	0.692	138	condensate /water/ methanol	70-120	-	$30 \cdot 10^{-6}$
	export line	0.438	48	condensate	75-100	-	$85 \cdot 10^{-6}$
Adewuni et al. (1989)	flowline	0.146	16	condensate /water	21	38	-
Fairhurst et al. (1997)	export line	0.743	50	condensate /water/ methanol	-	-	$38 \cdot 10^{-6}$ (condensate) $3 \cdot 10^{-6}$ (water)
Chen et al. (2000)	flowline	0.139	8	diesel/ water	128 (max)	-	$28 \cdot 10^{-6}$ (water)
Cochran et al. (2003)	flowline	0.254, 0.508, 0.610, 0.914	2-69	condensate /water/glycol+methanol	89 (arrival)	13	$28 \cdot 10^{-6}$ (condensate) $112 \cdot 10^{-6}$ (water)
Cochran et al. (2003)	flowline	0.305	92	condensate /water/ methanol	139 (arrival)	2	$11 \cdot 10^{-6}$ (condensate) $13 \cdot 10^{-6}$ (water)

a. Inlet conditions if not specified
b. At standard conditions of pressure and temperature (1 atm., 15 ^oC)

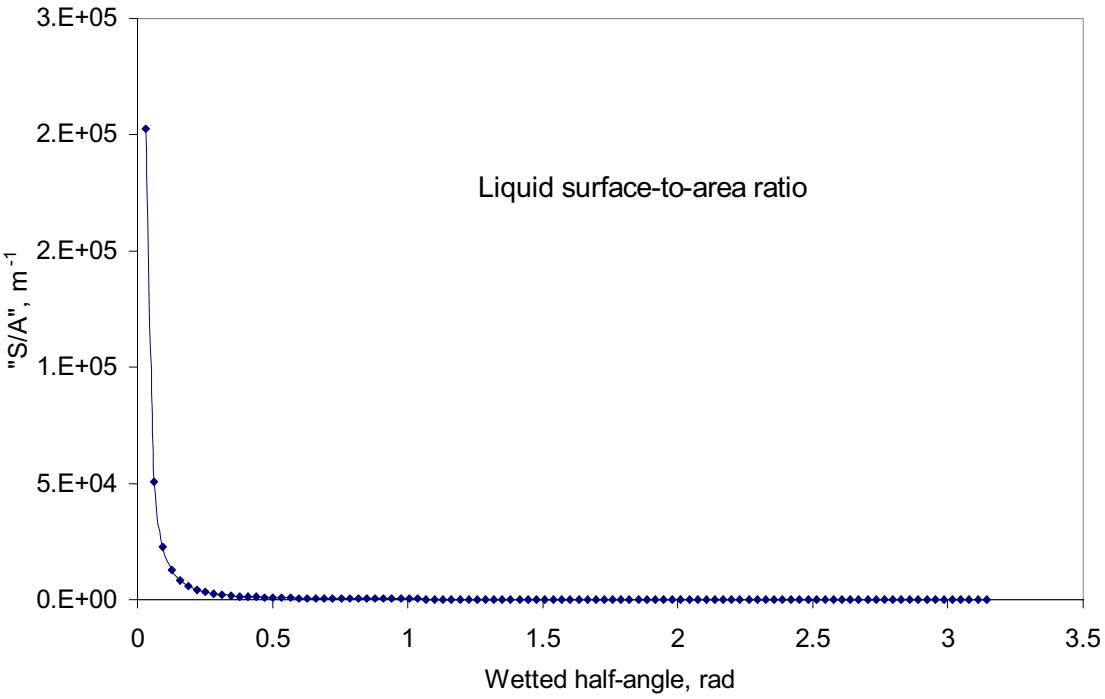

Figure 1–1: Surface-to-area ratio for the liquid phase versus the wetted half-angle. The gas-liquid interface is considered flat. The "surface" is the sum of the interfacial plus wall perimeters. The "area" is the portion of the pipe cross section occupied by the liquid. The computations are for a pipe of i.d. 0.06 m

Chapter 2 Literature review

2.1 Introduction

The literature reviewed in this chapter deals with gas-liquid and gas-oil-water flow, in horizontal and slightly inclined pipes. The review is restricted to gas dominated flows, at low liquid loading, for which the dominant flow regime is stratified flow but the transitions to slug flow and annular flow are also briefly explored. Such flow regimes are characteristic of gas-condensate pipe flow.

The literature review addresses only the hydrodynamical aspects of the flow and leaves aside the thermodynamical issues such as mass transfer or fluid properties. The details of the hydrodynamic models are dealt with in Chapter 3. The material of the review is taken from laboratory studies in the open literature. It particularly lays emphasis on the following aspects:

- The liquid holdup.
- The pressure drop.
- The liquid distribution: flow regimes, wall wetting, shape of the interface and droplets.
- The gas-liquid interactions: interfacial friction and waves.

The relevant literature has been searched within several media such as library, CD-ROM and on-line databases. Indicated below are the databases that contained the largest amount of information:

- The BIBSYS database (the university library system in Norway).
- CD-ROM databases: ISI, WebSPIRS, EI Compendex WEB, Petroleum Abstracts.
- The DIALOG on-line database which covers various sources such as US and European patents, Mc Graw Hill Publications, Fluidex, INSPEC, Chemical Abstracts and Mechanical Abstracts.

This chapter is organized in two main parts: two-phase gas-liquid flow is dealt with in Section 2.2 and three-phase gas-oil-water flow in Section 2.3. The most significant laboratory studies discussed in this chapter are summarized in Table 2–1 and Table 2–2, for two- and three-phase flow respectively.

2.2 Two-phase gas-liquid flow

2.2.1 Flow regimes

It is acknowledged that, despite the low liquid loadings, several gas-liquid flow regimes can be encountered in gas-condensate pipelines. According to Oliemans (1987), the most current flow regimes are:

- Stratified (smooth and wavy) flow.
- Annular dispersed flow.
- Slug flow.

The occurrence of flow regimes depends essentially on flow rates and local pipe inclination. Holdup can increase up to 40% or more for a few degrees upward inclination as mentioned in Meng et al. (1999) and Grolman (1994). This increases the chance for slug flow to occur. The gas flow rate at which liquid is continuously carried out of the pipeline is an important operating limit which defines the minimum gas flow rate for gas pipe steady production. Gas velocities may however occasionally fall under this limit causing liquid accumulation and possibly terrain induced slugging.

Usually, stratified flow (with or without droplets) and annular flow (for sufficiently high gas velocities and higher liquid flow rates) are the most frequent (and desired) flow regimes in gas-condensate pipelines. Badie et al. (2001) have illustrated with an axial viewing technique, two important features of the gas-liquid stratified flow regime at low liquid loading:

- The bulk of the liquid flows as a film at the pipe bottom. The film can be smooth or traversed by interfacial waves and exhibit a flat or concave curvature.
- There is significant droplet entrainment at high gas velocity. There can be partial or total wetting of the pipe circumference due to the entrained droplets re-depositing on the pipe wall.

Chen et al. (1997) distinguish between four gas-liquid interfacial structures as gas superficial velocity increases at constant liquid superficial velocity:

- Smooth interface.
- Two-dimensional (2D sinusoidal) interfacial waves.
- Three-dimensional (3D) interfacial waves.
- Large amplitude disturbance waves, also called roll waves.

At high enough gas velocity, annular flow occurs. Annular flow is characterized by a continuous wetting of the entire pipe periphery. Meng et al. (1999) and Badie et al. (2000) distinguish between:

- Annular flow with a slow moving liquid film on the upper pipe wall and a fast moving lower film with large amplitude waves. This annular flow is very asymmetric and can also be considered as a stratified/atomization flow.

- Annular flow with a liquid film that spreads around the whole pipe circumference and is traversed by large amplitude ring-shaped waves. This flow regime occurs at higher liquid flow rate and generates high pressure gradients.

2.2.2 Liquid holdup

From the literature, the following general trends can be drawn concerning the liquid holdup in stratified gas-liquid flow at low liquid loading:

- The liquid holdup increases with increasing liquid flow rate at constant gas flow rate in a less than linear way (Badie et al. 2000, Figure 2–1). A special case is reported by Meng et al. (1999) for air-oil horizontal flow at superficial gas velocity 25 m/s for which the liquid holdup decreased with increasing superficial liquid velocity. According to the authors, this is due to a more intense droplet generation.

- Liquid holdup strongly increases with decreasing gas flow rate at constant liquid flow rate as shown from measurements by Meng et al. (1999), Badie et al. (2000) and Olive et al. (2001). Liquid holdup reaches an almost constant asymptotic value at high gas flow rate as more liquid is entrained as droplets (Nuland et al. 1993, Badie et al. 2000). For one degree downward air-water flow, Olive et al. (2001) report an initial holdup increase when superficial gas velocity increases from 10 to 15 m/s. The reason invoked is that liquid-wall friction first increases in greater proportion than interfacial friction due to a large liquid spread around the wall circumference.

- Liquid holdup is sensitive to fluid properties, due in particular to the fluid ability to wet the pipe material. Badie et al. (2000) report higher holdup with oil than water as shown in Figure 2–1. This is not only due to the higher oil viscosity but also to the higher tendency of oil to wet the lateral and upper pipe walls.

- Liquid holdup is very sensitive to small upward inclinations. Grolman et al. (1997) report an eightfold increase of the total holdup with one degree upward inclination. Lunde et al. (1993) argue that, at low liquid loading, the necessary increase in gas velocity required to increase the drag at the gas-liquid interface requires a proportional higher increase of the liquid holdup than for systems with a higher liquid content. The holdup "heel" is thus more pronounced at small, rather than high, upward inclinations (Langsholt et al. 2001) and at low, rather than high, liquid loading.

2.2.3 Pressure drop

Chen et al. (1997), Meng et al. (1999), Badie et al. (2000) and Olive et al. (2001) all report that pressure drop continuously increases with liquid flow rate, starting from the "first drop" of liquid introduced in the pipe. This is illustrated by Badie et al. (2000) in Figure 2–2. The increase is all the sharper as the gas superficial velocity is high. As small amounts of liquid are introduced in the high velocity gas stream, an increasing portion of the pipe wall is replaced by a rough liquid interface. The degree of wall wetting, defined as the proportion of the pipe circumference covered by liquids, is considered to be of primary importance. With increasing gas flow rate, the pressure drop increases according to a law reminding of dry gas flow (proportional to the square rate of the gas flow rate) plus a magnification factor related to the liquid content in the pipe.

The pressure drop, as the liquid holdup, is sensitive to fluid properties. Badie et al. (2000) report a significantly higher pressure drop using oil instead of water (Figure 2–2) at otherwise identical conditions. The gas-oil interface is of a larger extent than the gas-water interface due to better wetting of the pipe wall by oil.

Olive et al. (2001) measured a pressure drop increase also at one degree downward pipe inclination. At low liquid loading, the static head contribution is generally too small to produce a significant pressure recovery in downward inclined pipes at high superficial gas velocity.

Smith et al. (1956) have conducted experiments in a three-inch “superfinished pipe” (the internal surface was honeyed and polished) and a standard rough four-inch seamless pipe at high gas Reynolds numbers. They report that, in presence of small amounts of condensate, the transmission factor, compared to dry gas flow, increases in the four-inch rough pipe at high Reynolds number but decreases at low Reynolds number. In the three-inch "superfinished" pipe, the transmission factor decreases in all cases. Measurements for the two cases are shown in Figure 2–3. Smith et al. (1956) argue that, in the rough pipe, the liquid film fills the valleys between the roughness peaks which reduces the apparent wall roughness. At lower gas Reynolds number, on the contrary, liquid drops and ripples coalesce and create an artificial roughness that increases the pressure drop. The same occurs at all Reynolds numbers in the three-inch "superfinished" pipe for which the surface is initially smooth.

2.2.4 High gas density

Gas density is high at normal gas pipeline operational pressure. Nuland et al. (1993) used Freon gas (density ten times that of methane) to approach this situation. They report new phenomena due to the high gas density.

Compared to low pressure gas, slug flow occurs at higher input liquid flow rates for a given gas flow rate. This is also observed by Wu et al. (1987). At the stratified-slug transition, high amplitude waves are formed with very aerated crests (Langsholt et al. 2001). Droplets are generated preventing the wave to evolve into long slugs. Wu et al. (1987) also

report that annular flow occurs at higher gas superficial velocity. As a result, the area of stable stratified flow is extended at high pressures.

At high gas flow rates, large amplitude interfacial waves are scarcer with dense gas and are more easily atomized. Waves may even disappear from the gas-liquid interface leaving only small scale film roughness with the bulk of the liquid flowing as a film at the pipe bottom and the rest as droplets. Langsholt et al. (2001) observed, at steep upward inclinations, droplet clouds shed at specific frequencies.

2.2.5 Wall wetting and shape of the gas-liquid interface

Hamersma et al. (1987), Hart et al. (1989), Grolman (1994), Chen et al. (1997) and Vlachos et al. (1999) have studied the shape of the gas-liquid interface in stratified flow but their observations differ, in part due to the different properties of the fluid and pipe materials used in their respective experiments. The interface is often described as either flat, concave or spread around the pipe circumference as a film of constant thickness. Representing the interface correctly is important for stratified flow modelling since the magnitude of the wall and interfacial shear forces depends on the interfacial perimeters.

At low liquid loading, the degree of liquid wall wetting reported is often incompatible with the representation of a liquid bulk flowing at the pipe bottom with a flat interface. For instance, Olive et al. (2001) report wetted wall fractions as high as 50% for a LGR as low as 0.03%.

There are, however, different interpretations on to which mechanism causes wall wetting. The most often invoked are:

- Droplet entrainment and deposition (Meng et al. 1999).
- Secondary flow in the gas phase (Flores et al. 1995).
- Conversion of the film kinetic energy into potential energy (Hart et al. 1989).
- Pumping actions due to disturbance waves (Chen et al. 1997).
- Surface tension (Brauner et al. 1998).

2.2.6 Droplet and bubble entrainment

Droplet generation is often reported in gas pipe flow at low liquid loading. Oliemans (1987) mentions significant droplet entrainment as the cause of model overestimation of field data holdup. For near horizontal flow, the droplet field presents a certain distribution, with a higher droplet concentration at the vicinity of the gas liquid interface (Nuland et al. 1993, Badie et al 2000).

Badie et al. (2001) have illustrated, with an axial viewing technique, the main mechanisms for droplet generation at low liquid loading:

• Intermittent bursting (Figure 2–4) and ballooning (Figure 2–5) of large amplitude waves producing a liquid filament that ruptures into droplets (primary mechanism).

• Ballooning and bursting of larger droplets (secondary mechanism).

Meng et al. (1999) report droplets only at conditions for which large amplitude waves are present at the interface. At gas superficial velocity near the point of droplet onset, few droplets reach the pipe wall. At higher gas velocity, more droplets hit the upper wall and form rivulets drained forward down in the flow direction. At even higher gas velocity, there is sufficient liquid at the wall to form a thin continuous film.

The consideration of droplet entrainment affects holdup predictions (Oliemans 1987) as droplet transport is a very effective way of moving liquids forward. Meng et al. (1999) and Badie et al. (2000) also consider droplet entrainment/deposition to be the primary mechanism for upper wall wetting which, in turn, increases holdup and pressure drop.

In addition to liquid exchange in the form of droplets, Meng et al. (1999) report significant aeration of the liquid layer. Gas bubbles are seen to penetrate two millimetres under the gas-liquid interface. Liquid layer aeration is also mentioned at high pressure (Nuland et al. 1993) and for experiments with formation fluids. Layer aeration can increase the interfacial friction, create viscous foams or induce drag reduction at the wall (Lunde et al. 1998).

2.2.7 Effect of added chemicals

2.2.7.1 Surface active agents

There are several effects of surfactants on gas-condensate flow reported in the literature with opposing effects on the pressure drop and liquid holdup, depending on the nature of the surfactant used.

Minami et al. (1983) observe that high concentrations of surfactant in water create a foamy mixture (high concentration of entrained air bubbles) at high gas superficial velocity. In that case, the liquid holdup is reduced due to the higher interfacial drag compared to the case without surfactant.

Hart et al. (1989) observe that pressure drop increases by 15% if the surface tension of the gas-liquid interface decreases by 50%. This is attributed to the promotion of interfacial waves and the resulting increase in apparent film roughness. No effect on holdup and wall wetting is reported.

Hand et al. (1992) have studied air-water and air-(water/surfactant) two-phase flow using a polymer surfactant. They report:

• An extension of the smooth stratified flow area. This is attributed to the damping of capillary ripples (interface stiffening) by the surfactant's molecular chain oriented

perpendicular to the interface. The holdup increases and the pressure drop decreases compared to no surfactant in this flow regime.

• The onset of atomization occurs at lower superficial gas velocity due to the weakening of surface tension. This is expected to result in premature wall wetting and increased pressure drop compared to the case with no surfactant.

• The surfactant has no effect in the well mixed regimes, in particular on roll wave initiation and frequency. This is due to the breaking of the polymer's molecular chain and loss of orientation.

2.2.7.2 Drag reducing agents

There are two types of drag reducing agents (DRAs) used in the oil and gas industry. DRAs for single phase liquid drag reduction are long chain molecules (usually polymers) that can absorb normal turbulent fluctuations near the wall and reduce the turbulent shear stress. DRAs for single phase gas flow are usually "film forming" molecules composed of a polar group at one end to bound to the inner pipe wall and a non-polar long chain at the other end. The product fills in roughness valleys and thus reduces the apparent wall roughness. Gas phase drag reduction is still a technique in its infancy. Some field trials are reported by Chen et al. (2000).

Al-Sarkhi et al. (2001) and Fernandes et al. (2003) measured the effect of liquid soluble DRA for liquid dominated gas-liquid flow. They show:

• An important effect of DRA on flow regimes. The stratified flow area is extended at the expense of slug and annular flow. In particular annular flow is changed into stratified flow with a smooth interface. In itself, this impact on flow regimes is the main cause of the pressure loss reduction observed in the presence of DRA.

• A significant pressure drop reduction in the stratified flow regime in presence of interfacial waves. DRA destroys the turbulence within disturbance waves that tend to disappear, with a resulting reduction in the interfacial drag and the amount of droplets generated. DRA is all the more effective as the turbulence level in the liquid is high as is the case at high liquid holdup and high liquid velocity.

2.2.8 Modelling

Gas pipe flow at low liquid loading can be seen as a regime halfway between dry gas flow and conventional gas-liquid flow. The traditional way of dealing with gas-liquid flow at low liquid loading has been to extrapolate from either one of these situations.

As evidenced in the previous paragraphs, gas-liquid pipe flows have complex hydrodynamics. Currently, there does not exist a "best" model that has sufficient generality to correctly predict integral flow properties for the broad range of situations encountered.

The modelling approaches in the literature can be grouped into:

- Modified one-phase models.
- Empirical two-phase models.
- Hydrodynamic (also called mechanistic) models.

The models considered hereafter are one-dimensional models for steady-state gas-liquid pipe flow with no consideration of mass exchange. This section is an introduction to Chapter 3 where some of the model equations are presented.

2.2.8.1 Modified single-phase models

The acknowledgement that small amounts of liquid in gas pipes considerably affect the transmission factor (Smith et al. 1956) has lead early investigators to modify single phase gas flow correlations by introducing an additional drag factor or an effective roughness. This approach is described in Gould et al. (1975) and Hope et al. (1977).

A major difficulty is to find an expression for the drag factor and effective roughness that encompasses the variety of fluid properties and flow regimes encountered in gas-condensate pipes. Asante et al. (1999) published charts of back-calculated drag factor and effective roughness from experimental data and field data acquired at LGR smaller than 0.004%. These are shown in Figure 2–6. Unfortunately, there does not seem to be a systematic relationship between drag factor, effective roughness and system variables.

Uhl (1975) questions the ability of such a modified single phase model to generate sound predictions of gas-liquid flow. If applicable, this approach is restricted to extremely small liquid loadings as suggested in Asante et al. (1999). In addition, it does not allow to trace the liquid holdup. Therefore a two-phase flow approach accounting specifically for the liquid phase is usually preferred.

2.2.8.2 Two-phase empirical models

Gregory et al. (1975), Minami et al. (1983), Baker et al. (1988) and Shea et al. (1997) have tested the accuracy of gas-liquid empirical models against field and laboratory data at low and high pressure. They show that empirical models are not to be recommended for wet gas pipe design due to, in particular, severe discrepancies between predictions and measurements in particular at high pressure. Shea et al. (1997) show that purely empiricial correlations over predict liquid holdup at high gas flow rates and under predict at low gas flow rates.

2.2.8.3 Two-phase mechanistic models

It can be distinguished between three classes of mechanistic models:

<u>Homogeneous models</u>

A homogeneous (no-slip) model is considered by Baker et al. (1988) in their comparative study with field data. Although it performs well in cases of high gas velocities and very

low liquid loading for which gas and liquid are well mixed, it results in severe discrepancies at lower gas velocities.

Drift-flux models

Drift-flux modelling consists in considering conservation equations for the gas-liquid mixture and introducing closure relationships to characterize the phase slip. From the analysis of high pressure data, Danielson (2003) reports that gas-liquid flow data at low liquid loading can not be represented by drift-flux relationships of the type used for liquid dominated flows. This modelling approach is therefore not considered appropriate for the modelling of gas-liquid pipe flow at low liquid loading.

Two-fluid models

Two-fluid models account for separate mass and momentum conservation equations for each phase.

Specific two-fluid models have been derived for the case of gas-liquid pipe flow at low liquid loading. The models are those of Oliemans (1987), Hamersma et al. (1987), Hart et al. (1989) (ARS model), Grolman et al. (1997) (MARS model), Chen et al. (1997) and Meng et al. (1999) (Double Circle model). Except for the ARS model, they are all based on the formulation of separate mass and momentum balance equations for each phase. The ARS model uses a correlation for the liquid holdup prediction and a composite gas friction factor equal to the sum of a wall term and a gas-liquid interfacial term.

The models differ in the treatment of the interfacial curvature and the friction closure laws. Hamersma et al. (1987), Hart et al (1989) and Grolman (1994) developed a correlation for liquid wall wetting. The correlation by Hart et al. has been compared successfully to experimental measurements by Chen et al. (1997), Meng et al. (1999) and Spedding et al. (1997). The models by Oliemans (1987), Grolman et al. (1997) and Meng et al. (1999) also include the influence of pipe inclination. Only Meng et al. (1999) consider liquid entrainment in the gas core.

Other stratified two-fluid flow models exist in the literature that can also be used for gas-condensate flow predictions. For stratified flow without droplet entrainment the most notable are those by Taitel et al. (1976), Espedal (1998) and Biberg (1998, 1999).

Minami et al. (1983) and Baker et al. (1988) have tested Taitel et al.'s model (1976) on their data, revealing severe holdup over predictions at low liquid loading and low gas flow rate. Badie et al. (2000) have tested the ARS and Double Circle models against their horizontal data. They show that neither model can scale the effect of high oil viscosity and oil spreading. In particular, pressure drop with oil is under predicted.

2.3 Three-phase gas-oil-water flow

In this section, gas-oil-water pipe flow literature is reviewed with gas and liquid flowing in the stratified and stratified/atomization flow regimes. The hydrodynamics borrow features from both two-phase gas-liquid and two-phase oil-water pipe flow.

2.3.1 Flow regimes

2.3.1.1 Classification and map

Acikgöz et al. (1992) and Pan (1996) suggest a classification of three-phase flow regimes based on visual observations in transparent pipes. The flow regime is identified in three sequences: 1) stratified or dispersed liquid, 2) oil or water continuous liquid, 3) gas-liquid flow pattern. In practice, the flow regime maps must be three-dimensional: gas, water and oil superficial velocities or combinations of these three variables must be plotted on independent axes. An example of a three-phase flow map given by Lahey et al. (1992) is reproduced in Figure 2–7.

2.3.1.2 Effect of superficial gas velocity on flow regimes

Sobocinski et al. (1958) describes the effect of increasing gas superficial velocity in a three-phase horizontal flow. At low gas velocity, the gas-liquid and oil-water interfaces are smooth. At higher gas velocity, capillary ripples form at the gas-oil interface. The oil-water slip velocity (oil velocity minus water velocity) increases but the oil-water interface remains undisturbed. At a certain gas velocity, large amplitude waves start to appear at the gas-oil interface causing disturbances at the oil-water interface and incipient emulsification of the liquid layer. Lunde et al. (1993) also observe water droplets being generated by shear instability of the oil-water interface as intermittent structures at the gas-liquid interface pass by.

At high gas velocity, water and condensate can form dispersions as mentioned in Sobocinski et al. (1958), Nuland et al. (1991) and Lunde et al. (1993). At low velocities, oil and water generally flow in two separate layers. The conditions at which dispersions form is very fluid dependent and not understood. The dispersion is usually unstable and separates rapidly. Its equivalent viscosity is generally higher than that of pure condensate or water. The water-in-oil type is the most current according to Sobocinski et al. (1958) and can exhibit a non-newtonian behaviour. When a dispersion is formed, the gas-liquid interface is unstable and some peculiar steep waves are triggered that make the gas-liquid interface very rough (Nuland et al. 1991).

2.3.1.3 Effect of superficial liquid velocity on flow regimes

Sobocinski et al. (1958) report that when increasing the superficial liquid velocity, the interfacial disturbances are triggered at lower superficial gas velocity due to the higher local

gas velocity. On the contrary, at high pressure, Elseth et al. (2003) observe a reduction of the slug flow pattern area at increasing superficial liquid velocity.

2.3.1.4 Effect of water fraction on flow regimes

Lee et al. (1993) have studied the effect of oil viscosity and water fraction on flow regime transitions. They observe that, compared to pure oil-gas flow, increasing the water fraction delays the transition to slug flow: slug flow appears at higher liquid superficial velocity at constant gas superficial velocity. Lunde at al. (1993) also observe that the presence of a free water layer can stabilize the gas-liquid interface by damping the turbulence in the disturbance waves. In three-phase flow, the transition to annular flow occurs at lower gas superficial velocity compared to two-phase flow. At intermediate water fractions, the area of the roll wave flow pattern tends to be larger at the expense of the regular wavy flow pattern. This is observed by Cai et al (1999) and Langsholt et al. (2001) in large diameter, high-pressure pipes.

2.3.2 Phase fractions

Compared to two-phase gas-liquid flow, the three-phase gas-oil-water phase fractions exhibit an additional sensitivity to input water fraction.

2.3.2.1 Total liquid holdup

In horizontal or slightly inclined pipes, Pan (1996) observed a clear liquid holdup peak close to the oil-water phase inversion point. This is shown in Figure 2–9 at 0 barg pressure and Figure 2–10 at 5 barg pressure. According to Pan, the holdup increase is due to a higher equivalent liquid viscosity close to phase inversion. In two-phase oil-water flow, phase inversion is defined as the passage from oil continuous to water continuous flow. Pan reports that the holdup peak slightly moves towards higher water fractions with increasing gas velocities. The experiments of Pan are performed at relatively high liquid content, thus at higher liquid content than gas-condensate pipelines.

Utvik et al. (1998) have carried out experiments in horizontal pipes at smaller liquid flow rates with formation fluids. Compared to Pan (1996), the holdup measured appears almost independent of water fraction as shown in Figure 2–11.

2.3.2.2 Oil and water holdup, phase slip

From Pan's Figure 2–9, it can be observed that the oil holdup often decreases at the passage from oil to water continuous flow. This is because oil, substracted from its contact with the pipe bottom, is better transported in dispersed form in the continuous water layer. It can also be seen that the water holdup first decreases then increases. At first, water transport is enhanced because water is in direct contact with the gas dragging force. At higher water fraction, this is balanced by the increasing wall drag which causes a water holdup increase.

In near horizontal pipes, the oil phase is in direct contact with the dragging gas. In addition, it runs on a moving water phase which reduces the oil-wall contact perimeter. As a result, the in-situ water-to-oil holdup ratio is usually higher that the input ratio, denoting a positive oil-water slip velocity and water accumulation, as shown in Sobocinski et al. (1958). At high superficial gas velocities, the water and condensate are better mixed and the slip velocity approaches zero. Valle (1998) reports cases in the literature for which the average water velocity is larger than the oil velocity.

2.3.2.3 Upward inclinations

A characteristic of gas-oil-water flow at upward inclinations is illustrated by Lunde et al. (1993) in Figure 2–12. It illustrates gravitational separation of water from oil in an inclined pipe due to the density difference between the two liquids. It usually results in a significant holdup increase in three-phase flow at equal liquid flowrate compared to two-phase gas-oil or gas-water flow.

The mechanism of phase separation is described in Lunde at al. (1993). Due to gravity, water separates from oil at low points, causing the hydrostatic pressure to increase. As a result, the gas needs to increase its velocity through a reduction of its cross section to increase the drag. The total liquid holdup therefore increases.

However, in case of little density difference between oil and water, gravity stratification does not result in a significant holdup increase since water is only replacing oil and the weight of the liquid column is less affected.

Elseth et al. (2003) observes that the holdup change is greatest in the range of inclinations between -1 and +1 degrees, after which, the holdup is less affected by a change of inclination.

2.3.3 Pressure drop

In near horizontal pipes, the three-phase pressure drop is sensitive to a change of the input water fraction. The pressure drop variations with water fraction are correlated to whether a liquid dispersion forms, or water and condensate flow in two continuous separate layers. It is acknowledged that dispersions, when formed, significantly increase the pressure drop in three-phase gas-oil-water pipes compared to two-phase gas-liquid flow.

Pan (1996) has conducted experiments at relatively high liquid loading so that liquid velocity is high and oil-water dispersions form. He observes a pressure drop peak at water fractions close to phase inversion, concomitant to the holdup peak. This can be seen in Figure 2–9. The peak magnitude increases with increasing gas velocity. Flow conditions are seen to oscillate between oil and water continuous close to the point of phase inversion resulting in oscillations of the pressure drop trace.

Sobocinski et al. (1958) also obtained a pressure drop maximum for water fractions around 60-70%, but identical pressure drop with pure water and pure oil. As in Pan's experiments, the pressure drop peak increases with increasing gas velocity. Sobocinski et al. (1958) observe that liquid dispersions offer an irregular gas-liquid interface that contributes to the pressure drop increase.

Lunde et al. (1993), Utvik et al. (1998) and Pettersen et al. (2001) have conducted three-phase gas-oil-water experiments at lower liquid loading than Pan (1996) and Sobocinski et al. (1958). They make consistent observations:

- When the flow regime in the liquid is water dispersed in a continuous oil phase, the pressure drop increases regularly with increasing water fraction up to a point where a free water phase forms. This appears from Utvik et al.'s experiments as shown in Figure 2–11. This behaviour is related to an increase of the apparent liquid viscosity with increasing volume fractions of the dispersed phase. The pressure drop peak usually shifts towards higher water fractions as superficial gas velocity increases. According to Langsholt et al. (2001), liquid turbulence is able to maintain a water-in-oil dispersion up to a higher input water fraction.

- When instead, a free water film forms at the pipe bottom (this occurs at lower gas velocities or at high water fractions), the pressure drop is less sensitive to water fraction and keeps values close to the two-phase gas-oil and gas-water pressure drop. Pettersen et al. (2001) and Utvik et al. (1998) observe that the pressure drop can reach a minimum at intermediate water fractions. This appears in Figure 2–11 and Figure 2–13.

2.3.4 High gas density

As in two-phase flow, it is reported a significant increase in the droplet generation (Lunde et al. 1993). The higher interfacial shear exerted by the dense gas also extends the area of stable stratified flow to higher liquid flow rates. Pan (1996) reports a decrease of the total liquid holdup at high pressure compared to atmospheric conditions. Elseth et al. (2003) show that the gas-liquid interface does not form a sharp density discontinuity. Instead, the local phase fractions vary gradually from liquid continuous to gas continuous. This denotes high levels of mutual phase transfer involving liquid phase aeration and droplet entrainment in the gas core.

2.3.5 Wall wetting and interfacial curvature

By numerical experimentation on a three-phase flow model, Hall (1992) shows that curving the oil-water interface from flat to concave results in better agreement with his experimental data.

Roberts (1996) performed measurements of chordal gamma densities from which the shape of the gas-oil and oil-water interface could be re-constituted. Obviously, the interface in his experiments is not flat with a tendency for the oil-water interface to be convex as shown in Figure 2–8. These results are not commented by Roberts.

2.3.6 Effect of added chemicals

Kang et al. (1998, 1999) and Tullius (2000) have studied the effect of DRAs in liquid dominated three-phase flow for which slug and dispersed bubble flow are the most probable flow regimes. They show that oil and water soluble DRAs are effective in reducing the pressure drop in stratified and slug flow as long as the liquid-liquid flow regime stays separated. At certain concentration, the DRA reduces the oil-water surface tension and a liquid dispersion forms. In the latter case, DRA efficiency can be negative (drag increase). DRA can also increase the area of stratified flow stability and reduce slug frequency. An associated but unexplored result is that DRA increases liquid wall wetting (Tullius 2000).

2.3.7 Material effect

At high LGR, Tullius (2000) compared measurements of pressure drop and phase fractions in acrylic and stainless steel pipes and did not observe any significant difference. On the contrary, Pettersen et al. (2001) measured pressure drop in slightly inclined pipes with SF_6 (high density gas), Exxsol D80 and water at moderate gas velocities and observed differences between steel and PVC pipes. An example measurement is shown in Figure 2–13. Steel gives higher pressure drop than PVC in three-phase flow but similar values in two-phase flow. The difference is less when the liquid loading is increased from 1% to 5%. Using a wetting probe, it can be shown that water flows dispersed in oil in the steel pipe and is not in contact with any part of the wall at superficial gas velocity equal to 4 m/s. In PVC, a free continuous water film forms at the pipe bottom at identical conditions of flow rates.

Angeli et al. (1998) have also studied the effect of pipe material in two-phase oil-water flow. In that case, the pressure gradient measured is higher in steel than acrylic (transpalite) for identical mixture velocities and volume fractions. The differences are highest at low mixture velocity where the two fluids are separated. The oil-water interface is shown to be more disturbed in steel. Angeli et al. (2000) also show with a local impedance probe that the stainless steel tube increases the tendency for oil and water to form dispersions.

Arney et al. (1996) have studied water lubrication of heavy viscous oil pipelines. They show that adhesion of oil to the pipe surface (fouling) can be reduced by increasing the water affinity of the pipe surface. One method is to add SiO_3^{2-} ions that increase the negative charge density of the electrical double layer at the steel pipe wall. Another option is a material that can be processed to form hydrophillic and oleophobic gels at the surface. Two such materials are sulphonated APS plastic that becomes durably water wet after immersion in water and mortar of Portland cement that naturally forms hydrophillic calcium silicate hydrate gels (C-S-H) while curing.

2.3.8 Modelling

The main difference between two and three-phase stratified gas-liquid flow lies in the fact that the simultaneous presence of two liquids gives rise to mutual interactions and results

in a wider variety of flow patterns. Models for three-phase gas-oil-water flow must account for the degree of mixing of the two-liquids (separated, mixing layer or fully dispersed), identify which phase is dispersed and which is continuous in case of dispersed liquid flow, and compute interfacial friction at the oil-water interface for separated flow or the equivalent liquid viscosity for dispersed flow.

There are currently two options for dealing with stratified gas-oil-water flow:

- Treat the oil and water as one liquid layer and use two-phase correlations or models.
- Use a mechanistic three-fluid model.

The first approach is adopted by Pan (1996). The liquid phase is represented as one equivalent liquid whose viscosity is calculated from an empirical mixing coefficient related to a three-phase Reynolds number. The method permits a straightforward use of two-phase flow equations for flow regime identification, pressure drop and holdup predictions. However it requires some empiricism and its generality can be questioned.

The second approach presents more complexity in forms of additional closure relationships but is also more rigorous. The mechanistic models applicable to stratified gas-oil-water flow found in the literature are based on:

- Drift-flux formulations as in Lahey et al. (1992).
- Three-fluid formulations (three-layer models) as in Hall (1992), Neogi et al. (1994), Taitel et al. (1995) and Khor et al. (1997).
- Combined two-fluid and drift-flux formulations (hereafter called "hybrid" models) as in Bonizzi et al. (2003).

2.3.8.1 Drift-flux model

Lahey et al. (1992) used phase fraction measurements to develop a drift-flux model for phase fractions. The standard drift-flux model is used for the gas phase but modified expressions are derived for the oil and water phases, with a distinction between oil continuous and water continuous flow. Drift-flux parameters (phase distribution parameter and drift velocity) are back-calculated from the experimental data. For water based separated flows (stratified and stratifying annular), the water drift velocity is always negative which hints at water accumulation. For oil based flows, it is interesting to note that the oil drift velocity approaches zero, meaning that water is not as well transported as oil in dispersed form.

2.3.8.2 Three-layer model

Three-layer models of steady stratified gas-oil-water flow are proposed by Hall (1992), Neogi et al. (1994) and Taitel et al. (1995). Khor et al. (1997) have performed numerical experiments where several combinations of closure laws (friction laws and hydraulic diameters) are tested against an experimental data bank.

Three-layer models are based on separate mass and momentum equations for the three phases (gas, oil and water) that are assumed to flow separated. They are direct generalizations to three fluids of the two-fluid separated flow one-dimensional steady-state pipe flow models. The various three-layer models in the literature assume separated phases and flat interfaces. They differ in the expression of the friction closures and the methods used for calculating the hydraulic diameters (especially for the oil phase). Details for the different models are given in Chapter 3.

2.3.8.3 "Hybrid" model

Bonizzi et al. (2003) have recently proposed a model initially developed for three-phase gas-oil-water slug flow but that also accounts for the stratified flow pattern within the bubble region. The approach combines separate momentum conservation equations for the gas and liquid phases (two-fluid approach) and an expression for the oil-water slip velocity (drift-flux approach). The determination of the latter is flow regime dependent and requires a closure for choosing between separated flow or dispersed flow. This closure is taken from Brauner et al. (2001). The model also includes a phase inversion model taken from Decarre et al. (1997) for the determination of the continuous phase in case of dispersed flow. Despite such simplification as a slip velocity assumed to be zero in the case of dispersed flow, the model yields good predictions in three-phase flow at LGR up to 12.5%. This approach also avoids the double looping on the liquid and water holdup equations inherent to three-fluid models and is therefore faster in terms of computations.

2.4 Summary

Literature of gas-liquid and gas-oil-water stratified pipe flow has been reviewed in this chapter. It has been emphasized on gas dominated flow at low liquid loading. In addition, the review has been restricted to a phenomenological description of the flow mechanisms based on laboratory studies and left aside the thermodynamical aspects of hydrocarbon mixture transport.

Two-phase gas-liquid flows at low liquid loading are characterized by:

- A significant fraction of the liquid transported as droplets and depositing at the wall.
- A high degree of liquid wall wetting and an often curved gas-liquid interface.
- Wavy, erratic gas-liquid interfacial structures and high interfacial friction at the gas-liquid film interface due to the high gas-liquid slip.
- A large surface-to-bulk ratio favouring the action of surface forces.

There is a lack of information concerning high pressure, two-phase flow in large diameter pipes at low liquid loading.

In three-phase gas-oil-water flow, additional complexity appears, related to liquid-liquid interactions within the liquid film. Three-phase gas-oil-water stratified flows are characterized by:

- Several, fluid dependent, liquid-liquid flow regimes.
- Water fraction dependent liquid holdup and pressure drop.
- Gravity separation of water and oil at positive inclinations.
- Potential formation of oil-water dispersions and phase inversion phenomenon.
- The curved shape of the fluid-fluid interfaces and the competitive wetting of the pipe wall by either one of the liquid phases depending on wall material.

Both pressure drop and holdup are influenced by these complex interactions within the liquid phase.

It is noticed a general lack of three-phase flow data at low liquid loading, both at low and high pressure.

As far as modelling is concerned, there appears to be few gas-oil-water flow models that encompass all phenomena occurring in the liquid phase: transition dispersed/separated, equivalent viscosity and phase inversion for dispersed flow, oil-water interfacial friction and surface effects (wall wetting and curvature of the interfaces) for separated flows. A complete flow model including more of these aspects as in Bonizzi et al. (2003) seems to be the key to improved prediction accuracy.

Table 2–1: Laboratory studies of two-phase, stratified, gas-liquid pipe flow at low liquid loading

Source	Measurement	Test Fluids	U_{SG} (m/s)	U_{SL} (m/s)	i.d. (m)	P (barg)	θ (deg.)	Purpose
Minami et al. (1983)	H	air-kerozene air-water	0.5-16.5	0.005-0.95	0.078 (PVC)	0	0	test holdup correlations
Hamersma et al. (1987)	H, dP/dx, δ	air-water/glycol	7-30	0.001-0.08	0.051 (copper)	0	0	new prediction model (ARS)
Hart et al. (1989)	H, dP/dx, δ	air-water/glycol/ Tween 80	5-30	0.00025-0.08	0.051 (copper)	0	0	improve ARS
Nuland et al. (1993)	H, dP/dx	Freon13B1- Exxsol D80	3-18	0.02-0.4	0.065 & 0.1 (PVC)	1,3,7,9	2,5,10	dense gas
Grolman (1994), Grolman et al. (1997)	H, dP/dx, δ	air-water air-tetradecane	2-34	<0.06	0.015, 0.026, 0.051 (glass)	0	-3 to +6	new prediction model (MARS)
Chen et al. (1997)	H, dP/dx, δ	air-kerozene	4-12	0.004-0.05	0.078 (steel)	0	0	new prediction model (Double Circle model)
Shea et al. (1997)	H	N_2-Naphta	0.5-12	0.005-0.1	0.189 (steel)	19, 89	+1	test holdup prediction models
Meng (1999), Meng et al. (1999)	H, dP/dx, film flow rate	air-Lubsnap 40	5-25	0.0015-0.053	0.051 (acrylic)	0	-2 to +2	improve Double Circle model
Asante et al. (1999)	H, dP/dx	air-light oil	15-30	0.0003-0.002	0.051 (acrylic)	0	0	low liquid loading
Badie et al. (2000), Badie et al. (2001)	H, dP/dx	air-water air-Tellus 22	15-25	0.0005-0.05	0.078 (steel)	0	0	test prediction models, axial viewing

Table 2–1: Laboratory studies of two-phase, stratified, gas-liquid pipe flow at low liquid loading

Source	Measurement	Test Fluids	U_{SG} (m/s)	U_{SL} (m/s)	i.d. (m)	P (barg)	θ (deg.)	Purpose
Olive et al. (2001)	H, dP/dx, film flow rate	air-water	5-25	0.0018-0.046	0.051 (acrylic)	0	-1	low liquid loading
Al- Sarkhi et al. (2001)	dP/dx	air-water/Percol 727	30-43	0.03-0.1	0.095 (acrylic)	0.03	0	effect of DRAs
Fernandes (2003)	dP/dx	methane-decane	2.5-18.9	0.01-0.7	0.019 (steel)	0	0	effect of DRAs

Table 2–2: Laboratory studies of three-phase, stratified, gas-oil-water pipe flow[a]

Source	Measurements	Test fluids	U_{SG} (m/s)	U_{SL} (m/s)	WF (%)	i.d. (m)	P (barg)	θ (deg.)	Purpose
Sobocinski et al. (1958)	H (QCV), dP/dx	air-gasoil (3.38 cp)-water	2.4-16.3	0.008-0.18	0-100	0.076 (plastic)	0	0	illustrate effect of water
Nuland et al. (1991)	H (QCV, gamma), dP/dx	air-Exxsol D80 (2 cp)-water	1-11	0.024-1.4	0-100	0.032	0	0	phase fraction measurement with gamma densitometer
Lahey et al. (1992)	H (QCV)	air-mineral oil (116 cp)-water	2.2-16.6	U_{SW}: 0.0036-0.6597 U_{SO}: 0.0024-0.2378	-	0.019 (acrylic)	0	0	develop drift-flux model for holdup predictions
Lunde et al. (1993)	H (QCV), dP/dx	Freon/SF_6-Exxsol D80 (2 cp)-water	2-6.3	0.016-0.25	0-100	0.100 (PVC)	1,3,7	+2, +15	combined effects of inclination and water
Pan (1996)	H (gamma), dP/dx	air-Tellus oil (40 cp)-water	0-25.9	U_{SO}: 0-0.565 U_{SW}: 0-0.615	0-100	0.078 (steel)	0,5,10	0, +1	test prediction models
Roberts (1996)	H (gamma), dP/dx	air-Tellus oil (40 cp)-water	1.1-9.8	U_{SO}: 0.018-0.104 U_{SW}: 0.015-0.204	-	0.078 (steel)	0.3-10.3	0	calibrate transient experiments
Utvik et al. (1998)	H (gamma, conductivity probes), dP/dx	field gas-crude oil-formation water (3.3% salt)	0.31-5.23	1.17	0-100	0.078 (steel)	105	0	effect of formation fluids

Table 2–2: Laboratory studies of three-phase, stratified, gas-oil-water pipe flow[a]

Source	Measurements	Test fluids	U_{SG} (m/s)	U_{SL} (m/s)	WF (%)	i.d. (m)	P (barg)	θ (deg.)	Purpose
Langsholt et al. (2001)	H (gamma), dP/dx	SF_6-Exxsol D80 (2cp) -tap water	0.3-8	0.05-0.1	1-30	0.1 (steel)	7	0 to +30	compare with OLGA
Pettersen et al. (2001)	dP/dx, water wetting (conductivity probe)	SF_6-Exxsol D80 (2cp) -water	2, 4	U_{SO}, U_{SW}: 0.0005-2	0-100	0.100 (steel and PVC)	7	+1, +5	effect of material on wall wetting
Elseth et al. (2003)	H (gamma), local phase distribution, dP/dx	recombined gas-recombined condensate-fresh water	0.3-8	0.15, 0.29	5	0.078 (duplex steel)	79	-6 to +10	compare with OLGA

a. Excluding mere flow regime studies

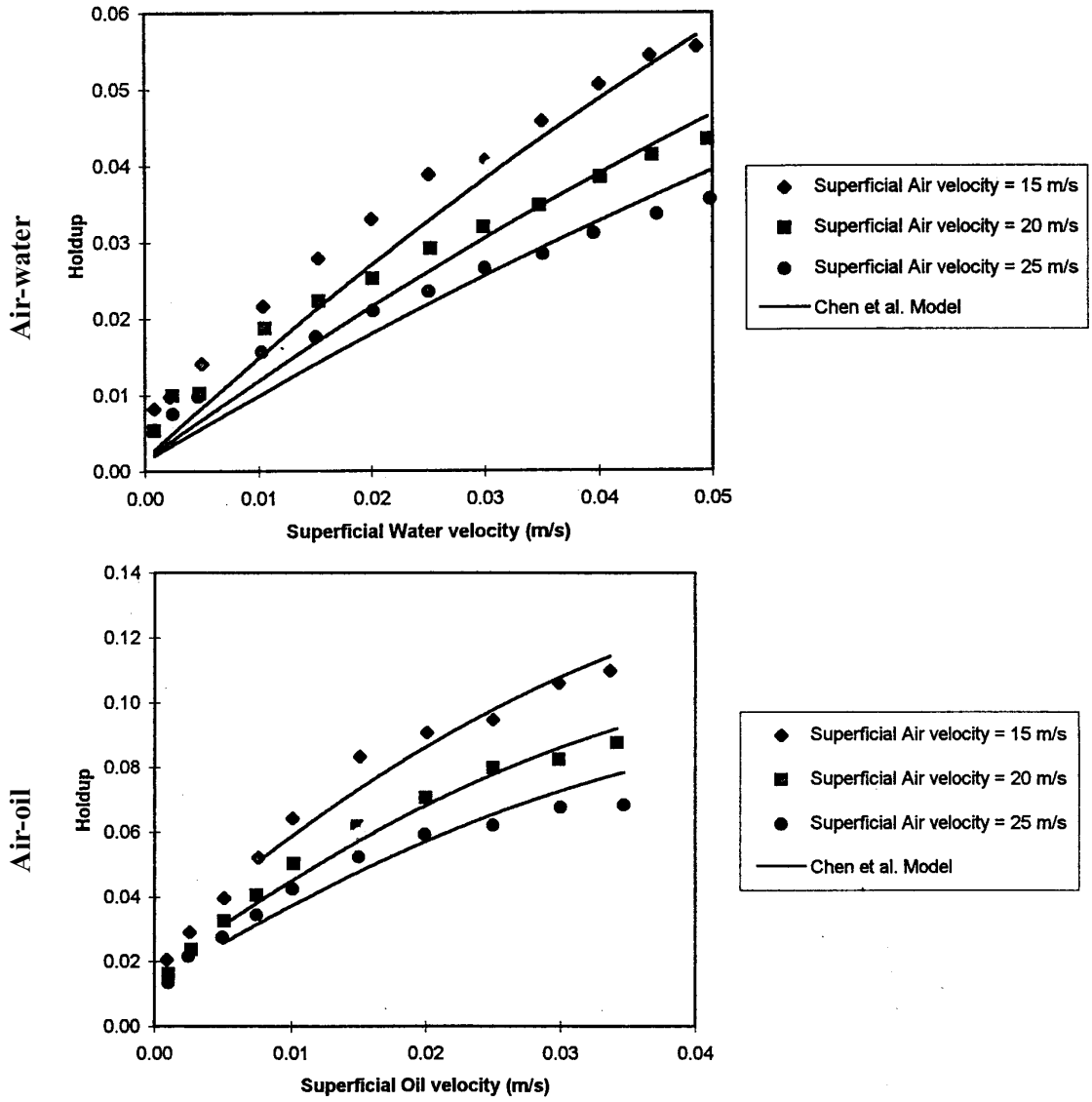

Figure 2–1: Liquid holdup versus liquid superficial velocity at constant gas superficial velocity in a horizontal pipe. Top: air-water; Bottom: air-oil (from Badie et al. 2000)

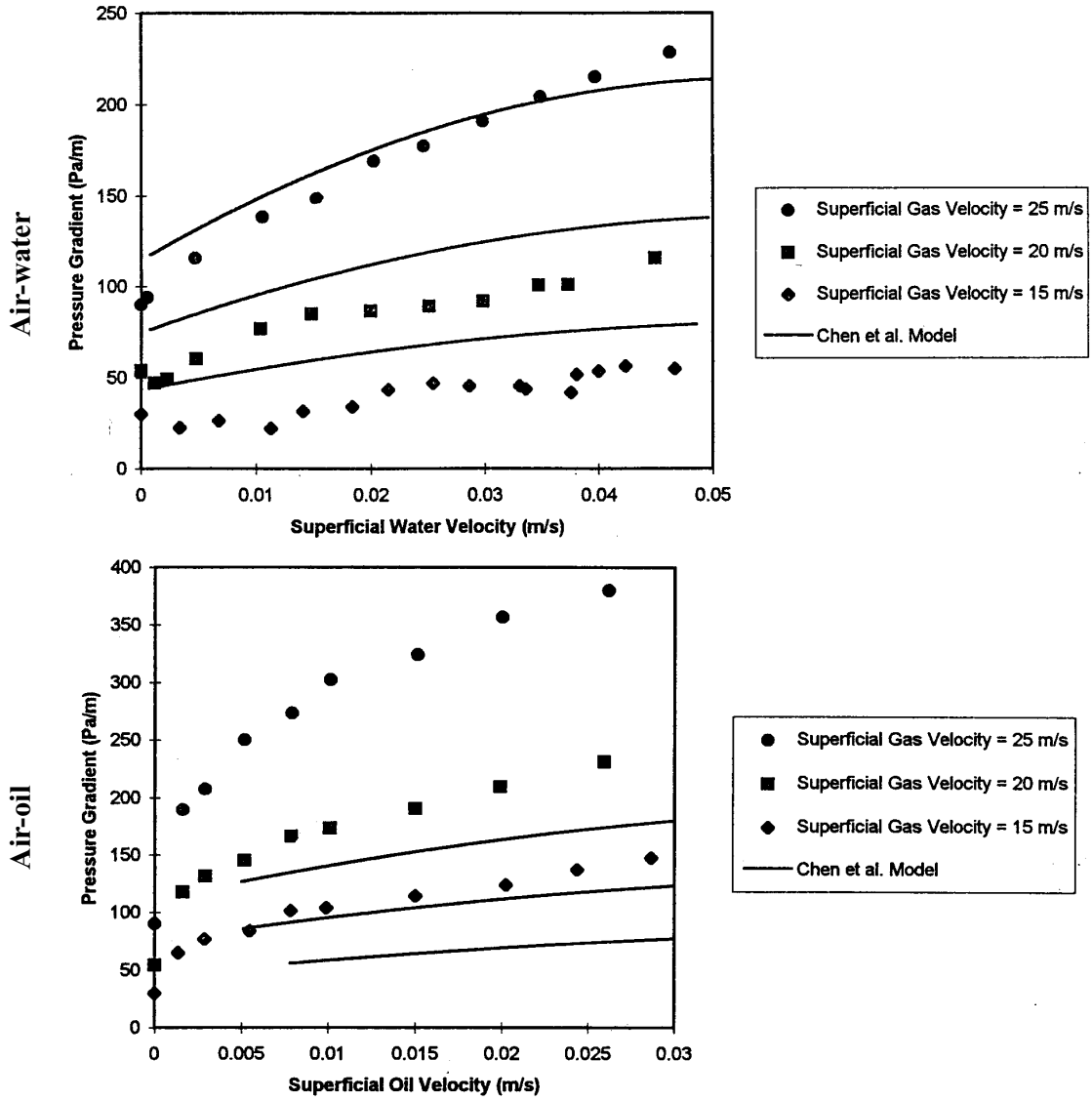

Figure 2–2: Pressure gradient versus liquid superficial velocity at constant gas superficial velocity in a horizontal pipe. Top: air-water; Bottom: air-oil (from Badie et al. 2000)

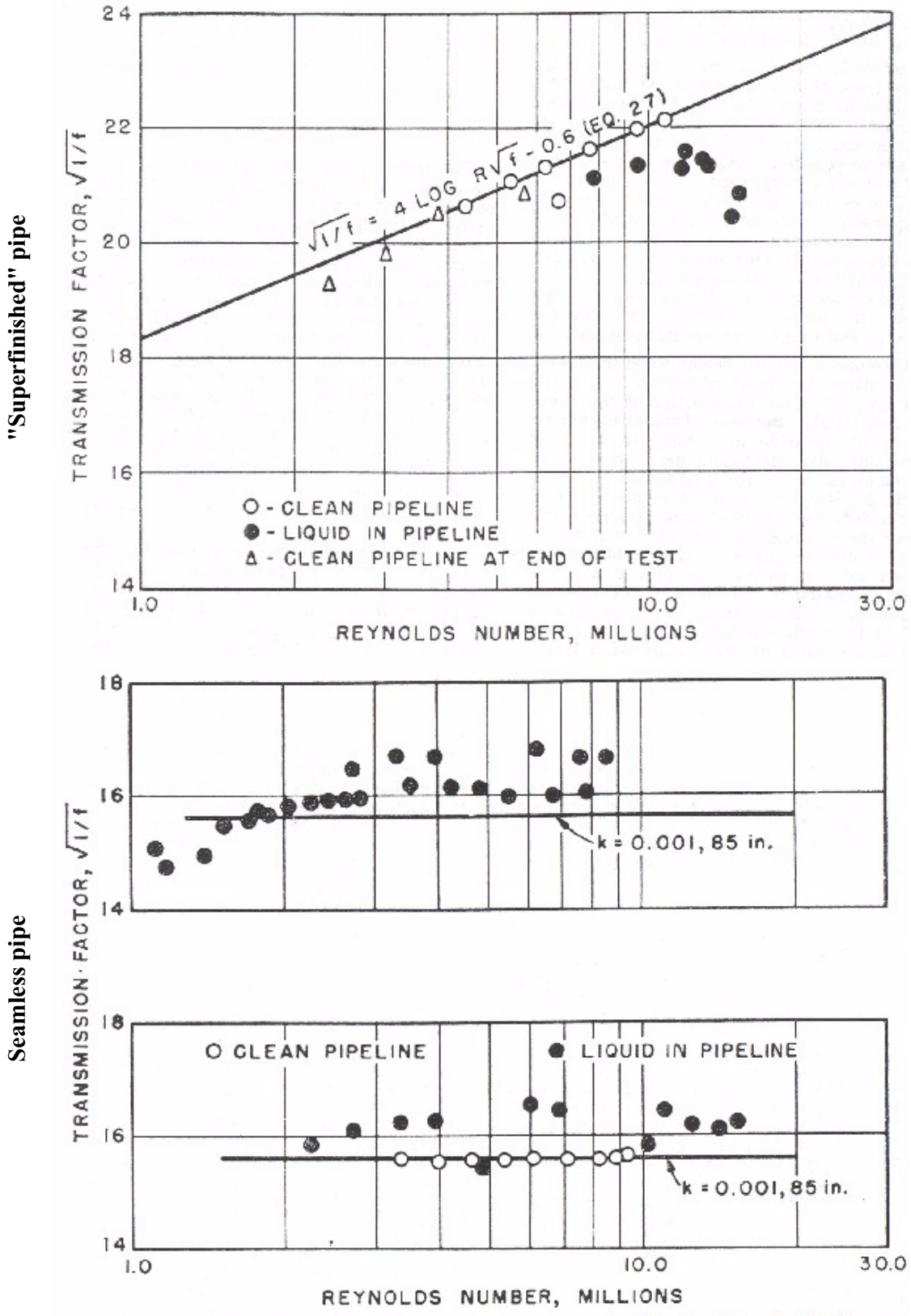

Figure 2–3: Measurement of the gas pipe transmission factor in presence of liquids. f is the Fanning gas-wall friction factor and k the hydraulic roughness. Top: "superfinished" (honeyed) 3 inch pipe. Bottom: seamless 4 inch pipe (from Smith et al. 1956)

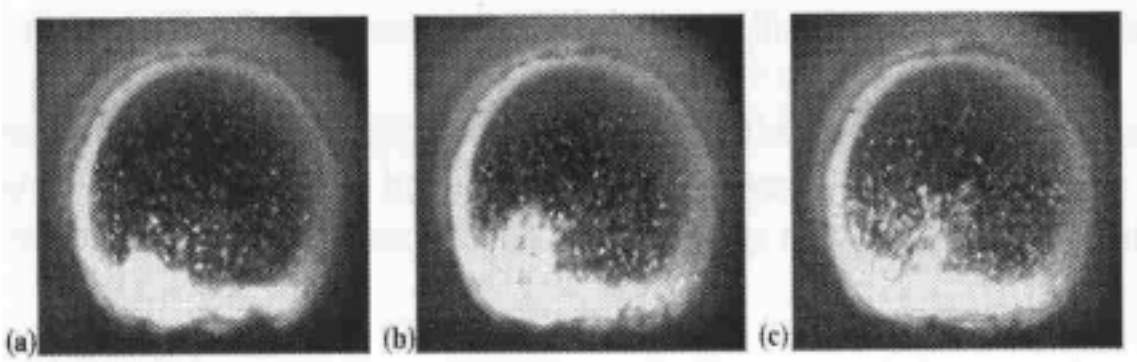

Figure 2–4: Successive frames for air-oil flow showing the bursting of a large amplitude wave into droplets (superficial gas velocity = 20 m/s, superficial liquid velocity = 0.02 m/s). (a) t = 0 s; (b) t = 0.005 s; (c) t = 0.010 s (from Badie et al. 2001)

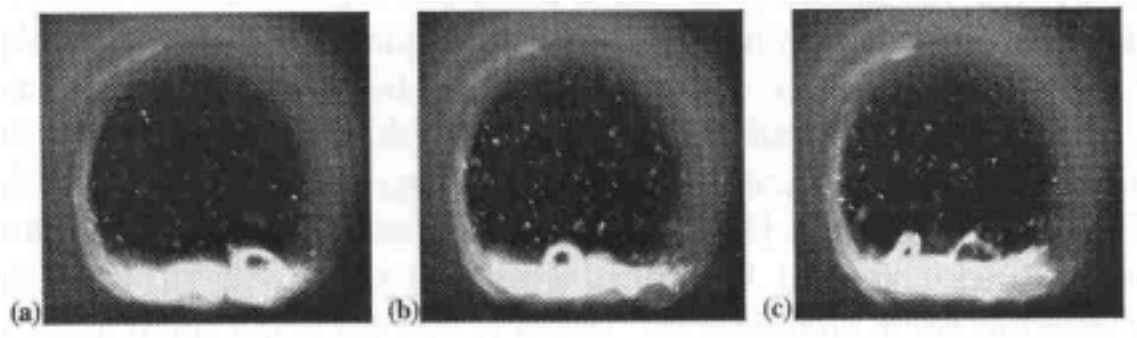

Figure 2–5: Successive frames for air-oil flow showing the ballooning of the liquid layer (superficial gas velocity = 15 m/s, superficial liquid velocity = 0.01 m/s). (a) t = 0.186 s; (b) t = 0.436 s; (c) t = 0.629 s (from Badie et al. 2001)

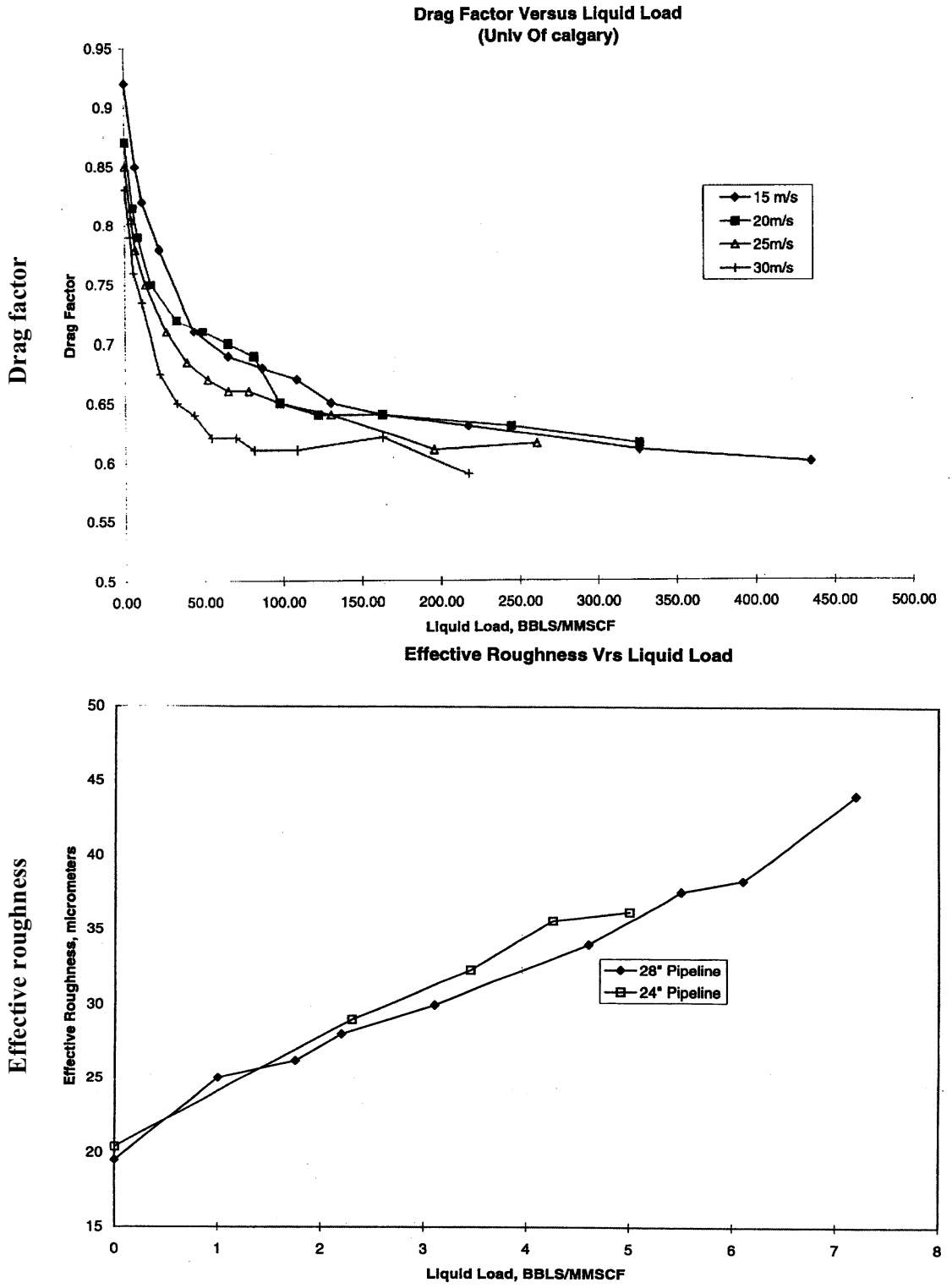

Figure 2–6: Modelling of gas-liquid flow at low liquid loading with a modified one-phase correlation. The liquid loading is expressed in barrels of liquid per million standard cubic feet of gas. Top: drag factor versus liquid loading; Bottom: effective roughness versus liquid loading (from Asante et al. 1999)

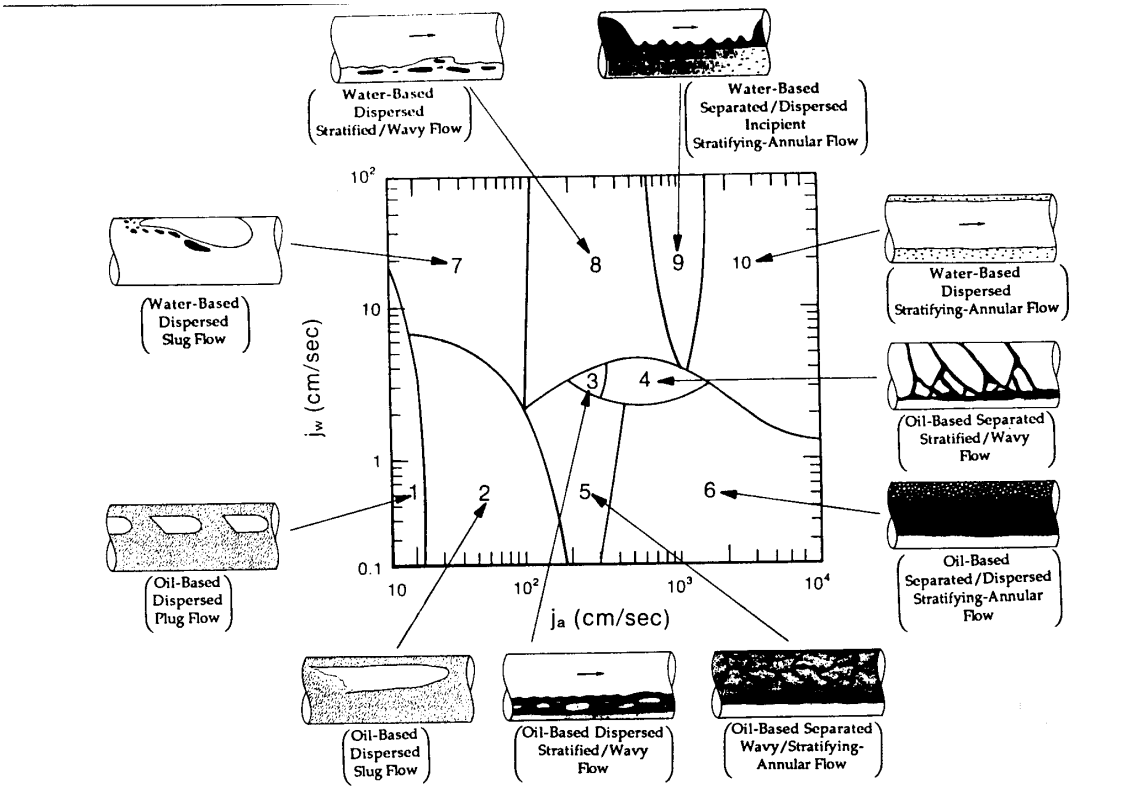

Figure 2–7: Three-phase flow regime map for horizontal air-oil-water flow. The map is for fixed oil superficial velocity. The flow map is plotted against superficial air velocity (j_a, in cm/s) and superficial water velocity (j_w, in cm/s) (from Lahey et al. 1992)

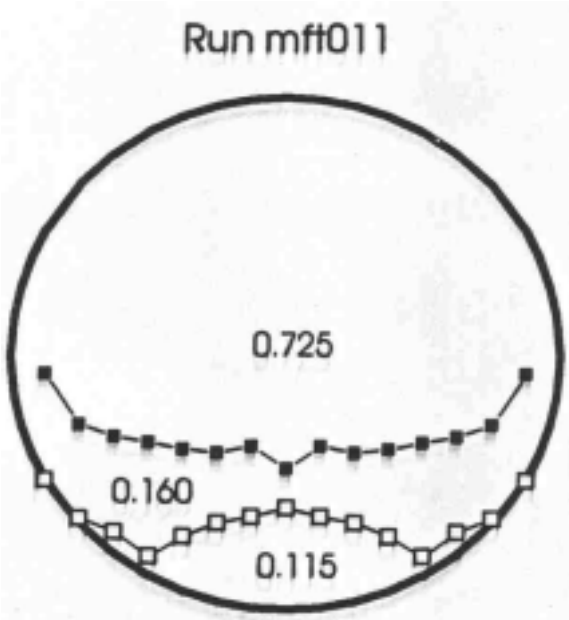

Figure 2–8: Interfacial profiles reconstructed from chordal density measurements with a dual energy gamma densitometer. Superficial gas velocity = 6.18 m/s, superficial oil velocity = 0.039 m/s and superficial water velocity = 0.041 m/s (from Roberts 1996)

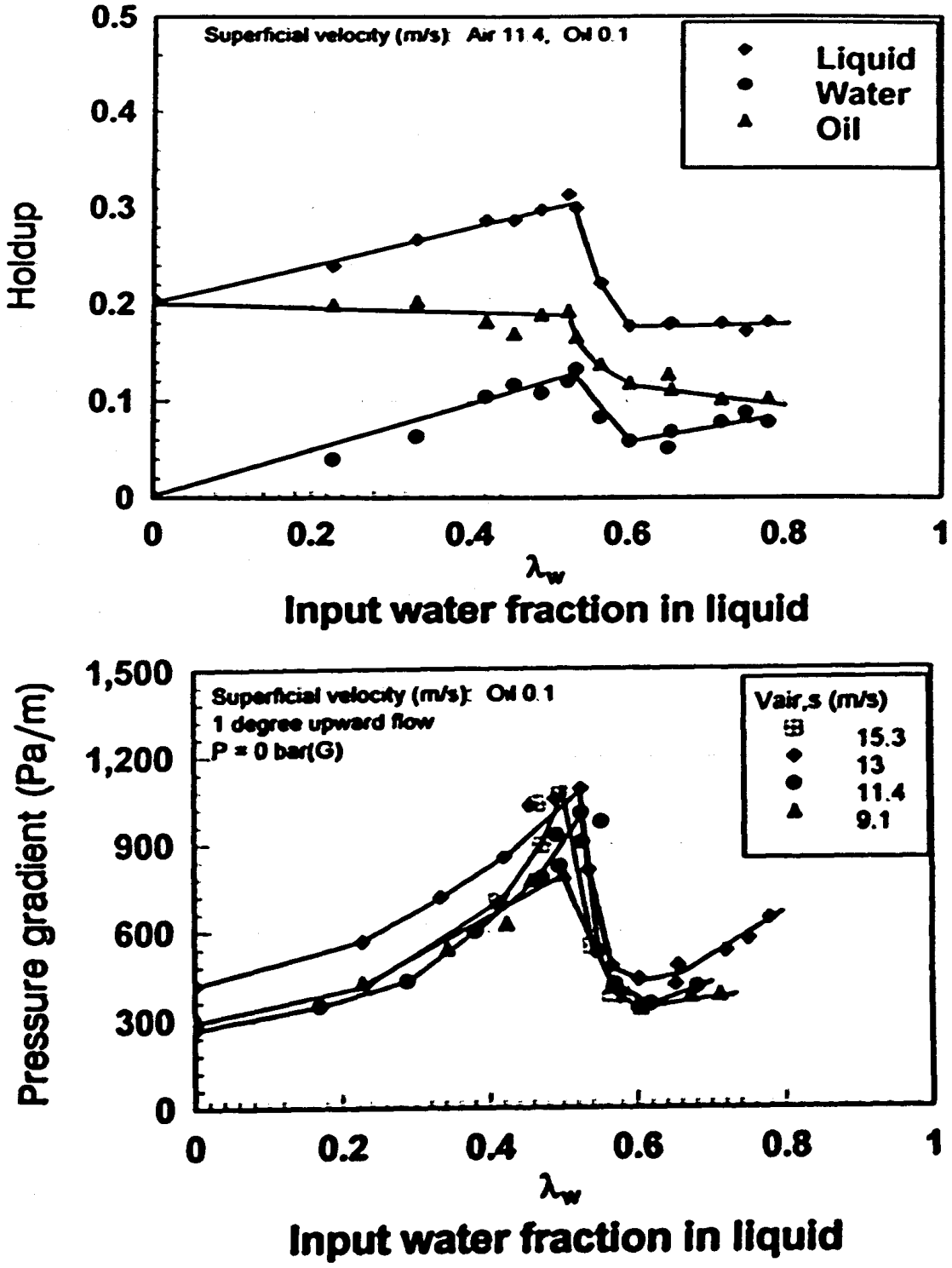

Figure 2–9: Total liquid holdup and pressure drop versus input water fraction for air-oil-water pipe flow at pressure = 0 barg. Air superficial velocity = 11.4 m/s, oil superficial velocity = 0.1 m/s and inclination = +1 deg. Oil viscosity = 40 cp (from Pan 1996)

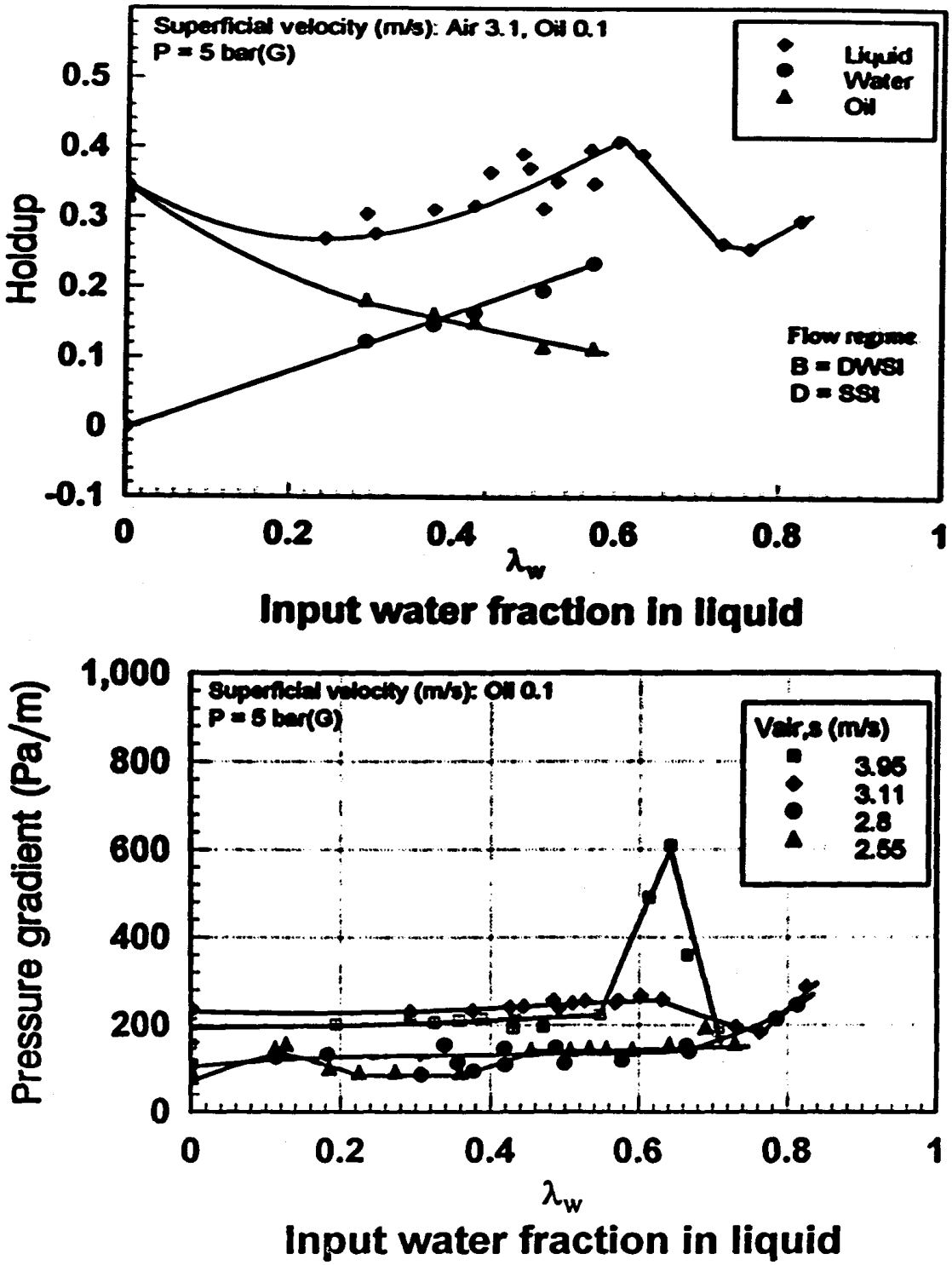

Figure 2–10: Total liquid holdup and pressure drop versus input water fraction for air-oil-water pipe flow at pressure = 5 barg. Air superficial velocity = 3.1 m/s, oil superficial velocity = 0.1 m/s and inclination = 0 deg. Oil viscosity = 40 cp (from Pan 1996)

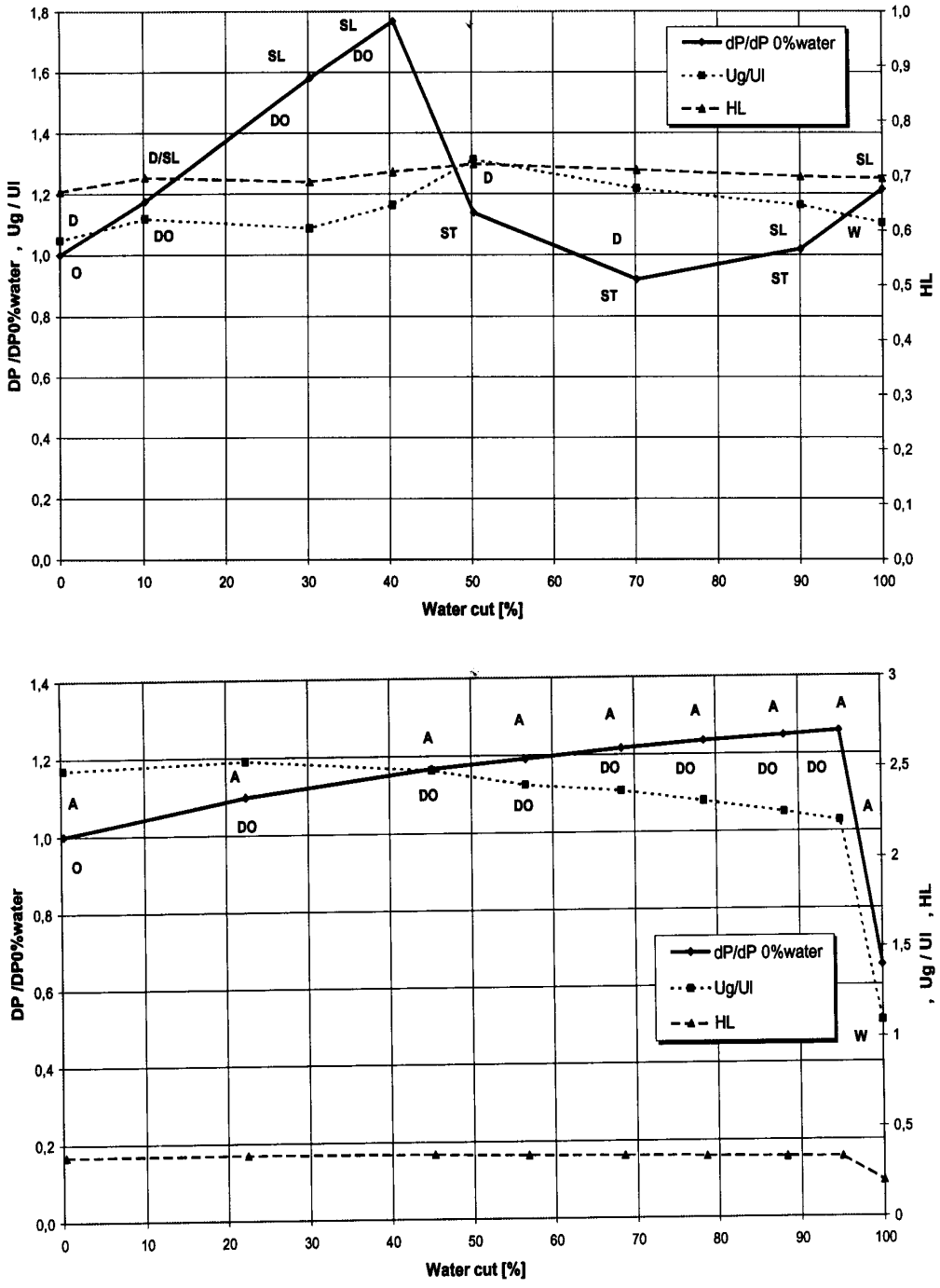

Figure 2–11: Pressure drop, flow pattern, gas-liquid slip and total liquid holdup in a three-phase gas-oil-water flow with formation fluids. Pressure = 105 barg, temperature = 70°C. The pressure drop is represented as a ratio of the measured pressure drop (DP) to the pressure drop measured in two-phase air-oil flow at the same flow rate conditions ($DP0\%_{water}$). Top: superficial gas velocity = 0.58 m/s and superficial liquid velocity = 1.17 m/s; Bottom: superficial gas velocity = 5.23 m/s and superficial liquid velocity = 1.17 m/s (from Utvik et al. 1998)

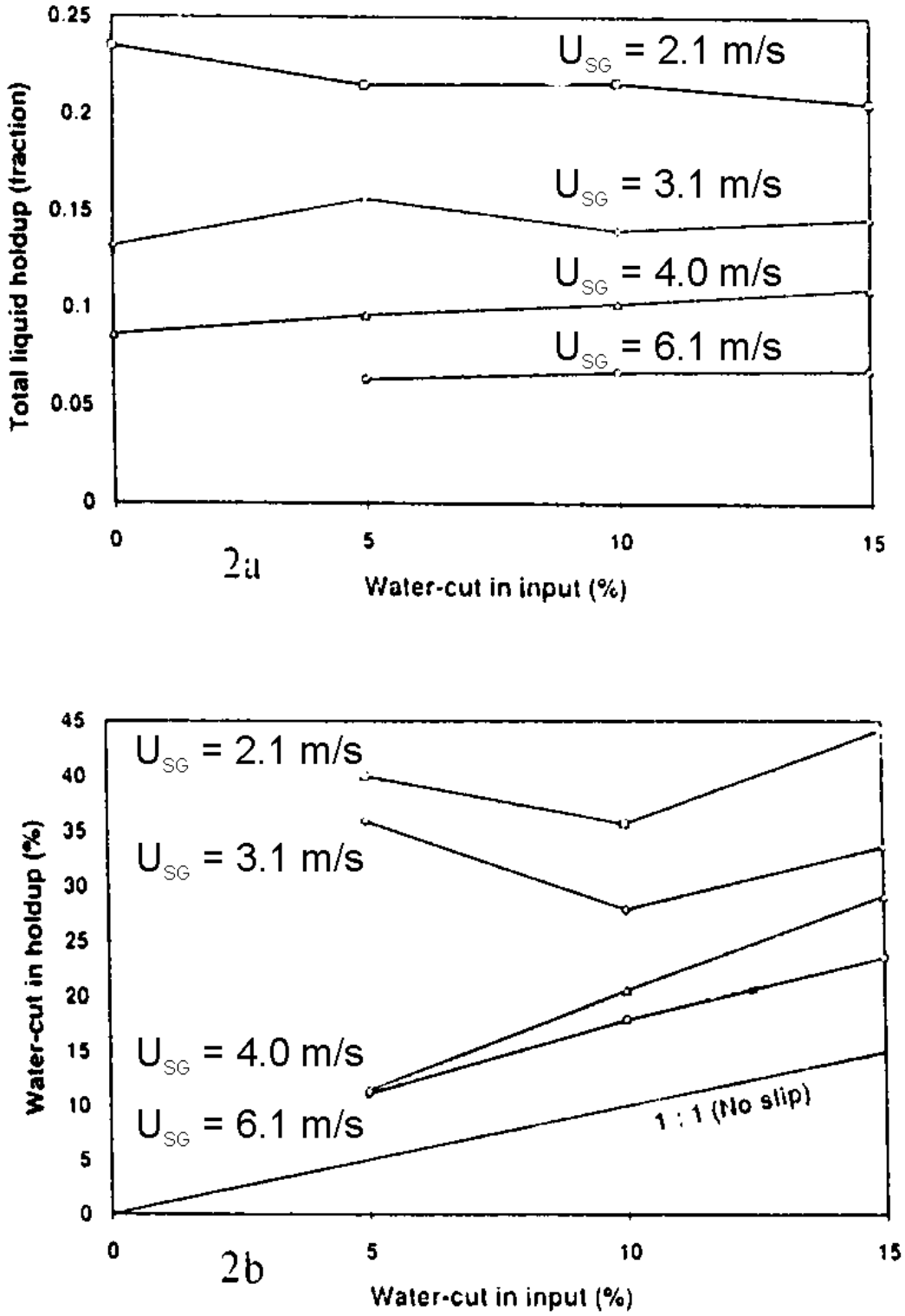

Figure 2–12: Liquid holdup and in-situ water fraction for Freon-Exxsol D80-water experiments at pressure = 8 bara and pipe inclination = +15 deg. (from Lunde et al. 1993)

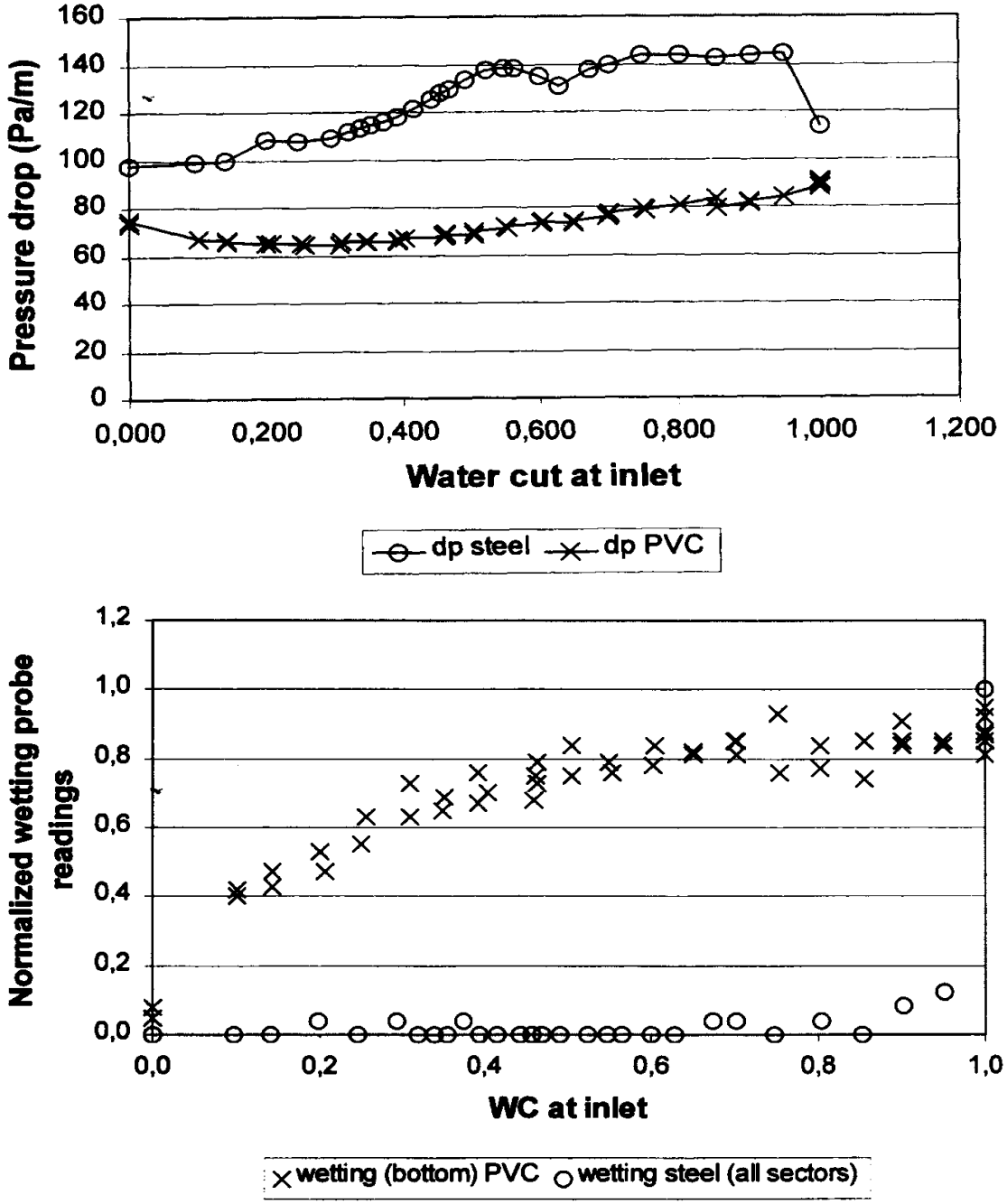

Figure 2–13: Measurements of pressure drop and wall wetting for two different pipe wall materials in SF6-Exxsol D80-water stratified flow. Pipe inclination = +1deg., superficial gas velocity = 4 m/s and LGR = 1%. The wetting probe sectors are normalized to yield 1.0 for water continuous flow (from Pettersen et al. 2001)

Chapter 3 Modelling

3.1 Introduction

In Chapter 2, literature dealing with gas-liquid pipe flow at low liquid loading has been reviewed with focus on a description of the flow mechanisms. In this chapter, current methods for predicting average integral steady flow properties are investigated. The models considered are based on the rigorous derivation of averaged, one-dimensional mass and momentum conservation equations for the phases involved, the so-called "two-fluid" and "three-layer" formulations. It is focused on the engineering type of predictions relevant for steady-state calculations in gas dominated pipelines.

After a brief review of single phase pipe flow in Section 3.2, stratified gas-liquid flow models are dealt with in Section 3.3. and stratified gas-oil-water flow models in Section 3.4.

3.2 Single phase flow

3.2.1 Gas momentum equation

Predictions of the pressure drop for steady flow of single phase gas are normally based on the one-dimensional averaged gas momentum equation given in Equation [3.1]:

$$0 = \frac{dP}{dx} + \rho_G g \sin\theta + \frac{\lambda_G}{8}\rho_G U_G^2 \frac{S}{A} + \frac{d}{dx}(\rho_G U_G^2) \qquad [3.1]$$

where

$$U_G = U_{SG} = Q_G / A \qquad [3.2]$$

Equation [3.2] expresses mass conservation. The pressure drop appears to be the sum of a gravity term, a gas-wall friction term and an acceleration term. The latter is small compared to the two others for fully developed flow and is usually neglected.

In the following, index k is used to designate a gas, a liquid or an interface.

Current practice is to express the wall shear stress in terms of a friction factor:

$$\tau_k = \frac{1}{8}\lambda_k \rho_k U_k^2 \qquad [3.3]$$

Friction factors are discussed in Section 3.2.2. In this dissertation, the Moody (Darcy) friction factor, λ_k, is normally preferred as opposed to the Fanning friction factor, f_k, defined by the relationship:

$$f_k = \frac{\lambda_k}{4} \qquad [3.4]$$

3.2.2 Friction factor

The friction factor for laminar, single phase flow is derived from an exact analytical solution of the velocity profile. It yields:

$$\lambda_k = \frac{64}{Re_k} \qquad [3.5]$$

Hereafter, Equation [3.5] is referred to as "Poiseuille's law".

For turbulent flow in smooth pipes, Blasius suggests:

$$\lambda_k = \frac{0.3164}{(Re_k)^{0.25}} \qquad [3.6]$$

This relation is known to be inaccurate at Reynolds number larger than 10^5. The empirical coefficients have been re-tuned to better agree with experimental pipe flow data. The modified Blasius equation is given in Equation [3.7]:

$$\lambda_k = \frac{0.184}{(Re_k)^{0.2}} \qquad [3.7]$$

Nikuradse (1933) shows good agreement between his smooth pipe flow measurements up to Reynolds number $3.4 \cdot 10^6$ and the following friction factor expression:

$$\lambda_k = \left(2\log\left(\frac{2.51}{Re_k\sqrt{\lambda_k}}\right)\right)^{-2} \qquad [3.8]$$

For turbulent fully rough pipe flow, Nikuradse (1933) suggests, based on experiments performed in artificially sanded pipes:

$$\lambda_k = \text{®}_{\text{TM}} 2\log \text{®}_{\text{TM}} \left(\frac{\varepsilon}{3.705D} \right)^{-2} \qquad [3.9]$$

Colebrook (1939) later derived a friction factor correlation for commercial steel pipes, known as the Colebrook's equation, that reduces to Equation [3.8] for hydraulically smooth pipes and Equation [3.9] for fully rough pipes:

$$\lambda_k = \text{®}_{\text{TM}} 2\log \text{®}_{\text{TM}} \left(\frac{2.51}{Re\sqrt{\lambda_k}} + \frac{\varepsilon}{3.7D} \right)^{-2} \qquad [3.10]$$

Colebrook claims that Equation [3.10] also agrees with experiments in the transition zone between the hydraulically smooth and fully rough regimes. The implicit Equation [3.10] was solved by Moody (1944) and the friction factor plotted against Reynolds number for various values of the hydraulic roughness.

For more computational convenience, Håland (1983) derived an explicit formulation of Colebrook's equation given by:

$$\lambda_k = \text{®}_{\text{TM}} 1.8\log \left[\frac{6.9}{Re_k} + \text{®}_{\text{TM}} \left(\frac{\varepsilon}{3.7D} \right)^{1.11} \right]^{-2} \qquad [3.11]$$

Håland claims agreement with Colebrook's equation within +/- 1.5% in the range $4.10^3 < Re_k < 10^8$ and $0 < \varepsilon / D < 5.10^{-2}$.

Another explicit version of the Colebrook's equation was derived by Eck (1973) and claimed applicable in the range $2.1.10^3 < Re_k < 10^8$:

$$\lambda_k = \text{®}_{\text{TM}} 2\log \left[\frac{15}{Re_k} + \frac{\varepsilon}{3.715D} \right]^{-2} \qquad [3.12]$$

Based on experiments in operating gas pipelines (Smith et al. 1956), Uhl et al. (1965) suggest to modify the smooth and fully rough friction factor equations, Equation [3.8] and Equation [3.9], to:

$$\lambda_G = \text{®}_{\text{TM}} 2F_f \log \text{®}_{\text{TM}} \left(\frac{2.83}{Re_G\sqrt{\lambda_G}} \right)^{-2} \qquad [3.13]$$

and

$$\lambda_G = \text{®}_{\text{TM}} 2\log \text{®}_{\text{TM}} \left(\frac{k_e}{3.7D} \right)^{-2} \qquad [3.14]$$

The drag factor, F_f, and the effective roughness, k_e, are introduced to take into account the reduction in the pipe transmission capacity due to bends, valves, fittings and welds. Equation [3.13] and Equation [3.14] are known as the AGA correlations.

Based on recent flow measurements in smooth and rough gas pipes, it is argued that the transition between hydraulic smooth and fully rough flow is sharper than suggested by the Colebrook's equation. Uhl et al. (1965) obtained better agreement with the AGA experimental database by taking the maximum of the smooth and fully rough pipe laws, respectively Equation [3.13] and Equation [3.14], instead of Colebrook's equation, Equation [3.10], to cover the transition zone. They suggest:

$$\lambda_G = max(\lambda_{G,\,smooth}, \lambda_{G,\,rough}) \qquad [3.15]$$

The issue of an adequate expression for the friction factor for single phase gas flow in commercial pipes is still open, especially at high Reynolds number. Other more recent expressions include those of Zaragola as cited in Slettfjerding (1999) for smooth pipes in the range $3.1.10^4 < Re_G < 3.5.10^7$ and Slettfjerding (1999) for fully rough pipes up to $Re_G = 3.10^7$. The latter is based on a direct characterization of the pipe inner wall roughness and texture.

3.3 Stratified gas-liquid flow

In this section, models are reviewed for stratified gas-liquid two-phase flow with a focus on gas flow at low liquid loading. The models considered are steady-state, one-dimensional, valid in horizontal or slightly inclined pipes. Such models are described in Taitel et al. (1976), Espedal (1998), Biberg (1998 and 1999), Oliemans (1987), Hart et al. (1989), Grolman (1994) and Grolman et al. (1997), Chen et al. (1997), Meng (1999) and Meng et al. (1999).

3.3.1 Conservation equations

Variables involved in the model derivation are shown in Figure 3–1.

The mass and momentum balance equations for the gas and liquid phases can be simplified upon assumption of:

- Steady-state flow.
- Fully developed flow.
- One-dimensional flow.
- Constant pipe cross sectional area.
- Separated phases.

- Negligible hydrostatic gradient.
- No mass transfer.

Upon the above assumptions, mass balance equations reduce to:

$$U_{SG} = \alpha U_G \quad [3.16]$$

$$U_{SL} = HU_L \quad [3.17]$$

Momentum conservation equations yield for the gas and liquid phases:

$$0 = -\alpha A\left(\frac{dP}{dx}\right) - \tau_G S_G - \tau_j S_j - \alpha A \rho_G g \sin\theta \quad [3.18]$$

$$0 = -HA\left(\frac{dP}{dx}\right) - \tau_L S_L + \tau_j S_j - HA \rho_L g \sin\theta \quad [3.19]$$

where j indexes the gas-liquid interface. Volumetric phase fractions verify:

$$\alpha + H = 1 \quad [3.20]$$

By analogy with single phase flow, the shear stresses are usually expressed in terms of friction factors:

$$\tau_k = \frac{1}{8}\lambda_k \rho_k |U_k| U_k \quad [3.21]$$

$$\tau_j = \frac{1}{8}\lambda_j \rho_j |U_k - U_j| (U_k - U_j) \quad [3.22]$$

where U_k is the upper phase velocity and U_j is a boundary velocity. Adding Equation [3.18] and Equation [3.19] to cancel out the interfacial friction term, an equation for the pressure gradient is obtained:

$$\left(\frac{dP}{dx}\right) = -\frac{S}{A}\tau_w - \rho_m g \sin\theta \quad [3.23]$$

where

$$\tau_w = \frac{1}{S}(\tau_G S_G + \tau_L S_L) \quad [3.24]$$

$$\rho_m = \alpha\rho_G + H\rho_L \quad [3.25]$$

are, respectively, the total shear stress and the mixture density.

Multiplying Equation [3.19] by α and Equation [3.18] by H and substracting, the pressure gradient term cancels out. The equation obtained is function of the liquid holdup, H:

$$0 = -H\tau_G S_G + (1-H)\tau_L S_L - \tau_j S_j + \alpha HA(\rho_L - \rho_G)g\sin\theta \quad [3.26]$$

At this point, models differ on how geometries (interfacial areas) and closures (friction factors) are calculated. In the rest of this section, it is distinguished between:

- General purpose stratified flow models based on a two-fluid formulation, hereafter called "standard" models. These are the models derived in Taitel et al. (1976), Espedal (1998) and Biberg (1998 and 1999).
- Models specifically derived for gas flow at low liquid loading hereafter called "specific" models. These are the models derived in Oliemans (1987), Hart et al. (1989), Grolman (1994) and Grolman et al. (1997), Chen et al. (1997), Meng (1999) and Meng et al. (1999).

3.3.2 Wetted perimeters

Wetted perimeters depend on whether the gas-liquid interface is considered to be flat or curved.

3.3.2.1 Standard models

Standard models generally consider a flat gas-liquid interface (Figure 3–1). The wetted perimeters are expressed in terms of the wetted half-angle δ by:

$$S_L = \delta D \quad [3.27]$$

$$S_G = D(\pi - \delta) \quad [3.28]$$

$$S_j = D\sin\delta \quad [3.29]$$

The liquid holdup is related to the wetted half-angle by the exact geometrical relationship:

$$H = \frac{1}{\pi}\left(\delta - \frac{1}{2}\sin 2\delta\right) \quad [3.30]$$

Biberg (1999) proposes an approximate solution for δ in terms of H, exact within +/- 0.002 rad:

$$\delta = \pi H + \left(\frac{3\pi}{2}\right)^{1/3}(1 - 2H + H^{1/3} - (1-H)^{1/3}) \quad [3.31]$$

The average liquid height h_L can also be expressed in function of the wetted half-angle δ:

$$h_L = \frac{D}{2}(1 - \cos\delta) \quad [3.32]$$

3.3.2.2 Low liquid loading

Specific models at low liquid loading generally consider a non-planar gas-liquid interface. The problem is now to predict the liquid wetted angle and wetted perimeters in terms of system parameters.

In the ARS model (Hart et al. 1989), the liquid is considered to creep up the pipe wall due to a fraction of the liquid phase kinetic energy being transformed into potential energy. Surface tension forces are not considered to be a driving mechanism. Hart et al. derived the following semi-empirical expression for the dimensionless wetted wall fraction, $\tilde{\delta}$:

$$\tilde{\delta} = \tilde{\delta}_0 + 0.26(Fr_L)^{0.58} \quad [3.33]$$

with

$$\tilde{\delta}_0 = 0.52H^{0.374} \quad [3.34]$$

and

$$Fr_L = \frac{\rho_L}{\rho_L - \rho_G}\frac{U_L^2}{gD} \quad [3.35]$$

Equation [3.33] is valid for horizontal pipes in the holdup range $0 < H < 0.06$.

Grolman (1994) argues that Hart et al.'s correlation gives serious discrepancies with experimental data in inclined pipes. Based on new data acquired at inclinations between -3 and +6 degrees, the following empiricial relationship is suggested:

$$\tilde{\delta} = \tilde{\delta}_0\left(\frac{\sigma_{wat}}{\sigma}\right)^{0.15} + (We_{SL})^{0.25}(Fr_G)^{0.8}\frac{\rho_G}{(\rho_L - \rho_G)\cos\theta} \quad [3.36]$$

with

$$We_{SL} = \frac{\rho_L U_{SL}^2 D}{\sigma} \quad [3.37]$$

$$Fr_G = \frac{U_G^2}{gD} \quad [3.38]$$

and

$$\tilde{\delta}_0 = 0.624 H^{0.374} \quad [3.39]$$

Equation [3.36] is obtained after re-arrangement of Equation [3.33] and least square fitting of 3500 measurements conducted in 15, 26 and 51 mm pipes with air-water and air-tetradecane. The agreement with measurement is within +/- 20% in the range $-3 < \theta < 6$ deg. and $0 < H < 0.42$.

The MARS model calculates the interfacial perimeter from a linear interpolation between the smooth/stratified and annular interfacial perimeters:

$$S_j = \pi D \left(\frac{(\delta - \tilde{\delta}_0)}{1 - \tilde{\delta}_0} (1 - H)^{0.5} + \frac{(1 - \delta)}{1 - \tilde{\delta}_0} \frac{\sin \pi \tilde{\delta}_0}{\pi} \right) \quad [3.40]$$

In the Double Circle model by Chen et al. (1997) and Meng (1999), the gas-liquid interface is modelled as a concave circle arc as shown in Figure 3–1. The gas-liquid interfacial perimeter is expressed in terms of the interfacial arc diameter D_j and the angle δ_j:

$$S_j = \delta_j D_j \quad [3.41]$$

D_j and δ_j are obtained from the consideration that the area between the pipe and the interfacial circle arc must equal the liquid cross sectional area. The following implicit equation in δ_j is then obtained (Chen et al. 1997):

$$\delta_j = \left(\frac{\sin \delta_j}{\sin \delta} \right)^2 \left(\delta + \frac{\sin^2 \delta}{\tan \delta_j} - \frac{\sin 2\delta}{2} - \pi H \right) \quad [3.42]$$

with

$$D_j = D \frac{\sin \delta}{\sin \delta_j} \quad [3.43]$$

To solve Equation [3.42], one must first determine the wetted half-angle δ. Chen et al. (1997) choose to compute δ from Hart et al.'s Equation [3.33] and limit themselves to horizontal flow. Meng et al. (1999) and Meng (1999) use two different correlations. In Meng et al. (1999), it is mentioned that the MARS correlation Equation [3.36] is used to compute δ. In Meng (1999), a new empirical correlation is suggested, based on measurements of the wetted angle:

$$\begin{aligned} \delta &= 0.624H^{0.374} + 0.21(Fr_L)^{0.21} \; for \; (\theta > 0) \\ \delta &= 0.624H^{0.374} + 0.10 \; for \; (\theta \le 0) \end{aligned} \qquad [3.44]$$

with

$$Fr_L = \frac{\rho_L}{\rho_L - \rho_G} \frac{U_L^2}{gD\cos\theta} \qquad [3.45]$$

3.3.3 Gas-wall friction

For calculating gas-wall shear stress, Equation [3.21] is generally used together with a gas-wall friction factor.

There are basically two approaches:

- Gas-wall friction models based on friction factors derived from single phase gas flow. Gas and liquid are assumed to flow as if in two separate ducts with diameters equal to the hydraulic diameters of the respective phases.
- Friction models specifically derived for gas driven gas-liquid stratified duct flow.

3.3.3.1 Hydraulic diameters

Hydraulic diameters are defined by:

$$D_k = \frac{4A_k}{S_k} \qquad [3.46]$$

The calculation of wall friction using hydraulic diameters gives good predictions for turbulent single phase flow in ducts with a non-circular cross section. For laminar flow, the accuracy is generally poor. The concept of single phase friction with hydraulic diameters is adapted in two-phase flow. A rigorous definition of hydraulic diameters for a general stratified two-phase system in ducts is given by Brauner et al. (1998), with 1 indexing the lighter phase and 2 the denser phase:

$$D_1 = \frac{4A_1}{S_1 + S_j};\ D_2 = \frac{4A_2}{S_2}\ for\ (U_1 > U_2)$$
$$D_1 = \frac{4A_1}{S_1};\ D_2 = \frac{4A_2}{(S_2 + S_j)}\ for\ (U_2 > U_1) \qquad [3.47]$$
$$D_1 = \frac{4A_1}{S_1};\ D_2 = \frac{4A_2}{S_2}\ for\ (U_1 \cong U_2)$$

For gas-liquid stratified flow, gas generally flows at higher speed than the liquid and the approximation is that of closed duct flow for the gas and open channel flow for the liquid yielding:

$$D_G = \frac{4A_G}{S_G + S_j};\ D_L = \frac{4A_L}{S_L} \qquad [3.48]$$

Hydraulic diameters are practical approximations in multiphase pipe flow but can result in significant errors for cross sectional flow areas with large aspect ratios, as occurs in the case of a small liquid holdup.

3.3.3.2 Standard models

Taitel et al. (1976) use Blasius smooth pipe Equation [3.7] for the turbulent gas-wall friction factor. The gas Reynolds number is defined based on the gas hydraulic diameter:

$$Re_G = \frac{\rho_G U_G D_G}{\mu_G} \qquad [3.49]$$

In his "simple" two-fluid model, Espedal (1998) uses Håland's equation, Equation [3.11], together with Equation [3.49] for the gas Reynolds number.

Biberg (1998) suggests a novel friction factor expression specially derived for gas driven two-phase gas-liquid stratified flow. He argues that the assumption that gas flows in a closed duct of equivalent diameter equal to the hydraulic diameter leads to an underestimation of the gas-wall friction in the presence of a rough gas-liquid interface. In the latter case, the gas velocity profile is indeed skewed towards the top of the pipe with a maximum local gas velocity occurring closer to the pipe wall than suggested if the gas flowed alone in an equivalent duct. Starting with an analysis of the gas phase velocity profiles in two-phase channel flow, Biberg (1998) suggests the following gas wall friction factor:

$$\lambda_G = \left(1.8\log\left[\frac{6.9}{Re_G} + \left(\frac{\varepsilon}{3.7D_G}\right)^{1.11}\right] - 2\log\left(\frac{S_j}{S_G}\left(1 + \mathrm{sgn}\left(\frac{\tau_j}{\tau_G}\right)\sqrt{\left|\frac{\tau_j}{\tau_G}\right|} - 1\right)\right)\right)^{-2} \qquad [3.50]$$

It appears from Equation [3.50] that λ_G is the sum of two terms, a closed duct flow term, given here by Håland's equation, and a correction term accounting for the presence of the wavy gas-liquid interface. The latter term requires modelling of the interfacial friction. Biberg (1999) proposes to calculate the ratio τ_j/τ_G through Equation [3.59].

Another more practical form of Equation [3.50] is suggested by Biberg (1998) using the gas-liquid interfacial friction factor instead of the interfacial shear stress:

$$\lambda_G = \left\{ 1.8\log\left[\frac{6.9}{Re_G} + \left(\frac{\varepsilon}{3.7D_G}\right)^{1.11}\right] + 2\log\left(1 + \frac{S_j}{S_G}\right)\right\}^{-2} \Bigg/ \left\{1 + 2\log\left(1 + \frac{S_j}{S_G}\right)\frac{U_r}{U_G}\sqrt{\lambda_j}\right\} \qquad [3.51]$$

3.3.3.3 Low liquid loading

Chen et al. (1997) and Meng (1999) recommend in the Double Circle model to use the Blasius smooth pipe equation, Equation [3.7], for the turbulent gas-wall friction factor together with Equation [3.49] for the gas Reynolds number.

Hart et al. (1989) and Grolman (1994) in, respectively, the ARS and MARS models, recommend a version of Eck's friction factor correlation for smooth pipes given by:

$$\lambda_G = \frac{0.309}{\{\log[Re_G/7]\}^2} \qquad [3.52]$$

However, Hart et al. use the pipe diameter D and the superficial gas velocity in the Reynolds number definition whereas Grolman employs the actual gas velocity and the hydraulic diameter D_G.

3.3.3.4 Transition laminar/turbulent

The conditions at which the flow of each phase goes from laminar to turbulent is an important issue for choosing which of the laminar or turbulent friction factor must be used.

Grolman et al. (1997) in the MARS model suggest to define a critical Reynolds number, $Re_k = 2100$, as a criterion for the laminar/turbulent transition. In other models, however, nothing is specified. Following a recommendation by Espedal (1998), it is chosen, for computational purposes, to use the maximum of the laminar and turbulent friction factors. This procedure is in practice important for transient computations, where discontinuities can cause numerical instabilities.

3.3.4 Liquid-wall friction

As for the gas-wall shear stress, Equation [3.21] is normally used together with a liquid-wall friction factor to compute the liquid-wall shear stress.

Two categories of liquid-wall friction factor correlations are used in stratified flow models:

- Correlations based on single phase flow.
- Empirical correlations derived for two-phase gas-liquid flow.

3.3.4.1 Standard models

Taitel et al. (1976) apply the Blasius smooth pipe Equation [3.7] to compute the liquid-wall friction factor for turbulent flow. The liquid Reynolds number is defined based on the liquid hydraulic diameter:

$$Re_L = \frac{\rho_L U_L D_L}{\mu_L} \qquad [3.53]$$

Espedal (1998) in his "simple" stratified flow model also uses Equation [3.53] for the liquid Reynolds number together with Håland's Equation [3.11].

It is argued by Espedal (1998) that liquid-wall friction factors derived from single phase flow expressions are under predicting liquid-wall friction. Therefore, it is often referred to empirical friction factor correlations for the liquid phase.

Biberg (1999) proposes an expression for the liquid-wall friction accounting empirically for the effect of interfacial waves on the liquid-wall shear stress:

$$\lambda_L = \left(1.47\log\left(\frac{Re_L}{1.44}\right) + 1.47\log\left(1 - \tanh\left(2.2\frac{\tau_j}{\tau_L}\left|\frac{S_j}{S_L}\right|\sqrt{\left|\frac{\tau_j}{\tau_L}\right|}\right)\right)\right)^{-2} \qquad [3.54]$$

It appears that the liquid-wall friction is the sum of a free surface flow term and a wave term. This expression agrees well with Espedal's air-water direct wall shear stress measurements (Biberg 1999).

As for gas-wall friction, the second term in Equation [3.54] requires the modelling of interfacial friction through the ratio τ_j/τ_L. This is provided in Equation [3.60].

3.3.4.2 Low liquid loading

Chen et al. (1997) and Meng (1999) recommend in the Double Circle model to use Blasius equation, Equation [3.7], to compute the liquid-wall friction factor together with Equation [3.53] for the liquid phase Reynolds number.

An empiricial liquid-wall friction factor is suggested by Grolman (1994) and Grolman et al. (1997) based on their experimental data. As in Biberg (1999), the friction factor is expressed as a function of the gas-liquid interfacial friction factor:

$$\lambda_L = \begin{cases} \lambda_j 202 \left(\frac{\mu_W}{\mu_L}\right)^{0.274} \delta_0 (Re_{SL})^{-1} (Re_G)^{0.25} \; when \; (Re_L < 2100) \\ \lambda_j 108 (Re_{SL})^{-0.726} \; when \; (Re_L \geq 2100) \end{cases} \quad [3.55]$$

3.3.5 Interfacial friction

The interfacial gas-liquid shear stress is generally calculated from Equation [3.22] together with a definition for the interfacial friction factor (λ_j) the boundary velocity (U_j) and the "interfacial" density (ρ_j).

3.3.5.1 Standard models

Taitel et al. (1976) make the following assumptions:

$$U_j = 0, \rho_j = \rho_G \quad and \quad \lambda_j = \lambda_G \; assuming \; U_G \gg U_L \quad [3.56]$$

Oliemans (1987) expresses the interfacial friction factor from Equation [3.10] (Colebrook) but uses an empirical apparent interfacial roughness ε_j taken from Cohen et al. (1968):

$$\begin{aligned} \varepsilon_j &= 3\sqrt{2} \; for \; (\Delta h < h_L) \\ \varepsilon_j &= 3\sqrt{2} \cdot h_L \; for \; (\Delta h \geq h_L) \end{aligned} \quad [3.57]$$

Oliemans (1987) does not specify how Δh, the mean wave height, can be evaluated in practical applications. Oliemans further calculates the interfacial shear stress from Equation [3.22] with $U_j = U_L$ and $\rho_j = \rho_G$.

Andritsos et al. (1987) derived a semi-empirical interfacial friction factor correlation that is generally acknowledged to be in good agreement with air-water measurements (Spedding et al. 1997). It is given by:

$$\frac{\lambda_j}{\lambda_G} - 1 = 0 \; for \; (U_{SG} \leq U_{SG,crit})$$
$$\frac{\lambda_j}{\lambda_G} - 1 = 15\sqrt{\frac{h_L}{D}}\frac{U_{SG}}{U_{SG,crit}} - 1 \; for \; (U_{SG} > U_{SG,crit}) \qquad [3.58]$$

The liquid height, h_L, is calculated from Equation [3.32] assuming a flat gas-liquid interface. $U_{SG,crit}$ is the gas velocity at the initiation of irregular large amplitude waves. For near atmospheric conditions in air-water systems, Andritsos et al. (1987) suggest $U_{SG,crit} = 5 \; m/s$.

In Andritsos et al. (1987), Equation [3.58] is associated with the modified Blasius equation, Equation [3.7], for the gas-wall friction factor. It is assumed that $\rho_j = \rho_G$ and $U_j = 0$.

Biberg (1999) suggests a novel expression for the interfacial shear stress based on elements from the exact solution for laminar-laminar stratified flow in circular pipes. Expressed in terms of the gas-wall shear stress, it yields:

$$\frac{\tau_j}{\tau_G} = \frac{\frac{S_G}{S_G + S_j} KC_a f(\delta)}{1 - \frac{S_j}{S_G + S_j} KC_a f(\delta)} \qquad [3.59]$$

where $K \cong 750$ is an empirical factor tuned against Espedal's (1998) air-water data, C_a is a capillary number and $f(\delta)$ is a holdup dependant amplification of the interfacial shear.

Expressed in terms of the liquid-wall shear stress, the interfacial shear stress yields (Biberg 1999):

$$\frac{\tau_j}{\tau_L} = \frac{\alpha \tau_j S_L}{H\tau_G S_G + \tau_j S_j - \alpha H(\rho_L - \rho_G) A g \sin\theta} \qquad [3.60]$$

More details on Equation [3.59] and Equation [3.60] are given in Biberg (1999).

3.3.5.2 Low liquid loading

Hart et al. (1989), in the ARS model, propose to use Eck's friction factor Equation [3.12] together with an empirical estimate of the interfacial hydraulic roughness. Based on experimental results, they suggest for the interfacial roughness:

$$\varepsilon_j = 2.3 h_L \qquad [3.61]$$

with, assuming low liquid loading,

$$h_L \approx \frac{H_L D}{4\delta} \qquad [3.62]$$

In the MARS model, Grolman (1994) and Grolman et al. (1997) compute the interfacial friction factor iteratively:

1. The interfacial friction factor is assumed to be equal to the gas-wall friction factor:

$$\lambda_j = \lambda_G \qquad [3.63]$$

2. An empirical friction number F_n is calculated according to:

$$F_n = \frac{\lambda_j}{(0.05+\lambda_j)(1-H)^{1.5}} \left(\frac{U_{SG}}{\sqrt{gD}} \right) \times \left(\frac{\sigma}{\mu_L \sqrt{gD}} \right)^{0.04} \left(\frac{\rho_L g D^2}{\sigma} \right)^{0.22} \qquad [3.64]$$

3. The apparent interfacial sand roughness is calculated according to:

$$\frac{\varepsilon_j}{D} = 0.5145 H_L \left(\frac{S_j}{\pi D} \right)^{-1.5} \times \{ \tanh([0.05762(F_n - 33.74)] + 0.9450) \} \qquad [3.65]$$

4. The interfacial friction factor λ_j is calculated from Eck's Equation [3.12].
5. The iteration is repeated with the new estimate of λ_j until convergence is achieved.

The interfacial shear stress is calculated taking $\rho_j = \rho_G$ and $U_j = U_L^*$ where U_L^*, the liquid velocity at the interface, is given by:

$$U_L^* = \begin{cases} 1.8 U_L \; for \; Re_L < 2100 \\ U_L \quad for \; Re_L \geq 2100 \end{cases} \qquad [3.66]$$

Chen et al. (1997) in the Double Circle model, modified Andritsos et al.'s Equation [3.58] to account for interfacial curvature and to better fit their experimental data. They suggest:

$$\begin{aligned} \frac{\lambda_j}{\lambda_G} - 1 &= 0 \; for \; (U_{SG} \leq U_{SG,crit}) \\ \frac{\lambda_j}{\lambda_G} - 1 &= 3.75 \left(\frac{H}{\delta} \right)^{0.20} \left(\frac{U_{SG}}{U_{SG,crit}} - 1 \right)^{0.08} for \; (U_{SG} > U_{SG,crit}) \end{aligned} \qquad [3.67]$$

$U_{SG,crit}$ is now the surperficial gas velocity at transition to stratified-wavy flow calculated according to Jeffrey's theory:

$$U_{SG,crit} = \alpha\left[\frac{4\nu_L(\rho_L-\rho_G)g}{0.06\rho_G U_L}\right]^{0.5} \quad [3.68]$$

Meng (1999), in his version of the Double Circle model for slightly inclined pipes, recommends using constant interfacial friction factors:

$$\begin{aligned}\lambda_j &= 0.12 \; for \; (\theta > 0)\\ \lambda_j &= 0.0568 \; for \; (\theta \le 0)\end{aligned} \quad [3.69]$$

In Meng et al. (1999), Equation [3.69] is modified to take into account the increase of the interfacial shear stress due to the presence of entrained droplets:

$$\lambda_j = \begin{cases} 0.12 + 8\dfrac{R_D}{\rho_G(U_G-U_L)} & (\theta > 0)\\ 0.0568 + 8\dfrac{R_D}{\rho_G(U_G-U_L)} & (\theta \le 0)\end{cases} \quad [3.70]$$

with

$$R_D = 0.05 C_D \quad [3.71]$$

and

$$C_D = \frac{\rho_L U_{SL} EF}{U_{SG} + U_{SL} EF} \quad [3.72]$$

A correlation for the entrained fraction, EF, is required and is taken from Equation [3.78] as suggested by Ishii et al. (1989).

3.3.6 Atomization and entrainment

3.3.6.1 Onset of atomization

Considering a mechanism where droplets are generated by the shearing of roll wave crests, Hanratty (1991) suggests that the critical gas velocity at the onset of atomization is given by:

$$U_{SG,crit} = 1.8 U_{SG}^{*} \quad [3.73]$$

where U_{SG}* is the critical superficial velocity at the initiation of large amplitude waves and is given by Hanratty (1991):

$$U_{SG}^{*} = \frac{U_{KH}}{\alpha}\left(\frac{\Theta_W}{\Theta}\right)^{0.025}\left(\frac{1}{\tanh\left(\frac{kh_L}{10}\right)}\right)^{0.1} \quad [3.74]$$

with

$$\Theta = \frac{\rho_L}{\rho_G}\frac{\sigma^2}{\mu_L^2 U_G^2} \quad [3.75]$$

and

$$k = \sqrt{\frac{\rho_L g}{\sigma}} \quad [3.76]$$

Θ_W stands for the Taylor dimensionless group Θ calculated for water as the liquid. U_{KH} is the critical gas velocity at the inception of irregular large amplitude waves calculated from inviscid Kelvin-Helmoltz theory:

$$(U_{KH} - U_L)^2 = \left[\frac{k\sigma}{\rho_G} + \frac{\rho_L g}{k\rho_G}\right]\tanh(k(1 - h_L)) \quad [3.77]$$

3.3.6.2 Entrained liquid fraction

Ishii et al. (1989) suggest the following empirical correlation to calculate the equilibrium entrained liquid fraction in the gas core, far from the pipe entrance:

$$EF = \tanh(7.25\,10^{-7} We^{1.25} (Re_{SL})^{0.25}) \quad [3.78]$$

with

$$We = \frac{\rho_G U_{SG}^2 D}{\sigma}\left(\frac{\rho_L - \rho_G}{\rho_G}\right)^{1/3} \quad [3.79]$$

This correlation was developed from dimensional analysis and was fitted to an experimental data bank primarily composed of measurements in vertical pipes. Therefore its general applicability to pipes of all inclinations can be questioned.

3.3.7 Method of solution

For flat interface models, three closure laws are required together with conservation equations, Equation [3.16] to Equation [3.19], in order to compute all system independent variables: phase fractions, pressure loss, shear stresses, velocities.

For models with a curved gas-liquid interface, a fourth closure equation is necessary. Traditionally, it is chosen to compute gas-wall, liquid-wall and gas-liquid friction using one of the friction factor correlations given in Section 3.3.3 to Section 3.3.5. The wetted angle is usually taken as the fourth closure. Table 3–1 summarizes the closures for the different models.

For the majority of models, the method for calculating pressure drop and phase fraction begins with an iteration on the holdup equation, Equation [3.26]. Once the holdup is determined, the pressure drop is obtained from the pressure drop equation, Equation [3.23]. Given system parameters, Equation [3.26] can yield several mathematical solutions but the only stable (physical) solution is the one corresponding to the thinnest liquid layer.

Hart et al. (1989) in the ARS model use instead an empirical correlation to compute the liquid holdup:

$$\frac{H}{1-H} = \frac{U_{SL}}{U_{SG}}\left[1 + 10.4(Re_{SL})^{-0.363}\left(\frac{\rho_L}{\rho_G}\right)^{1/2}\right] \qquad [3.80]$$

Using Equation [3.33] for the wetted perimeter, they calculate the frictional pressure drop from:

$$\left(\frac{dP}{dx}\right)_{fric} = \frac{1}{2D}\lambda_{TP}\rho_G U_G^2 \qquad [3.81]$$

with

$$\lambda_{TP} = (1-\delta)\lambda_G + \delta\lambda_j \qquad [3.82]$$

The predictions of the pressure drop and liquid holdup provided by the stratified flow models discussed in this section are compared with the data from an experimental data bank composed of gas-liquid steady flow measurements in pipes at low and high pressure. The database is composed of data at low liquid loading in near horizontal pipes. Results of the comparisons are presented in Appendix E.

3.4 Stratified gas-oil-water flow

As opposed to two-phase flow, there is no specific model for dealing with three-phase gas-liquid-liquid flow at low liquid loading. The available framework in this case is that of standard stratified flow models called "three-layer models". The principal assumption is that each phase, the gas and the two liquids, flows in separate layers with no mass exchange.

In this section, the general formulations proposed in the literature for standard three-layer models are reviewed. Such flow models are discussed in Hall (1992), Taitel et al. (1995), Neogi et al. (1994) and Khor et al. (1997).

3.4.1 Conservation equations

The variables involved in the model derivation are defined in Figure 3–2.

Three-layer models extend to the case of three immiscible phases the standard stratified two-fluid models presented in Section 3.3. In addition to the assumptions listed in Section 3.3.1, it is assumed that the phases distribute in three separate layers with the heaviest fluid flowing at the pipe bottom.

Upon model assumptions, mass conservation equations for each phase reduce to:

$$U_{SG} = \alpha U_G \qquad [3.83]$$

$$U_{SO} = H_O U_O \qquad [3.84]$$

$$U_{SW} = H_W U_W \qquad [3.85]$$

with

$$\alpha + H_O + H_W = 1 \qquad [3.86]$$

Momentum conservation equations can be written for each phase as:

$$0 = -\alpha A \frac{dP}{dx} - \tau_G S_G - \tau_j S_j - \alpha A \rho_G g \sin\theta \qquad [3.87]$$

$$0 = -H_O A \frac{dP}{dx} - \tau_O S_O - \tau_i S_i + \tau_j S_j - H_O A \rho_O g \sin\theta \qquad [3.88]$$

$$0 = -H_W A\frac{dP}{dx} - \tau_W S_W + \tau_i S_i - H_W A\rho_W g\sin\theta \quad [3.89]$$

Mean shear stresses are expressed in terms of friction factors:

$$\tau_k = \frac{1}{8}\lambda_k \rho_k |U_k| U_k \quad [3.90]$$

$$\tau_j = \frac{1}{8}\lambda_j \rho_j |U_k - U_j|(U_k - U_j) \quad [3.91]$$

$$\tau_i = \frac{1}{8}\lambda_i \rho_i |U_k - U_i|(U_k - U_i) \quad [3.92]$$

for, respectively, the gas- and liquid-wall shear stresses, the gas-liquid interfacial shear stress and the oil-water interfacial shear stress.

Adding Equation [3.87], Equation [3.88] and Equation [3.89], one obtains an expression for the pressure gradient similar to Equation [3.23] in two-phase flow:

$$\left(\frac{dP}{dx}\right) = -\frac{S}{A}\tau_w - \rho_m g\sin\theta \quad [3.93]$$

where

$$\tau_w = \frac{1}{S}(\tau_G S_G + \tau_O S_O + \tau_W S_W) \quad [3.94]$$

and

$$\rho_m = \alpha\rho_G + H_O\rho_O + H_W\rho_W \quad [3.95]$$

are, respectively, the total shear stress and the mixture density.

Adding Equation [3.88] and Equation [3.89], a momentum equation for the liquid phase can be obtained:

$$0 = -H_L A\frac{dP}{dx} - \tau_L S_L + \tau_j S_j - H_L A\rho_L g\sin\theta \quad [3.96]$$

where

$$\tau_L S_L = \tau_O S_O + \tau_W S_W \quad [3.97]$$

$$\rho_L = \frac{\rho_O H_O + \rho_W H_W}{H_L} \quad [3.98]$$

Multiplying Equation [3.87] by H_L and Equation [3.96] by α and substracting, the pressure gradient term cancels out and an equation for the total liquid holdup is obtained:

$$0 = -H_L \tau_G S_G + (1 - H_L)\tau_L S_L - \tau_j S_j + (1 - H_L) H_L A(\rho_L - \rho_G) g \sin\theta \quad [3.99]$$

In a similar manner, multiplying Equation [3.88] by H_W and Equation [3.89] by H_O and substracting, an equation for the water holdup is obtained, with the total liquid holdup as a parameter:

$$0 = -H_W \tau_O S_O + (H_L - H_W)\tau_W S_W + H_W \tau_j S_j - H_L \tau_i S_i + H_W (H_L - H_W) A(\rho_W - \rho_O) g \sin\theta \quad [3.100]$$

As in two-phase flow, the various models in the literature differ how the wetted perimeters and the friction closures are calculated.

3.4.2 Wetted perimeters

Assuming flat gas-liquid and liquid-liquid interfaces, the wetted perimeters can be obtained from exact geometrical relationships. Introducing δ_W and δ_L, respectively the water and liquid wetted half-angles, yields:

$$S_W = \delta_W D \quad [3.101]$$

$$S_O = D(\delta_L - \delta_W) \quad [3.102]$$

$$S_G = D(\pi - \delta_L) \quad [3.103]$$

$$S_j = D \sin\delta_L \quad [3.104]$$

$$S_i = D \sin\delta_W \quad [3.105]$$

For flat interfaces, the water and the total liquid holdup are geometrically related to the wetted half-angles by:

$$H_{W,L} = \frac{1}{\pi}\left(\delta_{W,L} - \frac{1}{2}\sin 2\delta_{W,L}\right) \quad [3.106]$$

Reciprocally, inversing Equation [3.106], δ_W and δ_L can be expressed in terms of the water and total liquid holdups using Biberg's approximation for flat interfaces (Biberg 1999):

$$\delta_{W,L} = \pi H_{W,L} + \left(\frac{3\pi}{2}\right)^{1/3}\left(1 - 2H_{W,L} + H_{W,L}^{1/3} - (1 - H_{W,L})^{1/3}\right) \quad [3.107]$$

The liquid heights, defined in Figure 3–2, are also unique functions of the wetted half-angles:

$$h_{W,L} = \frac{D}{2}(1 - \cos\delta_{W,L}) \quad [3.108]$$

3.4.3 Hydraulic diameters

Hall (1992) and Taitel et al. (1995) suggest, for the hydraulic diameters of each phase:

$$D_G = \frac{4A_G}{S_G + S_j} \quad [3.109]$$

$$D_O = \frac{4A_O}{S_O} \quad [3.110]$$

$$D_W = \frac{4A_W}{S_W} \quad [3.111]$$

Khor et al. (1997) discuss the case of very thin oil layers (S_O small) leading to unrealistic high values of the oil hydraulic diameter. They find that the calculation of integral flow properties is significantly affected by the definition of the oil hydraulic diameter but insensitive to the definition of the water and gas diameters. Khor et al. (1997) recommend for the oil hydraulic diameter:

$$D_O = \frac{4A_O}{S_O + S_i} \quad [3.112]$$

Equation [3.112] is also used by Neogi et al. (1994).

3.4.4 Wall friction

For the gas-wall, oil-wall and water-wall friction factors, Hall (1992), Neogi et al. (1994) and Taitel et al. (1995) use the Blasius equation (Equation [3.7]) for turbulent flow and Poiseuille's law (Equation [3.5]) for laminar flow. Khor et al. (1997) recommend to use the following empiricial correlation for oil-wall and water-wall shear stresses:

$$\lambda_{O,W} = 3.06(H_{O,W}Re_{O,W})^{-0.562} \quad [3.113]$$

3.4.5 Interfacial friction

For the gas-oil interface, Hall (1992) assumes smoothness and $U_G \gg U_O$, and so sets equal the interfacial gas-oil shear stress and the gas-wall shear stress:

$$\begin{aligned} \lambda_j &= \lambda_G \\ U_j &= U_O \\ \rho_j &= \rho_G \end{aligned} \quad [3.114]$$

For the oil-water interface, no such assumption can be made and Hall suggests that the oil-water interfacial shear is proportional to the oil-wall shear stress such that:

$$\tau_i = \gamma\tau_O \quad [3.115]$$

The proportionality factor γ is estimated from an analytical analysis of three-phase flow between flat plates. For computational purposes, Hall suggests the following approximation:

$$\gamma = \frac{\mu_W}{\mu_O} \quad [3.116]$$

Neogi et al. (1994) recommend using Equation [3.58] proposed by Andritsos et al. (1987) for computing the interfacial gas-oil friction factor. The interfacial shear stress is calculated assuming $\rho_j = \rho_G$ and $U_j = U_O$. For the oil-water shear stress, they suggest a smooth interface assumption that yields:

$$\begin{aligned} \lambda_i &= \lambda_O \\ U_i &= U_W \\ \rho_i &= \rho_O \end{aligned} \quad [3.117]$$

Taitel et al. (1995) use for the gas-liquid interfacial friction:

$$\begin{aligned} \lambda_j &= max(\lambda_G, 0.056) \\ U_j &= U_O \\ \rho_j &= \rho_G \end{aligned} \qquad [3.118]$$

For the oil-water interfacial friction factor, they suggest the similar expression:

$$\begin{aligned} \lambda_i &= max(\lambda_O, 0.056) \\ U_i &= U_W \\ \rho_i &= \rho_O \end{aligned} \qquad [3.119]$$

For the gas-liquid interfacial friction, Khor et al. (1997) adapted the definition proposed by Hart et al. (1989) in their ARS model. They suggest using Colebrook Equation [3.10] for λ_j with an expression of the interfacial roughness given by Equation [3.61] and Equation [3.62]. The wetted wall fraction is calculated from Equation [3.33] with a Froude number defined by:

$$Fr_O = \frac{\rho_O}{\rho_O - \rho_G} \frac{U_O^2}{gD} \qquad [3.120]$$

For the oil-water shear, Khor et al. (1997) recommend Equation [3.119] as in Taitel et al. (1995).

3.4.6 Method of solution

Solving the three-layer model involves solving simultaneously two holdup equations, Equation [3.99] and Equation [3.100] for, respectively, the total and water holdup. A calculation procedure is suggested by Taitel et al. (1995):

1. Start with a guess of the total liquid holdup (or, equivalently, h_L or δ_L).

2. Solve Equation [3.100] for the water holdup. There is only one solution for each value of the total liquid holdup.

3. Iterate on H_L (h_L or δ_L) until Equation [3.99] is satisfied. The search for successive values of the total liquid holdup is best achieved with a dichotomy method.

4. Search for additional solution pairs (H_W,H_L). The only physically stable solution is the one corresponding to the "thinnest" liquid layer (Taitel et al. 1995).

A summary of the closures associated with the three-layer models discussed in this section is given in Table 3–2. The method of solution for the three-layer model is summarized in the general algorithm displayed in Table 3–3.

3.5 Summary

In this chapter, one-dimensional models relevant to the calculation of average, steady-state, integral flow properties have been reviewed. It has been emphasized on stratified gas-liquid flow and stratified gas-oil-water flow. If the issue of gas-liquid flow at low liquid loading has motivated specific closures to be used in relation with standard two-fluid models, none can be said of stratified gas-oil-water flow. It is questionable on how accurate three-layer models can reproduce three-phase flow at low liquid loading since no experimental data was previously available in the literature. In the following chapters of this thesis, the models presented above will be systematically compared to the experimental measurements.

Table 3–1: Models for stratified two-phase gas-liquid flow at low liquid loading

Model	Gas-liquid interface	Entrain-ment	Limi-tations	Closures					Geometries		Holdup calc.	P drop calc.
				a_G	a_L	i_j		Y				
						a_j	U_j		S_L	S_j		
Taitel et al. (1976)	flat	no	stratified	Blasius Equation [3.7]	Blasius Equation [3.7]	$\lambda_j=\lambda_G$	0	geometric Equation [3.31]	geometric Equation [3.27]	geometric Equation [3.29]	iteration on Equation [3.26]	P drop Equation [3.23]
Oliemans (1987)	flat	no	stratified	Colebrook Equation [3.10]	Colebrook Equation [3.10]	Colebrook Equation [3.10] with ε_j Equation [3.57]	U_L	geometric Equation [3.31]	geometric Equation [3.27]	geometric Equation [3.29]	iteration on Equation [3.26]	P drop Equation [3.23]
Espedal (1998)	flat	no	stratified	Håland Equation [3.11]	Håland Equation [3.11]	Andritsos Equation [3.58]	U_L	geometric Equation [3.31]	geometric Equation [3.27]	geometric Equation [3.29]	iteration on Equation [3.26]	P drop Equation [3.23]
Biberg (1998, 1999)	flat	no	stratified	Biberg Equation [3.51]	Biberg Equation [3.54]	Biberg Equation [3.59]		geometric Equation [3.31]	geometric Equation [3.27]	geometric Equation [3.29]	iteration on Equation [3.26]	P drop Equation [3.23]
Grolman (1994), Grolman et al. (1997)	concave	no	$\varepsilon_L<0.47$ $-3<\theta<6$	Eck Equation [3.52]	MARS Equation [3.55]	Eck Equation [3.12] with ε_j Equation [3.65]	U_L^* with U_L^* Equation [3.66]	empirical Equation [3.36]	from δ Equation [3.27]	interpol-lation Equation [3.40]	iteration on Equation [3.26]	P drop Equation [3.23]

Table 3–1: Models for stratified two-phase gas-liquid flow at low liquid loading

Model	Gas-liquid interface	Entrainment	Limitations	Closures					Geometries		Holdup calc.	P drop calc.
				a_G	a_L	i_j		Υ	S_L	S_j		
						a_j	U_j					
Meng (1999)	concave	yes, Equation [3.78]	low liquid loading	Blasius Equation [3.7]	Blasius Equation [3.7]	empirical Equation [3.69]	U_L	empirical Equation [3.44]	from δ Equation [3.27]	from δ_j and D_j Equation [3.41]	iteration on Equation [3.26]	P drop Equation [3.23]
Hart et al. (1989)	concave	no	$\varepsilon_L<0.06$ horizontal	Eck Equation [3.52]	-	Eck Equation [3.12]+ε_j Equation [3.61]	0	energy min. Equation [3.33]	-	-	empirical Equation [3.80]	Equation [3.81]
Chen et al. (1997)	concave	no	low liquid loading horizontal	Blasius Equation [3.7]	Blasius Equation [3.7]	empirical Equation [3.67]	U_L	energy min. Equation [3.33]	from δ Equation [3.27]	from δ_j and D_j Equation [3.41]	iteration on Equation [3.26]	P drop Equation [3.23]

Table 3–2: Three-layer models for stratified three-phase gas-liquid-liquid flow

Model	Inter faces	Limita-tions	Closures										Holdup calc.	P drop calc.
			a_G	a_O	a_W	i_j			i_i			Y_O Y_W		
						a_j	U_j	g_j	λ_i	U_i	ρ_i			
Hall (1992)	flat	stratified flow separated phases	Blasius Equation [3.7]	Blasius Equation [3.7]	Blasius Equation [3.7]	λ_G	U_O	ρ_G	$\tau_i = \frac{\mu_W}{\mu_O}\tau_O$			geometric Equation [3.107]	double iteration Equation [3.99] and Equation [3.100]	Equation [3.93]
Neogi et al. (1994)	flat	stratified flow separated phases	Blasius Equation [3.7]	Blasius Equation [3.7]	Blasius Equation [3.7]	Andritsos et al. Equation [3.58]	U_O	ρ_G	λ_O	U_W	ρ_O	geometric Equation [3.107]	double iteration Equation [3.99] and Equation [3.100]	Equation [3.93]
Taitel et al. (1995)	flat	stratified flow separated phases	Blasius Equation [3.7]	Blasius Equation [3.7]	Blasius Equation [3.7]	$\max(\lambda_G, 0.056)$	U_O	ρ_G	$\max(\lambda_O, 0.056)$	U_W	ρ_O	geometric Equation [3.107]	double iteration Equation [3.99] and Equation [3.100]	Equation [3.93]
Khor et al. (1997)	flat	stratified flow separated phases	Blasius Equation [3.7]	empirical Equation [3.113]		Colebrook Equation [3.10] with ε_j Equation [3.61]	U_O	ρ_G	$\max(\lambda_O, 0.056)$	U_W	ρ_O	geometric Equation [3.107]	double iteration Equation [3.99] and Equation [3.100]	Equation [3.93]

Table 3–3: Solution algorithm for the three-layer model

start initialize variables read case and update input variables			
perform steps			
I	iterate on H_L		
	A	guess H_L in $0<H_L<1$	
	B	iterate on H_W	
		1	guess H_W in $0<H_W<1$
		2	compute interfacial geometries
		3	compute hydraulic diameters
		4	compute shear stresses
		5	repeat from step 1 until Equation [3.99] is satisfied
		6	return H_W
	C	repeat from step A until Equation [3.98] is satisfied	
	D	return H_L	
II	search for additional solution pair (H_W,H_L)		
III	return (H_W,H_L) corresponding to minimum H_L		
IV	terminate steps		
compute pressure drop from Equation [3.93] save data terminate			

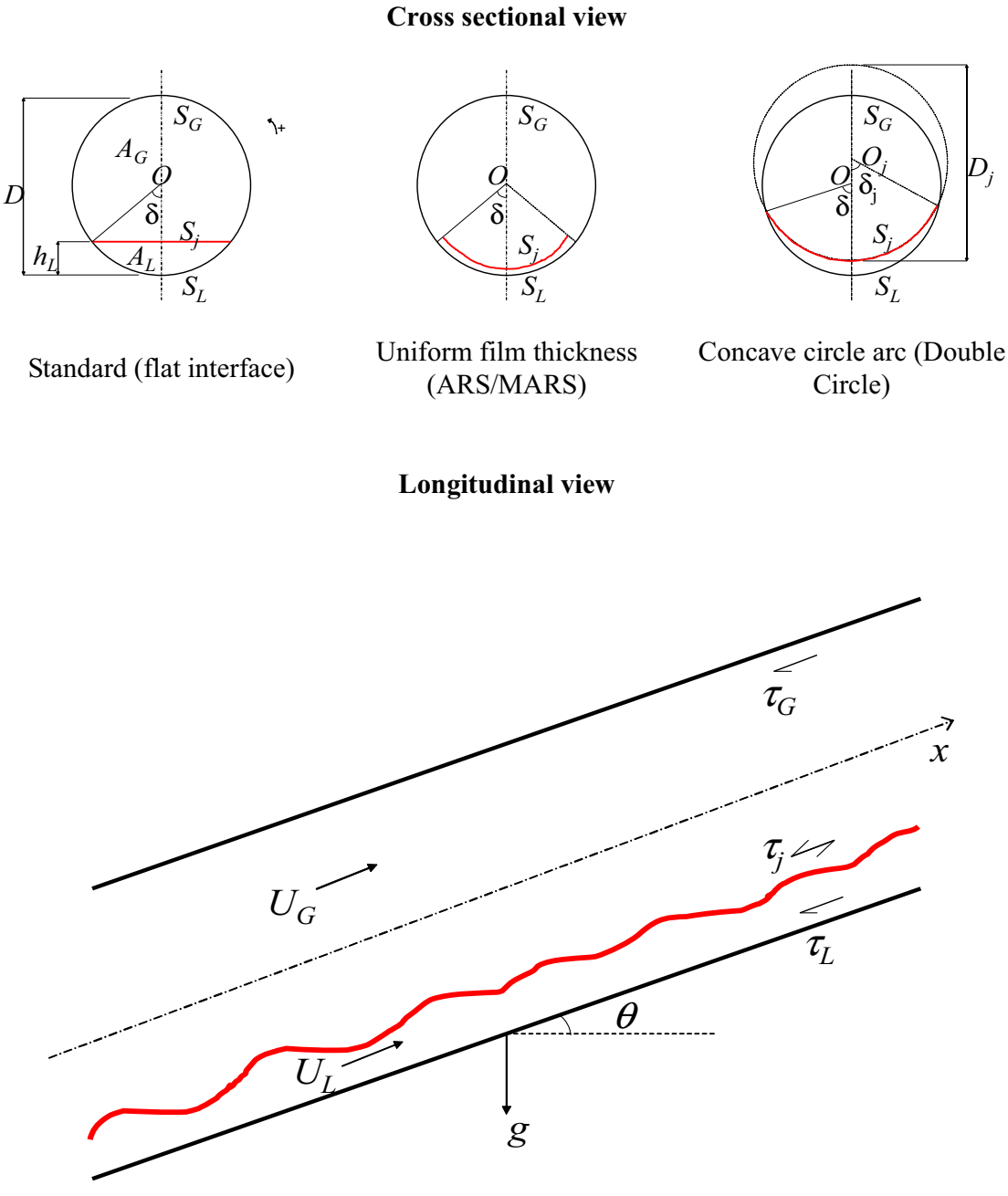

Figure 3–1: Geometries for two-phase stratified pipe flow models

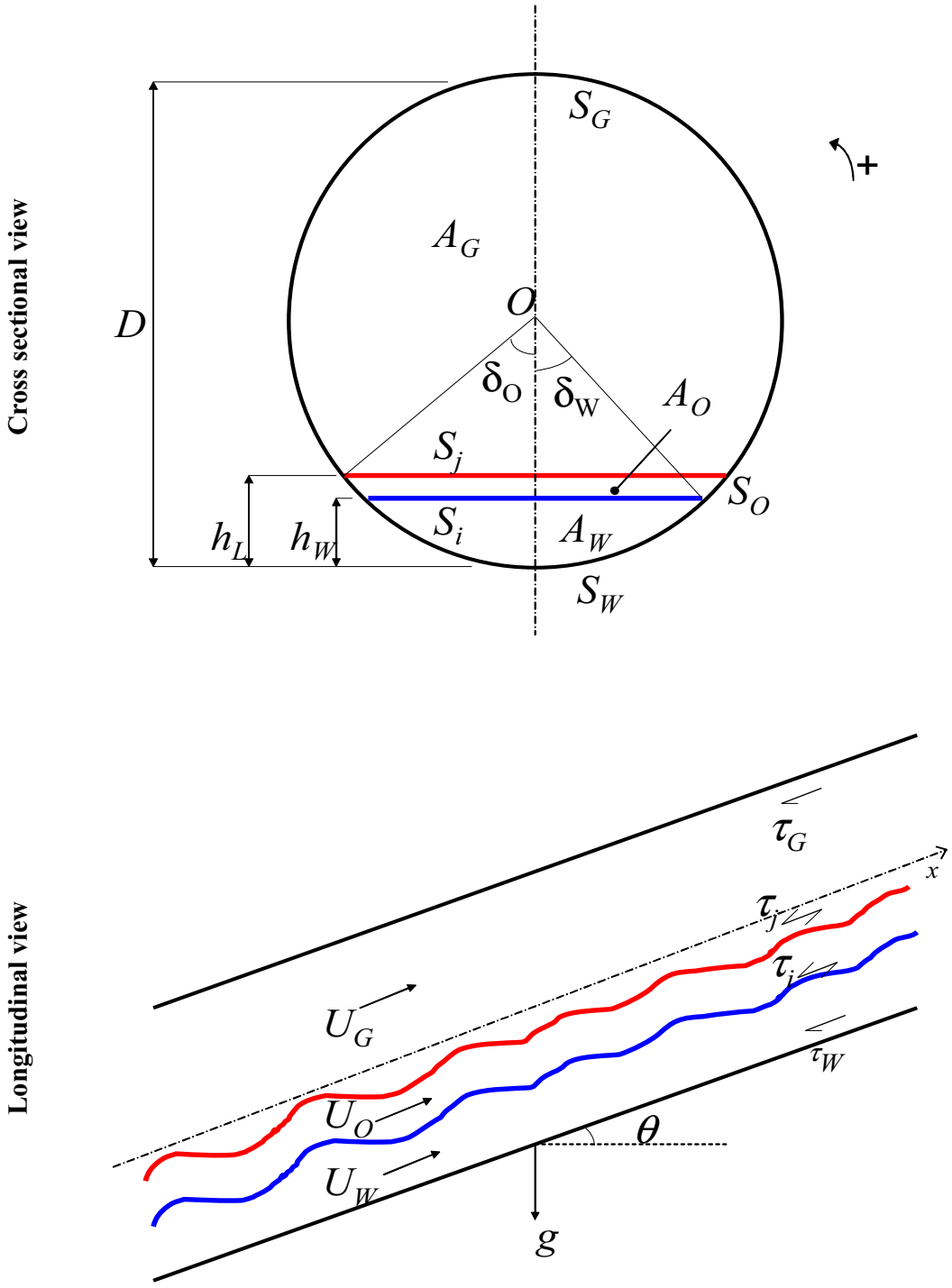

Figure 3–2: Geometries for the three-layer models with flat interfaces

Chapter 4 Flow facility

4.1 Introduction

The purpose of this chapter is to describe the multiphase flow loop used in this thesis and the measurements performed. In Section 4.2, the flow loop's infrastructure, working fluids and test sections are introduced. Test section physical characteristics such as physical roughness and contact angles with liquids are provided. In Section 4.3, the flow loop instrumentation is reviewed and the measurement accuracy is estimated. The experimental procedure for steady-state and transient measurements is presented in Section 4.4 as well as the flow loop control and data acquisition interface. Flow tests are performed to confirm the operability of the flow loop and results are presented in Section 4.5.

4.2 The flow loop infrastructure

4.2.1 General

An overall three-dimensional view of the multiphase flow rig is provided in Figure 4–1. The flow loop consists of a fluid supply system, test sections on their supports and a liquid return system dispatched on two floor levels. Three phases, air, water and oil, can be circulated simultaneously in the test sections. The flow loop is currently operated at atmospheric pressure and ambient temperature (approximately 20^{o}C).

Figure B–1 (Appendix B) gives a schematic representation of the fluid supply and fluid return systems. Air, water and oil are first transported in a separate piping and the flow rate of each phase is measured. The supply assembly is slightly tilted upwards to prevent the blockage of air bubbles in the liquid supply or liquid pockets in the air supply. Before entering the test section, the fluids are first introduced in an inlet section where they are put together in a stratified flow pattern according to their density. At the test section outlet, the fluids are collected in a slug catcher that aims at preventing eventual transients to impact on the flow upstream. Air is vented to the atmosphere while water and oil pass into a secondary tank and finally fall back into the separator tank at the ground floor. This tank has a volume of 3000 litres and contains mesh coalescers to improve separation of oil and water.

4.2.2 Fluids and fluid supply

The gas and liquid phases used in the flow loop are air, water and Exxsol D80. Air and water are abundant, inexpensive and innocuous fluids appropriate for laboratory experiments in a university environment. Exxsol D80 is a light hydrocarbon condensate (C11-C15) selected for its innocuity and fast separation capabilities. By its property, Exxsol D80 is similar to light condensate oils encountered in the field. In addition, Exxsol D80 has been used by other experimenters, which allows for comparisons.

Prior to introduction into the separator tank, water is filtered and mixed with 0.15 wt.% of Grotan WS plus. Grotan is a bactericide and fungicide chemical, fully soluble in water. To visually discriminate oil and water, 0.005 wt.% of a fluorochrome stain (fluoresceine-natrium) is added to the water phase. The molecule absorbs wave lengths in the visible blue range (around 490 nm) and re-radiate green light in the range 516-518 nm.

4.2.2.1 Fluid properties

Liquid properties are measured from samples taken in the flow loop separator. Fluid properties are summarized in Table 4–1.

Table 4–1: Flow loop fluid properties

Physical property	Air[a]	Water[b]	Exxsol D80[b]
density, kg/m^3	1.20	1000 +/- 0.2%	800 +/- 0.2%
viscosity, Pa.s	$1.8 \cdot 10^{-5}$	$1.11 \cdot 10^{-3}$ +/- 1.2%	$1.79 \cdot 10^{-3}$ +/- 1.2%
surface tension, N/m		0.0608 +/- 0.0005	0.0246 +/- 0.0005
Exxsol D80/Water interfacial tension, N/m		0.0301 +/- 0.0005	

a. Properties calculated at 1 atm. and 20°C
b. Properties measured at 1 atm. and 20°C

Oil and water densities were measured with a picnometer with an accuracy of +/- 0.2%. The water density appears to be non affected by the addition of Grotan and fluoresceine. From one experiment to the other, temperature and pressure variations are maintained within +/- 5°C and +/- 0.1 atm. Thus, variations of oil and water density with temperature and pressure are considered negligible. Air is considered an ideal gas and its density is derived from the ideal gas law.

Oil and water viscosities were measured with a capillary viscosimeter of accuracy +/- 1.2%. Viscosities calculated by this method are based on Poiseuille's law. From Table 4–1, it can be seen that the separator water viscosity is slightly higher than that of pure water due to emulsification with Exxsol D80.

Pressure is not considered to have an effect on the viscosity of liquids for the pressure variations at stake in the experiments. Effect of temperature on liquid viscosity is estimated from the Lewis-Squire correlation, Equation [4.1], from Reid et al. (1988):

$$\mu_L^{-0.2661} = \mu_K^{-0.2661} + \frac{T - T_K}{233} \quad [4.1]$$

where b_K is the measured liquid viscosity at $T_K = 293.15$ °K, T and T_K are in °K and $b_{L,K}$ in cp. Considering a +/- 5°K variation in temperature, the variations in water viscosity and oil viscosity do not exceed +/- $3 \cdot 10^{-5}$ Pa.s and +/- $5 \cdot 10^{-5}$ Pa.s respectively.

The surface tension of the water-air, Exxsol D80-air and water-Exxsol D80 interfaces has been measured with a ring tensiometer (De Noüy tensiometer). The principle consists in measuring the force necessary to withdraw a platinum ring from a bulk of liquid. A total of three repeated measurements were performed for each case with an accuracy of +/- 0.5 mN/m.

The surface tension of water appears to be lower than that of pure water (typically 72.8 mN/m) which probably results from a contamination by surface active agents coming from either the oil phase or small amounts of organisms living in water.

4.2.2.2 Fluid supply system

The air is supplied at 7 barg by the pressurized air network of the university. This pressure is reduced by a pressure reduction valve (PZV1.03) down to operational pressure (usually around 3 barg, measured in the buffer tank U1.26). After filtration of particles larger than 10 bm, the air is directed through either a large diameter (40 mm) or small diameter (15 mm) tubing where the flow rate is measured. The air flow rate is fine tuned by means of either one of the gate valves (HV1.16, HV1.17 or HV1.29).

Filtered tap water is introduced into the separator tank (U5.05) prior to operations. It is pumped through the flow loop with either a centrifugal pump (P2.22 or P2.23), for moderate to high flow rates, or a dosage pump (P2.26) for small flow rates. In the latter case, the metering infrastructure is bypassed. Pumping specifications are given in Table 4–2 below.

Table 4–2: Water supply: pump specifications

	Small water pump	Large water pump	Dosage pump
Name	Grundfoss	Gustavsberg C100-35	Prominent SIGMA 12090 PVT
Type	centrifugal	centrifugal	displacement (diaphragm)
Range (l/min)	unknown	unknown	0.048 - 1.661
U_{SW} (m/s)[a]	unknown	unknown	$0.3 \cdot 10^{-3}$ - $9.8 \cdot 10^{-3}$

a. In test section with i.d. = 60 mm at standard conditions

Water is further directed to either a large diameter (60.3 mm) or a small diameter (21.3 mm) tubing where the flow rate is metered.

Oil is introduced in the same separator tank as water from which it separates by density. The oil is pumped by either a centrifugal pump (P3.22 or P3.23) for high to moderate flow rates or a dosage pump (P3.26) for small flow rates. Pump specifications are given in Table 4–3.

Table 4–3: Oil supply: pump specifications

	Small oil pump	Large oil pump	Dosage pump
Name	Grundfoss CR 8-30	Grundfoss CR64-1	Prominent SIGMA 12090 PVT
Type	centrifugal	centrifugal	displacement (diaphragm)
Range (l/min)	99.7 - 199.5	498.7 - 1413.0	0.064 - 1.620
U_{SO} (m/s)[a]	0.59 - 1.18	2.94 - 8.34	$0.4 \cdot 10^{-3}$ - $9.5 \cdot 10^{-3}$

a. In test section with i.d. = 60 mm at standard conditions

As for water, the oil is further directed to either a large diameter (60.3 mm) or small diameter (21.3 mm) tubing where the flow rate is metered before introduction into the test section.

Further details concerning the gas, water and oil supply infrastructures are provided in Appendix B.

4.2.3 Test sections

4.2.3.1 General

A total of four test sections of different geometry and inner wall material are used in this thesis. A schematic of the test section arrangement is given in Figure 4–2 and dimensions are summarized in Table 4–4, Table 4–5 and Table 4–6. The acrylic test section arrangement was modified four times during the thesis period so as to accommodate laboratory upgrades and other experimental studies.

The straight sections are mounted on an inclinable, rigid supporting beam that can accommodate two of them in parallel. The supporting beam can be tilted around its central axis up to 15 deg. upward or downward using pre-defined anchors. The inclination is checked with a digital inclinometer with a precision of +/- 0.1 deg. The horizontal levelling of the pipe is performed with a binocular of the type used in construction engineering. The maximum deviation from the horizontal is estimated to be +/- 0.015 deg. which is equivalent to a maximum vertical deviation of 4 mm over a distance of 16 m.

The acrylic test section is assembled out from 2 m long pipe sections. The steel test sections (bare steel and epoxy coated) are made of 6 m long pipes made of stainless steel, cut

Table 4–4: Acrylic straight section dimensions

Description	Configuration 1[a]		Configuration 2[b]		Configuration 3[c]		Configuration 4[d]	
	Tag[e]	Dimension[f], m	Tag	Dimension[f], m	Tag	Dimension[f], m	Tag	Dimension[f], m
Total length	AK	16.640	AK	16.640	AK	16.555	AK	16.590
Flow development length	AB	4.660	AB	4.660	AB	4.705	AB	4.705
DP1	CE	1.745	EF	1.215	HJ	2.745	HJ	2.245
DP2	HJ	2.740	GH	1.195	CE	1.740	CE	1.740
DP3	EH	3.735	EH	3.705	CJ	8.195	CJ	7.695
Distance between quick closing valves	DI	5.210	DI	4.850	DI	4.845	DI	4.845
Distance to slug catcher[g]	JK	1.360	IK	3.540	JK	1.240	JK	1.767

a. Configuration 1: January 2001 to February 2002
b. Configuration 2: March 2002 to September 2002
c. Configuration 3: October 2002 to February 2003
d. Configuration 4: February 2003 to April 2003
e. Tags refer to drawing Figure 4–2
f. Dinension accuracy is +/- 0.005 m
g. Distance from last measuring device

Table 4–5: Steel test section dimensions

Description	Bare steel		Coated steel	
	Tag	Dimension[a], m	Tag	Dimension[a], m
Total length	AJ	16.620	AJ	16.620
Flow development length	AB	6.055	AB	6.055
DP1	EF	1.685	EF	1.655
DP2	FG	1.675	FG	1.650
DP3	BI	8.025	BI	7.535
Distance between quick closing valves	DH	4.470	DH	4.115
Distance to slug catcher[b]	IJ	2.545	IJ	3.035

a. Dimension accuracy is +/- 0.005 m
b. Distance from last measuring device

into 2.5 m long sections for the coated pipe. Pipe sections are assembled with a male-female flange junction in order to ensure smooth transitions. The pipes are supported by brackets that can be adjusted horizontally and vertically.

Table 4–6: L-shaped riser dimensions

Description	Tag	Dimension[a], m
Horizontal section length	AB	13.460
Total height	BH	6.435
Flow development length[b]	BD	3.740
Distance between quick closing valves	DG	1.690
DP	EF	1.000
Distance to slug catcher[c]	GH	1.000

a. Dimension accuracy is +/- 0.005 m
b. Vertical length to first measuring device
c. Vertical length from last measuring device

The L-shaped riser has been constructed in order to study vertical annular flow. A 13.5 m long, 2 deg. upward inclined section precedes a 92 deg. bend and a 6.5 m high vertical section on which the instrumentation is mounted. The test section is assembled from 2 m long, 50 mm i.d. transparent acrylic pipe sections and is mounted on fixed supports.

Average internal diameters and the volume of the "quick closed section" (part of the test section between quick closing valves) are indicated in Table 4–7.

Table 4–7: Summary of test section specifications

Specification	Acrylic	Steel	Coated steel	L-shape riser
Inner wall material	plexiglass (polymethyl methacrylate polymer)	stainless steel (min. 10% chromium-nickel)	epoxy resin (epoxy polymer + diamine)	plexiglass
Pipe section length, m	2	6	2.5	2
Average internal diameter, m	0.0600 +/- 0.0007	0.0604 +/- 0.0001	0.0601 +/- 0.0001	0.0500 +/- 0.0005
Volume of the quick closed section, m^3	$1.3726 \cdot 10^{-2}$ +/- $9 \cdot 10^{-6}$ (config. 1) $1.3453 \cdot 10^{-2}$ +/- $5 \cdot 10^{-6}$ (config. 2) $1.3493 \cdot 10^{-2}$ +/- $5 \cdot 10^{-6}$ (config. 3 & 4)	$1.2634 \cdot 10^{-2}$ +/- $5 \cdot 10^{-6}$	$1.2003 \cdot 10^{-2}$ +/- $5 \cdot 10^{-6}$	$3.388 \cdot 10^{-3}$ +/- $4 \cdot 10^{-6}$

To obtain a realistic value of the test section internal diameter, two methods have been used: an indirect measurement where diameter is obtained from the determination of the volume of a given length of pipe and a direct measurement with a calliper (Mitoyu cylin-

der gauge of precision +/- 0.01 mm). Several direct and indirect measurements have been treated statistically using t-test of hypothesis at 5% significance. The results indicated in Table 4–7 are average values given at 95% confidence.

Likewise, quick closed section volumes are determined from at least three repeated measurements. The fast closed section is first filled with water, taking care that no air bubble is trapped, then the water is drained and the fast closed section is pigged. After weighing on a Mettler-Toledo balance of accuracy +/- 0.1 g (range 32 kg), the entrapped water volume is obtained using the measured water density from Table 4–1.

4.2.3.2 Coating construction and coating control

To study the possibility of an impact of internal coatings on the flow of gas at low liquid loading, experiments have been performed in an internally coated pipe. The coating chosen is Copon EP 2306. It is a two-component epoxy paint used in several North-Sea gas transportation pipelines to mitigate pipe roughness and provide corrosion protection.

The pipe coated is the same stainless steel pipe as used in other experiments. Due to the small pipe i.d., it is not possible to spread the coating according to the normal industrial method that involves a rotating nozzle. The painting is instead applied manually.

The coating construction is performed in three steps:

1. Pipe preparation. The steel pipe is cut in maximum 2.5 m long sections, 2 mm pressure tappings are drilled and plugged with foam and the inner surface is scraped with fine sand paper.

2. Paint preparation. The paint quantity is computed for each section. The two components are mixed and stirred. The objective is to apply a 125 bm thick layer of paint. To achieve this film thickness, it is required 28 g of paint per meter of pipe, quantity that was doubled to account for contingency.

3. Pipe coating. The paint is introduced at the pipe upstream end and spread by manual rotation of the pipe until complete wetting of the pipe circumference. Excess paint is drained and the pipe is centrifuged at 125 rpm for 5 minutes. The drainage and centrifugation is repeated twice until an average of 20 g/m of excess paint is collected to achieve a film thickness as close as possible to specifications. The pipe section is finally dried for 24 hours in slow rotation on an electric motor and for further 7 days on a bench.

The criteria for accepting the coating are:

- Presence of dry patches: checked by visual control.
- Presence of castings: checked by visual control.
- Coating thickness: checked with a comparator.
- Surface roughness: checked with a roughness measurement.

The purpose of the shape control is to check that the paint is homogeneously spread around the pipe perimeter. Despite the centrifugations, it is indeed expected zones of paint accumulation along the path of the initial paint cast. A coarse control has been performed for all sections inlet and outlet using a comparator. Maximum deflections are summarized in Table 4–8.

Table 4–8: Maximum coating thickness variations for each coated section. Average deflection is 56 bm, about 45% of the targeted coating thickness

Section[a]	1-I	1-O	2-I	2-O	3-I	3-O	4-I	4-O	5-I	5-O	6-I	6-O
Measured deflection, bm	71	36	41	23	43	29	33	25	104	63	44	30

a. I stands for “inlet”; O stands for “outlet”

The comparator was also rotated by steps of 45 degrees and the measured deflections plotted. An example plot is given in Figure 4–3 for pipe section 1 at the outlet. A 40 bm thick paint accumulation can be seen along the line of paint introduction. This feature is encountered for nearly all pipe sections. During the assembly of the coated sections, the accumulations have been disposed in the upper, gas wetted half of the pipe to avoid a distortion of the liquid film.

The coating physical roughness is measured to ensure that the coating surface is not rougher that the initial substrate. In the normal situation, the coating is applied on a rough surface and the pipe roughness is significantly reduced. In the present case, the initial steel pipe is already hydraulically smooth and there is a risk that the method of applying the paint may alter the surface homogeneity. It is shown in Section 4.2.3.3 that the coating only slightly increases the surface roughness with a maximum 20% increase of mean peak-to-valley height.

4.2.3.3 Surface characterizations

In order to better interpret the differences in the flow measurements related to a change in the pipe material, it is important to define physical characterizations of the inner wall surface. The characterizations performed in this work include measurements of surface physical roughness and fluid/surface contact angles.

Surface roughness

Surface profiles of the inner pipe wall are acquired with a needle Pertometer S3P. For each pipe material, twelve profiles in the axial (main flow) direction are recorded. The instrument consists of a mechanical pick-up MFW-250 and a drive unit PGK. Log files are exported to a PC via a serial cable for further numerical processing. A schematic representation of the measurement setup is given in Figure 4–4. Instrument characteristics are summarized in Table 4–9.

Table 4–9: Pertometer S3P specifications

Item	Characteristic	Value
Stylus tip	radius of curvature	5 bm
	opening angle	90^o
Horizontal measuring range	cut-off wavelength	0.08,0.25, 0.8 or 2.5 mm
	digitized into	8064 intervals (1152 per cut-off)
Vertical measuring range	range	25 bm or 250 bm
	digitized into	16384 intervals

A total of twelve profiles has been acquired for each material at random places on the pipe inner wall. For the coated pipe, 12 measurements were performed for each coated section. The pipe to be measured was carefully laid and blocked on a weighted table to avoid vibrations and noise.

The following statistical parameters can be obtained from the vertical profile, z(x):

- R_a, the arithmetical mean roughness defined by:

$$R_a = \frac{1}{L}\int_L |z|\,dx \qquad [4.2]$$

- R_q, the root-mean-square roughness defined by:

$$R_q = \sqrt{\frac{1}{L}\int_L z^2\,dx} \qquad [4.3]$$

- R_z, the mean peak-to-valley height defined by.

$$R_z = \frac{1}{L}\int_L (z_{max} - z_{min})\,dx \qquad [4.4]$$

- R_y, the maximum profile height defined by:

$$R_y = (z_{max} - z_{min}) \qquad [4.5]$$

Roughness profile characterizations are summarized in Table 4–10.

From Table 4–10, it can be seen that acrylic is significantly smoother than steel and coated steel. The coated pipe is slightly rougher than the bare steel pipe by a factor of 20% on R_a. All three pipes are significantly smoother than commercial bare steel pipes and coated

Table 4–10: Summary of roughness measurements

Surface	R_a, bm	std, bm	R_q, bm	std, bm	R_z, bm	std, bm	Cut off, mm	# Meas.
Coated 1	0.40	0.14	0.49	0.16	2.71	0.71	0.8	8
Coated 2	0.38	0.17	0.51	0.21	2.59	1.13	0.8	8
Coated 3	0.41	0.32	0.60	0.45	2.92	1.72	0.8	8
Coated 4	0.33	0.14	0.44	0.17	2.26	0.77	0.8	16
Coated 5	0.36	0.15	0.47	0.19	2.27	0.71	0.8	16
Coated 6	0.35	0.09	0.47	0.12	2.71	0.61	0.8	8
Stainless steel	0.34	0.10	0.44	0.14	2.53	0.64	0.8	16
Acrylic	0.05	0.06	0.06	0.07	0.41	0.52	0.8	16

steel pipes that exhibit typical R_a in the order of 2 bm and 1 bm and R_q in the order of 4 bm and 2 bm respectively (Slettfjerding 1999).

Contact angles

Static (equilibrium) contact angles are defined in Figure 4–5. Contact angles vary with solid surfaces, liquid properties and surrounding media (solvent). Contact angles different from zero correspond to partial wetting systems whereas wetting systems are often characterized by a contact angle equal to zero (even though there is, formally speaking, no contact angle in this case). Advancing and receding angles are the contact angles observed at the contact line when a droplet is moved forward (advanced) or backward (receded) over a solid surface.

Table 4–11 summarizes the contact angle measurements performed. Several combinations of solid material (acrylic, steel and epoxy coated steel), liquids (water and Exxsol D80) and surrounding media (air, water or Exxsol D80) were considered. In addition, Table 4–11 indicates, for comparison, results obtained by Valle as cited by Angeli et al. (1998) for the same fluids and solid surfaces.

To perform the contact angle measurements, short lengths of test section pipe were opened in two-halves and droplets of fluids were deposited with a syringe on the pipe inner surface. No particular pre-treatment of the surface was performed other than cleaning with acetone. The fluids were taken directly from the laboratory separator tank. Contact angles displayed in Table 4–11 are averaged values obtained from at least 10 separate angle measurements for each solid/liquid/media system at ambient conditions of pressure and temperature. Measurement accuracy is estimated to +/- 1 deg.

Two methods have been considered for the measurements: a photographic method and a direct angle measurement with a goniometer. In the first case, the contact angle is obtained geometrically from measurements of droplet height and droplet diameter and assuming

Table 4–11: Summary of contact angle measurements (in deg.) for several solid/liquid/medium system. Accuracy is +/- 1 deg. Pressure = 1 atm; Temperature = 20°C

Solid	Type	Liquid/Solvent			
		Water/Air	Oil/Air	Water/Oil[a]	Oil/Water[a]
Acrylic	no pre-wetting	53	0	113	71
Steel	no pre-wetting	61	0	127	105
Epoxy	no pre-wetting	60	0	117	97
Acrylic	water pre-wetting	51	0	72 (106)	71 (88)
Steel	water pre-wetting	26	0	51 (0)	105 (143)
Epoxy	water pre-wetting	23	0	55	97
Acrylic	oil pre-wetting	52	0	115 (122)	0 (84)
Steel	oil pre-wetting	60	0	127 (129)	0 (0)
Epoxy	oil pre-wetting	66	0	117	0
Acrylic	advancing	72	0	117	-
Steel	advancing	86	0	115	-
Epoxy	advancing	63	0	96	-
Acrylic	receding	33	0	68	-
Steel	receding	19	0	37	-
Epoxy	receding	34	0	26	-

a. Figures in parenthesis are values by Valle as cited in Angeli et al. (1998)

spherical droplets. This method is not considered accurate and not pursued further. With the goniometer method, droplets are optically magnified and contact angles are measured directly by means of a graduation scale and a cross hair in the optical window. It is also possible to use a digital camera and a picture recognition software that can identify the liquid/media and liquid/solid interfaces based on pixel gray contrasts. Due to the curvature of the pipe surface, the measured angles have to be corrected by substracting the angle formed by the tangent to the liquid-solid contact line with the horizontal. A schematic representation of the measurement setup is given in Figure 4–6.

The results in Table 4–11 call for the following comments:

- Oil is wetting all solid materials but with water as the solvent, the surfaces have to be oil pre-wetted for oil droplets to wet.

- In all cases water is only partially wetting but the degree of wetting depends on both solid material and pre-wetting history. Without pre-wetting, average static angles are similar for all solid materials and the trend is for better wetting with air as the solvent than with oil as the solvent. With water pre-wetting however, steel and epoxy are better

water wetted than acrylic. A possible explanation is that the higher physical roughness of the steel and epoxy surfaces helps to trap water in roughness grooves during the pre-wetting. This creates a composite surface and the water droplet contact angle is lowered.

• The difference between the advancing and receding angles, called in the rest of this dissertation "contact angle hysteresis" or simply "hysteresis", is more pronounced with steel than with acrylic and epoxy. As will be seen, hysteresis can be related to droplet adhesion.

• The averaged values in Table 4–11 sometimes mask a large scatter in the measurements. This is reflected in the standard deviations given in Table 4–12. Contact angle measurements are difficult to perform and usually require, to be repeatable, clinical environments and the total absence of impurities in either the liquid bulk or at the solid surface. Often, the solid surfaces are polished to avoid contact angle hysteresis due to surface roughness. However, in the present case, it was not considered representative of the real flow situation to either work with pure fluids or to polish the pipe surface. On the contrary, the scatter in the results reveals the degree of contact angle hysteresis for each surface.

Table 4–12 shows results of water-surface contact angle measurements in air for several commercial coatings from three different manufacturers. The paint considered are all solvent based epoxy paint with different film thickness and applied on substrates of different initial roughness. As a result, the roughness of the coating varies from sample to sample. It is interesting to note the larger scatter in the contact angle measurement on un-painted substrates (sample quoted "no paint" and "Lab. steel"). This reflects the larger surface heterogeneity of the bare substrates compared to the coated substrates.

Table 4–12: Summary of water/surface contact angle measurements for several commercial coatings and comparisons with laboratory pipes

	En 223[a]	**En 123[a]**	**HL 248[b]**	**HL 225[b]**	**HL 48[b]**	**C0 EP2306[c]**	**No paint**	**Lab. acrylic**	**Lab. steel**
Roughness on substrate (R_y, bm)	20 +/- 5	50 +/-5	20 +/- 5	20 +/- 5	35 +/- 5	35 +/- 5	35 +/- 5	-	-
Dry film thickness, bm	50	45	53	221	57	93	-	-	-
Roughness on paint (R_y, bm)	6	21	3	1	5	5	-	-	-
Mean contact angle[d] (deg.)	62	70	57	66	65	66	69	53	61
std (deg.)	6	12	5	8	6	4	13	4	11

a. Solvent based epoxy paint from Endocote
b. Solvent based epoxy paint from Hempel (Hempel 87630)
c. Solvent based epoxy paint from Copon (EP 2306)
d. “trimmed mean”: +5% and -5% extreme values excluded

As mentioned earlier, it is possible to relate contact angle hysteresis to the adhesion force of a liquid droplet to a solid surface. Let us consider the schematic in Figure 4–7. It represents a liquid droplet on a plane surface submitted to a drag force in the x-direction. The force F resisting the drag results from interfacial tension acting at the contact line. Assuming a circular contact line, the x-component of F is:

[4.6]

$$F_x = \cos(\xi_R)\int_{-\frac{\pi}{2}}^{\frac{\pi}{2}} \sigma\cos\phi R d\phi - \cos(\xi_A)\int_{\frac{\pi}{2}}^{\frac{3\pi}{2}} \sigma R(-\cos\phi)d\phi = 2\sigma R(\cos\xi_R - \cos\xi_A)$$

The resistance to the drag is therefore proportional to the factor $\Delta = \cos\xi_R - \cos\xi_A$. This factor is enhanced by large differences between ξ_R and ξ_A (contact angle hysteresis).

F_x (Equation [4.6]) is calculated based on advancing and receding angle measurements in Table 4–11 for a water droplet on steel, acrylic and epoxy, in air and oil solvents. To simplify, the droplet radius is taken equal to one. Results are plotted in Figure 4–9. It shows that droplet adhesion in higher on steel than on either epoxy or acrylic in both air and Exxsol D80 as the solvent.

It is shown in Table 4–12 that contact angle hysteresis, reflected in the standard deviation around the mean, is in general less for coated pipes than for bare steel pipes. The difference is similar to the difference observed between the laboratory steel and acrylic pipes. Hysteresis is the result of surface heterogeneities such as adsorbed impurities or surface roughness. Figure 4–8 from De Gennes (1985) shows how hysteresis decreases with decreasing substrate roughness.

4.3 Instrumentation and flow loop control

4.3.1 Flow rate metering

4.3.1.1 Liquid

The flow loop is equipped with four flow meters for measuring liquid flow rates. Two are built on the water supply and two are built on the oil supply as shown in Figure B–1. Flow meter specifications are given in Table 4–13.

For liquid superficial velocity below 0.02 m/s in the 60 mm test section, the conventional centrifugal pumps are not able to deliver stable flow rates and liquid flow meters become out-of-range. In this case, the dosage pumps described in Section 4.2.2.2 must be used and

Table 4–13: Liquid flow meter specifications

Fluid	Name	Type	Range[a]	U_{sL} (m/s)[b]	Accuracy (+/-)	Repeata-bility	Temp. effects
Water	Endress & Hauser Promag 33	elmag	0.053-0.987 l/s	0.02-0.35	0.5%	0.5%	unknown
Water	Fisher-Porter COPA XM Series 3000	elmag	0.83-10 l/s	0.29-3.53	0.5%	0.5%	unknown
Oil	Micromotion F025	coriolis	100-1000 kg/h	0.01-0.09	0.20%	0.35%	0.0002% o.f.r[c]/^{o}C
Oil	Micromotion T150	coriolis	1000-5000 kg/h	0.09-4.91	0.15%	0.5%	0.0002% o.f.r/^{o}C

a. Factory calibrations
b. Reported in a 60 mm i.d. pipe
c. o.f.r. : of full range

the entire liquid metering section is bypassed to improve stability. Dosage pumps are connected directly to the inlet section through 19 mm flexible hoses. In the absence of low range liquid flow meters, flow rates are deducted directly from the pump stroke length and stroke frequency. This requires a careful calibration.

Calibration points for several piston courses and stroke frequencies are taken with a balance (Mettler Toledo, accuracy +/- 0.1 g) and a stop watch (accuracy +/- 0.5 s). The fixed root-mean-square error in the flow rate obtained by this method is estimated according to Equation [4.7] (Doebelin 1990):

$$\frac{\Delta Q}{Q} = \frac{1}{2}\sqrt{\left(\frac{\Delta M}{M}\right)^2 + \left(\frac{\Delta t}{t}\right)^2} \qquad [4.7]$$

Results of the calibration are shown in Figure 4–10 for the water pumps and Figure 4–11 for the oil pump. The calibration curve is linear for all piston lengths comprised between 100% and 10% of full piston course. The calibration is repeated before each experimental campaign. If changes are observed (due to setup modification or ageing of the supply hoses), a new calibration run for the entire pump range is carried out.

A linear interpolation curve passing through the origin is determined and used to back calculate the flow rates corresponding to a given frequency. A 97.7% prediction interval for the flow rates read from the interpolation line is given by (Doebelin 1990):

$$[\hat{y}_o - 3s, \hat{y}_o + 3s] \qquad [4.8]$$

where $\hat{y_o}$ is the interpolated value of the flow rate, $s = \sqrt{\frac{(y_i - \hat{y}_i)^2}{n-2}}$, is an unbiased estimator of the random error, y_i are the calibration points, $\hat{y}_i$ are the interpolations and n is the number of calibration points.

An upper limit of the total error on the flow rate obtained after calibration is given in Table 4–14 for the water pump and Table 4–15 for the oil pump.

Liquid metering accuracy is summarized in Table 4–16.

Table 4–14: Error on the flow rate for the water dosage pump

Stroke Length, % of full course	Range, l/min	Fixed error (calibration), %	Average error (linear fit, 97.7% confidence), l/min	Maximum error (linear fit), %	Total, %
100	1.28 - 1.66	0.3	0.009	0.70	1.00
75	0.84 - 1.28	0.3	0.009	1.07	1.37
50	0.40 - 0.84	0.3	0.012	3.30	3.60
25	0.13 - 0.40	0.3	0.002	1.54	1.84
10	0.03 - 0.13	0.3	0.002	6.67	6.97

Table 4–15: Error on the flow rate for the oil dosage pump

Stroke Length, % of full course	Range, l/min	Fixed error (calibration), %	Average error (linear fit, 97.7% confidence), l/min	Maximum error (linear fit), %	Total, %
100	1.36 - 1.72	0.3	0.017	1.25	1.55
75	0.93 - 1.36	0.3	0.008	0.86	1.16
50	0.45 - 0.93	0.3	0.001	0.22	0.52
25	0.17 - 0.45	0.3	0.009	5.29	5.59
10	0.06 - 0.17	0.3	0.004	6.67	6.97

4.3.1.2 Air

A low range coriolis meter and a high range vortex meter are used to measure air flow rate. The coriolis meter provides a direct measurement of the air mass flow rate whereas the vortex meter provides a volumetric flow rate measurement that needs to be extrapolated to test section conditions. In that purpose, a measurement of the absolute pressure is

Table 4–16: Summary: liquid metering accuracy reported in a 60 mm i.d. pipe

Fluid	Instrument	Range (+/- m/s)	Accuracy (+/-)
water	elmag (COPA XM)	0.29-3.53	0.5%
	elmag (Promag 33)	0.02-0.35	0.5%
	dosage (SIGMA 12090)	0.0075-0.0098	1.0%
		0.0049-0.0075	1.4%
		0.0024-0.0049	3.6%
		0.0008-0.0024	1.8%
		0.0002-0.0008	7.0%
oil	coriolis (T150)	0.09-4.91	0.2%
	coriolis (F025)	0.01-0.09	0.2%
	dosage (SIGMA 12090)	0.0100-0.0127	1.6%
		0.0068-0.0100	1.2%
		0.0033-0.0068	0.5%
		0.0013-0.0033	5.6%
		0.0004-0.0013	7.0%

performed just before the vortex meter and at the pipe inlet as shown in Figure B–1. The volumetric air flow rate at the test section inlet is calculated from Equation [4.9]:

$$Q_{inlet} = Q_{vortex}\frac{P_{vortex}}{P_{inlet}} \quad [4.9]$$

Flow meter specifications are summarized in Table 4–17.

Table 4–17: Air flow meter specifications

Specification	Low range	High range
Name	Micromotion CMF025 Elite	Endress & Hauser Flowirl 77A
Type	coriolis	vortex
Range[a]	0.12-80 kg/h	9-110 l/s
U_{SG} (m/s)[b]	0.01-6.5	3.2-39.3
Accuracy (+/- m/s)[c]	0.5%	1%
Repeatability[c]	0.25%	0.25%

a. Factory calibrations
b. At 1 atm, 20^{o}C in the 0.06 m i.d. pipe
c. Factory specifications

The manufacturer gives an instrument accuracy that can be checked as follows:

- Dry air is run in the 60 mm i.d. acrylic test section and metered. Several values of the steady state flow rate are tested to cover the whole metering range.
- The pressure drop is recorded over 3.735 m of test section. Three Fuji differential pressure cells are used of range 1000 Pa, 1000 Pa and 5000 Pa respectively.
- Using Håland's correlation, Equation [3.11], and plotting the gas friction factor λ_G versus the gas Reynolds number Re_G, a value of the hydraulic roughness ε can be obtained.
- Using the value of ε, the gas velocity is back-calculated using either Håland's, Prandtl's or Blasius' friction factor correlations for turbulent flow (Equation [4.10], Equation [4.11] and Equation [4.12] respectively). Equation [4.10] and Equation [4.11] are implicit and must be solved iteratively.

$$\frac{2\left(\frac{dp}{dx}\right)D}{\rho_G U_G^2} = 1.8\log\left[\frac{6.9\mu_G}{\rho_G U_G D} + \left(\frac{\varepsilon}{3.7D}\right)^{1.11}\right]^{-2} \qquad [4.10]$$

$$\frac{2\left(\frac{dp}{dx}\right)D}{\rho_G U_G^2} = 1.8\log\left(\frac{\rho_G U_G D}{6.9\mu_G}\right)^{-2} \qquad [4.11]$$

$$U_G = \left[\frac{6.3211\frac{dp}{dx}D^{5/4}}{\rho_G \nu_G^{1/4}}\right]^{4/7} \qquad [4.12]$$

- Calculated and measured gas velocities are then compared and a value for the metering accuracy is estimated graphically. This is shown in Figure 4–12 for the Prowirl 77 vortex meter and Figure 4–13 for the F025 coriolis meter.

For the Prowirl vortex meter, velocities calculated from the measured pressure loss are within +/- 2% of the values given by the gas meter. This is poorer than the specified accuracy of +/- 1% and +/- 2% is retained as a more realistic value.

For the Coriolis meter, the match is within +/- 1% in the high range but poor in the low range. This is due to inaccuracies in the pressure drop measurements and can be corrected if the pressure drop is measured over a longer distance. Based on the current data, the meter accuracy is estimated to be +/- 1%.

A summary of air metering accuracy is given in Table 4–18.

Table 4–18: Summary: air metering accuracy

Flow meter	Estimated accuracy (+/-)
Vortex (high range)	2%
Coriolis (low range)	1%

4.3.2 Pressure drop

As shown in Figure 4–2, differential pressure taps are mounted at different locations along the pipe which allows for multiple differential pressure measurements. Three Fuji differential pressure transmitters can be used allowing for three separate measurements of the pressure drop. Instrument specifications are given in Table 4–19.

Table 4–19: Differential pressure transmitter specifications

Specification	Low range transmitter	High range transmitter
Name	Fuji FHCW11	Fuji FKCW33
Type	membrane	membrane
Nominal range (kPa)	0-1	0-32
Calibrated range (kPa)	0-1	0-5
Specified accuracy (+/- Pa)[a]	1	5

a. +/- 0.1% of full range

In-house designed pressure taps were glued on the pipe outside wall at locations specified in Table 4–4, Table 4–5 and Table 4–6. Two millimetre wide holes were drilled through the pipe wall and carefully cleaned for burrs. The pressure transducers are connected to the upper wall pressure taps using 6 mm lines made of nylon, this material being chosen for its strength and hydrophobicity. The lines are air-filled and the differential pressure measurements are performed in the gas phase.

The factory specified accuracy of the transmitters has been checked by comparing their output for several flow rates while measuring the pressure loss with dry air over 3.735 m of the acrylic test section. The results of the comparisons are shown in Figure 4–14 and Figure 4–15. From the graphs, it appears that the accuracy specified in Table 4–19 is acceptable.

Error on the static pressure measurement due to finite hole size can be estimated according to the following equation mentioned in Slettfjerding (1999):

$$\frac{err(P)}{\tau_w} = 0.269(d^+)^{0.353} \qquad [4.13]$$

with

$$d^+ = \frac{d}{\nu_G}\sqrt{\frac{\tau_G}{\rho_G}} \qquad [4.14]$$

Considering the two cases where the transmitters are used up to saturation, the maximum pressure drop experienced by the FHC transmitters is estimated to 850 Pa/m for the straight 60 mm test sections and 1000 Pa/m for the 50 mm vertical test section. For the FKC transmitter, the maximum experienced pressure drop is 1350 Pa/m. Those figures are based on the pressure tap locations given in Table 4–4, Table 4–5 and Table 4–6. For 2 mm holes, this results in an error of 5.5% of full range for the FHC transmitters and 1% of full range for the FKC transmitter. These figures are high and regarded as little realistic based on the good value overlap obtained for the transmitter pair-wise comparison tests, Figure 4–14 and Figure 4–15.

The error on the static pressure measurement due to burrs is estimated according to an equation in Slettfjerding (1999):

$$err(P) = 8\tau_w \qquad [4.15]$$

Equation [4.15] is given for a burr height-to-tap diameter ratio of 2/63 = 0.03 (this corresponds to a burr height of 63 bm for a hole diameter of 2 mm). Such a burr would result in a 20% of full range inaccuracy in the pressure drop measurement for the FHC transmitters and 4% for the FKC transmitter. Particular care is therefore taken to eliminate burrs from pressure tap holes.

Pressure lines must be carefully cleaned for stagnant liquids prior to pressure drop measurements. For instance, a water plug of 5 mm blocked in the line can create an error in the order of 10 Pa/m equivalent to an inaccuracy of 1% of full FHC range.

Pressure transmitter accuracy is summarized in Table 4–20.

Based on the single transmitter accuracy given in Table 4–20, an estimate of the pressure drop measurement accuracy can be made. The steady-state pressure drop is obtained from an average of three pressure drop measurements (two for the vertical riser) performed at three different locations along the pipe. Indexing by 1, 2 and 3 the three measurements, the average pressure drop is calculated from Equation [4.16]:

$$\frac{dP}{dx} = \frac{1}{3}\left(\left.\frac{dP}{dx}\right|_1 + \left.\frac{dP}{dx}\right|_2 + \left.\frac{dP}{dx}\right|_3\right) \qquad [4.16]$$

Noting $\frac{dP}{dx}$ by P_x, the root mean square error on $\left.\frac{dP}{dx}\right|_k$ is given by:

Table 4–20: Differential pressure transmitter accuracy

Type of uncertainty	FHC transmitter (low range)	FKC transmitter (high range)
Specified accuracy (+/- Pa)	1	5
Zero stability (+/- Pa)[a]	0.5	2.5
Temperature effects	neglected	neglected
Pressure tap size	not considered	not considered
Burrs	not considered	not considered
Logger (+/-)[b]	0.001 Pa	0.005 Pa
Liquid plug	not considered	not considered
Total (+/-)	1.5 Pa	7.5 Pa

a. +/- 1 mV
b. +/-3 bV

$$\left(\frac{\Delta P_x}{P_x}\right)_k = \sqrt{\left(\frac{\Delta(\Delta P)}{\Delta P}\right)^2 + \left(\frac{\Delta L_k}{L_k}\right)^2} \qquad [4.17]$$

where <P is a given pressure difference between tappings, L is the distance between tappings and k indices a given pressure drop measurement (k = 1,2 or 3).

It is now possible to calculate the rms error on the pressure drop given by Equation [4.16] for given pressure differences <P. The results are shown in Figure 4–16.

It can be seen that there is little difference between the straight 60 mm sections. This shows that the averaging method is robust with respect to variations in pressure tap placement and setup changes. In the straight sections, for pressure differences higher than 100 Pa, which is the case for most of the experiments, the relative error on the pressure drop measured with the present tapping arrangement is less than 3.5%. For pressure differences in the order of 50 Pa, the error increases to 7%. For the vertical riser, the rms error is less than 3% for pressure differences larger than 50 Pa.

Based on the above considerations, the pressure drop measurement accuracy can be summarized in Table 4–21.

Table 4–21: Summary: pressure drop measurement accuracy

Section	Estimated accuracy (+/-)
Straight (60 mm i.d.)	3.5%
L-riser (50 mm i.d.)	3%

4.3.3 Phase fractions

At low liquid loading, the phase fractions are best determined by isolating a given length of the test section with quick closing valves, thereafter draining and measuring the volume of liquid collected. A picture of a quick closing valve with its drainage valve is given in Figure 4–28.

The liquid holdup is calculated from:

$$H_k = \frac{V_k}{V_{tot}} \qquad [4.18]$$

where k is the phase index (oil or water), V_k is the volume collected and V_{tot} is the total volume of the test section.

The quick closing valves are actuated manually. The closing time is evaluated to be maximum 0.5 s. The valves are connected together with a rigid steel wire and can be actuated simultaneously.

The volume V_{tot} needs to be carefully estimated to obtain a reasonable value of the liquid holdup. Quick closed section volumes are given in Table 4–7.

To determine V_k, the drained phase volume is collected in a graduated glass and measured with an accuracy of +/-1 ml. Special care is taken to also collect with a pig (Figure 4–28) the liquid fraction that remains on the wall after drainage. After pigging, the liquid volume still in the test section is considered to be less than 1 ml.

The estimated accuracy of the holdup measurement is summarized in Table 4–22.

Table 4–22: Summary: holdup measurement accuracy

Type of uncertainty	Value (+/-)	Comments
Fixed errors	1 ml	due to undrained liquid remaining in the test section
Accuracy	1 ml	accuracy of the graduated glass

4.3.4 Other measurements

4.3.4.1 Absolute pressure

Absolute pressure is monitored at vortex meter location (PE1.31) and at the test section inlet (PE1.24) as shown in Figure B–1. Absolute pressure cell specifications are given in Table 4–23.

Table 4–23: Absolute pressure transducer specifications

Name	Span	Calibrated range	Accuracy (+/-)	Time response
Siemens Sitrans P - 7MF4013	0-16 bara	0-7 bara	0.25%	<0.2 s

4.3.4.2 Temperature

Flow loop temperature is not regulated and varies with the room temperature. As the multiphase flow loop is situated in a closed laboratory, room temperature remains fairly constant at around 20^{o}C +/- 5^{o}C. Test section internal temperature is monitored during experiments (in the gas phase) with a chromel/alumel thermoelement and an Anritherm transducer of range -200 - 1200 ^{o}C and accuracy of +/- 0.1 ^{o}C. Temperature variations for the range at stake here are not considered to influence fluid properties significantly.

4.3.5 Flow loop control

Loop instruments, at the exception of temperature sensors and dosage pumps, can deliver a 4-20 mA signal. All instruments are wired to a central cabinet where their output is converted into a (0.8-4.0 V) voltage signal with a 200 kN resistor. This voltage is further directed to either an external logging instrument (HP34970 switch unit) from which it is digitized and sent to a PC for storage. The HP34790 switch unit has built-in electronics for various signal processing such as filtering or averaging. The switch unit is employed for logging slow varying signals such as flow rates, absolute pressures and differential pressures, typically at 1-2 Hz. Instrument specifications are given in Table 4–24.

Table 4–24: Specifications for logger HP34970

Specification	Value
Minimum sampling period	0.4 s
Number of channels	20
Buffer memory	50 000 readings
Accuracy[a]	+/- 3 bV

a. voltage reading for short circuited input

The user interface of the flow loop has been designed using the software Labview. Instrument setup, on-line visualization of signals and a rough post processing are among the interface capabilities. Log files are exported from the Labview interface as text files and stored on the hard-disk for later post-processing.

4.4 Operation of the flow loop and experimental procedure

The majority of the experiments performed in this thesis are steady-state measurements of pressure drop and phase fractions at low liquid content. Some experiments are also performed in a transient mode for which pressure drop and phase fractions are logged in the period following a fluid supply shut-down.

It has been observed that measurements repeatability and accuracy can be improved by following the same procedure for all experiments of the same kind. In the following, the experimental procedure is presented and the achieved level of repeatability shown. It is also explained how some difficulties related to the measurements have been identified and solved.

4.4.1 Experimental procedure for steady-state measurements

The experimental procedure for the steady-state measurements of phase fractions and pressure drop is described below. The experiments themselves are discussed in Chapter 6 and Chapter 7.

The experimental procedure is as follows:

1. A test section is selected and set in the horizontal position.
2. The instrument zeros are checked and adjusted if necessary.
3. The liquid flow rates are selected and the liquid pumps run for 5 minutes during which liquid flow rates are progressively lowered to the desired value. As a result, the liquid wetted perimeter is initially water wet.
4. The air flow rate is selected and air is progressively introduced up to the desired flow rate so as to avoid the formation of transient slugs and/or wetting of the upper pipe wall.
5. The test section is set to desired inclination.
6. The fluids are circulated in the test section for at least 30 minutes, or more if necessary, until steady-state conditions are reached.
7. The pressure taps are purged for stagnant liquid plugs and instruments are sampled for 10 minutes.
8. The quick closing valves are closed and the flow is shut down.
9. The quick closed section is drained and pigged and the collected volumes of liquid are measured in a graduated glass.
10. The rest of the test section is pigged and washed with water.
11. The next measurement is prepared and re-started from step 1.

Repeated experiments have been conducted to test the repeatability of the measurements performed in accordance with this experimental procedure. Results are summarized in Table 4–29 and plotted graphically in Figure 4–24 and Figure 4–25.

As shown in Figure 4–24, holdup measurement repeatability (precision) is kept within +/- 5% for holdup larger than 0.008 (100 ml) but scatter increases to over 10% for holdups smaller than 0.002 (25 ml). For the pressure drop, precision is in average kept under 2% for the measured range.

The lack of precision in holdup measurements develops as:

- Simultaneous quick closing of the valves is not achieved.
- The weight of fixed errors (liquid still trapped in the test section after drainage) in the total measurement increases. Fixed errors are greatly reduced by pigging the quick closed section in order to remove hanging droplets and thin liquid films at the pipe wall.
- The number of intermittent interfacial structures (waves or slugs) increases. The holdup becomes more dependent on the timing of the quick closing operation and on how many of the intermittencies are being trapped. In case of large amplitude waves bridging the entire pipe cross section or well developed slugs, the holdup measurement is repeated three times and the results averaged.

Other factors influencing measurement repeatability are:

- The time necessary for reaching the steady-state regime.
- The fluid contamination in the separator.
- The instability of the air supply.
- The contamination of the inner wall surface.
- The existence of liquid plugs in pressure tap hoses.

4.4.1.1 Steady-state conditions

Sufficient time is allowed for measurements to be representative of steady-state conditions. A test was carried out to estimate the necessary establishment time. Results are shown in Figure 4–17. There is a slight sensitivity of holdup and pressure drop with time up to 60 minutes but measured values are established within measuring accuracy after 30 minutes.

An optimal check for steady state conditions for each experiment is to measure the mass flow rate at the pipe outlet as performed by Hart et al. (1989) and Grolman (1994). In this thesis, it has been decided instead to start logging the pressure drop after a minimum waiting time of 30 min. and actuate the quick closing valves after a minimum elapsed time of 40 min. Based on the previous test, this is considered to be sufficient waiting time. Naturally, on-line plots of pressure drop time series and visual observations are always used as additional helps for deciding on whether steady-state conditions have been reached.

4.4.1.2 Fluid contamination in the separator

The fluids in the separator can be observed through an observation window. It has been detected, during the experimental campaigns, a biological contamination at the interface. The exact origin of this contamination however could not be determined. Preliminary analysis showed that it was neither bacterial nor fungal but probably resulted from an algae thriving in water and finding its nutrient in oil.

As long as there is little agitation in the separator tank, the algae colony does not spread and stays at the oil-water interface region. In the experiments of this thesis, small liquid flow rates are involved which do not induce important mixing of the fluids in the separator. In addition, fluid intake is kept at good distance from the interface. To restrict fluid contamination to a minimum, the content of the separator is replaced and the separator cleaned at regular intervals.

4.4.1.3 Instability of the air supply

Despite pressure regulating valve PZV1.03 and buffer tank U1.26, pressure oscillations in phase with compressor C1.02 cycles are not totally attenuated. This results in oscillations of the gas flow rate around its mean value as illustrated in Figure 4–26. The oscillations have a period of around two minutes. This situation is taken into account by allowing sufficient logging time to encompass several oscillation periods. Logging data is later processed so as to filter out all data that is not around the mean gas velocity plus/minus a tenth of the measuring accuracy.

4.4.1.4 Contamination of the pipe wall

It has been observed that the state of the pipe inner wall surface (clean or contaminated) can significantly influence the steady state measurements at low liquid loading, especially in the acrylic pipe. This is discussed further in Chapter 7. Special care has been taken to keep the pipe surface clean for adsorbed substances, at least at a macroscopic level. After each experiment, the entire pipe length is pigged and washed with clear water.

4.4.1.5 Liquid influx in pressure taps

As mentioned earlier, the presence of a liquid plug in the pressure tappings or the pressure tubes results in a measurement inaccuracy exceeding the expected accuracy. In general, the upper pipe wall where pressure intake holes are drilled is dry, except in the atomization regime where droplets are present and tend to flow into the pressure taps.

To ensure repeatable measurements, a purge system has been constructed where pressurized air is blown counter-current into the pressure tubing to clear them for stagnant liquids. This purge is systematically performed prior to pressure drop measurements.

In addition, the fact that three simultaneous differential pressure measurements are performed allows to detect pressure signals abnormally deviating from the others. A measu-

rement is considered acceptable when the three dp signals are deviating from each other by less than the expected measurement accuracy.

4.4.2 Experimental procedure for transient measurements

Transient two-phase flow measurements have been performed in this thesis where the liquid flow rate is shut down at constant gas flow rate and the pipe wall is allowed to dry up for liquids. These experiments are described in Chapter 5.

Experiments are conducted according to the following experimental procedure:

1. A test section is selected.
2. Instrument zeros are checked and adjusted if necessary.
3. The gas flow rate and the initial liquid flow rate are selected.
4. The fluids are circulated for at least 10 minutes.
5. The pressure taps are purged for stagnant liquids and instrument logging is started.
6. The liquid supply inlet valve is shut down and the clock watch is started simultaneously.
7. At desired time, quick-closing valves are actuated and the air flow rate is shut down.
8. The quick closed section is drained and pigged and the collected volumes of liquid are obtained from weighing on a Mettler-Toledo balance of precision +/- 0.1 g.
9. The rest of the test section is pigged and washed with water.
10. The next measurement is prepared and restarted from step 1.

Experiments are repeated, changing the elapsed time before quick closing until the pipe wall is entirely dry. This occurs when the measured pressure drop is equal to the pressure drop calculated for dry gas flow from the Blasius equation, Equation [3.7]. All experiments are carried out at ambient pressure and temperature.

Repeated experiments are performed to test the performance of this experimental procedure. The main concerns are to:

- Check that the pressure drop trace is repeatable from one experiment to another.
- Check that the holdup measured in the test section for identical elapsed time before quick closing is within expected accuracy.

A test with air and oil is performed where three identical experiments are conducted in accordance with the experimental procedure explained above. Elapsed timed before quick closing is set to 60 seconds. Test results can be seen in Figure 4–27 and are summarized in Table 4–25.

Table 4–25: Repeated experiments, transient measurements

Fluids	U_{SG}, m/s	Number of runs	Pressure drop at t = 60 s, Pa/m	Std (pressure drop), %	Holdup at t = 60 s, -	Std (holdup), %
Air-Exxsol D80	30	3	-379	2.1	0.014	4

Comparing standard deviations (std) for the pressure drop traces and the holdup with expected accuracy, these results are found to be acceptable.

Factors influencing measurement repeatability are:

- The instability of the air supply.
- The contamination of the wall surface.
- The existence of liquid plugs in pressure tap hoses.

Concerning the air supply instability, precautions are taken to start the transient experiment at identical periods in the oscillation cycle.

As for steady-state measurements, contamination of the pipe wall surface is kept to a minimum by regularly pigging the pipe and washing the inner wall with fresh water.

Formation of liquid plugs in pressure intake lines is a greater problem in the vertical pipe due to the presence of an annular liquid film at the wall. This problem is tackled by periodically isolating the differential pressure cells and purging the trapped liquid. Two simultaneous readings of the pressure drop are also taken and averaged. This allows to reject measurements when the difference between the two measured pressure drops is larger than the expected measuring accuracy.

4.5 System tests

System tests have been performed to evaluate overall flow loop performance. Tests include:

- Single phase air flow tests.
- Two-phase air/water flow tests.

4.5.1 Single phase flow tests

Single phase air flow tests are systematically performed prior to experiments in a new test section or after changes in the experimental setup. From test results, it is possible to check the accuracy of the pressure drop measurement and obtain the hydraulic roughness of the test section.

Figure 4–18 to Figure 4–21 show results of such tests. The gas friction factor is calculated from pressure drop measurements and is compared to Håland's explicit equation, Equation [3.11]. In each case, it is possible to compute an hydraulic roughness that gives a satisfactory fit with the measured values.

In the case of the L-riser test section, the fit can not be sustained down to small air Reynolds number. The reasons for this mismatch are:

- The test section being of i.d. 50 mm, smaller volumetric flow rates of air are needed to sustain the same superficial air velocities as in the 60 mm sections. This results in the vortex flow meter operating in its low range with reduced accuracy. As a consequence, superficial gas velocity in the L-riser below 25 m/s are not considered in the experiments.
- The pressure drop is measured over a 1.0 m long section of pipe. This results in smaller pressure differences and pressure transducers operating in their low range with reduced accuracy.

It is also possible to obtain a value of the hydraulic roughness for either the entire test section or a single pipe section. Test sections are made of assembled pipe sections, quick closing valves, pressure taps, drainage taps and, in the case of the acrylic test sections, impedance ring probes. These equipment generate an additional hydraulic roughness compared to that of single pipe sections. It is possible to quantify these effects by varying the locations of the pressure tapping points. Table 4–26 summarizes hydraulic roughness for the entire test sections and for single pipe sections.

Table 4–26: Summary of back calculated hydraulic roughness

Test section	Test section hydraulic roughness, εm	Single pipe section hydraulic roughness, εm
Acrylic 60 mm i.d.	31	4
Steel 60 mm i.d.	9	5
Epoxy 60 mm i.d.	4	1
Acrylic 50 mm i.d.	4	4

4.5.2 Two-phase flow tests

Espedal (1998) performed air-water two-phase flow measurements of steady-state pressure drop and holdup in an identical 60 mm acrylic pipe to that of the present flow loop. He obtained pressure drop from an average of three differential pressure measurements and phase factions with the quick closing valve method.

Selected air-water experiments from Espedal (1998) were repeated in the flow loop and comparisons with his data are summarized in Table 4–27. Plots are provided in Figure 4–22 for the pressure drop and Figure 4–23 for the holdup. Repeated and source data are found to agree within +/- 5%.

Table 4–27: Results of comparisons with Espedal (1998)

Exp #[a]	U_{SG}, m/s	U_{SW}, m/s	θ, deg.	H_{source}, %	$H_{meas.}$, %	err, %	dP/dx_{source}, Pa/m	$dP/dx_{meas.}$, Pa/m	err, %
fn0396	14.2	0.012	0.5	2.1	2.0	-6.0	70	69	-0.5
fn0412	8.0	0.030	0.5	10.9	10.5	-4.3	37	37	0.7
fn0167	14.2	0.023	-0.5	3.1	2.9	-4.8	83	82	-1.0
fn0118	9.0	0.020	-0.5	4.7	4.6	-0.7	29	27	-6.8
fn0125	13.1	0.020	-0.5	3.1	2.9	-6.8	68	68	-0.4
fn0154	8.1	0.024	-0.5	5.7	5.5	-4.8	22	23	1.3
fn0402	12.0	0.036	0.5	6.1	5.4	-11.5	71	73	3.6
fn0397	14.1	0.024	0.5	3.3	3.4	1.4	83	92	9.6
fn0398	12.0	0.012	0.5	2.7	2.4	-9.4	51	53	4.0
fn0162	12.2	0.012	-0.5	2.2	2.3	2.5	51	52	2.4

a. Refer to experiment numbers in Espedal (1998)

4.6 Summary

In this chapter, the multiphase flow loop used in this thesis and the type of measurements performed have been described. The multiphase flow loop can operate with air, water and oil at ambient temperature and pressure. Fluids have been chosen for their availability and innocuity. The oil is Exxsol D80 which is a light condensate, immiscible with water, with fast separation capabilities. Four test sections are used in this thesis, of varying inclination with the horizontal and made of different materials. An epoxy coated steel section has been constructed to test the effect of coating properties on the flow. Test sections exhibit different physical roughness and water contact angles which gives the possibility to test the sensitivity of the flow to these properties.

Very low liquid flow rates are provided by dosage displacement pumps which have been calibrated so as to obtain the average flow rate from set piston length and frequency. The measuring accuracy of the instrumentation used in this work has ben evaluated. System tests including repeatability tests, single and two-phase flow tests, have been conducted to validate the experimental procedure for steady-state and transient measurements and confirm the instrument accuracy.

A final summary of measurement accuracy is provided in Table 4–28.

Table 4–28: Summary of measurement accuracy

Measurement	Instrument	Accuracy (+/-)	Comment[a]
Water superficial velocity	elmag	0.5%	for $0.29 < U_{SW} < 3.53$ m/s
	elmag	0.5%	for $0.02 < U_{SW} < 0.35$ m/s
	dosage pump	1.0%	for $0.0075 < U_{SW} < 0.0098$ m/s
		1.4%	for $0.0049 < U_{SW} < 0.0075$ m/s
		3.6%	for $0.0024 < U_{SW} < 0.0049$ m/s
		1.8%	for $0.0008 < U_{SW} < 0.0024$ m/s
		7.0%	for $0.0002 < U_{SW} < 0.0008$ m/s
Oil superficial velocity	coriolis	0.2%	for $0.09 < U_{SO} < 4.91$ m/s
	coriolis	0.2%	for $0.01 < U_{SO} < 0.09$ m/s
	dosage pump	1.6%	for $0.0100 < U_{SO} < 0.0127$ m/s
		1.2%	for $0.0068 < U_{SO} < 0.0100$ m/s
		0.5%	for $0.0033 < U_{SO} < 0.0068$ m/s
		5.6%	for $0.0013 < U_{SO} < 0.0033$ m/s
		7.0%	for $0.0004 < U_{SO} < 0.0013$ m/s
Air superficial velocity	coriolis	1%	for $0.01 < U_{SG} < 6.5$ m/s
	vortex	2%	for $3.2 < U_{SG} < 39.3$ m/s
Pressure drop (60 mm test section)	3 dp cells	3.5%	Effect of temperature, tap hole size and burrs are not considered
Pressure drop (50 mm test section)	2 dp cells	3%	Effect of temperature, tap hole size and burrs are not considered
Phase fractions	quick closing valves	2 ml[b]	This corresponds to the following relative accuracy in the 60 mm i.d. test sections: +/- 10% for $H_k < 0.008$ +/- 5% for $0.008 < H_k < 0.015$ +/- 1% for $H_k > 0.015$
Absolute pressure	pressure cell	0.2%	-

Table 4–28: Summary of measurement accuracy

Measurement	Instrument	Accuracy (+/-)	Comment[a]
Pipe inclination	inclinometer	0.1 deg.	-
Temperature	thermoelement	0.1 ^{o}C	-

a. Superficial velocities are given in a 60 mm i.d. pipe
b. Including the fixed error due to liquid remaining in the test section after pigging

Table 4–29: Repeated experiments - Steady-state measurements

pipe	U_{SG}, m/s	U_{SL}, m/s	WF, %	j, deg.	Number of experiments	H_W[a], 10^{-6} m^3	std, %	H_O[a], 10^{-6} m^3	std, %	H_{tot}[a], 10^{-6} m^3	std, %	dP/dx[a], Pa/m	std, %
Acrylic 60 mm i.d.	14.8	0.0059	20	0	4	23	8.0	153	1.6	175	1.6	79	1.0
	14.8	0.0059	20	0	2	23	6.1	150	0.9	173	1.6	80	0.4
	7.5	0.0059	0	+1	2	-	-	-	-	-	-	26	0.1
	7.5	0.0059	100	+1	2	-	-	-	-	-	-	37	0.9
Steel 60 mm i.d.	14.8	0.0059	20	0	3	51	3.4	120	8.4	171	6.7	58	1.4
	14.8	0.0059	50	0	2	93	1.5	75	0	168	0.8	58	2.7
	14.8	0.0059	50	+1	2	104	5.4	83	16.3	187	4.2	60	5.2
	14.8	0.0059	90	+1	2	150	1.9	16	31.9	16.6	1.3	64	2.0
	7.5	0.0059	0	+1	2	-	-	-	-	-	-	24	0.9
	7.5	0.0059	90	+1	2	-	-	-	-	-	-	60	5.2

a. Average values

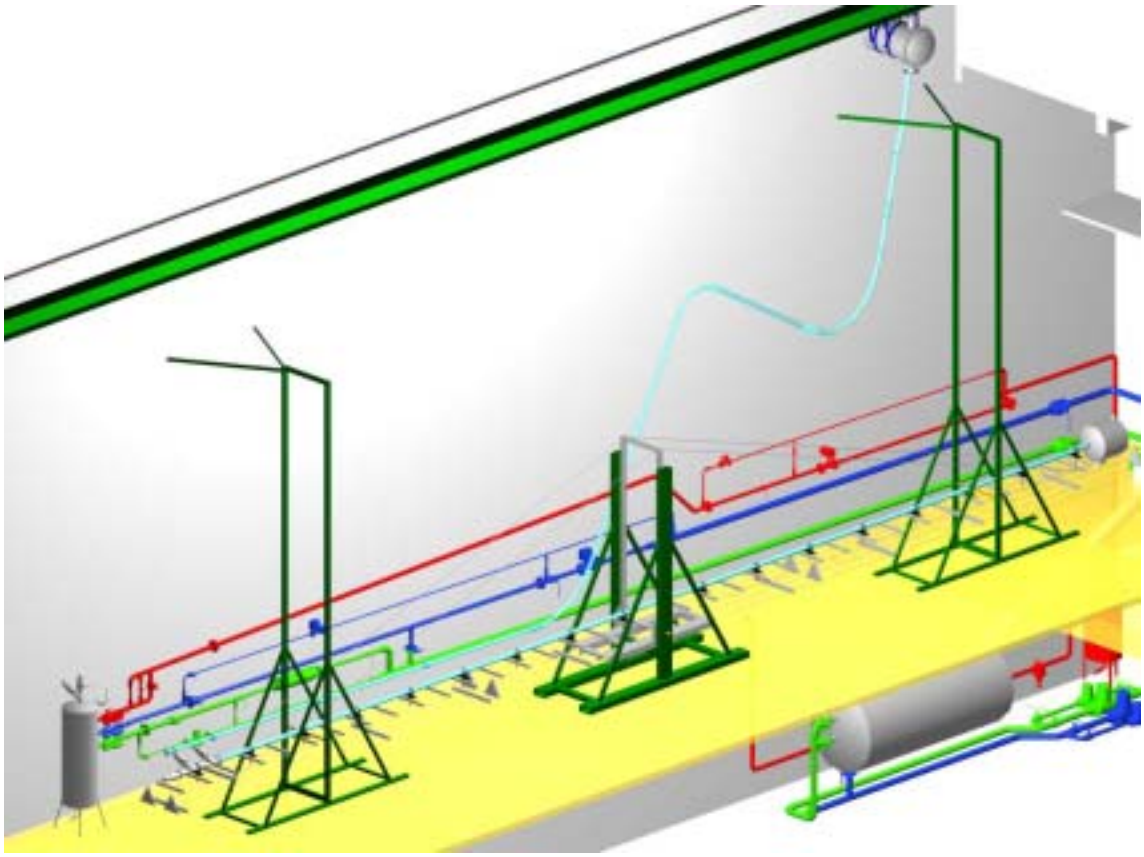

Figure 4–1: Three-dimensional view of the NTNU multiphase flow loop. The straight test sections on their supporting beam are located on the first floor. The main separator tank and pumping equipment are placed in the basement

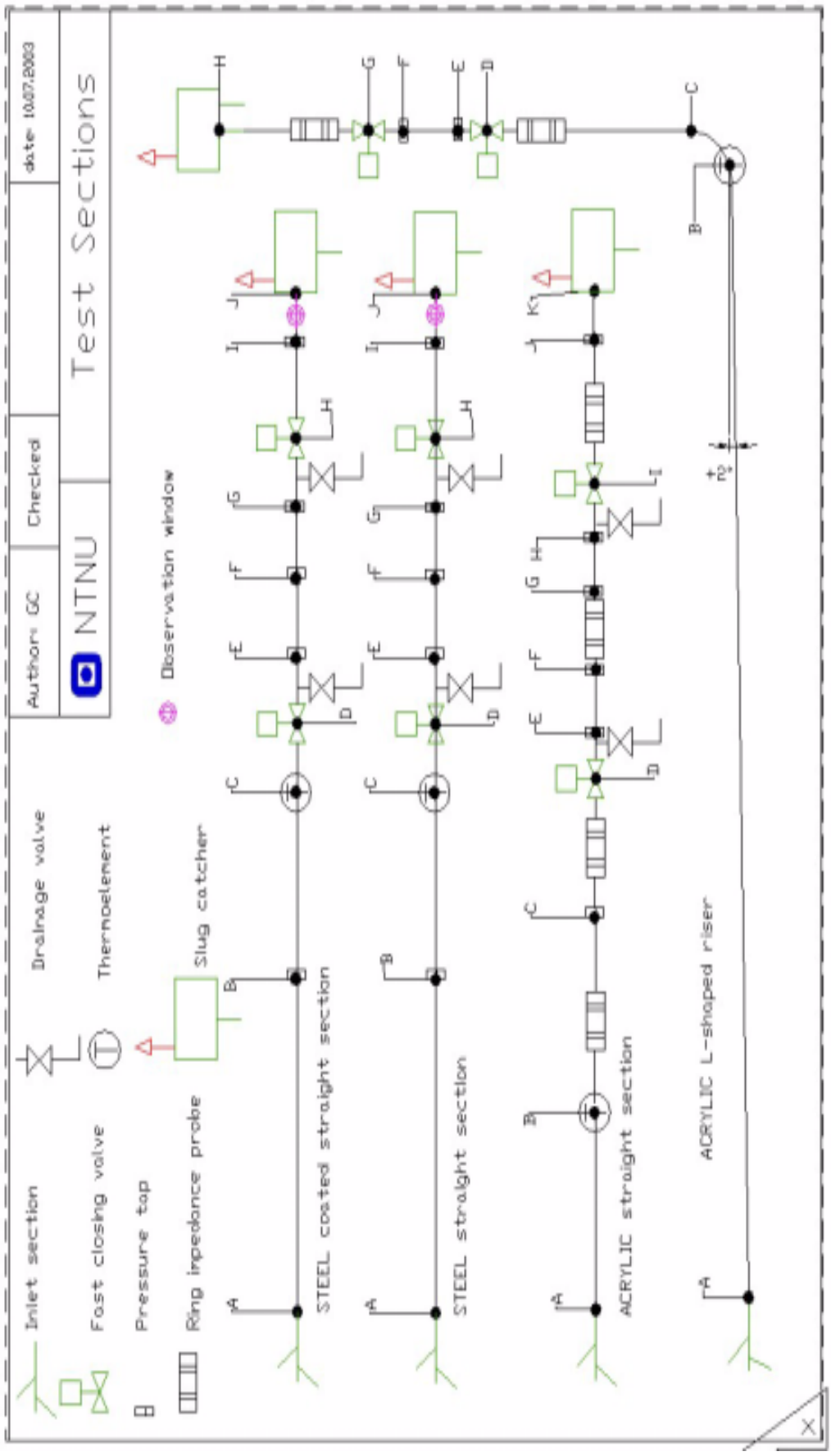

Figure 4–2: Schematic of the test section arrangements. Dimensions are given in Table 4–4, Table 4–5 and Table 4–6

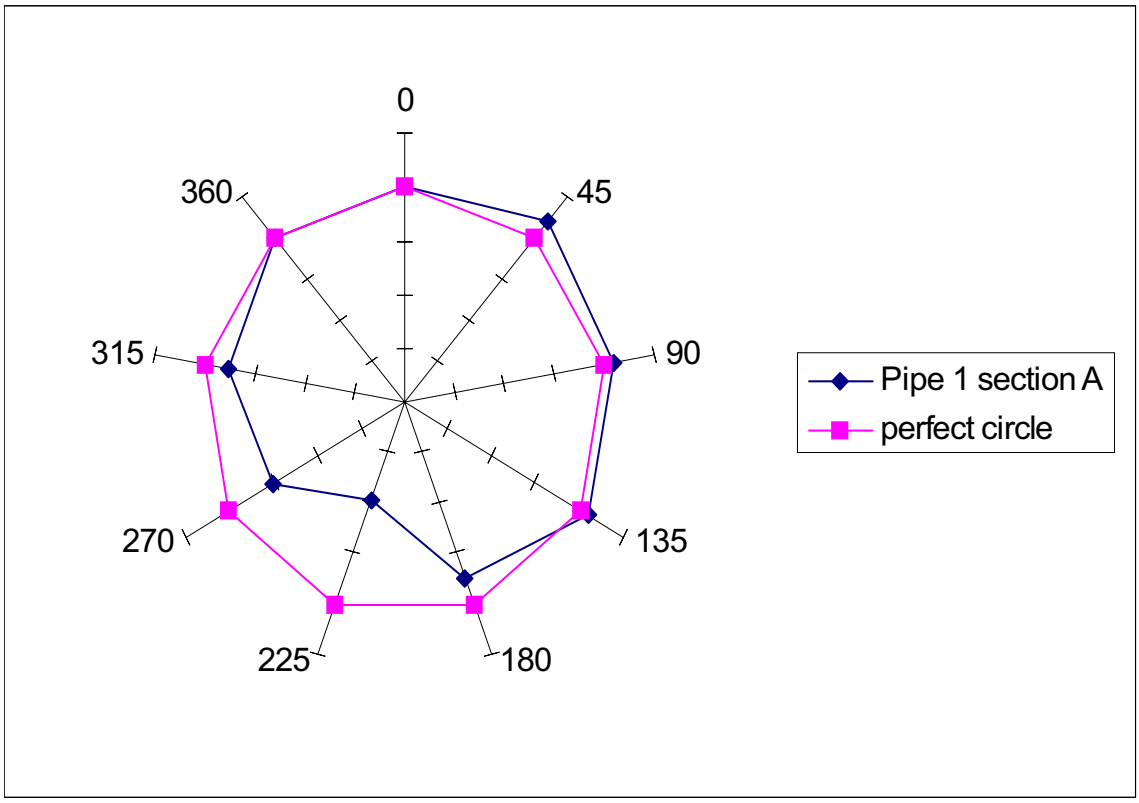

Figure 4–3: Shape plot for pipe 1 (outlet). 1 scale division = 20 bm

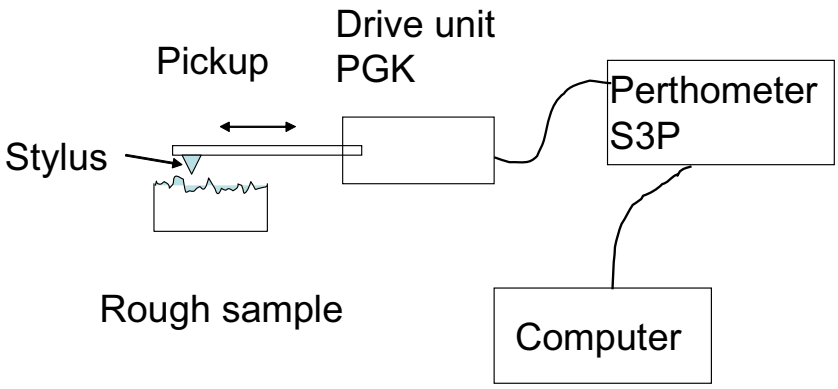

Figure 4–4: Schematic representation of the surface roughness measurement setup

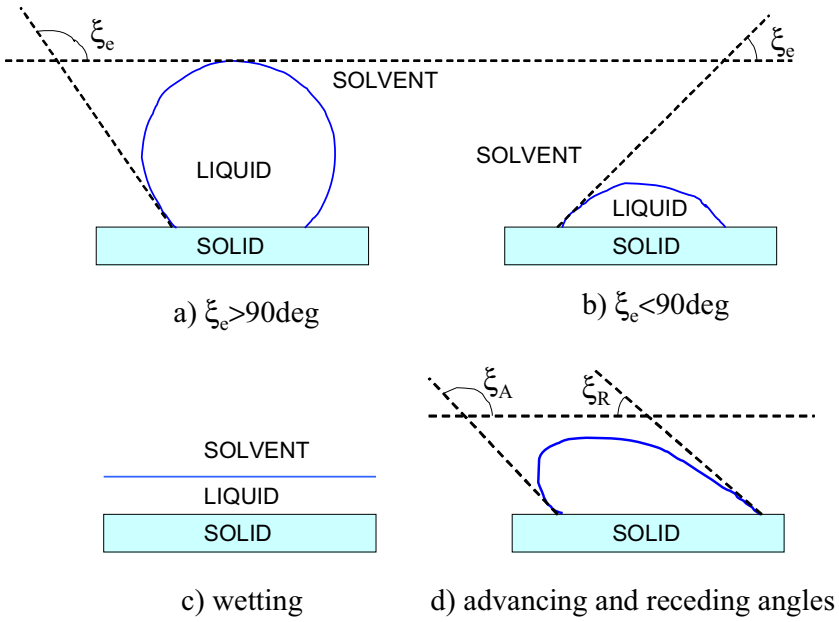

Figure 4–5: Definition of equilibrium (static) contact angles. a) and b) partial wetting with b) better wetting than a). c) corresponds to complete wetting. d) shows advancing and receding angles

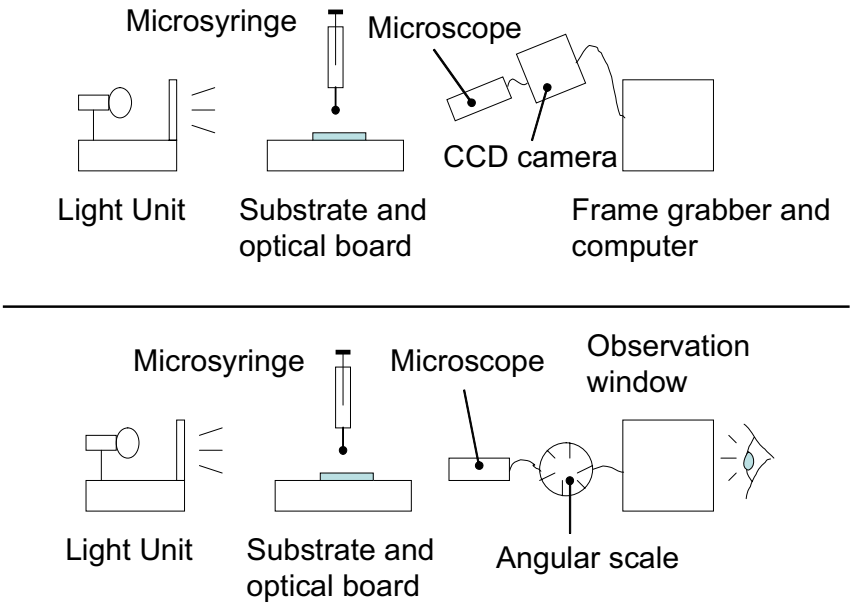

Figure 4–6: Schematic representation of the contact angle measurement setup. Top: image recognition software; Bottom: visual measurement with a goniometer

.

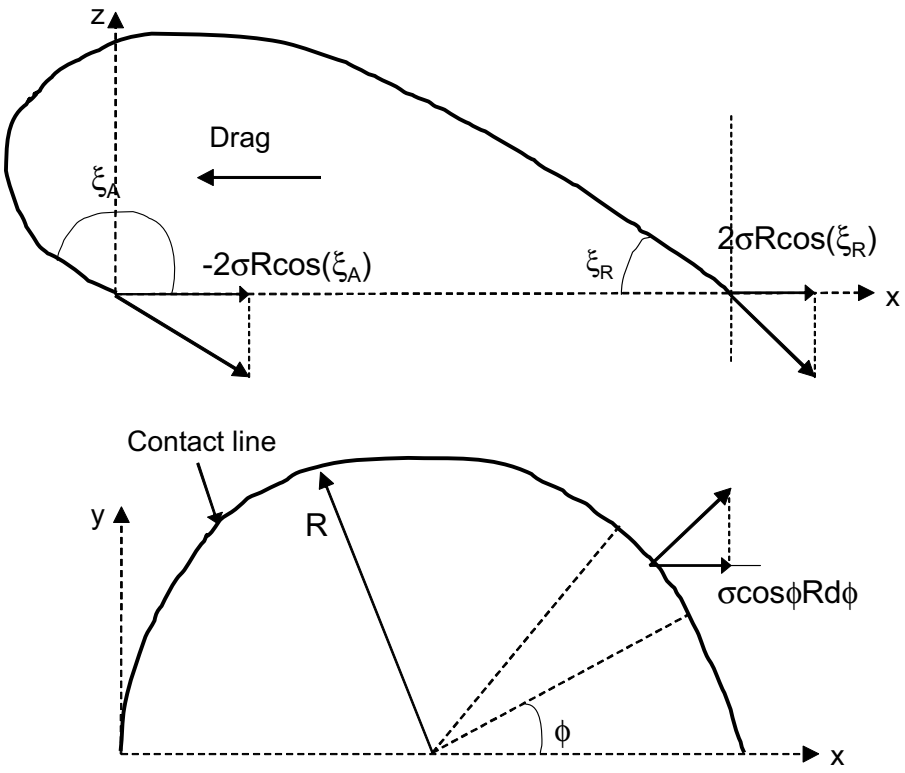

Figure 4–7: Surface tension forces acting on a static water droplet submitted to a drag force in the x-direction. ξ_A and ξ_R are the advancing and receding contact angles

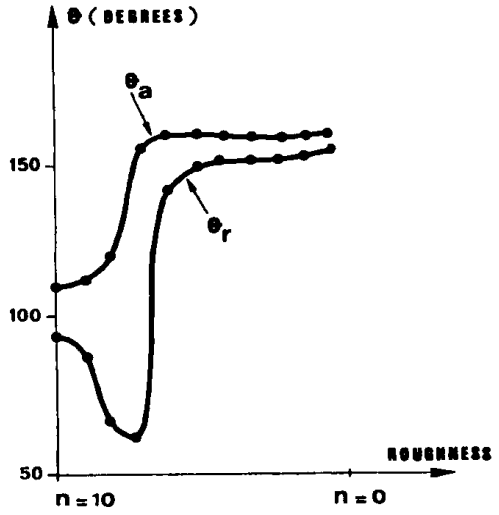

Figure 4–8: Advancing and receding angles for water on fluorocarbon wax. A rough surface is obtained by spraying the wax. It is then made smoother by heating in an oven. The number n on the horizontal scale (0, 1.0, 10) refers to the number of successive heat treatments (from De Gennes 1985)

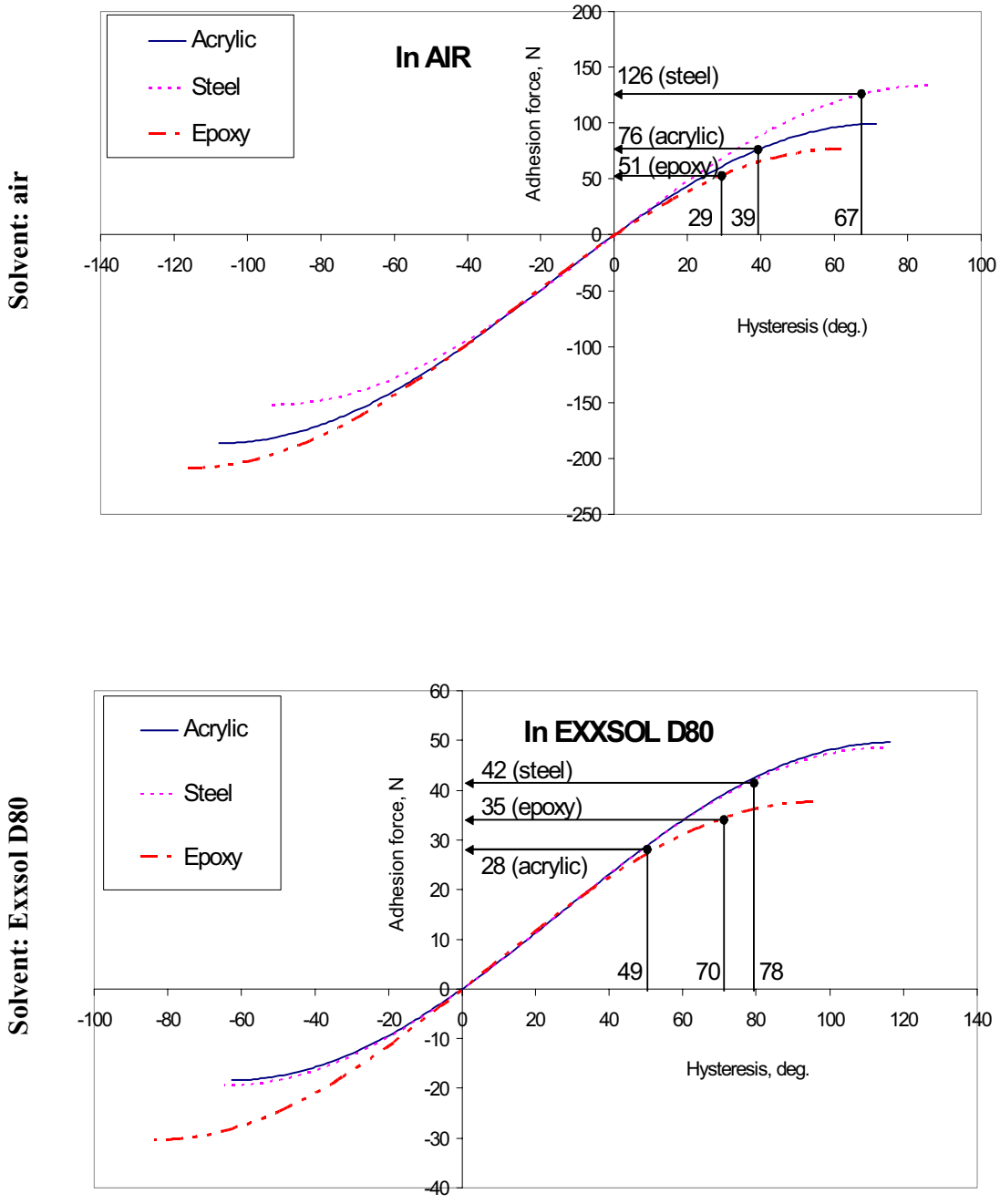

Figure 4–9: Adhesion force on three different solid surfaces for laboratory water droplets of radius unity

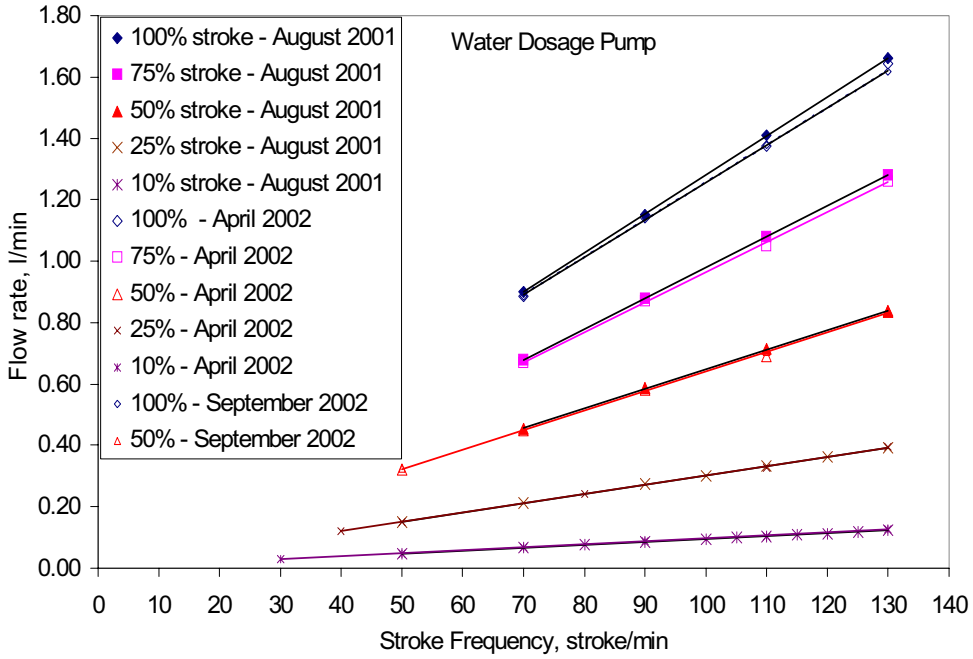

Figure 4–10: Calibration curves for the water dosage pump. The straight lines are linear interpolations of the calibrated data for various piston courses

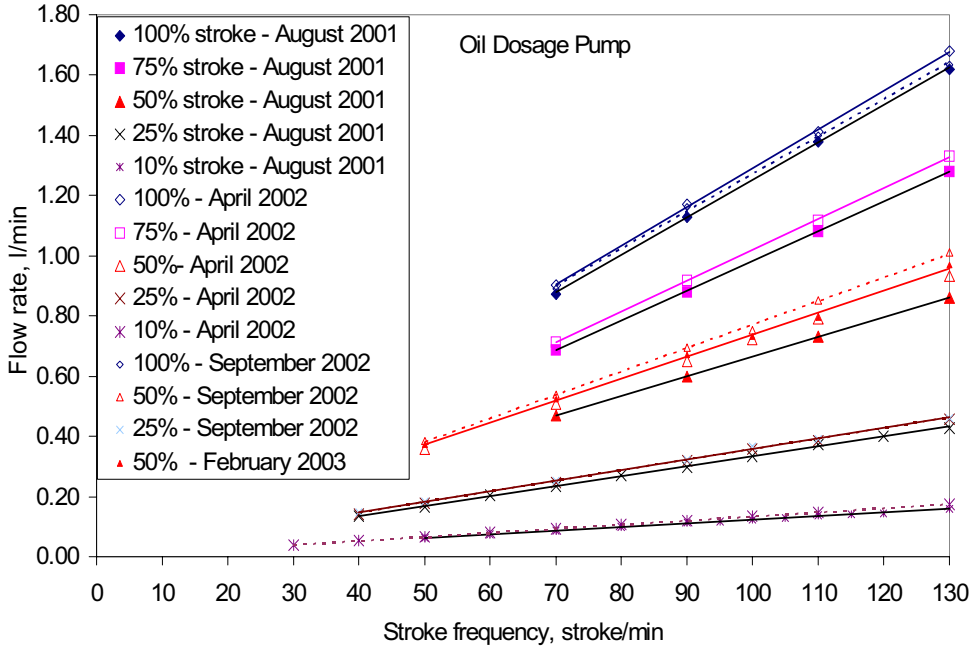

Figure 4–11: Calibration curves for the oil dosage pump. The straight lines are linear interpolations of the calibrated data for various piston courses

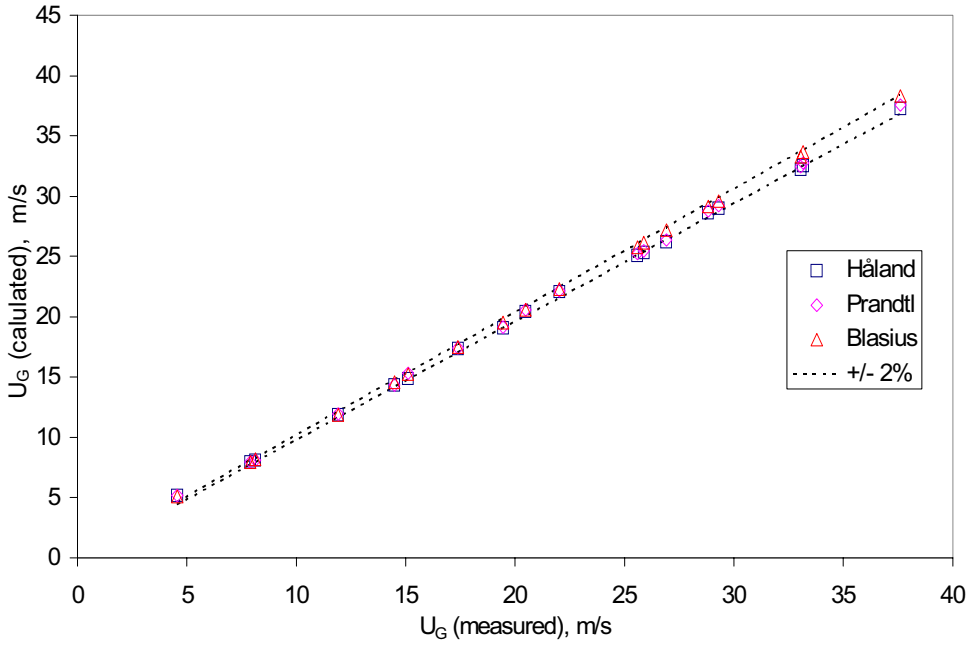

Figure 4–12: Calculated versus theoretical gas velocities in the 60 mm acrylic test section for the Prowirl 77 vortex meter. The dashed lines represent a variation of +/- 2% around the measured values

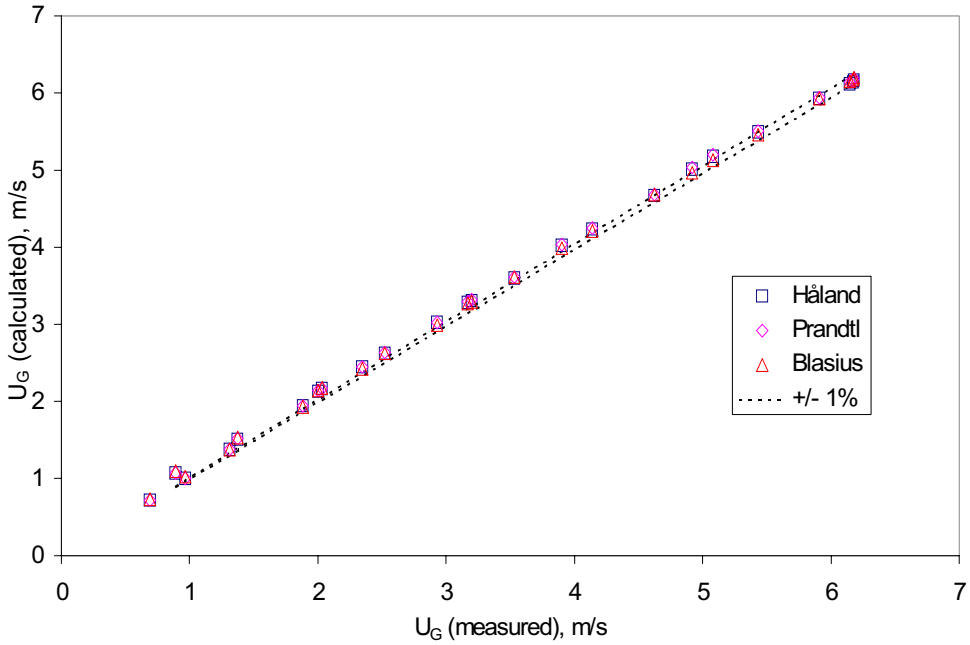

Figure 4–13: Calculated versus theoretical gas velocities in the 60 mm acrylic test section for the coriolis meter CMF025. The dashed lines represent a variation of +/- 1% around the measured values

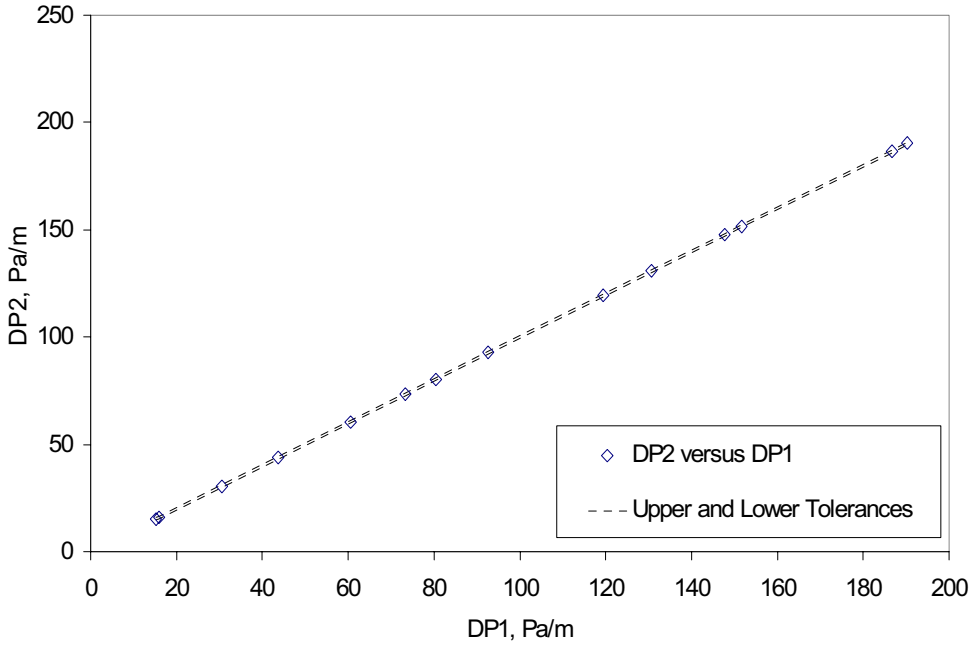

Figure 4–14: Comparison of the two FHC transmitters. The dashed lines represent upper and lower acceptable variations based on factory specifications

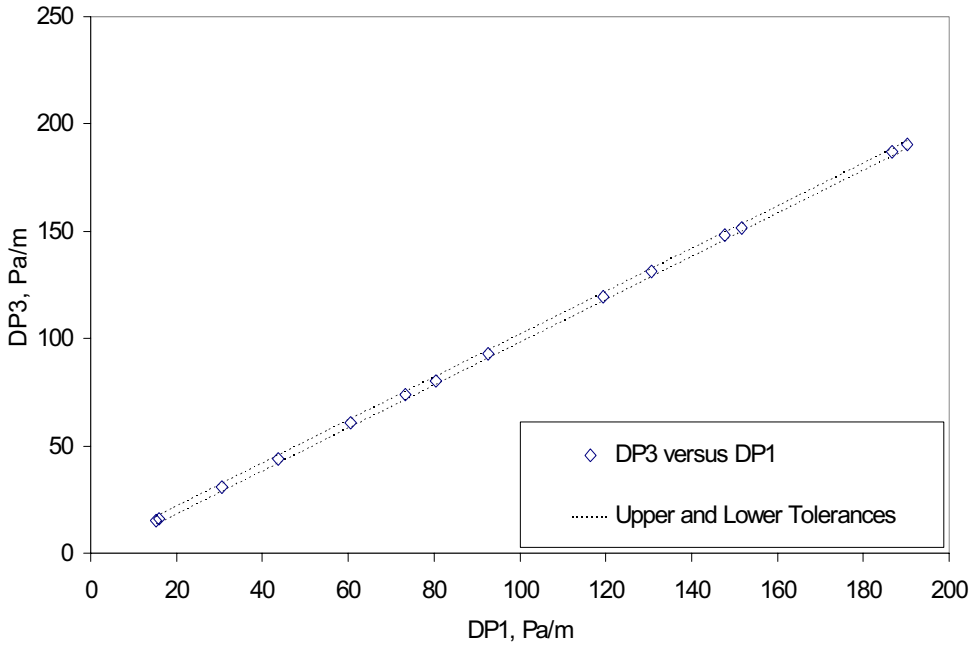

Figure 4–15: Comparison of one FHC transmitter with the FKC transmitter. The dashed lines represent upper and lower acceptable variations based on factory specifications

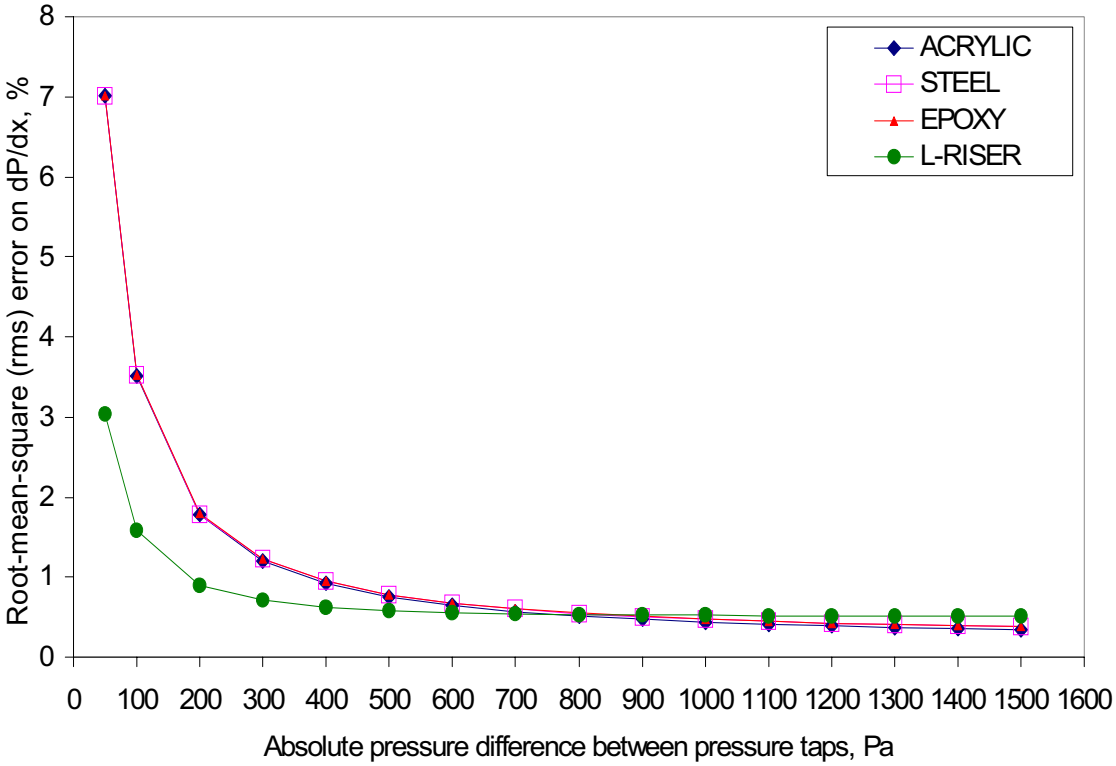

Figure 4–16: Error on the pressure drop measurement

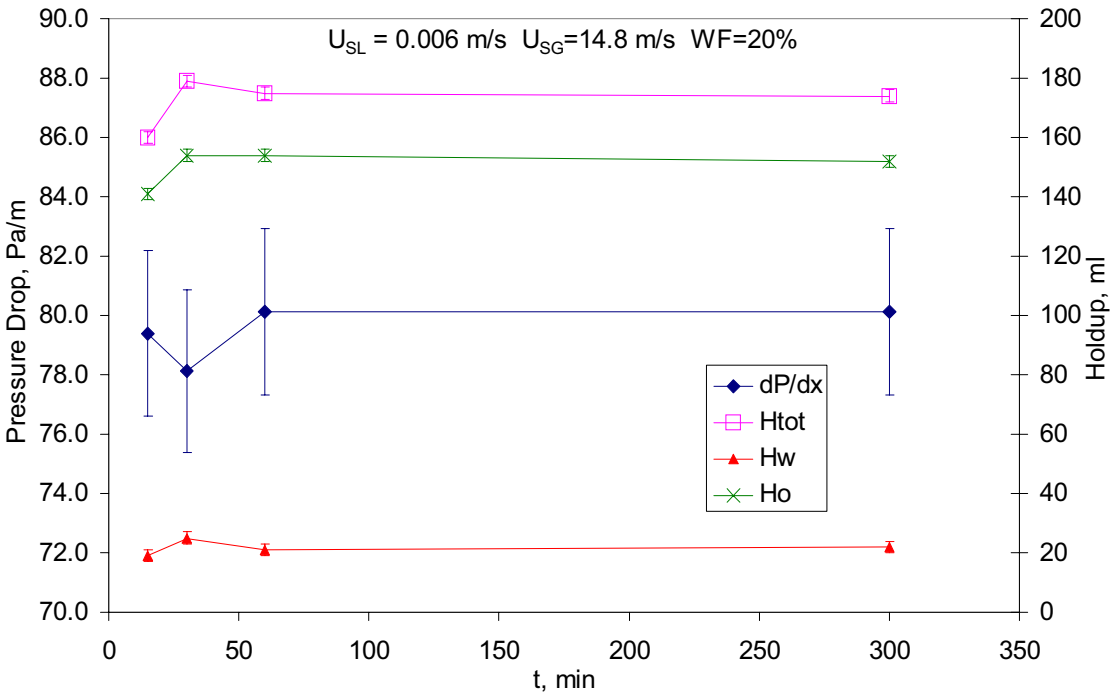

Figure 4–17: Sensitivity of measurements with experience time. The error bars represent the measuring accuracy

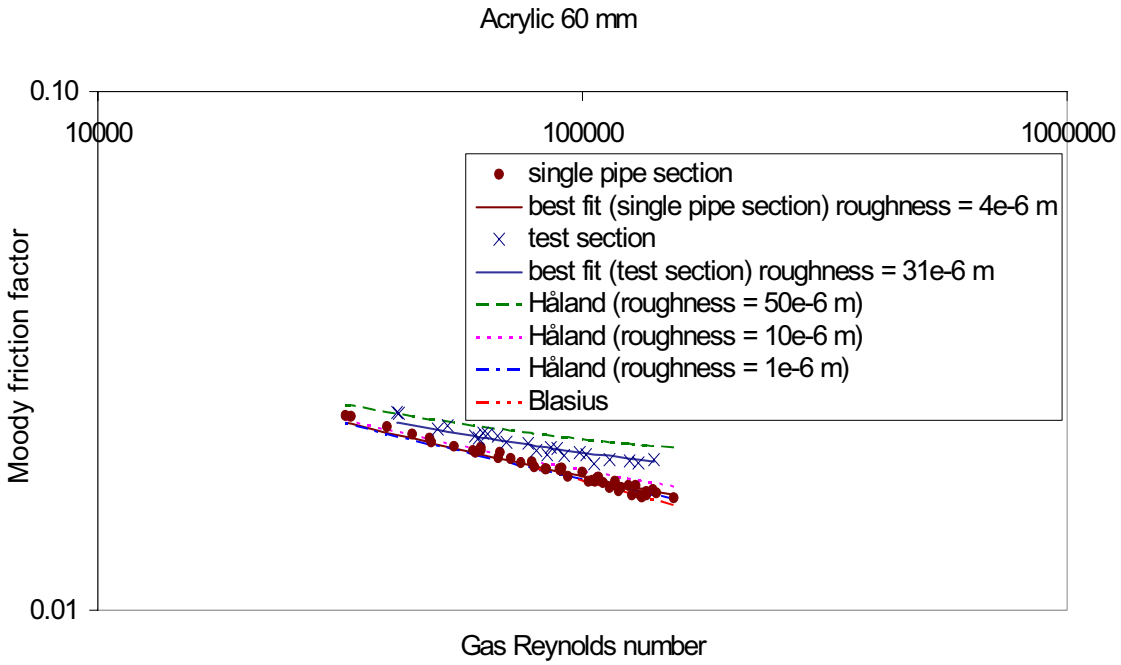

Figure 4–18: Measured friction factor compared with known correlations for single phase air in the 60 mm horizontal acrylic pipe

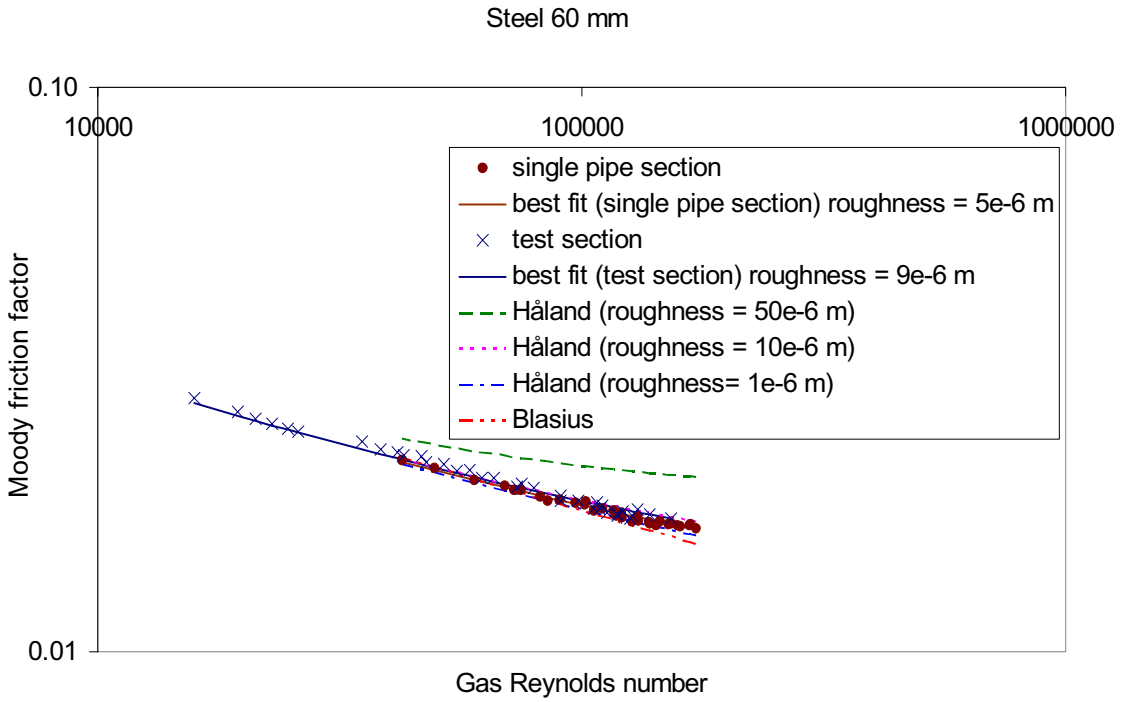

Figure 4–19: Measured friction factor compared with known correlations for single phase air in the 60 mm horizontal steel pipe

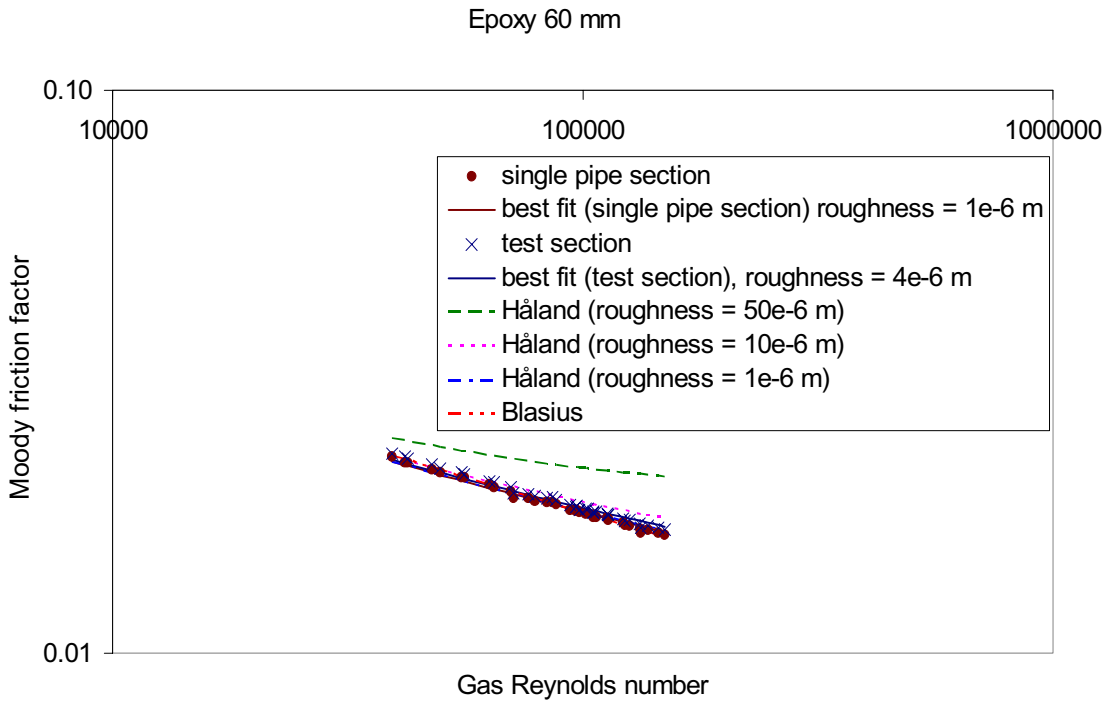

Figure 4–20: Measured friction factor compared with known correlations for single phase air in the 60 mm horizontal epoxy coated steel pipe

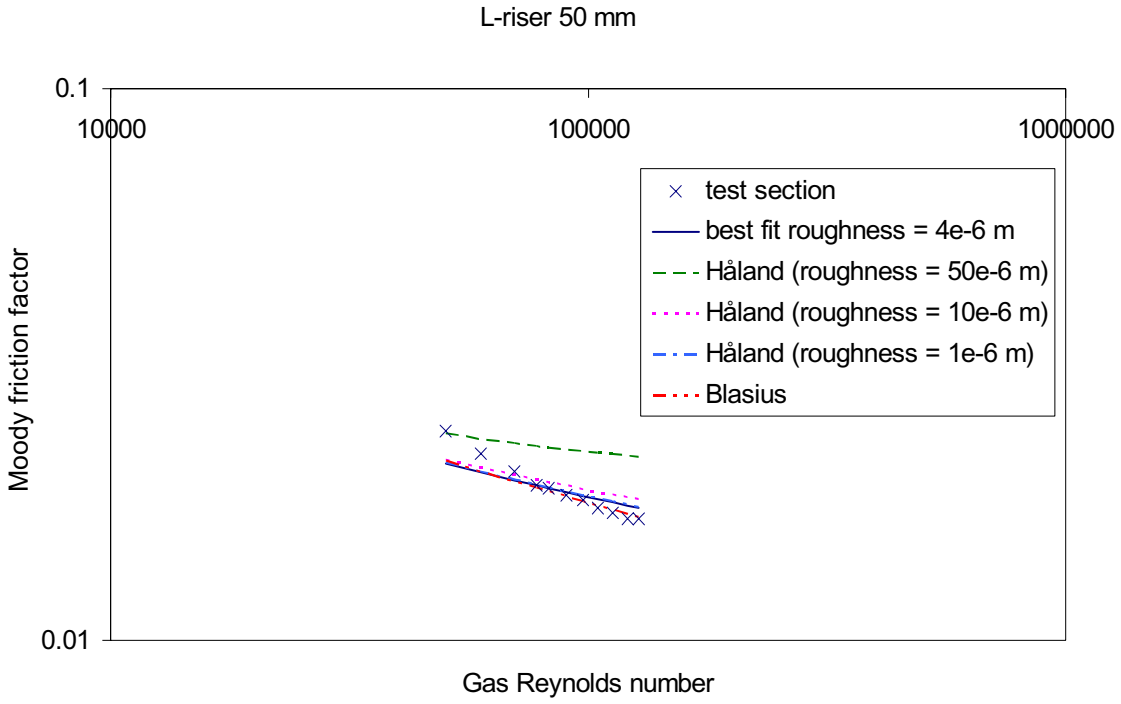

Figure 4–21: Measured friction factor compared with known correlations for single phase air in the 50 mm vertical acrylic riser

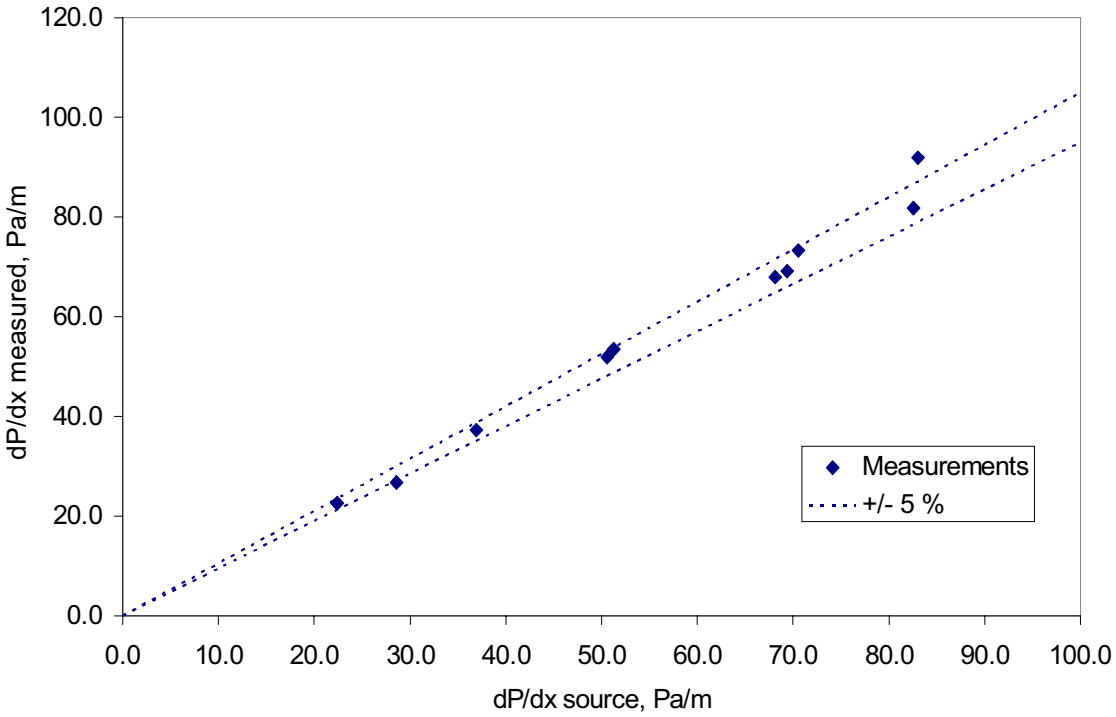

Figure 4–22: Pressure drop compared with Espedal (1998) for 10 repeated measurements

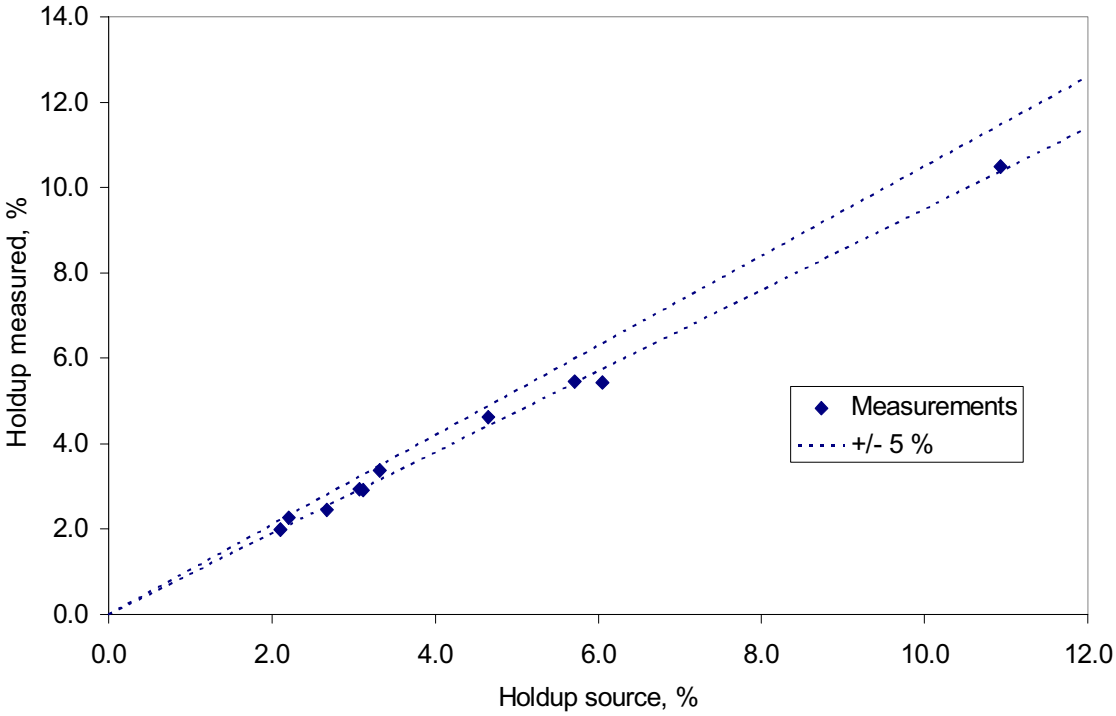

Figure 4–23: Phase fraction compared with Espedal (1998) for 10 repeated measurements

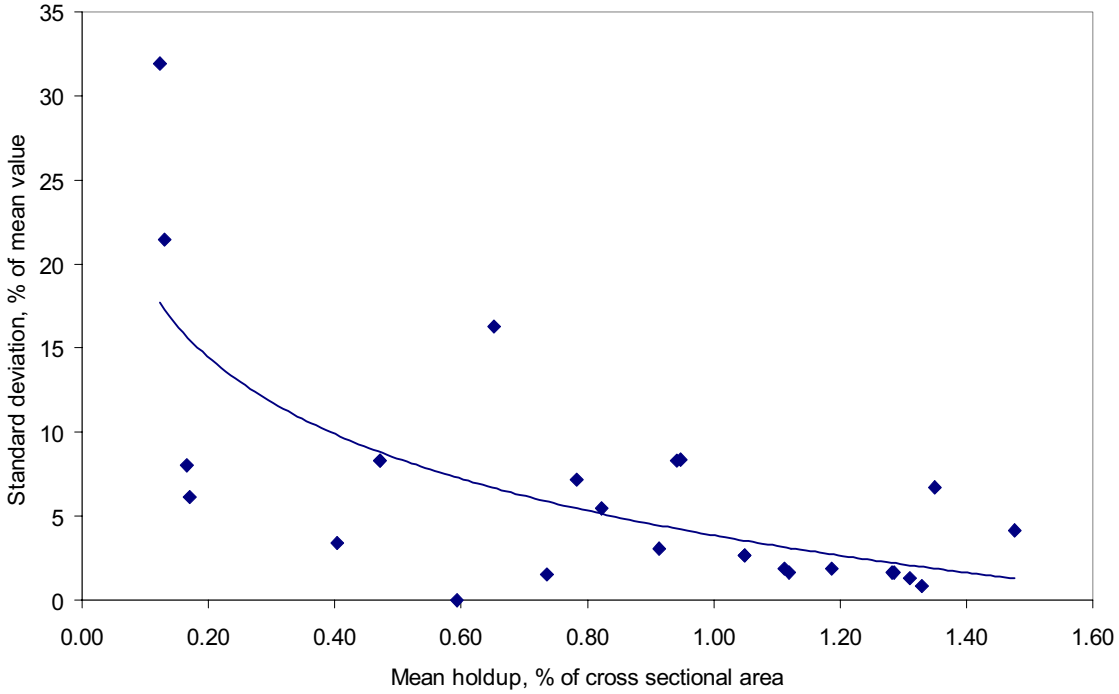

Figure 4–24: Repeatability of the holdup measurement expressed as the standard deviation around the mean value. The solid line is a logarithmic fit of the data.

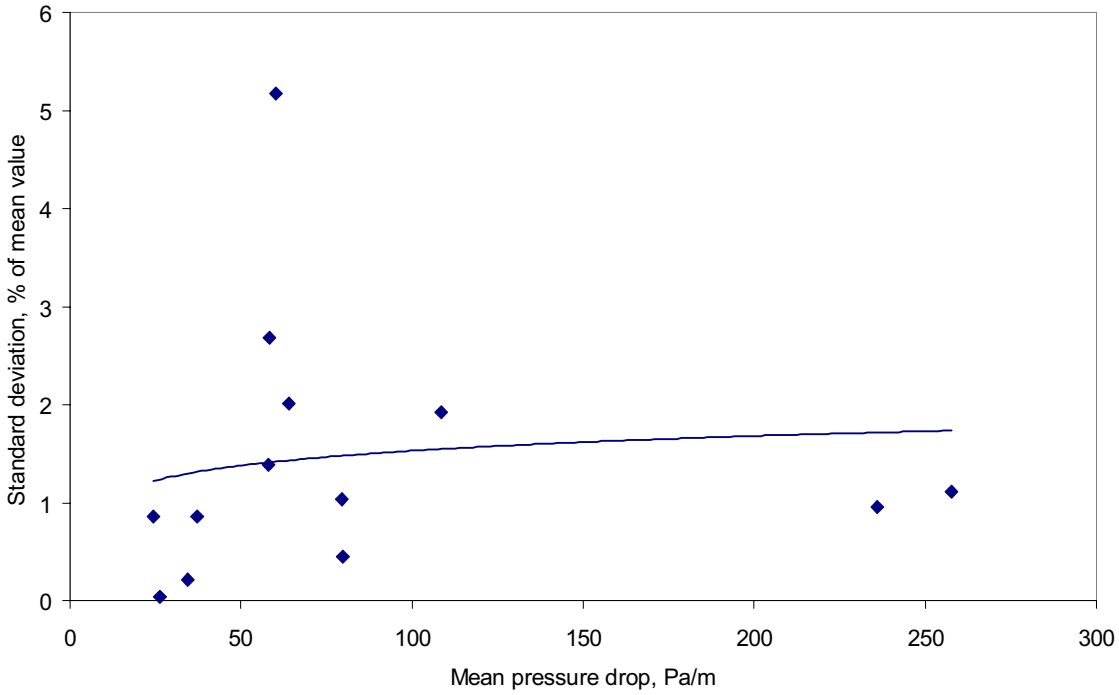

Figure 4–25: Repeatability of the pressure drop measurement expressed as the standard deviation around the mean value. The solid line is a logarithmic fit of the data.

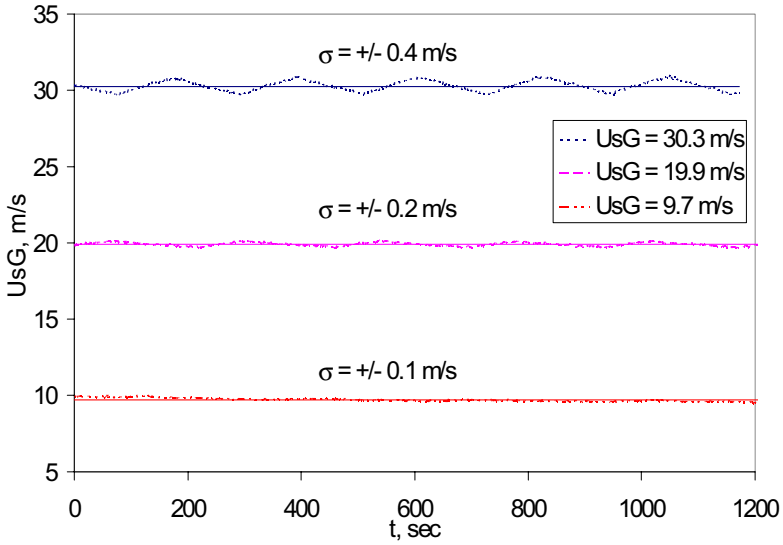

Figure 4–26: Time traces of gas flow rate for three different flow rates illustrating oscillations of the system air flow rate in phase with air compressor cycles. Average deviation around the mean value is indicated above each graph.

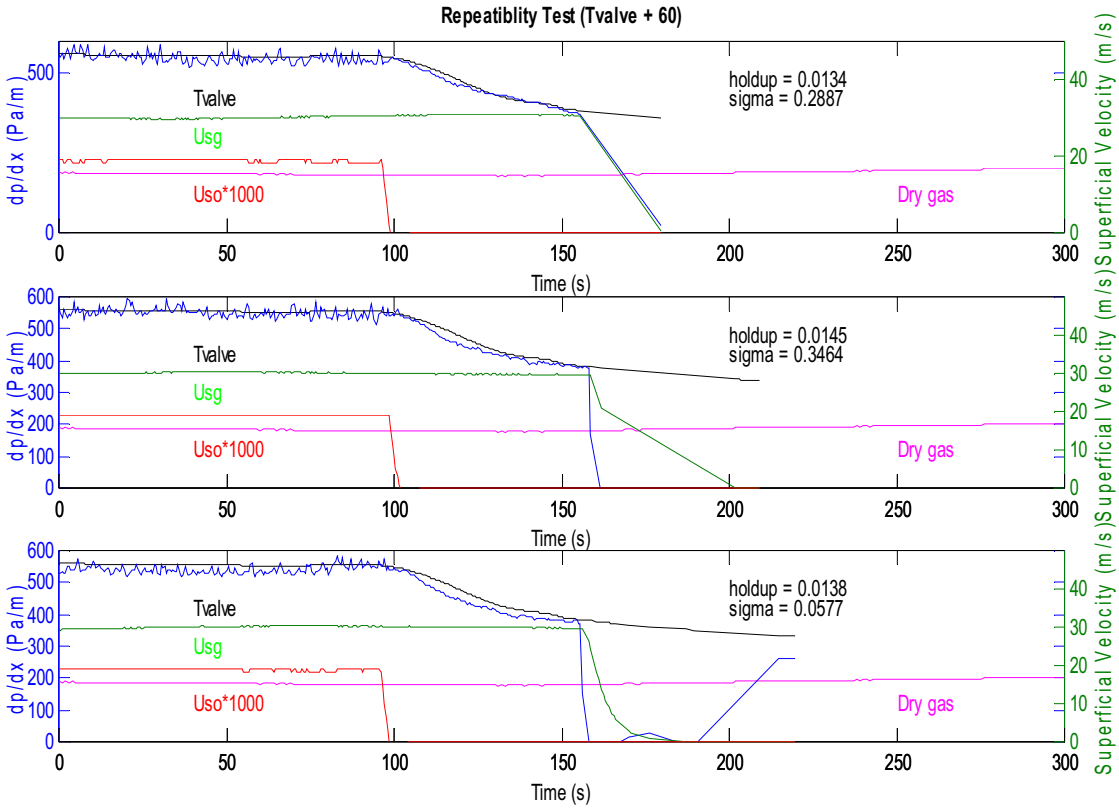

Figure 4–27: Air-oil transient experiments: repeatability tests (U_{SG} = 30 m/s, U_{SL} = 0.02 m/s

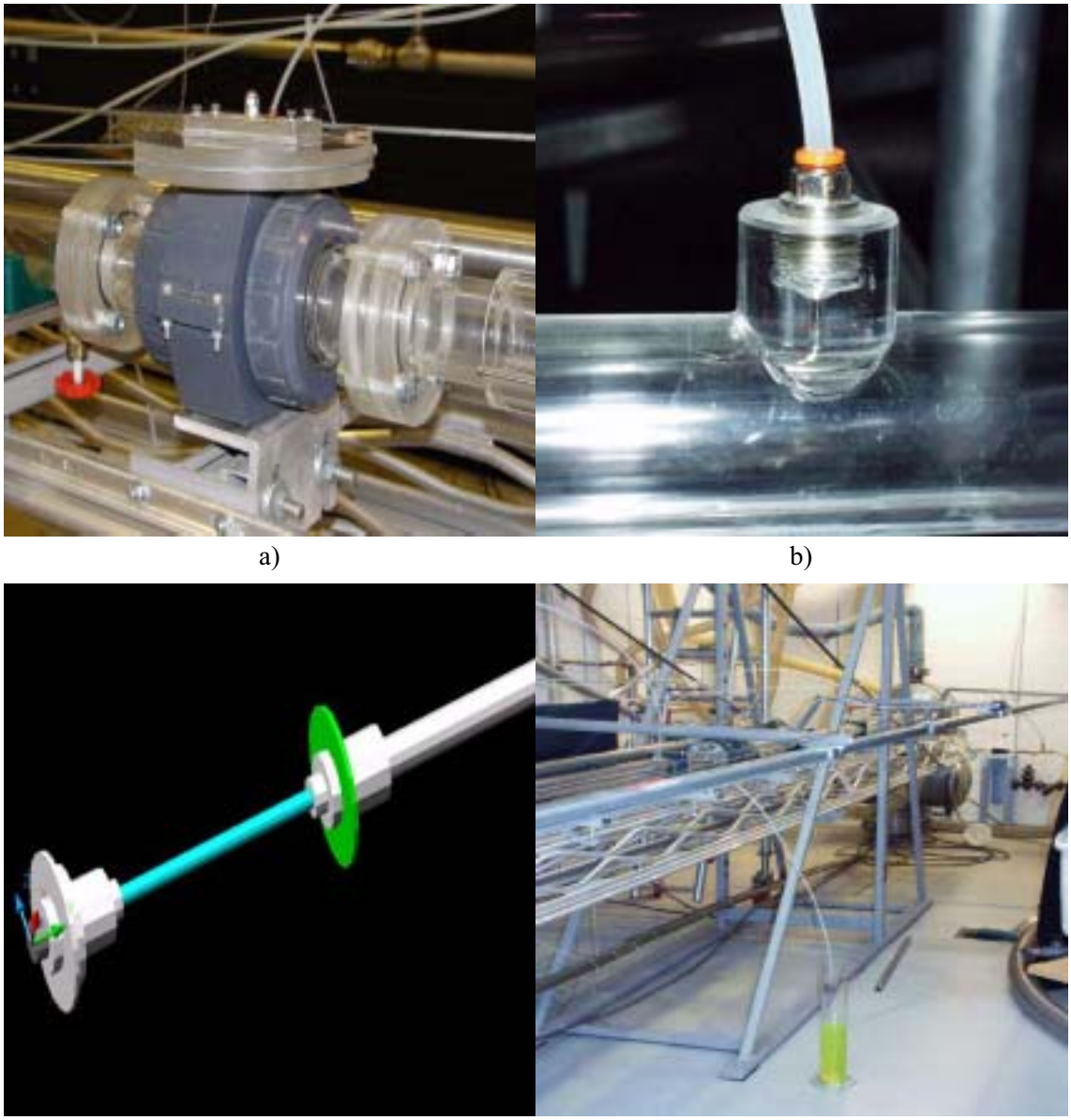

a) b)

c) d)

Figure 4–28: Flow loop details: a) quick closing valve with drainage valve, b) pressure tap, c) drainage pig (3D view), d) dosage glass

Chapter 5 Gas flow with wet walls

5.1 Introduction

Using the multiphase flow loop described in Chapter 4 and, in particular, the possibility to obtain accurate pressure differential and holdup measurements, a set of experiments has been carried out to investigate means of achieving drag reduction in gas pipes. The particular technique considered here consists in introducing a thin annular liquid film between the pipe wall and the turbulent gas core to reduce the frictional pressure loss.

As commented in Chapter 2, measurements of gas pipe transmission factors by Smith et al. (1956) show drag reduction in rough pipes in presence of small amounts of liquid. According to the authors, the most probable reason of the drag reduction observed is that liquid fills the roughness elements and smears the pipeline surface. The technique investigated here is of a different nature. By having a liquid film flowing at the wall, it is expected that the gas-liquid interface will act as a streamwise moving wall. Due to the apparent wall movement, the drag is reduced, resulting in an increase of the volumetric gas throughput.

Solbakken et al. (2000, 2002a) performed numerical experiments to investigate the technique's potential and gain understanding on how the thin liquid film can affect the turbulent gas core. Using simple turbulence modelling (RANS) for a turbulent gas flowing over a laminar film in a pipe, Solbakken et al. (2000) show the possibility of significant pressure loss reduction. In Section 5.2.1, their model is adapted to the vertical pipe geometry and hereafter called the Laminar Film model. The results from RANS models are confirmed by means of Direct Numerical Simulations (Solbakken et al. 2002a). An impermeability condition is imposed at the gas-liquid interface to prevent wall normal transport of momentum. It can be seen that near-wall streamwise vortices are thereby pushed further into the flow and results in an increase of the viscous sub-layer thickness. The liquid film furthermore prevents local regions of high skin friction to develop.

Solbakken et al. (2002a) have also carried out DNS and LES to study the effect of gas Reynolds number, liquid film thickness and liquid viscosity on the level of drag reduction achieved. A result plot is shown in Figure 5–1. It reveals that the region where possible drag reduction can be attained is increasing with gas Reynolds number, provided that the gas-liquid interface is stable. Drag reduction can be maintained for higher viscosity ratio between the liquid film and the gas if the gas Reynolds number is increased.

In the present study, the conditions necessary for drag reduction in presence of an annular liquid film have been approached experimentally and the frictional pressure drop has been

measured in presence of films and droplets at the wall. The experiments also provide data for the flow of gas in pipes of gradually changing wall wetting.

This chapter is dealt into four sections. After deriving annular flow models for laminar and turbulent liquid films in Section 5.2, the experiments are described in Section 5.3 and the results are analysed and compared with model predictions in Section 5.3 and Section 5.4.

5.2 Annular flow models

Simplified analytical annular flow models are derived in this section. The models are based on several underlying assumptions which are most probably fulfilled at low liquid loading (for instance, the no-droplet-entrainment assumption). Two classes of models are derived: models assuming laminar flow in the liquid film (in Section 5.2.1) and models assuming turbulent flow (in Section 5.2.2).

5.2.1 Laminar Film model

As mentioned in introduction, the Laminar Film model has been first derived by Solbakken et al. (2000) for horizontal gas-liquid pipe flow. The model has been re-written to include the effect of gravity.

5.2.1.1 Model derivation

The model is a two-phase gas-liquid annular flow model assuming laminar flow in the liquid film and turbulent flow in the gas core. The gas-liquid interface is also assumed to behave as a smooth wall moving in the streamwise direction. It is assumed continuity of the velocity at the gas-liquid interface and continuity of the shear stress. Analytical expressions for the liquid and gas velocity can be derived considering Navier-Stockes equations for the laminar liquid film and the Law of the Wall for the turbulent gas core. Other assumptions are:

- Constant pipe geometry and fluid properties.
- Constant and uniform film thickness.
- Fully developed, one-dimensional flow.
- Upward vertical flow.
- No slip at the wall.
- No droplet entrainment.

Model variables are defined in Figure 5–2.

Liquid film properties

The streamwise component of the Navier-Stokes equations describing the motion of the laminar film reduces, upon model assumptions, to the following equation:

$$0 = -r\left(\frac{dP}{dx} + \rho_L g\right) + \mu_L \frac{d}{dr}\left(r\frac{du_L}{dr}\right) \quad [5.1]$$

After integration between the wall (r = R) and the interface ($r = r_G$), an expression for the interfacial velocity can be obtained:

$$u_j = -\frac{1}{4\mu_L}\left(\frac{dP}{dx} + \rho_L g\right)(R^2 - r_G^2) + \frac{r_G^2 g}{2\mu_L}(\rho_L - \rho_G)\ln\frac{R}{r_G} \quad [5.2]$$

Under the assumption of laminar flow, the velocity profile is almost linear for thin films and the mean liquid velocity is given by:

$$U_L = \frac{u_j}{2} \quad [5.3]$$

The liquid film Reynolds number is given by:

$$Re_L = \frac{\rho_L U_L D_L}{\mu_L} \quad [5.4]$$

where D_L is the hydraulic diameter of the liquid film defined by (open channel assumption):

$$D_L = \frac{4A_L}{S} = 2HR \quad [5.5]$$

The liquid film thickness can be calculated from the liquid fraction @ and the assumption of a uniform, constant thickness film:

$$m = R(1 - \sqrt{1 - H}) \quad [5.6]$$

The position of the gas-liquid interface is obtained from:

$$r_G = R - m \quad [5.7]$$

Gas core properties

The gas core velocity is assumed to be given by the Law of the Wall where the velocity profile is split into the viscous sub-layer in the direct vicinity of the gas-liquid interface (considered as a rigid wall) and the logarithmic region. Under model assumptions, the gas core velocity can be written as:

$$\begin{aligned} u_G &= u_j + \frac{(r_G - r)(u_{jG}^*)^2}{\nu_G} \quad for\ (r_{10} < r < r_G) \\ u_G &= u_j + \frac{u_{jG}^*}{\kappa} \ln\left(\frac{(r_G - r)u_{jG}^*}{\nu_G}\right) + Bu_{jG}^* \quad for\ (0 < r < r_{10}) \end{aligned} \qquad [5.8]$$

where the viscous sub-layer thickness is given by:

$$r_{10} = r_G - 10\frac{\nu_G}{u_\tau} \qquad [5.9]$$

and the friction velocity at the interface by:

$$u_{jG}^* = \sqrt{\frac{\tau_j}{\rho_G}} \qquad [5.10]$$

By integration of the velocity over the cross sectional area of the turbulent core, the volumetric gas flow rate per unit area can be calculated according to:

$$U_{SG} = \frac{1}{A}\int_{A_G} u_G dA \qquad [5.11]$$

For vertical annular flow, the gas and liquid combined momentum and mass conservation equations, Equation [3.18] and Equation [3.19], reduce to:

$$0 = -\alpha A\frac{dP}{dx} - \tau_j S_j - \alpha A\rho_G g \qquad [5.12]$$

$$0 = -HA\frac{dP}{dx} + \tau_j S_j - \tau_L S_L - HA\rho_L g \qquad [5.13]$$

The interfacial gas-liquid and liquid-wall frictional pressure drop can be expressed using Moody friction factors. From Equation [5.12] and Equation [5.13] it is obtained:

$$F_j = \frac{\tau_j S_j}{A} = \frac{\lambda_j}{8}\rho_G U_r^2 \frac{S_j}{A} = -\alpha\left(\frac{dP}{dx} + \rho_G g\right) \quad [5.14]$$

$$F_L = \frac{\tau_L S_L}{A} = \frac{\lambda_L}{8}\rho_L U_L^2 \frac{S}{A} = -\left[\frac{dP}{dx} + (\alpha\rho_G + H\rho_L)g\right] \quad [5.15]$$

In case of single-phase gas flow, the gas-wall frictional pressure drop reduces to:

$$F_G = -\left(\frac{dP}{dx} + \rho_G g\right) \quad [5.16]$$

The Fanning friction factors are also used in this chapter and are defined by:

$$f_k = \frac{\lambda_k}{4} \quad [5.17]$$

From Equation [5.14], the interfacial shear stress, or alternatively the interfacial friction factor, can be expressed in terms of the measured pressure drop and phase fraction:

$$\tau_j = -\frac{r_G}{2}\left(\frac{dP}{dx} + \rho_G g\right) \quad [5.18]$$

$$f_j = \frac{-\frac{r_G}{2}\left(\frac{dP}{dx} + \rho_G g\right)}{\frac{1}{2}\rho_G U_r^2} \quad [5.19]$$

Likewise, the liquid-wall shear stress is obtained from Equation [5.15]:

$$\tau_L = -\frac{R}{2}\left[\frac{dP}{dx} + (\alpha\rho_G + H\rho_L)g\right] \quad [5.20]$$

In case of single-phase gas flow, the interfacial shear stress reduces to:

$$\tau_G = -\frac{R}{2}\left(\frac{dP}{dx} + \rho_G g\right) \quad [5.21]$$

Velocity profiles in the liquid film and the gas core are calculated on an example case with air and water for a given pressure drop of -500 Pa/m and a liquid fraction of 10%. Profiles are shown in Figure 5–3.

5.2.1.2 Horizontal flow

In case of horizontal annular flow, the gravity terms disappear. In particular, interfacial velocity and interfacial shear stress reduce to Equation [5.22] and Equation [5.23] respectively:

$$u_j = -\frac{1}{4\mu_L}\frac{dP}{dx}(R^2 - r_G^2) \qquad [5.22]$$

$$\tau_j = -\frac{r_G}{2}\frac{dP}{dx} \qquad [5.23]$$

5.2.1.3 Vertical flow

Upon Laminar Film model assumptions, the pressure drop expected in the 50 mm vertical acrylic riser available at the NTNU multiphase flow laboratory can be calculated at given gas superficial velocity and for different film thicknesses. Sensitivities with film thickness and superficial gas velocities are carried out and results are shown in Figure 5–5. The plots represent the ratio of the pressure drop in presence of a film at the wall to that without the film for various film thicknesses and gas superficial velocities.

Figure 5–5 indicates that for vertical experiments, pressure drop can not be expected to fall much under the dry gas pressure drop. With water as the liquid, there is a slight drop of the pressure drop under the dry gas pressure drop but the difference is small compared to measuring accuracy. In vertical flow, the gravity component of the pressure drop tends to compensate for the film drag reducing effect and the overall pressure loss reduction is small. In order to conclude on the eventual drag reduction due to the film, one needs to extract the frictional pressure drop from the total pressure drop. This requires a phase fraction measurement. Figure 5–6 shows the ratio of gas friction in the presence of a film to that at the wall without a film for vertical experiments in the 50 mm NTNU riser. Gas frictional pressure drop with the film, F_j is calculated from Equation [5.14] and the frictional pressure drop without the film, F_G, from Equation [5.16].

5.2.2 Turbulent Film Model

A Turbulent Film model similar to the laminar Film model has been derived for gas-liquid steady-state annular flow model at low liquid loading. The liquid film is now assumed to be turbulent. Two cases are distinguished on whether the gas-liquid interface is assumed smooth or wavy.

5.2.2.1 Smooth interface model

Biberg (1998) suggests to use a double logarithmic velocity profile (excluding the viscous sub-layer) to represent the gas flow field in gas-liquid stratified flow. This approach is ex-

tended to the liquid phase in Helleren (1999). In the present work, the equations taken from Helleren (1999) are adapted to the vertical annular flow geometry.

The assumptions of the Laminar Film model are retained except for the liquid film for which a turbulent profile is now assumed.

Liquid film properties

Upon model assumptions, the velocity profile in the liquid film can be written as follows:

$$u_L = a_L \ln\left(\frac{r - r_G}{R - r_G}\right) + b_L \ln\left(\frac{R - r}{R - r_G}\right) + c_L \quad for \quad (r_G < r < R) \qquad [5.24]$$

Constants a_L, b_L and c_L can be determined by matching boundary conditions at the wall and gas-liquid interfaces.

Close to the pipe wall:

$$u_L \approx \frac{u_L^*}{\kappa}\left[\ln\left(\frac{u_L^*}{\nu_L}(R - r)\right) + \kappa B\right] \approx b_L \ln\left(\frac{R - r}{R - r_G}\right) + c_L \qquad [5.25]$$

and at the gas-liquid interface:

$$u_L \approx \frac{u_{jL}^*}{\kappa}\left[\ln\left(\frac{-u_{jL}^*}{\nu_L}(r - r_G)\right) + \kappa B\right] + u_j \approx a_L \ln\left(\frac{r - r_G}{R - r_G}\right) + c_L \qquad [5.26]$$

It is obtained:

$$a_L = \frac{u_{jL}^*}{\kappa} \qquad [5.27]$$

$$b_L = \frac{u_L^*}{\kappa} \qquad [5.28]$$

$$c_L = \frac{u_L^*}{\kappa}\left[\ln\frac{u_L^*}{\nu_L}(R - r_G) + \kappa B\right] \qquad [5.29]$$

$$u_j = \frac{u_L^*}{\kappa}\left[\ln\frac{u_L^*}{\nu_L}(R - r_G) + \kappa B\right] - \frac{u_{jL}^*}{\kappa}\left[\ln\frac{-u_{jL}^*}{\nu_L}(R - r_G) + \kappa B\right] \qquad [5.30]$$

Friction velocities are given by:

$$u_{jL}^{*} = \sqrt{\tau_j / \rho_L} \qquad [5.31]$$

and

$$u_{L}^{*} = \sqrt{\tau_L / \rho_L} \qquad [5.32]$$

The gas-liquid and liquid-wall shear stresses are calculated from Equation [5.20] and Equation [5.18] knowing the pressure drop and the liquid holdup.

Gas core properties

The annular gas core velocity profile can be written as follows:

$$u_G = a_G \ln\left(\frac{r}{r_G}\right) + c_G \qquad [5.33]$$

At the gas-liquid interface:

$$u_G \approx \frac{u_{jG}^{*}}{\kappa}\left[\ln\frac{u_{jG}^{*}}{\nu_G}(r_G - r) + \kappa B\right] + u_j \approx a_G \ln\left(\frac{r}{r_G}\right) + c_G \qquad [5.34]$$

from which it is obtained:

$$a_G = \frac{u_{jG}^{*}}{\kappa} \qquad [5.35]$$

$$c_G = u_j + \frac{u_{jG}^{*}}{\kappa}\left[\ln\frac{u_{jG}^{*}}{\nu_G} r_G + \kappa B\right] \qquad [5.36]$$

The friction velocity u_{jG}^{*} is calculated from Equation [5.10] and Equation [5.18] knowing the pressure drop and the liquid holdup.

Note that the final expression for u_G is the same as formulated in Equation [5.8] for the turbulent gas core for $0 < r < r_{10}$.

An example velocity plot calculated by this method for air and water and a given pressure drop of -500 Pa/m and liquid fraction of 10% is given in Figure 5–4.

5.2.2.2 Rough interface model

In Equation [5.26] and Equation [5.34], the gas liquid interface is assumed to behave as a smooth solid wall. It is possible to replace the hydraulically smooth velocity profile at the

vicinity of the interface with the corresponding rough velocity profile if the interface should now behave as a solid rough wall.

The boundary conditions at the interface are now, for the liquid and the gas respectively:

$$u_L \approx \frac{u_{jL}^*}{\kappa}\left[\ln\left(\frac{r - r_G}{k_S}\right) + \kappa A\right] + u_j \approx a_L \ln\left(\frac{r - r_G}{R - r_G}\right) + c_L \qquad [5.37]$$

$$u_G \approx \frac{u_{jG}^*}{\kappa}\left[\ln\left(\frac{r_G - r}{k_S}\right) + \kappa A\right] + u_j \approx a_G \ln\left(1 - \frac{r}{r_G}\right) + c_G \qquad [5.38]$$

giving:

$$u_j = \frac{u_L^*}{\kappa}\left[\ln\left(\frac{u_L^*}{\nu_L}(R - r_G)\right) + \kappa B\right] - \frac{u_{jL}^*}{\kappa}\left[\ln\left(\frac{R - r_G}{k_S}\right) + \kappa A\right] \qquad [5.39]$$

$$c_G = u_j + \frac{u_{jG}^*}{\kappa}\left[\ln\left(\frac{r_G}{k_S}\right) + \kappa A\right] \qquad [5.40]$$

The rough interface model is used in Section 5.4.2 to calculate a value for the equivalent sand roughness k_S that matches the vertical annular flow measurements.

5.3 Experiments

Laboratory experiments have been carried out to investigate the potential drag reducing effect of having a liquid film at the wall. To meet the conditions of validity of the Laminar Film model, very thin films of constant thickness are required. It has been investigated on whether such films can be created by progressively thinning an annular film by a gas flow at constant flow rate. Hereafter, such experiments are called "film thinning" experiments. Results are presented hereby for experiments carried out in horizontal and vertical pipes.

5.3.1 Horizontal flow

5.3.1.1 Description of the experiments

The film thinning experiments are first carried out in the 60 mm i.d. acrylic and steel test pipes in the horizontal position. Test sections are described in Chapter 4. For these particular experiments, ring probe sections and quick closing valves are taken out and replaced

by spool pieces. Therefore, the test section hydraulic roughness is expected to be close to the single pipe section hydraulic roughness given in Table 4–26.

The experimental procedure is described in Section 4.4.2. In the case of horizontal experiments, no holdup measurement is required since the frictional pressure drop is directly measured. The measuring accuracy is indicated in Table 4–28.

If a drag reducing film forms at the pipe wall during the film thinning process, it is expected that the pressure drop will fall momentarily under the computed value for dry gas flow. Four combinations of pipe material and fluids are tried out in order to investigate the influence of material and fluid properties. Runs are summarized in Table 5–1.

Table 5–1: Test matrix for the horizontal experiments

Run #	U_{SG}, m/s	U_{SL}[a], m/s	Test section	Liquid film
1	43.1	0.21	acrylic 60 mm	water
2	38.1	0.22	steel 60 mm	water
3	43.0	0.08	acrylic 60 mm	Exxsol D80
4	37.9	0.14	steel 60 mm	Exxsol D80

a. Initial liquid superficial velocity prior to liquid shut-down

5.3.1.2 Results

The pressure drop measured during the film thinning experiments is plotted in Figure 5–7 for the four combinations of pipe materials and fluids. The dry pipe pressure drop calculated from the Blasius' equation is plotted on the same graph. Pressure drop oscillations of period approximately two minutes are due to slow variations of the rig air supply.

Pictures of flow regimes are shown in Figure 5–8 for the particular case of water film thinning in the acrylic pipe. The process goes through the following successive stages:

- Immediately after valve shut-down, the annular film at the wall breaks down, starting from the top of the pipe and begins to fall down the wall. With oil, the film integrity is maintained longer after shut-down.
- A few minutes after liquid shut-down, the flow regime is stratified gas-liquid flow with a thin liquid film at the bottom of the pipe. Droplets are observed running on the upper wall in the mainstream direction, especially with water. Some droplets are already too small to offer sufficient drag to the air and hang without motion on the pipe wall.
- As the liquid holdup decreases, the film gets thinner with capillary ripples forming at the free surface and eventually turns into a meandering rivulet.
- At the end of the process, the rivulet breaks down. Liquid drops remain at the wall until total evaporation.

5.3.1.3 Discussion

Neither plot gives reason to believe that drag reduction has been achieved at any time during the horizontal experiments. The pressure drop falls strongly in the first minutes, just after the liquid supply valve is shut, until it starts to converge slowly to the dry pipe pressure drop but never falls under the dry gas values.

Failure to achieve drag reduction is caused by the following:

- The film is not symmetrically distributed around the pipe circumference.
- The film is not continuous and breaks down starting from the top of the pipe. In other words, the de-wetting process is too fast.
- The film has no constant thickness. It is thicker at the bottom and thinner at the wall flanks.
- The gas-liquid interface is not smooth but traversed by capillary ripples.
- The liquid film flow is not laminar.

In all the experiments, it is observed that the de-wetting process is too quick compared to the film thinning process. In that respect, it is easier to get closer to the assumptions of the Laminar Film model using oil which is both wetting (slower de-wetting) and more viscous (higher tendency to laminar flow) than water. However the problem of asymmetric film distribution is inherent to the horizontal annular flow. Capillary ripples are observed at the gas-liquid interface even for very thin films and are prone to increase interfacial friction.

5.3.2 Vertical flow

In a second stage, experiments have been conducted in a vertical pipe in order to improve film symmetry and slow down the de-wetting of the pipe wall.

5.3.2.1 Description of the experiments

This serie of film thinning experiments is performed in the 50 mm i.d. L-shaped riser described in Chapter 4, at ambient pressure and temperature. Measurements are carried out in the 6.4 m high vertical section of the riser.

The experimental procedure is the same as for the horizontal experiments and is described in Section 4.4.2. After the establishment of a steady-state annular two-phase flow, the liquid supply is shut-down whilst leaving the air thin the liquid film until the pipe wall is completely dry. Two series of experiments are conducted with water and Exxsol D80 so as to vary liquid viscosity and wall wetting. The actual test matrix is summarized in Table 5–2.

For each case, several runs are repeated at the same average air superficial velocity and initial liquid superficial velocity and the pressure drop is recorded. The aim of these initial

Table 5–2: Test matrix for the vertical experiments

Run #	U_{SG}, m/s	U_{SL}[a], m/s	Test section	Liquid film
1	30.0	0.02	acrylic 50 mm	water
2	30.0	0.02	acrylic 50 mm	Exxsol D80

a. Initial liquid superficial velocity prior to liquid shut-down

runs is to construct the pressure trace of the film thinning experiment. This curve is obtained by averaging the runs and computing an interpolation 8^{th} order polynomial. The process is illustrated in Figure 5–9.

At selected times during the experiment, the average liquid holdup is measured using quick closing valves. Good repeatability is obtained by following an identical experimental procedure from one run to the other as explained in Section 4.4.2.

In order to determine an initial liquid flow rate achieving an annular two-phase flow without flow reversal, preliminary annular flow experiments are conducted at varying superficial gas velocity and constant liquid superficial velocity. Figure 5–10 shows plots of such experiments for superficial gas velocity between 15 and 40 m/s. It reveals that, at air and liquid superficial velocities of respectively 30 m/s and 0.02 m/s, there is effectively no liquid backflow.

5.3.2.2 Results

During the film thinning experiments, five flow regimes can be identified of which photographs are shown in Figure 5–12 for the air-water flow case. These flow regimes are:

- Initial annular flow. In general, large amplitude waves are seen running across the liquid film.
- Film thinning. In this flow regime, the liquid flows as a film at the wall. There is no noticeable droplet generation.
- Film break down. At a certain time in the film thinning process (dependent on fluid properties), the continuous liquid film breaks down into liquid rivulets.
- Rivulets. The liquid is now flowing as one or several rivulets.
- Hanging droplets. The remaining liquid forms droplets that cannot be moved by the gas and hang on the pipe wall until total evaporation.

With Exxsol D80, which is both more viscous and wets better acrylic than water, the film breakdown occurs later after the supply is cut. Also, the hanging droplets are smaller and tend to be smeared by the gas over the wall surface.

From average phase fraction measurements, it is possible to calculate average film thickness from Equation [5.7], assuming a uniform film of constant thickness and no droplets in the gas stream. Film thicknesses achieved in the experiments prior to film break down

are in the range 59-330 bm with oil and 136-314 bm with water. Average thicknesses are compared with those achieved by other authors in Figure 5–11.

Air-water experiment

Results of the pressure drop and holdup measurements for the water film thinning run are shown in Figure 5–13.

The following data is indicated on the pressure drop plot:

- The "measured" interfacial frictional pressure drop, F_j, obtained from Equation [5.14] using the measured total pressure drop and the measured phase fraction.
- The theoretical interfacial frictional pressure drop experienced by the gas in a smooth pipe, whose wall position corresponds to the location of the gas-liquid interface. This term, tagged $F_{j,SLF}$, is calculated from:

$$F_{j,\,SLF} = \frac{\lambda_{j,\,SLF}}{8}\rho_G U_G^2 \frac{S_j}{A} \qquad [5.41]$$

with

$$\lambda_{j,\,SLF} = \frac{0.184}{(Re_G)^{0.2}} \qquad [5.42]$$

$$Re_G = \frac{\rho_G U_G (D-2m)}{\mu_G} \qquad [5.43]$$

$$U_G = \frac{U_{SG}}{1-H} \qquad [5.44]$$

and

$$S_j = \pi(D-2m) \qquad [5.45]$$

- The theoretical interfacial frictional pressure drop computed from the Laminar Film model, $F_{j,LF}$.
- The theoretical frictional pressure drop for the gas flowing alone in the pipe at the same superficial velocity as the experiments. This term, tagged F_G, is calculated from:

$$F_G = \frac{2}{R}\tau_G \qquad [5.46]$$

with

$$\tau_G = \frac{\lambda_G}{8}\rho_G U_{SG}^2 \quad [5.47]$$

and

$$\lambda_G = \frac{0.184}{(Re_{SG})^{0.2}} \quad [5.48]$$

The holdup plot in Figure 5–13 shows values of the holdup in the pipe versus time. The line marked "*Film breakdown*" shows the time at which the liquid film is no longer continuous and breaks down.

Additional calculations were performed based on the measurements and are shown in Figure 5–15. These are:

• The film thickness based on the Laminar Film model assumptions. The line marked "*Dry gas: viscous sub-layer thickness*" is a computation of the viscous sub-layer thickness for single phase air flowing at superficial gas velocity of 30 m/s in the 50 mm riser. It is computed according to:

$$\partial = 5\frac{\nu_G}{\tau_G} \quad [5.49]$$

with, τ_G, given by Equation [5.47].

• The liquid film Reynolds number upon Laminar Film model assumptions. The line marked "*Onset droplet entrainment*" is the critical liquid Reynolds number below which there is no expected entrainment at the gas velocity considered. A critical liquid Reynolds number of 330 is suggested by Asali et al. (1985) in their upward annular flow experiments and is consistent with the observations in Hewitt et al. (1970, p. 142) that no entrainment is possible below a critical liquid Reynolds number.

Air-Exxsol D80 experiment

Similar plots for the oil film thinning experiments are presented in Figure 5–14 and Figure 5–15. Due to its higher viscosity, it takes longer for the oil film to break down. More holdup points could therefore be taken in the film thinning region.

5.3.2.3 Discussion

Drag reduction

Figure 5–13 and Figure 5–14 show that the frictional pressure drop at the interface does not fall below the smooth static interface value. This indicates that the moving liquid film, while thinning and before break down, generates drag increase instead of drag reduction.

Film thickness

Film thicknesses achieved range from 300 to 50 bm, based on the assumptions of a uniform constant thickness film and no entrainment. It has not been possible to verify, in the experiments, that the film was effectively symmetric. It is also worthwhile to notice that film breaks down below a thickness of about 50 bm for both water and oil. 50 bm also approximately corresponds to the single-phase gas viscous sub-layer thickness at the studied superficial velocity of 30 m/s.

Liquid Reynolds number

The liquid Reynolds number calculated from the measured holdup is higher with water than oil. In most cases, it stays below 2100. However, this condition is not sufficient to stipulate the film is flowing laminar. Turbulent films are reported in the literature at Reynolds number as low as 500.

The liquid Reynolds number is kept below the critical Reynolds number suggested by Asali et al. (1985) for the onset of droplet entrainment, except for the initial annular flow conditions in the air-water case. This tends to confirm the no-entrainment assumption.

Interfacial shear stress

The "experimental" interfacial friction factor obtained from Equation [5.19] is compared to the following correlations:

- Wallis' correlation (1969), Equation [5.50]. The interfacial (Fanning) friction factor is defined by Equation [5.51].

$$f_j = 0.079 Re_{SG}^{-1/4}[1 + 90(1 - \alpha)] \qquad [5.50]$$

with

$$f_j = \frac{\tau_j}{1/2 \rho_G U_{SG}^2} \qquad [5.51]$$

- Asali et al's correlation (1985), Equation [5.52]:

$$\frac{f_j}{f_s} - 1 = 0.045(m_G^+ - 4) \qquad [5.52]$$

where f_s, the Fanning friction factor for the gas flowing alone in the pipe assumed hydraulically smooth, is given by the Blasius' equation, Equation [5.53], and m_G^+ is a dimensionless film thickness given by Equation [5.54]. In this case, the interfacial friction factor, f_j, is defined by Equation [5.55] based on the actual velocity.

$$f_s = 0.046 Re_{SG}^{-0.20} \quad [5.53]$$

$$m_G^+ = m \left(\frac{\tau_i}{\rho_G} \right)^{1/2} \frac{1}{\nu_G} \quad [5.54]$$

$$f_j = \frac{\tau_j}{1/2 \rho_G U_G^2} \quad [5.55]$$

The empirical correlation by Wallis (1969), Equation [5.50], is a widely used correlation for one-dimensional modelling of annular flow. Asali et al.'s correlation (1985) has been developed from an extensive database of annular flow experiments down to very thin film thicknesses.

The root-mean-square (rms) error on the interfacial friction factor calculated from Equation [5.19] is, according to Doebelin (1990):

$$\frac{df_j}{f_j} = \sqrt{\left(\frac{dm}{R - m} \right)^2 + \left(\frac{\frac{dP}{dx}}{\frac{dP}{dx}} \right)^2 + \left(\frac{dU}{U} \right)^2} \quad [5.56]$$

where U is either the actual or superficial gas velocity depending on the definition of the interfacial friction factor. Based on the measurement accuracy estimations given in Table 4–28, the r.m.s error on the interfacial friction factor is estimated to be +/- 7.3%.

A plot of the ratio of the measured interfacial friction factor to the interfacial friction factor calculated with Wallis' correlation is shown in Figure 5–16. It can be seen that Wallis' correlation over predicts interfacial friction by up to 20%. This is higher than the estimated 7.3% error on the friction factor. The correlation performs better for air-water flow than for air-oil flow. Figure 5–17 shows that measurements agree better with Asali et al.'s correlation but there are discrepancies for large film thicknesses.

The equivalent sand roughness, calculated from the interfacial friction factor assuming Håland's equation (Equation [3.11]) is also compared to Hart et al's (1989) ARS model expression, Equation [5.57]:

$$\varepsilon_j = 2.3m \quad [5.57]$$

Hart et al's Equation [5.57] has been proposed for thin liquid films at low liquid loading. It suggests a simple relation between film roughness and film thickness. Comparisons between measured and calculated hydraulic roughness are shown in Figure 5–18. It shows that Hart et al's correlation overestimates hydraulic roughness for thin films. Interestingly,

the sand grain roughness of the interface calculated with this method seems to scale with the film thickness, as shown in Figure 5–18.

5.4 Comparison of experiments with annular flow models

The experimental results have been compared with predictions from the annular flow models derived in Section 5.2. Only vertical experiments were considered.

5.4.1 Laminar Film model

Equation [5.11] is an implicit function of pressure drop. Starting from a gas superficial velocity and a film thickness, it is possible to compute the corresponding pressure gradient upon Laminar Film model assumptions. This is given in Figure 5–19 for the average film thicknesses measured with water and oil in the 50 mm vertical riser at 30 m/s superficial gas velocity. Had the assumptions of the Laminar Film model been achieved, experimental and theoretical pressure gradients would have matched within measuring accuracy. The fact that this is not the case indicates that at least one assumption of the model is not fulfilled.

The frictional pressure drop from the Laminar Film model, $F_{j,LM}$, is calculated for the conditions corresponding to the experiments and compared with the experimental frictional pressure drop. This is shown in Figure 5–13 and Figure 5–14. It can be seen that gas experiences a higher interfacial friction than expected upon Laminar Film model assumptions.

In the following section, it is investigated the effect of considering instead a turbulent liquid film with a rough interface.

5.4.2 Turbulent Film model

The Turbulent Film model with rough gas-liquid interface (Section 5.2.2.2) assumes that the interface behaves as a rough rigid wall that moves co-current with the gas at velocity equal to the interfacial velocity. It is possible to compute an interfacial equivalent sand roughness for which, given the experimental pressure gradient and film thickness, the experimental air flow rate is matched. This is shown in Figure 5–20. It is also indicated on the graph the value of the hydraulic roughness computed by matching Håland's equation to the experimental value of the interfacial friction factor. Both quantities converge for thin films, as expected.

5.4.3 Discussion

Comparisons with the rough Turbulent Film model together with estimates of film hydraulic roughness (Figure 5–18 and Figure 5–20) suggest that the gas-liquid interface is not smooth contrary to the Laminar Film model pre-requisites for achieving drag reduction. This agrees with visual observations that the gas-liquid interface in the experiments is always wavy, independent of film thickness.

Solbakken et al. (2002b) have performed a literature review on the topic of sheared viscous liquid film stability. They identify three forms of instability:

• Instability of a free surface film submitted to a constant shear. This has been studied by Miles (1960). Miles concludes that a sufficient condition for stability with respect to small wave disturbances is either $Re_L < 203$ or $We_L < 3$, independent of liquid Reynolds number. The film Weber number is defined as:

$$We_L = \frac{\rho_L U_L^2 m}{\sigma} \qquad [5.58]$$

• Instability of a free surface submitted to a turbulent gas. This instability has been studied by Cohen et al. (1965). From experiments with air and glycerine-water solutions in horizontal channels, they demonstrate the existence of a critical gas Reynolds number above which waves are triggered by pressure and shear stress fluctuations at the interface. A theoretical analysis is also developed that confirms the experimental observations. Viscosity has a stabilizing effect with respect to this type of instability and critical gas Reynolds increases with decreasing liquid Reynolds number. Experiments reveal typical critical gas Reynolds in order of $4 \cdot 10^3$ for liquid Reynolds number between $1 \cdot 10^2$ and $2 \cdot 10^2$.

• Slow wave instability (Craik 1966). It occurs for very thin sheared film for which surface tension is too small to overcome the destabilizing effect of surface stresses. The instability is seen as a slow wave, moving with a a velocity less than the interface velocity. Miesen et al. (1995) and Craik (1966) show, with two different approaches, that films thinner than approximately 40 micrometers are liable to develop slow waves, independent of the gas Reynolds number.

Another form for film instability is surface de-wetting. Hewitt et al. (1970) show that stability to de wetting is increased by low contact angles and high fluid inertia (high density and high local velocity).

The film Weber numbers for the vertical experiments are calculated and given in Appendix A, Table A–17 and Table A–18. They show that films achieved in the experiments are stable with respect to Miles' instability. Also, film thicknesses attained are too large for slow waves to develop at the interface.

The most probable cause of instability is therefore high shear and pressure oscillations at the gas-liquid interface in presence of the turbulent gas core. Gas Reynolds numbers

achieved in this study are in order of 10^5 and are therefore well above critical gas Reynolds number identified by Cohen et al. (1965).

Ways of achieving drag reducing films are suggested below:

- Increase the liquid viscosity but not too much since high liquid viscosities have a negative effect with respect to drag reduction potential.
- Use a polymer additive in the liquid phase that stiffens the interface and makes it less sensitive to normal fluctuations of interfacial stresses due to the gas turbulence.
- Increase surface wettability in order to reduce the occurrence of dry patches and attain thinner liquid films.

5.5 Summary

An experimental study has been conducted to investigate the potential drag reducing effect in gas pipelines of having a liquid film at the pipe wall. Simple flow models such as the Laminar Flow model but also numerical experimentation (Solbakken et al. 2002a) demonstrate the possibility of pressure loss reduction in gas pipes with this technique. Pre-requisites are of a stable smooth gas-liquid interface, symmetric thin film and low liquid-to-gas viscosity ratio.

An experimental procedure has been developed to meet the requirements on the liquid film in terms of film thicknesses and film symmetry. Thin films have been achieved by thinning the liquid film at the wall through a transient experiment. Symmetric film conditions have been attained in vertical pipes only. A combination of pressure drop and holdup measurements during the film thinning process in a 50 mm i.d. vertical riser allows to compare gas friction with and without the film.

Results show that friction at the gas-liquid interface is always higher than either the smooth static film friction and the interfacial friction assuming a smooth laminar film. The liquid film develops an equivalent sand roughness that scales with the film thickness and is well above the gas viscous sub-layer thickness. Other requirements such as the condition of no droplet generation and stability with respect to Miles instability criterion (Miles 1960) are otherwise met.

The most probable cause of film instability are waves induced by gas turbulent fluctuations of surface stresses. Ways of reducing interface compliance are suggested for improving future experiments.

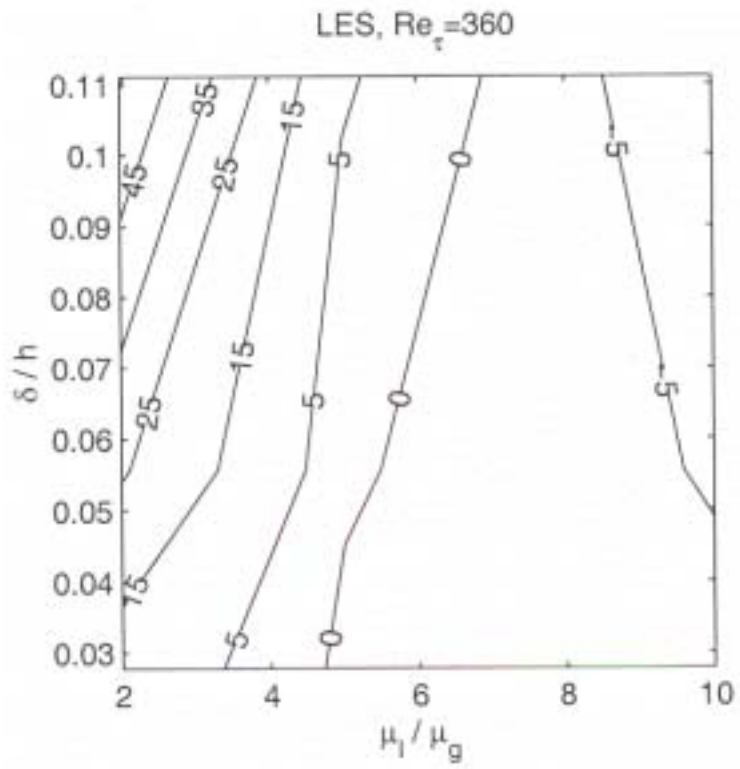

Figure 5–1: Change of gas volumetric flow rate in presence of a liquid film compared to dry channel flow. Results are from LES simulations with Re_τ = 360. The changes in flow rates are indicated on the solid lines in percent of dry gas flow rate. Sensitivities are performed with liquid-to-gas viscosity ratio, b_l/b_g, and film-thickness-to-channel-height ratio, Y/h (from Solbakken et al. 2002a)

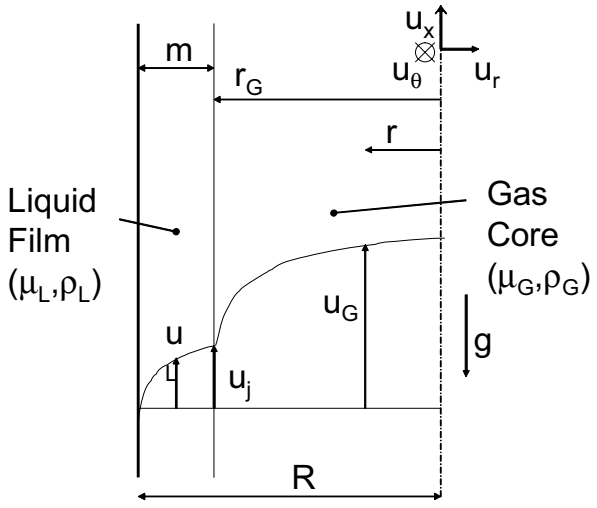

Figure 5–2: Variable definitions for annular flow models

.

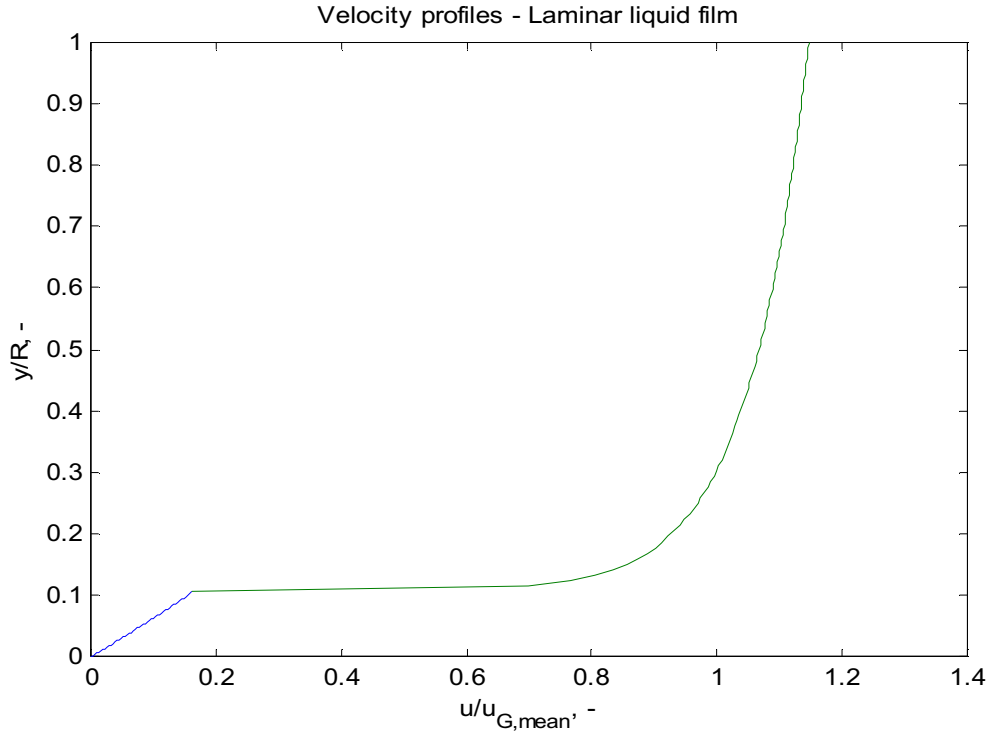

Figure 5–3: Water and air velocity profiles upon Laminar Film model assumptions. Liquid holdup = 10%, pressure drop = -500 Pa/m

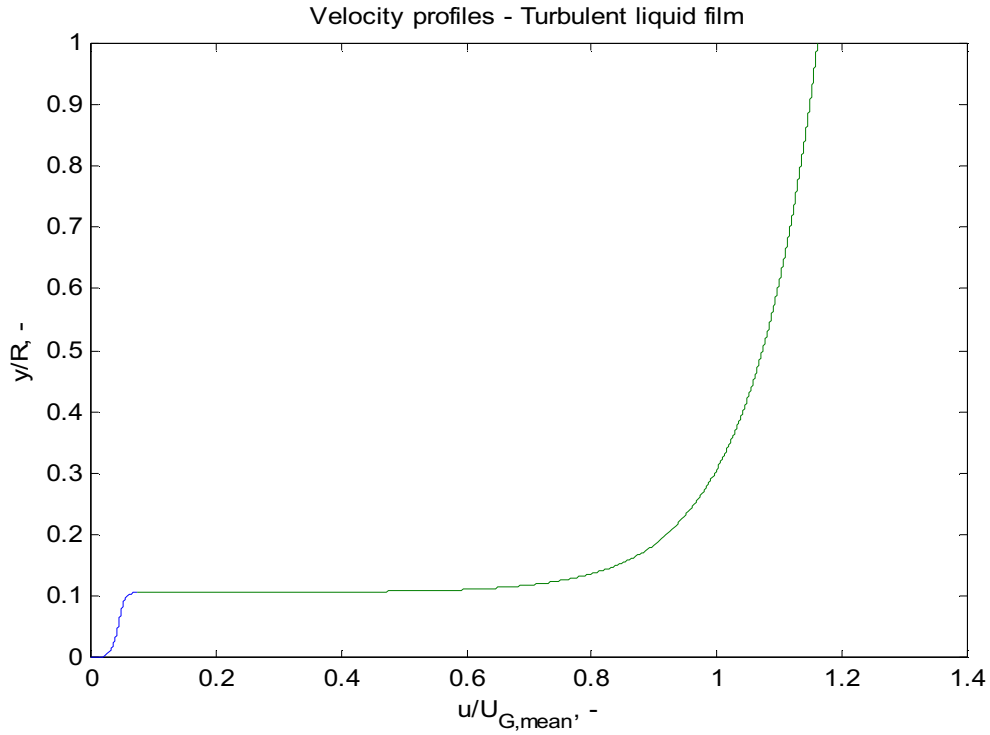

Figure 5–4: Water and air velocity profiles upon smooth Turbulent Film model assumptions. Liquid holdup = 10%, pressure drop = -500 Pa/m

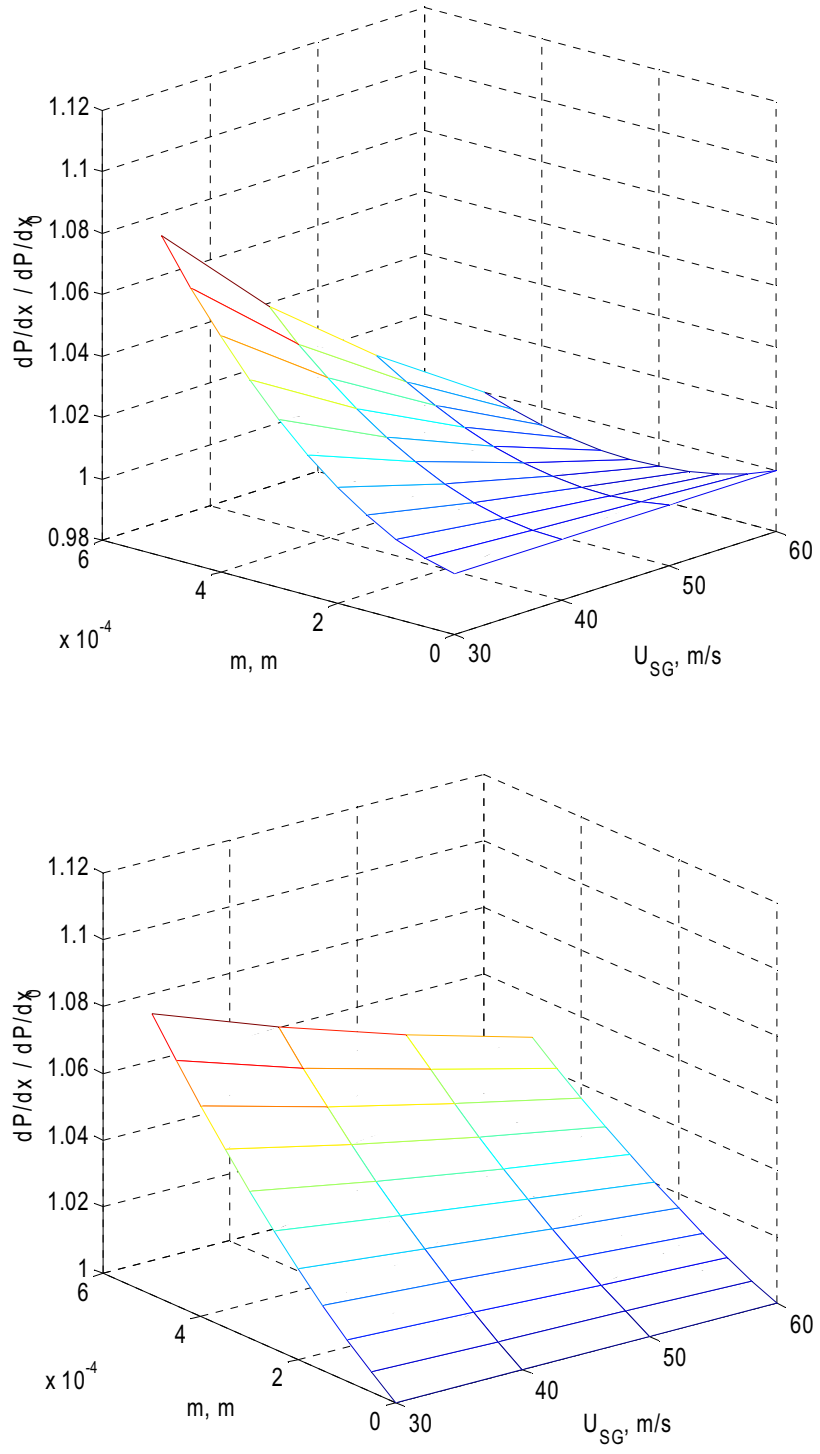

Figure 5–5: Ratio of the pressure drop with an annular liquid film (dP/dx) to the pressure drop without the film (dP/dx_0) calculated upon Laminar Film model assumptions, for various film thicknesses and gas superficial velocities. The laboratory 50 mm i.d. vertical riser geometry and laboratory fluid properties are used in the calculations. Top: air-water; Bottom: air-oil

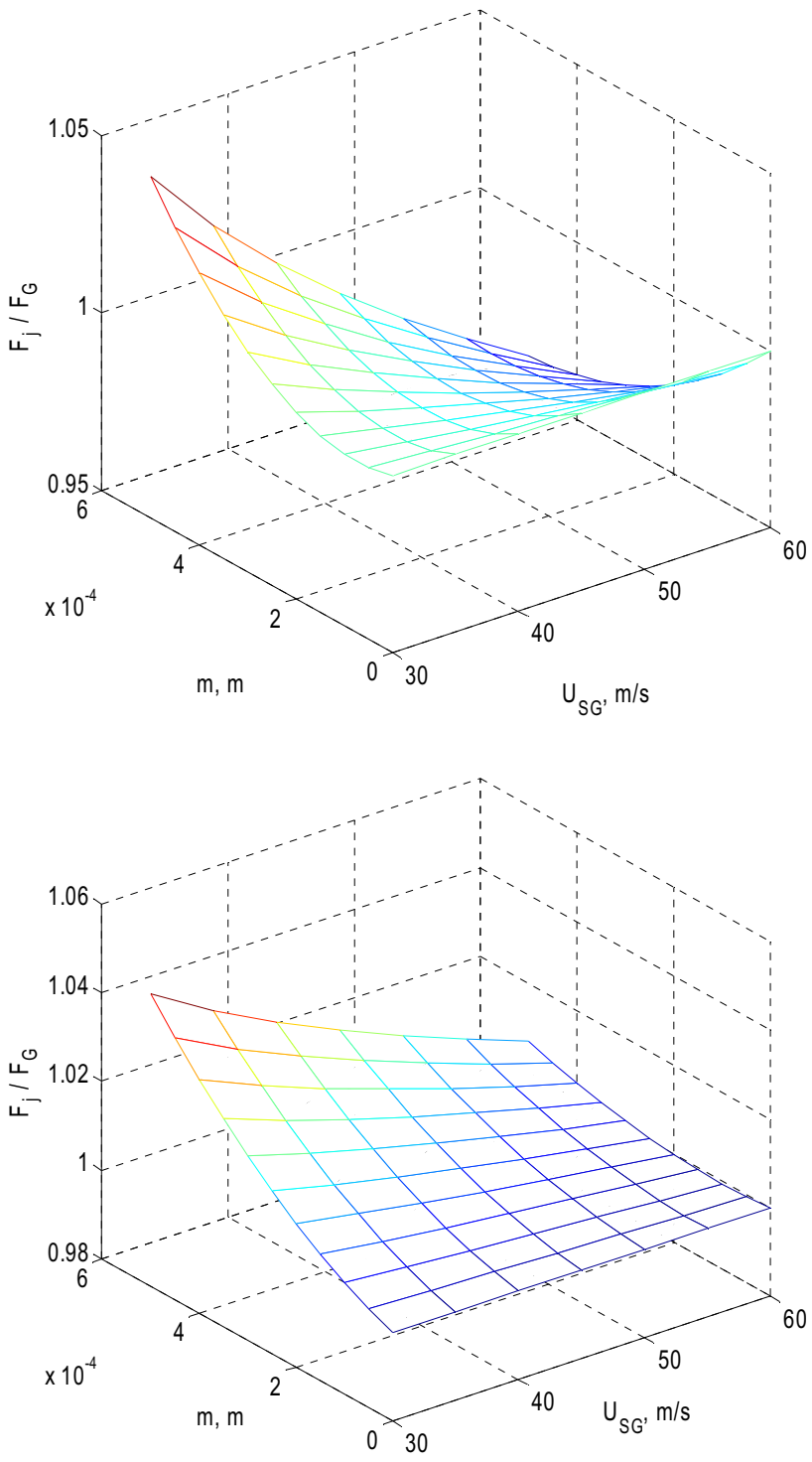

Figure 5–6: Ratio of the gas frictional pressure drop with an annular liquid film (F_j) calculated upon Laminar Film model assumptions to the gas frictional pressure drop without the film (F_G), for various film thicknesses and gas superficial velocities. The laboratory 50 mm vertical riser geometry and laboratory fluid properties are used in the calculations. Top: air-water; Bottom: air-oil

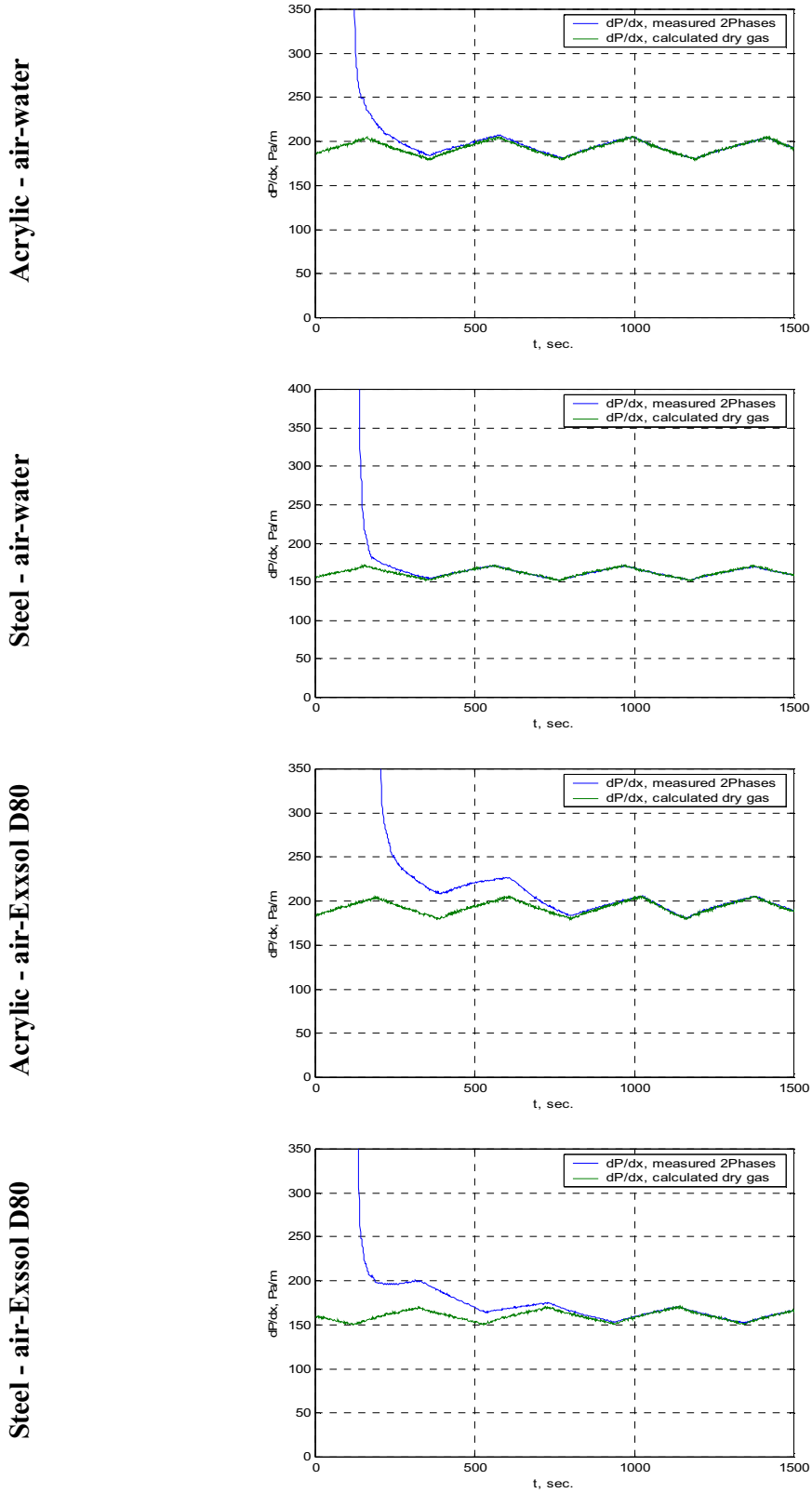

Figure 5–7: Horizontal film thinning runs. The frictional pressure drop is recorded versus time during the film thinning process and compared with the corresponding dry pipe pressure drop calculated with the Blasius equation

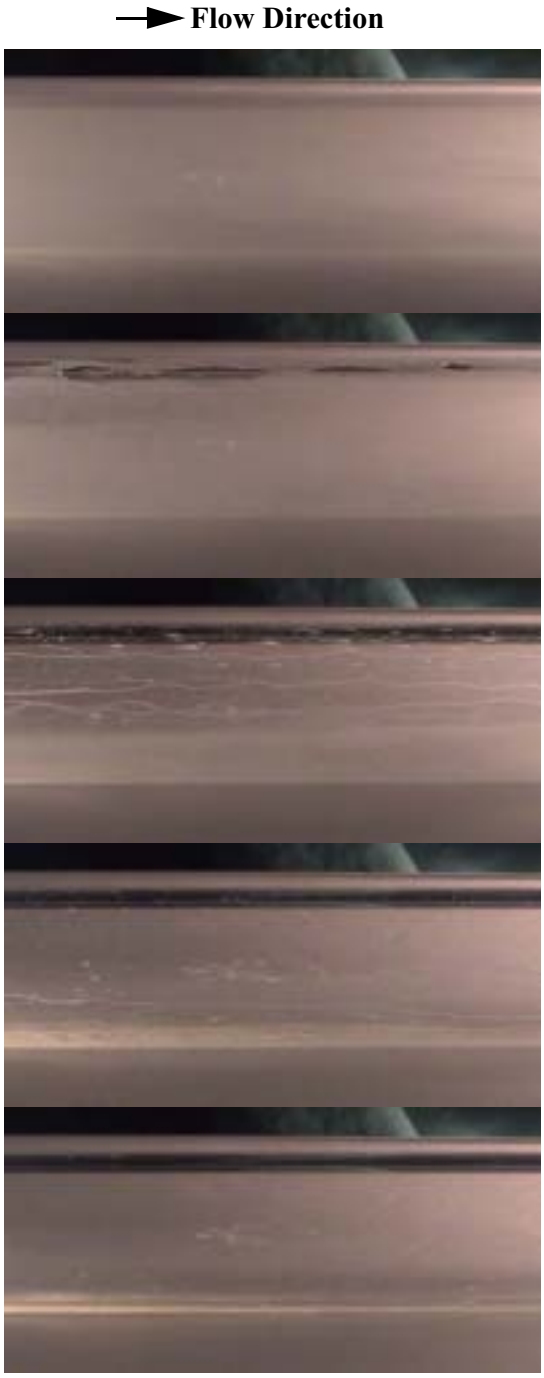

Figure 5–8: Pictures of flow regimes during water film thinning in the horizontal acrylic 60 mm pipe

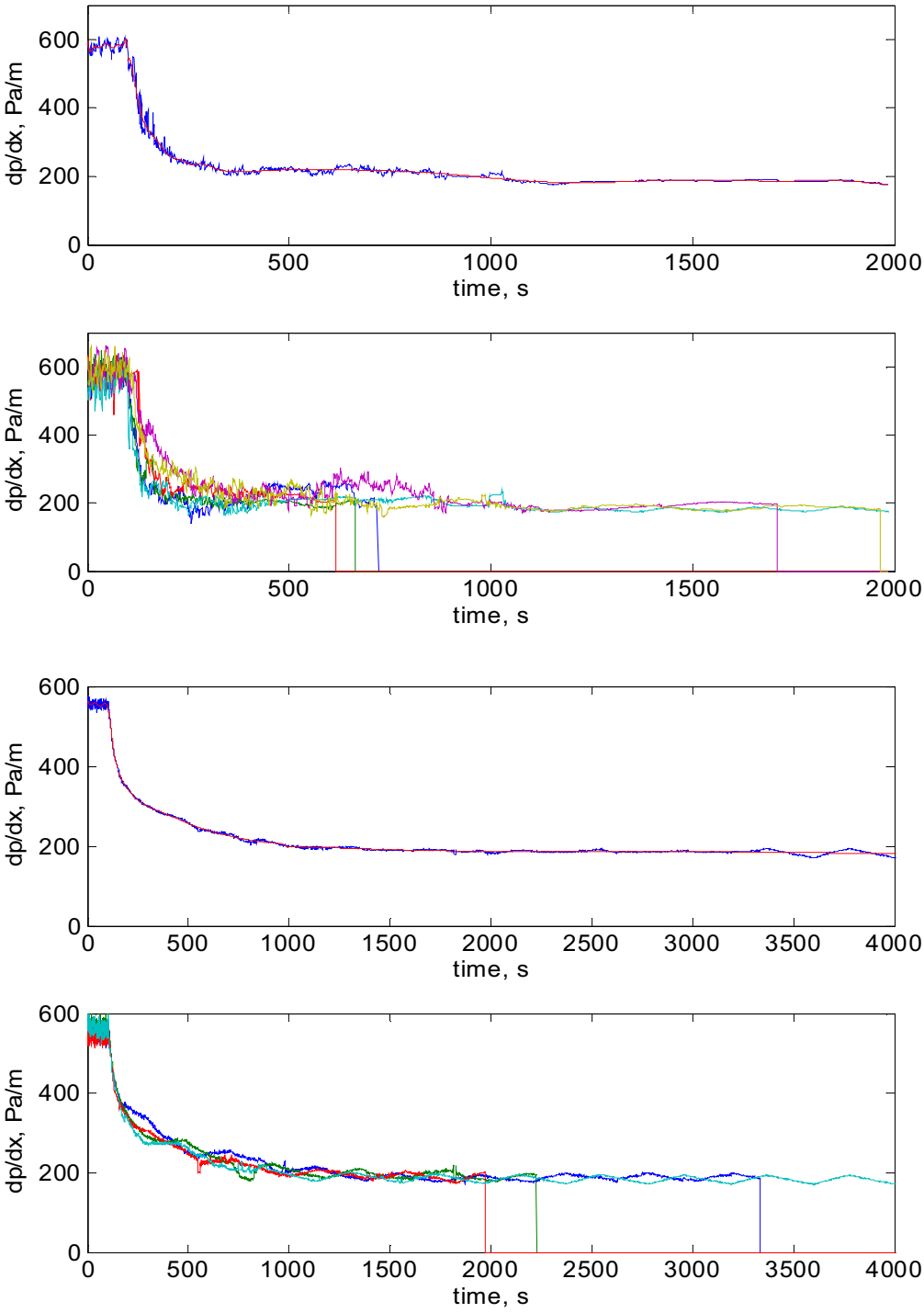

Figure 5–9: Averaging of pressure drop traces for obtaining the pressure drop for vertical film thinning runs. The pressure drop measurements for at least three repeated runs are first superimposed to match the valve shutdown time (lower plot). The time traces are averaged and an 8^{th} order polynomial interpolation is calculated (upper plot). Top: air-water experiments; Bottom: air-Exxsol experiments

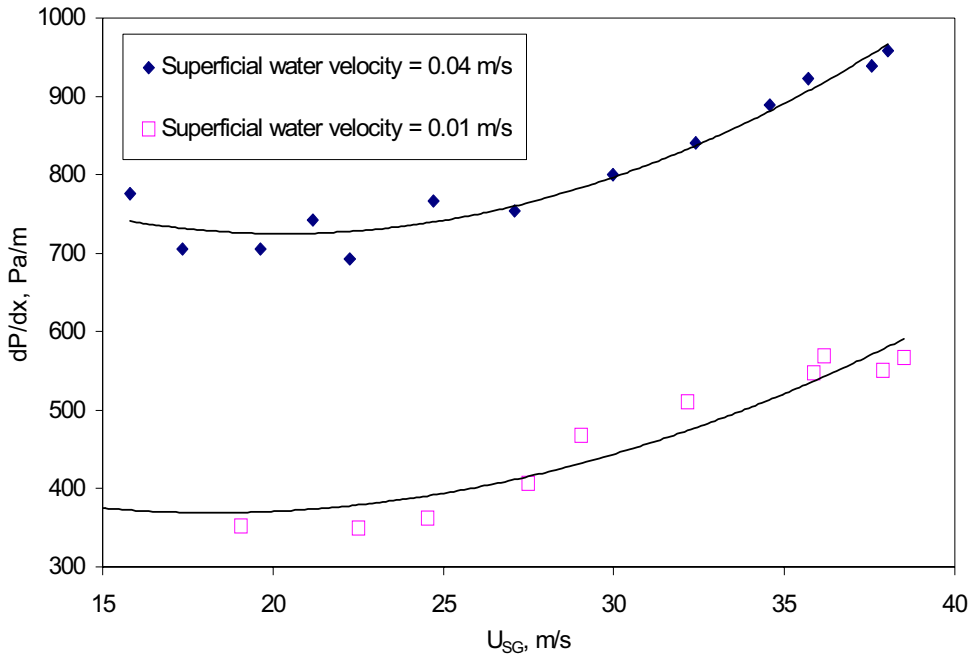

Figure 5–10: Pressure drop versus air flow rate at various water flow rates in the 50 mm i.d. vertical acrylic pipe. The curve's minimum corresponds to the onset of flow reversal (liquid backflow)

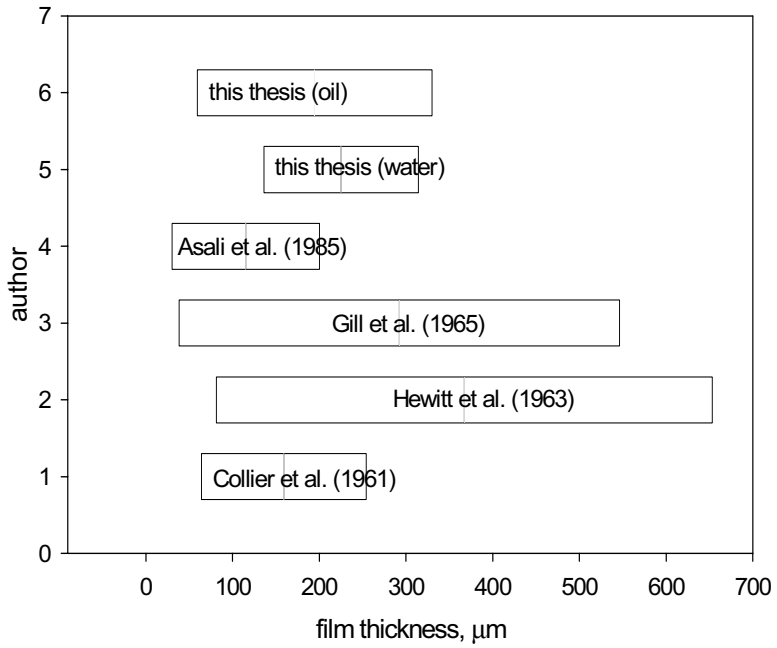

Figure 5–11: Average film thickness achieved in the vertical film thinning experiments compared to other authors. Data from Asali et al. (1985), Gill et al. (1965), Hewitt et al. (1963) and Collier et al. (1961)

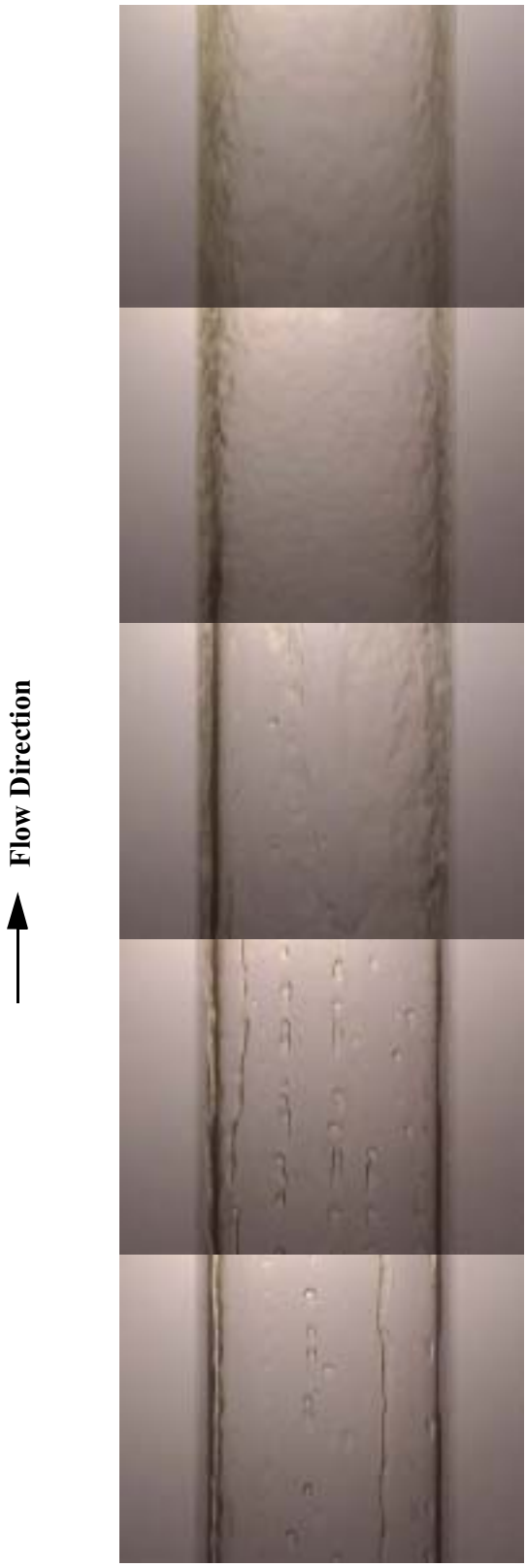

Figure 5–12: Pictures of flow regimes during water film thinning in the vertical acrylic 50 mm i.d. pipe

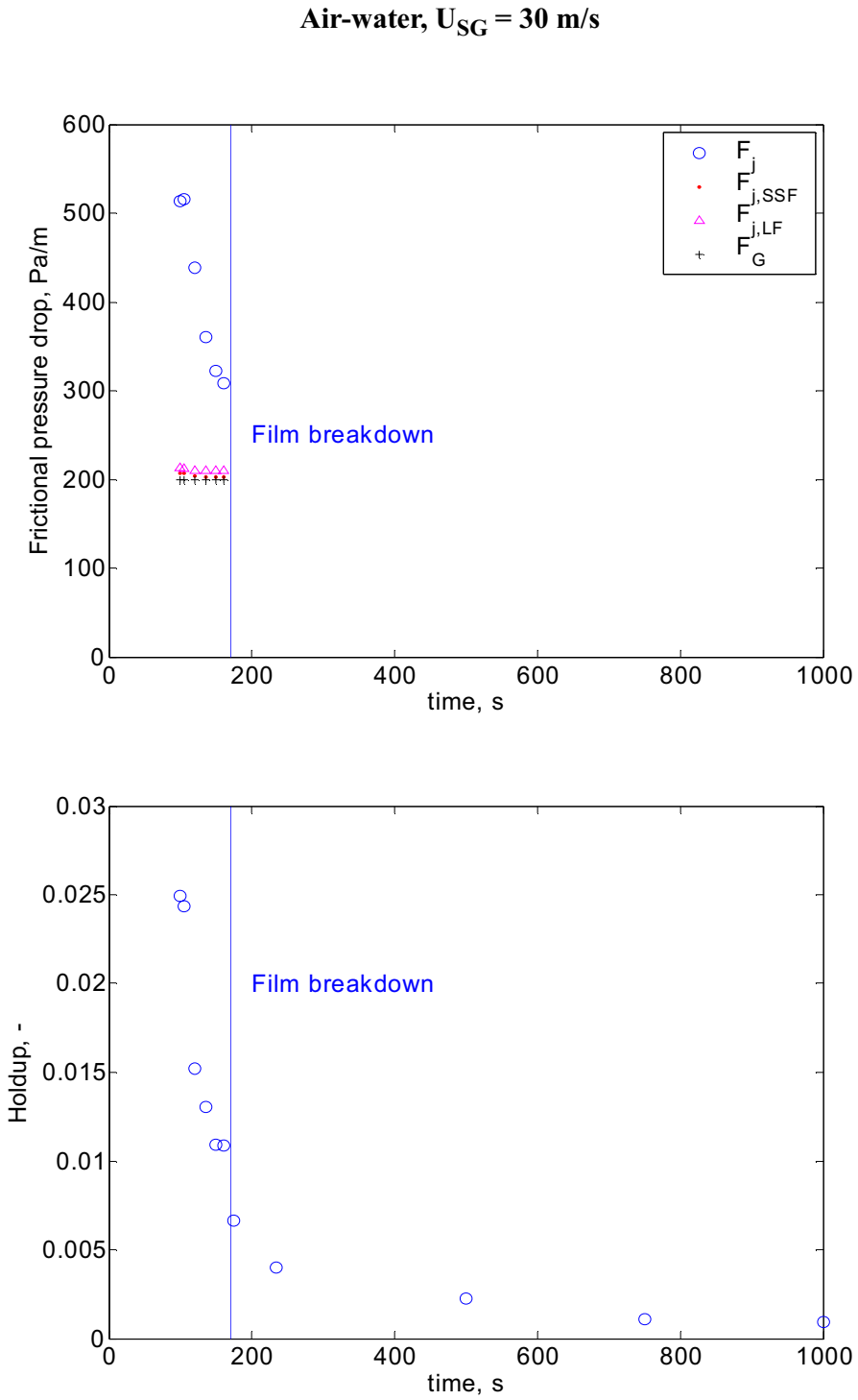

Figure 5–13: Measurement of the frictional pressure drop and liquid holdup for the water film thinning experiment in the vertical 50 mm i.d. acrylic pipe. F_j is the measured frictional pressure drop in the gas phase, $F_{j,SSF}$ is the computed frictional pressure drop assuming a smooth static film, $F_{j,LF}$ is the computed frictional pressure drop assuming a laminar flowing film and F_G is the computed frictional pressure drop for the gas alone in the pipe. The holdup is obtained from average phase fraction measurements with quick-closing valves

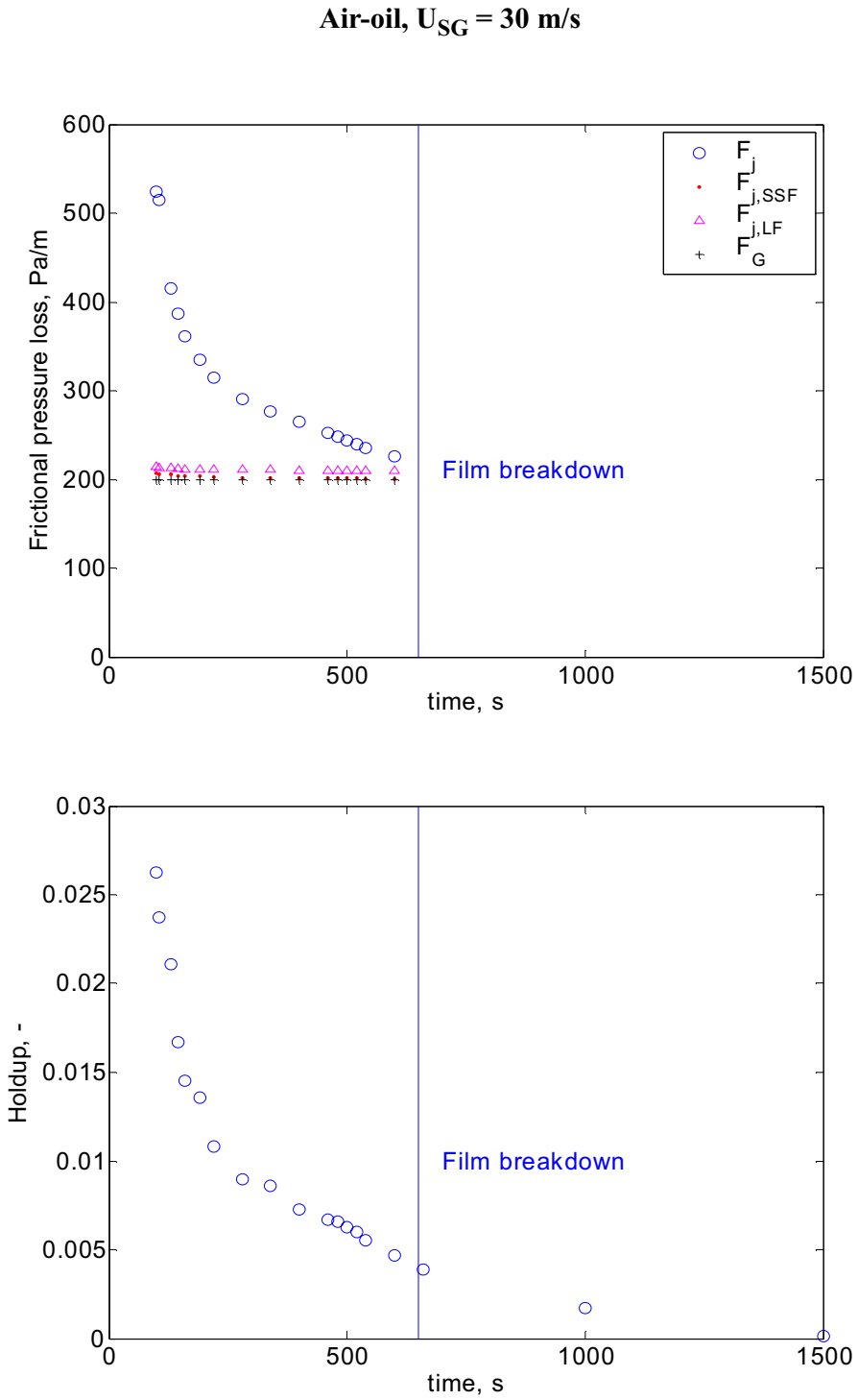

Figure 5–14: Measurement of the frictional pressure drop and liquid holdup for the Exxsol D80 film thinning experiment in the vertical 50 mm i.d. acrylic pipe. F_j is the measured frictional pressure drop in the gas phase, $F_{j,SSF}$ is the computed frictional pressure drop assuming a smooth static film, $F_{j,LF}$ is the computed frictional pressure drop assuming a laminar flowing film and F_G is the computed frictional pressure drop for the gas alone in the pipe. The holdup is obtained from average phase fraction measurements with quick-closing valves

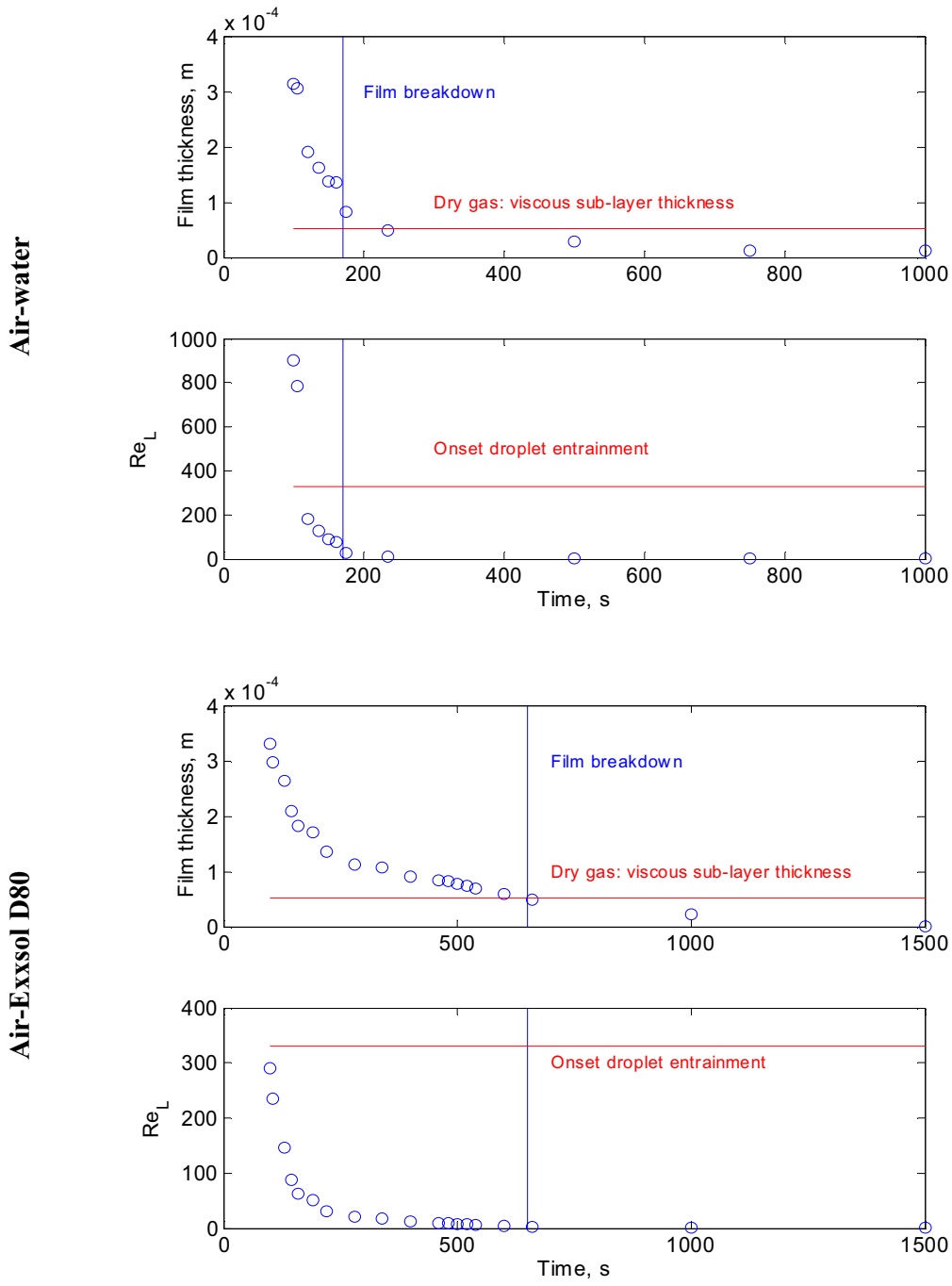

Figure 5–15: Calculated film thickness and liquid Reynolds number for the film thinning experiments. The time at liquid film break-down is indicated as well as the viscous sub-layer thickness computed for the gas flowing alone in the pipe. Top: air-water; Bottom: air-oil

.

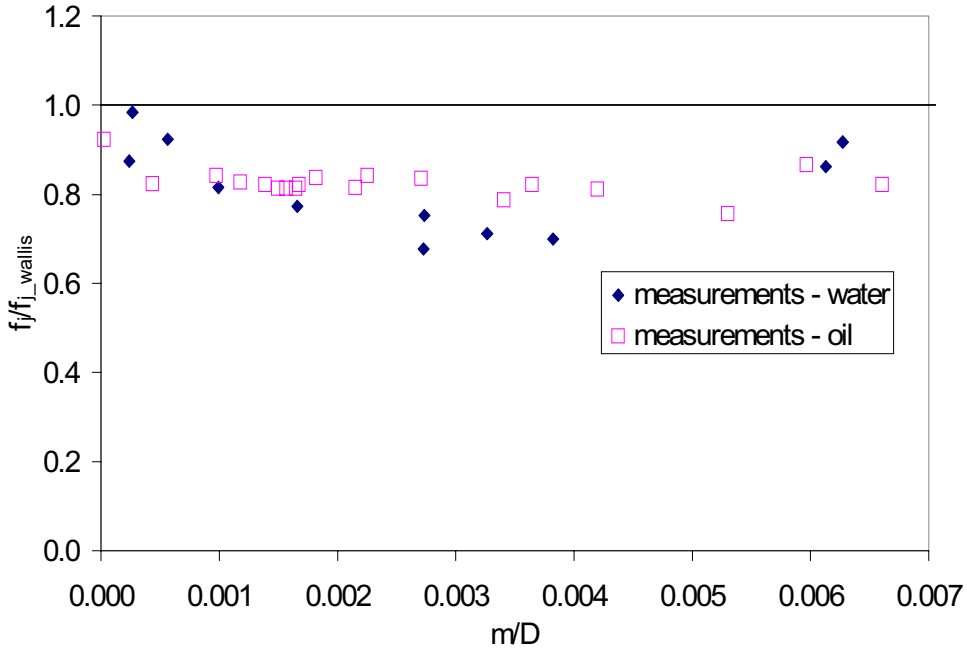

Figure 5–16: Comparison of the measured interfacial friction factor with Wallis' correlation (Wallis 1969)

.

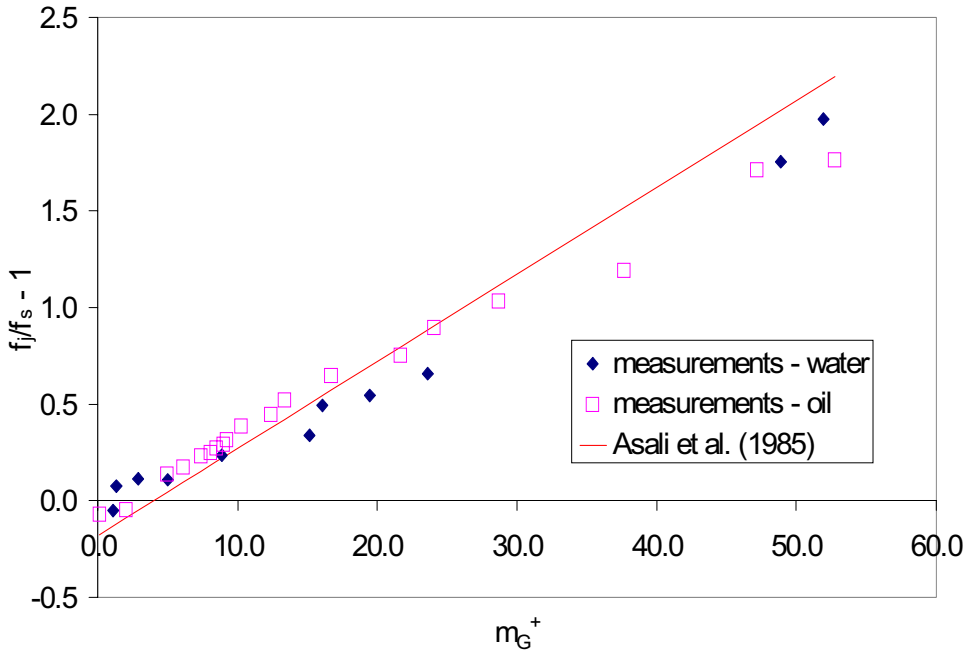

Figure 5–17: Comparison of the measured interfacial friction factor with Asali et al.'s correlation (Asali et al. 1985)

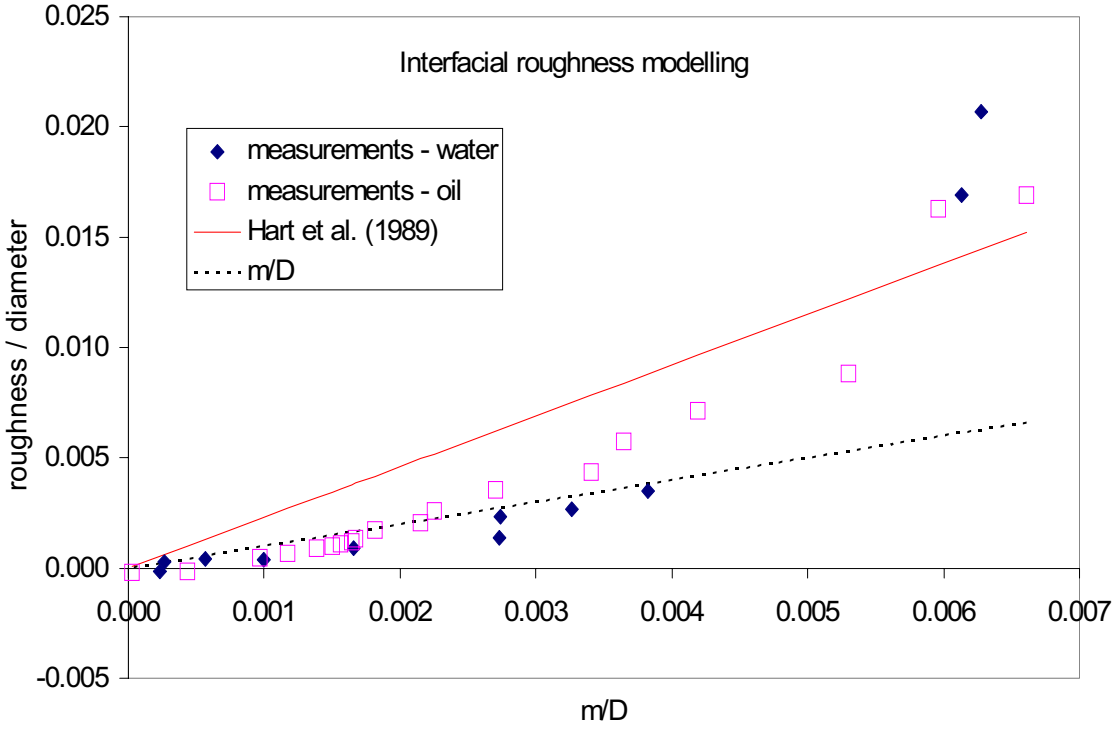

Figure 5–18: Comparison of the interfacial roughness calculated from the measured interfacial friction factor assuming Håland's equation with the correlation proposed by Hart et al. (1989)

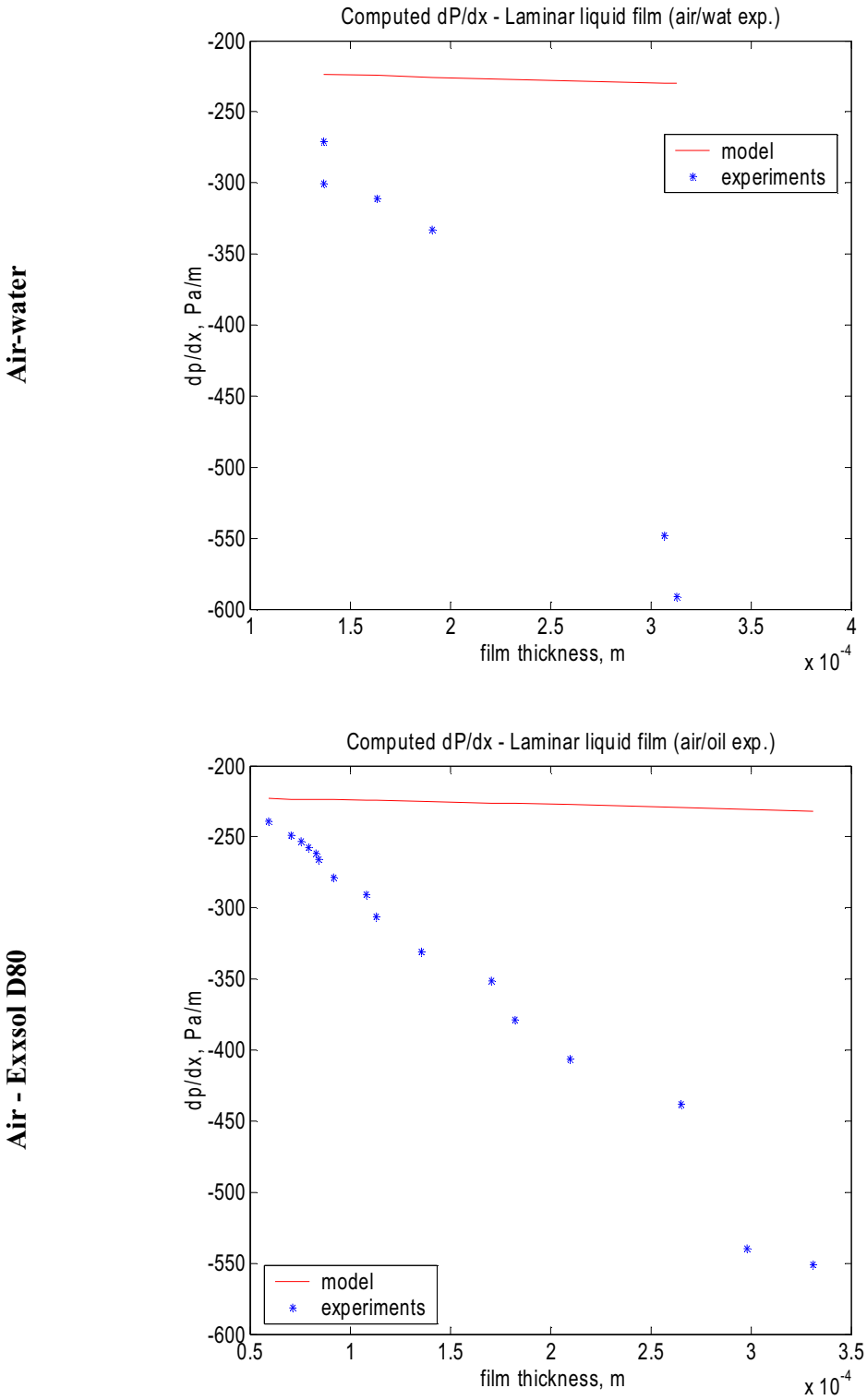

Figure 5–19: Comparison of the experimental pressure drop with the pressure drop calculated from the Laminar Film model. Top: air-water experiments; Bottom: air-oil experiments

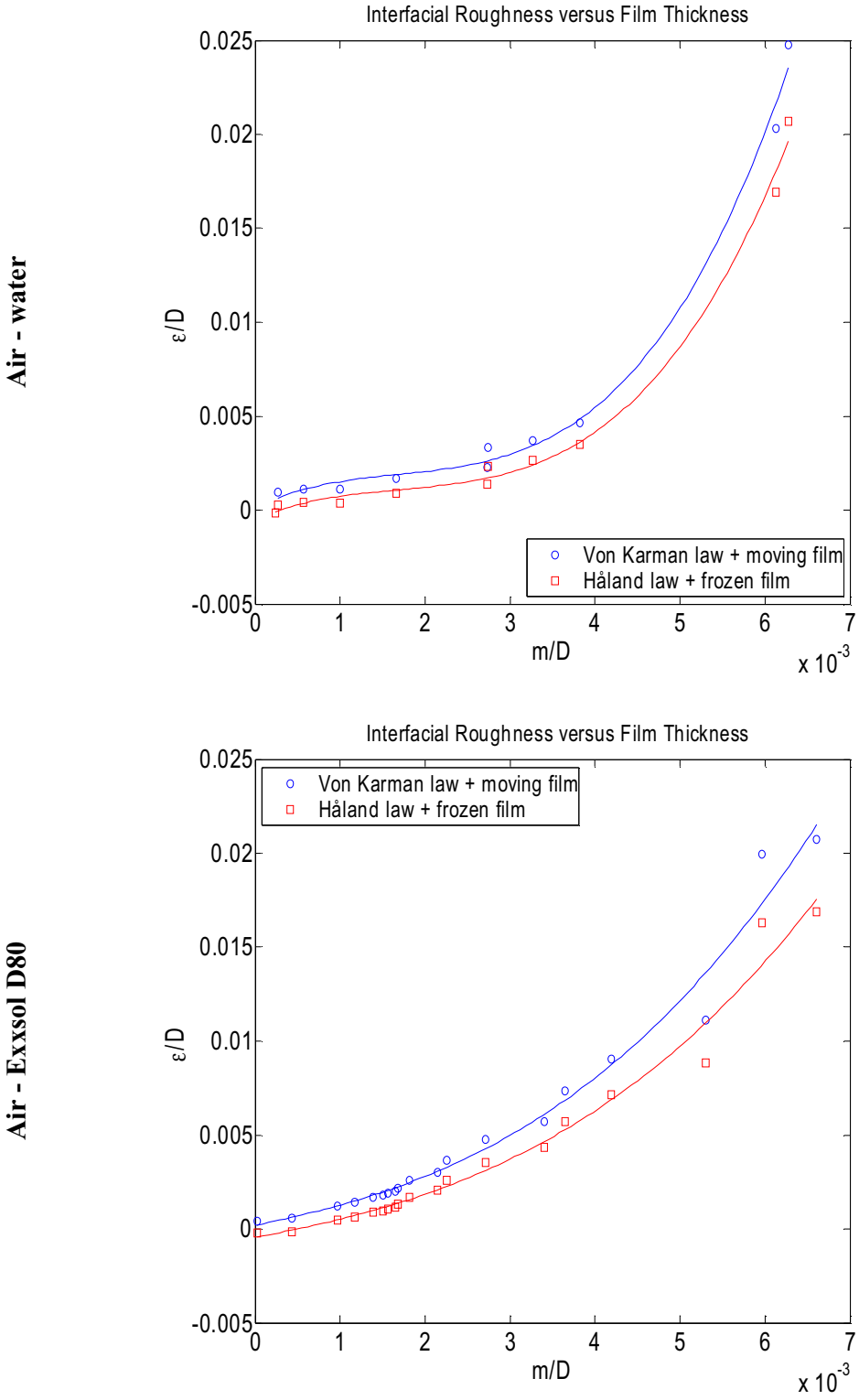

Figure 5–20: Back-calculated interfacial roughness. Circles: using Von Karman's law Equation [5.37] and Equation [5.38], for a moving interface; Squares: by matching Håland's Equation [3.11] with the measured interfacial friction factor assuming the interface is a fixed rough wall. Top: air-water experiments; Bottom: air-oil experiments

Chapter 6 Two-phase gas-liquid flow at low liquid loading

6.1 Introduction

In this chapter are described steady-state two-phase gas-liquid flow experiments carried out at low liquid loading in near horizontal pipes. The goals of the two-phase flow experiments are to:

- Obtain new pressure drop and holdup measurements at low liquid loading that can be compared to data from the literature.
- Provide a two-phase gas-liquid reference to the three-phase gas-oil-water flow experiments at low liquid loading described in Chapter 7.
- Test the possible effect of test section material.
- Provide new data to be compared with one-dimensional model predictions.

This chapter is divided in two main parts. In Section 6.2, the test matrix is presented, the flow regimes and the measurements are described. In Section 6.3 the pressure drop and holdup measurements are compared with predictions from one-dimensional models. Standard stratified flow models, specific models for low liquid loading and the multiphase flow general purpose simulator PETRA are tested and discussed. Liquid-wall friction and interfacial friction calculated from measurements are compared with wall-friction and interfacial friction correlations from the literature.

6.2 Experiments

6.2.1 Test matrix

The experiments performed are steady-state air-water and air-Exxsol D80 flow experiments in horizontal or slightly upward pipes at atmospheric conditions. Three different 60 mm i.d. test sections were used, made of acrylic, bare steel and epoxy coated steel. They are described in Chapter 4.

For each test section, one serie of experiments was run at fixed gas velocity and varying liquid velocity (serie #1) and one serie was run at fixed liquid velocity and varying gas velocity (serie #3). Serie #3.3 is a particular case of serie #3 run in the acrylic pipe at a higher liquid flow rate. Table 6–1 summarizes the two-phase flow test matrix.

Table 6–1: Test matrix for two-phase flow experiments

Serie	U_{SG}, m/s	U_{SL}, m/s	θ, deg.	Material
#1	14.8	0.0002-0.04	0	Acrylic Steel Epoxy
#3.1	4.93-29.6	0.0059	0,+1	Acrylic Steel Epoxy (0 deg. only)
#3.3	5.7-25	0.04	+0.5	Acrylic

Except for serie #3.3, experiments were performed at very low liquid loading, with a LGR down to 0.00135%. Figure 6–1 compares the range of superficial liquid velocities with that of other authors.

6.2.2 Experimental procedure

Experiments were performed in a steady-state mode according to the methodology presented in Section 4.4.1. After a settling period of minimum 30 minutes, differential pressure cells were logged for 10 minutes after which a phase fraction measurement was taken with quick-closing valves. The measuring accuracy attained is indicated in Table 4–28.

6.2.3 Flow regimes

The flow regimes observed are slug flow, stratified smooth and wavy flow, stratified/atomization flow with large amplitude waves and annular flow. Table 6–2 gives labels associated with the observed flow regimes. Detailed flow regime observations are tabulated in Appendix A. In this work, slug flow is defined when bridging of the pipe cross section occurs and encompasses such regimes as pseudo-slug flow, frothy slug flow or churn flow. Annular flow is defined when a continuous liquid film forms around the entire pipe circumference.

Figure 6–2 shows how air-water experiments distribute on the flow regime maps generated from the general flow regime identification algorithm of Barnea (1986). Results are similar for the air-oil experiments.

Longitudinal views and cross sectional views of flow regimes are provided at superficial liquid velocity equal to 0.0059 m/s in Figure 6–3 and Figure 6–4. Water appears green due

Table 6–2: Simplified two-phase flow pattern code

Flow regime	Detail	Label
Bubbly flow		BU
Stratified flow	smooth	ST1
	wavy, 2D regular waves	ST2
	wavy, 3D regular waves	ST3
	wavy, large amplitude irregular waves	ST4
	droplets	o
Slug flow		SL
Annular flow		AN

to the fluoresceine dye dissolved in it. Longitudinal views are taken facing the liquid phase from under the pipe. Cross sectional views are obtained by removing the slug catcher tank (U4.03) and placing a camera at the pipe outlet. Air needs to be continuously blown in front of the camera lens in order to prevent droplet impidgment. This is provided by a nozzle blowing compressed air, located at about 10 cm from the pipe end in front of the camera lens.

From the observation of flow regimes, it appears that:

- The flow regimes are identical in both acrylic and steel pipes.
- With oil (Exxsol D80), small amplitude three dimensional gravity and capillary waves form at the interface at 9 m/s air superficial velocity. The waves are crescent shaped when seen from above. With increasing air velocity, wave amplitude and wavelength decrease. Liquid tends to creep slightly up the pipe wall at high air velocities but in average, the gas-liquid interface appears flat.
- With water, the gas-liquid interface is smooth at 9 m/s air superficial velocity. As air superficial velocity increases to 11.5 m/s, irregular large amplitude gravity waves of random frequency start to develop at the interface. Wave amplitude and frequency increase as gas velocity is further increased. Between waves, the interface is rippled with capillary waves. The gas-liquid interface appears slightly convex at 9 m/s. In general, water creeps less up the pipe wall than oil.
- At conditions of droplet entrainment, water droplets deposited on the pipe wall protrude more into the gas core than oil droplets that tend to spread and merge into a thin liquid film.

6.2.4 Results

Measurements of steady-state pressure drop and holdup were performed for the flow ranges described in the test matrix, Table 6–1. Tabulated results are available in Appendix A.

Plots of the measurements versus input data were generated and summarized in Table 6–3.

Table 6–3: Summary of plots for two-phase, steady-state flow experiments

Label	Page	Topic
Figure 6–5	p. 172	Serie #1, pressure drop and holdup sensitivity with liquid superficial velocity at fixed gas superficial velocity
Figure 6–6	p. 173	Serie #3, pressure drop sensitivity with gas superficial velocity at fixed liquid superficial velocity
Figure 6–7	p. 174	Serie #3, holdup sensitivity with gas superficial velocity at fixed liquid superficial velocity

6.2.5 Analysis

A method of analysis of two-phase flow data is presented in Appendix D: assuming gas-wall friction can be calculated from a standard friction factor correlation, it is possible to extract and compare the terms contributing to the holdup and pressure drop. The involved contributions are frictional (wall and interfacial) and gravitational. More details concerning the extraction and scaling of the terms are given in Appendix D.

The term extraction was performed for selected series of measurements. The plots generated are summarized in Table 6–4.

Table 6–4: Summary of plots giving the relative magnitude of the terms of the holdup and pressure drop equations for a selection of two-phase flow data

Label	Page	Topic
Figure 6–8	p. 175	Holdup and pressure drop contributions: air-Exxsol D80 flow, acrylic pipe, inclination = +1 deg.
Figure 6–9	p. 176	Holdup and pressure drop contributions: air-Exxsol D80 flow, acrylic pipe, inclination = 0 deg.
Figure 6–10	p. 177	Pressure drop contributions: air-water, acrylic pipe, inclination = 0 deg. - Comparison with data by Espedal (1998)
Figure 6–10	p. 177	Pressure drop contributions: air-oil, steel pipe, inclination = 0 deg. - Comparison with data by Meng (1999)

With respect to which physical effects dominate pressure drop and holdup, the present two-phase data undergoes two distinct flow regimes:

1. Holdup and pressure drop dominated by gravity contributions. This can be seen in Figure 6–8 as superficial gas velocity decreases below 10 m/s. For gravity dominated flow, holdup is more sensitive to changes in operational conditions than pressure drop.

2. Holdup and pressure drop dominated by frictional contributions. This can be seen in

Figure 6–8 as superficial gas velocity increases above 10 m/s. At very low liquid superficial velocities, gas-wall friction dominates. This can be seen in Figure 6–9 for superficial liquid velocities below 0.02 m/s. At moderate to high superficial liquid velocities (above 0.02 m/s), liquid-wall friction dominates. For friction dominated flows, pressure drop is more sensitive to changes in operational conditions than the liquid holdup.

The present data compares well with two-phase flow data at low liquid loading from other authors. Figure 6–10 shows how the current data extends the trends observed by Espedal (1998) to lower superficial liquid velocities. Figure 6–10 shows that the data of Meng (1999) is also dominated by liquid-wall friction when the liquid superficial velocity increases but in a larger extent, due to the higher oil viscosity.

6.2.5.1 Holdup

Holdup tends to a constant asymptotic value at high gas velocity that seems independent of pipe material and fluid properties, and little sensitive to inclination. The fact that the liquid holdup tends to a constant value at high gas superficial velocity is due to the improved liquid transport due to droplet generation.

Holdup increases exponentially at low gas flow rates (gravity dominated flow). The relative increase compared to the asymptotic value at high gas superficial velocity is three times in horizontal flow and 6 times at +1 deg. inclination just prior to slug flow.

The sharpness of the holdup increase is function of the liquid superficial velocity. The increase is sharper at superficial liquid velocity equal to 0.0059 m/s than at 0.04 m/s, as shown in Figure 6–7. This agrees qualitatively with results by Lunde et al. (1993). At low liquid loading, a reduction of the gas velocity requires a larger relative increase in the liquid holdup in order to maintain the force balance necessary for liquid transport. In the present experiments, this increase appears to be little dependent on fluid viscosity and test section material.

6.2.5.2 Pressure drop

In all cases, the two-phase pressure drop is higher than the single phase pressure drop. Starting from no liquid and increasing liquid superficial velocity (Figure 6–5), pressure drop starts to increase with water for liquid-to-gas ratio larger than 0.003%, but with oil, the increase is significant from the first drop.

Pressure drop is fluid sensitive. At low liquid superficial velocity, pressure drop tends to be higher with oil than water. This is due to the liquid viscosity which results in slightly larger liquid holdup with oil. At higher liquid superficial velocity, pressure drop is higher with water than oil. This is a combined effect of the rougher air-water interface (large amplitude waves) and increased gas-wall friction (water droplets are non wetting and protrude more into the viscous sub-layer than oil droplets that are wetting and tend to spread on the wall surface).

Pressure drop is only slightly sensitive to a change in test section material at high gas velocities and is always larger in the acrylic pipe, all other conditions being the same. Even though the internal test section diameters are somewhat different, this does not significantly affect the single phase gas pressure drop as shown in Figure 6–6. A possible explanation is that the larger heterogeneity of the acrylic test section, reflected by its higher hydraulic roughness as shown in Table 4–26, causes more droplets to be generated and deposited on the wall in acrylic and this contributes to an increase in the gas-wall friction.

6.3 Comparison with prediction models

6.3.1 Liquid-wall friction

Using the procedure described in Appendix D, it is possible to calculate liquid-wall friction from measurements of two-phase pressure drop and holdup. Experimental data is selected in the stratified and stratified/atomization flow regimes and the liquid-wall friction is computed. Only data from the steel pipe experiments is considered for this comparison since the pressure drop and holdup results are, in general, not significantly different between test sections, as discussed in Section 6.2.5. The correlation by Biberg (1998), Equation [3.50], is used for the gas-wall friction.

It is chosen to compare the measured liquid-wall friction, $\tau_L * S_L$, with the following calculations:

1. The liquid-wall friction is obtained from a liquid-wall friction factor given by Poiseuille's law for laminar flow, Equation [3.5].

2. The liquid-wall friction is obtained from a liquid-wall friction factor given by Blasius' law for turbulent flow in smooth pipes Equation [3.7].

3. The liquid-wall friction is obtained from a liquid-wall friction factor given by Håland's equation, Equation [3.11].

4. The liquid-wall friction is obtained from a liquid-wall friction factor given by Kowalski's correlation (as cited in Espedal 1998):

$$\lambda_L = 1.052 H^2 Re_L \frac{D}{D_L}\Bigg|^{-0.5} \qquad [6.1]$$

5. The liquid-wall friction is obtained from a liquid-wall friction factor given by Hand's correlation (as cited in Espedal 1998):

$$\begin{cases} \lambda_L = 0.1048 H^2 Re_L \left(\frac{D}{D_L}\right)^{-0.139} & for\ Re_L > 2100 \\ \lambda_L = \frac{24}{Re_L} & for\ Re_L < 2100 \end{cases} \quad [6.2]$$

These friction factor correlations are chosen because they are among the most used correlations for calculating liquid-wall friction in two-phase pipe flow.

Results of comparisons are given in Figure 6–11. It reveals that correlations derived from single phase flow friction factors (Blasius or Håland) underestimate liquid-wall friction whereas the correlation by Kowalski severely overestimates the liquid-wall friction in addition to giving a larger spread. Best match is obtained with Hand's correlation. Similar conclusions were drawn by Espedal (1998) after comparisons with his own air-water data acquired in a 60 mm acrylic pipe.

Note that the liquid Reynolds number involved in the present study are close to the transition laminar-turbulent ($Re_L = 2100$). A reason for the good behaviour of Hand's correlation is, perhaps, the good performance of his friction factor expression for laminar flow.

6.3.2 Interfacial friction

Similar to liquid-wall friction, gas-liquid interfacial friction is extracted from pressure drop and holdup measurements in the stratified and stratified/atomization regimes. The extraction methodology and assumptions are described in Appendix D.

Interfacial friction, $\tau_j * S_j$, is compared with interfacial friction calculated from:

1. An interfacial friction factor assumed equal to the gas-wall friction factor given by Biberg (1998), Equation [3.50].

2. An interfacial friction factor given by Cheremisinoff et al. for small amplitude waves (as cited in Espedal 1998):

$$\lambda_j = 0.0142 \left(\frac{U_G}{U_r}\right)^2 \quad [6.3]$$

3. An interfacial friction given by Cheremisinoff et al. for roll waves (as cited in Espedal 1998):

$$\lambda_j = 0.032 + 810^{-5} \left(\frac{3}{8} Re_L\right) \quad [6.4]$$

4. An interfacial friction correlation from the ARS model by Hart et al. (1989), conside-

ring interfacial curvature in the calculation of S_j.

5. An interfacial friction factor from Andritsos et al. (1987), Equation [3.58].

These expressions for calculating interfacial friction are widely used in one-dimensional modelling of stratified two-phase flow.

Results of comparisons are shown in Figure 6–12. Severe under predictions of interfacial friction are obtained when assuming a smooth interface and $\lambda_j = \lambda_G$, even at low liquid loading. Cheremisinoff et al.'s roll wave correlation performs well with water, in agreement with observations that large amplitude waves form at the air-water interface at low liquid loading. Surprisingly, this same correlation underestimates interfacial friction with oil even though roll waves do not form at the air-oil interface. The Hart et al.'s ARS model and Andritsos et al.'s correlation generally over predict interfacial friction. These observations are in agreement with similar conclusions by Espedal (1998) with air-water stratified flow.

6.3.3 Pressure drop and holdup

The two-phase measurements are compared with pressure drop and holdup predictions given by one-dimensional models. Two classes of models, adequate for comparisons with the present data, are defined in Chapter 3. These are the "standard" stratified flow models and the "specific" models specifically derived for dealing with low liquid loading. The models considered are summarized in Table 6–8.

Models M3 to M7 are described in Chapter 3. Under model label M10 are presented results obtained with the general purpose three-phase flow pipe simulator PETRA. PETRA builds on OLGA concepts (Bendiksen et al. 1991) but is specially designed to track flow discontinuities such as gas-liquid fronts and pigs. PETRA can simulate three-phase gas-oil-water, steady-state and transient non isothermal pipe flows. The constitutive equations are three separate mass balance equations, combined as in OLGA to give a volume conservation equation or pressure equation, three momentum conservation equations for each phase and an energy balance equation for the mixture. Details of the closure laws, in particular wall and interfacial friction laws, are protected by confidentiality. Closure laws have been tuned against an extensive data bank of high pressure data.

The comparison between models and experimental data are conducted as follows:

1. For a given set of experimental conditions, the models are run for a standard pipe of i.d. 60 mm and hydraulic roughness 5 bm. Models M3 to M7 are programmed with MATLAB 6.5 and the method of solution is described in Section 3.3.7. Some assumptions are made that are listed in Appendix E. The PETRA model is run with PETRA 2.4. The more recent version 2.5 has also been tested a posteriori on some selected cases and gave exactly identical results.

2. Computed and measured data are treated statistically: a relative algebraic error for each data point is calculated according to Equation [E.4]. A gaussian probability density

function (pdf) is assumed for the error distribution as given by Equation [E.5], with mean and standard deviation given by Equation [E.6] and Equation [E.7] respectively. Tables of mean and standard deviation of errors are given in Table 6–5 and Table 6–6 for horizontal and inclined data.

3. Plots are generated of "point-by-point" comparisons, pdf functions and detail comparisons. The plots are summarized in Table 6–7. For the purpose of the detail comparisons, only the steel pipe data has been considered, except at superficial liquid velocity equal to 0.04 m/s where experiments have only been performed in the acrylic pipe.

Table 6–5: Statistic summary for the comparison of horizontal two-phase flow data with prediction models

Model	Holdup		Pressure drop	
	b_{err}	h_{err}	b_{err}	h_{err}
M3	-0.05	0.29	-0.22	0.12
M4	-0.41	0.13	0.02	0.07
M5	0.04	0.24	0.11	0.10
M6	0.09	0.16	-0.07	0.07
M7	-0.34	0.21	-0.02	0.13
M10	0.01	0.18	0.05	0.15

Table 6–6: Statistic summary for the comparison of inclined two-phase flow data with prediction models

Model	Holdup		Pressure drop	
	b_{err}	h_{err}	b_{err}	h_{err}
M3	4.62	6.58	0.78	1.42
M4	-0.51	0.09	-0.06	0.15
M5	0.15	0.55	0.19	0.15
M6	0.12	0.32	-0.06	0.10
M7	-0.57	0.14	0.53	0.33
M10	-0.08	0.26	0.06	0.24

6.3.4 Analysis

6.3.4.1 Overall statistics and point-by-point comparisons

Figure 6–13 and Figure 6–14 provide the following information:

Table 6–7: Summary of plots for comparisons between two-phase steady-state flow measurements and one-dimensional prediction models

Label	Page	Topic
Figure 6–13	p. 180	Holdup: point-by-point and PDF error comparisons
Figure 6–14	p. 180	Pressure drop: point-by-point and PDF error comparisons
Figure 6–15	p. 181	Serie #1: sensitivity with liquid superficial velocity at fixed gas superficial velocity. Comparison with models
Figure 6–16	p. 182	Serie #3: pressure drop sensitivity with superficial gas velocity at fixed liquid superficial velocity. Comparison with models
Figure 6–17	p. 183	Serie #3: holdup sensitivity with superficial gas velocity at fixed liquid superficial velocity. Comparison with models

- Best holdup predictions are obtained with Grolman's MARS model and PETRA, but PETRA gives more scatter.
- Best pressure drop predictions are obtained with Espedal's "simple" stratified flow model, Grolman's MARS model and PETRA.
- Specific models for dealing with low liquid loading perform slightly better than general purpose stratified flow models. A possible explanation is that specific models take into account interfacial curvature.
- Among specific models, Grolman's MARS model gives better overall predictions than Meng's Double Circle model.
- Few models can correctly predict pressure drop and especially holdup at slight upward inclination. Grolman's MARS model and PETRA are performing best in that respect.

6.3.4.2 Detail plots

The performance of each model in reproducing the experimental data is analysed in light of the following criteria:

For gravity dominated flows:

- Correct holdup inflexion with decreasing gas superficial velocity.
- Sharpness of the holdup increase with decreasing gas superficial velocity.
- Accuracy of the holdup prediction at +1 deg. upward inclination.

For friction dominated flows:

- Correct pressure drop and holdup sensitivity with increasing superficial liquid velocity.
- Accuracy of the pressure drop prediction at high gas velocity.

- Accuracy of the holdup prediction at high gas velocity.

Gravity dominated flows

As seen in Figure 6–17, no model can accurately predict, at low liquid loading, both the gas velocity at holdup inflexion and the magnitude of the holdup increase in the +1 deg. inclined pipe. Among the two best holdup models, Grolman's MARS model gives an inflexion that is too sharp compared to the measured data whereas PETRA gives an inflexion that is too slack. However, PETRA performs significantly better at higher liquid loading and superficial liquid velocity of 0.04 m/s.

Holdup accuracy prediction in inclined pipes is poor with Taitel et al's model (Taitel et al. 1976) and Meng's Double Circle model (Meng 1999). The unrealistic increase of holdup with decreasing gas superficial velocity given by the Taitel et al.'s model is also reported by other investigators (e.g. Baker et al. 1988). It results from the too low interfacial friction predicted by the assumption of interfacial friction equalling gas-wall friction. A similar explanation can be invoked for Meng's model which uses a constant value for the interfacial friction factor, a consideration that proves to be too simplistic.

In horizontal pipes, Biberg's model (Biberg 1998 and 1999) and Grolman's MARS model (Grolman 1994) give best holdup overall match with measurements. Standard stratified flow models are expected to perform worse close to the slug flow transition.

Friction dominated flows

Figure 6–15 shows that no model is able to reproduce with good overall accuracy both holdup and pressure drop variations with superficial liquid velocity at constant gas velocity. Among standard models, Espedal's "simple" model performs best for the pressure drop and Biberg's model performs best for the holdup. Grolman's MARS model performs best among specific models but generally under predicts the pressure drop. Espedal's "simple" model severely under predicts holdup as a consequence of the too high interfacial friction prediction by Andritsos et al. (1987) (see Section 6.3.2). PETRA does not predict the sharp pressure drop increase due to the introduction in the flow of small amount of liquids. This results in a significant under prediction of the pressure drop at very low liquid loading. At higher liquid loading, PETRA tends to overestimate the pressure drop but underestimates the liquid holdup.

Model prediction spread is large at high gas velocities as shown in Figure 6–16. Among standard stratified flow models, Espedal's (1998) "simple" model performs very well to predict pressure drop increase with increasing gas superficial velocity. This is surprising since the holdup predicted is too low and closures for gas-wall friction and liquid-wall friction are considered to predict too low values of the wall shear, as shown in Section 6.3.1 for the liquid-wall friction.

Among specific models at low liquid loading, Grolman's MARS model performs best in predicting pressure drop and holdup at high gas velocities. PETRA severely under predicts pressure drop at high gas superficial velocity, close to the transition with annular flow.

6.4 Summary

In this chapter, two-phase flow experiments have been carried out in straight 60 mm i.d. test sections at near horizontal inclinations. Experiments have been performed at lower liquid loading than previous studies in the literature. Sensitivities with flow rate, pipe inclination, pipe material and fluid properties have been investigated. The dominant flow regime was stratified flow, but the transitions to slug flow and annular flow were approached. Steady-state pressure drop and holdup have been measured and compared to one-dimensional prediction models and to the multiphase flow simulator PETRA.

The main topics discussed in this chapter are summarized below:

- Low liquid loaded flow can be friction or gravity dominated depending on experimental conditions. For gravity dominated flows, holdup shows the greatest sensitivity with changes of experimental conditions whereas pressure drop is the sensitive design parameter for friction dominated flows.

- At constant liquid superficial velocity and decreasing gas superficial velocity, holdup increases sharply at low liquid loading.

- At high superficial gas velocity, holdup tends to a constant asymptotic value whereas pressure drop is fluid and test section dependent.

- Few significant differences are observed between test section materials in two-phase flow. In general, steel and epoxy coated pipes exhibit a slightly higher holdup and slightly smaller pressure drop than the acrylic pipe. It is not obvious on whether this is an effect of the higher acrylic pipe hydraulic roughness or an effect of different surface wetting.

- Liquid-wall friction and interfacial friction are extracted from pressure drop and holdup measurements, assuming Biberg's closure law for gas-wall friction (Biberg 1998). Hand's correlation, as cited in Espedal (1998), is in best agreement with measured liquid-wall friction. No correlation agrees overall with measured interfacial friction. Cheremisinoff's roll wave correlation (Cheremisinoff et al. 1979) performs well with water data and Hart et al.'s ARS rough surface interfacial friction model (Hart et al. 1989) performs best with oil data.

- No one-dimensional stratified flow model gives good overall predictions for both gravity and friction dominated flows.

- Specific low liquid loading models perform only slightly better than standard stratified flow models for predicting steady-state holdup and pressure drop at low liquid loading. Among them, Grolman's MARS model (Grolman 1994) reproduces the present data with better accuracy than Meng's Double Circle model (Meng 1999).

- PETRA's overall performance is acceptable knowing that this software is not specifically calibrated against atmospheric data at low liquid loading. Nevertheless, some discrepancies appear at very low liquid loading: PETRA under predicts pressure drop in friction dominated flows and under predicts holdup for gravity dominated flows. Accuracy is improved when liquid loading increases.

Table 6–8: Models for stratified two-phase gas-liquid flow at low liquid loading

Label	Ref.	Gas-liquid interface	Entrain-ment	Limi-tations	Closures					Geometries		Holdup calc.	Pressure drop calc.
					a_G	a_L	i_j		Y				
							a_j	U_j		S_L	S_j		
M3	Taitel et al. (1976)	flat	no	stratified	Blasius Equation [3.7]	Blasius Equation [3.7]	$\lambda_j=\lambda_G$	0	geometric Equation [3.31]	geometric Equation [3.27]	geometric Equation [3.29]	iteration on Equation [3.26]	P drop Equation [3.23]
M4	Espedal (1998)	flat	no	stratified	Håland Equation [3.11]	Håland Equation [3.11]	Andritsos Equation [3.58]	U_L	geometric Equation [3.31]	geometric Equation [3.27]	geometric Equation [3.29]	iteration on Equation [3.26]	P drop Equation [3.23]
M5	Biberg (1998, 1999)	flat	no	stratified	Biberg Equation [3.51]	Biberg Equation [3.54]	Biberg Equation [3.59]		geometric Equation [3.31]	geometric Equation [3.27]	geometric Equation [3.29]	iteration on Equation [3.26]	P drop Equation [3.23]
M6	Grolman (1994)	concave	no	$\varepsilon_L<0.47$ $-3<\theta<6$	Eck Equation [3.52]	MARS Equation [3.55]	Eck Equation [3.12] with ε_j Equation [3.65]	U_L^* with U_L^* Equation [3.66]	empirical Equation [3.36]	from δ Equation [3.27]	interpol-lation Equation [3.40]	iteration on Equation [3.26]	P drop Equation [3.23]
M7	Meng (1999)	concave	yes, Equation [3.78]	low liquid loading	Blasius Equation [3.7]	Blasius Equation [3.7]	empirical Equation [3.69]	U_L	empirical Equation [3.44]	from δ Equation [3.27]	from δ_j and D_j Equation [3.41]	iteration on Equation [3.26]	P drop Equation [3.23]
M10	PETRA 2.4	flat	yes	general purpose model	unknown								

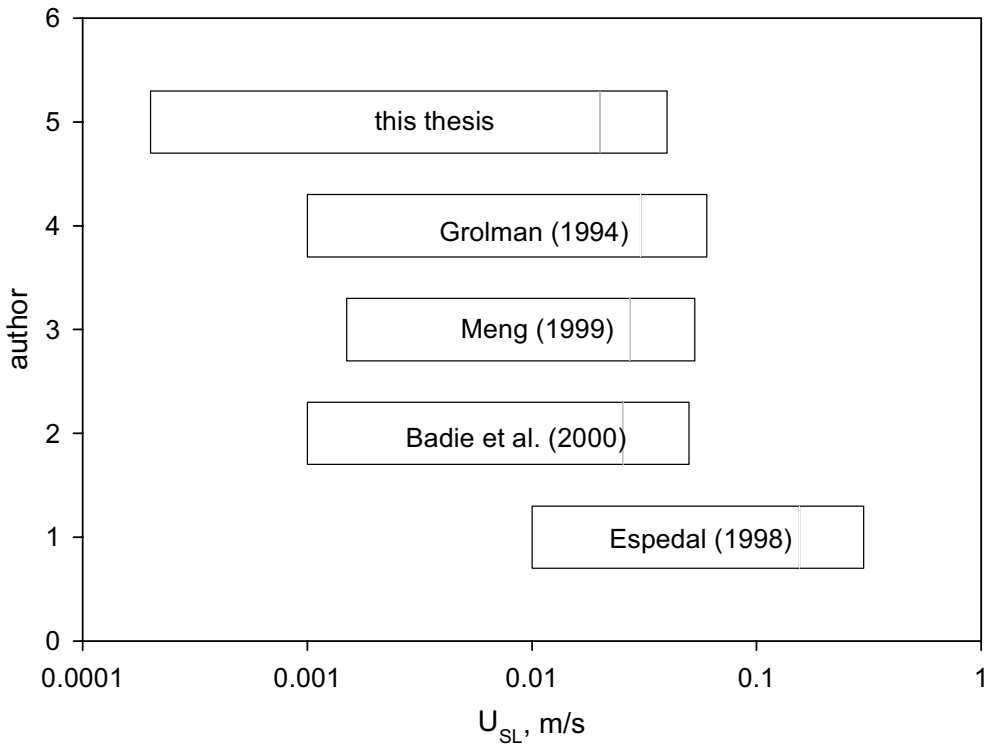

Figure 6–1: Liquid loading compared to other authors. Data from Grolman (1994), Meng (1999), Badie et al. (2000) and Espedal (1998)

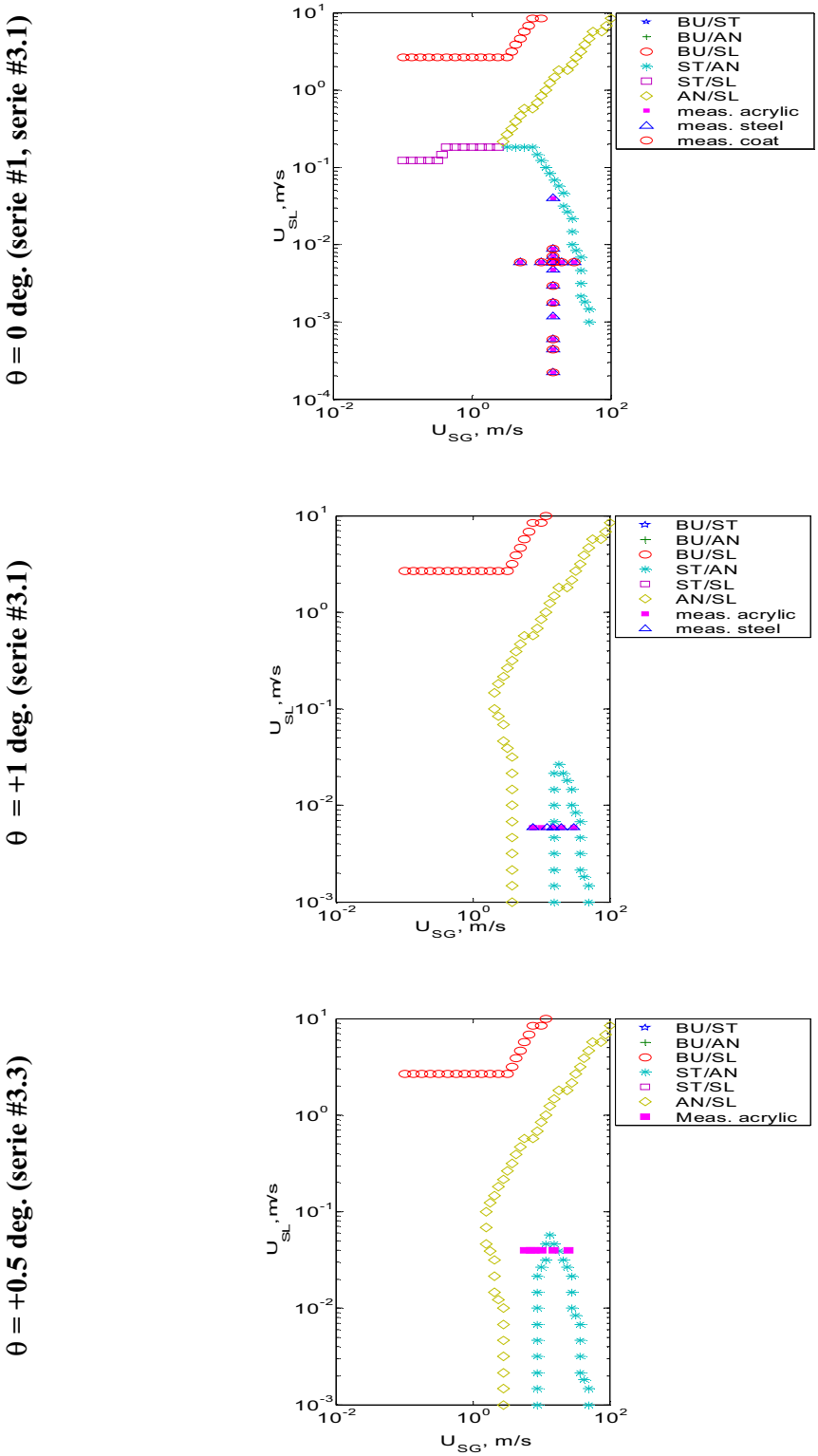

Figure 6–2: Air-water experiments located on the flow regime map according to Barnea (1986). Transition lines between flow regimes are obtained by numerically testing the transition criteria algorithm provided by Barnea (1986) for each pair of gas and liquid superficial velocities

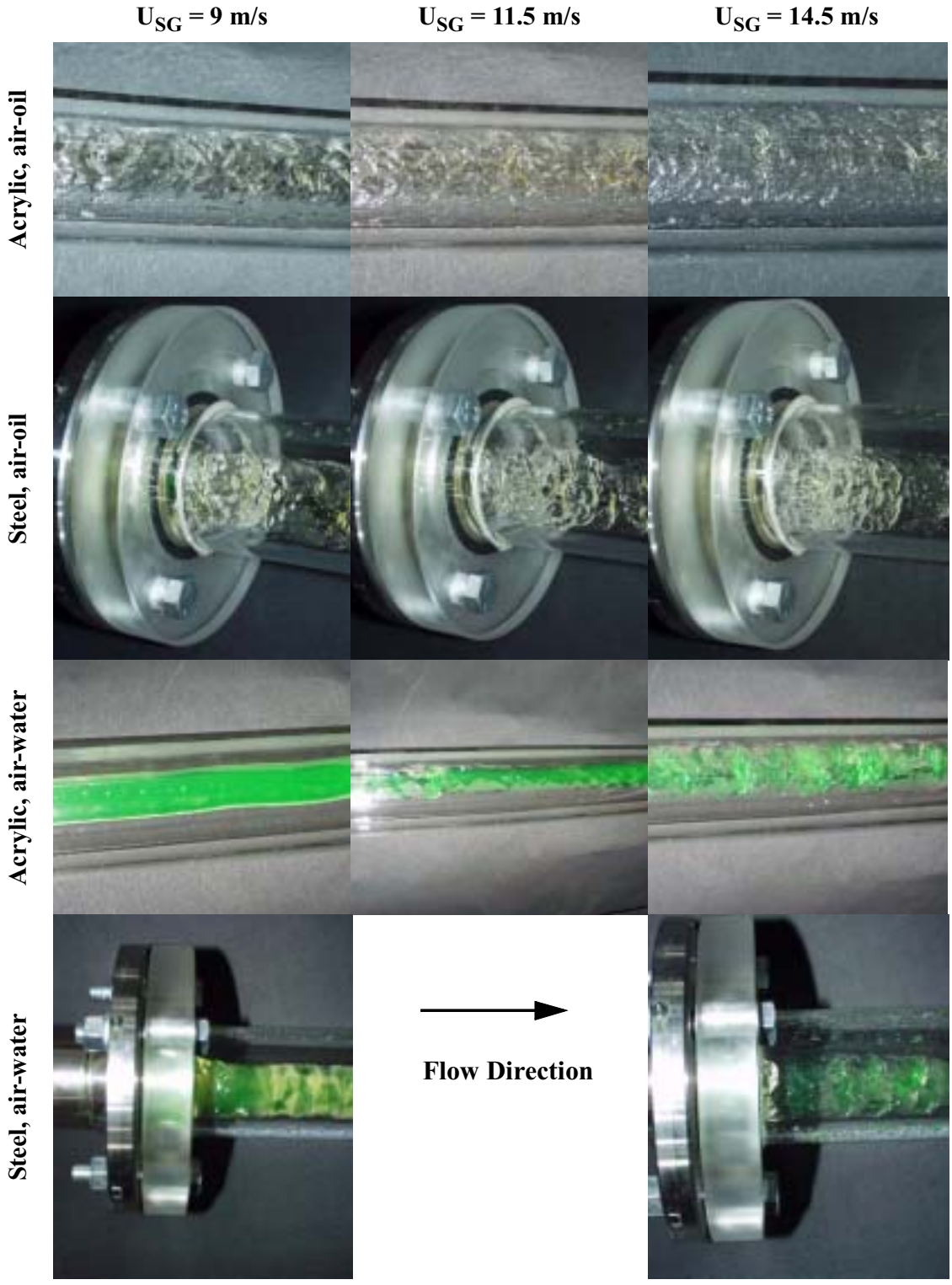

Figure 6–3: Flow regimes in the steel and acrylic pipes at liquid superficial velocity = 0.0059 m/s: longitudinal views, viewpoint from under the pipe

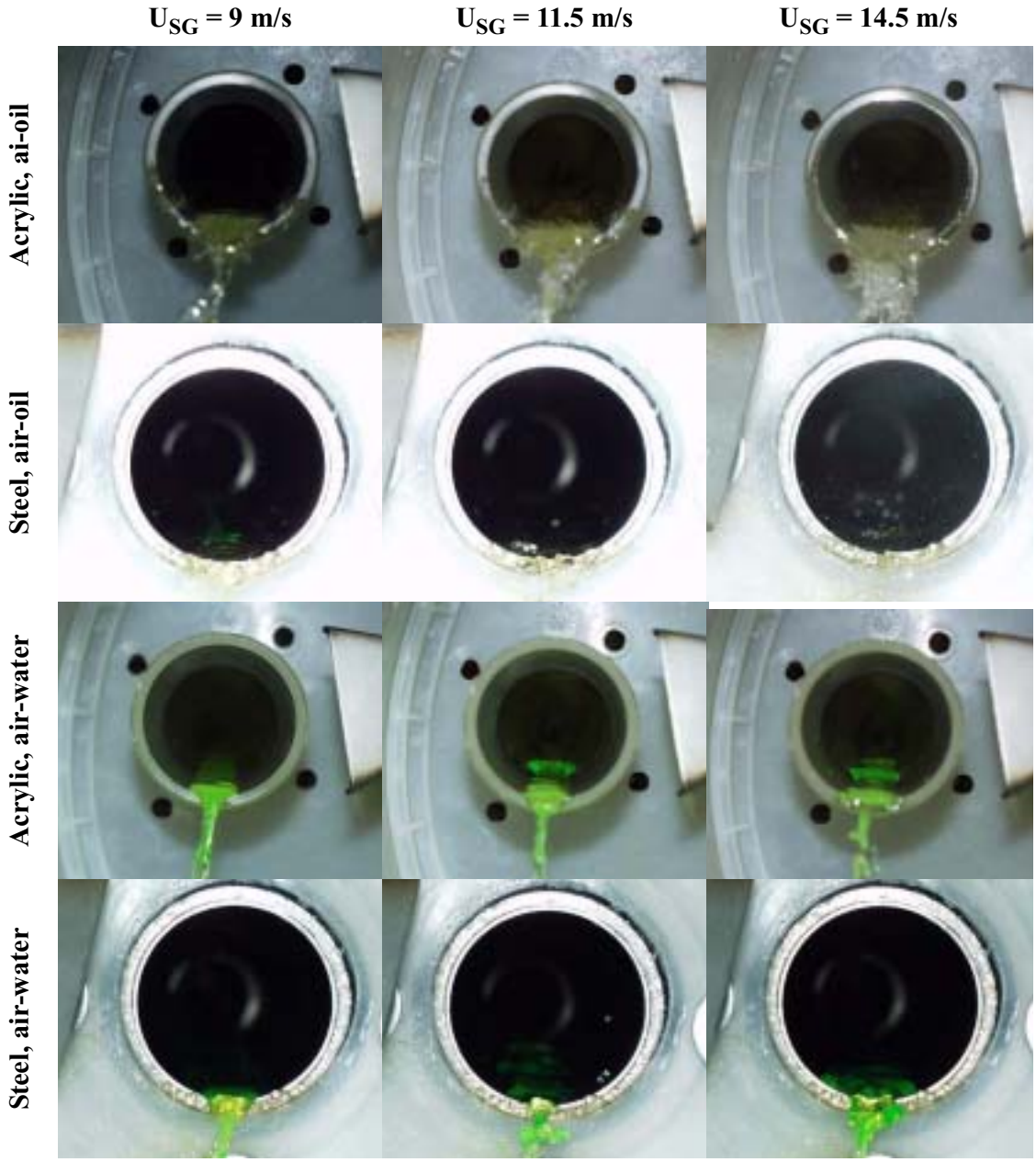

Figure 6–4: Flow regimes in the steel and acrylic pipes at liquid superficial velocity = 0.0059 m/s: cross sectional views

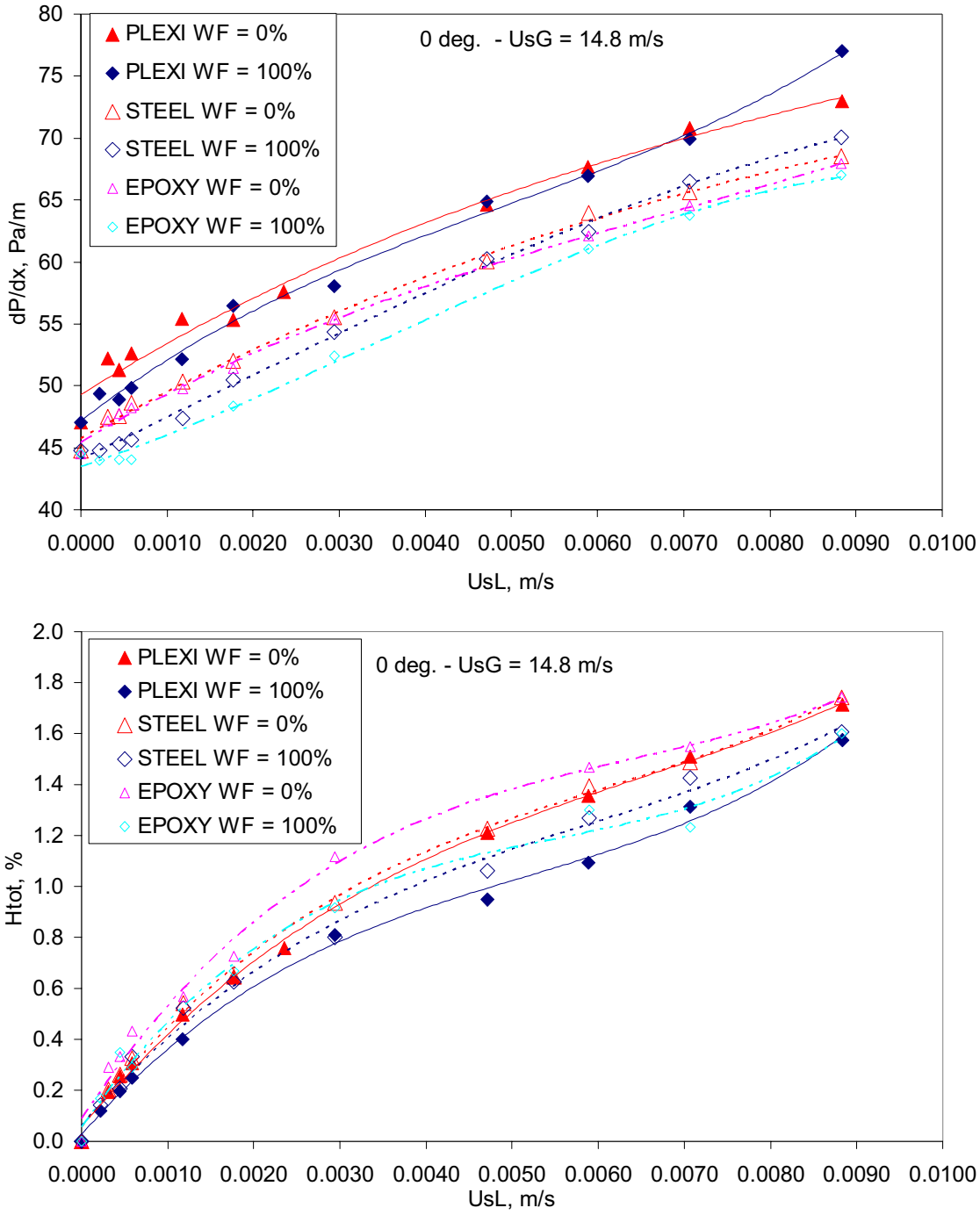

Figure 6–5: Serie #1, sensitivity with liquid superficial velocity at fixed gas superficial velocity; Top: pressure drop, Bottom: liquid holdup

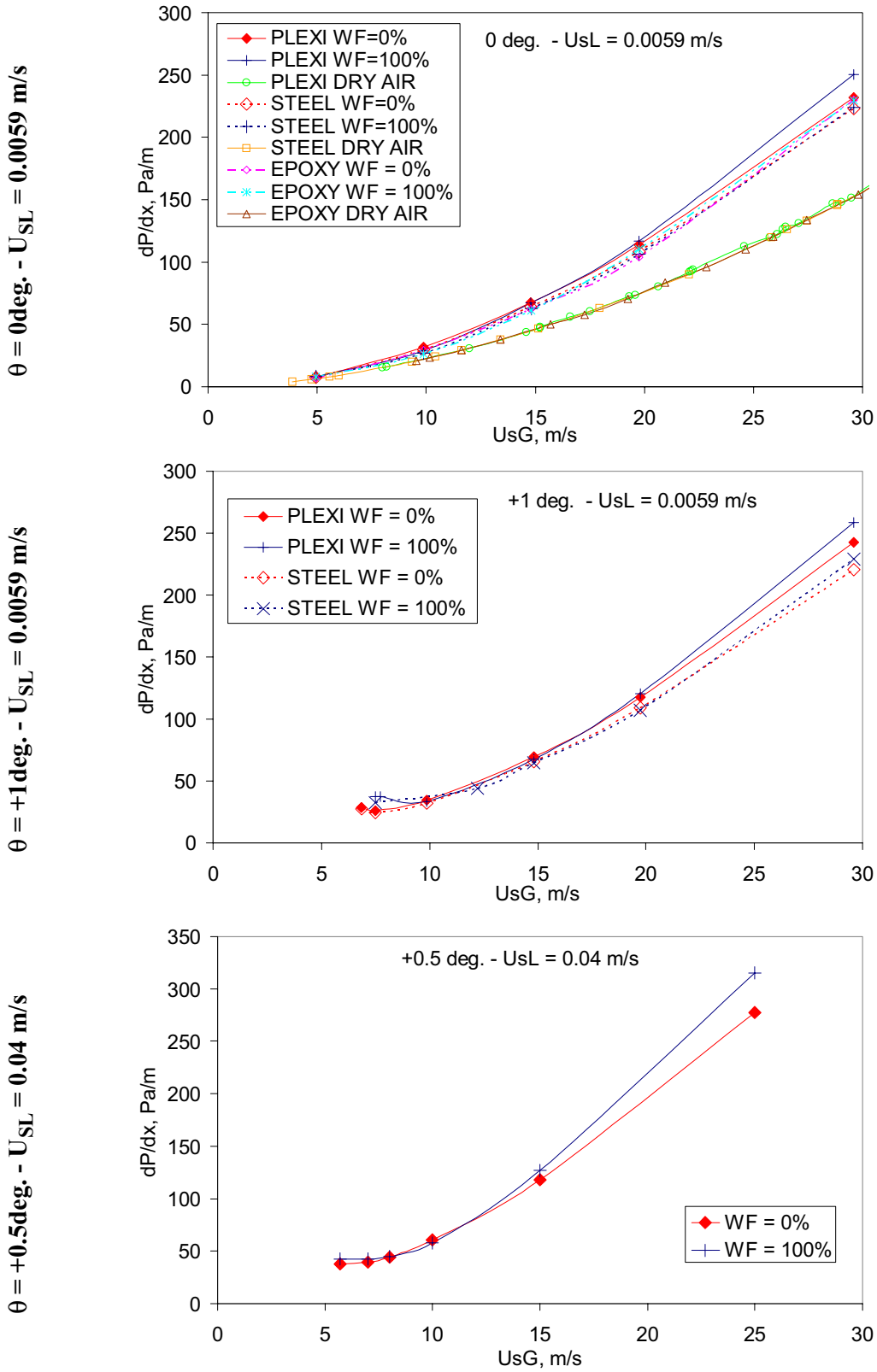

Figure 6–6: Serie #3, pressure drop sensitivity with superficial gas velocity at fixed liquid superficial velocity and inclination

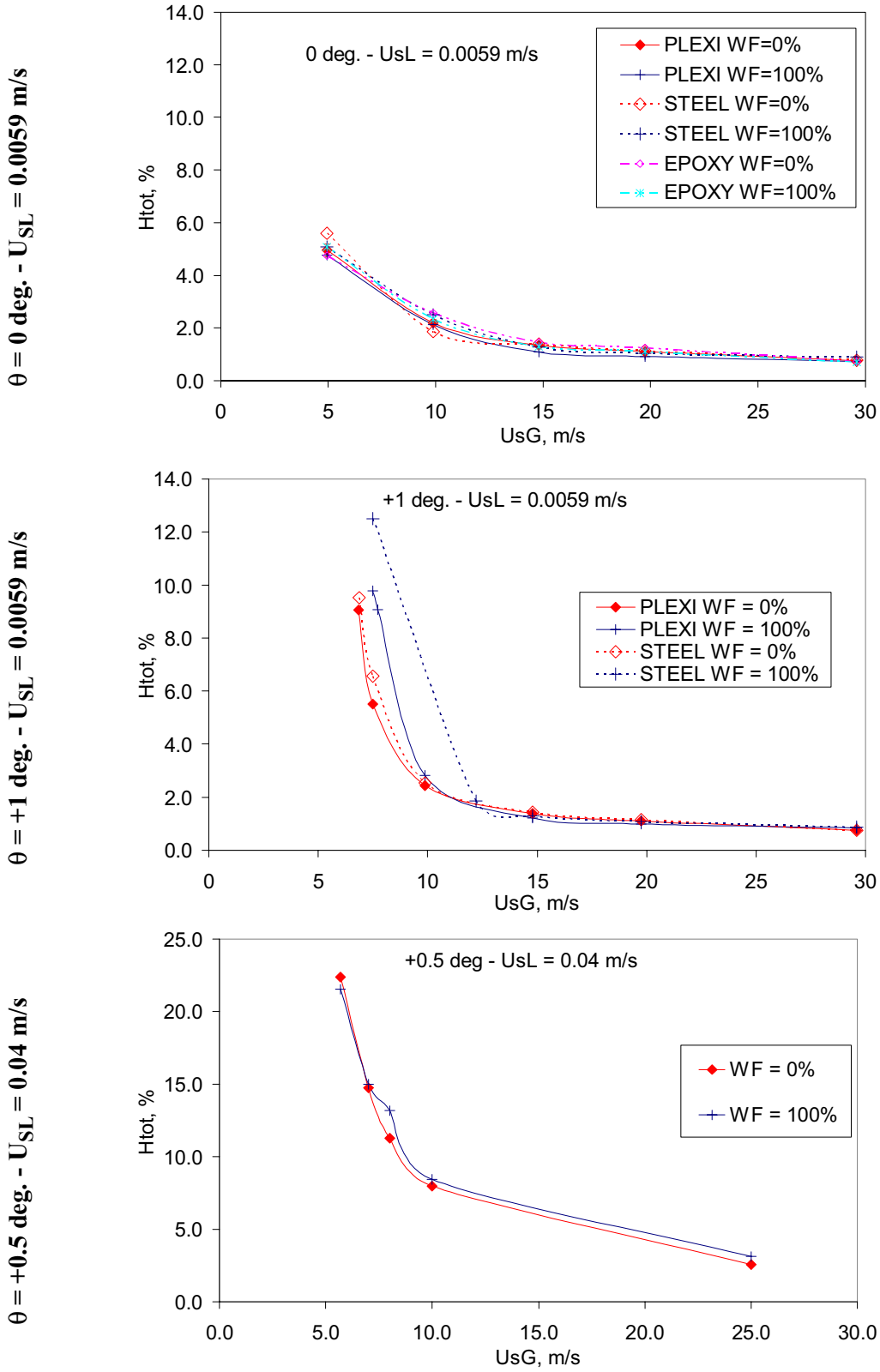

Figure 6–7: Serie #3 holdup sensitivity with superficial gas velocity at fixed liquid superficial velocity and inclination

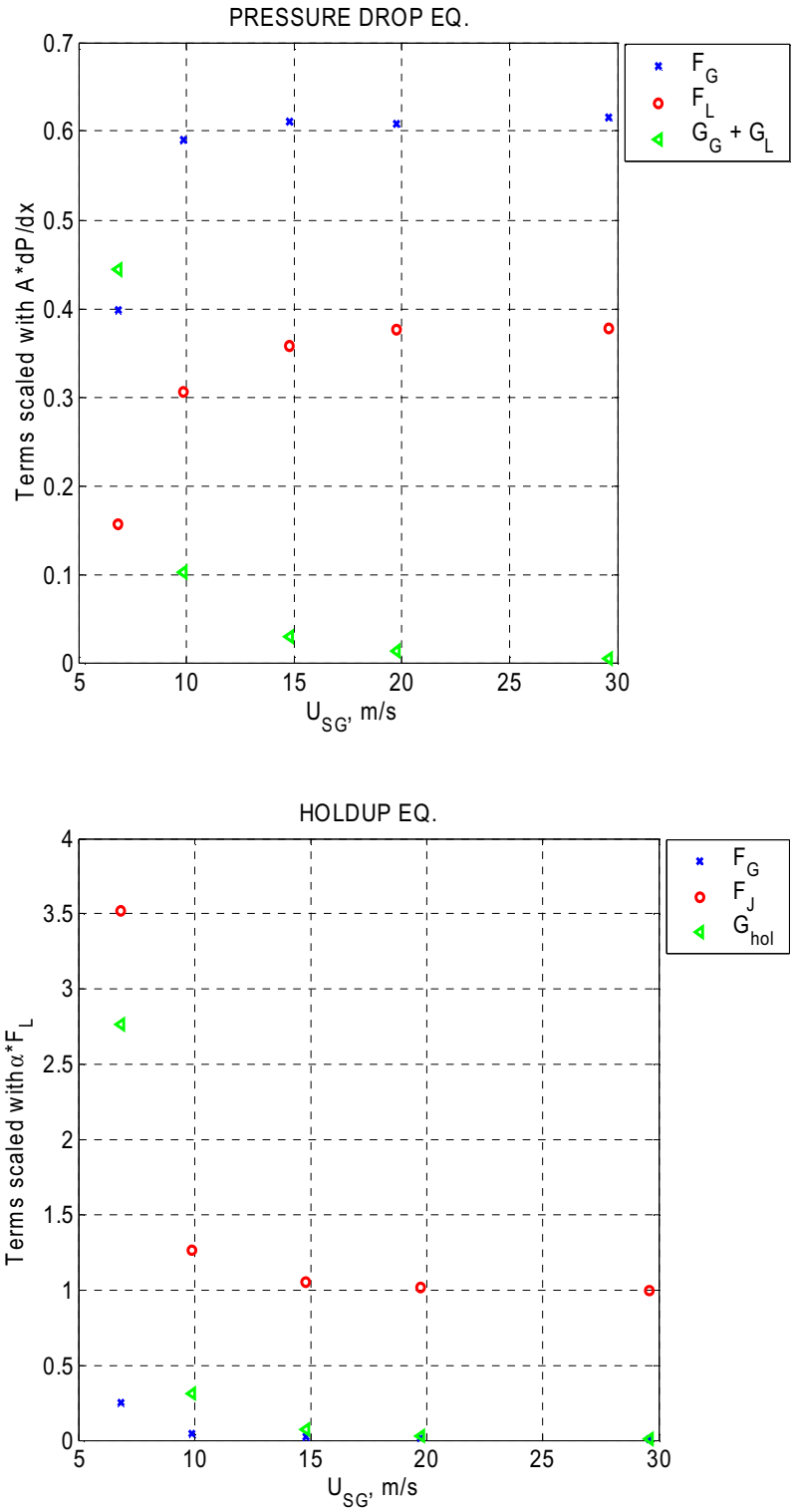

Figure 6–8: Scaled contributions to the liquid holdup and pressure drop for the following case: air-Exxsol D80, superficial liquid velocity = 0.0059 m/s, inclination = +1 deg. Respective contributions are: F_G, gas-wall friction, F_L, liquid-wall friction, F_J gas-liquid interfacial friction and (G_G+G_L) and G_{hol}, gravity. Top: pressure drop; Bottom: holdup

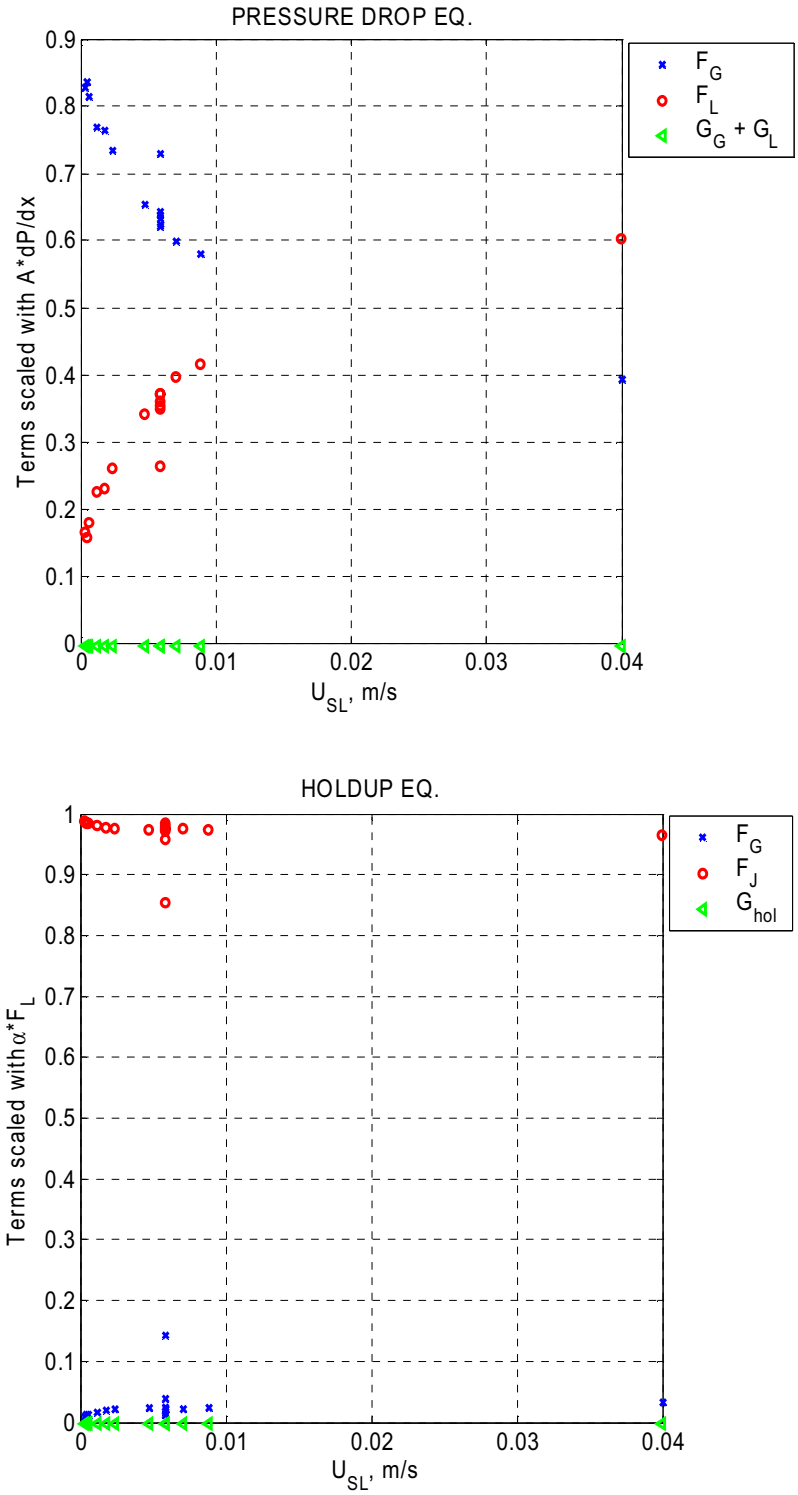

Figure 6–9: Scaled contributions to the liquid holdup and the pressure drop for the following case: air-Exxsol D80, superficial gas velocity = 14.8 m/s, inclination = 0 deg. Respective contributions are: F_G, gas-wall friction, F_L, liquid-wall friction, F_J gas-liquid interfacial friction and (G_G+G_L) or G_{hol}, gravity. Top: pressure drop; Bottom: holdup

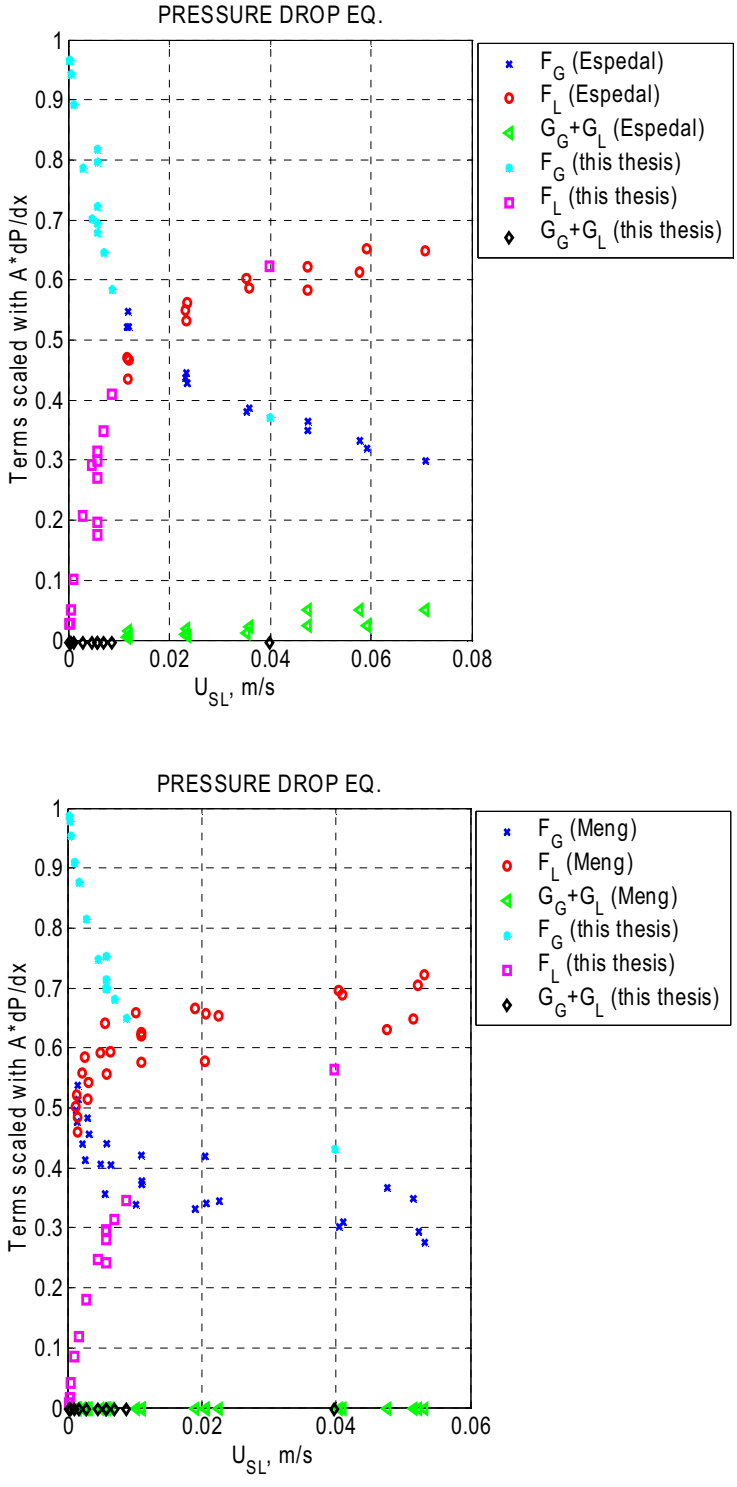

Figure 6–10: Scaled contributions to the pressure drop for the 60 mm i.d. horizontal acrylic pipe. Respective contributions are: F_G, gas-wall friction, F_L, liquid-wall friction and (G_G+G_L), gravity. Top: comparison with data from Espedal (1998); Bottom: comparison with data from Meng (1999)

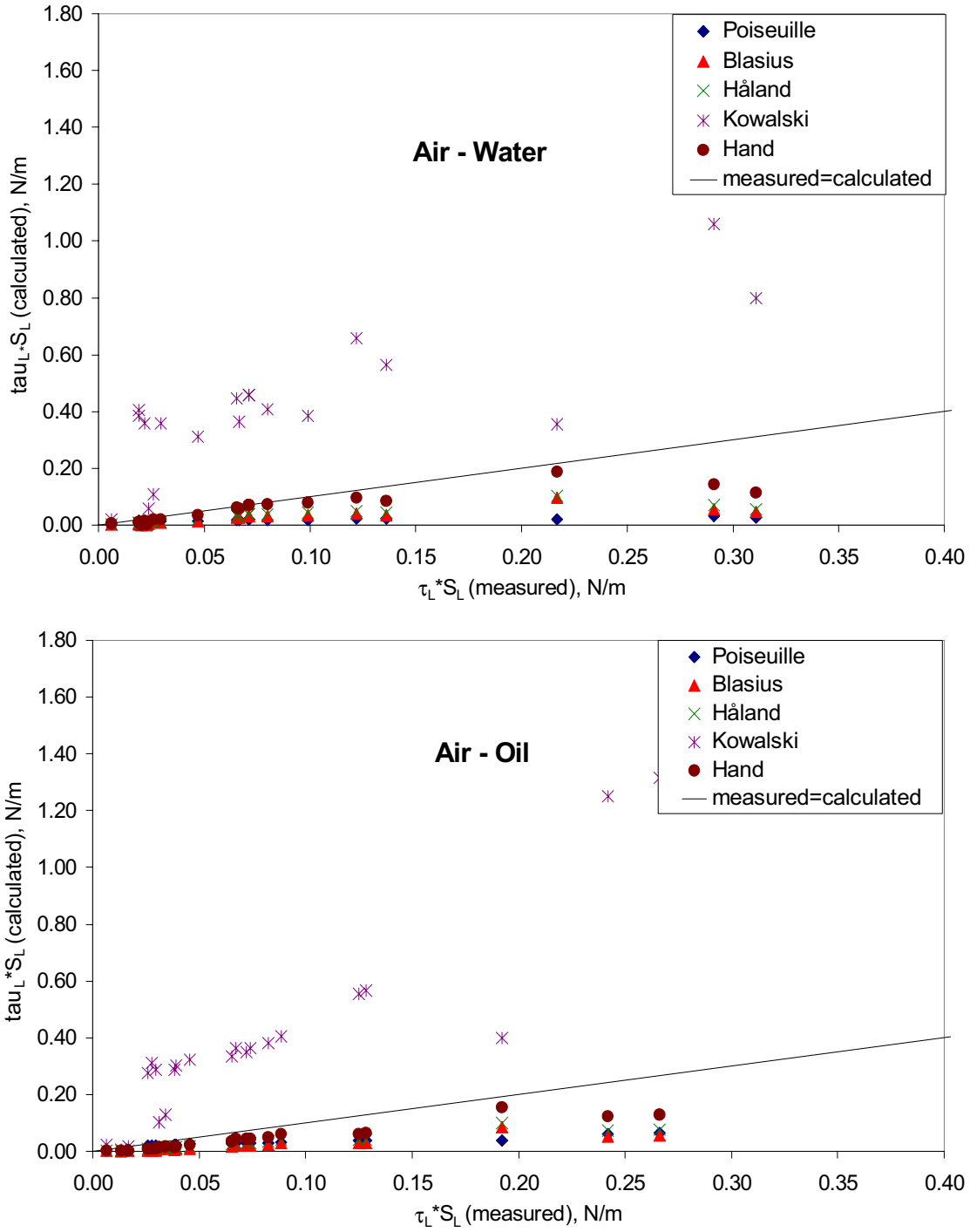

Figure 6–11: Liquid-wall friction from measurements compared with prediction models

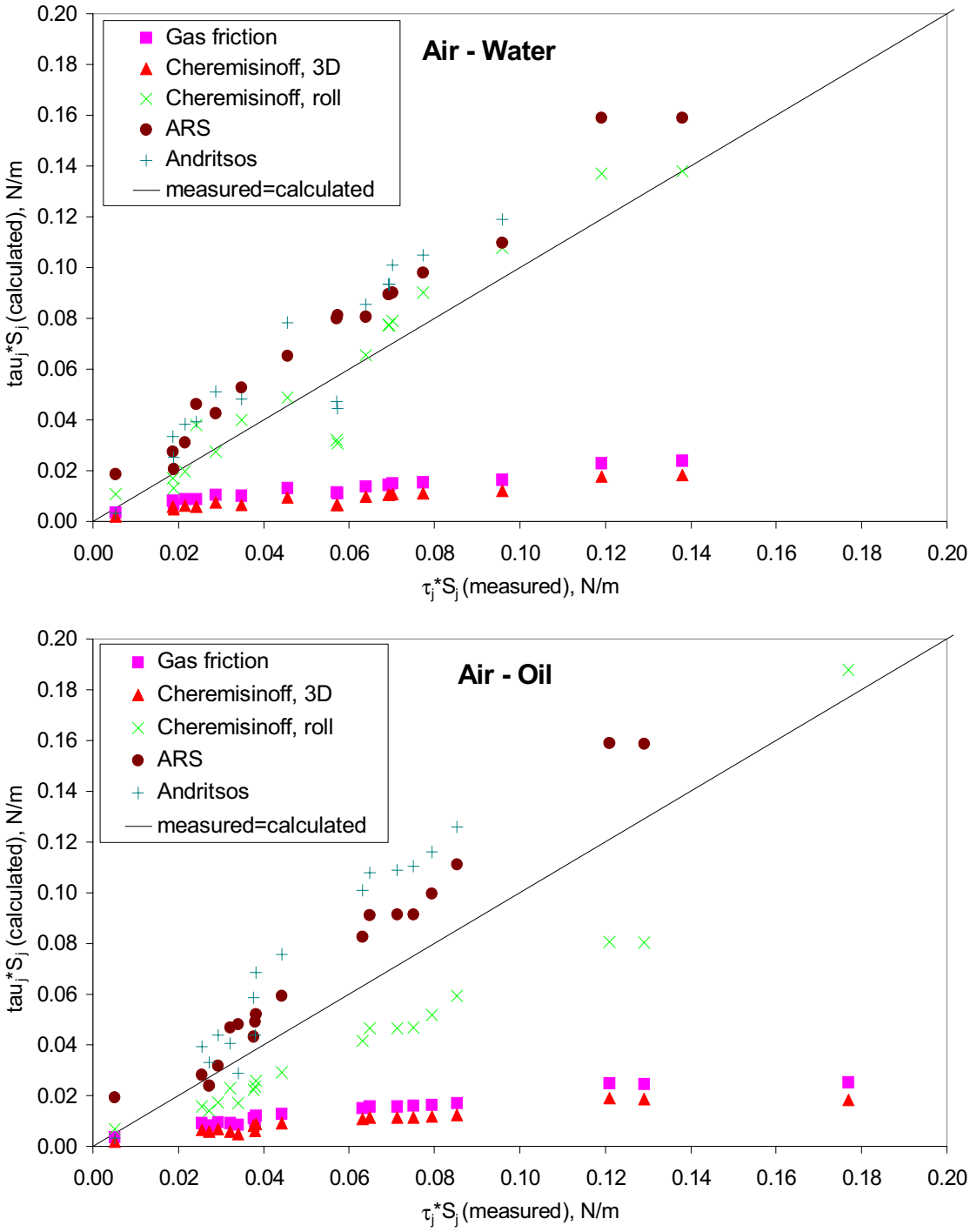

Figure 6–12: Interfacial friction from measurements compared with prediction models

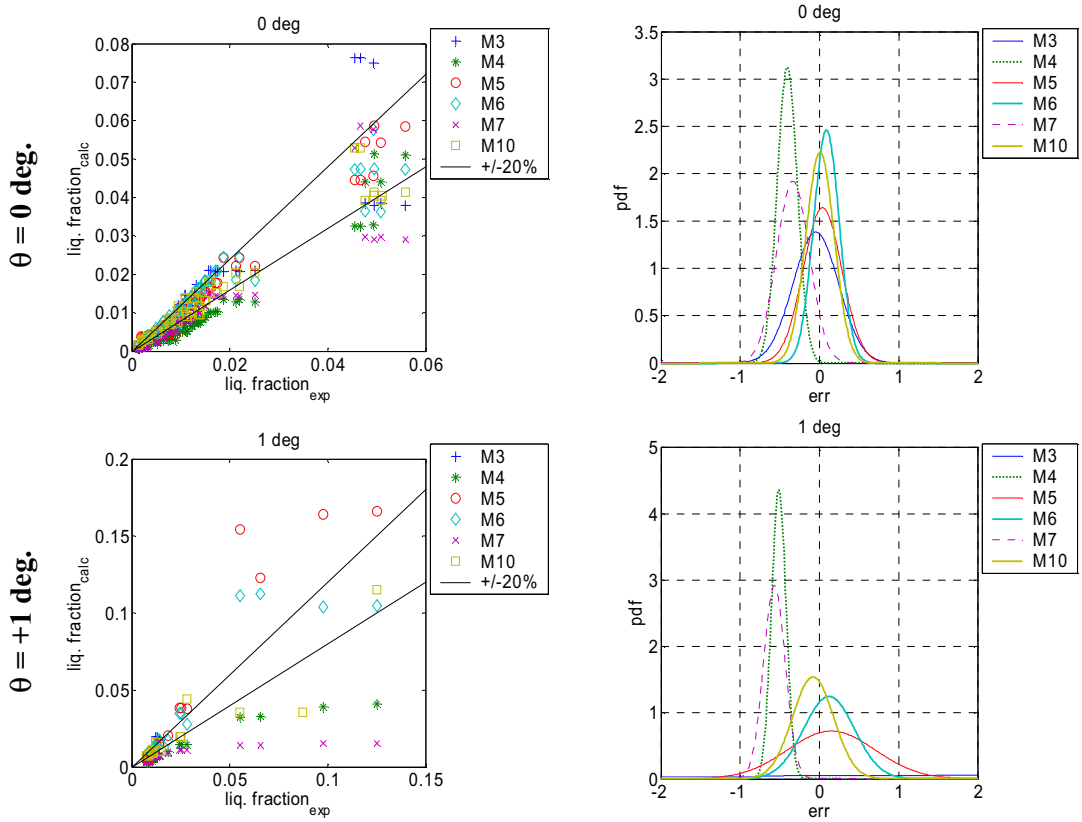

Figure 6–13: Two-phase holdup measurements: point-by-point and pdf error comparison with models; Top: horizontal data; Bottom: +1 deg inclined data

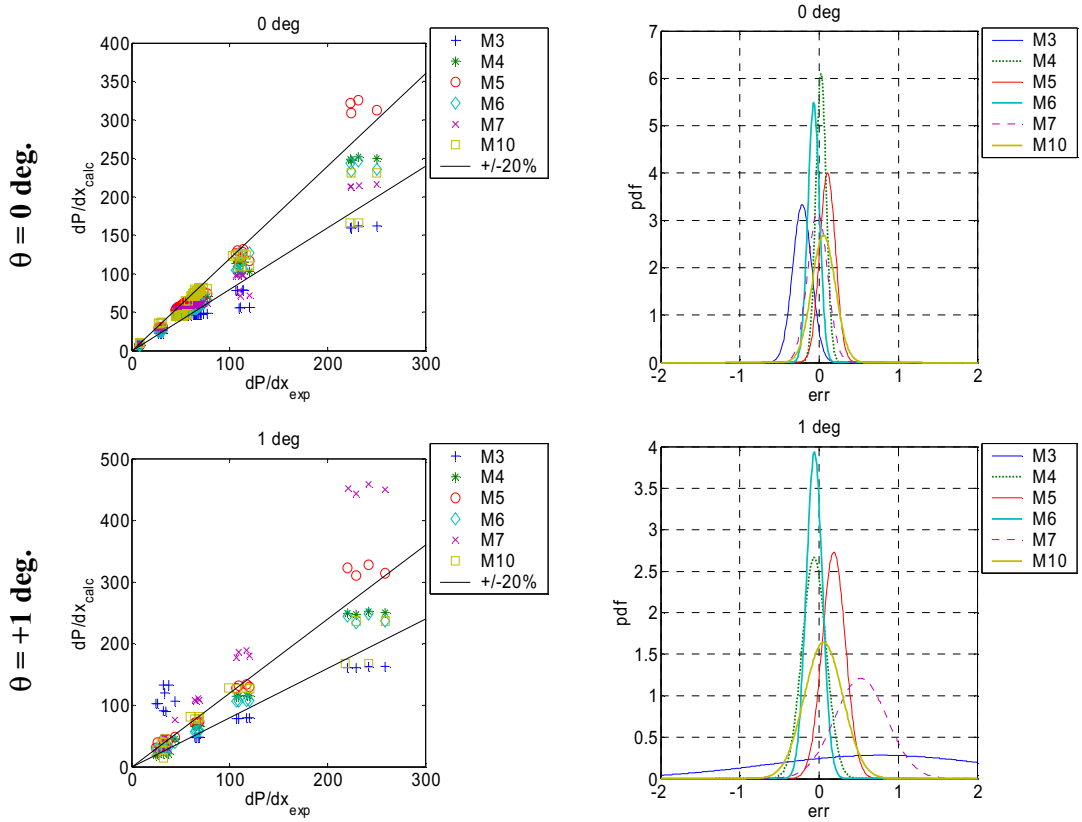

Figure 6–14: Two-phase pressure drop measurements: point-by-point and pdf error comparison with models; Top: horizontal data; Bottom: +1 deg. inclined data

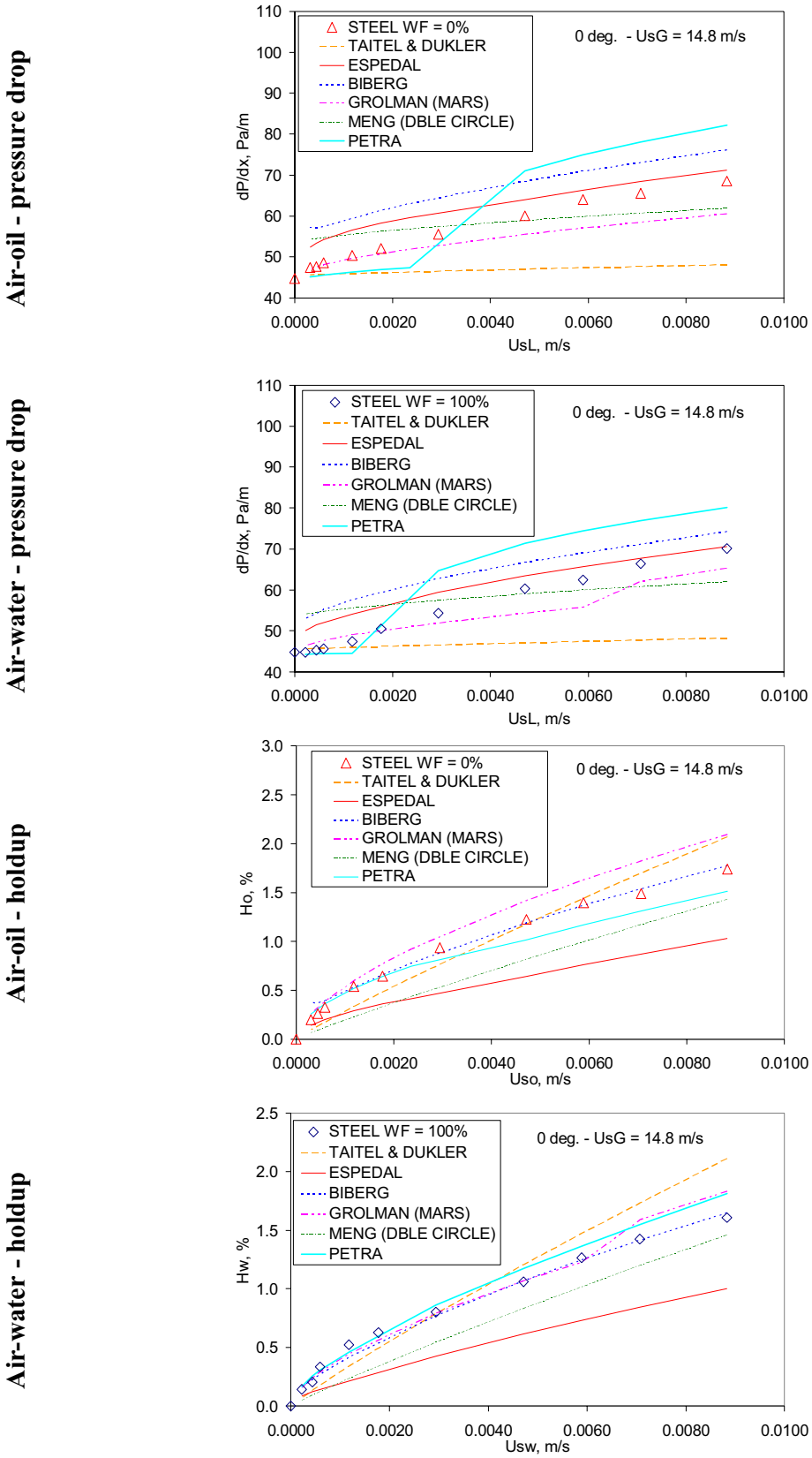

Figure 6–15: Serie #1, sensitivity with liquid superficial velocity at fixed gas superficial velocity. Comparison of measurements with model predictions

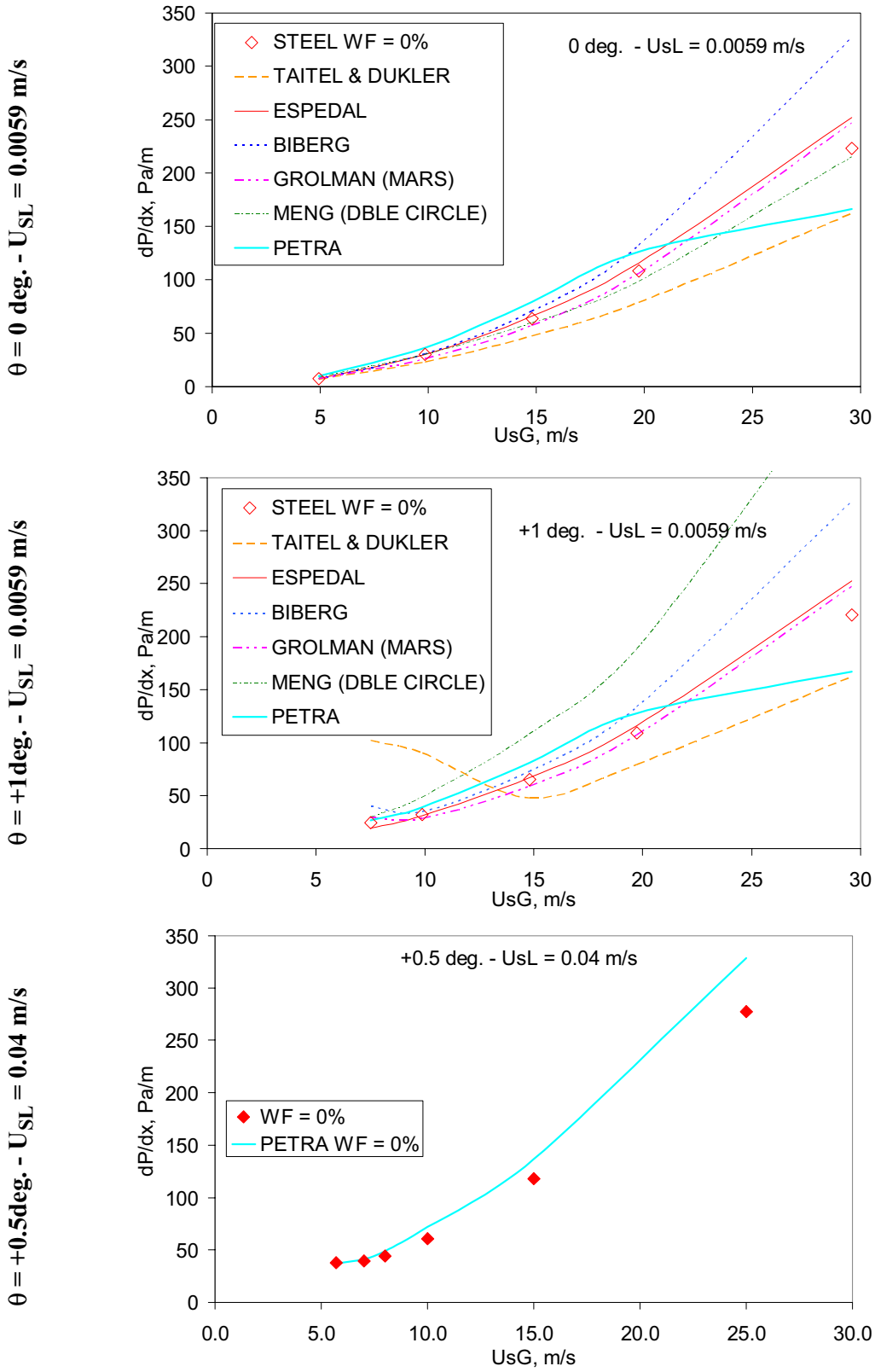

Figure 6–16: Serie #3, pressure drop sensitivity with superficial gas velocity at fixed liquid superficial velocity and inclination. Comparison of measurements with models

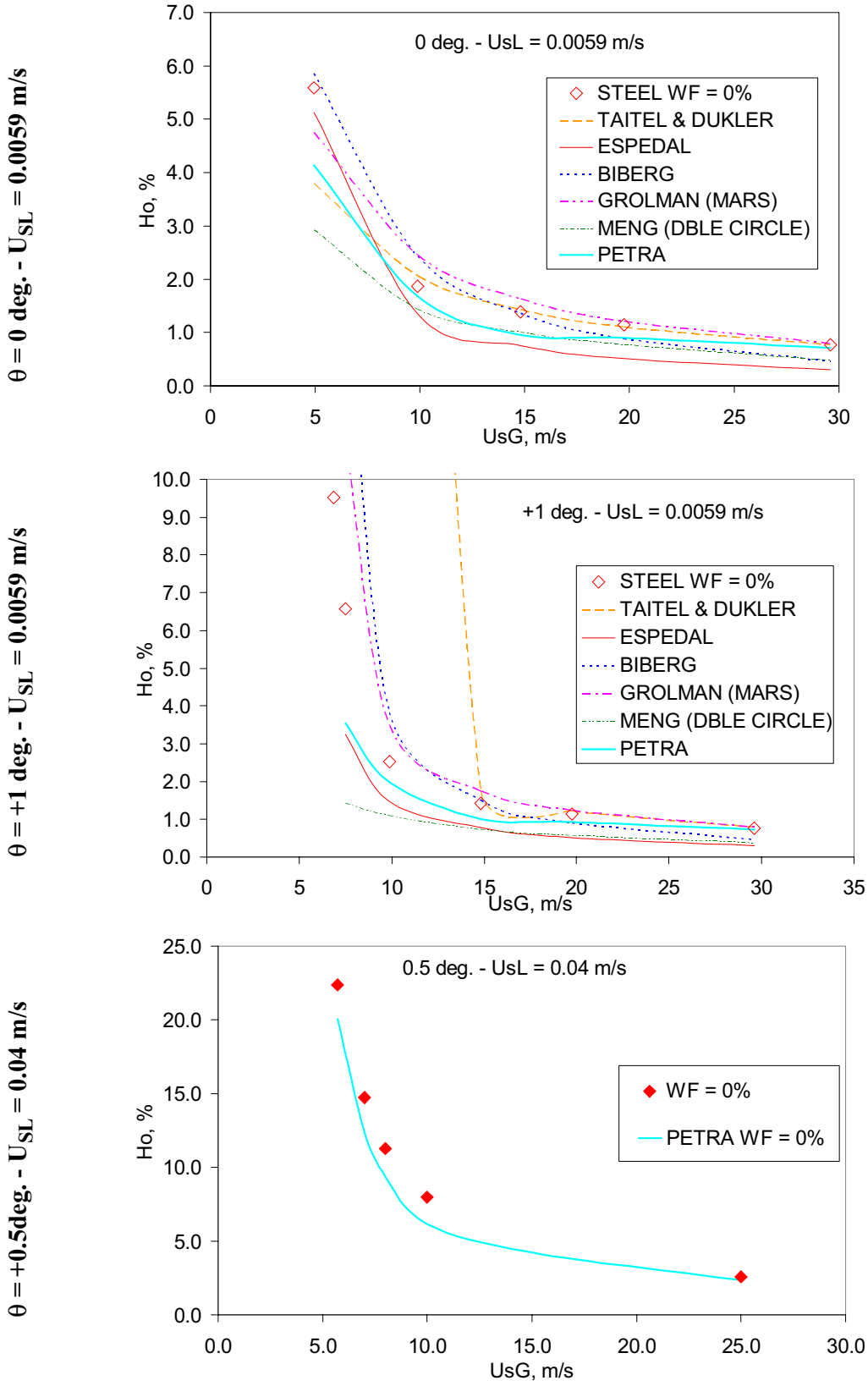

Figure 6–17: Serie #3, holdup sensitivity with superficial gas velocity at fixed liquid superficial velocity and inclination. Comparison of measurements with models

Chapter 7 Three-phase gas-oil-water flow at low liquid loading

7.1 Introduction

The two-phase flow experiments described in Chapter 6 are, in this chapter, extended to three-phase flow using, for the liquid phase, a mixture of oil and water. It is still focused on low input liquid loading (superficial liquid velocities smaller than 0.01 m/s) and friction dominated flows at high gas superficial velocities but some data points have been taken at moderate liquid loading (superficial liquid velocity of 0.04 m/s) in a slightly inclined upward pipe to investigate gravity dominated three-phase flows. The purpose of the three-phase flow experiments are to:

- Supplement literature with new three-phase gas-oil-water flow data.
- Explore the region of low liquid loadings for which there is no data in the open literature.
- Test the influence of test section material.
- Test how accurate three-layer models and three-phase pipe flow simulators extrapolate at these particular conditions and identify the main shortcomings.

Due to the high surface-to-volume ratio for the liquid phase, interfacial effects are expected to be important at low liquid loading. One goal of the experiments has been to test the effect of different wall material properties on the flow.

This chapter is divided in two main sections. In Section 7.2, the test matrix is presented and the measurements are described, analysed and discussed. In Section 7.3, pressure drop and phase fraction measurements are compared with one-dimensional three-layer models and the multiphase pipe flow simulator PETRA.

7.2 Experiments

7.2.1 Test matrix

The three-phase flow experiments were performed at atmospheric conditions using air, water and Exxsol D80. Fluid properties are summarized in Table 4–1. The fluids were run in one of three 60 mm i.d. test sections made of acrylic, steel or epoxy coated steel, at horizontal or slightly upward inclinations. Test sections are described in Chapter 4.

Experiments cover sensitivities with gas and liquid flow rates, inclination and test section material for a total of 209 three-phase flow tests. Because different test sections were used, experiments were carried out within different campaigns spanning from July 2001 to March 2003.

For each test section, one serie was run at fixed superficial gas velocity and water fraction and varying superficial liquid velocity (serie #1). One serie was run at fixed gas and liquid superficial velocities and varying water fraction (serie #2). Finally, one serie was run at fixed liquid superficial velocity and water fraction and varying gas superficial velocity (serie #3). For serie #2 and serie #3, runs were conducted at two different liquid superficial velocities: 0.0059 m/s (series #2.1 and #3.1) and 0.04 m/s (serie #2.2 and #3.2). This is to compare low to moderate liquid loadings. The test matrix for the three-phase flow experiments is given in Table 7–1.

Table 7–1: Test matrix for the three-phase flow experiments

Serie	U_{SG} , m/s	U_{SL}, m/s	WF, %	θ, deg.	Material
#1	14.8	0.0006-0.04	20,50	0	acrylic steel epoxy (20% only)
#2.1	4.93, 7.5, 9.87, 14.8, 19.74, 29.6	0.0059	5-95	0,+1	acrylic steel epoxy (0 deg. only)
#2.2	5.7, 7.0, 8.0, 10.0, 15.0, 25.0	0.04	5-90	+0.5	acrylic
#3.1	4.93-29.6	0.0059	20,50,90	0,+1	acrylic steel epoxy (0 deg. only)
#3.2	5.7-25	0.04	20,50,90	+0.5	acrylic

Except for serie #2.2 and #3.2, experiments were performed at low liquid loading, with LGR down to 0.002%. Figure 7–19 compares the range of superficial liquid velocities for the present three-phase experiments with that of other authors.

7.2.2 Experimental procedure

Experiments were performed at steady-state conditions according to the experimental procedure presented in Section 4.4.1. After a settling period of about 30 minutes, diffe-

rential pressure cells were logged for 10 minutes after which phase fractions were measured with quick-closing valves. Measuring accuracy is indicated in Table 4–28.

7.2.3 Flow regimes

Three-phase flow regimes are more diverse than two-phase flow regimes because specific oil-water flow regimes superpose to the traditional gas-liquid flow patterns. This work at low liquid loading makes no exception.

The flow regimes observed were found to be well described by the classification initially suggested by Acikgöz et al. (1992) and later simplified by Pan (1996). Both authors suggest to identify gas-oil-water flow regimes in three steps:

1. State of the oil-water mixture: dispersed or separated. In this work, a three-layer liquid-liquid flow pattern with two continuous zones separated by a mixing zone of mutual oil-in water and water-in-oil dispersions is also considered as separated flow.

2. State of the liquid mixture, in case of a dispersed liquid phase: oil continuous, water continuous or undefined.

3. State of the gas-liquid interface: bubbly, stratified, annular or slug.

Flow regime labels associated with this classification are indicated in Table 7–2 while detailed flow regime observations are tabulated in Appendix A.

Table 7–2: Simplified three-phase flow pattern code

I water-oil interface		**II liquid-liquid distribution**		**III gas-liquid interface**		
Flow regime	**Label**	**Flow regime**	**Label**	**Flow regime**	**Detail**	**Label**
dispersed	D	oil continuous	O	bubbly		BU
		water continuous	W	stratified	smooth	ST1
		undefined	?		wavy, 2D regular waves	ST2
separated	S	-			wavy, 3D regular waves	ST3
					wavy, large amplitude irregular waves	ST4
					droplets	o
				slug		SL
				annular		AN

Using visual observations, flow regime maps were generated for the cases summarized in Table 7–3. In the steel and epoxy coated pipes, flow regimes were observed through an observation spool piece made of acrylic and located at the pipe outlet (Figure 4–2). The accuracy of the transition line location is indicated with error bars and is based on how close observations are performed from each other. As can be seen, the accuracy is coarse, +/- 5 m/s in average on the superficial gas velocity, except for the stratified/slug transition that is identified with an accuracy of +/- 0.25 m/s. Accurate determination of flow regime transitions is not specifically studied in this work and the indicated transition lines are treated as qualitative information only.

Table 7–3: Summary of experimentally determined flow regime maps

Label	Page	Serie	θ, deg.	Topic
Figure 7–1	p. 210	#1 and #3.1	0	stratified/atomization transition
Figure 7–2	p. 211	#3.1 and #3.2	+1, +0.5	stratified/slug transition
Figure 7–3	p. 212	#3.1	0, +1	separated/dispersed transition

The following comments can be made on the flow regime maps:

- The onset of atomisation occurs at different gas superficial velocities in the acrylic and steel pipes at intermediate water fractions.
- The stratified/slug transition is not very much affected by water fraction. This lack of sensitivity may be due to the physical properties of oil and water (density and viscosity) being very close.
- The separated/dispersed transition in the liquid phase at superficial liquid velocity equal to 0.0059 m/s is also affected by the test section material. The water phase stays longer continuous in the steel pipe at intermediate water fractions. The better stability of water in steel is probably an effect of interfacial forces at small liquid loading as discussed in Section 7.2.6.2.

Longitudinal and cross sectional views of flow regimes are provided at superficial liquid velocity equal to 0.0059 m/s in Figure 7–38, Figure 7–39, Figure 7–40 and Figure 7–41. Longitudinal views at superficial liquid velocity equal to 0.04 m/s are provided in Figure 7–42. Water is coloured green due to the fluoresceine dye dissolved in it. The setup for the flow regime photography is described in Section 6.2.3.

It is observed that:

- At low liquid loading (superficial liquid velocity equal to 0.0059 m/s), there is a difference in flow regimes between the acrylic and the steel pipes. In steel, water flows as a continuous rivulet up to a superficial gas velocity of 14.5 m/s (Figure 7–39). In acrylic, water flows continuous only at 9 m/s but at 11.5 m/s and 14.5 m/s, the water rivulet gets unstable and disperses in oil, in particular at water fractions equal to 20% and 50% (Figure 7–38).

• At 11.5 m/s and 14.5 m/s gas superficial velocity, peculiar large amplitude waves develop at the gas-liquid interface in the acrylic pipe. At their front, water droplets are seen to accumulate. A picture of such waves is given in Figure 7–43. These waves are prone to atomize into large amounts of droplets at high gas velocity. Incidentally, oil droplets tend to spread at the top of the pipe forming a rippled film whereas water droplets are non-wetting and tend to run along the wall, forming narrow meandering rivulets. An example of an oil rippled film can be seen in Figure 7–42 at superficial gas velocity 25 m/s and water fraction 20%. An example of water rivulet flow can be seen in the same figure at water fraction 90%.

• The gas-liquid interface appears smoother in steel, as seen in Figure 7–41. The water film is continuous, also at superficial gas velocity equal to 14.5 m/s and the water-oil interface develops a convex shape.

• Increasing liquid superficial velocity from 0.0059 m/s to 0.04 m/s, the water film is no longer unstable at intermediate gas superficial velocities in acrylic. For example at 10 m/s, there is a continuous water film at the pipe bottom as seen in Figure 7–42.

7.2.4 Results

The steady-state pressure drop and phase fractions were measured for the sensitivities in flowrates, test section material and inclination described in Table 7–1. Quantitative results are tabulated in Appendix A.

Plots were generated from the measured data and are summarized in Table 7–7.

7.2.5 Analysis

As in two-phase flow, it is possible to distinguish between flows dominated by (bulk) gravity forces and flows dominated by (surface) friction forces. The former case occurs at small upward inclinations and small gas superficial velocities close to the stratified/slug transition. The latter occurs at high gas velocities in horizontal or slightly inclined pipes close to the transition with annular flow.

It is convenient, for the purpose of the data analysis to distinguish between these two situations. For gravity dominated flows, it is looked especially at the holdup variations with gas and liquid superficial velocity, water fraction, test section material and inclination. For friction dominated flows, it is focused on pressure drop variations with gas and liquid superficial velocity, water fraction and test section material.

In addition, it is possible to compare low liquid loadings, at superficial liquid velocity up to 0.0059 m/s, with moderate liquid loadings, at superficial liquid velocity equal to 0.04 m/s.

7.2.5.1 Gravity dominated flows

This concerns measurements at superficial gas velocity between 5 and 10 m/s, superficial liquid velocity 0.0059 m/s at +1 deg. inclination (serie #2.1 and #3.1) and 0.04 m/s at +0.5 deg. inclination (serie #2.2 and #3.2).

At superficial liquid velocity equal to 0.04 m/s, the following observations can be made:

- Close to the slug flow transition, pressure drop goes through a minimum with decreasing gas superficial velocity (Figure 7–14) and varies little with neither gas superficial velocity nor water fraction (Figure 7–9 at superficial gas velocity equal to 5.7, 7 and 8 m/s).
- Close to the slug flow transition, the liquid holdup increases sharply with decreasing superficial gas velocity, as in two-phase flow (Figure 7–14).
- In three-phase flow, the total liquid holdup is also dependent on input water fraction and is governed by water gravity stratification at slight upward inclination. For example in Figure 7–9 at superficial gas velocities 5.7 m/s, 7 m/s and 8 m/s, the total liquid holdup goes through a maximum at intermediate water fractions when in the same time the proportion of water in the holdup is higher than the input water fraction.

At superficial liquid velocity 0.0059 m/s:

- As in two-phase flow, the magnitude of the holdup increase with decreasing gas superficial velocity is higher at lower liquid loading (Figure 7–13).
- There is a holdup material sensitivity with differences between acrylic and steel as shown in Figure 7–11 at superficial gas velocity equal to 4.93, 7.5 and 9.87 m/s. The water holdup is generally higher in steel and the oil holdup is generally higher in acrylic. The two effects compensating, the total holdup is comparable in both pipes.
- In the horizontal pipe, there is no clear maximum of the total liquid holdup at intermediate water fraction as is the case for the upward inclined case (Figure 7–11). The dominant mechanism, as water fraction increases, is the replacement of oil by the less viscous water which results in a more monotonic decrease of the total liquid holdup with increasing input water fraction.

7.2.5.2 Friction dominated flows

This concerns measurements at high gas superficial velocity (between 10 and 30 m/s) and superficial liquid velocity 0.0059 m/s (serie #1, #2.1 and #3.1) or 0.04 m/s (serie #2.2 and #3.2).

Both at low and moderate liquid loading, there are the following trends:

- As in two-phase flow, the total liquid holdup tends to an asymptotic value at high superficial gas velocities. This is due to an increasing liquid fraction being transported as droplets in the gas core. The total liquid holdup also appears to be less sensitive to input water fraction.

- The pressure drop increases exponentially with increasing gas superficial velocity.
- The pressure drop exhibits variations with input water fraction at given superficial gas and liquid velocities.

At superficial liquid velocity 0.04 m/s, the following is observed:

- The total liquid holdup has not yet reached its asymptote at superficial gas velocity equal to 25 m/s (Figure 7–14).
- The total liquid holdup is less sensitive to input water fraction at given superficial liquid velocity than for gravity dominated flows but exhibits a peak at water fraction around 50% (Figure 7–12 at superficial gas velocity equal to 25 m/s).
- Increasing the superficial liquid velocity towards the transition to annular flow, the in-situ liquid composition tends to the input (no-slip) liquid composition (Figure 7–9 at superficial gas velocity equal to 25 m/s).
- The pressure drop is water fraction sensitive and reaches a maximum at water fraction 80% for superficial gas velocity equal to 25 m/s (Figure 7–9).
- The pressure drop is sensitive to pipe wall contamination (discussed in Section 7.2.6.4). Pressure drop is less in a contaminated acrylic pipe compared to a clean (pigged) surface.

At superficial liquid velocity 0.0059 m/s:

- There is little effect of a slight upward inclination on the total liquid holdup (Figure 7–10).
- There is a significant effect of wall material on holdup composition at intermediate gas superficial velocities (corresponding to a stratified flow regime with little atomization). The water holdup is higher in steel, the oil holdup is higher in acrylic resulting in a total liquid holdup higher in steel than in acrylic (Figure 7–10). Compared to input composition, water accumulates in steel (in-situ water fraction above input water fraction) but oil accumulates in acrylic as shown in Figure 7–10. These differences are smeared off as superficial gas velocity approaches the critical velocity at the transition to annular flow.
- As in two-phase flow, pressure drop increases with superficial liquid velocity at given gas superficial velocity (Figure 7–5).
- Pressure drop sensitivity with water fraction is emphasized compared to superficial liquid velocity equal to 0.04 m/s (Figure 7–10). Pressure drop tends to a maximum at intermediate water fractions in acrylic but tends to a minimum at intermediate water fractions in steel and epoxy coated steel.
- At low gas velocity, the pressure drop in all materials is similar. Increasing gas superficial velocity, there is a critical velocity over which the pressure drop in acrylic starts to diverge away from the pressure drop in steel (Figure 7–15). This gas velocity corresponds approximately to the velocity at the onset of liquid film atomization

observed visually. The differences between materials is therefore particularly pronounced in the stratified/atomization regime.

• There is a sensitivity with wall contamination at high water fractions in acrylic, as seen in Figure 7–10 (discussed in Section 7.2.6.4).

The effect of the internal epoxy coating on the flow has been tested only for friction dominated flow at low liquid loading for which surface effects are expected to be greatest. The following comments can be made:

• In the epoxy coated pipe, the pressure drop and the holdup variations are close to that of bare steel for the sensitivities studied.

• There is a slight difference in holdup composition with varying water fraction. Compared to bare steel, the oil holdup is significantly higher in epoxy and the water holdup is equal or slightly lower in epoxy, resulting in a slightly higher liquid holdup (Figure 7–10).

• Compared to bare steel, the pressure drop is slightly smaller in two-phase flow but slightly higher at intermediate water fractions (Figure 7–10). At high gas velocities (stratified-atomization flow), the pressure drop in epoxy is the least of the three materials tested (Figure 7–15).

7.2.6 Discussion

In this section, selected issues are discussed in more details. They are specifically related to the experiments carried out at low liquid loading for a superficial liquid velocity equal to 0.0059 m/s.

The topics discussed are:

• The effect of varying water fraction on the pressure drop and phase fractions (three-phase effect).

• The effect of varying pipe wall material (material effect).

• The internal epoxy coating.

• The sensitivity to pipe wall surface contamination.

• Transient experiments.

7.2.6.1 Three-phase effect

The present three-phase flow experiments illustrate a sensitivity of holdup and pressure drop to input water fraction at constant gas and liquid superficial velocity. There is a holdup variation with water fraction for gravity dominated flows at moderate to high liquid loading and a pressure drop variation with water fraction for friction dominated flows at low liquid loading.

In gravity dominated flows, the water holdup sensitivity is primarily due to local separation of water and oil at slight upward inclinations and water replacing oil as water fraction increases in horizontal pipes. This is a combined effect of:

- The density difference between water and oil.
- The higher drag exerted by the gas on the oil.
- The reduced oil-wetted perimeter.

For friction dominated flows, the reason for the water fraction sensitivity is less obvious. It appears to depend, for instance, on the liquid phase flow regime. Within the liquid phase, two flow regimes can occur: either water and oil flow separated (with perhaps, a mixing layer at the oil-water interface) or, a dispersion of water in oil or oil in water forms.

To investigate further the water fraction sensitivity of the measurements, it has been undertaken:

1. Comparisons with oil-water measurements.
2. Visual observations of flow regimes.

Oil-water measurements

Figure 7–18 shows a typical pressure gradient plot for two-phase water and Exxsol D80 obtained in the 60 mm acrylic and steel pipes (Ioannou et al. 2003). The mixture superficial velocity is 4.5 m/s corresponding to conditions where the liquid phase is a dispersion of one phase into the other.

The following can be said of Figure 7–18:

- Phase inversion occurs for input water fractions between 35% and 50%.
- Inversion is pipe material dependent. Inversion peak is sharper with acrylic than with stainless steel.
- The water fraction at inversion is dependent on whether the pipe is initially water or oil wetted.

In the present experiments in three-phase flow, the pressure drop peak occurs first at water fraction around 70-80% and is displaced towards smaller water fractions (around 40-50%) at increasing gas velocity. This appears for instance in Figure 7–8. In addition, the peak is not as sharp as in oil-water flow but instead, there is a gradual increase of the pressure drop with increasing water fraction. Although phase inversion may play a role at conditions where a dispersion forms in the liquid layer (typically at high gas superficial velocity), this is not obvious from the present experiments and the cause for the pressure drop peak is to be searched elsewhere.

Visual observations

As mentioned in Section 7.2.3, the liquid phase is often seen as dispersed in the acrylic pipe at conditions where there are two separated continuous phases in steel. In such a case, it can be expected that the apparent liquid viscosity increases in acrylic compared to steel. More important is the fact that there are differences in the wetting of the upper pipe wall depending on test section material. This is discussed in the following section.

7.2.6.2 Material effect

Differences between pipe materials are small at low liquid loading in two-phase gas-liquid flow but are marked in three-phase, friction dominated, gas-oil-water flow.

The differences between acrylic and steel are best described by looking at a case into details. The case chosen is from Figure 7–10 in horizontal pipes at superficial gas velocity equal to 14.8 m/s, superficial liquid velocity equal to 0.0059 m/s and water fraction equal to 50%.

In acrylic, the pressure drop at 50% input water fraction is 43% higher than for either pure oil or pure water. The total liquid holdup is 1.1% at input water fraction 50% against 1.4% for pure oil and 1.2% for pure water. The peak in pressure drop corresponds to a minimum in the holdup. The in-situ water fraction is below the first bisector, meaning that water is better transported than oil or equivalently, that oil is accumulating.

In steel, the pressure drop at 50% input water fraction is 10.8% lower than for either pure oil or water. The total liquid holdup is 1.3%, 1.4% for pure oil and 1.25% for pure water. The in-situ water fraction is above the first bisector, meaning that water accumulates in steel, or, in other words, that oil is better transported than water.

The flow regimes for the same conditions are water dispersed in oil in the acrylic pipe with irregular large amplitude interfacial waves together with droplet generation. In the steel pipe, the flow regime is water continuous-oil continuous separated flow in the liquid layer, no large amplitude interfacial waves at the gas-liquid interface and less droplet generation.

The pressure drop and holdup measurements in acrylic and steel can be interpreted as follows:

- In acrylic, the fact that water is dispersed in oil enhances overall water transport. Even though liquid viscosity may increase due to the dispersion, the liquid holdup does not increase. Instead, the picture is dominated by a destabilization of the gas-liquid interface. Large amplitude waves form and enhance overall liquid transport reducing the total holdup. On the other hand, pressure drop increases due to the rougher interface and the higher droplet field. Oil droplets depositing on the upper pipe wall form a thin annular oil film, enhancing oil accumulation on the one hand and gas-wall friction on the other hand. Protruding non-wetting water droplets also contribute to a pressure drop increase at intermediate water fractions.
- In steel, water is present as a continuous phase under the oil phase and is not as well transported as in acrylic. The water holdup is higher. In the same time, the oil phase

flows over a moving water phase, offering less resistance to motion, and is better dragged by the gas than water, in contact with the wall. The total holdup is higher than in acrylic and is characterized by a higher water content. In presence of a continuous oil-water interface, the gas-liquid interface is more stable and large amplitude waves are not triggered. This phenomenon of gas-liquid interface stabilization in presence of a continuous oil-water interface has been observed by others, for instance Lee et al. (1993) and Lunde et al. (1993). Due to the smoother interface and reduced droplet field, the pressure drop is smaller in steel than in acrylic and smaller in three-phase flow than in two-phase flow.

In summary, it has been seen that three-phase effects are dependent on the nature of the flow regime in the liquid layer (separated and dispersed) and the latter seems to be influenced by an interaction with the wall material that becomes significant at low liquid holdup. One can wonder whether this interaction can be related to a characterization of the pipe material surface. In Section 4.2.3.3, it has been demonstrated, from a simplified force balance and data on contact angles, that steel is expected to develop a higher affinity for water than acrylic in presence of an oily media. In other words, a drop of water, being displaced by oil adheres more to the steel surface (a larger force is required for displacing it) than to the acrylic surface. This can explain why water rather disperses in the oil phase in acrylic but that this process requires more energy (it occurs at larger gas superficial velocities) in steel.

7.2.6.3 Epoxy coating

The effects foreseen of having an internal coating in a bare steel pipe are:

- Reduced wall friction due to the smaller physical roughness.
- Reduced water affinity in presence of an oily media due to the surface being chemically and physically more homogeneous (thus reduced contact angle hysteresis).

Surface characterizations carried out in Section 4.2.3.3 suggest that:

- The local physical roughness measured is slightly higher in the coated pipe compared to the steel pipe.
- The "global" test section hydraulic roughness is smaller in epoxy compared to steel and acrylic.
- The water-in-oil static contact angles are between those of acrylic and steel.
- The contact angle hysteresis is between that of acrylic and steel.

The epoxy coating has been studied at conditions of friction domination in horizontal pipes. Figure 7–10 shows that water transportation is enhanced in the coated pipe. Since the surface is chemically more homogeneous, heterogeneities disappear that would otherwise enhance contact angle hysteresis and water affinity. However the most significant difference is the higher oil holdup in epoxy compared to steel. A possible explanation is that the water film retracts more in presence of oil on the epoxy coated surface, therefore

leaving a larger oil-wetted perimeter and smaller water wetted perimeter. Visual observations show that, as in bare steel, the water film flows rather continuous in epoxy at conditions where water is dispersed in oil in the acrylic pipe.

At superficial gas velocity equal to 20 and 30 m/s (Figure 7–8) corresponding to stratified-atomization flow, the pressure drop in epoxy is smaller than in steel. In the present experiments, gas-wall friction is the dominant term in the pressure drop and its contribution increases at higher gas superficial velocities as shown in Section 6.2.5. Reasons for the lower pressure drop in epoxy in the atomization flow regime may therefore be searched in a smaller upper-wall apparent roughness and/or in the fact that less droplets are generated. More experiments with other coatings are needed to confirm this hypothesis.

7.2.6.4 Effect of pipe wall contamination

It has been discovered that measurements in the stratified/atomization flow regime in the acrylic pipe are affected by whether the pipe wall is "cleaned" prior to experiment or not.

Indeed, at high superficial gas velocities, the inner wall of the acrylic pipe gets progressively covered with small unfiltered rust particles (dimensions in the order of the micrometer) coming from the air supply. The phenomenon is particularly clear with the acrylic surface that accumulates static electricity and at high superficial air velocities for which there are more particles and less filter efficiency.

Surface contamination results in:

- An additional artificial roughness.
- An inner pipe surface being more impure therefore less homogeneous. Thus, water hysteresis (and surface water affinity) is expected to increase.

Neither the physical roughness nor the contact angles were measured for the contaminated surface. The discussion that follows is therefore only a possible interpretation of what is observed experimentally.

The difference in the state of the wall has an impact on the three-phase flow measurements in two ways. The first effect occurs in the liquid phase. In the contaminated (unpigged) pipe, water forms a continuous film, similar to what is observed in steel. In the "clean" (pigged) pipe, the film breaks into droplets and clusters of droplets. The picture in Figure 7–44 illustrates how the water film contracts while flowing from the contaminated surface (left) to the cleaned surface (right). Eventually, the water film may break if sufficient turbulence is induced in the liquid phase by the gas. Figure 7–45 illustrates how the water rivulet destabilises (meanders) and eventually breaks down into droplets.

The second effect occurs at the upper wall. In the contaminated pipe, there are fewer water droplets and the upper pipe wall is mostly oil wetted with water droplets running on top. In the clean pipe, water droplets protrude more into the gas-phase forming a "creamy"

granular film at the pipe wall. A picture of the upper pipe at the transition between a contaminated pipe section and a clean pipe section is shown in Figure 7–46.

In terms of holdup and pressure drop, it can be seen that the water holdup increases in the contaminated, unpigged pipe. The reason for this is probably due to a higher water affinity of the wall surface. The effect is particularly marked at high water fractions (Figure 7–10). The pressure drop is higher in the pigged, clean pipe. This can be explained by the more unstable gas-liquid interface giving enhanced droplet generation. In addition the wetted upper pipe wall results in a higher gas-wall friction.

7.2.6.5 Transient experiments

Transient tests were carried out to illustrate effects related to water phase wetting and de-wetting of the pipe wall.

The following test was considered: starting from a steady state three-phase flow at superficial gas velocity 14.8 m/s, superficial liquid velocity 0.0059 m/s and water fraction 20%, the water supply is shut down. After the pressure drop has reached a new steady-state, the water phase is re-introduced in the pipe.

Three transient experiments were performed:

1. In the contaminated acrylic pipe. Results are given in Figure 7–20.
2. In the clean, pigged acrylic pipe. Results are given in Figure 7–21.
3. In the clean, pigged steel pipe. Results are given in Figure 7–22.

In the contaminated acrylic pipe, the initial pressure drop is abnormally low at 65 Pa/m instead of 80 Pa/m for the clean pipe. The flow regime in the liquid phase is separated oil-water flow. After water is shut down, the pressure drop first decreases due to the decreasing holdup then, surprisingly, increases again as water disappears from the system and oil is left as the only liquid phase. Immediately after water is re-introduced, a peak of pressure drop is obtained at 82-83 Pa/m which is roughly the value of the steady-state pressure drop in the cleaned pipe for which the flow regime in the liquid phase is water dispersed in oil. In the first minutes following water re-introduction, there is indeed no continuous water film. After some time, water re-wets the pipe surface and pressure drop falls back to its initial value.

In the second experiment, the acrylic pipe is carefully cleaned (pigged) prior to experiment and washed with water, according to the normal experimental procedure detailed in Section 4.4.1. Initially, the pressure drop is 81 Pa/m and water flows dispersed in oil. After water is shut down, the pressure drop falls down to 66 Pa/m (as in the first experiment). This illustrates that two-phase flow is less sensitive to wall contamination. After water is re-introduced, the pressure drop increases immediately back to its initial value, without a peak.

In the third experiment, the steel pipe is now used instead of the acrylic pipe. The transient experiment illustrates a behaviour very similar to that of the contaminated acrylic pipe. The flow regime in the liquid phase is initially separated oil-water flow. After water shut down, the pressure drop first decreases but then increases to a two-phase value that is higher than the three-phase value despite the lower liquid flow rate. After water is re-introduced into the flow, the pressure drop peaks and remains to a high value as long as water is dispersed in oil. After some time, the water film is reconstituted and the pressure drop falls back to its initial value.

These transient experiments, though not pursued further, demonstrate some interesting effects related to the degree of surface water wetting. This suggests that a considerable effect on wet gas flow can be foreseen if the water affinity of the pipe surface can be changed in three-phase gas-oil-water flow.

7.3 Comparison with prediction models

7.3.1 Introduction

The experimental three-phase flow data at low liquid loading presented in Section 7.2.4 has been compared with predictions from one-dimensional models in the literature. As mentioned in Chapter 2, there is currently no model developed specifically for three-phase gas-oil-water flow at low liquid loading but there are models for stratified gas-liquid-liquid flow, called three-layer models. It is chosen here to consider the following three-layer models:

- The model by Taitel et al. (1995).
- The model constructed from the closure recommendations by Khor et al. (1997).

In addition, data is also compared to the general purpose multiphase pipe flow simulator PETRA. Model characteristics are summarized in Table 7–8.

With this choice of models, it is possible to investigate:

- The ability of three-layer models to reproduce three-phase stratified flow data at low liquid loading.
- The effect of changing the friction laws by comparing M1 (Taitel et al. 1995) with M2 (Khor et al. 1997).
- Three-layer models contra general purpose simulators.

The comparisons are organized as follows:

1. Flow regime observations are compared with PETRA predictions. Only the strati-

fied/slug transition is considered for upward inclined flow at superficial liquid velocity 0.0059 m/s and 0.04 m/s.

2. Statistical analysis: predicted pressure drop, total liquid holdup, water and oil fractions are plotted against the measured values. The pdf distribution function of the mean algebraic errors is plotted assuming a gaussian distribution.

3. Detailed plots: predicted sensitivities of pressure drop and phase fractions with superficial liquid velocity, superficial gas velocity, water fraction and inclination are compared with the experimental.

None of the models are expected to reproduce the sensitivity with test section material observed in this study. The simulations are therefore carried out on a generic pipeline of internal diameter equal to 60 mm and hydraulic roughness 5 μm.

7.3.2 Flow regimes

The stratified/slug transitions plotted in Figure 7–2 are compared with flow regime predictions obtained with PETRA. The critical gas velocity at transition is obtained by trial-and-error, guessing a superficial gas velocity and comparing the flow regime predicted by PETRA with the experimental. In the experiments, slug flow is defined by the bridging of the pipe cross section, not regarding whether the subsequent slug is stable or rapidly decays.

The following two cases are considered:

1. Stratified/slug transition at superficial liquid velocity equal to 0.0059 m/s, inclination +1 deg. with the horizontal and varying water fraction.

2. Stratified/slug transition at superficial liquid velocity equal to 0.04 m/s, inclination +0.5 deg. with the horizontal and varying water fraction.

Results are shown in Figure 7–23. At superficial liquid velocity equal to 0.0059 m/s, there is good agreement between the predicted and the experimental except at high water fractions. PETRA also predicts a slight sensitivity of the transition line with varying water fraction as observed experimentally. In particular, it correctly predicts that the region of stable stratified flow is reduced when going from water fraction 0% (two-phase air-oil) to water fraction 20% (three-phase air-oil-water). Introduction of water has therefore a slight destabilizing effect on the flow.

At superficial liquid velocity equal to 0.04 m/s, there are discrepancies, and the predicted critical superficial gas velocity at transition is too low by up to 1 m/s. This can be due to the definition of slug flow adopted experimentally. The variations with water fraction, however, seem to match qualitatively with the experimental, in particular the fact that the area of stable stratified flow is larger at intermediate water fractions than for pure water.

7.3.3 Pressure drop and holdup

Comparison of models with experimental three-phase flow data are conducted as follows:

1. For a given set of experimental conditions, the models listed in Table 7–8 are run for the generic pipe of internal diameter 60 mm and hydraulic roughness 5 micrometer. Models M1 and M2 are programmed with MATLAB 6.5 and the method of solution is described in Table 3–3. The PETRA model was run with PETRA 2.4.

2. Computed and measured pressure drop and phase fractions are treated statistically: a relative algebraic error for each data point is first calculated according to Equation [E.4]. A gaussian probability density function (pdf) is assumed for the error distribution as given by Equation [E.5] with mean and standard deviation given by Equation [E.6] and Equation [E.7] respectively. Tables of mean and standard deviation of errors are given in Table 7–4, Table 7–5 and Table 7–6 for horizontal and inclined data.

3. Plots are generated of point-by-point comparisons, pdf functions and comparisons with experimental sensitivities. For the detail comparisons, only the steel pipe data is compared with model predictions, wherever measurements are available. The plots are summarized in Table 7–9.

Table 7–4: Statistic summary for the comparison of three-phase flow data with prediction models (Superficial liquid velocity = 0.0059 m/s, horizontal pipe)

Model	Pressure drop		Total liquid holdup		Water holdup		Oil holdup	
	b_{err}	h_{err}	b_{err}	h_{err}	b_{err}	h_{err}	b_{err}	h_{err}
M1	-0.35	0.12	0.07	0.45	-0.55	0.15	-0.21	0.16
M2	1.04	0.37	2.39	1.64	0.53	0.37	0.10	0.28
M3	-0.11	0.11	0.26	0.52	-0.25	0.17	-0.06	0.28

Table 7–5: Statistic summary for the comparison of three-phase flow data with prediction models (Superficial liquid velocity = 0.0059 m/s, inclination = +1 deg.)

Model	Pressure drop		Total liquid holdup		Water holdup		Oil holdup	
	b_{err}	h_{err}	b_{err}	h_{err}	b_{err}	h_{err}	b_{err}	h_{err}
M1	-0.16	0.83	0.14	1.07	-0.59	0.14	-0.10	0.51
M2	0.92	0.53	1.70	1.18	0.50	0.43	0.03	0.22
M3	-0.18	0.21	0.00	0.40	-0.25	0.20	-0.12	0.22

Table 7–6: Statistic summary for the comparison of three-phase flow data with prediction models (Superficial liquid velocity = 0.04 m/s, inclination = +0.5 deg.)

Model	Pressure drop		Total liquid holdup		Water holdup		Oil holdup	
	b_{err}	h_{err}	b_{err}	h_{err}	b_{err}	h_{err}	b_{err}	h_{err}
M1	0.25	0.43	0.50	0.48	-0.31	0.13	-0.21	0.24
M2	0.07	0.37	0.22	0.64	-0.05	0.17	0.00	0.17
M3	-0.26	0.14	-0.27	0.17	-0.25	0.17	0.05	0.12

7.3.4 Analysis

7.3.4.1 Overall statistics

Figure 7–24 to Figure 7–27 together with Table 7–4 and Table 7–5 deal with data at low liquid loading (maximum superficial liquid velocity equal to 0.0059 m/s) and provide the following information:

- PETRA gives better overall predictions than three-layer models. It gives better accuracy (mean error closer to zero), less spread (smaller standard deviation). In particular, PETRA gives better predictions of the phase fractions at upward inclinations.
- PETRA yet under predicts the water holdup at upward inclinations. In other terms, the mechanism by which water and oil stratify by gravity at upward inclinations is not reproduced with sufficient accuracy.
- PETRA under predicts the pressure drop in the stratified/atomization regime.
- Taitel et al.'s (1995) three-layer model tends to over predict phase fractions, especially at upward inclinations, and under predict the pressure drop. The same behaviour is observed with Taitel et al's (1976) two-phase flow model. The main cause of this discrepancy is a weakness in the interfacial friction models.
- Khor et al's (1997) model overestimates phase fractions at low liquid loading but falls correctly back on the pressure drop. This highlights the impact of friction laws on the predictions: Taitel et al. (1995) and Khor et al. (1997) use the same geometrical model but different closure laws.

Figure 7–28 together with Table 7–6 deal with data at moderate liquid loading (superficial liquid velocity equal to 0.04 m/s) and provide the following information:

- Khor et al.'s (1997) model gives best prediction accuracy despite a larger spread. The closures selected by Khor et al. apparently perform better at moderate liquid loading than low liquid loading.

• Taitel et al's (1995) model still over predicts phase fractions and under predicts the pressure drop.

• PETRA under predicts the holdup at high liquid holdup both for water and oil.

7.3.4.2 Detail plots

The relative performance of three-layer models and PETRA is analysed in light of the following criteria:

For gravity dominated flows:

• Correct pressure drop sensitivity with water fraction.

• Correct gas superficial velocity at holdup inflexion and magnitude of the holdup increase with decreasing gas velocity.

• Correct holdup sensitivity with water fraction.

• Accuracy of the water and oil holdup predictions.

For friction dominated flows:

• Correct asymptotic holdup value at high gas velocities.

• Correct holdup composition with varying water fraction.

• Magnitude of the pressure drop increase with increasing gas superficial velocity.

• Correct pressure drop sensitivity with water fraction in the stratified and stratified/atomization regimes.

• Correct pressure drop sensitivity with liquid superficial velocity at low liquid loading.

• Correct holdup sensitivity with liquid superficial velocity at low liquid loading.

Gravity dominated flows

All three models correctly predict the pressure drop in stratified flow at low gas velocity and the fact that pressure drop is little sensitive to water fraction. This can be seen in Figure 7–31 at superficial gas velocity 7 m/s.

PETRA correctly predicts the gas superficial velocity at holdup inflexion but, as in two-phase flow, the holdup increase with decreasing superficial gas velocity is too slack. This appears in Figure 7–33 and Figure 7–36. This is especially true at low liquid loading (superficial liquid velocity 0.0059 m/s) and at low water fractions. The three-layer models do not correctly predict the superficial gas velocity at inflexion nor the magnitude of the holdup increase.

PETRA's prediction accuracy of the individual holdup is poor, and PETRA under predicts the water holdup at low gas velocity, upward inclination and low liquid loading as shown

in Figure 7–34. Holdup predictions are improved at moderate liquid loading but PETRA still slightly under predicts.

All models predict water accumulation at low gas velocities, in accordance with experiments (Figure 7–31). On the other hand, the holdup sensitivity with water fraction is not well predicted and the holdup peak at 50% water fraction is overlooked by, for instance, PETRA (Figure 7–31 at superficial gas velocity 7 m/s). The reason for this is the under prediction of the water holdup at small inclinations.

Friction dominated flows

The asymptotic holdup at large gas velocity in the stratified/atomization regime is well predicted by PETRA and less accurately by three-layer models. This is true at both low and moderate liquid loading. The measured holdup sensitivity with water fraction at 25 m/s is not reproduced by PETRA (Figure 7–31) that predicts a flat holdup with changing water fraction The phase fraction variations with water fraction at low liquid loading (Figure 7–30) are, however, well reproduced by PETRA. Khor et al's model severely over predicts the phase fractions in this case.

Water accumulation is predicted by all models both at low and high liquid loading (Figure 7–30 and Figure 7–31), with PETRA being the closest to the measured data.

The magnitude of the pressure drop increase with superficial gas velocity is not well predicted by any of the models at low liquid loading but reasonably well predicted by PETRA at moderate liquid loading (Figure 7–32 and Figure 7–36). At low liquid loading PETRA severely under predicts the pressure drop and this represents a major problem for predicting gas condensate pipe flow. It is probably related to the handling of droplets. Three-layer models also under predict in a slightly lesser extent. One possible remedy would be to re-model gas-wall friction to account for the droplets depositing at the upper pipe wall.

No model can correctly predict the sensitivity of pressure drop with water fraction. At moderate superficial gas velocity and low liquid loading (Figure 7–30), the model of Taitel et al. actually gives good agreement with the steel data. PETRA exhibits a peculiar loss of pressure drop at intermediate water fractions which reminds of the drag reduction effect observed in steel but it can not be reproduced with good accuracy. A possible explanation is that PETRA assumes dispersed flow in the liquid phase at small and high water fractions and separated flow at intermediate water fractions. At moderate liquid loading (Figure 7–31), PETRA can reproduce with good accuracy the almost constant value of the pressure drop in the case of the unpigged acrylic pipe.

Finally, neither the three-layer models nor PETRA can match the pressure drop sensitivity with increasing superficial liquid velocity at low liquid loading. (Figure 7–29). At very low loading, PETRA yields a pressure drop close to the dry gas pressure drop and this underestimates the data. At a certain liquid superficial velocity, the pressure drop predicted by PETRA increases to over the measured pressure drop. The reason for this behaviour is perhaps the triggering of the droplet entrainment criterion at high liquid superficial velocity.

7.4 Summary

This chapter has dealt with three-phase steady-state flow experiments performed at conditions involving small and moderate liquid loading. Stratified flows of air, water and Exxsol D80 spanning from the transition with slug flow to the stratified/atomization regime have been studied in near horizontal 60 mm pipes of different wall properties in terms of surface roughness and contact angles. Measurements of steady-state pressure drop and phase fractions have been performed and compared with predictions from three-layer one-dimensional models and the multiphase pipe flow simulator PETRA.

The main topics discussed in this chapter are summarized below:

• For gravity dominated flows, the holdup is water fraction dependent and goes through a maximum at low water fractions due to local separation of water and oil. The magnitude of the phenomenon is emphasized at low liquid loading. For friction dominated flows, the pressure drop is water dependent especially in the atomization regime at the highest gas velocities. The traditional explanation is that the equivalent fluid viscosity increases close to water-oil phase inversion leading to a peak in the total liquid holdup and the pressure drop. This is only partly verified in the acrylic pipe at moderate liquid loading where a peak in the total holdup is effectively obtained at moderate gas flow rate. At low liquid loading, a peak is obtained only at high gas flowrates.

• Other mechanisms, however, come into play at low liquid loading. One of them is the significant effect of wall material property on the flow. This concerns essentially friction dominated flows, at conditions where oil and water are flowing together in the liquid phase and compete for the wetting of the pipe wall. The material effects observed are twofold:

– On the flow regime in the liquid layer. At conditions where a separated oil-water flow exists in the steel pipe, the flow is dispersed in the pigged, water-washed acrylic pipe. In the acrylic pipe, large amplitude irregular waves form at the interface between the gas and the liquid dispersion, carrying batches of water droplets at their front and resulting in increased droplet generation.

– On the wetting of the upper pipe wall in the atomization regime. The wall in the clean acrylic pipe exhibits a granular creamy structure where large amounts of water droplets are seen protruding into the gas phase, either hanging or running streamwise. In the steel pipe, the upper film is smoother and fewer protruding water droplets can be seen.

• In terms of pressure drop and holdup, the pressure drop is generally higher in acrylic with more sensitivity with water fraction and a peak at middle to high water fractions. The pressure drop in steel also exhibits a peak but at higher gas superficial velocities and less marked. The holdup composition is different in steel and acrylic with water accumulating in steel and oil accumulating in acrylic relative to input water fraction.

• The epoxy coating of the bare steel pipe does not result in a fundamentally different flow behaviour compared to the bare steel pipe. The coating has been studied for friction dominated flows. It has little effect on the pressure drop as the initial steel pipe is already

hydraulically smooth. It has an effect on liquid composition with enhanced oil accumulation. Pressure drop is also less in the atomization regime.

• The reason for the material differential affinity has been investigated. Water affinity can be related to contact angle hysteresis. Hysteresis is, in turn, very affected by surface physical roughness and chemical homogeneity. An illustration is given by the differences observed between the clean and contaminated acrylic pipe. The contaminated acrylic pipe develops more contact angle hysteresis as the surface heterogeneity increases and water droplet adhesion is higher on this surface. This results in a larger holdup and a smaller pressure drop. Transient experiments also illustrates the effect of water wetting and de-wetting in three-phase flow.

• Comparisons of data with predictions from three-layer models and the general purpose multiphase flow simulator PETRA show that PETRA gives overall best accuracy and less spread and is able to reproduce stratified three-phase flow data both at moderate and low liquid loading. Two major shortcomings however are noticed:

– PETRA under predicts holdup for gravity dominated flows and this is due to the fact that the water stratification mechanism is not correctly reproduced. A possible reason is that PETRA assumes an oil-water dispersion instead of a separated regime in the liquid layer.

– PETRA under predicts the pressure drop at conditions of atomization flow. That may be due to non-conservative friction closures in presence of droplets. A more conservative gas-wall friction is needed to represent the droplet wetting of the upper pipe wall.

In addition, PETRA somewhat under predicts the pressure drop at very low liquid loading for which the pressure drop calculated is very close to that of the dry pipe. In other words, small liquid quantities are ignored when in fact they have an important impact on the pressure drop.

Khor et al's closure proposals (Khor et al. 1997) perform well at moderate liquid loading but result in severe over prediction of the phase fractions at low liquid loading.

Table 7–7: Summary of plots for three-phase steady-state flow experiments

Label	Page	Serie	Main variables	Primary sensitivity	Secondary sensitivity	Fixed parameter
Figure 7–4	p. 213	#1	pressure drop total liquid holdup in-situ water fraction	input water fraction	superficial liquid velocity material	$\theta = 0$ deg. $U_{SG} = 14.8$ m/s
			pressure drop	input water fraction	superficial liquid velocity	$\theta = 0.5$ deg. $U_{SG} = 25$ m/s material = acrylic
Figure 7–5	p. 214	#1	pressure drop total liquid holdup water and oil holdup	superficial liquid velocity	input water fraction material	$\theta = 0$ deg. $U_{SG} = 14.8$ m/s
Figure 7–6	p. 215	#1 details	pressure drop total liquid holdup	superficial liquid velocity	input water fraction material	$\theta = 0$ deg. $U_{SG} = 14.8$ m/s
Figure 7–7	p. 216	#1 details	water and oil holdup	superficial liquid velocity	input water fraction material	$\theta = 0$ deg. $U_{SG} = 14.8$ m/s
Figure 7–8	p. 217	#2.1	pressure drop in-situ water fraction total liquid holdup water and oil holdup	input water fraction	material superficial gas velocity	$\theta = 0$ deg. $U_{SL} = 0.0059$ m/s
						$\theta = 1$ deg. $U_{SL} = 0.0059$ m/s
Figure 7–9	p. 218	#2.2	pressure drop in-situ water fraction total liquid holdup	input water fraction	material superficial gas velocity	$\theta = 0.5$ deg. $U_{SL} = 0.04$ m/s
Figure 7–10	p. 219	#2.1 details	pressure drop in-situ water fraction total liquid holdup water and oil holdup	input water fraction	material inclination	$U_{SL} = 0.0059$ m/s $U_{SG} = 14.8$ m/s

Table 7–7: Summary of plots for three-phase steady-state flow experiments

Label	Page	Serie	Main variables	Primary sensitivity	Secondary sensitivity	Fixed parameter
Figure 7–11	p. 220	#2.1 details	phase fractions	input water fraction	Material superficial gas velocity	$\theta = 0$ deg. $U_{SL} = 0.0059$ m/s
						$\theta = 1$ deg. $U_{SL} = 0.0059$ m/s
Figure 7–12	p. 221	#2.2 details	phase fractions	input water fraction	superficial gas velocity	$\theta = 0.5$ deg. $U_{SL} = 0.04$ m/s material = acrylic
Figure 7–13	p. 222	#3.1	pressure drop total liquid holdup water and oil holdup	superficial gas velocity	material input water fraction	$\theta = 0$ deg. $U_{SL} = 0.0059$m/s
						$\theta = 1$ deg. $U_{SL} = 0.0059$ m/s
Figure 7–14	p. 223	#3.2	pressure drop total liquid holdup	superficial gas velocity	input water fraction	$\theta = 0.5$ deg. $U_{SL} = 0.04$ m/s material = acrylic
Figure 7–15	p. 224	#3.1 details	pressure drop	superficial gas velocity	input water fraction material inclination	$U_{SL} = 0.0059$ m/s
Figure 7–16	p. 225	#3.1 details	phase fractions	superficial gas velocity	input water fraction material	$\theta = 0$ deg. $U_{SL} = 0.0059$ m/s
						$\theta = 1$ deg. $U_{SL} = 0.0059$ m/s
Figure 7–17	p. 226	#3.2 details	phase fractions	superficial gas velocity	input water fraction	$\theta = 0.5$ deg. $U_{SL} = 0.04$ m/s material = acrylic

Table 7–8: Models for stratified three-phase gas-liquid-liquid flow

Label	Ref.	Inter-faces	Limi-tations	Closures											Holdup calc.	P drop calc.
				a_G	a_O	a_W	i_j			i_i			Y_O	Y_W		
							a_j	U_j	g_j	a_i	U_i	g_i				
M1	Taitel et al. (1995)	flat	stratified flow seprated phases	Blasius Equation [3.7]	Blasius Equation [3.7]	Blasius Equation [3.7]	max(λ_G, 0.056)	U_O	ρ_G	max(λ_O, 0.056)	U_W	ρ_O	geometric Equation [3.107]	geometric Equation [3.107]	double iteration Equation [3.99] and Equation [3.100]	Equation [3.93]
M2	Khor et al. (1997)	flat	stratified flow separated phases	as M1	empirical Equation [3.113]		Colebrook Equation [3.10] + ε_j Equation [3.61]	U_O	ρ_G	as M1			geometric Equation [3.107]	geometric Equation [3.107]	double iteration Equation [3.99] and Equation [3.100]	Equation [3.93]
M3	PETRA 2.4	flat	general purpose simulator	unknown												

Table 7–9: Summary of plots for comparisons between three-phase steady-state flow measurements and one-dimensional prediction models

Label	Page	Topic
Figure 7–24	p. 232	Total liquid holdup at low liquid loading: point-by-point and pdf error comparaisons
Figure 7–25	p. 232	Water holdup at at low liquid loading: point-by-point and pdf error comparaisons
Figure 7–26	p. 233	Oil holdup at at low liquid loading: point-by-point and pdf error comparaisons
Figure 7–27	p. 233	Pressure drop at at low liquid loading: point-by-point and pdf error comparaisons
Figure 7–28	p. 234	Moderate liquid loading (Superficial liquid velocity 0.04 m/s): point-by-point and pdf error comparaisons
Figure 7–29	p. 235	Serie #1 at 20% water fraction: sensitivity with liquid superficial velocity at fixed gas superficial velocity. Comparaison with models
Figure 7–30	p. 236	Serie #2.1: sensitivity with water fraction at fixed gas superficial velocity 14.8m/s and fixed liquid superficial velocity 0.0059 m/s. Comparaison with models
Figure 7–31	p. 237	Serie #2.2: sensitivity with water fraction at fixed gas superficial velocity 14.8m/s and fixed liquid superficial velocity 0.04 m/s. Comparaison with models
Figure 7–32	p. 238	Serie #3.1: pressure drop sensitivity with gas superficial velocity and fixed liquid superficial velocity 0.0059 m/s. Comparaison with models
Figure 7–33	p. 239	Serie #3.1: total liquid holdup sensitivity with gas superficial velocity and fixed liquid superficial velocity 0.0059 m/s. Comparaison with models
Figure 7–34	p. 240	Serie #3.1: water holdup sensitivity with gas superficial velocity and fixed liquid superficial velocity 0.0059 m/s. Comparaison with models
Figure 7–35	p. 241	Serie #3.1: oil holdup sensitivity with gas superficial velocity and fixed liquid superficial velocity 0.0059 m/s. Comparaison with models
Figure 7–36	p. 242	Serie #3.2: pressure drop and total liquid holdup sensitivity with gas superficial velocity and fixed liquid superficial velocity 0.04 m/s. Comparaison with models
Figure 7–37	p. 243	Serie #3.2: water and oil holdup sensitivity with gas superficial velocity and fixed liquid superficial velocity 0.04 m/s. Comparaison with models

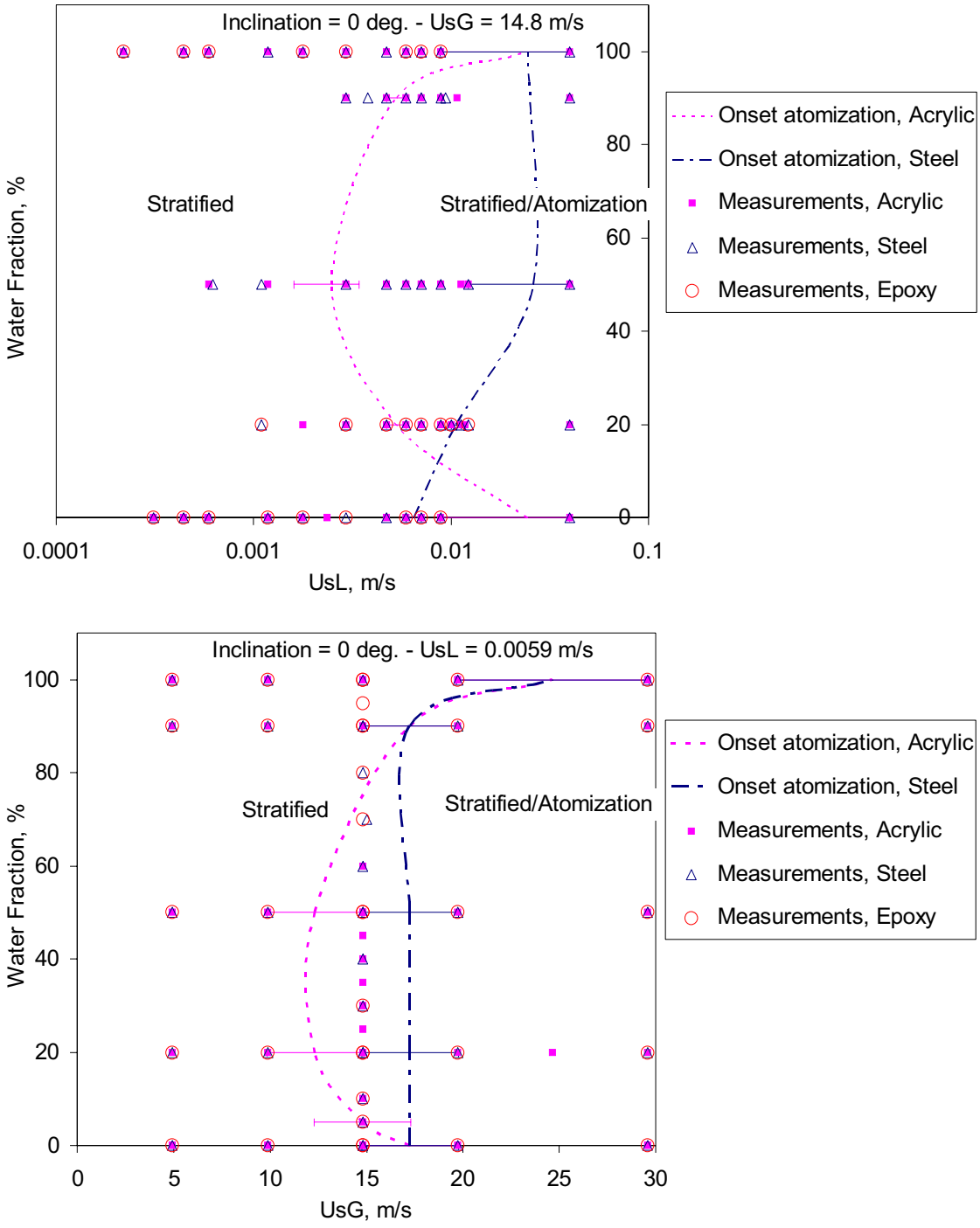

Figure 7–1: Stratified/atomization transition in the acrylic and steel horizontal pipes. The location accuracy of the transition line is indicated as an error bar on the plot. Markers indicate the locations of the steady-state pressure drop and phase fractions measurements. Top: superficial gas velocity = 14.8 m/s (serie #1); Bottom: superficial liquid velocity = 0.0059 m/s (serie #3.1)

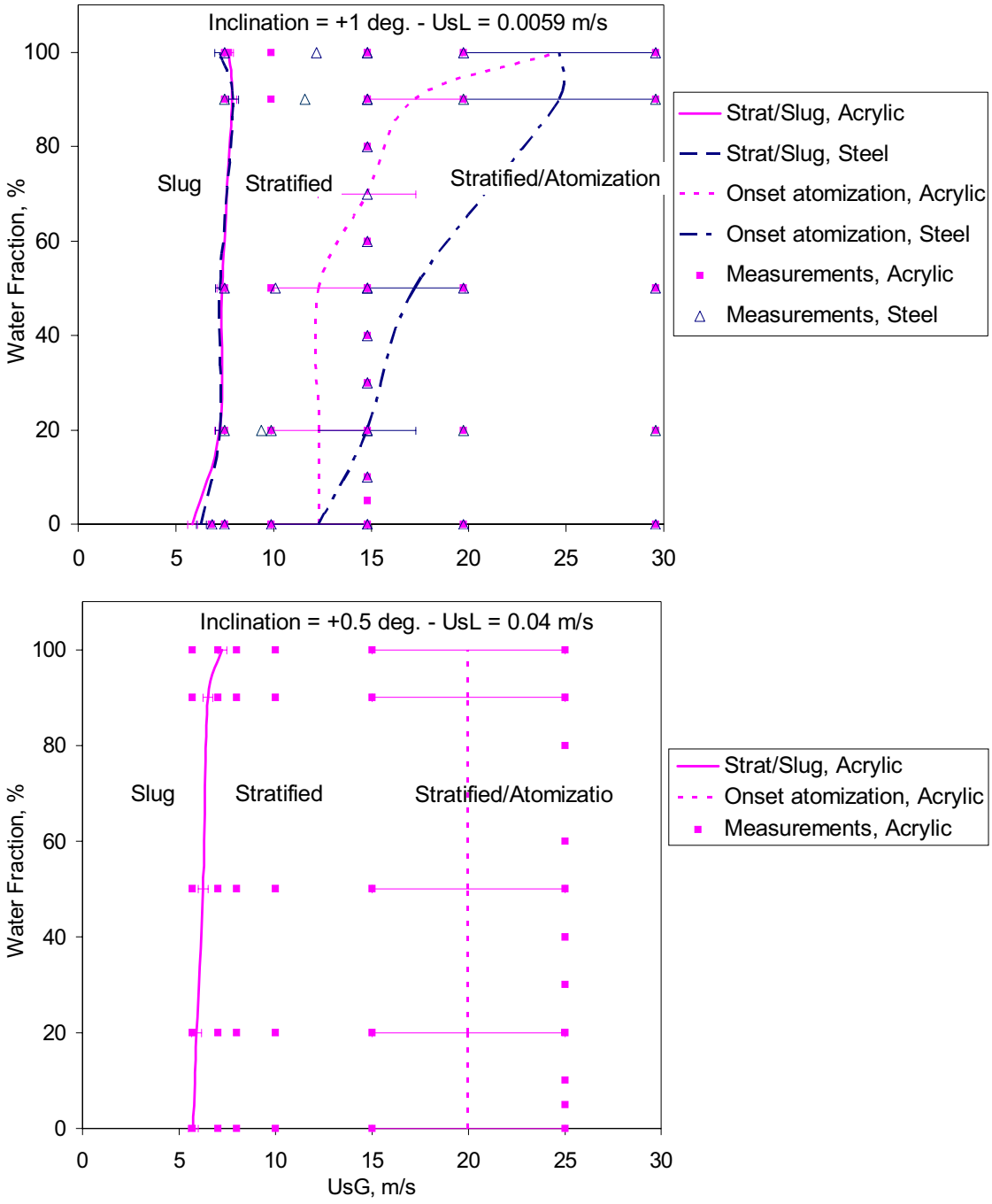

Figure 7–2: Slug/stratified and stratified/atomization transitions in the acrylic and steel inclined pipes. The location accuracy of the transition lines is indicated as an error bar on the plot. Markers indicate the locations of the steady-state pressure drop and phase fractions measurements. Top: superficial liquid velocity = 0.0059 m/s and inclination = +1 deg. (serie #3.1); Bottom: superficial liquid velocity = 0.04 m/s and inclination = +0.5 deg. (serie #3.2)

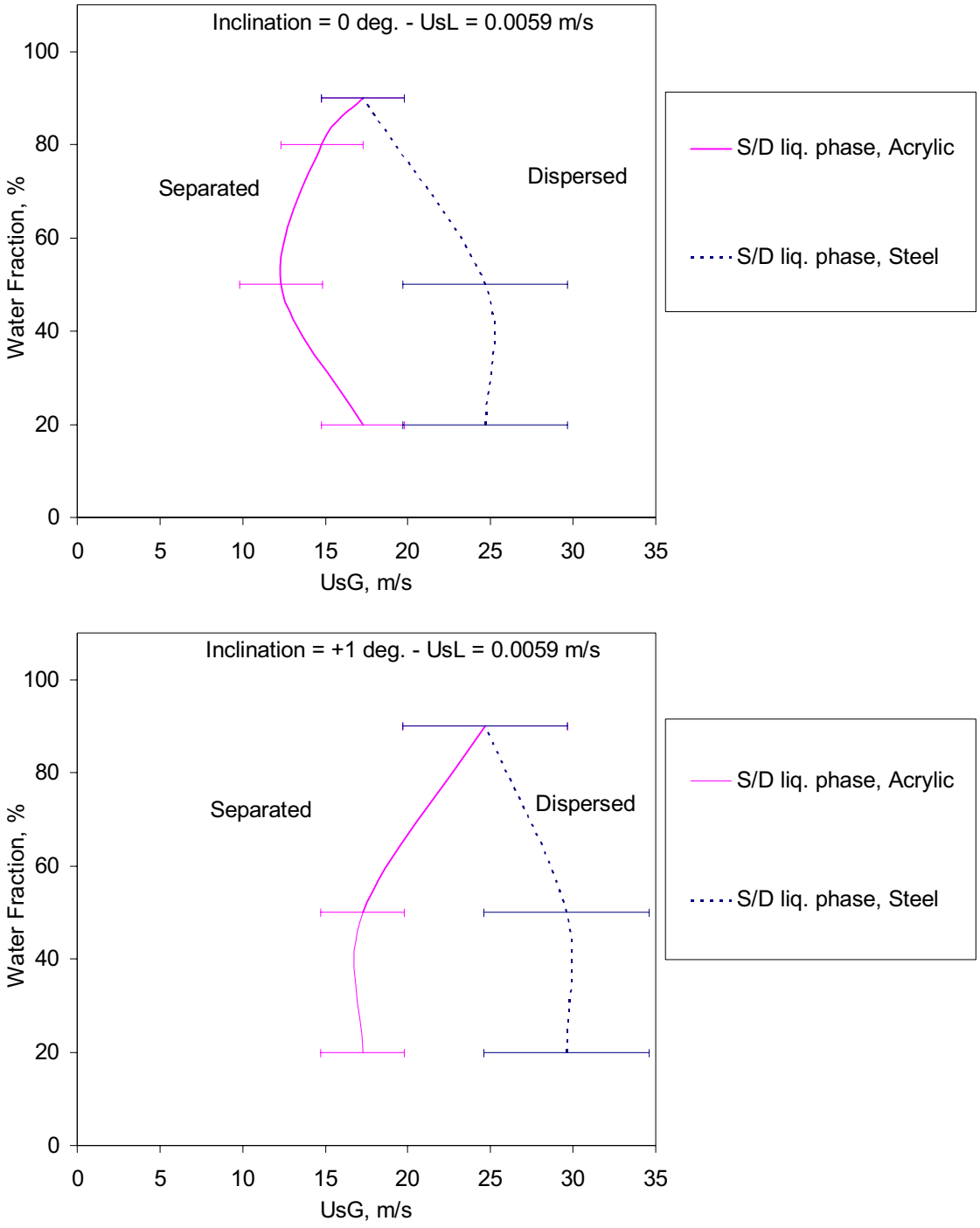

Figure 7–3: Separated/dispersed transition in the acrylic and steel pipes. The location accuracy of the transition lines is indicated as an error bar on the plot. Top: superficial liquid velocity = 0.0059 m/s and inclination = 0 deg. (serie #3.1); Bottom: superficial liquid velocity = 0.0059 m/s and inclination = +1 deg. (serie #3.1)

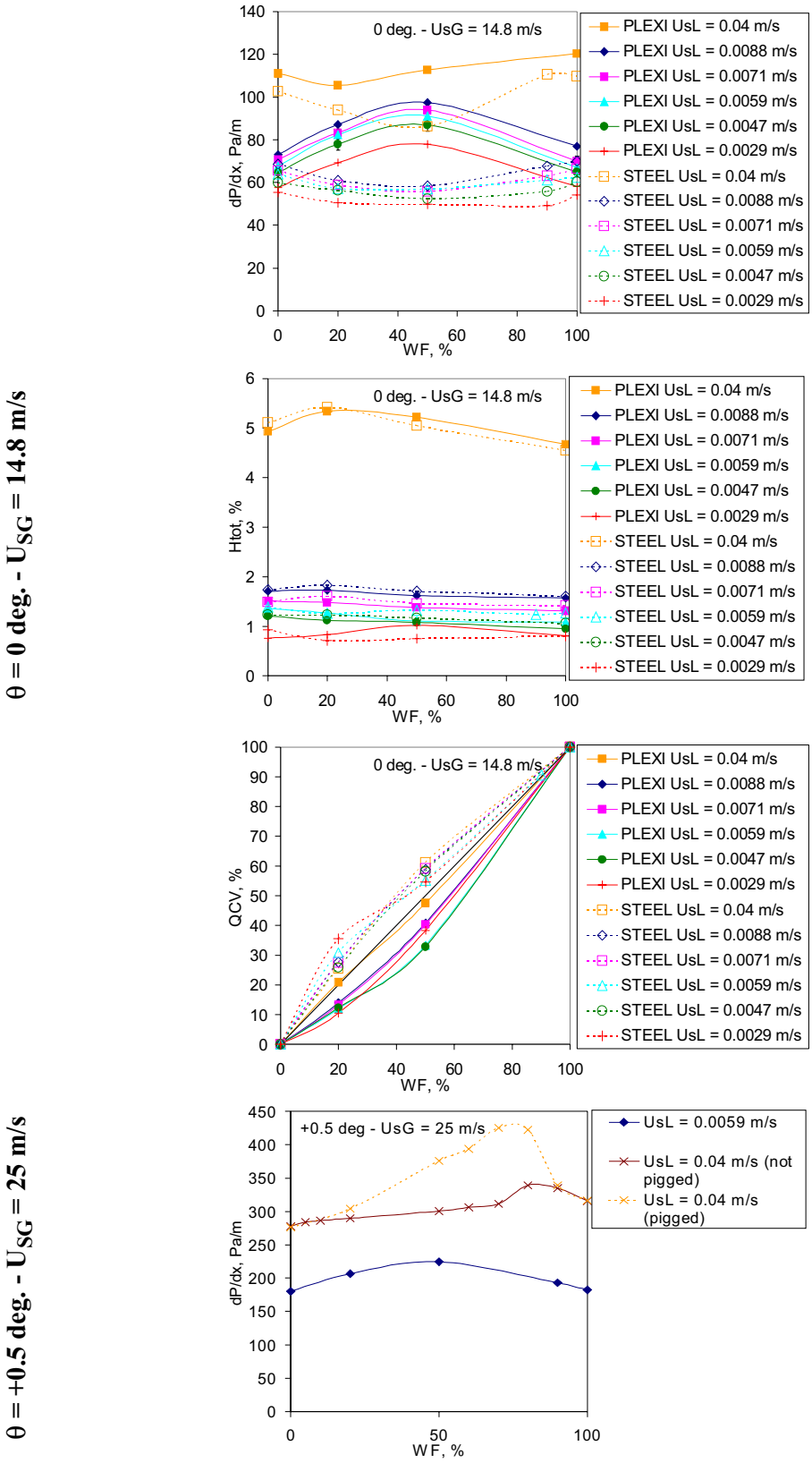

Figure 7–4: Serie #1, sensitivity with water fraction for various superficial liquid velocities at fixed air superficial velocity and inclination

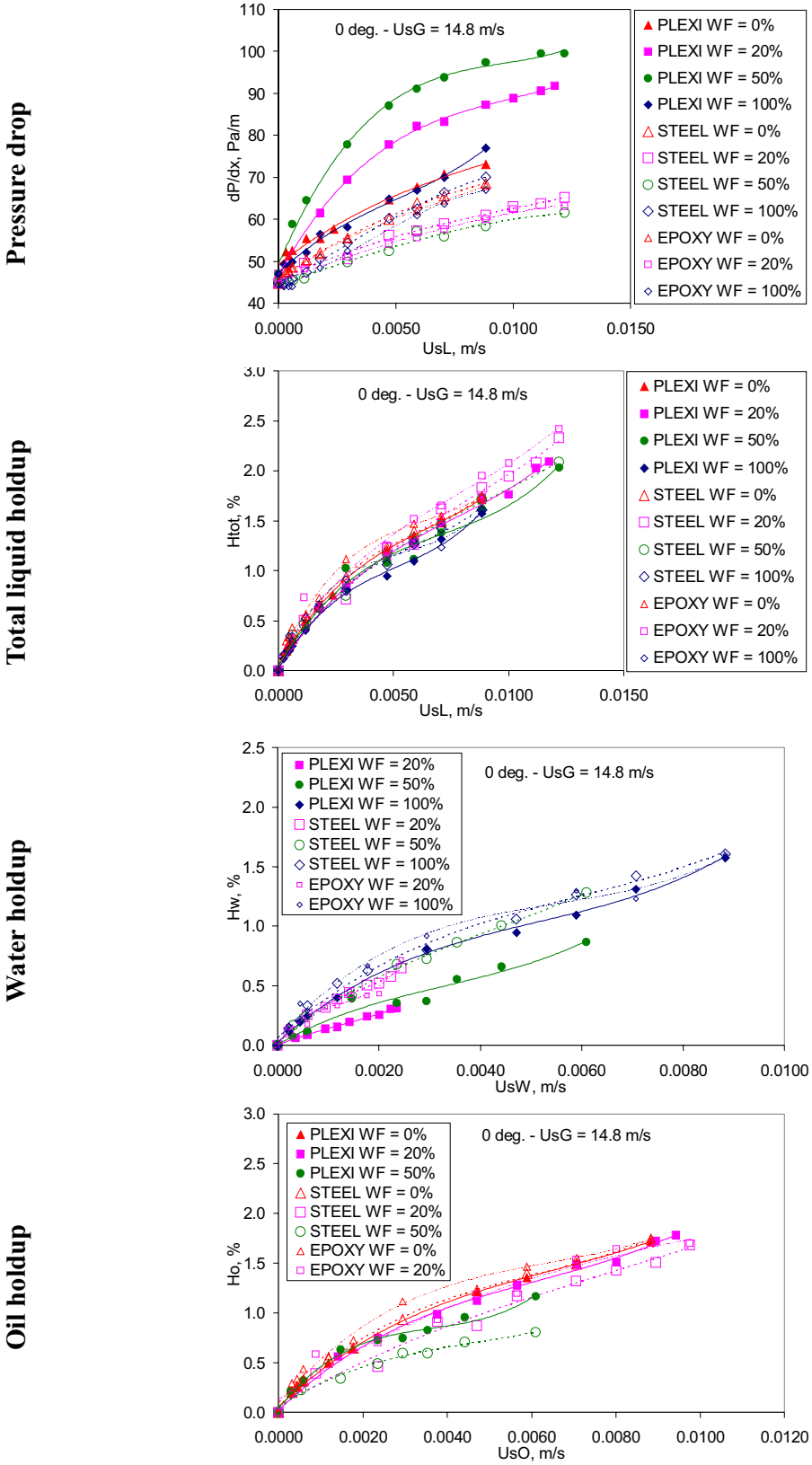

Figure 7–5: Serie #1, sensitivity with superficial liquid velocity for various water fractions at constant superficial air velocity = 14.8 m/s and inclination = 0 deg.

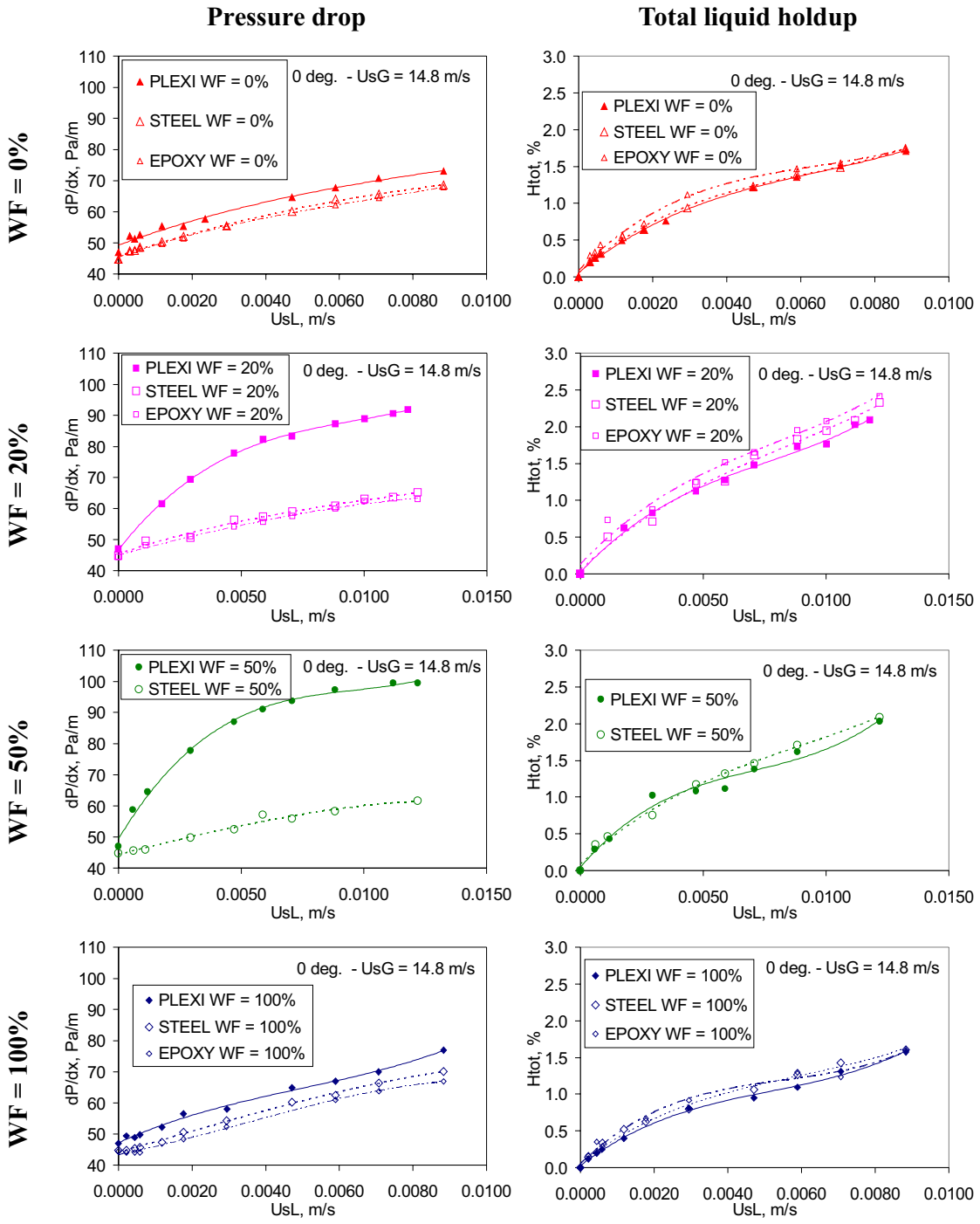

Figure 7–6: Serie #1, sensitivity of pressure drop and total liquid holdup with liquid superficial velocity at constant superficial air velocity = 14.8 m/s and inclination = 0 deg. - Details

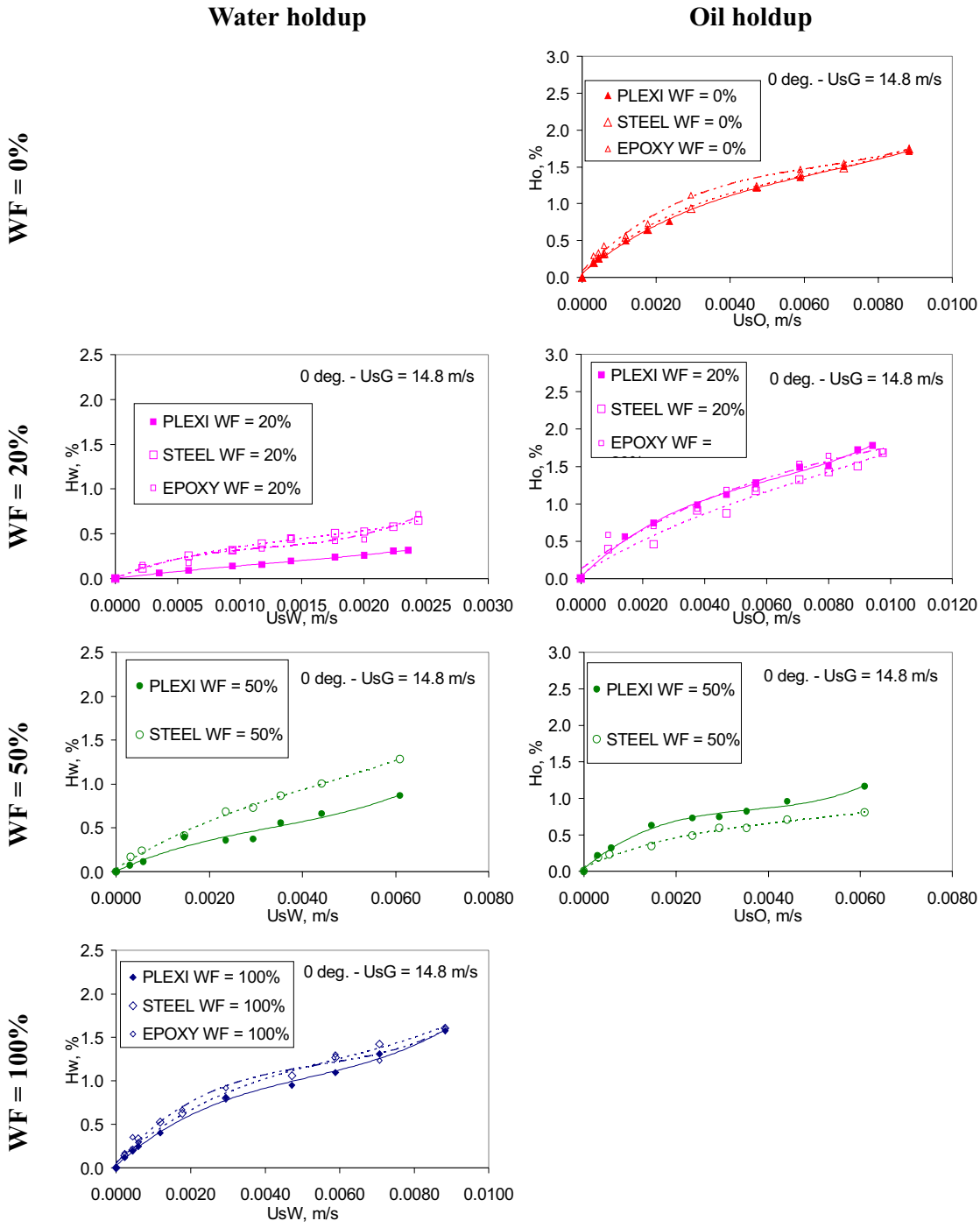

Figure 7–7: Serie #1, sensitivity of water and oil phase fractions with liquid superficial velocity at constant superficial air velocity = 14.8 m/s and inclination = 0 deg. - Details

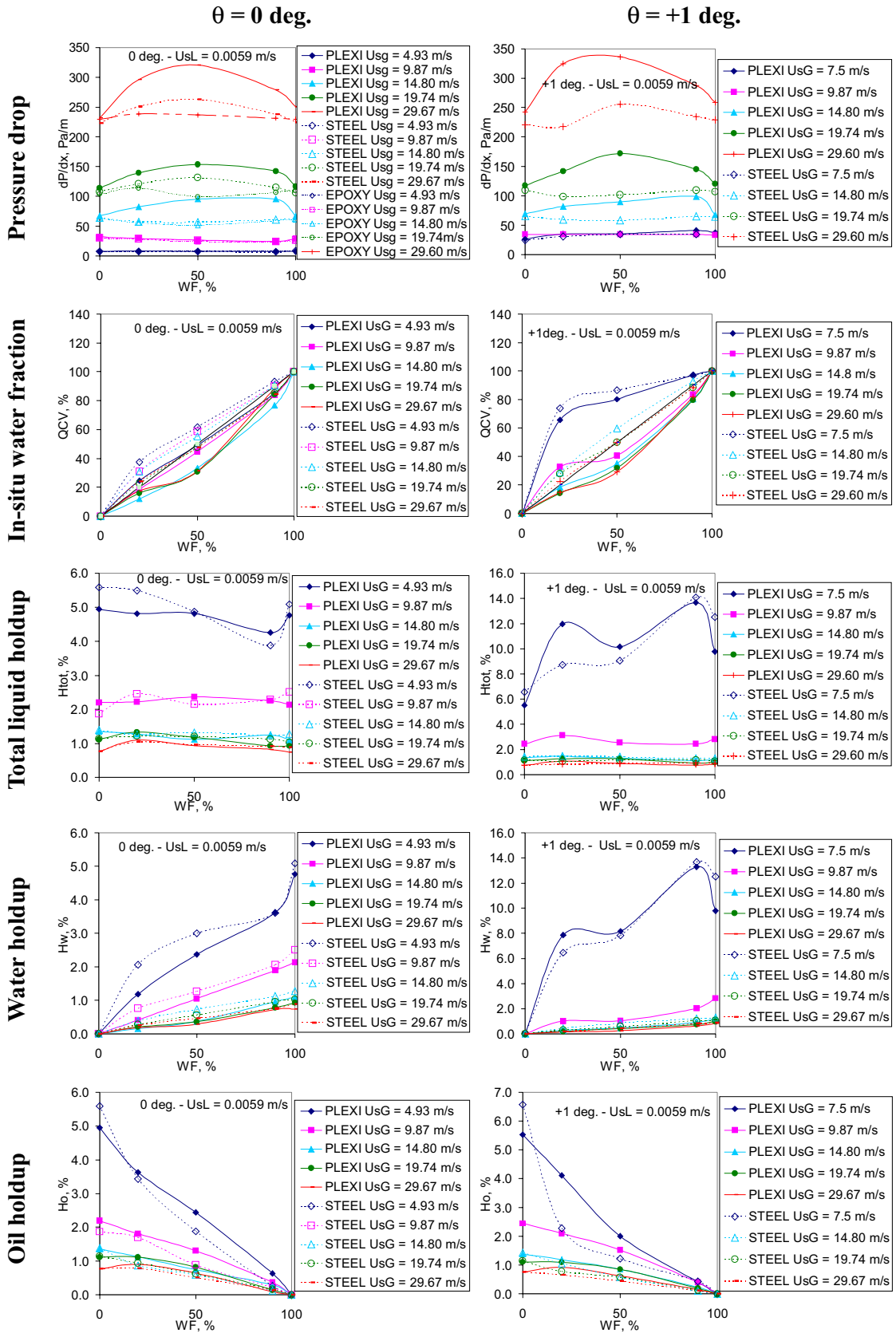

Figure 7–8: Serie #2.1, sensitivity with input water fraction for various superficial air velocities and liquid superficial velocity = 0.0059 m/s

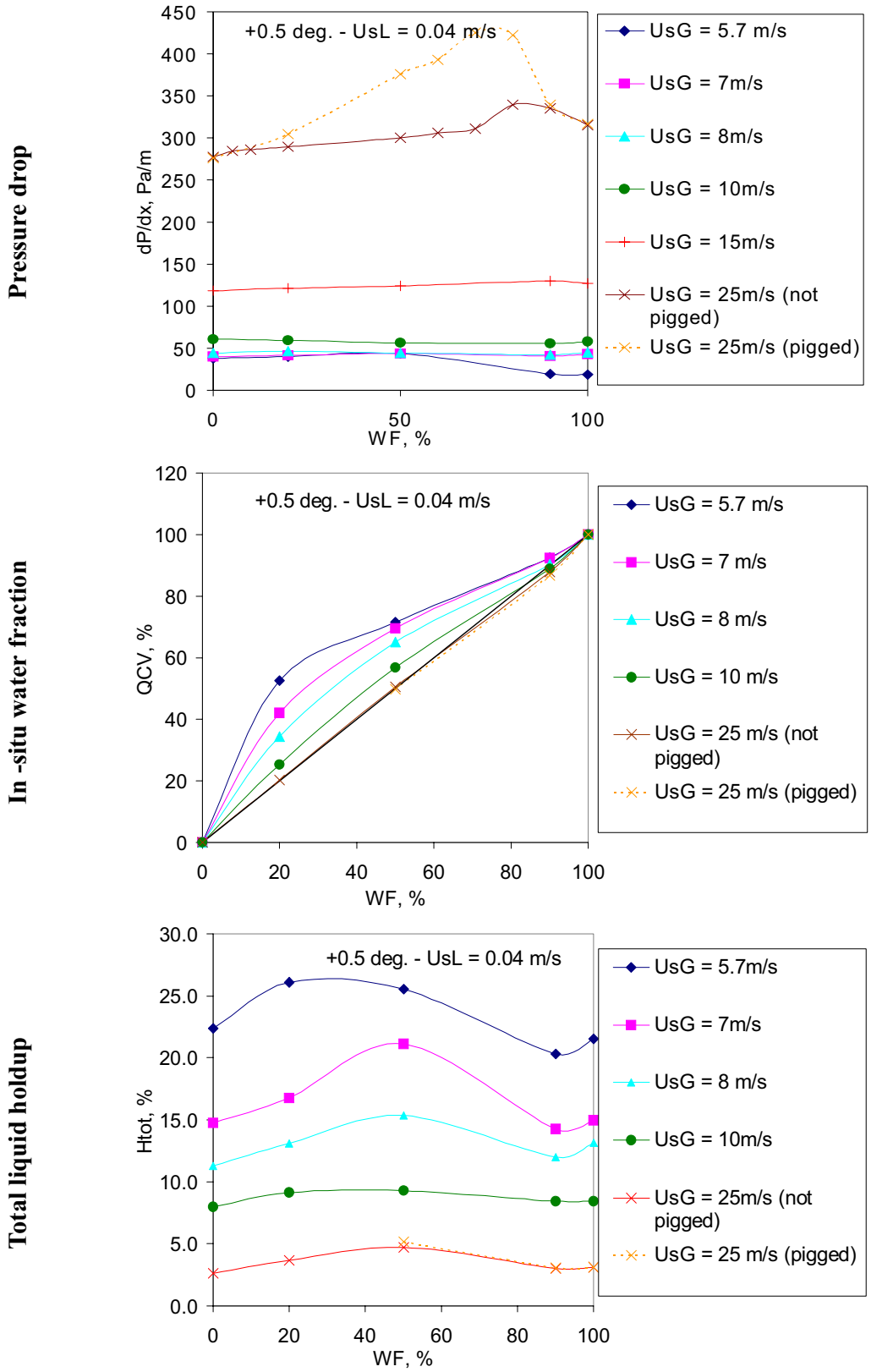

Figure 7–9: Serie #2.2, sensitivity with input water fraction for various air superficial velocities and superficial liquid velocity = 0.04 m/s. Inclination = +0.5 degree with the horizontal

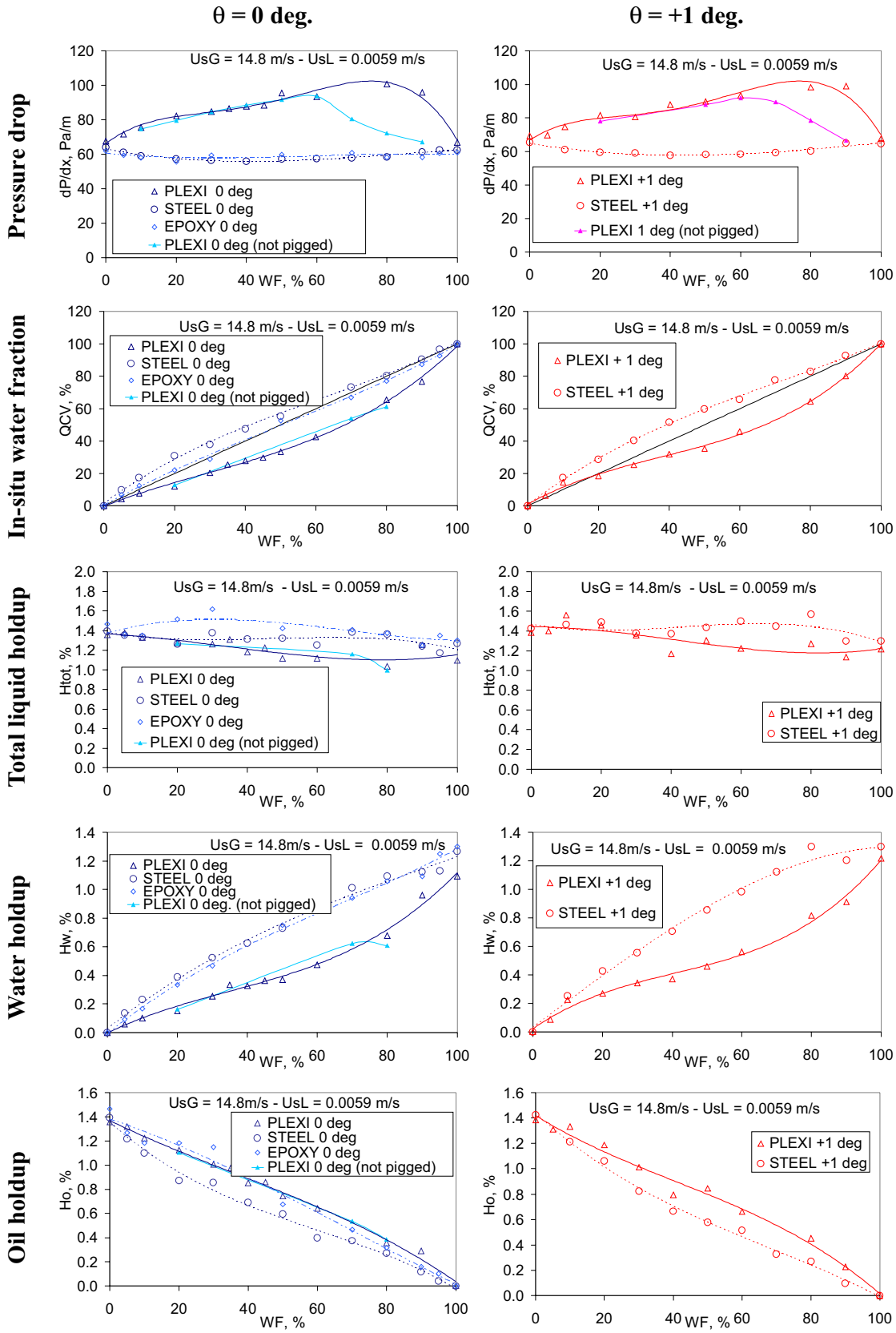

Figure 7–10: Serie #2.1, sensitivity with water fraction, details for superficial liquid velocity = 0.0059 m/s and superficial gas velocity = 14.8 m/s

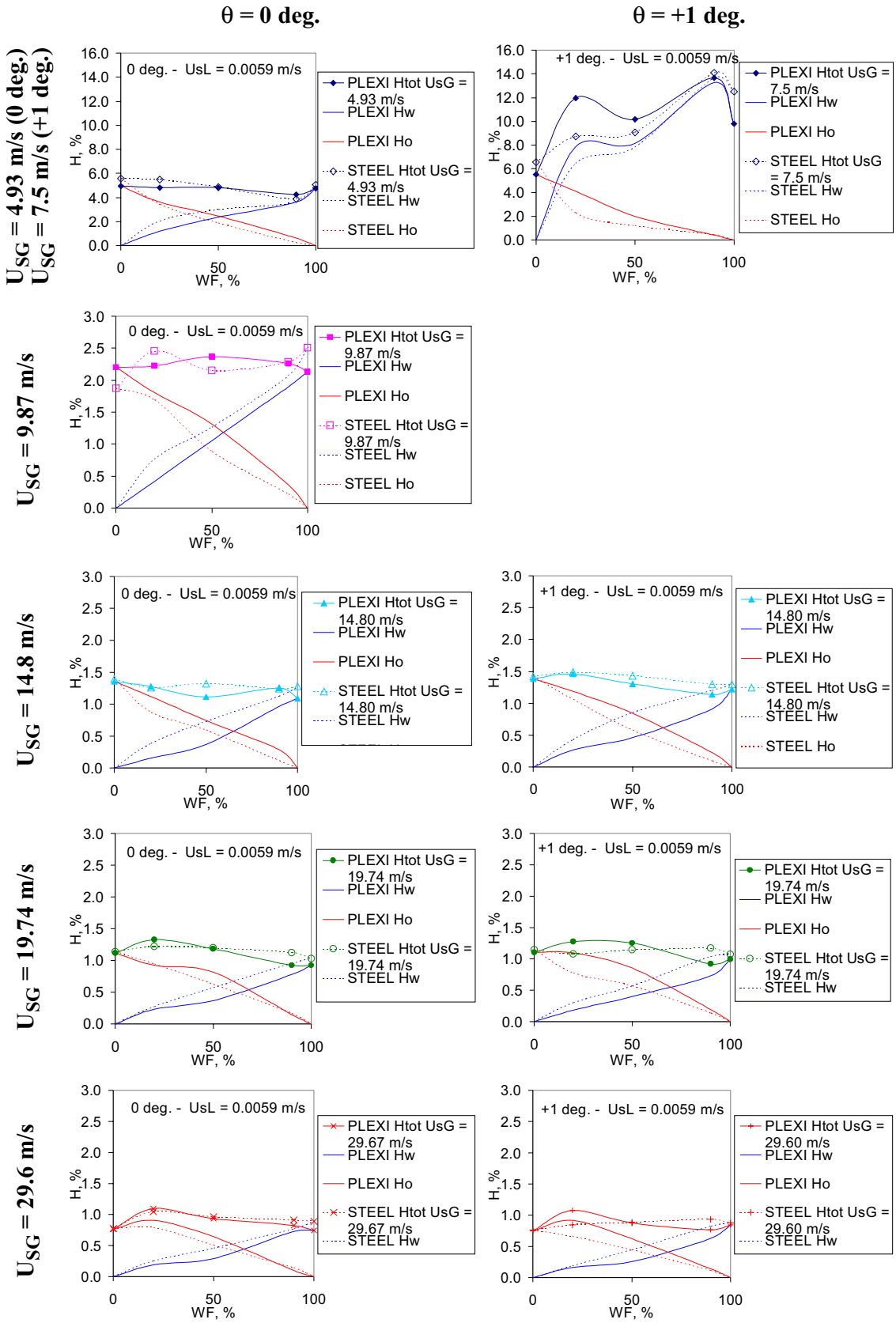

Figure 7–11: Serie #2.1, sensitivity of phase fractions with input water fraction. Details for superficial liquid velocity = 0.0059 m/s

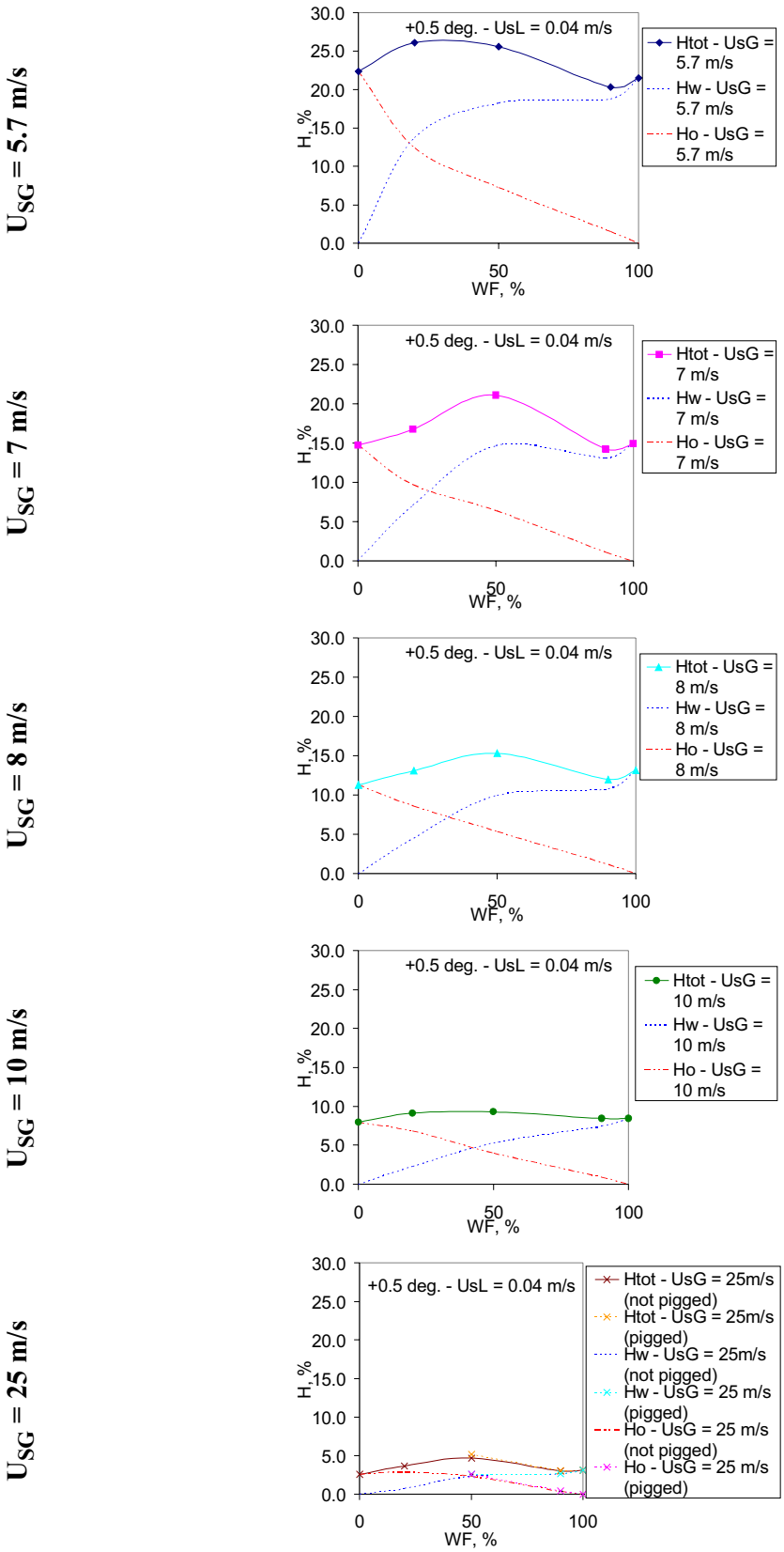

Figure 7–12: Serie #2.2, sensitivity of phase fractions on water fraction. Details for superficial velocity = 0.04 m/s, inclination = +0.5 deg.

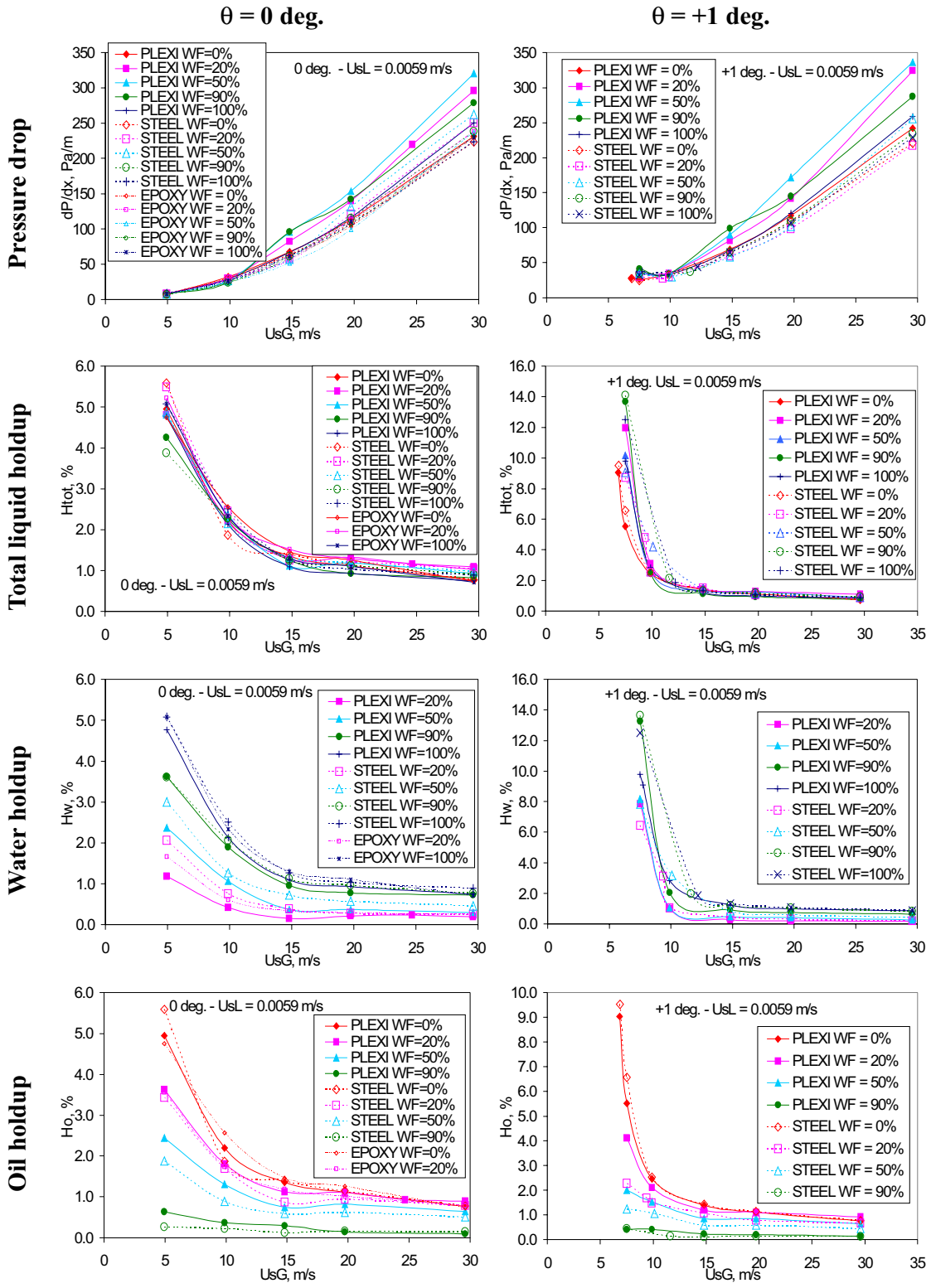

Figure 7–13: Serie #3.1, sensitivity with superficial gas velocity at given water fraction and superficial liquid velocity = 0.0059 m/s

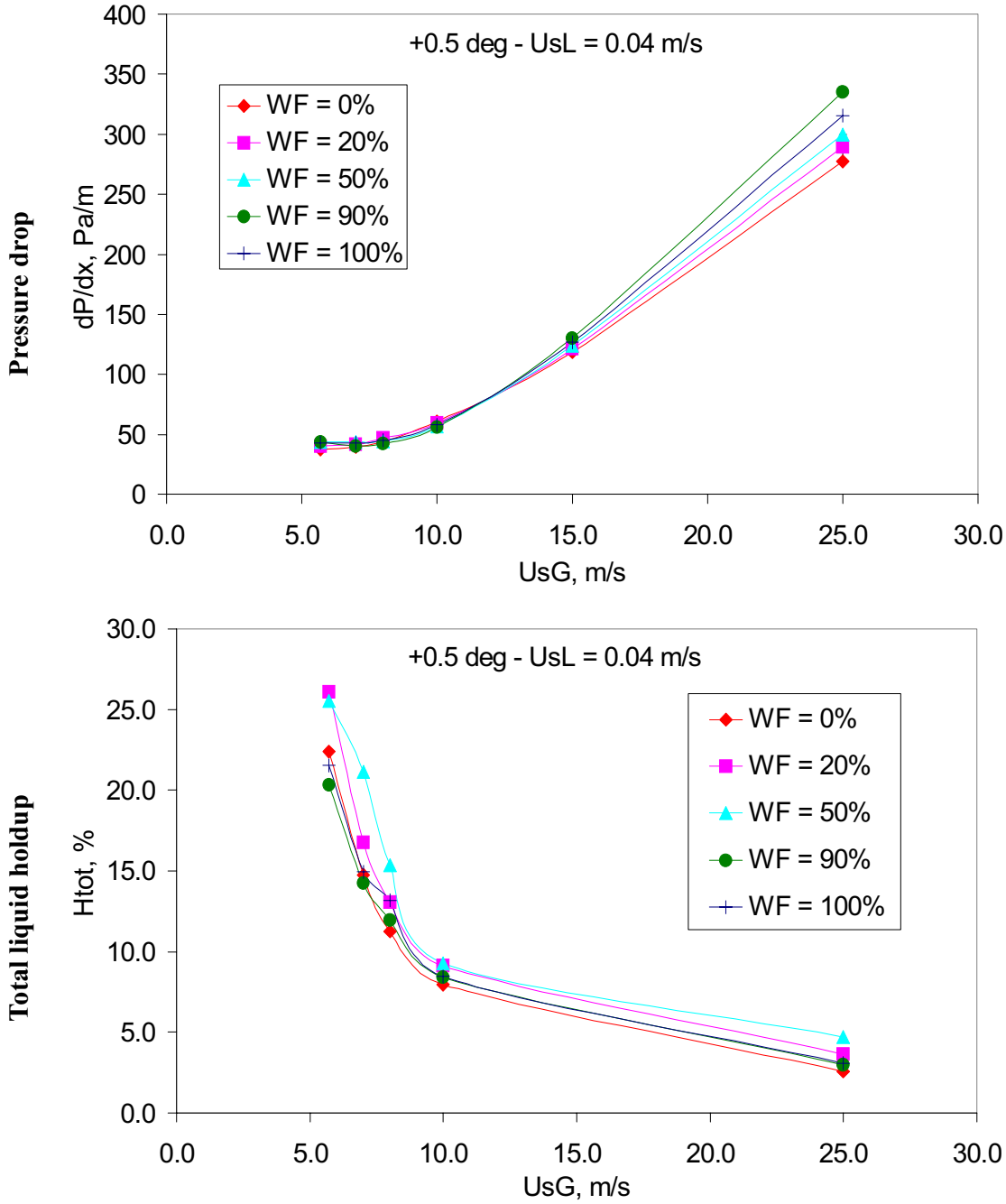

Figure 7–14: Serie #3.2, sensitivity with superficial gas velocity at given water fraction and superficial liquid velocity = 0.04 m/s. Pipe inclination = +0.5 deg.

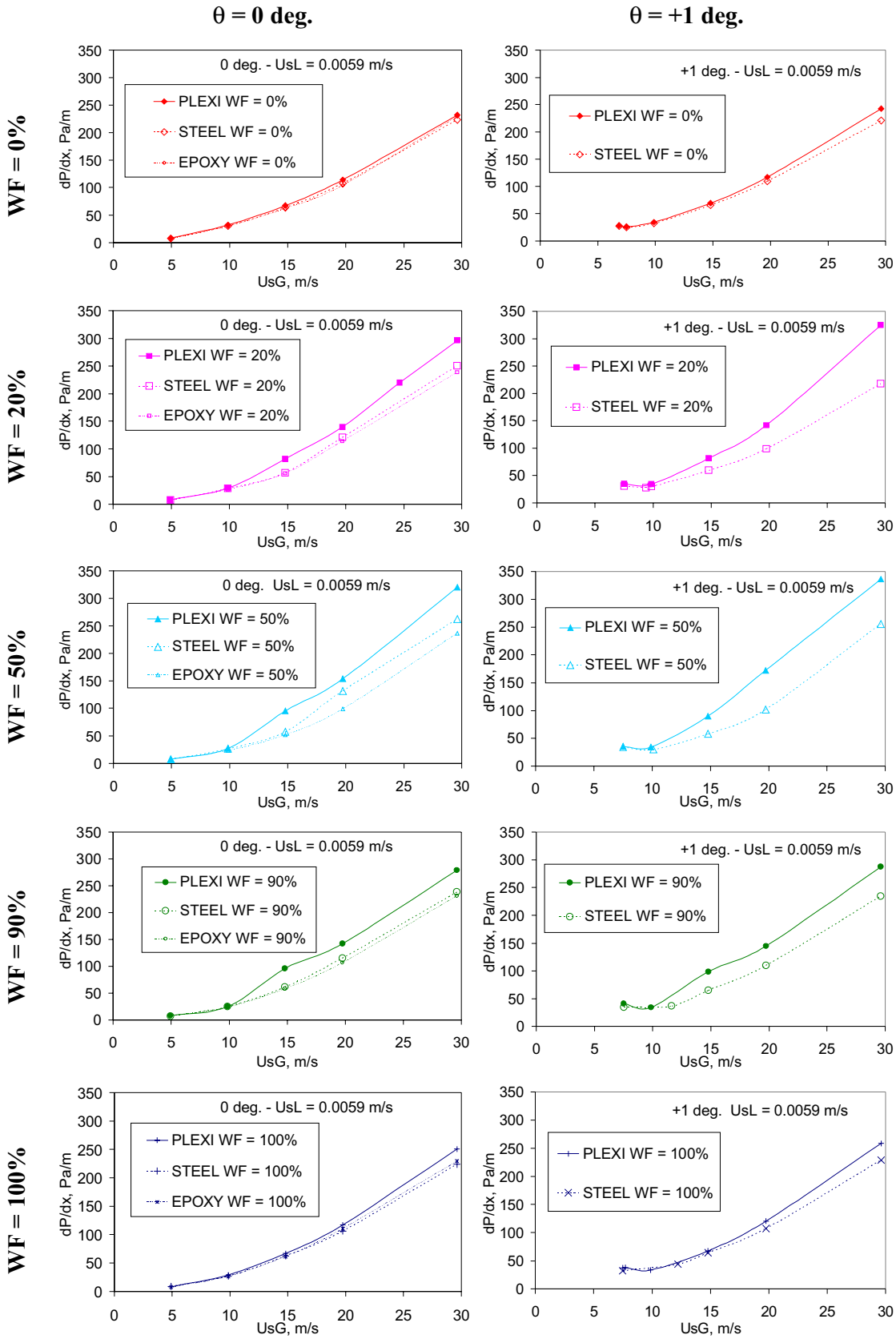

Figure 7–15: Serie #3.1, sensitivity of pressure drop with superficial gas velocity. Details for superficial liquid velocity = 0.0059 m/s

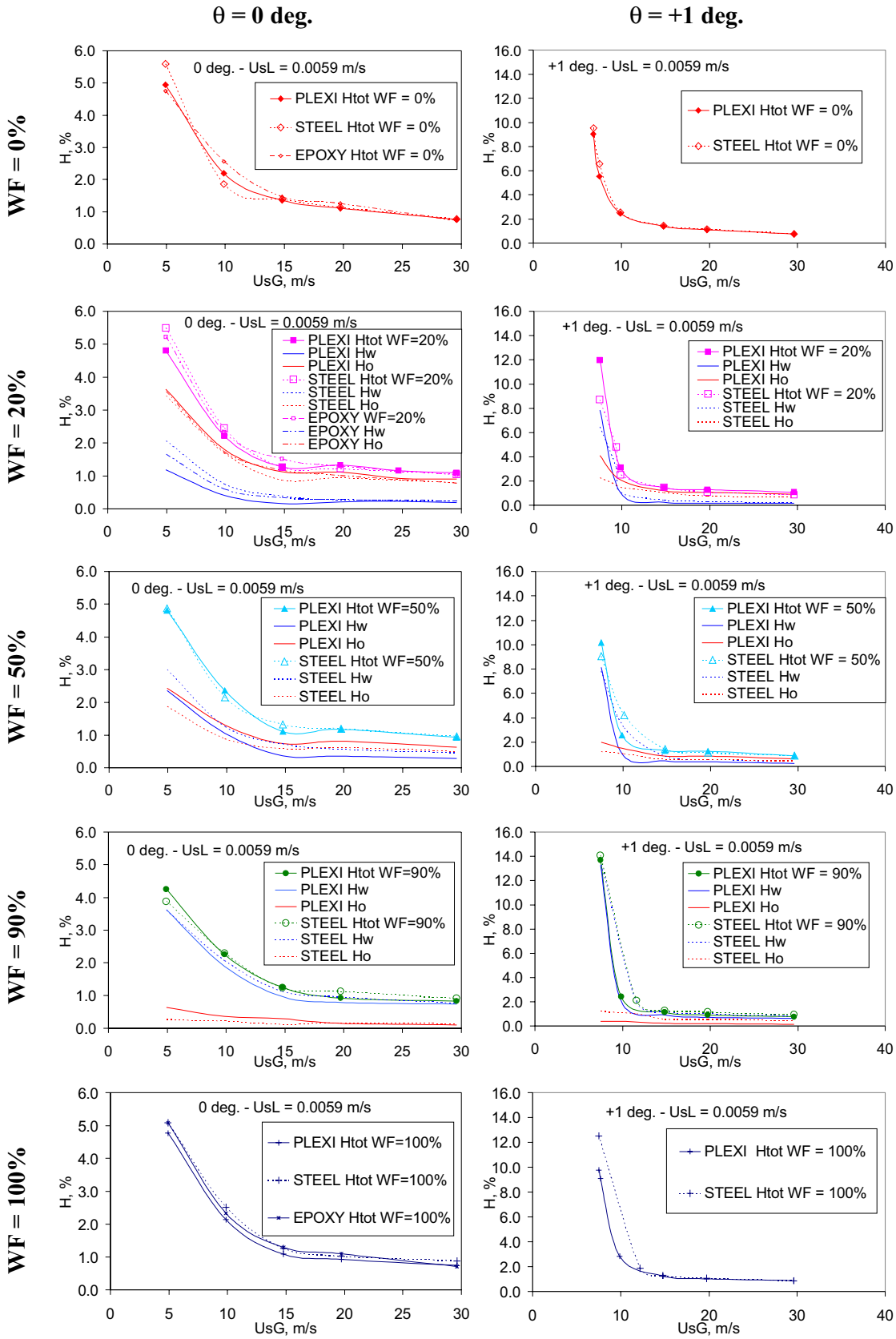

Figure 7–16: Serie #3.1, sensitivity of phase fractions with superficial gas velocity. Details for superficial liquid velocity = 0.0059 m/s

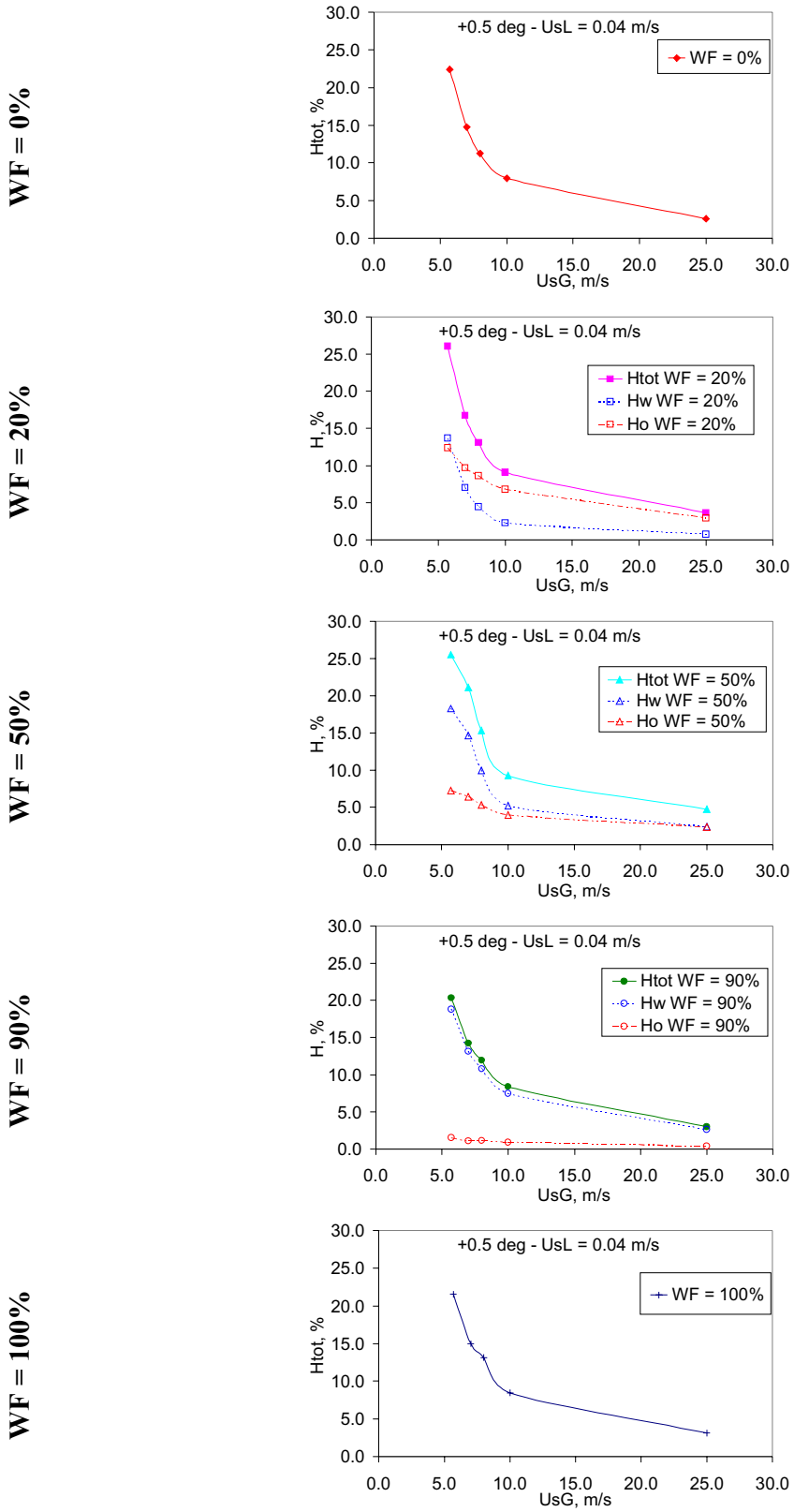

Figure 7–17: Serie #3.2 sensitivity of phase fractions with superficial gas velocity. Details for superficial liquid velocity = 0.04 m/s, inclination = +0.5 deg.

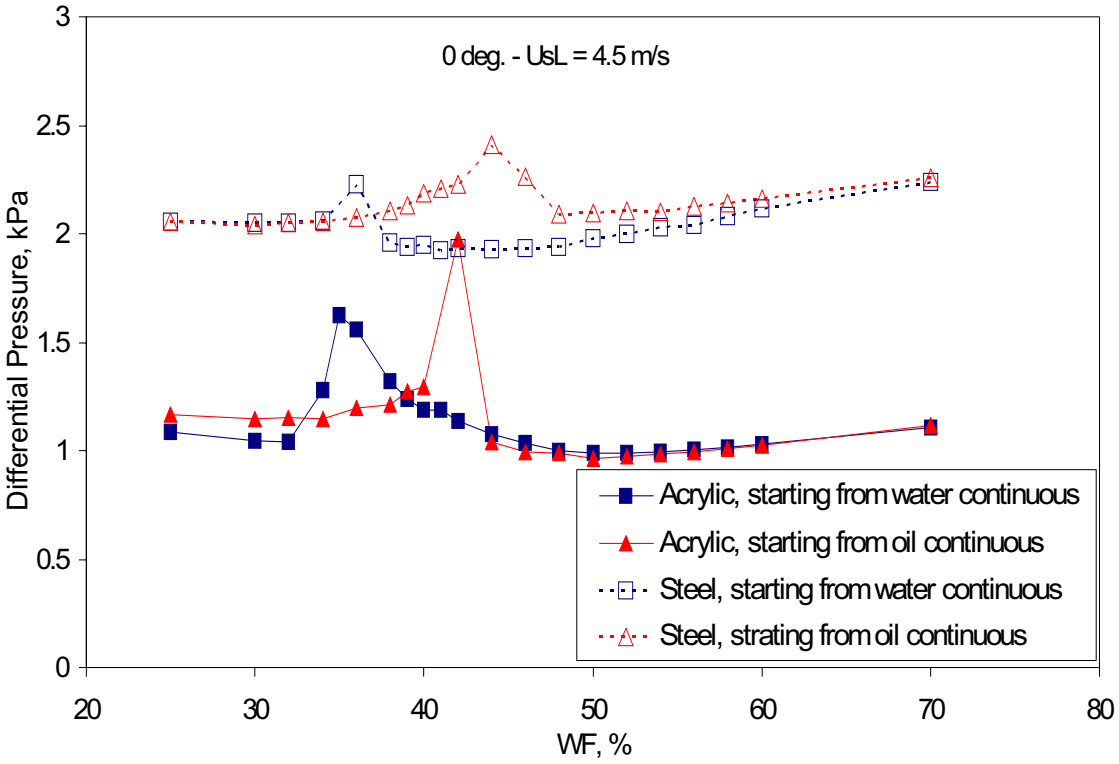

Figure 7–18: Differential pressure versus input water fraction for two-phase water-Exxsol D80 flow. The total superficial liquid velocity is equal to 4.5 m/s. Differential pressure measurements are carried out in the 60 mm i.d. steel and acrylic pipes. Experimental series are taken either starting from a water fraction 100% (single phase water) and progressively replacing water by oil or inversely from a water fraction of 0% (single phase oil), gradually replacing oil by water (from Ioannou et al. 2003)

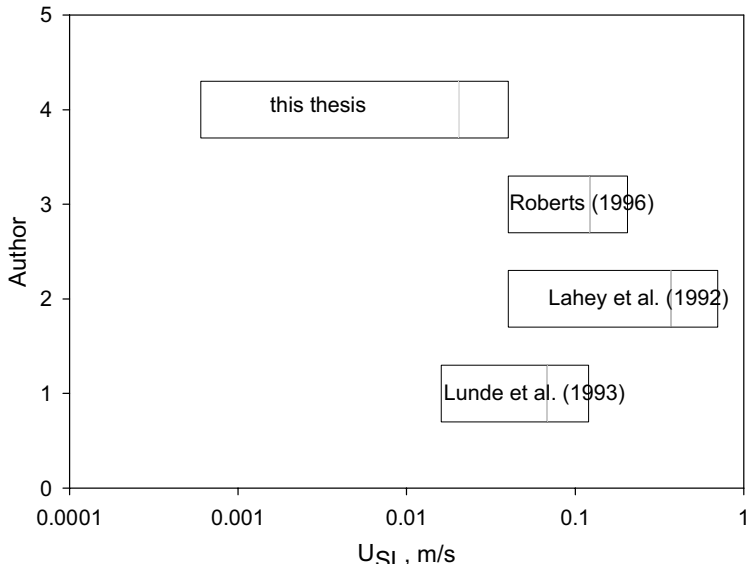

Figure 7–19: Liquid loading compared to other authors. Data from Lahey et al. (1992), Lunde et al. (1993), Roberts (1996)

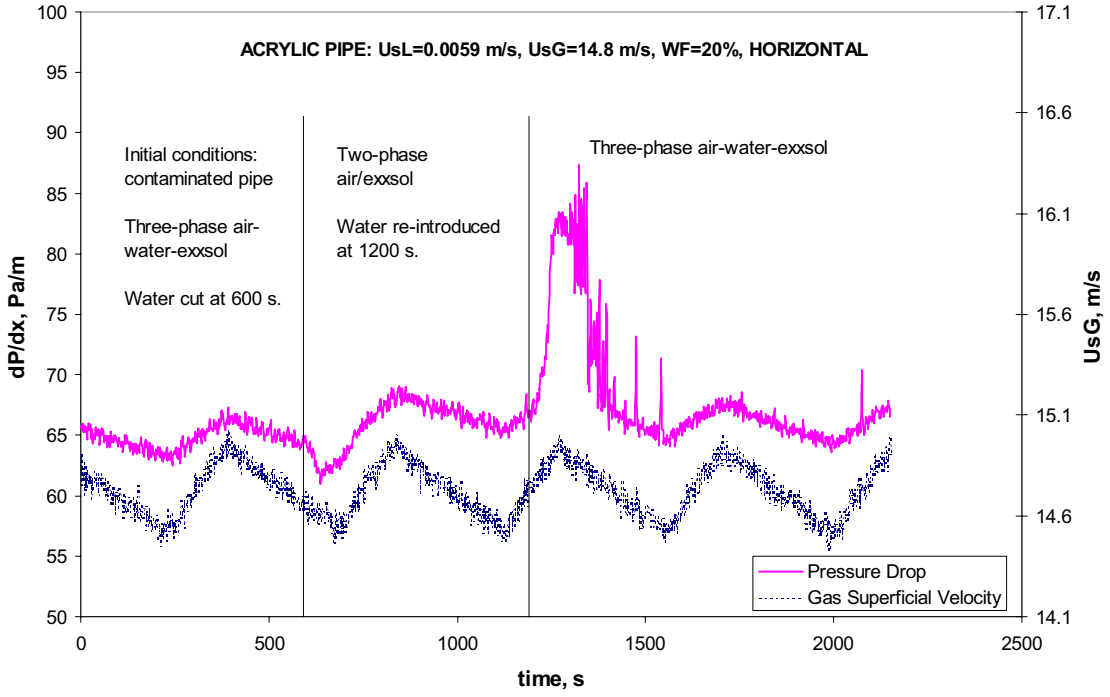

Figure 7–20: Transient experiment in the acrylic 60 mm test section for a contaminated (unpigged) pipe wall. Initial conditions are for liquid superficial velocity = 0.0059 m/s, superficial gas velocity = 14.8 m/s, water fraction = 20%. The flow regime in the liquid phase is separated oil-water stratified flow. After 600 seconds, the water supply is shut down. The pressure drop first decreases as water is washed away but then slightly increases despite the lower liquid loading. After 1200 seconds, the water phase is re-introduced giving a pressure drop peak as water is first dispersed in oil. After about 200 seconds, water starts to re-wet the pipe surface and the pressure drop falls back to its initial value

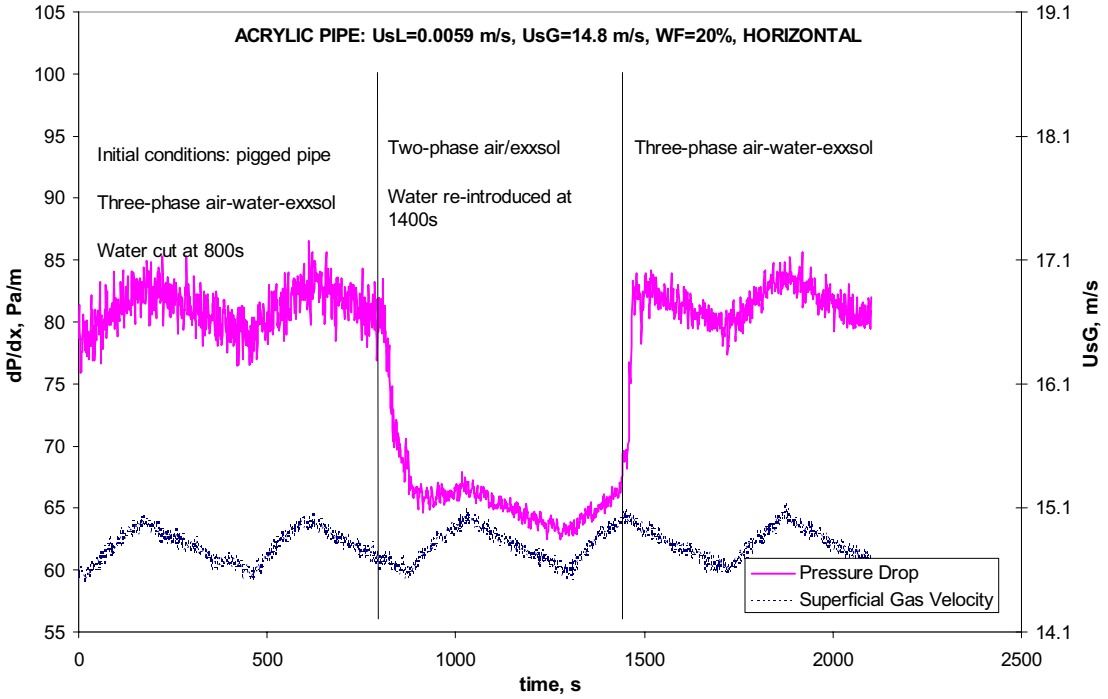

Figure 7–21: Transient experiment in the acrylic 60 mm test section for a clean (pigged) pipe wall. Initial conditions are for liquid superficial velocity = 0.0059 m/s, superficial gas velocity = 14.8 m/s and water fraction = 20%. The flow regime in the liquid phase is dispersed water in oil. After 800 seconds, the water supply is shut down. The pressure drop decreases strongly to that of two-phase air-oil at superficial liquid velocity 0.0047 m/s. After 1400 seconds, the water phase is re-introduced. Pressure drop increases to its initial value. The value of the pressure drop is equal to that of the peak of pressure drop in the case of the contaminated pipe

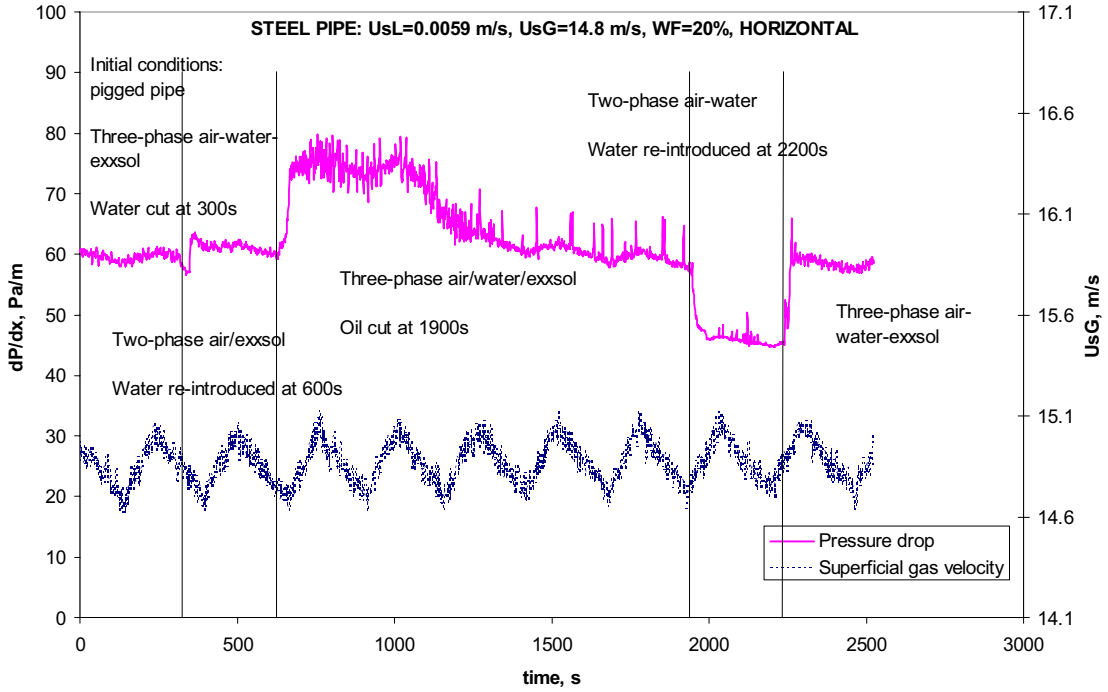

Figure 7–22: Transient experiment in the steel 60 mm test section for a clean (pigged) pipe wall. Initial conditions are for liquid superficial velocity = 0.0059 m/s, superficial gas velocity = 14.8 m/s and water fraction = 20%. The flow regime in the liquid phase is separated oil-water stratified flow. After 300 seconds, the water supply is shut down. The pressure drop first decreases as water is washed away but then slightly increases despite the lower liquid loading. After 600 seconds, the water phase is re-introduced giving a pressure drop peak as water is first dispersed in oil. After about 500 seconds water starts to re-wet the pipe surface and the pressure drop falls gradually back to its initial value. No such peak in pressure drop is observed if now oil is shut down and then re-introduced

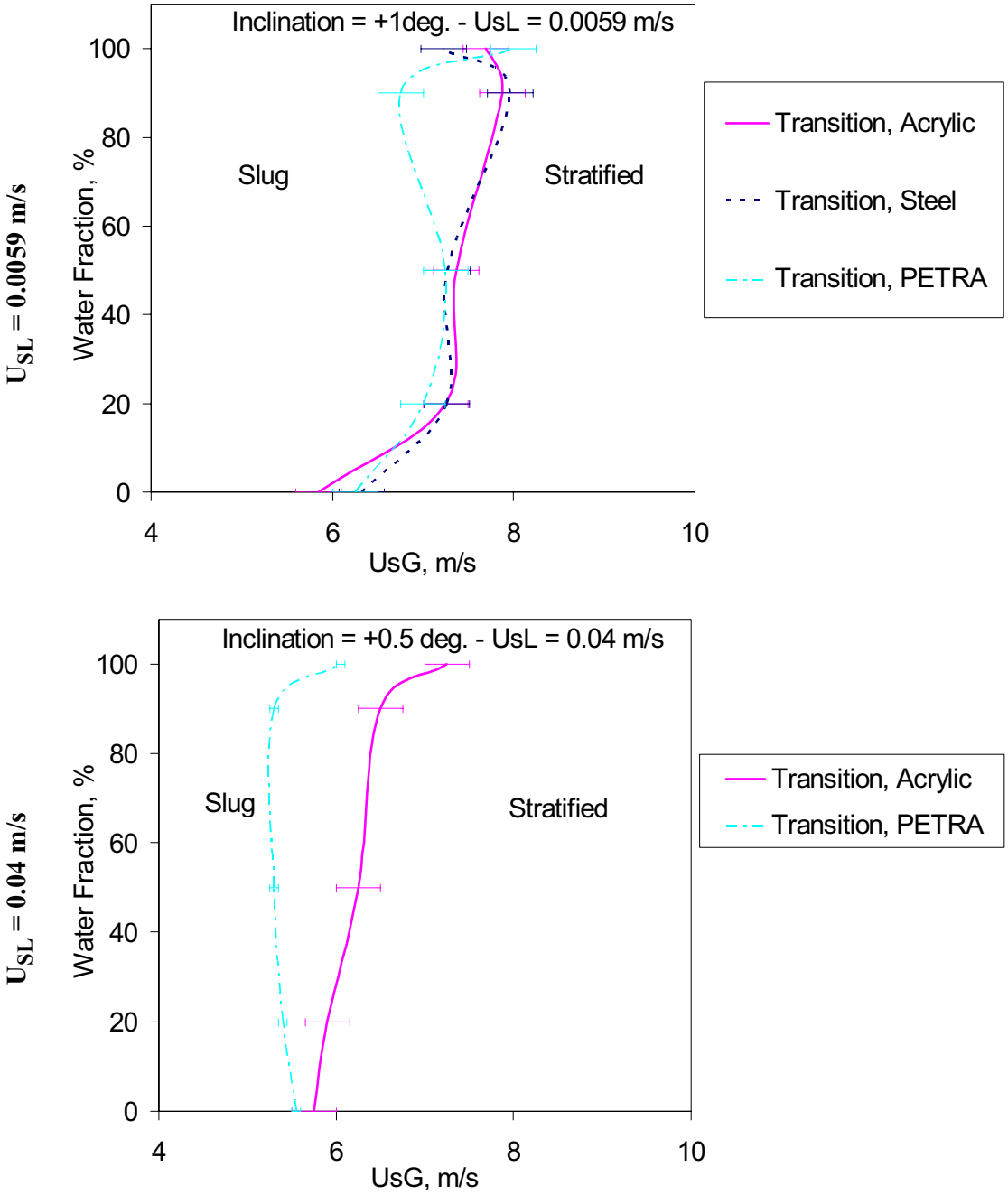

Figure 7–23: Stratified/slug transition compared to PETRA predictions. The error bars indicate the accuracy of the transition line location. Top: superficial liquid velocity = 0.0059 m/s, inclination = +1deg; Bottom: superficial liquid velocity = 0.04 m/s, inclination = +0.5 deg.

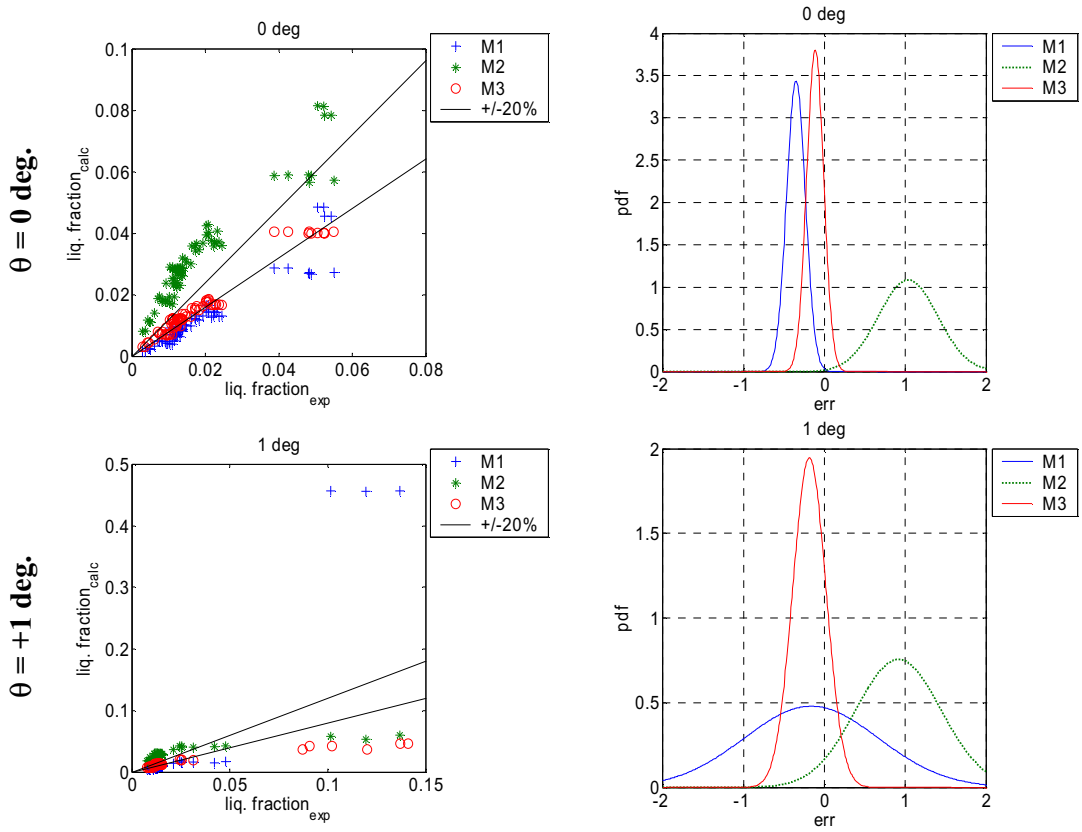

Figure 7–24: Three-phase total holdup measurements at low liquid loading: point-by-point and pdf error comparison with models; Top: horizontal data; Bottom: +1deg.

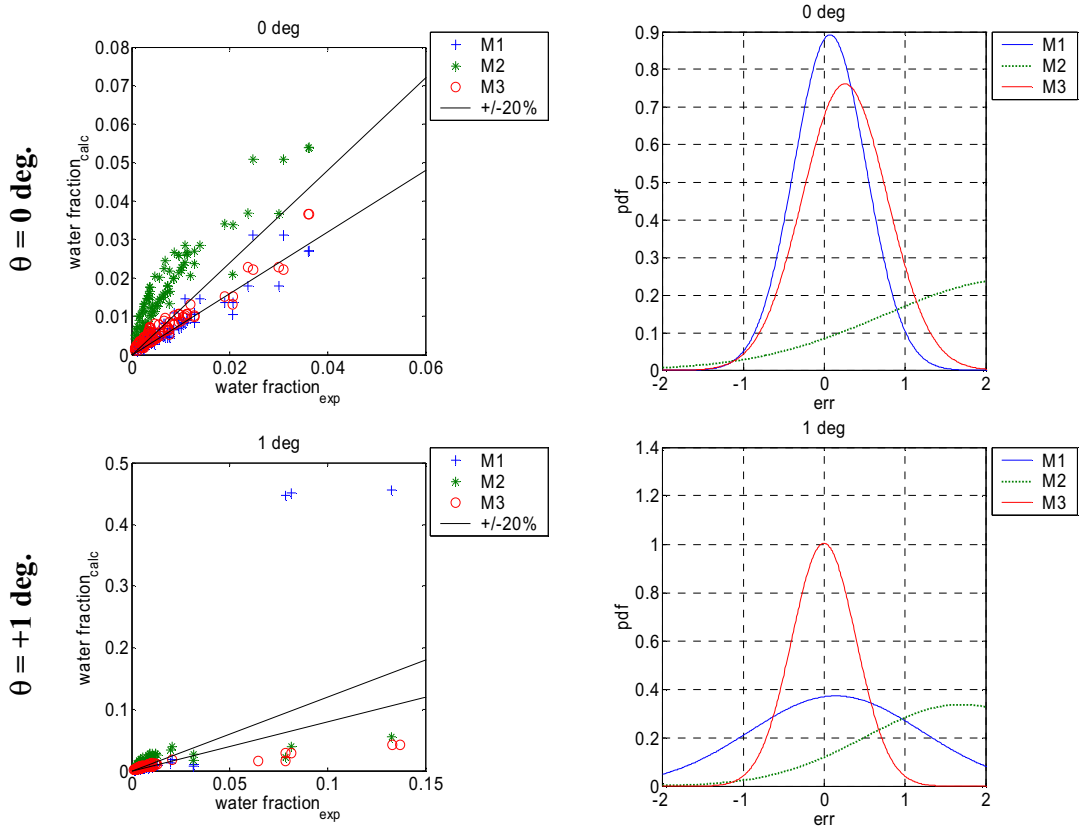

Figure 7–25: Three-phase water holdup measurements at low liquid loading: point-by-point and pdf error comparison with models; Top: horizontal data; Bottom: +1deg.

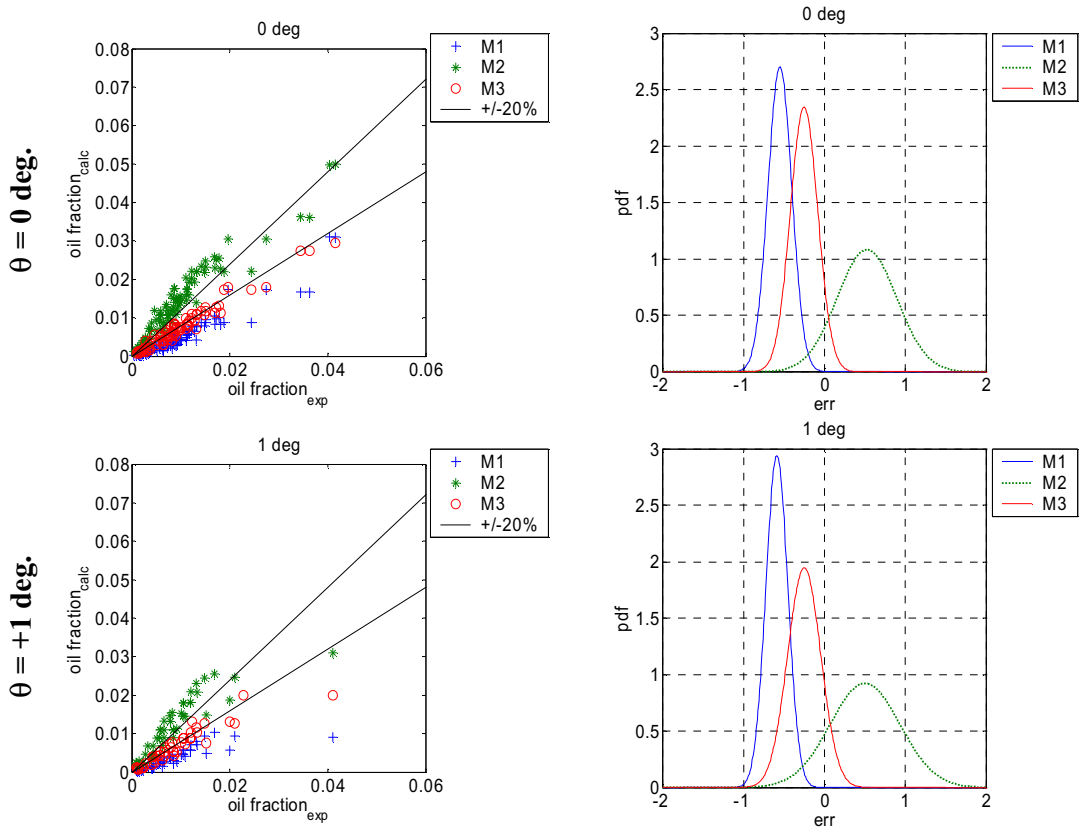

Figure 7–26: Three-phase oil holdup measurements at low liquid loading: point-by-point and pdf error comparison with models; Top: horizontal data; Bottom: +1 deg.

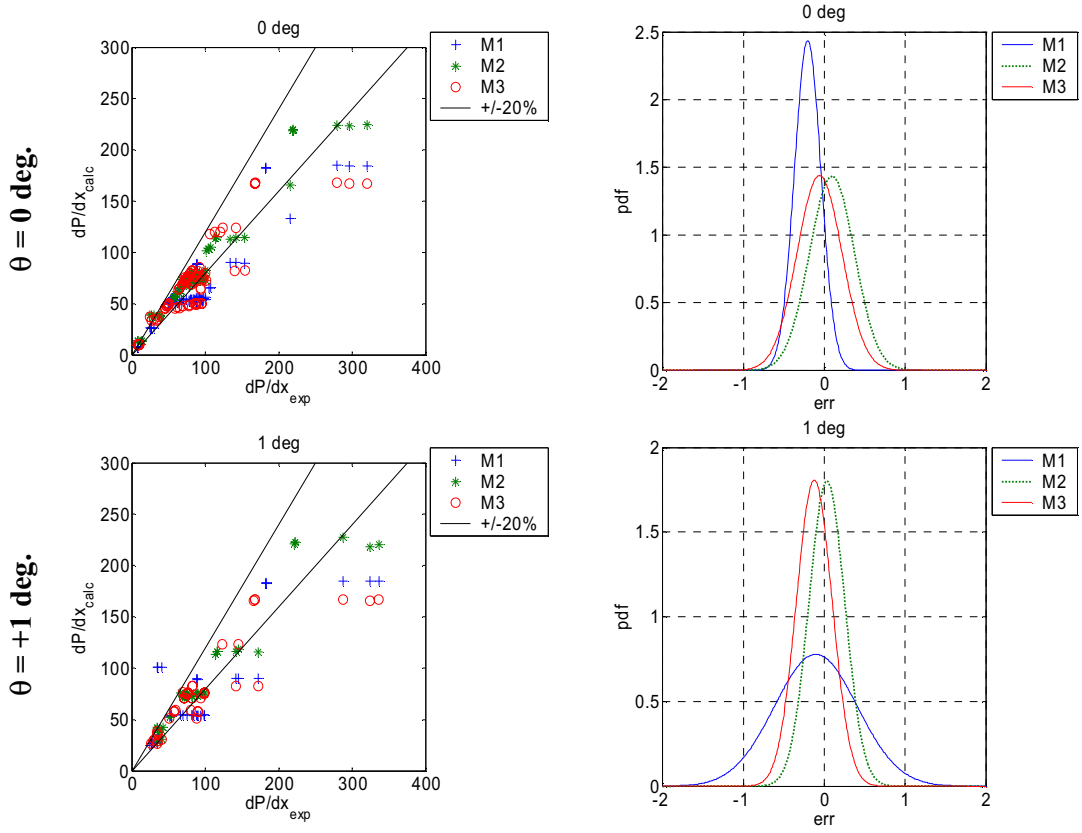

Figure 7–27: Three-phase pressure drop measurements at low liquid loading: point-by-point and pdf error comparison with models; Top: horizontal data; Bottom: +1 deg.

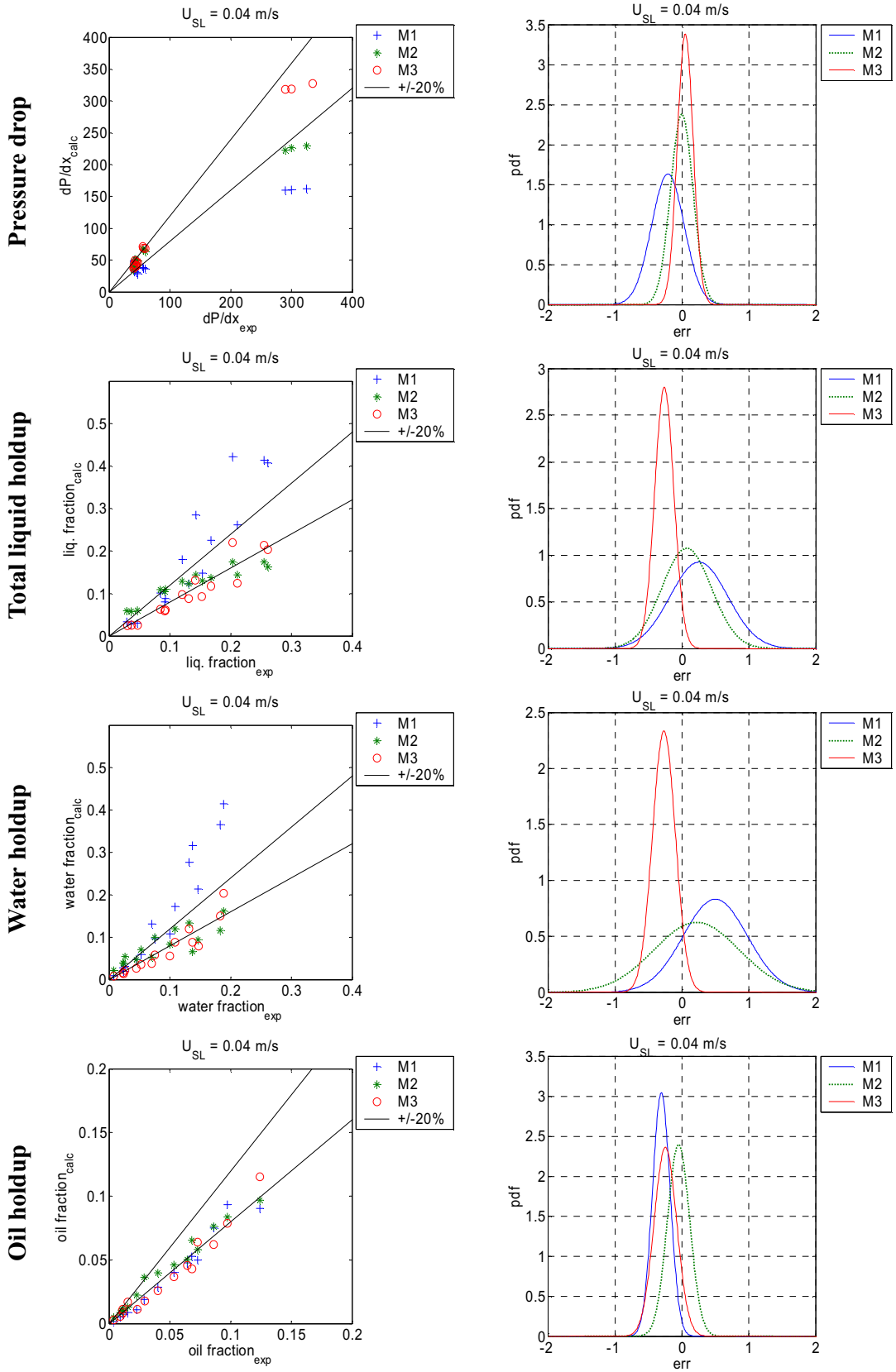

Figure 7–28: Measurements at moderate liquid loading (superficial liquid velocity = 0.04 m/s). Point by point and pdf error comparison with models

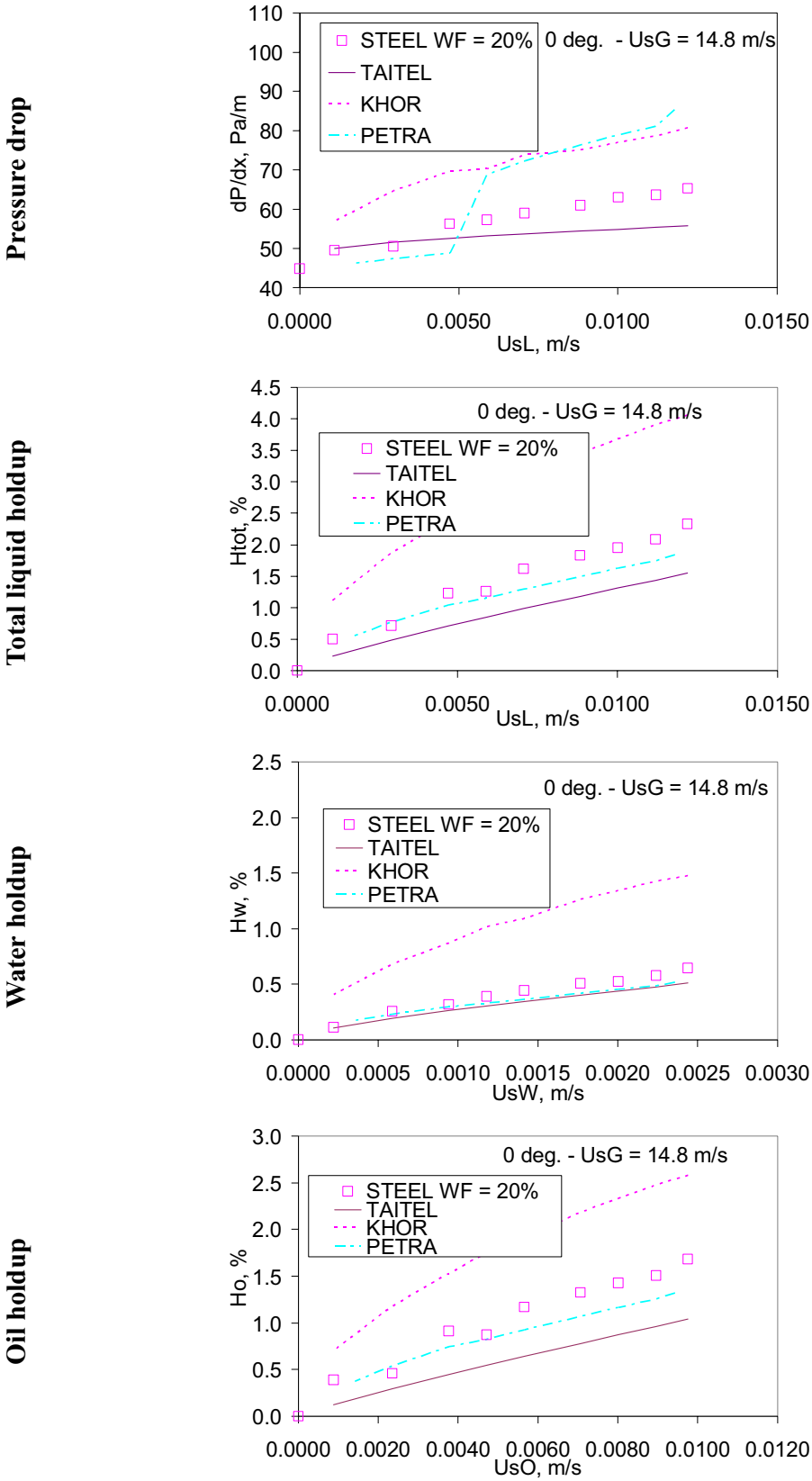

Figure 7–29: Serie #1, sensitivity with liquid superficial velocity at fixed gas superficial velocity. Comparison of measurements with model predictions

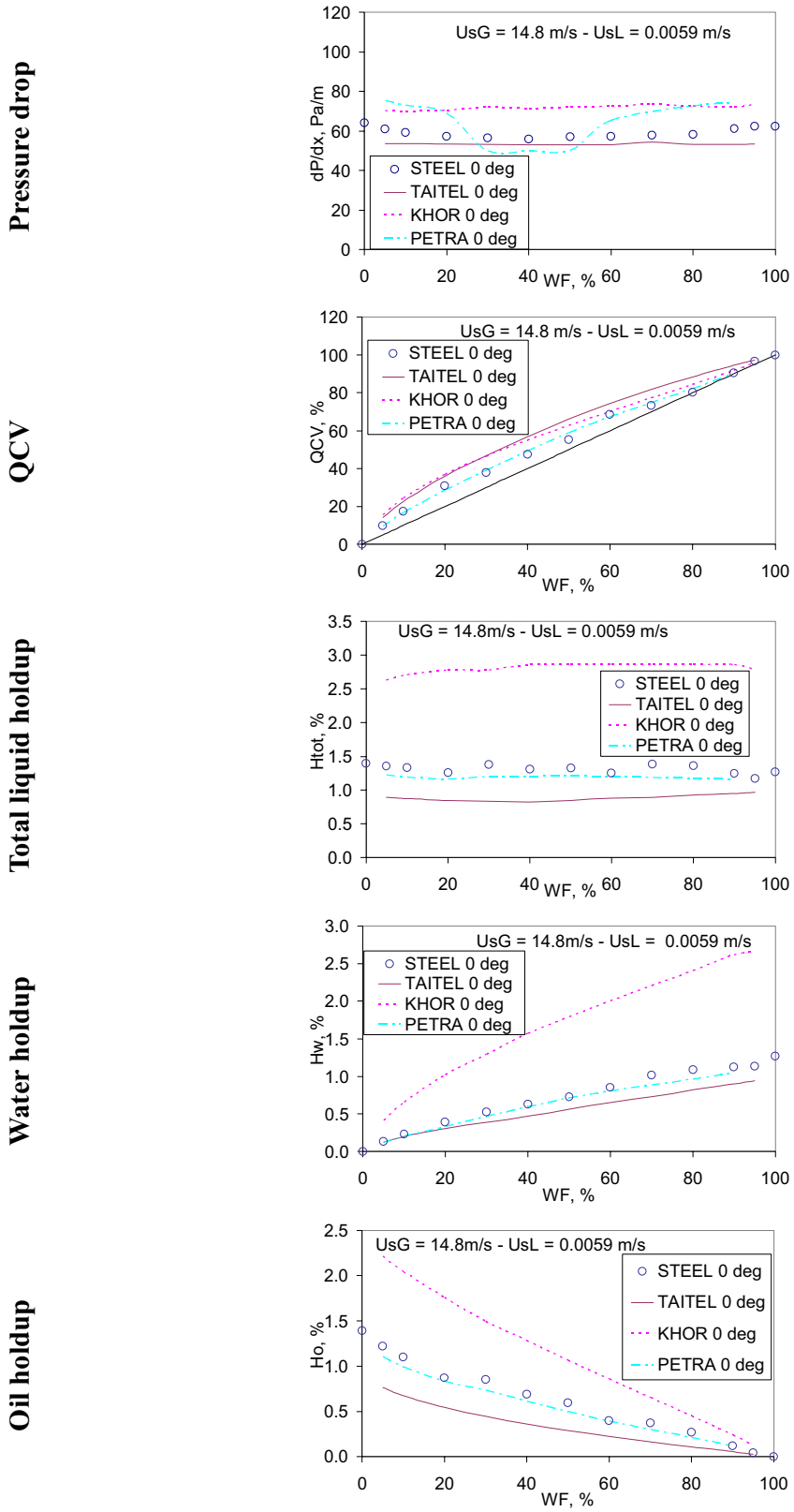

Figure 7–30: Serie #2.1, sensitivity with input water fraction at fixed liquid superficial velocity = 0.0059 m/s and gas superficial velocity = 14.8 m/s in horizontal pipes. Comparison of measurements with model predictions

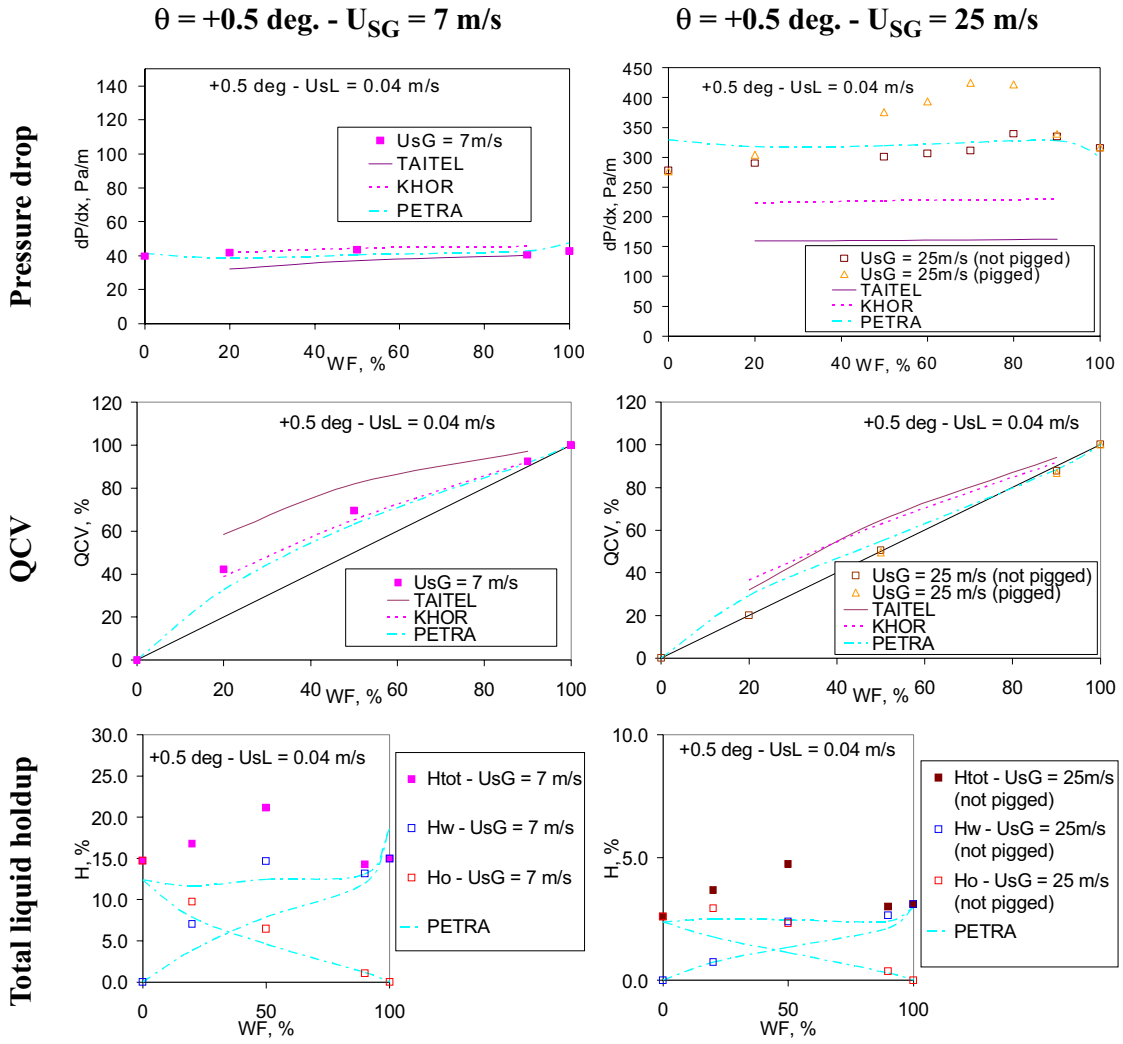

Figure 7–31: Serie #2.2, sensitivity with input water fraction at fixed liquid superficial velocity = 0.04 m/s. Comparison of measurements with model predictions

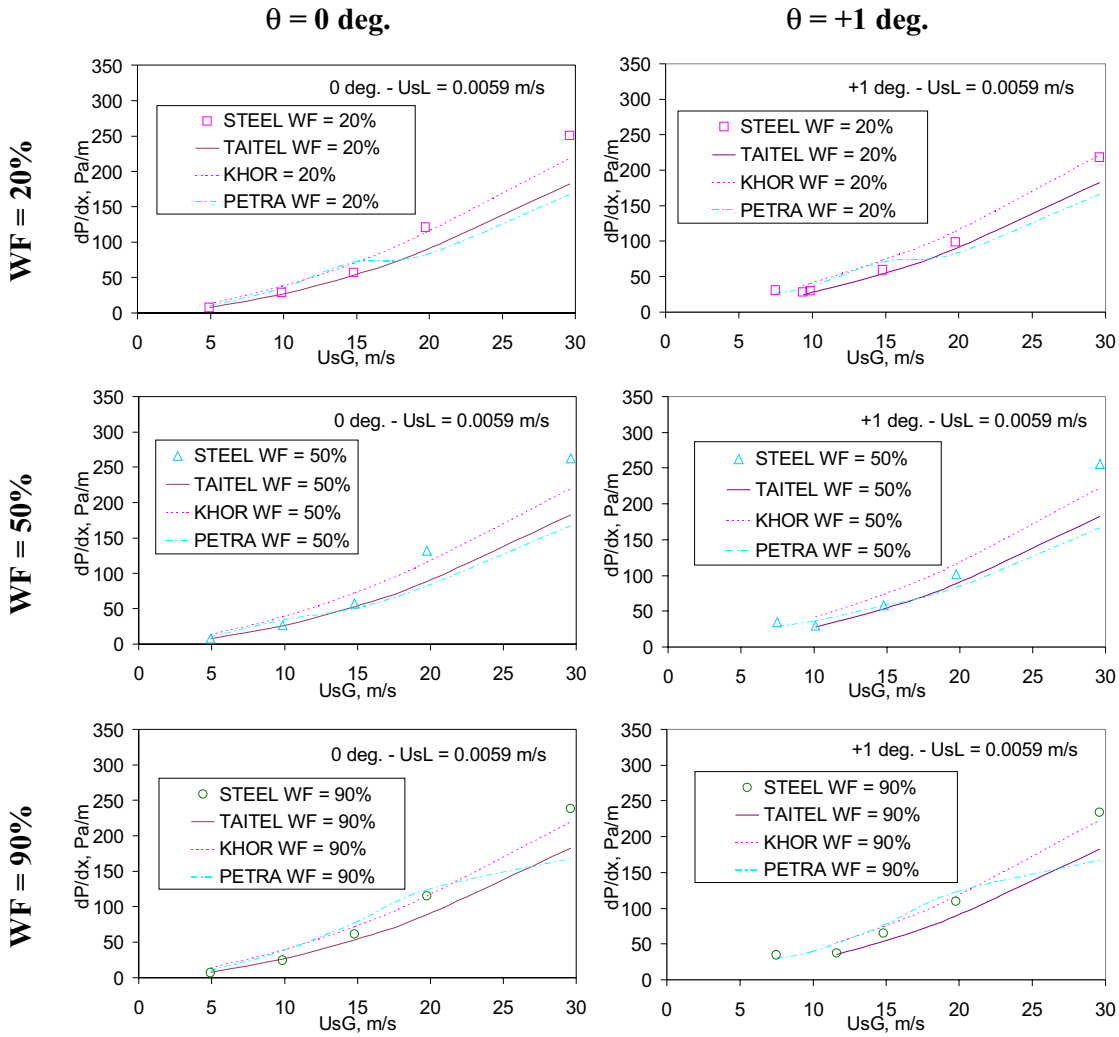

Figure 7–32: Serie #3.1, pressure drop sensitivity with superficial gas velocity at fixed liquid superficial velocity = 0.0059 m/s. Comparison of measurements with model predictions

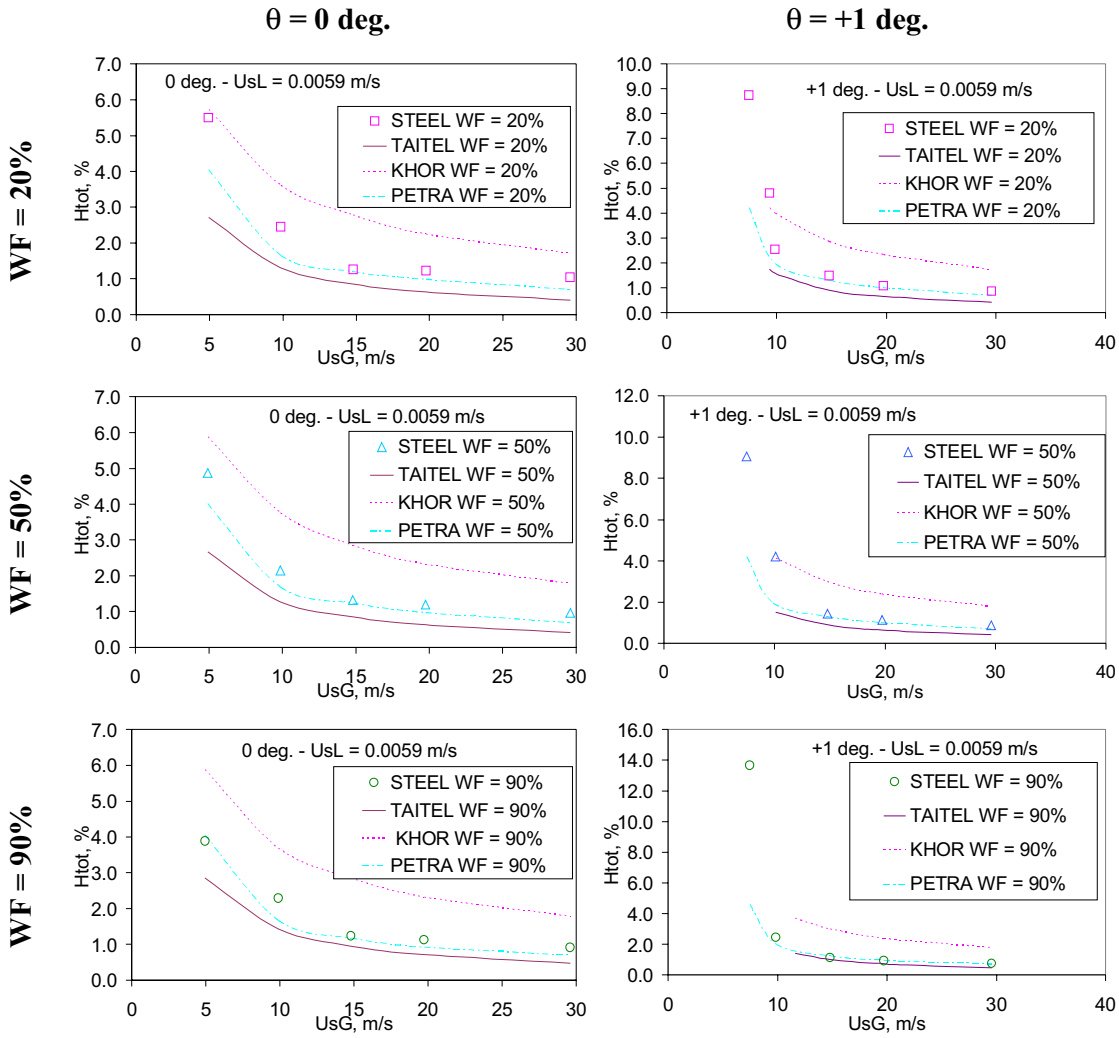

Figure 7–33: Serie #3.1, total liquid holdup sensitivity with superficial gas velocity at fixed liquid superficial velocity = 0.0059 m/s. Comparison of measurements with model predictions

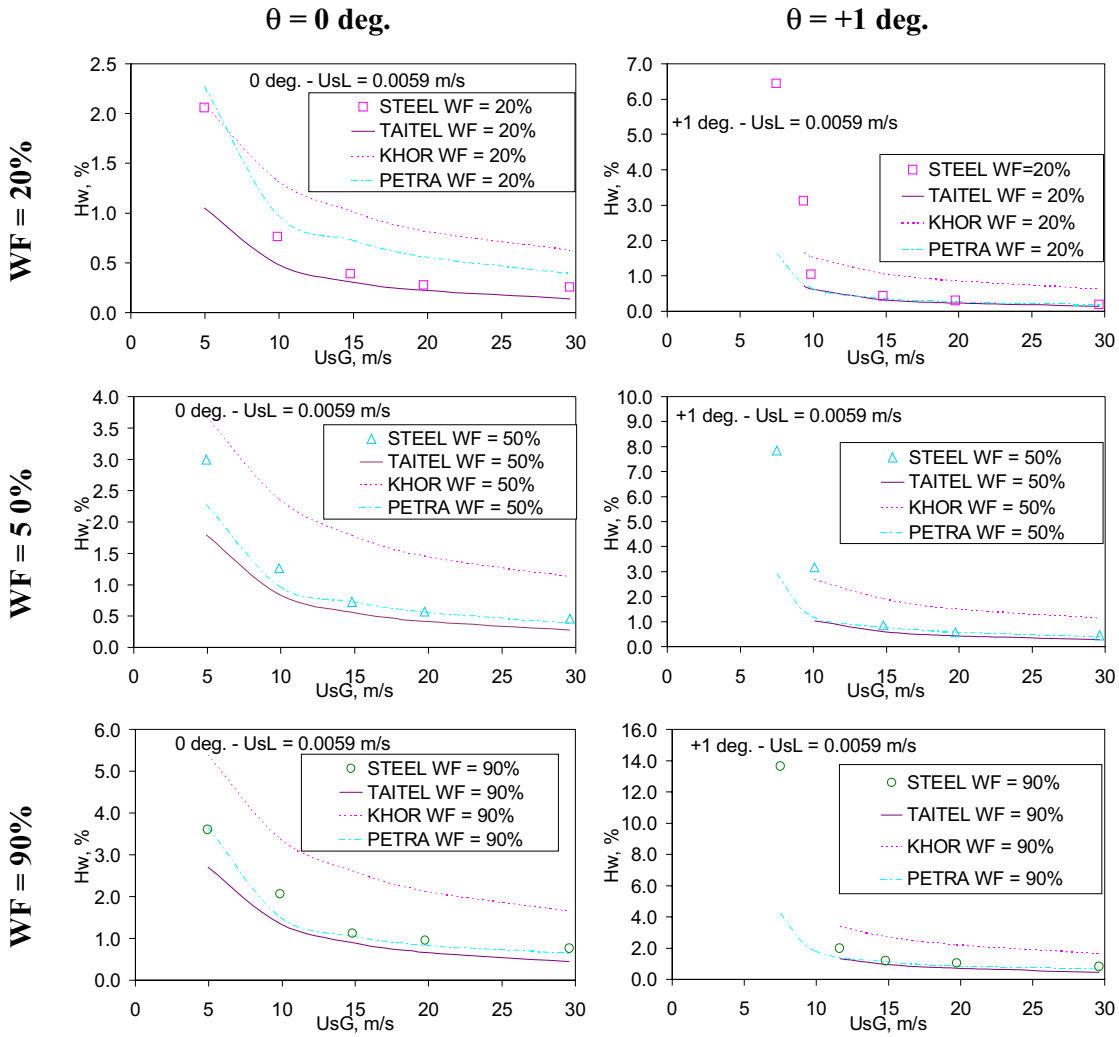

Figure 7–34: Serie #3.1, water holdup sensitivity with superficial gas velocity at fixed liquid superficial velocity = 0.0059 m/s. Comparison of measurements with model predictions

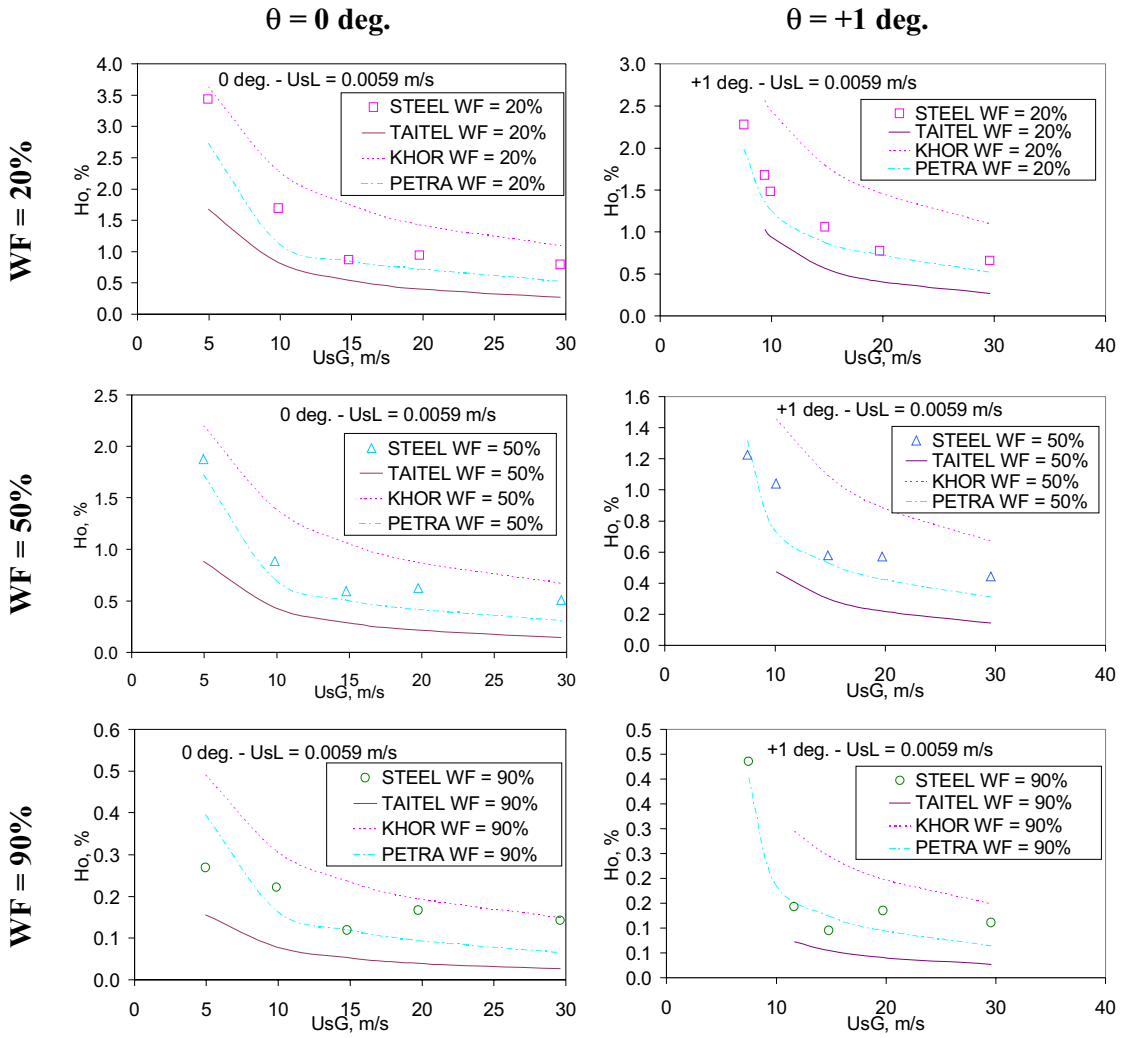

Figure 7–35: Serie #3.1, oil holdup sensitivity with superficial gas velocity at fixed liquid superficial velocity = 0.0059 m/s. Comparison of measurements with model predictions

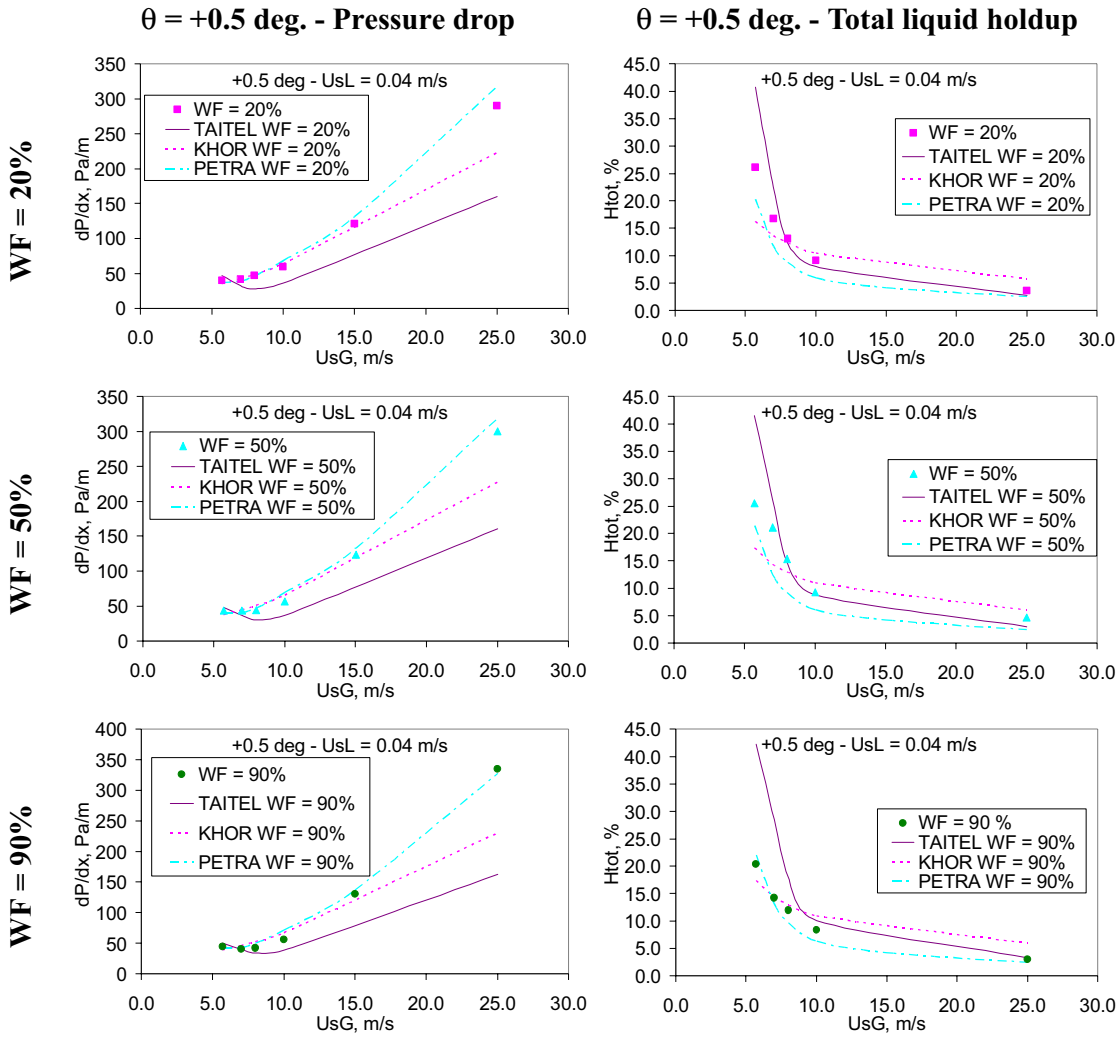

Figure 7–36: Serie #3.2, pressure drop and total liquid holdup sensitivity with superficial gas velocity at fixed liquid superficial velocity = 0.04 m/s. Comparison of measurements with model predictions

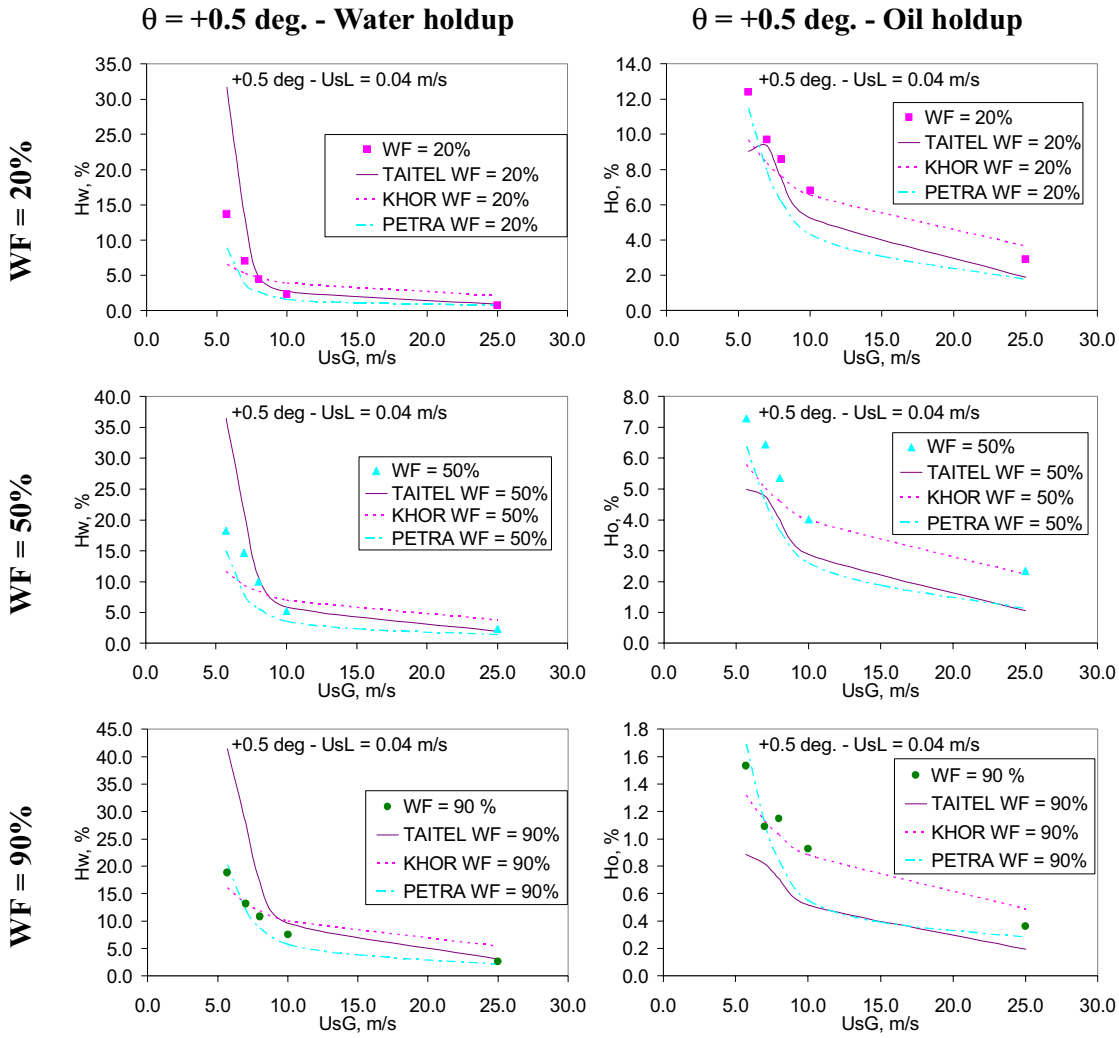

Figure 7–37: Serie #3.2, water and oil holdup sensitivity with superficial gas velocity at fixed liquid superficial velocity = 0.04 m/s. Comparison of measurements with model predictions

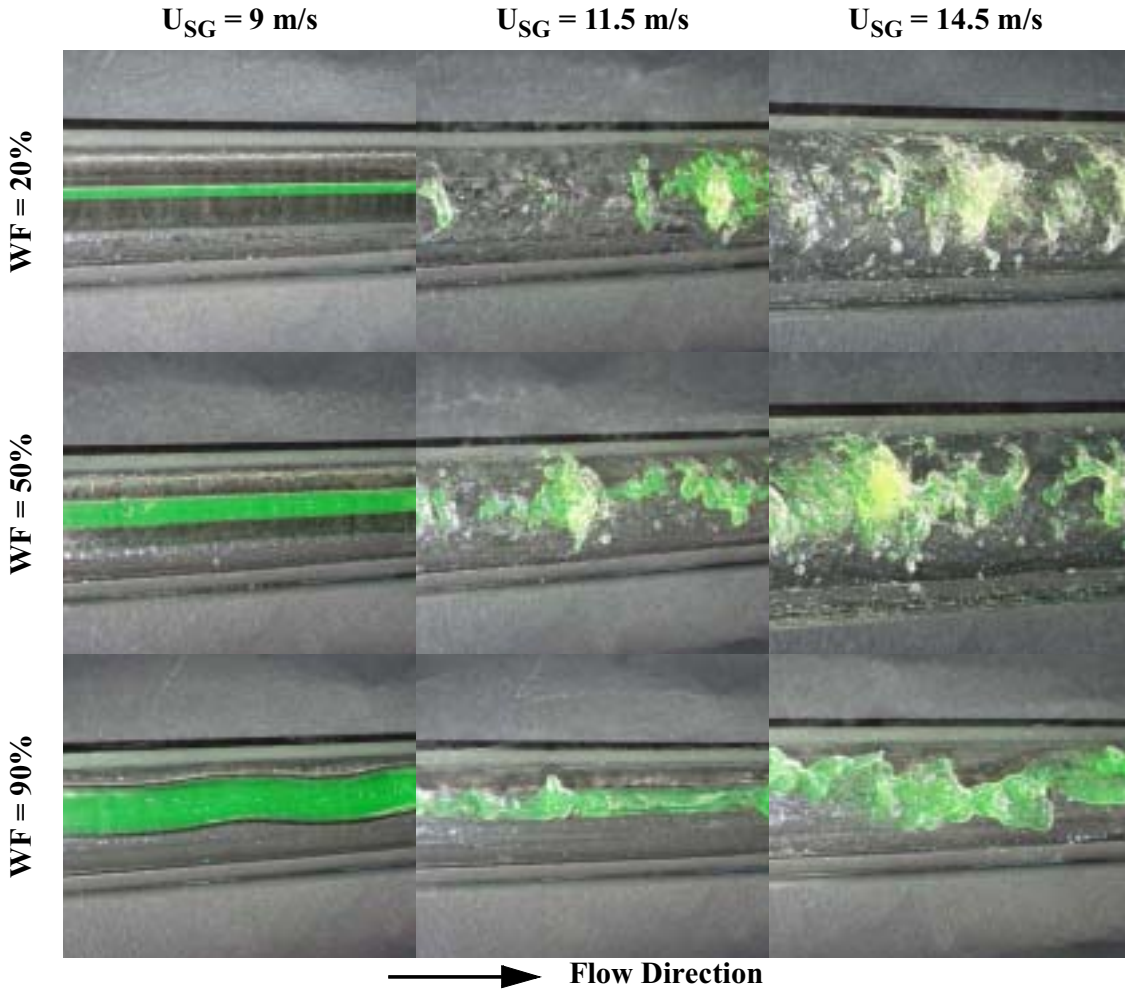

Figure 7–38: Flow regimes in the horizontal acrylic pipe at superficial liquid velocity = 0.0059 m/s: longitudinal views, viewpoint from under the pipe

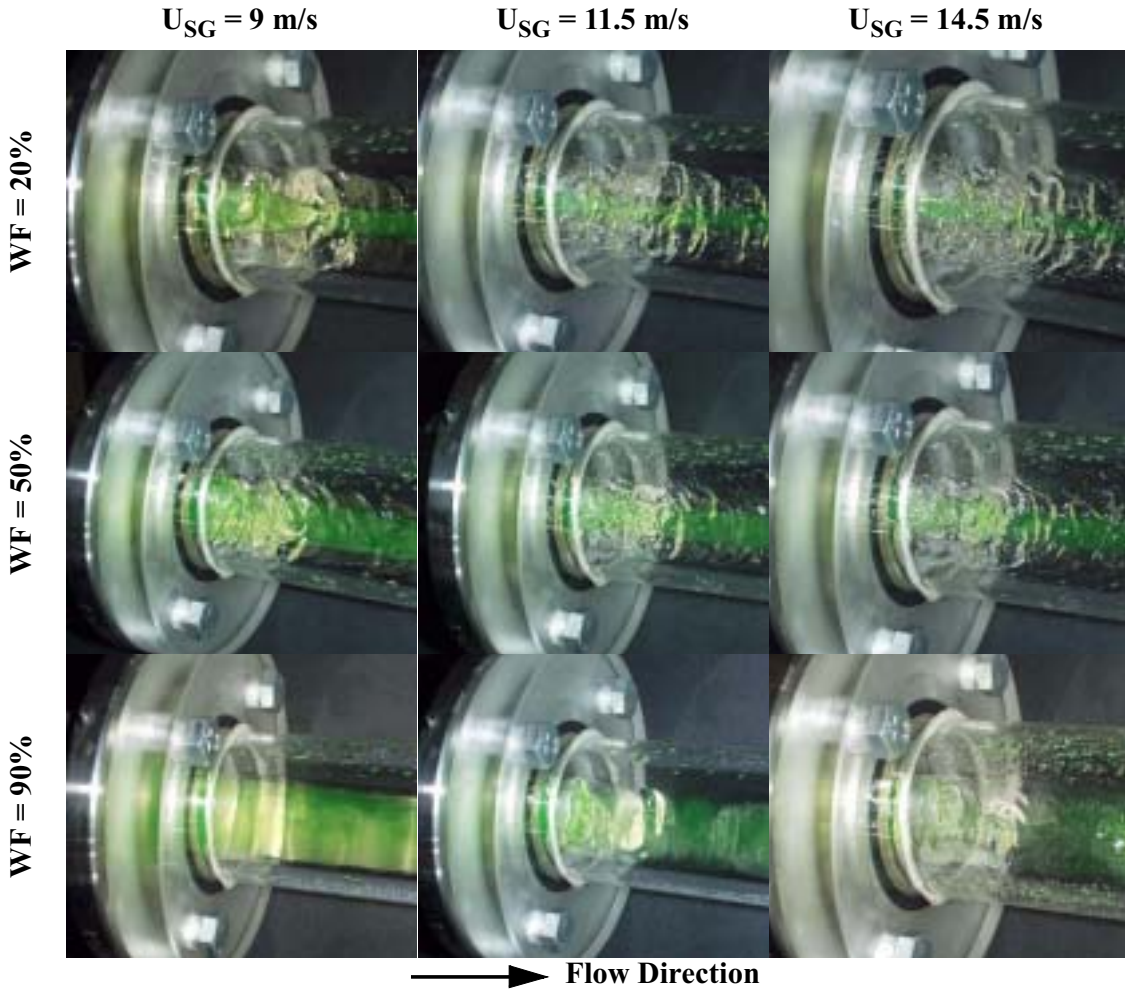

Figure 7–39: Flow regimes in the horizontal steel pipe at superficial liquid velocity = 0.0059 m/s: longitudinal views, viewpoint from under the pipe

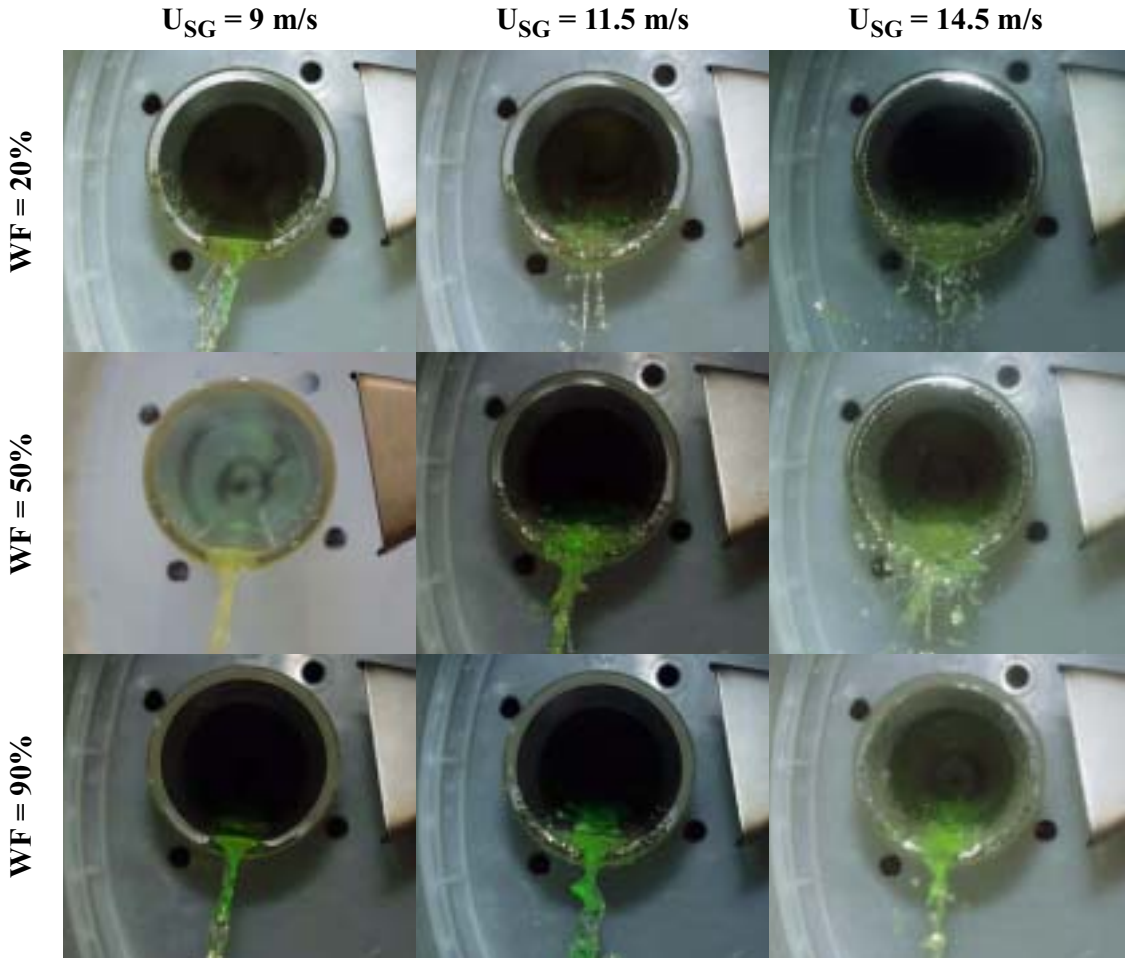

Figure 7–40: Flow regimes in the horizontal acrylic pipe at superficial liquid velocity = 0.0059 m/s: cross sectional views

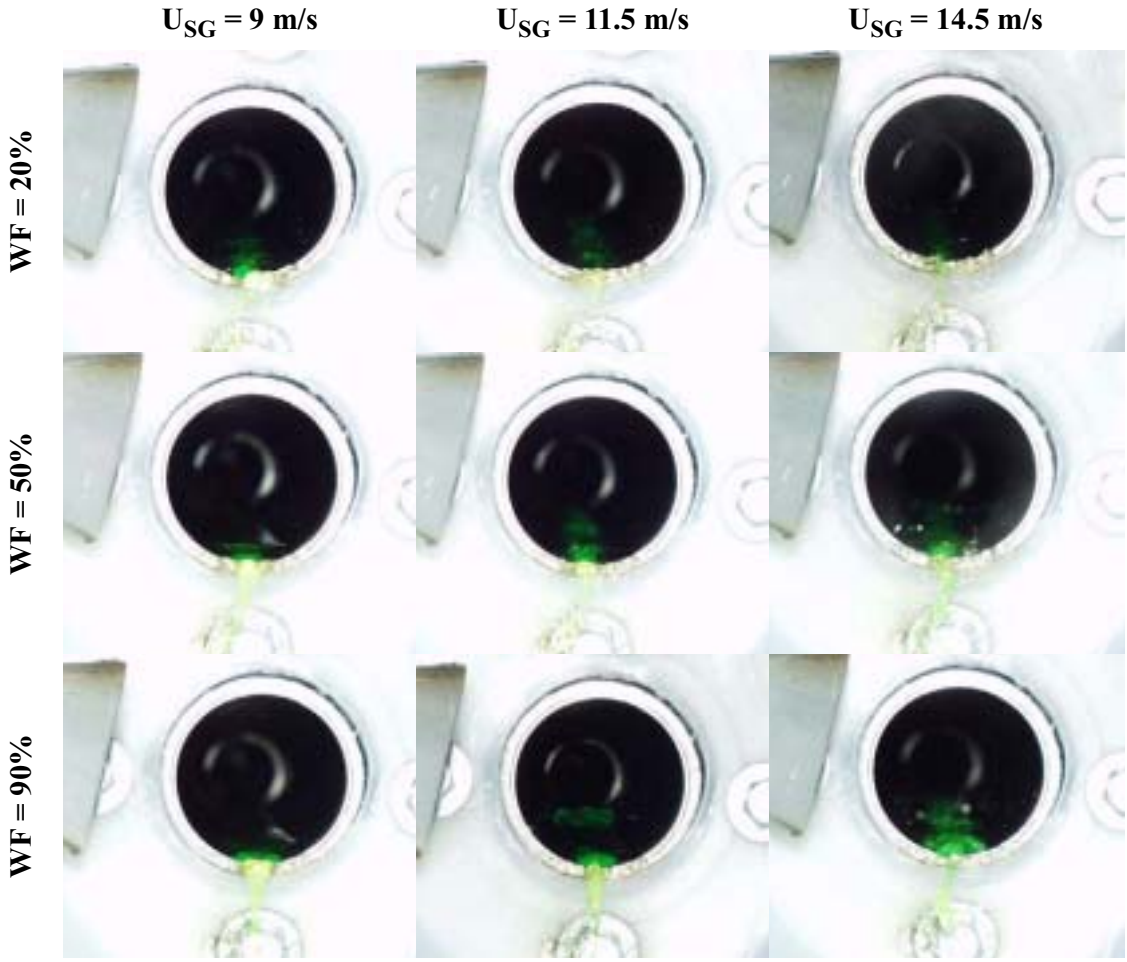

Figure 7–41: Flow regimes in the horizontal steel pipe at superficial liquid velocity = 0.0059 m/s: cross sectional views

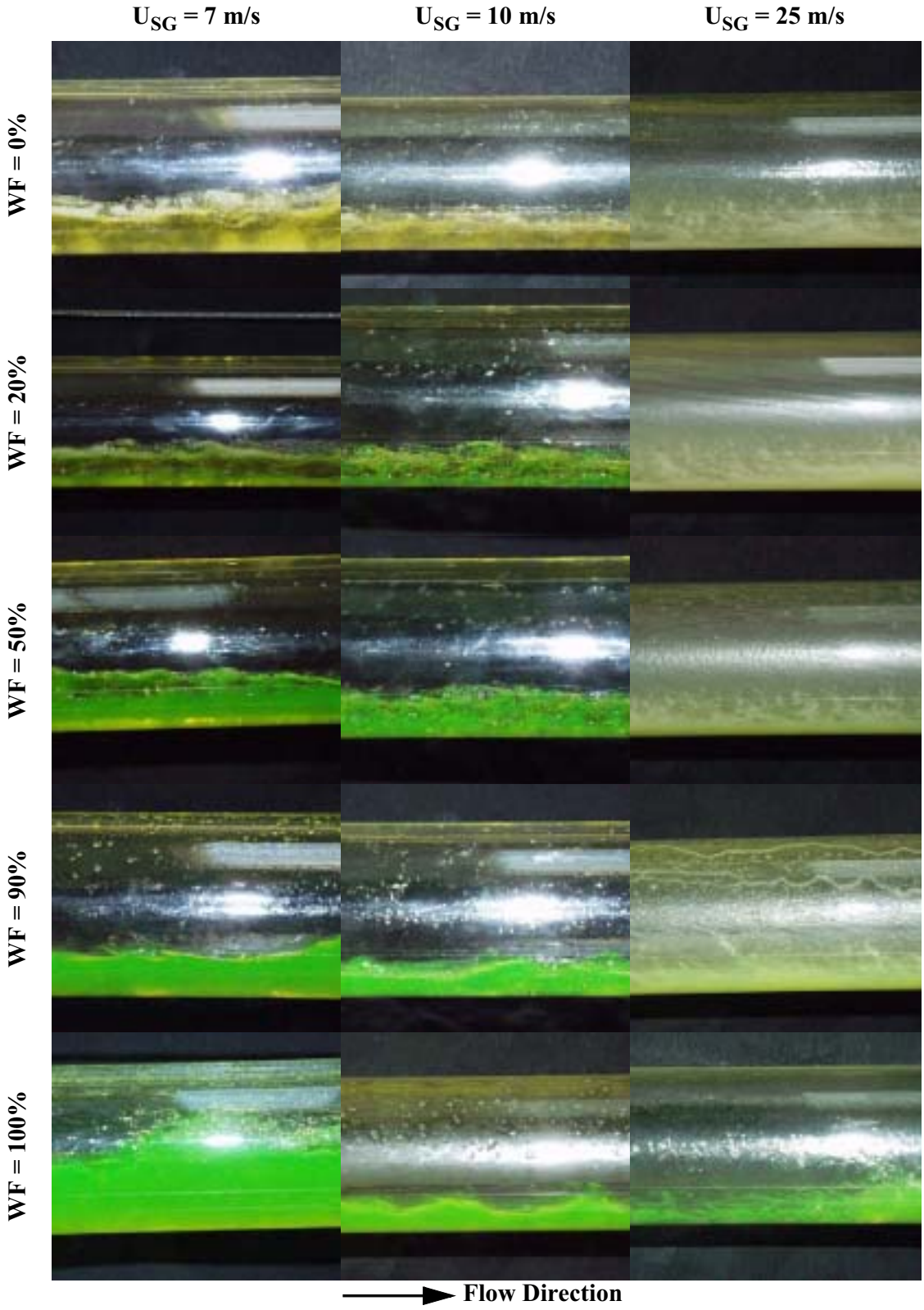

Figure 7–42: Flow regimes in the acrylic pipe at superficial liquid velocity = 0.04 m/s and inclination = +0.5 deg. with the horizontal: longitudinal views

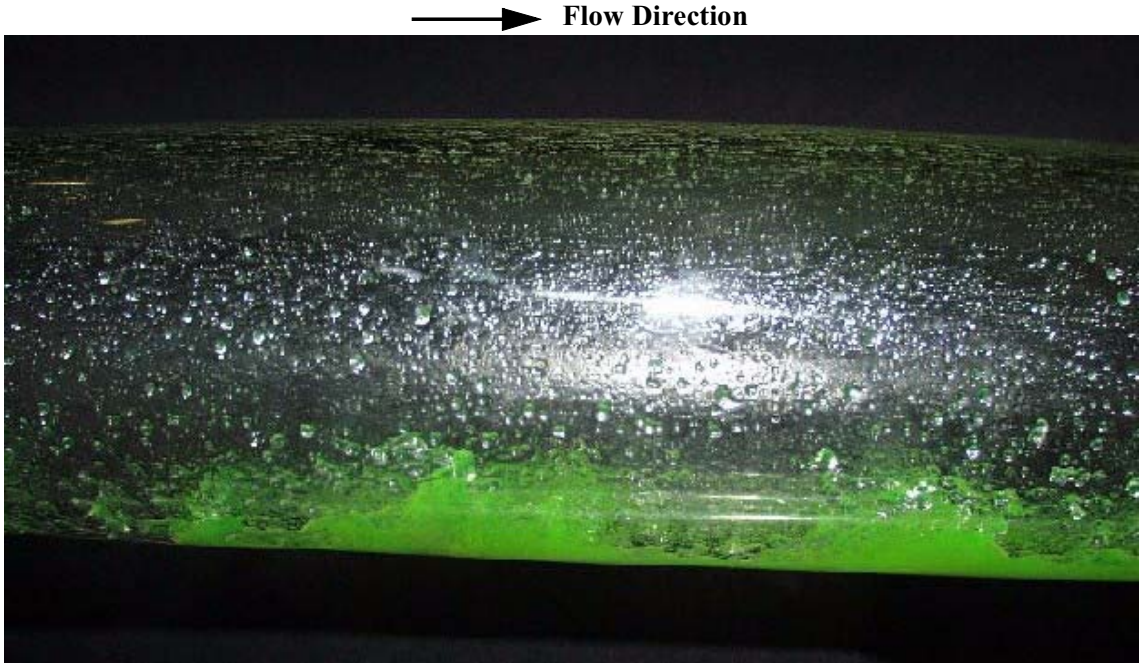

Figure 7–43: Picture of irregular large amplitude waves developing in the acrylic pipe in three-phase air-Exxsol D80-water flow. The water is dyed in green. This particular case is at water fraction = 20%, superficial liquid velocity = 0.0059 m/s and superficial gas velocity = 14.8 m/s. Note the droplets (water) depositing on the pipe wall

Figure 7–44: Picture taken from under the pipe of the water film contracting at the passage between a contaminated pipe wall (at the left) to a clean (pigged) pipe wall (at the right). This case is for input water fraction = 50%, superficial gas velocity = 10.5 m/s and superficial liquid velocity = 0.0059 m/s in the acrylic pipe

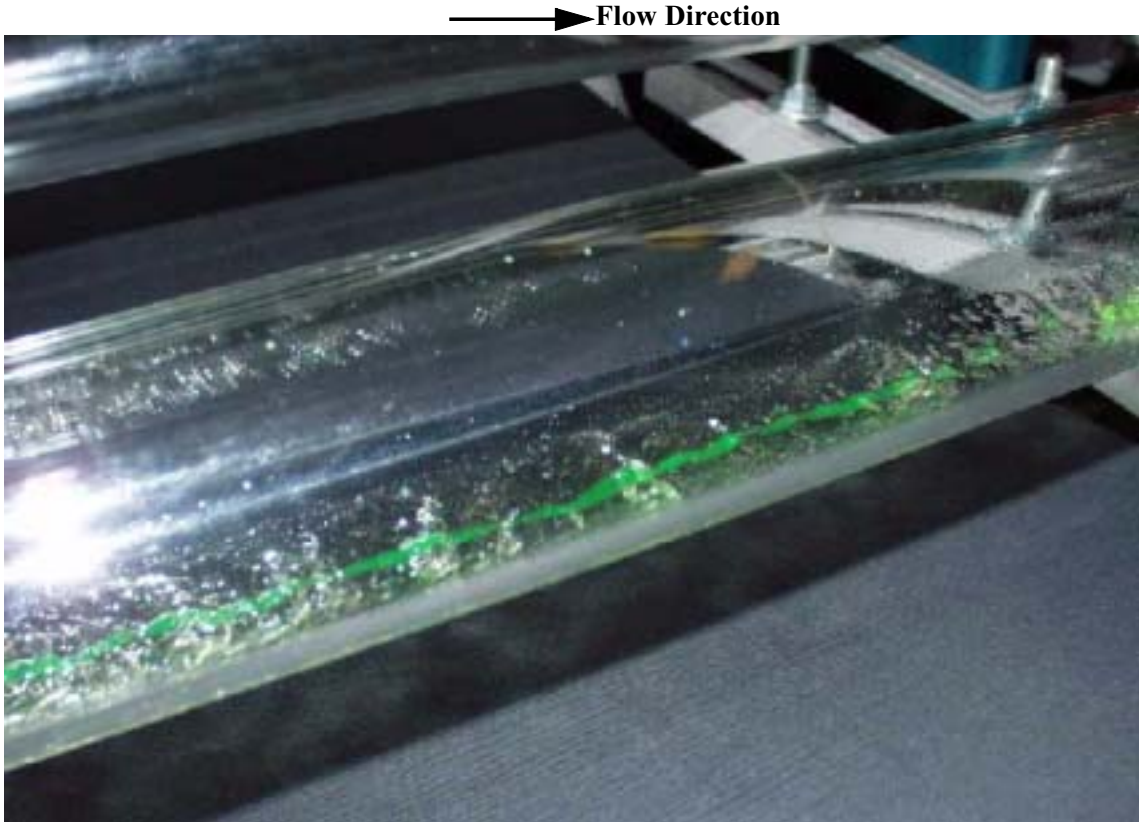

Figure 7–45: Picture of the water rivulet instability in three-phase flow in the acrylic pipe. The rivulet (in green) starts to meander and eventually breaks down into water droplets dispersed in oil. The case is for water fraction = 20%, air superficial velocity = 14.8 m/s and superficial liquid velocity = 0.0059 m/s in the acrylic pipe

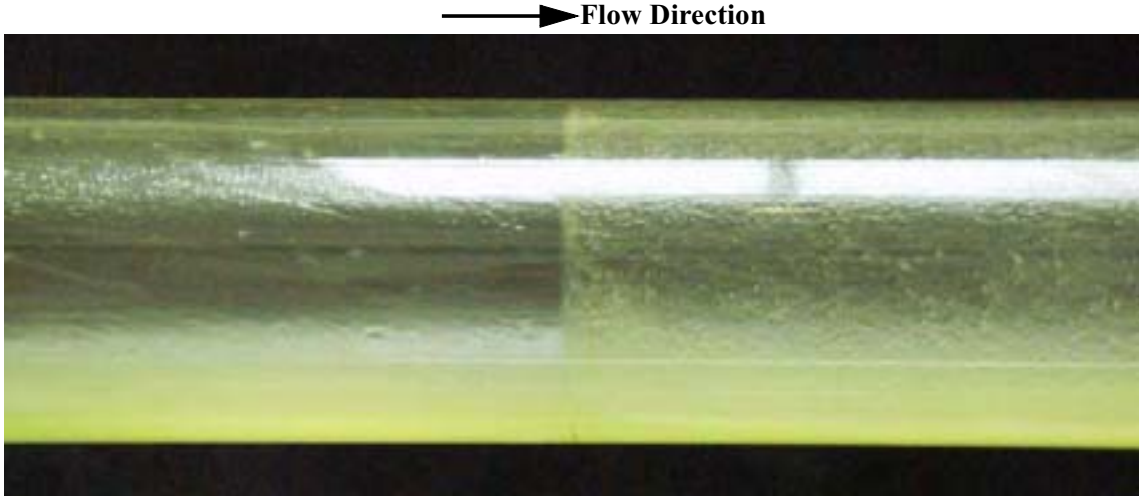

Figure 7–46: Picture of the upper pipe wall at the transition between a contaminated wall (left) and a clean wall (right). the picture is taken in the stratified/atomization flow regime with 60% water fraction, superficial gas velocity = 25 m/s and superficial liquid velocity = 0.04 m/s

Chapter 8 A three-layer model with curved interfaces

8.1 Introduction

In Chapter 6, it has been shown that two-fluid one-dimensional models that consider a concave gas-liquid interface are slightly more accurate in predicting pressure drop and holdup at low liquid loading than standard models assuming flat interfaces. In Chapter 7, it has been observed experimentally that the oil-water interface was convex under conditions of stratified separated three-phase flow at low liquid loading. In addition, three-layer models assuming flat interfaces proved inaccurate in their predictions of phase fractions at conditions of low liquid loading.

To investigate whether, at low liquid loading, the consideration that the fluid-fluid interfaces are not flat but curved could influence one-dimensional model predictions, a stratified gas-oil-water steady-state flow model has been derived that incorporates interfacial curvature in the calculation of integral flow properties.

This chapter is divided into three sub-sections. In Section 8.2, methods are reviewed for predicting the interfacial shape for a two-fluid system in a circular duct. Section 8.3 is devoted to the model derivation: the hydraulic model, the interfacial shape predictions and the method of solution. Finally in Section 8.4, the model is tested against experimental three-phase flow data acquired in the steel pipe (Chapter 7).

8.2 Interfacial shape prediction in two-phase flow

In stratified two-fluid computations in circular conduits, it is usually assumed that the fluid-fluid interface is flat. This is generally a good approximation when the density difference between the two fluids is large and surface forces are small compared to bulk gravitational forces.

In Chapter 6, it has been shown that at low liquid loading, or more generally, in the case of a small phase fraction of the lower phase, better agreement with experiments is achieved by considering interfacial curvature. In the case of gas-liquid systems, Hart et al. (1989), Grolman et al. (1994), Chen et al. (1997) and Meng (1999) consider a concave gas-liquid interface and propose ways of predicting the interfacial shape. However, these are often based on mechanistic semi-empiricial considerations and make no mention of surface forces.

Brauner et al. (1998) have published a general two-fluid model assimilating the fluid-fluid interface to a circular arc. The interfacial curvature is solved by taking surface forces into consideration. It is recognized that, at low (and high) phase fractions of the lower phase, the interface generally deviates from the flat configuration. The magnitude of this deviation is shown by Brauner et al. to be a function of contact angle, phase fraction and a dimension less parameter, the Eötvös number, defined as:

$$\varepsilon_v = \frac{2\sigma_{12}}{(\rho_2 - \rho_1) g \cos\theta R^2} \qquad [8.1]$$

where 2 indexes the denser (lower) fluid, 1 indexes the lighter (upper) fluid and σ_{12} is the interfacial tension between fluid 1 and 2. Alternatively, the Bond number can be used defined as:

$$B_o = \frac{2}{\varepsilon_v} \qquad [8.2]$$

The Eötvös number is a measure of the ratio of surface forces to gravity forces. It tends to zero for low surface tension and high density difference between the two fluids as is the case for gas-liquid flow. However, for fluids of close densities such as oil and water, the Eötvös number can be large. Also, according to Figure 8–1, even at low Eötvös number, for partial wetting of the denser fluid (contact angles departing from zero), the interface is not flat at holdup approaching zero. This is in particular the case for gas-liquid pipe flow at low liquid loading.

In Brauner et al. (1996), the interfacial curvature is solved by minimizing the change of the system total energy (potential plus surface energy) associated with a change of the interfacial curvature. Quoting Brauner et al. (1996): "Taking the configuration of plane interface as a reference, the curving of the interface to either concave or convex shape is associated with an elevation of the system centre of gravity, thereby increasing the potential energy. It also results in a change of the phases contact area with the tube wall and the phases interfacial area, resulting in a change of the system surface energy". For a given holdup, contact angle and Eötvos number, the change in the total system energy associated with the process of curving the interface from the plane configuration is given by (Brauner et al. 1996):

$$\frac{\Delta E}{R^3 L(\rho_2 - \rho_1) g \cos\theta]} = \left[\frac{\sin^3\delta}{\sin^2\phi_j}(\cot\phi_j - \cot\delta)\left(\pi - \phi_j + \frac{1}{2}\sin(2\phi_j)\right) + \frac{2}{3}\sin^3\delta^P\right] + \varepsilon_v\left[\sin\delta\frac{(\pi - \phi_j)}{\sin\phi_j} - \sin\delta^P + \cos\xi(\delta^P - \delta)\right] \qquad [8.3]$$

where variables are defined in Figure 8–3. δ^P is the wetted angle in the case of a plane interface and ξ the contact angle at the contact line between fluid 1, fluid 2 and the wall

solid surface. Note that the interfacial curvature Φ_j, the view angle δ_j and the lower phase fraction H are related geometrically by the following relationships:

$$0 = H - \frac{1}{\pi}\delta - \frac{1}{2}\sin(2\delta) - \frac{\sin\delta}{\sin\phi_j}\left[\phi_j - \pi - \frac{1}{2}\sin(2\phi_j)\right] \qquad [8.4]$$

$$\delta_j = \phi_j - \pi \qquad [8.5]$$

Equation [8.4] is derived in Appendix C. In the case of a flat interface: $\phi_j = \pi$, $\delta = \delta^P$ and Equation [8.4] reduces to Equation [3.30].

By searching for the minimum of the total system energy change, one can determine the optimal interfacial curvature that the system, for a given holdup, would spontaneously adopt to minimize its total energy. Plots of the computed optimal interfacial curvature for a two-fluid system of given Eötvos number and contact angle are given in the form of an interface monogram. The monogram computed by Brauner et al. (1998) is reproduced in Figure 8–1.

Once the interfacial curvature Φ_j is known (or equivalently δ_j), the interfacial perimeter can be readily calculated as well as the gas and liquid wetted perimeters.

Ng et al. (1999, 2001) argue that the circular shape is only an approximation of the exact interfacial shape, which results in a loss of information. They also highlight a discrepancy between the physical contact angle (ξ) and the contact angle effectively obtained by solving the circular arc analysis (δ). At low holdup, the predicted contact angle is too small compared to the real (physical) contact angle when the latter is large (Ng et al. 1999).

Considering, as in Brauner et al. (1996), a static two-fluid system, Ng et al. (1999) compute the exact interfacial shape by solving numerically the Young-Laplace equation and imposing physical contact angles as boundary conditions at the triple line (wall-interface contact line). As in Brauner et al., shapes are a function of three parameters: the contact angle (ξ), the Bond number (or Eötvos number) and the lower phase fraction (H). Computed interfacial shapes are shown in Figure 8–2 for various combinations of those three parameters.

It can be seen from Figure 8–2 that, at low Bond number (high Eötvös number), the exact interfacial shape closely approaches the circular shape. However, at high Bond number, the interface adopts a more elliptical shape with a significant change of curvature from the centre of the interface to the wall, the interface being nearly flat at the centre but highly curved near the wall (meniscus). In this case, the circular arc models predict an almost flat interface and neglect the existence of a meniscus at the wall. Apart from this aspect, the circular arc approximation is considered to be in close agreement with the exact interfacial shape (Ng et al., 1999).

By considering the interfacial shape, one can improve precision in the prediction of shear stresses, pressure drop and phase fractions. Even though the flat interface models are good

approximations for gas-liquid flows, large diameter pipes and moderate holdups, improvements can be foreseen by considering interfacial curvature in cases such as oil-water flows, small diameters or limit conditions such as very small or very high holdup.

Both Brauner et al. and Ng et al.'s analysis consider a static two-fluid system for the determination of the interfacial shape and do not consider the mechanical contributions of fluid inertia, waves and turbulence to the interfacial shape. The approach, therefore, is appropriate for laminar flow modelling but can nevertheless yield interesting approximations in the case of turbulent gas-laminar liquid flow and fully turbulent flow.

8.3 The Three-Circle model

8.3.1 Motivation

Building on the two-fluid model of Brauner et al. (1998), a three-layer model with curved gas-liquid and liquid-liquid interfaces has been developed. For convenience, the model is named hereafter the Three-Circle model by extension of the Two-Circle model by Chen et al. (1997).

The motivation for considering curved interfaces is the following:

- There are experimental observations that the oil-water interface is convex in three-phase gas-oil-water flow at low liquid loading (Section 7.2.3).
- In two-phase stratified flow, it is theoretically demonstrated by Brauner et al. (1998) and Ng et al. (1999) that, at small holdup and partial wetting of the lower phase, the interfacial shape deviates from the flat configuration even at low Eötvos number.
- There are discrepancies between conventional three-layer model predictions and the experimental measurements performed in this thesis even in the case of separated three-phase flow. For instance, this is the case for steel at moderate gas superficial velocity. The predicted oil and water fractions are in general too low (Figure 7–30).

The consideration of curved interfaces seems therefore relevant for simulating the present experiments performed at low liquid loading, in a relatively small diameter pipe and for oil and water of relatively small density difference. The model presented below however has the generality that it yields nearly flat interfaces for the conventional three-phase flows in large diameter pipes with large density differences between fluids.

As indicated in introduction, the Three-Circle model is merely an extension of Brauner et al's (1998) model. It now takes into account two fluid interfaces instead of one: a gas-liquid interface and a liquid-liquid interface. Other assumptions are those of classical three-layer models and in particular, the phases are considered to flow in three separate layers without mass exchange. The determination of the interfacial shape is based on sys-

tem total energy minimization assuming static fluids. Some limitations are therefore expected in the case of fully turbulent flow. However, the Reynolds number in the liquid phase is usually small at low liquid loading, close to laminar conditions.

In the following sections, the geometry of the Three-Circle model is discussed (Section 8.3.2), then the prediction of interfacial curvature (Section 8.3.3) and, finally, the calculation of integral flow properties (Section 8.3.4 to Section 8.3.6).

8.3.2 Model geometry

As in Brauner et al. (1998), the gas-liquid and liquid-liquid interfacial shapes are approximated by circular arcs. Liquid holdups are thus function of two parameters: a wetted half-angle (δ_W or δ_O) and a view angle (δ_i or δ_j). These variables are defined in Figure 8–5 for the four possible combinations of interfacial curvature:

- Concave gas-liquid / concave liquid-liquid.
- Concave gas-liquid / convex liquid-liquid.
- Convex gas-liquid / concave liquid-liquid.
- Convex gas-liquid / convex liquid-liquid.

In the rest of this chapter, variables relative to the gas-liquid interface are indexed by j and variables relative to the liquid-liquid interface are indexed by i. Subscript k is used to index the water or the oil phases (k = W,O).

It was found convenient, as far as computations are concerned, to introduce the following variable as an alternative to the wetted half-angle:

$$c_k = \begin{cases} \dfrac{\delta_k - \delta_k^P}{\delta_k^P} \; for \; (0 < \delta_k < \delta_k^P) \\ \dfrac{\delta_k - \delta_k^P}{\pi - \delta_k^P} \; for \; (\delta_k^P < \delta_k < \pi) \end{cases} \qquad [8.6]$$

c_k is called hereafter the "curvature index" and is a measure of how the interface deviates from the plane configuration ($c_k = 0$ for $\delta_k = \delta_k^P$). For $-1 < c_k < 0$, the interface is convex and for $0 < c_k < 1$, the interface is concave.

Reciprocally, given holdups (H_W, H_L) and interfacial curvature index (c_W, c_O):

- The wetted half angles for flat interfaces (δ_k^P) are calculated using Biberg's Equation [3.31] with H_W for δ_W^P and H_L for δ_O^P:

$$\delta_{W,O}^{P} = \pi H_{W,L} + \left(\frac{3\pi}{2}\right)^{1/3}(1 - 2H_{W,L} + H_{W,L}^{1/3} - (1 - H_{W,L})^{1/3}) \qquad [8.7]$$

- The actual wetted half-angle is obtained by reversing Equation [8.6]:

$$\delta_k = \begin{cases} \delta_k^P(1 - c_k) \ \ for\ (c_k < 0) \\ \delta_k^P(1 + c_k) + \pi c_k \ \ for\ (c_k > 0) \end{cases} \qquad [8.8]$$

In the following, it is assumed:

1. $0 < \delta_k < \pi$, meaning the model is valid for three-phase flow only.
2. $0 < \delta_{i,j} < \pi$, meaning the interface is neither flat nor concentric to the pipe.

Two situations must be distinguished:

1. The interfacial arcs do not intersect.

2. The interfacial arcs intersect. The latter case is called in subsequent paragraphs the "critical case".

In the first case, the view angles $\delta_{i,j}$ can simply be expressed in terms of phase holdups using H_W for δ_i and H_L for δ_j:

$$0 = H_{W,L} - \frac{1}{\pi}\left[\delta_{W,O} - \frac{\sin 2\delta_{W,O}}{2}\right] - \left(\frac{\sin\delta_{W,O}}{\sin\delta_{i,j}}\right)^2\left[\delta_{i,j} - \frac{\sin 2\delta_{i,j}}{2}\right] \ if\ (c_{W,O} > 0) \qquad [8.9]$$

$$0 = H_{W,L} - \frac{1}{\pi}\left[\delta_{W,O} - \frac{\sin 2\delta_{W,O}}{2}\right] + \left(\frac{\sin\delta_{W,O}}{\sin\delta_{i,j}}\right)^2\left[\delta_{i,j} - \frac{\sin 2\delta_{i,j}}{2}\right] \ if\ (c_{W,O} < 0)$$

$$D_{i,j} = D\frac{\sin\delta_{W,O}}{\sin\delta_{i,j}} \qquad [8.10]$$

Equation [8.9] and Equation [8.10] are derived in Appendix C.

The view angles $\delta_{i,j}$ are solved iteratively using Equation [8.9], given phase fractions H_W and H_L. Once $\delta_{i,j}$ and $D_{i,j}$ are known, wetted and interfacial perimeters are readily calculated using the following geometrical relationships:

$$S_W = D\delta_W \qquad [8.11]$$

$$S_O = D(\delta_O - \delta_W) \qquad [8.12]$$

$$S_G = D(\pi - \delta_O) \quad [8.13]$$

$$S_i = D_i \delta_i \quad [8.14]$$

$$S_j = D_j \delta_j \quad [8.15]$$

In the critical case, interfacial arcs intersect as shown in Figure 8–6. The view angle δ_j can no longer be defined using Equation [8.9] on the basis of H_L. Indeed, this would overestimate H_O. The equations defining δ_j for the critical cases defined in Figure 8–6 are detailed in Appendix C.

Angles $w_{i,j}$ are defined in Figure 8–6 and characterize the intersection of the two interfacial circle arcs. They are required for the calculation of the interfacial perimeters in the critical case. Equations defining $w_{i,j}$ are given in Appendix C.

Once $\delta_{i,j}$ and $w_{i,j}$ are determined, wetted and interfacial perimeters can be calculated using the following geometrical relationships:

$$S_W = D\delta_W \quad [8.16]$$

$$S_G = D(\pi - max(\delta_W, \delta_O)) \quad [8.17]$$

$$\begin{aligned} S_O &= D(\delta_O - \delta_W) \; if \; (\delta_O \geq \delta_W) \\ S_O &= 0 \; if \; (\delta_O < \delta_W) \end{aligned} \quad [8.18]$$

$$\begin{aligned} S_i &= D_i(\delta_i - w_i) \; if \; (\delta_O \geq \delta_W) \\ S_i &= D_i w_i \; if \; (\delta_O < \delta_W) \end{aligned} \quad [8.19]$$

$$\begin{aligned} S_{jO} &= D_j(\delta_j - w_j) \; if \; (\delta_O \geq \delta_W) \\ S_{jO} &= D_j w_j \; if \; (\delta_O < \delta_W) \\ S_{jW} &= D_i w_i \; if \; (\delta_O \geq \delta_W) \\ S_{jW} &= D_i(\delta_i - w_i) \; if \; (\delta_O < \delta_W) \end{aligned} \quad [8.20]$$

In the critical case, the geometrical model predicts an hybrid gas-liquid interface with part being a gas-oil interface of perimeter S_{jO} and part being a gas-water interface of perimeter S_{jW}. It is questionable whether this situation can actually occur in practice but must be taken into account to insure the consistency of the model.

8.3.3 Prediction of interfacial curvature

The system energy considerations of Brauner et al. (1998) for a two-fluid pipe system are extended to deal with the three-phase situation. Brauner et al. state that for given phase fractions, the interfacial curvature is such that the system total energy, sum of the potential energy and surface energy, is minimized. Brauner et al. (1996) derive an expression for the system total energy variation caused by curving the interface from the flat configuration, given in Equation [8.3].

With three immiscible phases, the problem is more complicated because one has to deal with two interfacial curvatures simultaneously. In theory, the system energy should be expressed for a simultaneous change of both the gas-liquid and liquid-liquid curvatures and a two variable minimization algorithm should be run on the system energy to obtain the curvatures at equilibrium. In first approximation, it is possible to decompose the search for the optimal interfacial curvatures into two steps.

1. First, the water-oil interfacial curvature is considered. The oil and water holdup being given, the upper phase is considered to be an equivalent fluid of density equal to the volume average of the oil and gas phase as shown in Figure 8–4. The optimal interfacial curvature for this two-phase system at given water holdup is searched using Brauner et al.'s (1996) analysis. The optimum interfacial curvature Φ_i is such that Equation [8.21] is minimized:

$$\frac{\Delta E_i}{R^3 L(\rho_W - \rho_{eqi})g\cos\theta]} = \left[\frac{\sin^3\delta_W}{\sin^2\phi_i}(\cot\phi_i - \cot\delta_W)\pi - \phi_i + \frac{1}{2}\sin(2\phi_i)\right] + \frac{2}{3}\sin^3\delta_W^P + \varepsilon_{vi}\left[\sin\delta_W\frac{(\pi-\phi_i)}{\sin\phi_i} - \sin\delta_W^P + \cos\xi_i(\delta_W^P - \delta_W)\right] \quad [8.21]$$

The Eötvos and contact angle, in this case, are:

$$\varepsilon_{vi} = \frac{2\sigma_{water-oil}}{(\rho_W - \rho_{eqi})g\cos\theta R^2} \quad [8.22]$$

$$\xi_i = \xi_{water-oil} \quad [8.23]$$

with the equivalent upper phase density given by:

$$\rho_{eqi} = \frac{H_O}{H_O + (1-H_L)}\rho_O + \frac{1-H_L}{H_O + (1-H_L)}\rho_G \quad [8.24]$$

Once Φ_i is known, δ_W and c_W are calculated using Equation [8.25], knowing the holdup H_W.

$$0 = H_W - \frac{1}{\pi}\left\{\delta_W - \frac{1}{2}\sin(2\delta_W) - \left(\frac{\sin\delta_W}{\sin\phi_i}\right)^2\left[\phi_i - \pi - \frac{1}{2}\sin(2\phi_i)\right]\right\} \qquad [8.25]$$

2. After the water-oil interfacial curvature is determined, the gas-oil interface is considered. The phase fractions being given, the lower liquid is assumed to be an equivalent liquid of density equal to the volume average of the oil and water density, the upper phase being pure gas. Brauner et al's (1996) analysis is applied to this two-phase system in order to determine the optimal interfacial curvature using Equation [8.26]:

$$\frac{\Delta E_j}{R^3 L(\rho_{eqj} - \rho_G)g\cos\theta] = \left[\frac{\sin^3\delta_O}{\sin^2\phi_j}(\cot\phi_j - \cot\delta_O)\left\{\pi - \phi_j + \frac{1}{2}\sin(2\phi_j)\right\} + \frac{2}{3}\sin^3\delta_O^P\right] + \varepsilon_{vj}\left[\sin\delta_O\frac{(\pi-\phi_j)}{\sin\phi_j} - \sin\delta_O^P + \cos\xi_j(\delta_O^P - \delta_O)\right] \qquad [8.26]$$

The Eötvos and contact angle are now:

$$\varepsilon_{vj} = \frac{2\sigma_{oil-gas}}{(\rho_{eqj} - \rho_G)g\cos\theta R^2} \qquad [8.27]$$

$$\xi_j = \xi_{oil-gas} \qquad [8.28]$$

with the equivalent lower phase density given by:

$$\rho_{eqj} = \frac{H_O}{H_L}\rho_O + \frac{H_W}{H_L}\rho_W \qquad [8.29]$$

Φ_j is used as an alternative variable for δ_j. Knowing the liquid holdup H_L, δ_O and c_O are calculated from Equation [8.30]:

$$0 = H_L - \frac{1}{\pi}\left\{\delta_O - \frac{1}{2}\sin(2\delta_O) - \left(\frac{\sin\delta_O}{\sin\phi_j}\right)^2\left[\phi_j - \pi - \frac{1}{2}\sin(2\phi_j)\right]\right\} \qquad [8.30]$$

Some examples of interfacial shapes predicted by this method are given in Figure 8–7 and Figure 8–8. Figure 8–7 shows the computed and measured interfacial shapes for a test case at relatively high liquid content. The measured profiles were obtained by Roberts (1996) using a dual gamma densitometer and recording chordal attenuations. Figure 8–8 shows the predicted interfacial shapes and liquid heights for serie #3.1 of the present experiments at 20% water fraction in the steel pipe (Chapter 7). One can notice the increase of the interfacial curvatures (especially for the water-oil interface) as the holdup decreases.

8.3.4 Closure laws

Once interfacial geometries are determined, integral flow properties are calculated as for classical three-layer models. One needs to make a selection of friction laws to be able to compute pressure drop and phase fractions.

The choice of the most adequate friction laws for three-phase steady stratified flow is still an open issue and, as mentioned in Chapter 3, Khor et al. (1997) have formulated some recommendations based on comparisons with an extensive three-phase flow database. A three-layer model with flat interfaces is considered in their analysis.

It is not the object of the present chapter to recommend certain closure laws before others but merely to illustrate the effect of considering a curved interface model instead of flat approximations. It is chosen to take the same friction laws as in Taitel et al's model (1995). Taitel et al. (1995) have proposed simple friction laws that are fast and easy to compute.

For the wall friction factors, Blasius' equation, Equation [3.7], is used for turbulent pipe flow (Poiseuille's Equation [3.5] for laminar flow) and the maximum of the two at transition. The hydraulic diameter definitions are those according to Khor et al. (Equation [3.109], Equation [3.111] and Equation [3.112]). In those definitions, S_j is taken as:

$$S_j = S_{jW} + S_{jO} \qquad [8.31]$$

with $S_{jW} \neq 0$ in the critical case.

Gas-liquid interfacial friction is defined by Equation [3.118]. For the critical case, both a gas-oil interfacial shear τ_{jO} and a gas-water interfacial friction τ_{jW} are defined according to:

$$\begin{aligned} \tau_{jk} &= \frac{1}{8}\lambda_j \rho_G |U_{jk}| U_{jk} \\ U_{jk} &= U_G - U_k \end{aligned} \qquad [8.32]$$

Oil-water friction is computed from Equation [3.119] by Taitel et al. (1995).

8.3.5 Holdup equations

As in standard three-layer models, a double iteration on the total and water holdup equations must be performed to obtain the phase fractions. The total liquid holdup equation for the Three-Circle model is slightly modified to account for the critical case for which $S_{jW} \neq 0$. It is given by solving Equation [8.33]:

$$0 = -H_L\tau_G S_G + (1-H_L)\tau_L S_L - (\tau_{jO}S_{jO} + \tau_{jW}S_{jW}) + (1-H_L)H_L A(\rho_L - \rho_G)g\sin\theta \quad [8.33]$$

The water holdup equation is also modified and is given by solving Equation [8.34]:

$$\begin{aligned} 0 = &-H_W\tau_O S_O + (H_L - H_W)\tau_W S_W + H_W\tau_{jO}S_{jO} - (H_L - H_W)\tau_{jW}S_{jW} \\ &-H_L\tau_i S_i + H_W(H_L - H_W)A(\rho_W - \rho_O)g\sin\theta \end{aligned} \quad [8.34]$$

8.3.6 Solution algorithm

The search for the steady-state solution requires several parallel iterations and thus is rather heavy in terms of computation.

The solution algorithm is schematically represented in Table 8–3. First, it is searched for interfacial curvatures. The hydraulic model converges towards a unique (minimal) holdup solution pair (H_W, H_L) for any given pair of interfacial curvature (c_W, c_O). An iteration must be performed in order to determine the pair (c_W, c_O) that minimizes the energy equations, Equation [8.21] and Equation [8.26]. This iteration is conducted as follows:

1. A value of c_O is guessed.

2. A value of c_W is guessed.

3. Holdups H_W and H_L are calculated by double iteration on the total liquid and water holdup equations, Equation [8.33] and Equation [8.34] respectively. Several solutions are searched and only the solution pair giving the thinnest liquid layer is retained.

4. Equation [8.21] is minimized by iteration on c_W and the optimum c_W is returned.

5. With c_W from step 4, Equation [8.26] is minimized by iteration on c_O and the optimum c_O is returned.

6. The returned c_O and the guessed c_O are compared. If they differ, a new c_O is guessed and step 1-6 are repeated until convergence.

At convergence, c_O and c_W define the optimum interfacial curvatures for which the system total energy is minimum. The water and liquid holdup are calculated and finally the pressure drop.

The Three-Circle model algorithm requires solving several implicit equations. The solution search procedure can be any mathematical algorithm for continuous or non continuous functions changing sign in the solution interval. In the computations performed in this thesis, the MATLAB's function FZERO has been used. It uses a combination of bisection, secant, and inverse quadratic interpolation methods (MATLAB's User Guide 2002).

For the minimization of the energy equations, the minimization search algorithm used is that of MATLAB's FMINDBD routine which searches for the minimum of continuous

function of one variable on an interval. The algorithm is based on golden section search and parabolic interpolation (MATLAB's User Guide 2002).

8.4 Comparison with experimental data

The Three-Circle model predictions are compared with the experimental three-phase flow data acquired in the steel pipe at low liquid loading. The reason for this choice is that, as shown in Chapter 7, the acrylic pipe exhibits an atypical behaviour due to a more hydrophobic surface and a tendency to dispersed flow in the liquid layer. The Three-Circle model, by assumption, is relevant for modelling separated three-phase flow only and this flow regime is effectively observed at moderate gas superficial velocities (up to 15 m/s) in the steel pipe. Significant surface effects are expected to occur at low liquid loading and the Three-Circle model should bring improvements upon Taitel et al.'s three-layer model (Taitel et al. 1995) developed for flat interfaces.

Two types of comparisons are performed:

1. A statistical analysis of the relative error between prediction and measurement. A relative algebraic error for each data point is calculated according to Equation [E.4]. A gaussian probability density function (pdf) is assumed for the error distribution as given by Equation [E.5] with mean and standard deviation given by Equation [E.6] and Equation [E.7] respectively. A table of mean and standard deviation of errors for the comparison with the steel pipe data is given in Table 8–1.

Table 8–1: Statistics summary for the comparison between this thesis' three-phase flow data in the steel pipe and three-layer models with flat and curved interfaces

	Taitel et al. (1995)		**Three Circle model**	
	b_{err}	h_{err}	b_{err}	h_{err}
Total liquid holdup	-0.38	0.11	0.10	1.23
Water holdup	-0.26	0.13	0.32	2.71
Oil holdup	-0.50	0.13	0.09	0.45
Pressure drop	-0.10	0.09	0.01	0.31

2. Detail plots of comparisons with experimental series. This is to compare predicted variations of integral flow properties with flow parameters with the measured variations. The plots are summarized in Table 8–2.

Table 8–2: Comparisons between three-phase flow data in the 60 mm i.d. steel pipe and the Three-Circle model (Detail plots)

Label	Page	Topic
Figure 8–9	P 272	Serie #1 at 20% water fraction: sensitivity with liquid superficial velocity at fixed gas superficial velocity
Figure 8–10	P 273	Serie #2.1: sensitivity with water fraction at fixed gas superficial velocity 14.8 m/s and fixed liquid superficial velocity 0.0059 m/s
Figure 8–11	P 274	Serie #3.1: total liquid holdup sensitivity with gas superficial velocity and fixed liquid superficial velocity 0.0059 m/s
Figure 8–12	P 275	Serie #3.1: water holdup sensitivity with gas superficial velocity and fixed liquid superficial velocity 0.0059 m/s
Figure 8–13	P 276	Serie #3.1: oil holdup sensitivity with gas superficial velocity and fixed liquid superficial velocity 0.0059 m/s
Figure 8–14	P 277	Serie #3.1: pressure drop sensitivity with gas superficial velocity and fixed liquid superficial velocity 0.0059 m/s

8.4.1 Overall statistics

From results in Table 8–1, it can be said that the Three-Circle model displaces Taitel et al.'s model results towards higher oil and water holdups, in better agreement with the experimental data. The pressure drop also gains from the better holdup predictions. However, the standard deviation of the mean error is generally higher and this is due, as seen in the detail plots, to the performance of the model in the upward inclined case.

8.4.2 Detail plots

The following can be said of the detail plots in Table 8–2:

• The consideration of the interfacial curvature for the experiments in the 60 mm i.d. steel pipe yields a three-layer geometry where the gas-oil interface is nearly flat (slightly concave) and where the oil-water interface has a tendency to be convex at low liquid loading, as shown in Figure 8–8. Due to the increased oil-wall contact, the predicted oil fraction is higher than if the interfaces are considered flat and this is in better agreement with the experimental data. The predicted water holdup is also higher, compared to Taitel et al.'s predictions. This is due to the reduced drag at the oil-water interface due to the smaller oil-water relative velocity (oil experiences a higher wall drag and its mean velocity is reduced). The increased water holdup is also in better agreement with the experimental data. This is apparent both at low gas velocity and high gas velocity in Figure 8–12 and Figure 8–13. The total holdup benefits from these trends (Figure 8–11).

• There is yet a severe over prediction of the phase fractions close to the transition to slug flow in the inclined case. The situation is actually worsened compared to Taitel et al.'s model due to the increase of the total holdup. As mentioned in Chapter 7, the reason

for this discrepancy is a weakness in the interfacial friction models. Due to the overestimated holdup, the pressure drop also mismatches with the experimental data close to the slug transition.

• The agreement with measured holdup and pressure drop is improved in the stratified flow regime at moderate gas velocities (gas superficial velocity comprised between 10 m/s and 20 m/s) compared to Taitel et al.'s model. There is good agreement with the holdup and liquid composition data for the Serie #2.1 in Figure 8–10. However, the agreement is poor at high gas velocities. There are two reasons for this discrepancy. First, at high gas velocities, the flow regime in the liquid phase is no longer separated but dispersed flow and the real situation departs from the model assumptions. Second, there is intense droplet generation and deposition in this regime whereas no droplet field is considered in the Three-Circle model.

• There is good agreement with the holdup data at the limit of the very low liquid loadings (Serie #1, Figure 8–9). However, there are discrepancies at higher liquid superficial velocities.

8.5 Summary

In this chapter, a new three-layer model has been derived for one-dimensional computations of steady-state pressure drop and phase fractions in three-phase gas-liquid-liquid flow. Unlike standard three-layer models, this model considers the effect of curved gas-liquid and liquid-liquid interfaces on flow properties. The physical principle for determining the interfacial shape is that of minimum system total energy (potential and surface) for the static three-layer system. The analysis builds on Brauner et al.'s theory (1998) developed for a general two-fluid system in a circular duct with interfacial shapes assimilated to circle arcs. An approximate two-step search of the optimal interface curvature has been used. In the future, the more rigorous calculation of the exact interfacial shape using Young-Laplace equation is recommended.

The effect of considering curved interfaces has been compared to the companion three-layer model of Taitel et al. (1995) with flat interfaces but identical friction laws. At identical closures, the Three-Circle model yields higher oil and water fractions, in better agreement with the experimental data. The prediction of the Three-Circle model are not satisfactory at small upward inclinations due to non adequate interfacial friction closures.

Table 8–3: Solution algorithm for the Three-Circle model

start initialize variables read case and update input variables perform steps										
	iterate on c_O									
	A	guess c_O in $-1<c_O<1$								
		iterate on c_W								
		1	guess c_W in $-1<c_W<1$							
			iterate on H_L							
			I	guess H_L in $0<H_L<1$						
				iterate on H_W						
				a	guess H_W in $0<H_W<1$					
				b	compute wetted half-angles, Equation [8.8]					
				c	iterate on water circle equation					
				d	i	guess δ_i in $0<\delta_i<\pi$				
					ii	return to step i until Equation [8.9] is satisfied				
					iii	return δ_i				
				e	iterate on oil circle equation					
					i	guess δ_j in $0<\delta_j<\pi$				
					ii	return to step i until Equation [8.9] is satisfied				
					iii	return δ_j				
I	B	2	II	f	if not critical					
					i	compute interfacial geometries, Equation [8.11] to Equation [8.15]				
				g	if critical					
					i	iterate on δ_j				
					ii	a	guess δ_j on appropriate interval (see Appendix C)			
						b	return to step a until Equation [C.16] is satisfied			
						c	return δ_j			
					iii	compute interfacial geometries Equation [8.16] to Equation [8.20]				
				h	compute hydraulic diameters					
				i	compute shear stresses					
				j	repeat from step a until Equation [8.34] is satisfied					
				k	return H_W					
			III	repeat from step I until Equation [8.33] is satisfied						
			IV	return H_L						
		3	return to step 1 until energy equation Equation [8.21] is minimized							
		4	return c_W							
	C	return to step A until energy equation Equation [8.26] is minimized								
	D	return c_O								
II	terminate steps									

Table 8–3: Solution algorithm for the Three-Circle model

compute (H_W, H_L) for (c_W, c_O)
compute pressure drop from Equation [3.93]
save data
terminate

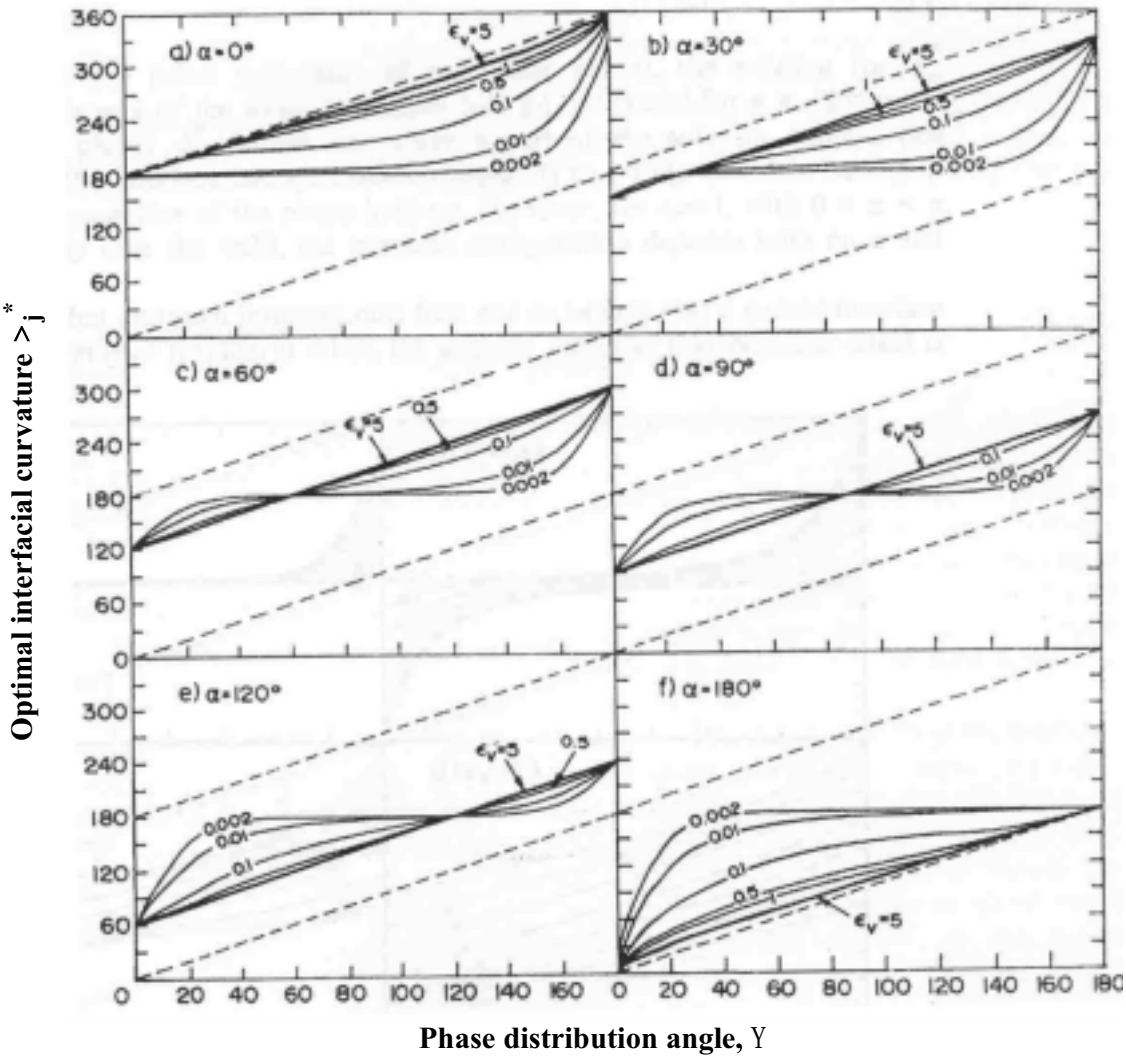

Figure 8–1: Optimal interfacial curvature versus phase distribution angle for given Eötvos number and contact angle. In the figure, α indicates the contact angle (ξ in this dissertation) (from Brauner et al. 1998)

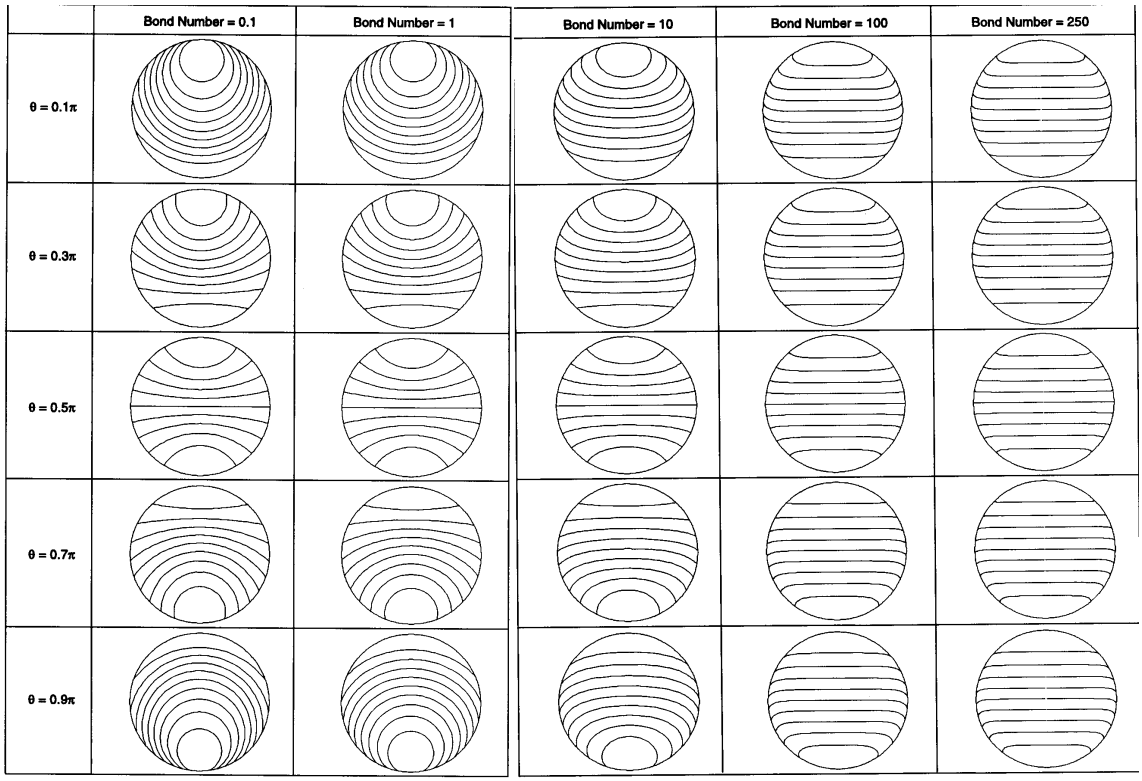

Figure 8–2: Variation of the interfacial shape with holdup for constant Bond number and contact angle. In this figure, θ indicates the contact angle (ξ in this dissertation). H = 0.1, 0.2,...0.9 (from Ng et al. 2001)

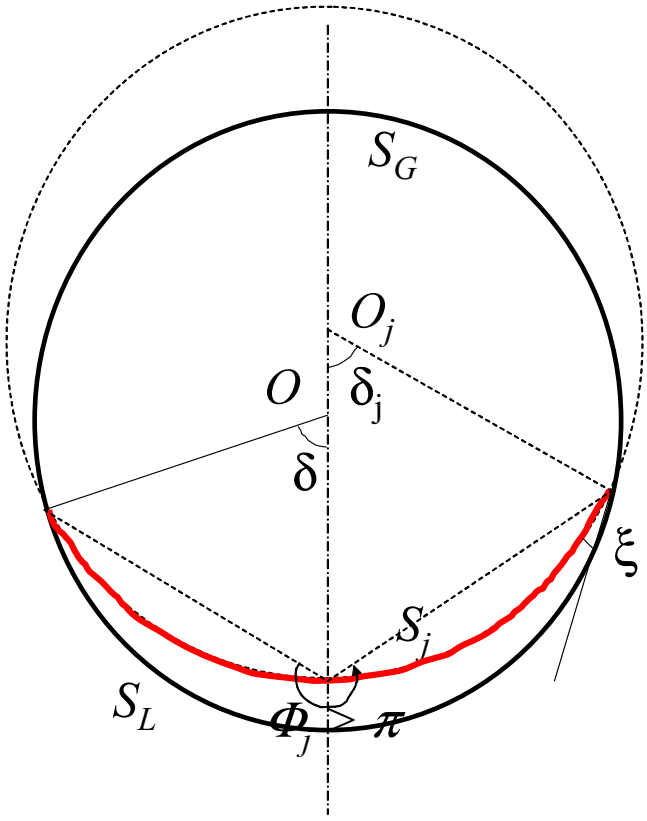

Figure 8–3: Variable definitions for curved circular arc interface models

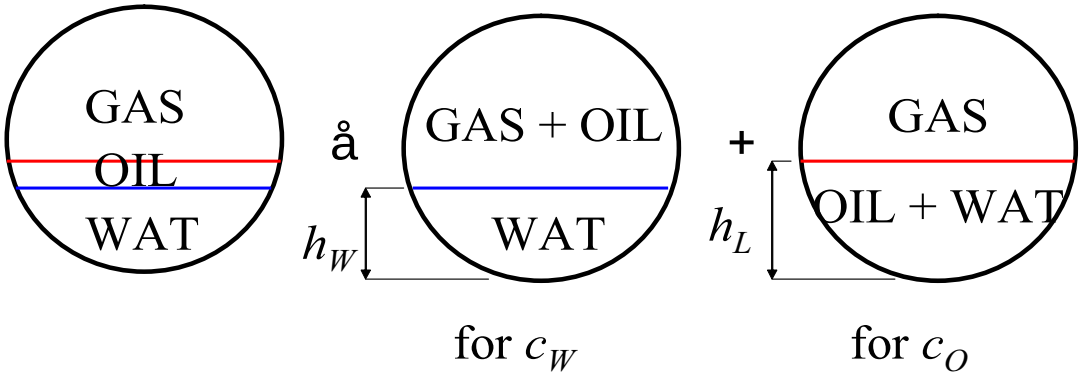

Figure 8–4: Search for optimal system interfacial curvatures

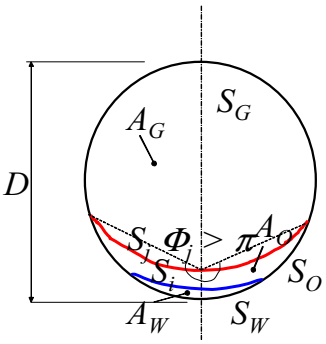

concave gas-liquid - concave liquid-liquid

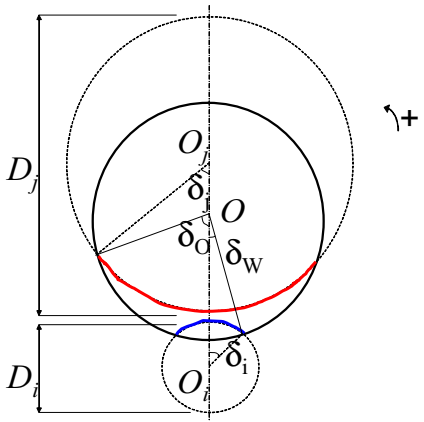

concave gas-liquid - convex liquid-liquid

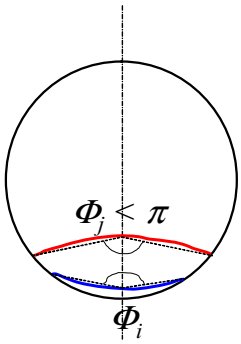

convex gas-liquid - concave liquid-liquid

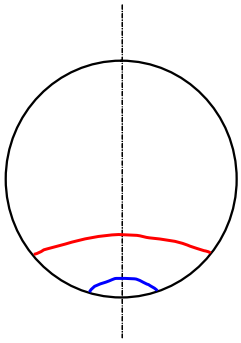

convex gas-liquid - convex liquid-liquid

Figure 8–5: Geometries for the Three Circle model

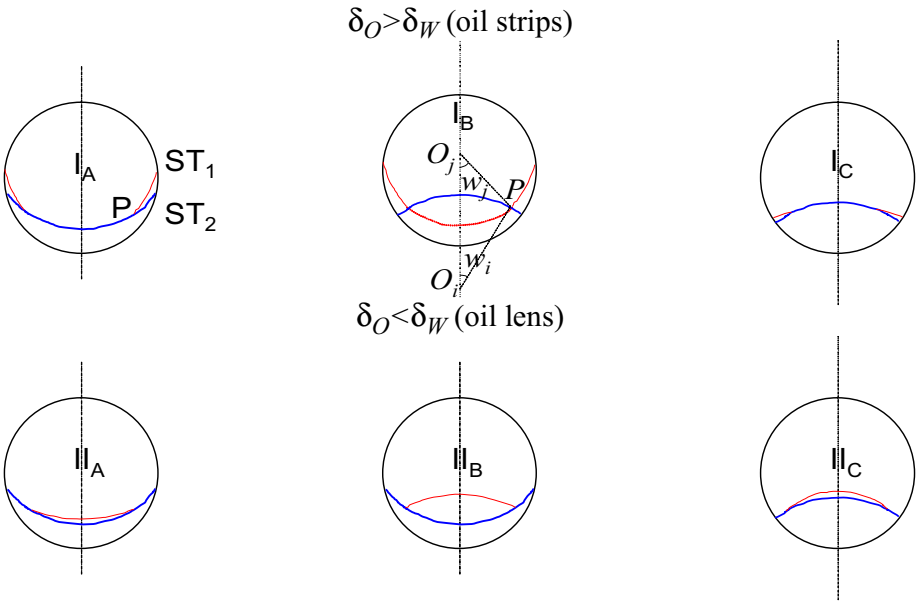

Figure 8–6: Critical geometries for the Three Circle model

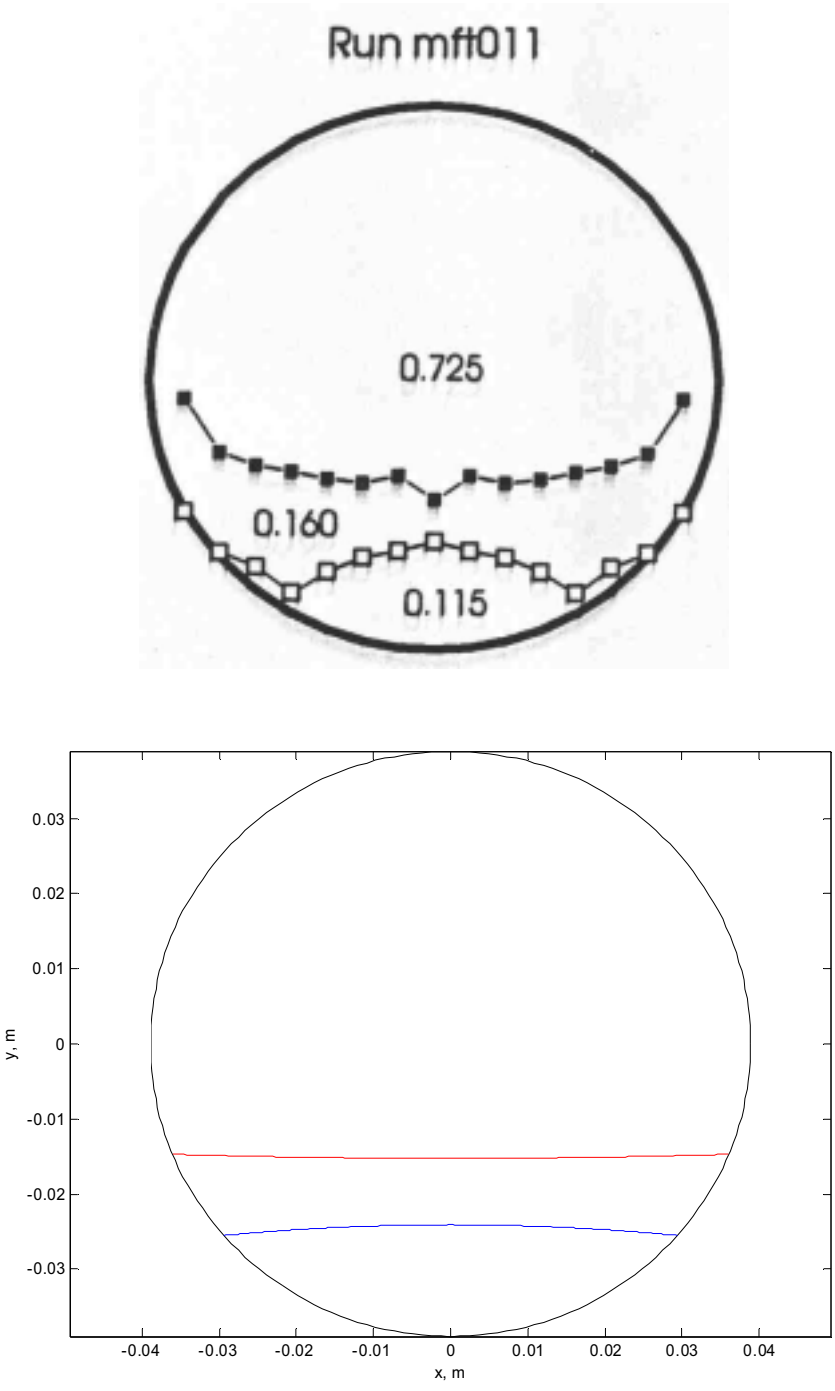

Figure 8–7: Measured and computed interfacial shapes and liquid heights for a three-phase stratified flow example. Superficial gas velocity = 6.18 m/s, superficial oil velocity = 0.039 m/s, superficial water velocity = 0.041 m/s, gas density = 2.204 kg/m^3, oil density = 862.6 kg/m^3, oil viscosity = 0.046 Pa.s, oil/water/pipe contact angle = 80 deg., air/oil/pipe contact angle = 0 deg., internal pipe diameter = 0.0779 m, inclination = 0 deg. Top: interfacial profiles as measured by Roberts (1996); Bottom: profiles and liquid heights calculated with the Three-Circle model

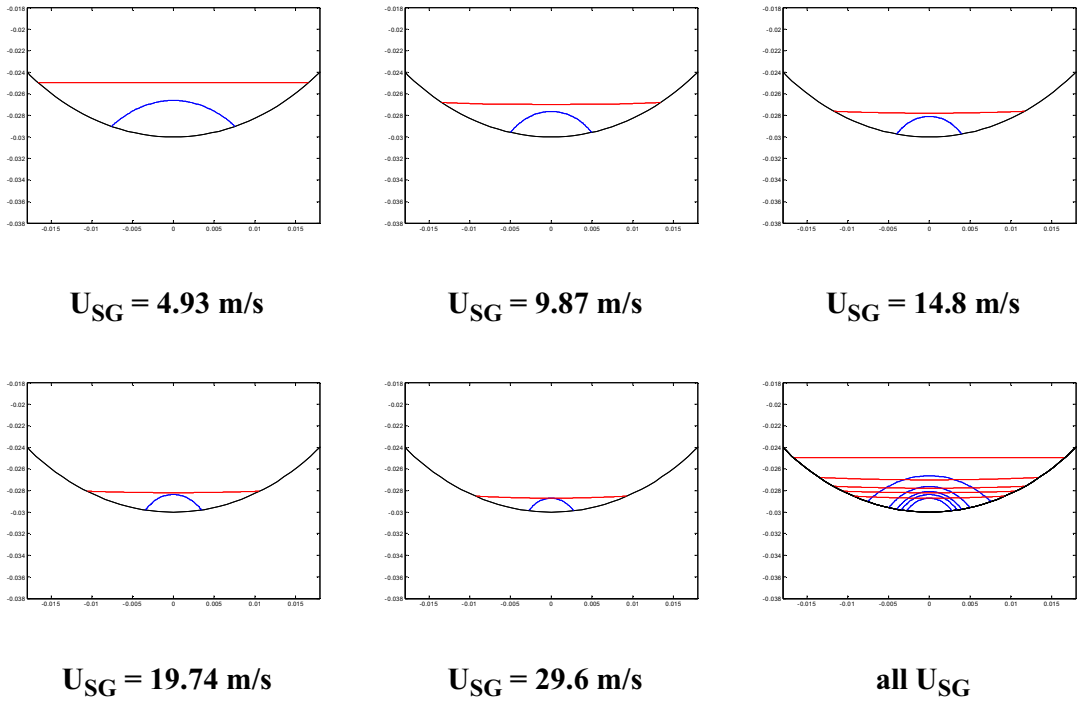

U_{SG} = 4.93 m/s U_{SG} = 9.87 m/s U_{SG} = 14.8 m/s

U_{SG} = 19.74 m/s U_{SG} = 29.6 m/s all U_{SG}

Figure 8–8: Interfacial shapes and liquid heights calculated with the Three-Circle model. Test cases are those of serie #3.1 at superficial liquid velocity = 0.0059 m/s, water fraction = 20% in the horizontal steel pipe

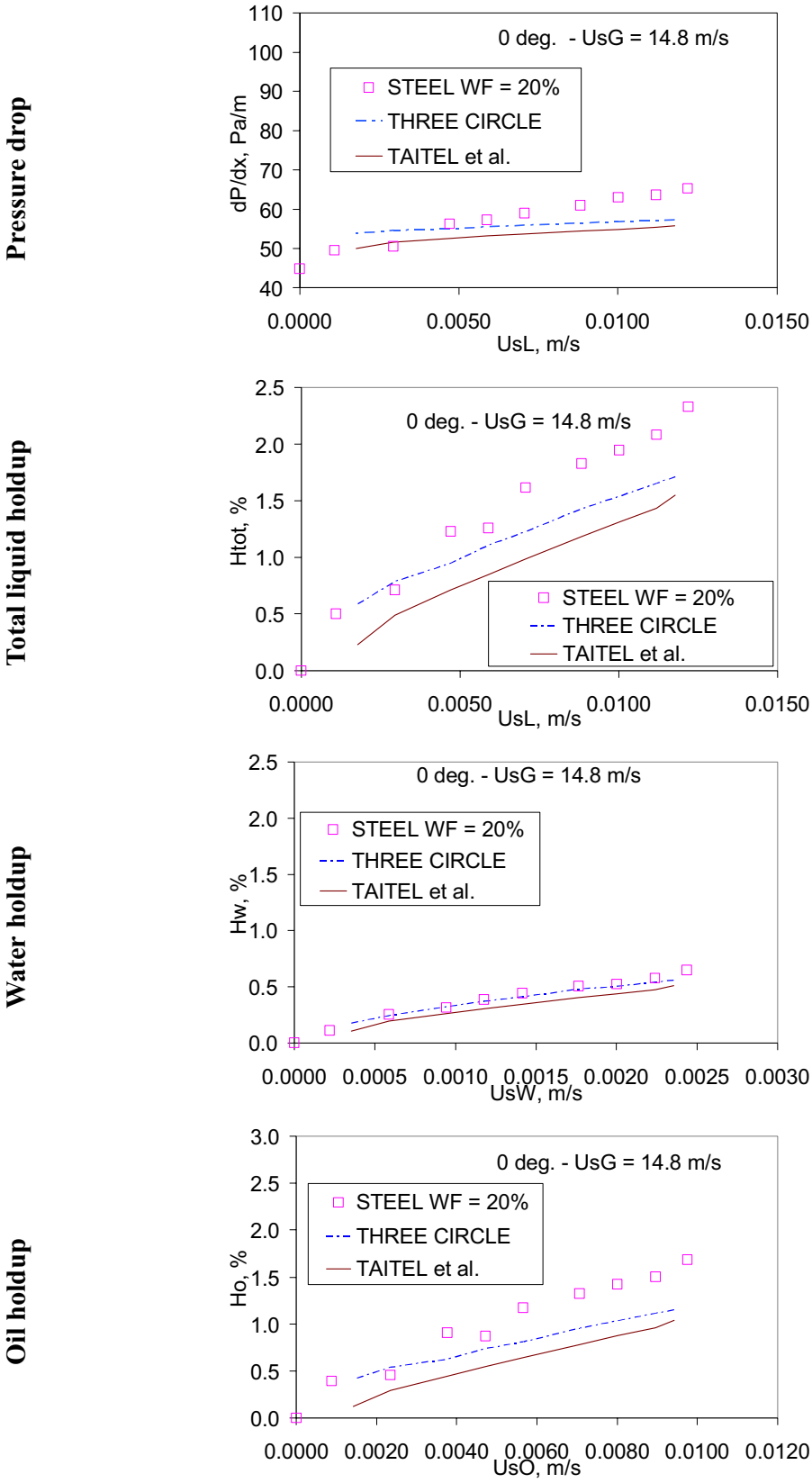

Figure 8–9: Serie #1, sensitivity with liquid superficial velocity at fixed gas superficial velocity. Comparison of measurements with the Three-Circle model

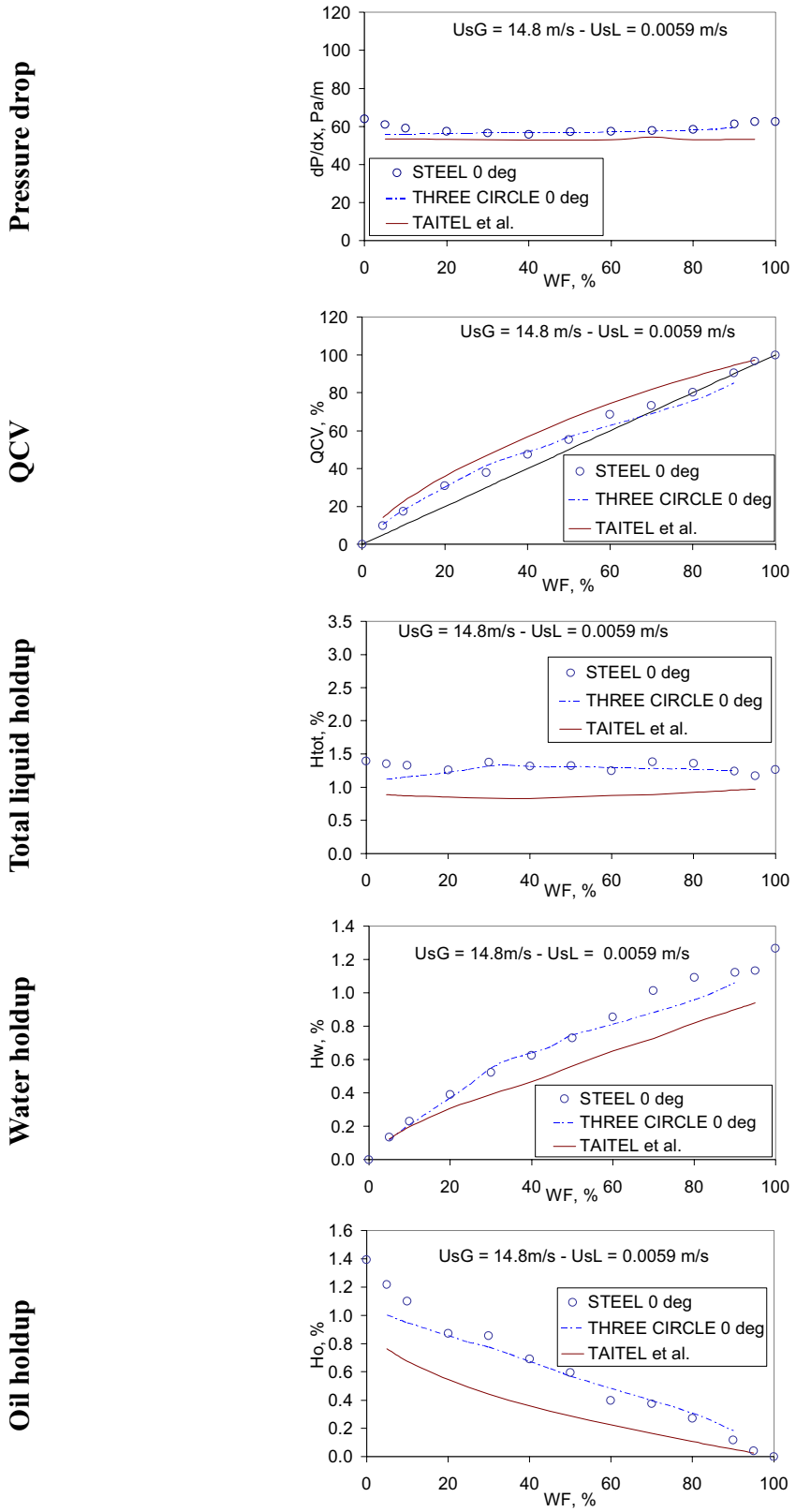

Figure 8–10: Serie #2.1, sensitivity with input water fraction at fixed liquid superficial velocity = 0.0059 m/s and fixed gas superficial velocity = 14.8 m/s in horizontal pipes. Comparison of measurements with the Three-Circle model

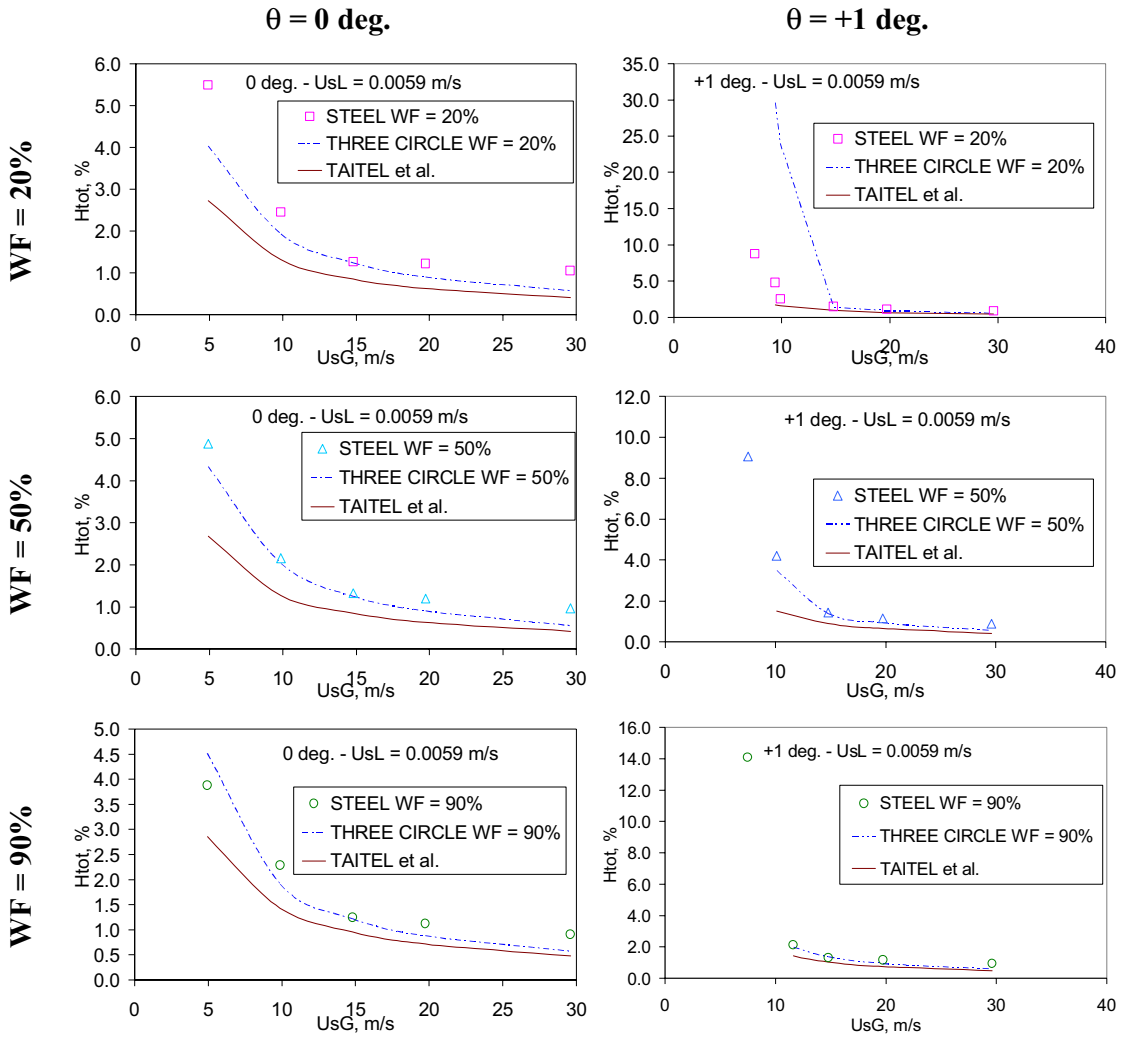

Figure 8–11: Serie #3.1, total liquid holdup sensitivity with superficial gas velocity at fixed liquid superficial velocity = 0.0059 m/s. Comparison of measurements with the Three-Circle model

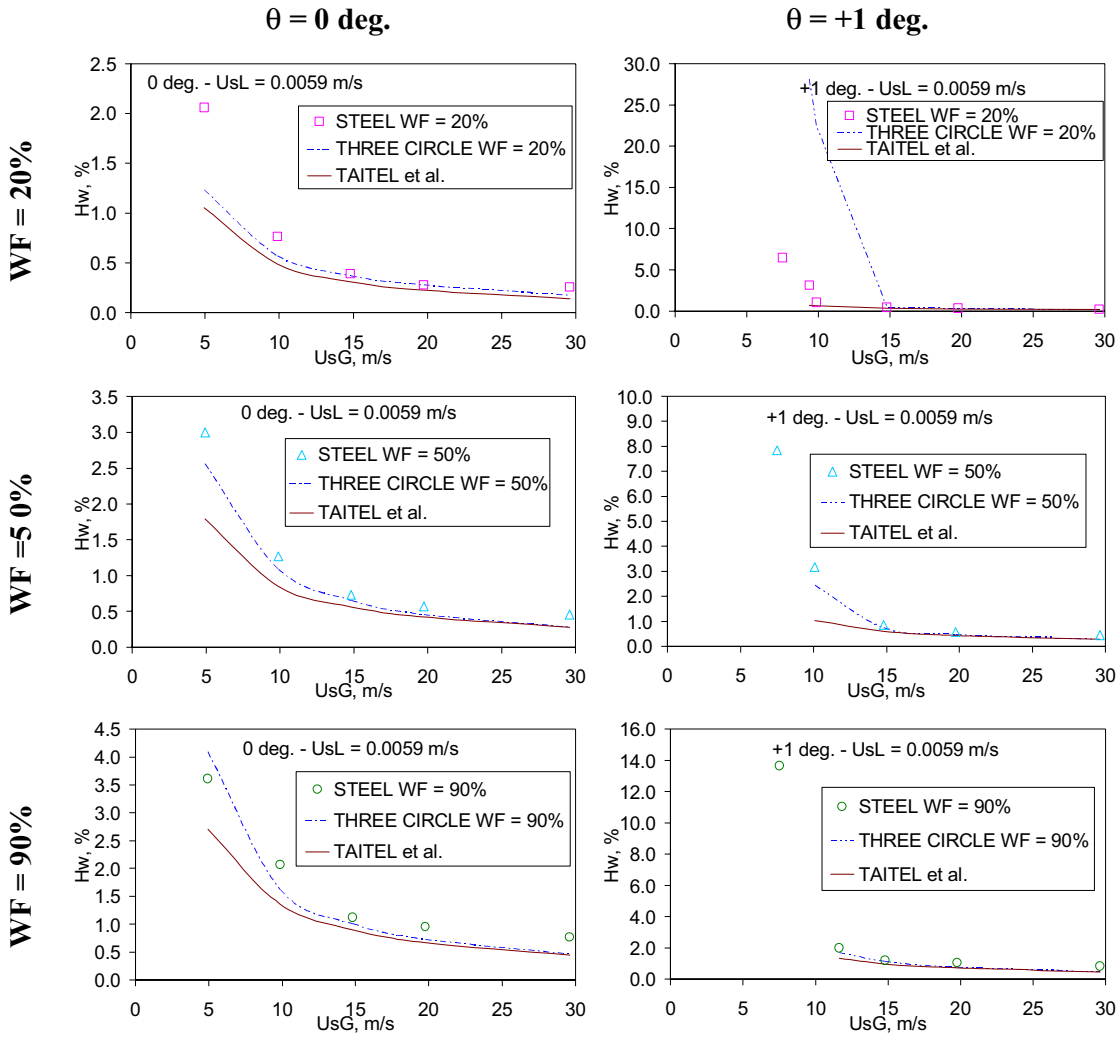

Figure 8–12: Serie #3.1, water holdup sensitivity with superficial gas velocity at fixed liquid superficial velocity = 0.0059 m/s. Comparison of measurements with the Three-Circle model

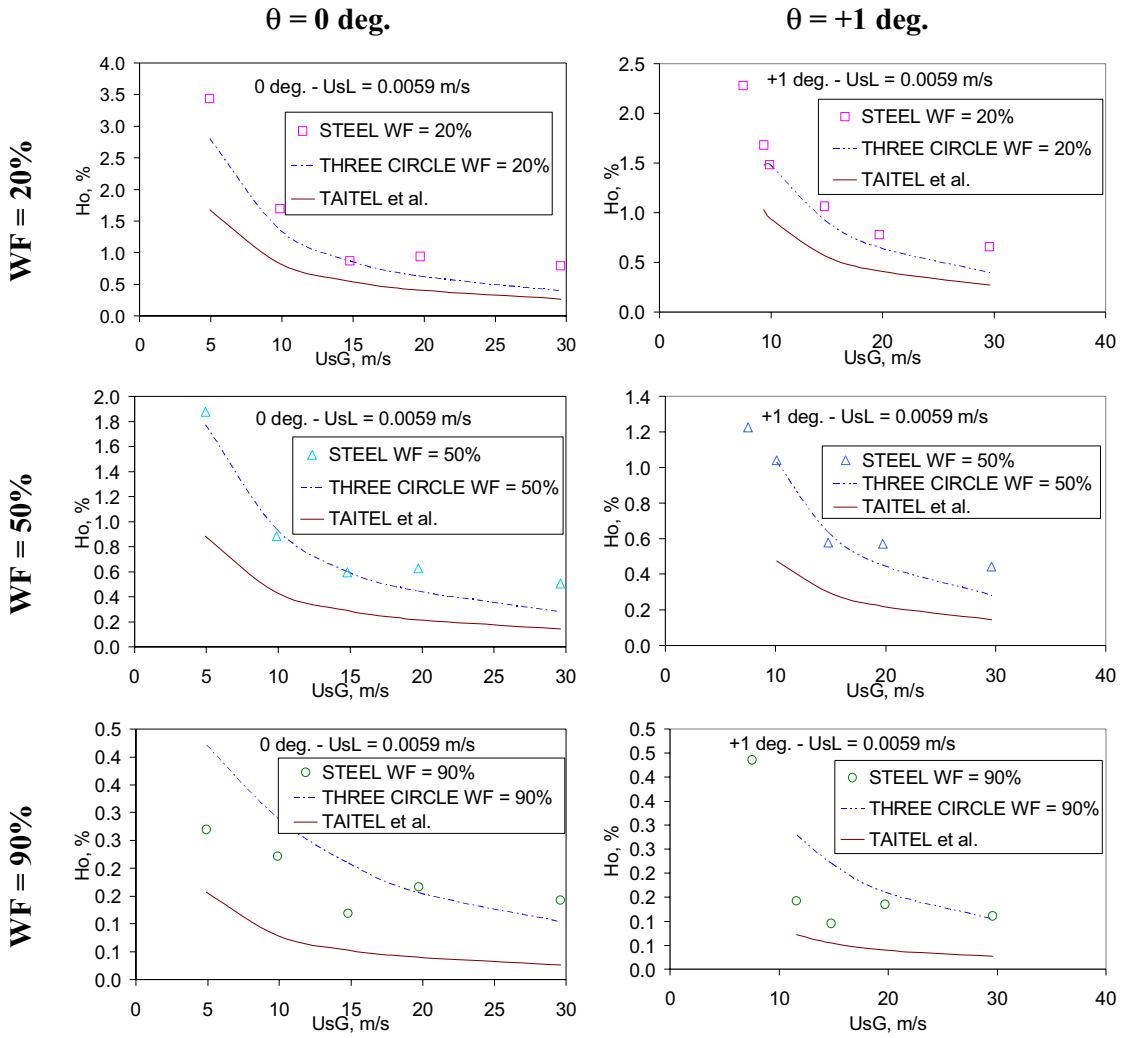

Figure 8–13: Serie #3.1, oil holdup sensitivity with superficial gas velocity at fixed liquid superficial velocity = 0.0059 m/s. Comparison of measurements with the Three-Circle model

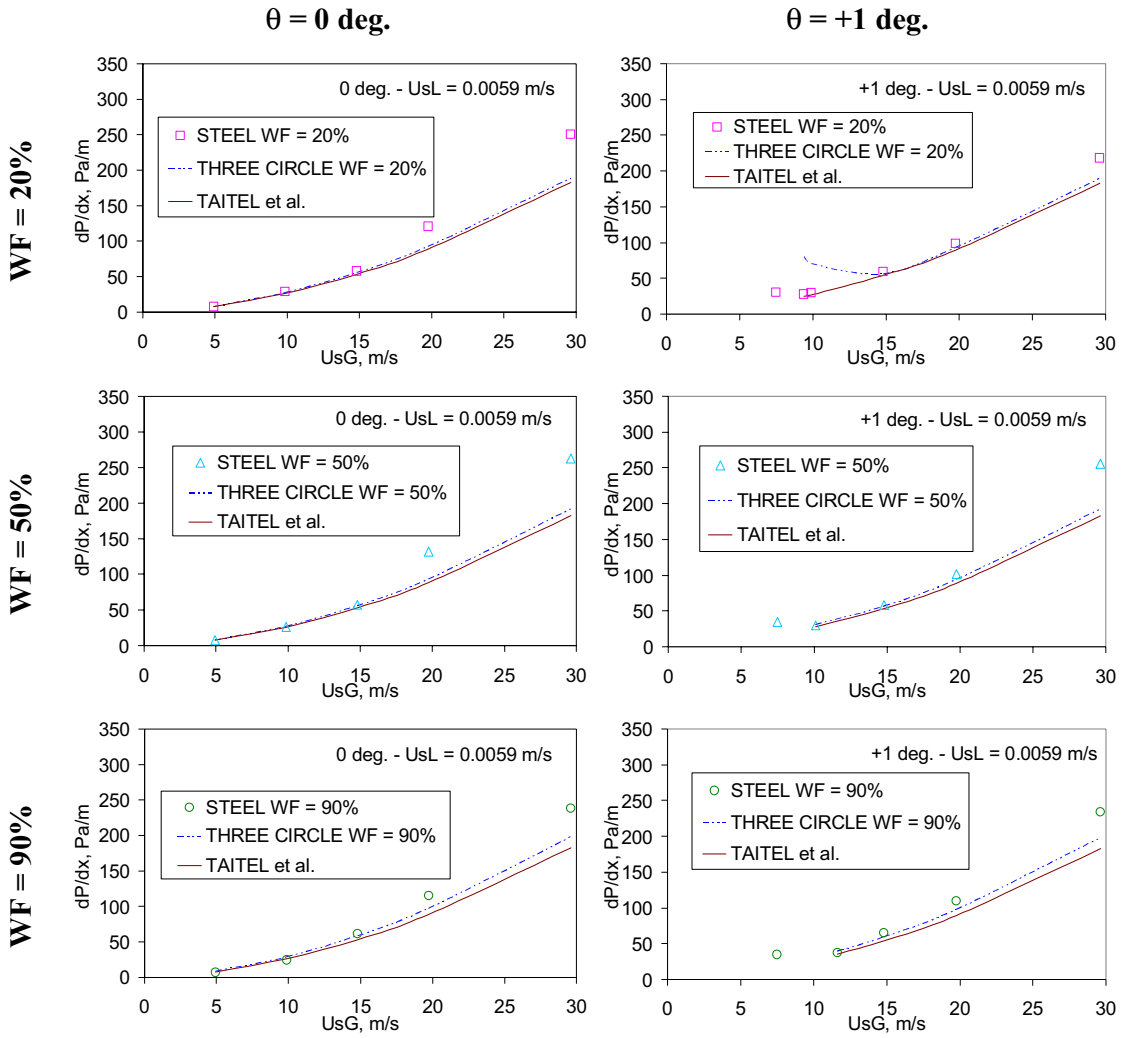

Figure 8–14: Serie #3.1, pressure drop sensitivity with superficial gas velocity at fixed liquid superficial velocity = 0.0059 m/s. Comparison of measurements with the Three-Circle model

Chapter 9 Conclusions

9.1 Summary of the thesis

The work performed in this thesis can be roughly divided into four main parts:

1. A review of the literature on stratified gas-liquid and gas-oil-water pipe flow with focus on the flow hydrodynamics (Chapter 2) and one-dimensional models (Chapter 3).

2. The qualification of measurement techniques for steady gas-liquid flow at low liquid loading (Chapter 4).

3. Three experimental studies: a study of gas flow on wet walls (Chapter 5), measurements of pressure drop and holdup for steady-state two-phase gas-liquid flow at low liquid loading (Chapter 6) and measurements of pressure drop and holdup for steady-state three-phase gas-oil-water flow at low and moderate liquid loading (Chapter 7).

4. Modeling of gas-liquid flow at low liquid loading including comparisons of measurements with annular flow models (Chapter 5), comparisons with one-dimensional stratified flow models and the multiphase flow simulator PETRA (Chapter 6, Chapter 7) and the derivation of a three-layer model with curved interfaces (Chapter 8).

9.2 Conclusions

The following conclusions can be drawn from the results obtained in this thesis:

Two-phase flow

- Despite the low input liquid loading, the in-situ liquid holdup can be high in upward inclined pipes at low gas flow rates, such that the flow becomes gravity dominated. At conditions of high gas flowrates where the flow is friction dominated, gas-wall friction dominates at low liquid loading but liquid-wall friction can be at least as important as gas-wall friction, especially for high viscosity oils. There is a large increase of the pressure drop at conditions of atomization flow for which wetting of the upper pipe wall occurs.

- For the experiments performed in stratified flow, liquid-wall friction is best represented by Hand's friction factor correlation (Espedal 1998). Gas-liquid interfacial friction is best represented by Hart et al's correlation (Hart et al. 1989) though the latter generally over predicts.

• Best holdup and pressure drop predictions at low liquid loading are obtained from Grolman's MARS model (Grolman 1994), but the general purpose multiphase flow simulator PETRA also gives acceptable results. However, there is currently no model that can accurately predict the holdup increase close to the transition to slug flow nor the pressure drop increase due to droplets in stratified/atomization flow.

Three-phase flow

• Three-phase flow at low liquid loading is dominated by a dependency with input water fraction. In gravity dominated flows, the holdup is the most sensitive parameter and exhibits a peak at intermediate water fractions, due to local separation of water and oil. This is enhanced at upward inclinations and high density differences between the two liquids. In friction dominated flows, the pressure drop can exhibit a dip or a peak, depending on the gas-liquid flow regime (stratified / atomization) and the state (separated / dispersed) of the liquid layer. At increasing gas flowrate, the peak is enhanced and displaced towards lower water fractions.

• At low liquid loading, there is an effect of pipe wall material in three-phase gas-oil-water flow. This is because water and oil are competing for the wetting of the wall surface. In two-phase gas-liquid flow, the effect of pipe material is not significant. In three-phase gas-oil-water flow, the wall material interacts with the flow regime in the liquid layer (separated or dispersed) and the degree and nature of the wetting of the upper pipe wall. In the acrylic pipe, the liquid forms a dispersion at smaller gas velocity compared to steel when the gas velocity increases. When a dispersion forms, large amplitude waves appear at the gas liquid interface and increase the amount of droplets in the gas core and depositing at the wall. As a result, oil is accumulating in acrylic whereas water is accumulating in steel. The pressure drop is also higher in acrylic compared to steel. The significance of the material effect decreases as the liquid holdup in the pipe increases.

• A characterization of the wall surface has been suggested to predict the effect of wall material in three-phase flow at low liquid loading. It consists in measuring the difference between advancing and receding contact angles on the pipe wall material for a water droplet in oil. It can be shown that the higher the hysteresis, the higher the adhesion of the water droplet on the material when displaced by oil.

• Compared to bare steel, the epoxy coating has little influence on the flow which conserves the characteristics observed in steel.

• One-dimensional gas-oil-water three-layer models can not reproduce with acceptable accuracy the measured three-phase stratified flow data at low liquid loading. The agreement is improved using Khor et al.'s model closures (Khor et al. 1997) in case of moderate liquid loading. The multiphase pipe flow simulator PETRA provides better overall prediction of three-phase gas-oil-water flow at low liquid loading than three-layer models. However, two discrepancies are identified. First, for gravity dominated flows, the holdup is under predicted compared to experiments. The holdup dependency to water fraction is not well accounted for. Second, for friction dominated flows in the atomization regime, the pressure drop is underestimated.

• The Three-Circle model, a three-layer model with curved interfaces, can reproduce measurements in horizontal pipes with better accuracy than if the interfaces are assumed to be flat, provided the flow regime is separated gas-oil-water flow. In inclined pipes, more accurate interfacial friction closures are required to achieve better agreement with the experimental measurements.

Wet walls

• No drag reduction has been obtained with a thin moving liquid film at the wall due to the premature film de-wetting and the occurrence of instabilities at the gas-liquid interface. The pressure drop is enhanced with partial wall wetting compared to a dry wall. The measured gas-liquid interfacial friction is not correctly reproduced by Wallis' friction factor correlation (Wallis 1969). For very thin films, the pressure drop is best predicted with Hart et al.'s interfacial friction correlation (Hart et al. 1989) and an apparent interfacial roughness that scales with the film thickness.

9.3 Recommendations for future work

The following recommendations can be made for further work on the topic of low liquid loaded gas flow in pipes:

• Some effects have been identified in this thesis that require confirmation from detailed measurements. Measurements needed are the intensity of the droplet field, the regime (dispersed / separated) of the liquid layer depending on wall material, the magnitude of the wall and interfacial friction and the degree of wall wetting in three-phase flow.

• It would be relevant to further investigate the effect of material water affinity on three-phase gas-oil-water flow. New wall materials, proven hydrophobic or hydrophillic, could be tested. Arney et al. (1995) give suggestions of hydrophillic walls (Chapter 2). Another test would consist in temporarily altering the water affinity of the material by injecting a chemical. As shown by Mannes et al. (1997), glycol based corrosion inhibitors are expected to modify the water-wall contact angle in presence of oil in steel pipes. Other classes of chemicals called "superspreaders" could also be tested such as silicon based surfactants. Such products are used in agriculture to render surfaces hydrophillic and improve the spreading of water based pesticides (Adamson et al. 1997, p. 467).

• The suggested method for characterizing the water affinity of a material, based on contact angle measurements, needs to be tested on a wider range of surfaces. A method for measuring contact angle hysteresis, based on the measurement of the "drop-off" angle, is described in Kvernvold et al. (1981). It consists in measuring the angle at which a drop of water starts to slide down an inclined plane of a selected material. Based on a static force balance, this angle can be shown to be proportional to the contact angle hysteresis.

• It would be interesting to test the influence of varying wall sand grain roughness on the flow at low liquid loading. In particular, it is expected that surface roughness has an impact on contact angle hysteresis and therefore can have an effect on wall wetting in three-phase gas-oil-water flow.

• Experiments on walls artificially wetted with liquid droplets would permit to improve gas-wall friction laws in atomization flow.

• Three-phase gas-oil-water transient flow experiments have been tried out in this thesis and more transient experiments are required for testing against transient multiphase flow codes. Transient experiments are relevant to engineering issues such as pipeline shut-down, start-up and pigging operations.

• New experiments may be performed to further investigate the theoretical possibility of pressure loss reduction in gas pipes using a liquid film at the wall. Chemicals could be used to improve film behaviour. Two classes of chemicals may be investigated: wetting agents, to delay film de-wetting and therefore achieve thinner films, and surfactant polymers, that can stiffen the gas-liquid interface and hence reduce the effect of gas induced turbulence.

• A more comprehensive three-phase one-dimensional stratified flow model is required that can extrapolate correctly to the case of small phase fractions. Such a model may include:

- a model for predicting the transition from stratified to dispersed flow in the liquid phase, if possible including surface effects.
- in case of dispersed liquid flow, a viscosity model and a model for phase inversion.
- in case of separated oil-water flow, a three-layer model including interfacial curvature. It is recommended that the prediction of exact interfacial curvature should be pursued through the resolution of the Young-Laplace equation.
- A model for droplets: onset, entrainment and deposition.
- Friction laws based on velocity profiles derived from first principles.

References

Acikgöz M., França F., Lahey Jr. R.T., 1992, *An Experimental Study of Three-Phase Flow Regimes*, Int. J. of Multiphase Flow, Vol. 18, pp. 327-336

Adamson A.W., Gast A.P., 1997, *Physical Chemistry of Surfaces*, Sixth Edition, John Wiley & Sons

Adewuni A., Mucharam L., Watson R.W., Campbell L.D., 1989, *Field Study and Modelling of Condensation in a Gas Distribution Pipeline*, 64th Annual Technical Conference and Exhibition of the SPE, San Antonio, Tx, October 8-11, 1989, SPE 19811

Al-Sarkhi A., Hanratty T.J., 2001, *Effect of Drag-Reducing Polymers on Annular Gas-Liquid Flow in a Horizontal Pipe,* Int. J. of Multiphase Flow, Vol. 27, pp. 1151-1162

Andritsos N., Hanratty T.J., 1987, *Influence of Interfacial Waves in Stratified Gas-Liquid Flows,* AIChE Journal Vol. 33, No. 3, pp. 444-454

Angeli P., Hewitt G.F., 1998, *Pressure Gradient in Horizontal Liquid-Liquid Flows,* Int. J. of Multiphase Flow, Vol. 24, pp. 1183-1203

Angeli P., Hewitt G.F., 2000, *Flow Structure in Horizontal Oil-Water Flow,* Int. J. of Multiphase Flow, Vol 26, pp. 1117-1140

Arney M.S., Ribeiro G.S., Guevara E., Bai R., Joseph D.D., 1995, *Cement-Lined Pipes for Water Lubricated Transport of Heavy Oil,* Int. J. of Multiphase Flow, Vol. 22, pp. 207-221

Asali J.C., Hanratty T.J., 1985, *Interfacial Drag and Film Height for Vertical Annular Flow,* AIChE Journal, Vol. 31, No. 6, pp. 895.902

Asante B., Stanislav J.F., Pan Lei, 1999, *Multiphase Transport of Gas and Low Loads of Liquids in Pipelines,* 31st Annual Pipeline Simulation Interest Group Meeting

Badie S., Hale C.P., Lawrence C.J., Hewitt G.F., 2000, *Pressure Gradient and Holdup in Horizontal Two-Phase Gas-Liquid flows with Low Liquid Loading,* Int. J. of Multiphase Flow, Vol. 26, pp. 1525-1543

Badie S., Lawrence C.J., Hewitt G.F., 2001, *Axial Viewing Studies of Horizontal Gas-Liquid Flows with Low Liquid Loading*, Int. J. of Multiphase Flow, Vol. 27, pp. 1259-1269

Baker A., Nielsen K., Gabb A., 1988, *Field Data Test New Holdup, Pressure-Loss Calculations for Gas-Condensate Pipelines,* Oil & Gas Journal, Mars 21, 1988

Barnea D., 1986, *A Unified Model for Predicting Flow-Pattern Transitions for the Whole Range of Pipe Inclinations,* Int. J. of Multiphase Flow, Vol. 13, pp. 1-12

Bendiksen K.H, Malnes D., Moe R., Nuland S., 1991, *The Dynamic Two-Fluid Model OLGA: Theory and Application,* SPE Production Engineering, SPE 19451

Biberg D., 1998, *A Simple Friction Model for Two Phase Stratified Pipe Flow,* 3rd Int. Conference on Multiphase Flow, Lyon, France, June 8-12, 1998

Biberg D., 1999, *Two-Phase Stratified Pipe Flow Modelling. A New Expression for the Interfacial Shear Stress,* Two-Phase Flow Modelling and Experimentation 1999, pp. 99-108

Brauner N., Moalem-Maron D., 2001, *The Prediction of Dispersed Flow Boundaries in Liquid-Liquid and Gas-Liquid Systems,* Int. J. of Multiphase Flow, Vol. 27, pp. 885-910

Brauner N., Moalem Maron D., Rovinsky J., 1998, *A Two-Fluid Model for Stratified Flows with Curved Interfaces,* Int. J. of Multiphase Flow, Vol. 24, pp. 975-1004

Brauner N., Rovinsky J., Maron D.M., 1996, *Determination of the Interface Curvature in Stratified Two-Phase Systems by Energy Considerations,* Int. J. of Multiphase Flow, Vol. 22, pp. 1167-1185

Cai J.Y., Gopal M., Jepson W.P., 1999, *Investigation of Flow Regime Transitions in Large-Diameter Inclined Pipes,* Journal of Energy Ressources Technology, Transactions ASME, Vol. 121, No. 2, June 1999, pp. 91-95

Chen H.J., Kouba G.E., Fouchi M.S., Fu B., Rey D.G., 2000, *DRA for Gas Pipelining Successful in Gulf of Mexico Trial,* Oil & Gas Journal, June 5, 2000

Chen X.T., Cai X.D., Brill J.P., 1997, *Gas-Liquid Stratified Wavy Flow in Horizontal Pipelines,* J. of Energy Ressources Technology, Vol. 119

Cheremisinoff N.P., Davis E.J., 1979, *Stratified Turbulent-Turbulent Gas-Liquid Flow,* AIChE Journal, Vol. 25, No. 1, January 1979

Chupin G., Nydal O.J., 2003a, *An Experimental Study of Air/Oil/Water Pipe Flow at Low Liquid Loading,* 11th International Conference on Multiphase Flow, Multiphase 03, San Remo, Italy, June 11-13, 2003

Chupin G., Nydal O.J., 2003b, *Stratified Gas/Liquid Flow at Low Liquid Loading,* 2nd International Conference on Heat Transfer, Fluid Mechanics and Thermodynamics, Livingstone, Zambia, June 23-26, 2003

Cochran S., Gudimetia R., Choate T., Harun A., Nelson S., Wallace B., 2003, *Flow Assurance Comparison of Two Long Distance Gas Tiebacks: Canyon Express and Scarab/*

Saffron, 11th International Conference on Multiphase Flow, Multiphase 03, San Remo, Italy, 11-13 June, 2003

Cohen L.S., Hanratty T.J., 1968, *Effects of Waves at a Gas-Liquid Interface on a Turbulent Air Flow,* J. Fluid Mech., Vol. 31, Part 3, pp. 467-479

Colebrook C., 1939, *Turbulent Flow in Pipes with Particular Reference to the Transition Regime between Smooth and Rough Pipe Laws,* Institution of Civ. Eng. Journal, Vol. 11, pp. 133-156, paper No. 5204

Collier J.G., Hewitt G.F., 1961, *Data on The Vertical Flow of Air-Water Mixtures in the Annular and Dispersed Flow Regions. Part II: Film Thickness and Entrainment Data and Analysis of Pressure Drop Measurements,* Trans. Inst. Chem. Eng., Vol. 39, pp. 127-144

Craik A.D.D., 1966, *Wind-Generated Waves in Thin Liquid Films,* J. Fluid Mech., Vol. 26, Part 2, pp. 369-392

Decarre S., Fabre J., 1997, *Etude sur la Prédiction de l'Inversion de Phase,* Revue de l'Institut Français du Pétrole, Vol. 52, No. 4, Juillet-Août 1997

De Gennes P.G., 1985, *Wetting: Statics and Dynamics*, Reviews of Modern Physics, Vol. 57, No. 3, Part 1, July 1985, pp. 827-863

Doebelin E.O., 1990, *Measurement Systems, Application and Design, Fourth Edition*, McGraw-Hill International Editions

Eck B., 1973, *Technische Strömunglehre,* Springer, New York

Elseth G., Holm H., Munaweera S., Duchet-Suchaux P., Vandersippe W., 2003, *High Pressure Recombined Gas-Condensate-Water Flow at Inclined Conditions*, 11th International Conference on Multiphase 03, San Remo, Italy, June 11-13, 2003

Espedal M., 1998, *An Experimental Investigation of Stratified Two-Phase Pipe Flow at Small Inclinations,* PhD dissertation, Department of Mechanical Engineering, NTNU

Fabre J., Masbernat L., Fernandez-Flores R., Suzanne C., 1987, *Stratified Flow, Part II: Interfacial and Wall Shear Stress,* Multiphase Science and Technology, No. 8

Fairhurst C.P., Barrett N., 1997, *Oil/Water/Gas Transport in Undulating Pipelines - Field Observations, Experimental Data, and Hydraulic Model Comparisons,* SPE 38811

Fernandes R., 2003, *Multiphase Drag Reduction in Horizontal Flows,* 11th International Conference on Multiphase Flow, Multiphase 03, San Remo, Italy, June 11-13, 2003

Flores A.G., Crowe K.E., Griffith P., 1995, *Gas-Phase Secondary Flow in Horizontal, Stratified and Annular Two-Phase Flow*, Int. J. of Multiphase Flow, Vol. 21, pp. 207-221

Furukawa H., Kohda K., Suzukawa Y., 1987, *Evaluation of Compositional Two-Phase Liquid Holdup and Pressure-Loss Correlation,* 1987 ASME Pipeline Engineering Symposium ETCE, Dallas, Tx

Gill L.E., Hewitt G.F., Lacey P.M.C., 1965, *Data on the Upwards Annular Flow of Air-Water Mixtures,* Chemical Engineering Science, Vol. 20, pp. 71-88

Gould T.L., Ramsey E.L., 1975, *Design of Offshore Gas Pipelines Accounting for Two-Phase Flow,* SPE 4844

Gregory G.A., Aziz K., 1975, *Design of Pipelines for Multiphase (Gas-Condensate) Flow,* Journal of Canadian Petroleum Technology, July-September 1975

Grolman E., 1994, *Gas-Liquid Flow with Low Liquid Loading in Slightly Inclined Pipes,* PhD dissertation, University of Amsterdam

Grolman E., Fortuin J.M.H., 1997, *Gas-Liquid Flow in Slightly Inclined Pipes,* Chemical Engineering Science, Vol. 52, No. 24, pp. 4461-4471

Hall A.R., 1992, *Multiphase Flow of Oil, Water and Gas in Horizontal Pipes,* PhD Dissertation, Imperial College of Science, Technology and Medicine, University of London

Hamersma P.J., Hart J., 1987, *A Pressure Drop Correlation for Gas/Liquid Pipe Flow with a Small Liquid Holdup,* Chemical Engineering Science, Vol. 42, No. 5, pp. 1187-1196

Hand N.P., Spedding P.L., Ralph S.J., 1991, *The Effect of Surface Tension on Flow Pattern, Holdup and Pressure Drop during Horizontal Air-Water Pipe Flow at Atmospheric Conditions,* The Chemical Engineering Journal, Vol. 48, pp. 197-210

Hanratty T.J., 1991, *Separated Flow Modelling and Interfacial Transport Phenomena,* Applied Scientific Research, Vol. 48, pp. 353-390

Hart J., Hamersma P.J., Fortuin J.M.H., 1989, *Correlations Predicting Frictional Pressure Drop and Liquid Holdup during Horizontal Gas-Liquid Pipe Flow with a Small Liquid Holdup,* Int. J. of Multiphase Flow, Vol. 15, pp. 947-964

Helleren T., 1999, *Gass-Olje-Vann Slugstrømning (Gas-Oil-Water Slug Flow),* Project work, Norwegian University of Science and Technology, Trondheim, Norway (in Norwegian)

Hewitt G.F., Hall-Taylor N.S., 1970, *Annular Two-Phase Flow,* First Edition, Pergamon Press

Hewitt G.F., King I., Lovegrove P.C., 1963, *Holdup and Pressure Drop Measurements in the Two-Phase Annular Flow of Air-Water Mixtures,* British Chemical Engineering, Vol. 8, No. 5, pp. 311-318

Hope P.M., Nelson R.G., 1977, *Improved Calculations Aid Design of Wet Gas Pipelines,* The Oil and Gas Journal, Oct. 31, 1977

Håland S.E., 1983, *Simple and Explicit Formulas for the Friction Factor in Turbulent Pipe Flow,* J. of Fluids Engineering, Vol. 105, No. 89

Ioannou K., Nydal O.J., Angeli P., 2003, *Phase Inversion in Liquid-Liquid Concentrated Dispersions,* Technical Report, Norwegian University of Science and Technology, Trondheim, Norway

Ishii M., Mishima K., 1989, *Droplet Entrainment Correlation in Annular Two-Phase Flow,* Int. J. Heat Mass Transfer, Vol. 32, No. 10, pp. 1835-1846

Kang. C., Jepson W.P., 1999, *Multiphase Flow Conditioning Using Drag-Reducing Agents,* SPE 56569

Kang C., Vansko R.M., Green A.S., Kerr H., Jepson W.P., 1998, *Effect of Drag-Reducing Agents in Multiphase Flow Pipelines,* Journal of Energy Ressources Technology, Transactions ASME, Vol. 120, No. 1, pp. 15-19

Khor S.H., Mendes-Tatsis M.A., Hewitt G.F., 1997, *One-Dimensional Modelling of Phase Holdups in Three-Phase Stratified Flow,* Int. J. of Multiphase Flow, Vol. 23, No. 5, pp. 885-897

Kvernvold O., Friisk H., Søntvedt T., 1981, *Entrainment of Settled Corrosive Water in Oil. Contact Angles and Drop off Angles for Water Droplets on Duran Glass, Acrylic, C-Steel and Stainless Steel,* Technical Report No. 81-0368, Project No. 433001, Det Norske Veritas

Lahey R.T, Acikgös M., França F., 1992, *Global Volumetric Phase Fractions in Horizontal Three-Phase Flows,* AIChE Journal, Vol. 38, No. 7, pp. 1049-1058

Langsholt M., Holm H., 2001, *Oil-Water-Gas Flow in Steeply Inclined Pipes,* 10th International Conference on Multiphase Flow, Multiphase '01, Cannes France, June 13-15, 2001

Lee A.H., Sun J.Y., Jepson W.P., 1993, *Study of Flow Regime Transition of Oil-Water-Gas Mixtures in Horizontal Pipelines,* 3rd International Offshore and Polar Engineering Conference, Singapore, pp. 159-164

Lunde K., Nossen J., 1998, *Self-Aeration and Drag Reduction in Stratified, Two-Phase Pipe Flow,* 3rd Int. Conf. on Multiphase Flow, June 8-12, 1998, Lyon, France

Lunde K., Nuland S., Lindelem M., 1993, *Aspects of Three-Phase Flows in Gas Pipelines,* 6th International Conference on Multiphase Flow, Cannes 1993, pp. 291-307

Mc Cain W.D. Jr., 1990, *The Properties of Petroleum Fluids*, Second Edition, PennWell Books

Mannes T., Urdahl O., 1997, *The Effect of Chemicals on Flow Characteristics in a Condensate-Water Pipeline,* BHR Group 1997

Matlab Release 13, 2002, *User's Manual, Matlab Version 6.5,* MathWorks Inc.

Meng W., 1999, *Low Liquid Loading Gas-Liquid Two-Phase Flow in Near-Horizontal Pipes,* PhD dissertation, University of Tulsa

Meng W., Chen X.T., Kouba G., Sarica. C., Brill J.P., 1999, *Experimental Study of Low Liquid Loading Gas-Liquid Flow in Near Horizontal Pipes,* SPE 56466, 1999 SPE Annual Technical Conference and Exhibition, Houston, Texas, Oct. 3-6, 1999

Miesen R., Bendiks J.B., 1995, *Hydrodynamic Stability of a Sheared Liquid Film,* J. Fluid Mech., Vol. 301, pp. 175-202

Miles J.W., 1960, *The Hydrodynamic Stability of a Thin Film of Liquid in Uniform Shearing Motion,* J. Fluid Mech., Vol. 8, pp. 593-610

Minami K., Brill J.P., 1983, *Liquid Holdup in Wet-Gas Pipelines,* University of Tulsa

Moody L.F., 1944, *Friction Factors for Pipe Flow,* Transactions of the ASME, Nov. 1944, pp. 671-684

Neogi S., Lee A.H., Jepson W.P., 1994, *A Model for Multiphase (Gas-Water-Oil) Stratified Flow in Horizontal Pipelines,* SPE 28799

Newton C.H., Behnia M., 1998, *On the Use of the Stratified Momentum Balance for the Deduction of Shear Stress in Horizontal Gas-Liquid Pipe Flow,* Int. J. of Multiphase Flow, Vol. 24, pp. 1407-1423

Ng T.S., Lawrence C.J., Hewitt G.F., 1999, *Exact Interface Shape Calculations for a Two-Phase Stratified Flow System,* Multiphase flow systems report WASP/46, MPS/122, Imperial College, London

Ng T.S., Lawrence C.J., Hewitt G.F., 2001, *Interface Shapes for Two-Phase Laminar Stratified Flow in a Circular Pipe, Brief Communication,* Int. J. of Multiphase Flow, Vol. 27., pp. 1301-1311

Nikuradse J., 1933, *Stromungsgesetze in Rauhen Rohren,* In Forshungsheft 361, Vol. B., VDI Verlag Berlin. Translated in NACA Technical Memorandum No. 1292, 1950

Nuland S.T., Lingelem M.N., 1993, *Two-Phase Flow in Inclined Pipes at High Gas Density,* 1993 OMAE, Volume V: Pipeline Technology, ASME, pp. 411-425

Nuland S., Skarsvåg K., Sæther G., Fuchs P., 1991, *Phase Fractions in Three-Phase Gas-Oil-Water Flow,* 5th Int. Conference on Multiphase Production, Cannes, France, June 1991

Oliemans R.V.A., 1987, *Modelling of Gas-Condensate Flow in Horizontal and Inclined Pipes,* 1987 ASME Pipeline Engineering Symposium, ETCE, Dallas, Tx

Olive N.R., Zhang H.Q., Redus C.L., Brill J.P., 2001, *Experimental Study of Low Liquid Loading Gas-Liquid Flow in Near Horizontal Pipes,* ETCE 2001, Feb. 5-7, 2001, Houston

Pan L., 1996, *High Pressure Three-Phase (Gas/Liquid/Liquid) Flow,* PhD dissertation, Dep. of Chemical Engineering, Imperial College of Science, Technology and Medicine, London

Pettersen B.H., Langsholt M., 2001, *Pressure Drop and Wall Wetting; The Effect of Pipe Wall Material in Multiphase Flow,* 10th Int. Conference on Multiphase Flow, Multiphase 01, Cannes, France, pp. 177-192

Reid R.C., Prausnitz J.M., Poling B.E., 1988, *The Properties of Gases and Liquids, Fourth Edition,* McGraw-Hill International Editions, Chemical Engineering Series, p. 439

Roberts I., 1996, *Modelling and Experimental Studies of Transient Stratified Multiphase Flows,* PhD dissertation, Imperial College of Science, Technology and Medicine, University of London

Shea R.H., Rasmussen J., Hedne P., Malnes D., 1997, *Holdup Predictions for Wet-Gas Pipelines Compared,* Oil & Gas Journal, May 19, 1997

Sletfjerding E., 1999, *Friction Factor in Smooth and Rough Gas Pipelines,* PhD dissertation, Norwegian University of Science and Technology, Trondheim, Norway

Smith R.V., Miller J.S., Ferguson J.W., 1956, *Flow of Natural Gas Through Experimental Pipe Lines and Transmission Lines,* AGA Monograph 9, US Bureau of Mines

Sobocinski D.B., Huntington R.L., 1958, *Concurrent Flow of Air, Gas-Oil, and Water in a Horizontal Pipe,* Transactions of the ASME, pp. 252-256

Solbakken S., Andersson H.I., 2000, *Turbulent Pipe Flow with a Laminar Liquid Film at the Wall*, Technical Report, Norwegian University of Science and Technology, Trondheim, Norway

Solbakken S., Andersson H.I, 2002a, *On the Potential Drag Reduction in Gas Pipelines Using a Thin Liquid Film at the Wall, a Parameter Study,* Technical Report, Norwegian University of Science and Technology, Trondheim, Norway

Solbakken S., Andersson H.I., 2002b, *On the Stability of Sheared Liquid Films, a Literature Review,* Technical Report, Norwegian University of Science and Technology, Trondheim, Norway

Solbakken T., Schuller R.B., 2001, *Multiphase Flow Experiments on a High Pressure Recombined Gas/Condensate System,* 10th Int. Conference on Multiphase Flow, Multiphase 01, BHR group 2001, Cannes, France, pp. 163-176

Spedding P.L., Hand N.P., 1997, Prediction in Stratified Gas-Liquid Co-Current Flow in Horizontal Pipelines, Int. J. Heat Mass Transfer, Vol. 40, No. 8, pp. 1923-1935

Taitel Y., Dukler A.E., 1976, *A Model for Predicting Flow Regime Transitions in Horizontal and Near Horizontal Gas-Liquid Flow,* AIChE Journal, Vol. 22, No.1 pp. 47-55

Taitel Y., Barnea D., Brill J.P., 1995, *Stratified Three-Phase Flow in Pipes,* Int. J. of Multiphase Flow, Vol. 21, pp. 53-60

Tayebi D., Nuland S., Fuchs P., 1999, *Droplet Transport in Oil/Gas and Water/Gas Flow at High Gas Densities,* Int. J. of Multiphase Flow, Vol. 26, pp. 741-761

Tullius L., 2000, *A Study of Drag Reducing Agents in Multiphase Flow in Large Diameter Horizontal Pipelines,* PhD dissertation, Ohio University

Uhl A.E., 1975, *Discussion: Design of Offshore Gas Pipelines Accounting for Two-Phase Flow,* J. of Pet. Technology, pp. 648-652

Uhl A.E., Bischoff K.B., Bukacek R.F., Burket P.V., Ellington R.T., Kniebes D.V., Staats W.R., 1965, *Steady Flow in Gas Pipelines,* American Gas Association, Technical Report No. 10

Utvik O.H., Valle A., Rinde T., 1998, *Pressure Drop, Flow Pattern and Slip for a Multi-Phase Crude Oil-Water-Hydrocarbon Gas System,* 3rd Int. Conf. on Multiphase Flow, ICMF'98 Lyon, France, June 8-12, 1998

Valle A., 1998, *Multiphase Pipeline Flows in Hydrocarbon Recovery,* Multiphase Science and Technology, Vol. 10, No. 1, pp. 1-139

Vlachos N.A., S.V., Karabelas A.J., 1999, *Brief Communication - Prediction of Holdup, Axial Pressure Gradient and Wall Shear Stress in Wavy Stratified and Stratified/Atomization Gas/Liquid Flow,* Int. J. of Multiphase Flow, Vol. 25, pp. 365-376

Wallis G.B., 1969, *One-Dimensional Two-Phase Flow,* McGraw-Hill, Inc., pp. 318-323

Wu H.L., Pots B.F.M., Hollenberg J.F., Meerhoff R., 1987, *Flow Pattern Transitions in Two-Phase Gas/Condensate Flow at High Pressure in an 8-inch Horizontal Pipe,* 3rd Int. Conf. on Multiphase Flow, Paper A2, The Hague, Netherlands, May 18-20, 1987

Appendix A Tabulated experimental data

A.1 Introduction

This appendix contains the following tabulated data:

- Steady-state pressure drop and phase fraction measurements (Section A.2).
- Measurements for the transient film thinning experiments (Section A.3).
- Measured and computed shear forces for the case of the acrylic pipe in two-phase flow as discussed in Chapter 6 (Section A.4).

The flow regime code for the steady-state experiments is described in Chapter 7.

A.2 Tabulated data, steady-state measurements

Table A–1: Serie #1, Acrylic pipe

Exp.	U_{SG}	U_{SL}	WF	U_{SW}	U_{SO}	H_W		H_O		H_{TOT}		Re_G	Re_O	Re_W	dP/dx	T	Visual
#	m/s	m/s	%	m/s	m/s	ml	%	ml	%	ml	%	-	-	-	Pa/m	^oC	
1 U_{SL} sensitivity WF = 0%																	
1	14.80	0.0400	0	0.0000	0.0400	0	0.00	665	4.93	665	4.93	6.0E+04	4.3E+03	-	111	21.6	ST4o
2	14.80	0.0088	0	0.0000	0.0088	0	0.00	235	1.71	235	1.71	5.9E+04	1.4E+03	-	73	-	ST4
3	14.80	0.0071	0	0.0000	0.0071	0	0.00	207	1.51	207	1.51	5.9E+04	1.2E+03	-	71	-	ST4
4	14.80	0.0059	0	0.0000	0.0059	0	0.00	186	1.36	186	1.36	5.9E+04	1.0E+03	-	68	-	ST4
5	14.80	0.0047	0	0.0000	0.0047	0	0.00	166	1.21	166	1.21	5.9E+04	8.3E+02	-	65	-	ST4
6	14.80	0.0024	0	0.0000	0.0024	0	0.00	104	0.76	104	0.76	5.9E+04	4.9E+02	-	58	-	ST4
7	14.80	0.0018	0	0.0000	0.0018	0	0.00	88	0.64	88	0.64	5.9E+04	3.9E+02	-	55	-	ST4
8	14.80	0.0012	0	0.0000	0.0012	0	0.00	68	0.50	68	0.50	5.9E+04	2.8E+02	-	55	-	ST3
9	14.80	0.0006	0	0.0000	0.0006	0	0.00	42	0.31	42	0.31	5.9E+04	1.7E+02	-	53	-	ST2
10	14.80	0.0004	0	0.0000	0.0004	0	0.00	35	0.25	35	0.25	5.9E+04	1.3E+02	-	51	-	ST2
11	14.80	0.0003	0	0.0000	0.0003	0	0.00	26	0.19	26	0.19	5.9E+04	1.0E+02	-	52	20.9	ST1
1 U_{SL} sensitivity WF = 20%																	
12	14.80	0.0400	20	0.0080	0.0320	150	1.11	570	4.22	720	5.34	6.0E+04	3.4E+03	3.6E+03	106	-	SST4o
13	14.80	0.0118	20	0.0024	0.0094	43	0.31	244	1.78	287	2.09	6.0E+04	1.4E+03	1.6E+03	92	-	DOST4o
14	14.80	0.0112	20	0.0022	0.0090	42	0.31	236	1.72	278	2.03	6.0E+04	1.3E+03	1.6E+03	91	-	DOST4o
15	14.80	0.0100	20	0.0020	0.0080	35	0.25	207	1.51	242	1.76	5.9E+04	1.2E+03	1.5E+03	89	-	DOST4o
16	14.80	0.0088	20	0.0018	0.0071	33	0.24	204	1.49	237	1.73	5.9E+04	1.1E+03	1.3E+03	87	-	DOST4o
17	14.80	0.0071	20	0.0014	0.0057	27	0.20	176	1.28	203	1.48	5.9E+04	9.3E+02	1.1E+03	83	-	DOST4o
18	14.80	0.0059	20	0.0012	0.0047	21	0.15	154	1.12	175	1.27	5.9E+04	8.2E+02	1.0E+03	82	-	DOST4o

Table A–1: Serie #1, Acrylic pipe

Exp.	U_{SG}	U_{SL}	WF	U_{SW}	U_{SO}	H_W		H_O		H_{TOT}		Re_G	Re_O	Re_W	dP/dx	T	Visual
#	m/s	m/s	%	m/s	m/s	ml	%	ml	%	ml	%	-	-	-	Pa/m	^oC	
19	14.80	0.0047	20	0.0009	0.0038	19	0.14	135	0.98	154	1.12	5.9E+04	6.8E+02	8.6E+02	78	-	DOST4
20	14.80	0.0029	20	0.0006	0.0024	12	0.09	102	0.74	114	0.83	5.9E+04	4.7E+02	6.3E+02	69	-	DOST4
21	14.80	0.0018	20	0.0004	0.0014	9	0.06	76	0.56	84	0.62	5.9E+04	3.1E+02	4.2E+02	62	21.3	DOST4
1 U_{SL} sensitivity WF = 50%																	
22	14.80	0.0400	50	0.0200	0.0200	335	2.48	370	2.74	705	5.22	6.0E+04	2.2E+03	6.9E+03	113	21.0	SST4o
23	14.80	0.0122	50	0.0061	0.0061	117	0.87	157	1.16	274	2.03	6.0E+04	9.1E+02	3.0E+03	100	21.0	SST4o
24	14.80	0.0112	50	0.0056	0.0056	-	-	-	-	-	-	-	-	-	100	20.9	SST4o
25	14.80	0.0088	50	0.0044	0.0044	89	0.66	129	0.96	218	1.62	5.9E+04	7.1E+02	2.4E+03	97	20.2	SST4o
26	14.80	0.0071	50	0.0035	0.0035	75	0.56	111	0.82	186	1.38	5.9E+04	6.0E+02	2.0E+03	94	20.8	SST4o
27	14.80	0.0059	50	0.0029	0.0029	51	0.37	102	0.74	153	1.11	5.9E+04	5.4E+02	1.9E+03	91	21.7	DOST4o
28	14.80	0.0047	50	0.0024	0.0024	48	0.36	98	0.73	146	1.08	5.9E+04	4.3E+02	1.6E+03	87	20.4	DOST4o
29	14.80	0.0029	50	0.0015	0.0015	53	0.39	85	0.63	138	1.02	5.9E+04	2.8E+02	9.5E+02	78	21.1	DOST4
30	14.80	0.0012	50	0.0006	0.0006	15	0.11	43	0.32	58	0.43	5.9E+04	1.5E+02	5.8E+02	65	21.0	DOST4
31	14.80	0.0006	50	0.0003	0.0003	10	0.07	29	0.21	39	0.29	5.9E+04	8.5E+01	3.3E+02	59	21.0	DOST4
1 U_{SL} sensitivity WF = 100%																	
32	14.80	0.0400	100	0.0400	0.0000	630	4.67	0	0.00	630	4.67	6.0E+04	-	1.1E+04	120	21.0	ST4o
33	14.80	0.0088	100	0.0088	0.0000	216	1.57	0	0.00	216	1.57	5.9E+04	-	3.6E+03	77	-	ST4
34	14.80	0.0071	100	0.0071	0.0000	180	1.31	0	0.00	180	1.31	5.9E+04	-	3.0E+03	70	-	ST4
35	14.80	0.0059	100	0.0059	0.0000	150	1.09	0	0.00	150	1.09	5.9E+04	-	2.7E+03	67	-	ST4
36	14.80	0.0047	100	0.0047	0.0000	130	0.95	0	0.00	130	0.95	5.9E+04	-	2.3E+03	65	-	ST4
37	14.80	0.0029	100	0.0029	0.0000	111	0.81	0	0.00	111	0.81	5.9E+04	-	1.5E+03	58	-	ST3
38	14.80	0.0018	100	0.0018	0.0000	-	-	-	-	-	-	-	-	-	57	-	ST2

Table A–1: Serie #1, Acrylic pipe

Exp.	U_{SG}	U_{SL}	WF	U_{SW}	U_{SO}	H_W		H_O		H_{TOT}		Re_G	Re_O	Re_W	dP/dx	T	Visual
#	m/s	m/s	%	m/s	m/s	ml	%	ml	%	ml	%	-	-	-	Pa/m	^oC	
39	14.80	0.0012	100	0.0012	0.0000	55	0.40	0	0.00	55	0.40	5.9E+04	-	7.5E+02	52	-	ST2
40	14.80	0.0006	100	0.0006	0.0000	34	0.25	0	0.00	34	0.25	5.9E+04	-	4.4E+02	50	-	ST2
41	14.80	0.0004	100	0.0004	0.0000	27	0.20	0	0.00	27	0.20	5.9E+04	-	3.6E+02	49	-	ST1
42	14.80	0.0002	100	0.0002	0.0000	16	0.12	0	0.00	16	0.12	5.9E+04	-	2.1E+02	49	19.8	ST1

Table A–2: Serie #1, Steel pipe

Exp.	U_{SG}	U_{SL}	WF	U_{SW}	U_{SO}	H_W		H_O		H_{TOT}		Re_G	Re_O	Re_W	dP/dx	T	Visual
#	m/s	m/s	%	m/s	m/s	ml	%	ml	%	ml	%	-	-	-	Pa/m	^oC	
1 U_{SL} sensitivity WF = 0%																	
43	14.80	0.0400	0	0.0000	0.0400	-	-	645	5.11	645	5.11	6.0E+04	4.3E+03	-	103	-	ST4o
44	14.80	0.0088	0	0.0000	0.0088	-	-	220	1.74	220	1.74	5.9E+04	1.4E+03	-	69	20.6	ST4o
45	14.80	0.0071	0	0.0000	0.0071	-	-	188	1.49	188	1.49	5.9E+04	1.2E+03	-	66	21.1	ST4o
46	14.80	0.0059	0	0.0000	0.0059	-	-	176	1.39	176	1.39	5.9E+04	9.9E+02	-	640	19.9	ST4
47	14.80	0.0047	0	0.0000	0.0047	-	-	155	1.23	155	1.23	5.9E+04	8.3E+02	-	60	20.8	ST3
48	14.80	0.0029	0	0.0000	0.0029	-	-	118	0.93	118	0.93	5.9E+04	5.7E+02	-	56	20.6	ST3
49	14.80	0.0018	0	0.0000	0.0018	-	-	82	0.65	82	0.65	5.9E+04	3.9E+02	-	52	20.5	ST3
50	14.80	0.0012	0	0.0000	0.0012	-	-	69	0.54	69	0.54	5.9E+04	2.7E+02	-	50	20.6	ST3
51	14.80	0.0006	0	0.0000	0.0006	-	-	41	0.32	41	0.32	5.9E+04	1.6E+02	-	49	21.1	ST3
52	14.80	0.0004	0	0.0000	0.0004	-	-	33	0.26	33	0.26	5.9E+04	1.3E+02	-	48	20.4	ST3
53	14.80	0.0003	0	0.0000	0.0003	-	-	26	0.20	26	0.20	5.9E+04	1.0E+02	-	48	20.6	ST3

Table A–2: Serie #1, Steel pipe

Exp.	U_{SG}	U_{SL}	WF	U_{SW}	U_{SO}	H_W		H_O		H_{TOT}		Re_G	Re_O	Re_W	dP/dx	T	Visual
#	m/s	m/s	%	m/s	m/s	ml	%	ml	%	ml	%	-	-	-	Pa/m	^oC	
1 U_{SL} sensitivity WF = 20%																	
54	14.80	0.0400	20	0.0080	0.0320	175	1.39	510	4.04	685	5.42	6.0E+04	3.4E+03	3.4E+03	94	-	SST4o
55	14.80	0.0122	20	0.0024	0.0098	82	0.65	213	1.68	294	2.33	6.0E+04	1.4E+03	1.3E+03	65	20.6	SST4o
56	14.80	0.0112	20	0.0022	0.0090	73	0.58	190	1.50	263	2.08	6.0E+04	1.3E+03	1.3E+03	64	20.5	SST4o
57	14.80	0.0100	20	0.0020	0.0080	66	0.52	180	1.42	246	1.95	5.9E+04	1.2E+03	1.2E+03	63	19.8	SST4
58	14.80	0.0088	20	0.0018	0.0071	64	0.51	167	1.32	231	1.83	5.9E+04	1.1E+03	1.0E+03	61	20.4	SST4
59	14.80	0.0071	20	0.0014	0.0057	56	0.44	148	1.17	204	1.61	5.9E+04	9.1E+02	8.7E+02	59	20.4	SST4
60	14.80	0.0059	20	0.0012	0.0047	49	0.39	110	0.87	159	1.26	5.9E+04	8.3E+02	7.6E+02	57	19.9	SST4
61	14.80	0.0047	20	0.0009	0.0038	40	0.32	115	0.91	155	1.23	5.9E+04	6.6E+02	6.5E+02	56	20.4	SST3
62	14.80	0.0029	20	0.0006	0.0024	32	0.25	58	0.46	90	0.71	5.9E+04	5.0E+02	4.4E+02	51	20.0	SST3
63	14.80	0.0011	20	0.0002	0.0009	14	0.11	50	0.39	64	0.50	5.9E+04	2.1E+02	2.2E+02	50	20.5	SST3
1 U_{SL} sensitivity WF = 50%																	
64	14.80	0.0400	50	0.0200	0.0200	390	3.09	248	1.96	638	5.05	6.0E+04	2.2E+03	6.4E+03	86	-	SST4o
65	14.80	0.0122	50	0.0061	0.0061	162	1.28	102	0.80	264	2.09	6.0E+04	9.1E+02	2.6E+03	62	22.0	SST3
66	14.80	0.0088	50	0.0044	0.0044	127	1.01	89	0.70	216	1.71	5.9E+04	7.0E+02	2.1E+03	58	21.8	SST3
67	14.80	0.0071	50	0.0035	0.0035	109	0.86	75	0.59	184	1.46	5.9E+04	5.9E+02	1.7E+03	56	21.9	SST3
68	14.80	0.0059	50	0.0029	0.0029	92	0.73	75	0.59	167	1.32	5.9E+04	5.1E+02	1.5E+03	57	20.6	SST3
69	14.80	0.0047	50	0.0024	0.0024	86	0.68	62	0.49	148	1.17	5.9E+04	4.3E+02	1.3E+03	52	21.9	SST3
70	14.80	0.0029	50	0.0015	0.0015	52	0.41	43	0.34	95	0.75	5.9E+04	3.1E+02	9.3E+02	50	21.9	SST3
71	14.80	0.0011	50	0.0006	0.0006	30	0.24	29	0.23	59	0.46	5.9E+04	1.4E+02	4.2E+02	46	21.9	SST2
72	14.80	0.0006	50	0.0003	0.0003	21	0.17	24	0.19	45	0.36	5.9E+04	8.3E+01	2.7E+02	46	22.1	SST1
1 U_{SL} sensitivity WF = 100%																	

Table A–2: Serie #1, Steel pipe

Exp.	U_{SG}	U_{SL}	WF	U_{SW}	U_{SO}	H_W		H_O		H_{TOT}		Re_G	Re_O	Re_W	dP/dx	T	Visual
#	m/s	m/s	%	m/s	m/s	ml	%	ml	%	ml	%	-	-	-	Pa/m	^oC	
73	14.80	0.0400	100	0.0400	0.0000	575	4.55	-	-	575	4.55	6.0E+04	-	1.1E+04	110	-	ST4o
74	14.80	0.0088	100	0.0088	0.0000	203	1.61	-	-	203	1.61	5.9E+04	-	3.5E+03	70	16.7	ST4
75	14.80	0.0071	100	0.0071	0.0000	180	1.42	-	-	180	1.42	5.9E+04	-	2.9E+03	66	16.7	ST4
76	14.80	0.0059	100	0.0059	0.0000	160	1.27	-	-	160	1.27	5.9E+04	-	2.6E+03	63	16.7	ST4
77	14.80	0.0047	100	0.0047	0.0000	134	1.06	-	-	134	1.06	5.9E+04	-	2.2E+03	60	16.7	ST4
78	14.80	0.0029	100	0.0029	0.0000	101	0.80	-	-	101	0.80	5.9E+04	-	1.5E+03	54	16.9	ST4
79	14.80	0.0018	100	0.0018	0.0000	79	0.63	-	-	79	0.63	5.9E+04	-	9.8E+02	51	16.8	ST3
80	14.80	0.0012	100	0.0012	0.0000	66	0.52	-	-	66	0.52	5.9E+04	-	6.9E+02	47	16.8	ST3
81	14.80	0.0006	100	0.0006	0.0000	42	0.33	-	-	42	0.33	5.9E+04	-	4.0E+02	46	16.7	ST3
82	14.80	0.0004	100	0.0004	0.0000	26	0.21	-	-	26	0.21	5.9E+04	-	3.5E+02	45	16.7	ST3
83	14.80	0.0002	100	0.0002	0.0000	18	0.14	-	-	18	0.14	5.9E+04	-	2.0E+02	45	18.0	ST3

Table A–3: Serie #1, Epoxy coated steel pipe

Exp.	U_{SG}	U_{SL}	WF	U_{SW}	U_{SO}	H_W		H_O		H_{TOT}		Re_G	Re_O	Re_W	dP/dx	T	Visual
#	m/s	m/s	%	m/s	m/s	ml	%	ml	%	ml	%	-	-	-	Pa/m	^oC	
1 U_{SL} sensitivity WF = 0%																	
84	14.80	0.0088	0	0.0000	0.0088	-	-	209	1.74	209	1.74	5.9E+04	1.4E+03	-	68	-	-
85	14.80	0.0071	0	0.0000	0.0071	-	-	186	1.55	186	1.55	5.9E+04	1.1E+03	-	66	-	-
86	14.80	0.0059	0	0.0000	0.0059	-	-	176	1.47	176	1.47	5.9E+04	9.7E+02	-	62	21.0	-
87	14.80	0.0029	0	0.0000	0.0029	-	-	134	1.12	134	1.12	5.9E+04	5.3E+02	-	55	20.9	-
88	14.80	0.0018	0	0.0000	0.0018	-	-	87	0.72	87	0.72	5.9E+04	3.7E+02	-	51	21.4	-

Table A–3: Serie #1, Epoxy coated steel pipe

Exp.	U_{SG}	U_{SL}	WF	U_{SW}	U_{SO}	H_W		H_O		H_{TOT}		Re_G	Re_O	Re_W	dP/dx	T	Visual
#	m/s	m/s	%	m/s	m/s	ml	%	ml	%	ml	%	-	-	-	Pa/m	^oC	
89	14.80	0.0012	0	0.0000	0.0012	-	-	68	0.57	68	0.57	5.9E+04	2.7E+02	-	50	-	-
90	14.80	0.0006	0	0.0000	0.0006	-	-	52	0.43	52	0.43	5.9E+04	1.5E+02	-	48	22.3	-
91	14.80	0.0004	0	0.0000	0.0004	-	-	40	0.33	40	0.33	5.9E+04	1.2E+02	-	48	21.9	-
92	14.80	0.0003	0	0.0000	0.0003	-	-	35	0.29	35	0.29	5.9E+04	8.8E+01	-	47	22.6	-
1 U_{SL} sensitivity WF = 20%																	
93	14.80	0.0122	20	0.0024	0.0098	86	0.72	204	1.70	290	2.42	6.0E+04	1.4E+03	1.3E+03	63	23.0	-
94	14.80	0.0100	20	0.0020	0.0080	52	0.43	197	1.64	249	2.07	6.0E+04	1.2E+03	1.2E+03	62	23.1	-
95	14.80	0.0088	20	0.0018	0.0071	50	0.42	184	1.53	234	1.95	6.0E+04	1.1E+03	1.1E+03	60	23.3	-
96	14.80	0.0071	20	0.0014	0.0057	54	0.45	144	1.20	198	1.65	5.9E+04	9.0E+02	8.7E+02	58	23.4	-
97	14.80	0.0059	20	0.0012	0.0047	40	0.33	142	1.18	182	1.52	5.9E+04	7.7E+02	8.0E+02	56	23.1	-
98	14.80	0.0047	20	0.0009	0.0038	38	0.32	112	0.93	150	1.25	5.9E+04	6.6E+02	6.5E+02	54	23.4	-
99	14.80	0.0029	20	0.0006	0.0024	21	0.17	84	0.70	105	0.87	5.9E+04	4.6E+02	5.0E+02	51	24.3	-
100	14.80	0.0011	20	0.0002	0.0009	18	0.15	70	0.58	88	0.73	5.9E+04	1.8E+02	2.0E+02	48	23.9	-
1 U_{SL} sensitivity WF = 100%																	
101	14.80	0.0088	100	0.0088	0.0000	192	1.60	-	-	192	1.60	5.9E+04	-	3.5E+03	67	19.9	-
102	14.80	0.0071	100	0.0071	0.0000	148	1.23	-	-	148	1.23	5.9E+04	-	3.1E+03	64	23.1	-
103	14.80	0.0059	100	0.0059	0.0000	156	1.30	-	-	156	1.30	5.9E+04	-	2.5E+03	61	22.0	-
104	14.80	0.0029	100	0.0029	0.0000	110	0.92	-	-	110	0.92	5.9E+04	-	1.4E+03	52	-	-
105	14.80	0.0018	100	0.0018	0.0000	80	0.67	-	-	80	0.67	5.9E+04	-	9.5E+02	48	22.1	-
106	14.80	0.0006	100	0.0006	0.0000	35	0.29	-	-	35	0.29	5.9E+04	-	4.2E+02	44	21.7	-
107	14.80	0.0004	100	0.0004	0.0000	42	0.35	-	-	42	0.35	5.9E+04	-	2.9E+02	44	21.6	-
108	14.80	0.0002	100	0.0002	0.0000	20	0.17	-	-	20	0.17	5.9E+04	-	1.9E+02	44	21.7	-

Table A–4: Serie #2.1, acrylic pipe, horizontal

Exp.	U_{SG}	U_{SL}	WF	U_{SW}	U_{SO}	H_W		H_O		H_{TOT}		Re_G	Re_O	Re_W	dP/dx	T	Visual
#	m/s	m/s	%	m/s	m/s	ml	%	ml	%	ml	%	-	-	-	Pa/m	^oC	
2.1 WF sensitivity (pipe pigged prior to experiment)																	
109	14.80	0.0059	5	0.0003	0.0056	8	0.06	181	1.32	189	1.38	5.9E+04	9.4E+02	3.6E+02	72	19.0	DOST4o
110	14.80	0.0059	10	0.0006	0.0053	14	0.10	168	1.22	182	1.33	5.9E+04	9.1E+02	6.0E+02	76	18.0	DOST4o
111	14.80	0.0059	30	0.0018	0.0041	35	0.25	138	1.01	173	1.26	5.9E+04	7.2E+02	1.3E+03	85	18.0	DOST4o
112	14.80	0.0059	35	0.0021	0.0038	46	0.34	134	0.98	180	1.31	5.9E+04	6.6E+02	1.4E+03	86	18.0	DOST4o
113	14.80	0.0059	40	0.0024	0.0035	45	0.33	117	0.85	162	1.18	5.9E+04	6.3E+02	1.6E+03	88	18.0	DOST4o
114	14.80	0.0059	45	0.0027	0.0032	50	0.36	118	0.86	168	1.22	5.9E+04	5.7E+02	1.8E+03	88	16.0	DOST4o
115	14.80	0.0059	60	0.0035	0.0024	65	0.47	88	0.64	153	1.11	5.9E+04	4.3E+02	2.1E+03	93	17.0	DOST4o
116	14.80	0.0059	80	0.0047	0.0012	93	0.68	49	0.36	142	1.03	5.9E+04	2.2E+02	2.5E+03	101	-	DWST4o
117	14.80	0.0059	90	0.0053	0.0006	132	0.96	40	0.29	172	1.25	5.9E+04	1.0E+02	2.5E+03	96	16.0	DWST4o
2.1 WF sensitivity (pipe not pigged prior to experiment)																	
118	14.80	0.0059	10	0.0006	0.0053	-	-	-	-	-	-	-	-	-	75	22.1	DOST4o
119	14.80	0.0059	20	0.0012	0.0047	22	0.16	149	1.10	171	1.27	5.9E+04	8.2E+02	1.0E+03	80	21.7	DOST4o
120	14.80	0.0059	30	0.0018	0.0041	-	-	-	-	-	-	-	-	-	85	21.9	DOST4o
121	14.80	0.0059	40	0.0024	0.0035	-	-	-	-	-	-	-	-	-	88	21.8	DOST4o
122	14.80	0.0059	50	0.0029	0.0029	-	-	-	-	-	-	-	-	-	91	21.7	DOST4o
123	14.80	0.0059	60	0.0035	0.0024	-	-	-	-	-	-	-	-	-	94	21.5	DOST4o
124	14.80	0.0059	70	0.0041	0.0018	84	0.62	72	0.53	156	1.16	5.9E+04	3.2E+02	2.3E+03	80	21.7	SST4o
125	14.80	0.0059	80	0.0047	0.0012	82	0.61	52	0.39	134	0.99	5.9E+04	2.2E+02	2.6E+03	72	21.8	SST4o
126	14.80	0.0059	90	0.0053	0.0006	-	-	-	-	-	-	-	-	-	67	21.7	SST4o

Table A–5: Serie #2.1, acrylic pipe, +1deg. upward

Exp.	U_{SG}	U_{SL}	WF	U_{SW}	U_{SO}	H_W		H_O		H_{TOT}		Re_G	Re_O	Re_W	dP/dx	T	Visual
#	m/s	m/s	%	m/s	m/s	ml	%	ml	%	ml	%	-	-	-	Pa/m	^oC	
2.1 WF sensitivity (pipe pigged prior to experiment)																	
127	14.80	0.0059	0	0.0000	0.0059	-	-	190	1.38	190	1.38	5.9E+04	9.9E+02	-	69	17.0	ST3
128	14.80	0.0059	5	0.0003	0.0056	12	0.09	180	1.31	192	1.40	5.9E+04	9.4E+02	3.1E+02	70	18.0	DOST4o
129	14.80	0.0059	10	0.0006	0.0053	31	0.23	183	1.33	214	1.56	5.9E+04	8.6E+02	4.6E+02	75	17.0	DOST4o
130	14.80	0.0059	20	0.0012	0.0047	37	0.27	163	1.19	200	1.46	5.9E+04	7.8E+02	8.6E+02	82	18.0	DOST4o
131	14.80	0.0059	30	0.0018	0.0041	47	0.34	139	1.01	186	1.36	5.9E+04	7.0E+02	1.2E+03	81	17.0	DOST4o
132	14.80	0.0059	40	0.0024	0.0035	51	0.37	109	0.79	160	1.17	5.9E+04	6.4E+02	1.5E+03	88	17.0	DOST4o
133	14.80	0.0059	50	0.0029	0.0029	63	0.46	116	0.85	179	1.30	5.9E+04	5.1E+02	1.8E+03	90	18.0	DOST4o
134	14.80	0.0059	60	0.0035	0.0024	77	0.56	91	0.66	168	1.22	5.9E+04	4.2E+02	2.0E+03	93	17.0	DOST4o
135	14.80	0.0059	80	0.0047	0.0012	112	0.82	62	0.45	174	1.27	5.9E+04	2.1E+02	2.4E+03	99	16.0	DWST4
136	14.80	0.0059	90	0.0053	0.0006	125	0.91	31	0.23	156	1.14	5.9E+04	1.1E+02	2.6E+03	99	16.0	DWST4
137	14.80	0.0059	100	0.0059	0.0000	167	1.22	-	-	167	1.22	5.9E+04	-	2.6E+03	68	17.0	ST4
2.1 WF sensitivity (pipe not pigged prior to experiment)																	
138	14.80	0.0059	20	0.0012	0.0047	-	-	-	-	-	-	-	-	-	78	20.3	SST4o
139	14.80	0.0059	50	0.0029	0.0029	-	-	-	-	-	-	-	-	-	88	19.8	SST4o
140	14.80	0.0059	60	0.0035	0.0024	-	-	-	-	-	-	-	-	-	92	19.8	SST4o
141	14.80	0.0059	70	0.0041	0.0018	-	-	-	-	-	-	-	-	-	89	19.9	SST4
142	14.80	0.0059	80	0.0047	0.0012	-	-	-	-	-	-	-	-	-	79	19.8	SST4
143	14.80	0.0059	90	0.0053	0.0006	-	-	-	-	-	-	-	-	-	66	20.3	SST4

Table A–6: Serie #2.1, steel pipe, horizontal

Exp.	U_{SG}	U_{SL}	WF	U_{SW}	U_{SO}	H_W		H_O		H_{TOT}		Re_G	Re_O	Re_W	dP/dx	T	Visual
#	m/s	m/s	%	m/s	m/s	ml	%	ml	%	ml	%	-	-	-	Pa/m	^oC	
2.1 WF sensitivity																	
144	14.80	0.0059	5	0.0003	0.0056	17	0.13	154	1.22	171	1.35	5.9E+04	9.5E+02	2.7E+02	61	21.3	SST4
145	14.80	0.0059	10	0.0006	0.0053	29	0.23	139	1.10	168	1.33	5.9E+04	9.1E+02	4.5E+02	59	19.7	SST4
146	14.80	0.0059	30	0.0018	0.0041	66	0.52	108	0.85	174	1.38	5.9E+04	7.0E+02	1.0E+03	57	21.4	SST3
147	14.80	0.0059	40	0.0024	0.0035	79	0.63	87	0.69	166	1.31	5.9E+04	6.1E+02	1.3E+03	56	19.6	SST3
148	14.80	0.0059	60	0.0035	0.0024	108	0.85	50	0.40	158	1.25	5.9E+04	4.2E+02	1.8E+03	57	20.5	SST3
149	15.00	0.0059	70	0.0041	0.0018	128	1.01	47	0.37	175	1.39	6.0E+04	3.0E+02	1.9E+03	58	20.0	SST3
150	14.80	0.0059	80	0.0047	0.0012	138	1.09	34	0.27	172	1.36	5.9E+04	2.0E+02	2.1E+03	58	20.1	SST3
151	14.80	0.0059	90	0.0053	0.0006	142	1.12	15	0.12	157	1.24	5.9E+04	1.1E+02	2.4E+03	61	19.0	SST3
152	14.80	0.0059	95	0.0056	0.0003	143	1.13	5	0.04	148	1.17	5.9E+04	5.4E+01	2.5E+03	62	19.1	SST4

Table A–7: Serie #2.1, steel pipe, +1deg. upward

Exp.	U_{SG}	U_{SL}	WF	U_{SW}	U_{SO}	H_W		H_O		H_{TOT}		Re_G	Re_O	Re_W	dP/dx	T	Visual
#	m/s	m/s	%	m/s	m/s	ml	%	ml	%	ml	%	-	-	-	Pa/m	^oC	
2.1 WF sensitivity																	
153	14.80	0.0059	0	0.0000	0.0059	-	-	180	1.42	180	1.42	5.9E+04	9.8E+02	-	65	19.4	ST4o
154	14.80	0.0059	10	0.0006	0.0053	32	0.25	153	1.21	185	1.46	5.9E+04	8.8E+02	4.4E+02	61	19.4	SST4o
155	14.80	0.0059	20	0.0012	0.0047	54	0.43	134	1.06	188	1.49	5.9E+04	7.8E+02	7.4E+02	60	19.1	SST4
156	14.80	0.0059	30	0.0018	0.0041	70	0.55	104	0.82	174	1.38	5.9E+04	7.0E+02	1.0E+03	59	18.6	SST4
157	14.80	0.0059	40	0.0024	0.0035	89	0.70	84	0.66	173	1.37	5.9E+04	6.0E+02	1.2E+03	58	19.0	SST4

Table A–7: Serie #2.1, steel pipe, +1deg. upward

Exp.	U_{SG}	U_{SL}	WF	U_{SW}	U_{SO}	H_W		H_O		H_{TOT}		Re_G	Re_O	Re_W	dP/dx	T	Visual
#	m/s	m/s	%	m/s	m/s	ml	%	ml	%	ml	%	-	-	-	Pa/m	^oC	
158	14.80	0.0059	50	0.0029	0.0029	108	0.85	73	0.58	181	1.43	5.9E+04	5.0E+02	1.5E+03	58	19.1	SST4
159	14.80	0.0059	60	0.0035	0.0024	124	0.98	65	0.51	189	1.50	5.9E+04	3.9E+02	1.7E+03	58	19.2	SST4
160	14.80	0.0059	70	0.0041	0.0018	142	1.12	41	0.32	183	1.45	5.9E+04	3.0E+02	1.9E+03	59	18.4	SST4
161	14.80	0.0059	80	0.0047	0.0012	164	1.30	34	0.27	198	1.57	5.9E+04	1.9E+02	2.0E+03	60	18.4	SST4
162	14.80	0.0059	90	0.0053	0.0006	152	1.20	12	0.09	164	1.30	5.9E+04	1.0E+02	2.3E+03	65	17.8	DWST4
163	14.80	0.0059	100	0.0059	0.0000	164	1.30	-	-	164	1.30	5.9E+04	-	2.5E+03	65	16.1	ST4

Table A–8: Serie #2.1, epoxy coated steel pipe, horizontal

Exp.	U_{SG}	U_{SL}	WF	U_{SW}	U_{SO}	H_W		H_O		H_{TOT}		Re_G	Re_O	Re_W	dP/dx	T	Visual
#	m/s	m/s	%	m/s	m/s	ml	%	ml	%	ml	%	-	-	-	Pa/m	^oC	
2.1 WF sensitivity																	
164	14.80	0.0059	5	0.0003	0.0056	11	0.09	152	1.27	163	1.36	5.9E+04	9.5E+02	3.1E+02	59	24.3	-
165	14.80	0.0059	10	0.0006	0.0053	20	0.17	142	1.18	162	1.35	5.9E+04	9.0E+02	5.1E+02	58	24.3	-
166	14.80	0.0059	30	0.0018	0.0041	56	0.47	138	1.15	194	1.62	5.9E+04	6.6E+02	1.1E+03	59	24.3	-
167	14.80	0.0059	50	0.0029	0.0029	90	0.75	81	0.67	171	1.42	5.9E+04	5.0E+02	1.5E+03	60	21.6	-
168	14.80	0.0059	70	0.0041	0.0018	113	0.94	56	0.47	169	1.41	5.9E+04	3.0E+02	2.0E+03	61	21.2	-
169	14.80	0.0059	80	0.0047	0.0012	127	1.06	38	0.32	165	1.37	5.9E+04	2.0E+02	2.2E+03	58	-	-
170	14.80	0.0059	90	0.0053	0.0006	131	1.09	19	0.16	150	1.25	5.9E+04	1.0E+02	2.4E+03	58	22.7	-
171	14.80	0.0059	95	0.0056	0.0003	150	1.25	12	0.10	162	1.35	5.9E+04	5.1E+01	2.4E+03	61	26.8	-

Table A–9: Serie #2.1, acrylic pipe, +0.5 deg. upward

Exp.	U_{SG}	U_{SL}	WF	U_{SW}	U_{SO}	H_W		H_O		H_{TOT}		Re_G	Re_O	Re_W	dP/dx	T	Visual
#	m/s	m/s	%	m/s	m/s	ml	%	ml	%	ml	%	-	-	-	Pa/m	^oC	
2.1 WF sensitivity (pipe pigged prior to experiment)																	
277	25.00	0.0059	0	0.0000	0.0059	-	-	-	-	-	-	-	-	-	181	-	-
278	25.00	0.0059	20	0.0012	0.0047	-	-	-	-	-	-	-	-	-	207	-	-
279	25.00	0.0059	50	0.0029	0.0029	-	-	-	-	-	-	-	-	-	225	-	-
280	25.00	0.0059	90	0.0053	0.0006	-	-	-	-	-	-	-	-	-	193	-	-
281	25.00	0.0059	100	0.0059	0.0000	-	-	-	-	-	-	-	-	-	182	-	-

Table A–10: Serie 2.2, acrylic pipe, +0.5 deg. upward

Exp.	U_{SG}	U_{SL}	WF	U_{SW}	U_{SO}	H_W		H_O		H_{TOT}		Re_G	Re_O	Re_W	dP/dx	T	Visual
#	m/s	m/s	%	m/s	m/s	ml	%	ml	%	ml	%	-	-	-	Pa/m	^oC	
2.2 WF sensitivity (pipe pigged prior to experiment)																	
282	25.00	0.0400	0	0.0000	0.0400	-	-	-	-	-	-	-	-	-	276	20.6	ST4o
283	25.00	0.0400	20	0.0080	0.0320	-	-	-	-	-	-	-	-	-	304	20.6	D?ST4o
284	25.00	0.0400	50	2.0000	2.0000	348	2.58	352	2.61	700	5.19	1.0E+05	2.2E+05	6.8E+05	376	20.8	D?ST4o
285	25.00	0.0400	60	0.0240	0.0160	-	-	-	-	-	-	-	-	-	393	21.0	D?ST4o
286	25.00	0.0400	70	2.8000	1.2000	-	-	-	-	-	-	-	-	-	425	-	D?ST4o
287	25.00	0.0400	80	3.2000	0.8000	-	-	-	-	-	-	-	-	-	422	20.5	D?ST4o
288	25.00	0.0400	90	0.0360	0.0040	360	2.67	55	0.41	415	3.08	1.0E+05	5.3E+02	1.2E+04	340	20.2	D?ST4o
289	25.00	0.0400	100	0.0400	0.0000	420	3.11	-	-	420	3.11	1.0E+05	-	1.3E+04	316	19.4	ST4o
2.2 WF sensitivity (pipe not pigged prior to experiment)																	

Table A–10: Serie 2.2, acrylic pipe, +0.5 deg. upward

Exp.	U_{SG}	U_{SL}	WF	U_{SW}	U_{SO}	H_W		H_O		H_{TOT}		Re_G	Re_O	Re_W	dP/dx	T	Visual
#	m/s	m/s	%	m/s	m/s	ml	%	ml	%	ml	%	-	-	-	Pa/m	^oC	
290	25.00	0.0400	0	0.0000	0.0400	-	-	350	2.59	350	2.59	1.0E+05	5.4E+03	-	278	21.0	ST4o
291	25.00	0.0400	5	0.0020	0.0380	-	-	-	-	-	-	-	-	-	284	20.1	D?ST4o
292	25.00	0.0400	10	0.0040	0.0360	-	-	-	-	-	-	-	-	-	286	20.1	D?ST4o
293	25.00	0.0400	20	0.0080	0.0320	100	0.74	395	2.93	495	3.67	1.0E+05	3.9E+03	4.2E+03	290	20.5	D?ST4o
294	25.00	0.0400	50	0.0200	0.0200	322	2.39	315	2.33	637	4.72	1.0E+05	2.3E+03	7.0E+03	300	20.7	D?ST4o
295	25.00	0.0400	60	0.0240	0.0160	-	-	-	-	-	-	-	-	-	306	20.1	D?ST4o
296	25.00	0.0400	70	0.0280	0.0120	-	-	-	-	-	-	-	-	-	311	20.1	D?ST4o
297	25.00	0.0400	80	0.0320	0.0080	-	-	-	-	-	-	-	-	-	339	20.1	D?ST4o
298	25.00	0.0400	90	0.0360	0.0040	356	2.64	49	0.36	405	3.00	1.0E+05	5.4E+02	1.2E+04	335	20.3	D?ST4o
299	25.00	0.0400	100	0.0400	0.0000	420	3.11	-	-	420	3.11	1.0E+05	-	1.3E+04	315	19.2	ST4o

Table A–11: Serie #3.1, acrylic pipe, horizontal

Exp.	U_{SG}	U_{SL}	WF	U_{SW}	U_{SO}	H_W		H_O		H_{TOT}		Re_G	Re_O	Re_W	dP/dx	T	Visual
#	m/s	m/s	%	m/s	m/s	ml	%	ml	%	ml	%	-	-	-	Pa/m	^oC	
3.1 U_{SG} sensitivity WF = 0%																	
172	4.93	0.0059	0	0.0000	0.0059	-	-	679	4.95	679	4.95	2.0E+04	6.4E+02	-	8	20.0	ST1
173	9.87	0.0059	0	0.0000	0.0059	-	-	302	2.20	302	2.20	4.0E+04	8.5E+02	-	32	21.0	ST3
174	19.74	0.0059	0	0.0000	0.0059	-	-	153	1.11	153	1.11	7.9E+04	1.1E+03	-	114	19.0	ST4o
175	29.60	0.0059	0	0.0000	0.0059	-	-	105	0.76	105	0.76	1.2E+05	1.2E+03	-	232	19.0	ST4o
3.1 U_{SG} sensitivity WF = 20%																	

Table A–11: Serie #3.1, acrylic pipe, horizontal

Exp.	U_{SG}	U_{SL}	WF	U_{SW}	U_{SO}	H_W		H_O		H_{TOT}		Re_G	Re_O	Re_W	dP/dx	T	Visual
#	m/s	m/s	%	m/s	m/s	ml	%	ml	%	ml	%	-	-	-	Pa/m	^oC	
176	4.93	0.0059	20	0.0012	0.0047	163	1.19	498	3.63	661	4.82	2.0E+04	5.2E+02	5.2E+02	8	18.0	SST1
177	9.87	0.0059	20	0.0012	0.0047	57	0.42	248	1.81	305	2.22	4.0E+04	6.8E+02	7.4E+02	30	18.0	SST2
178	19.74	0.0059	20	0.0012	0.0047	29	0.21	153	1.11	182	1.33	7.9E+04	8.1E+02	9.4E+02	140	18.0	DOST4o
179	24.67	0.0059	20	0.0012	0.0047	32	0.23	127	0.93	159	1.16	9.9E+04	8.5E+02	9.0E+02	220	17.0	DOST4o
180	29.60	0.0059	20	0.0012	0.0047	26	0.19	124	0.90	150	1.09	1.2E+05	8.6E+02	9.7E+02	296	17.0	D?ST4o
3.1 U_{SG} sensitivity WF = 50%																	
181	4.93	0.0059	50	0.0029	0.0029	325	2.37	335	2.44	660	4.81	2.0E+04	3.3E+02	1.0E+03	8	19.0	SST1
182	9.87	0.0059	50	0.0029	0.0029	145	1.06	180	1.31	325	2.37	4.0E+04	4.2E+02	1.4E+03	27	19.0	SST2
183	19.74	0.0059	50	0.0029	0.0029	50	0.36	112	0.82	162	1.18	7.9E+04	5.3E+02	1.9E+03	154	17.0	DOST4o
184	29.60	0.0059	50	0.0029	0.0029	40	0.29	88	0.64	128	0.93	1.2E+05	5.7E+02	2.1E+03	320	-	D?ST4o
3.1 U_{SG} sensitivity WF = 90%																	
185	4.93	0.0059	90	0.0053	0.0006	497	3.62	87	0.63	584	4.25	2.0E+04	7.1E+01	1.6E+03	8	17.0	SST1
186	9.87	0.0059	90	0.0053	0.0006	260	1.89	50	0.36	310	2.26	4.0E+04	8.7E+01	2.0E+03	24	19.0	SST2
187	19.74	0.0059	90	0.0053	0.0006	107	0.78	20	0.15	127	0.93	7.9E+04	1.2E+02	2.7E+03	142	13.0	DWST4o
188	29.60	0.0059	90	0.0053	0.0006	100	0.73	13	0.09	113	0.82	1.2E+05	1.2E+02	2.8E+03	279	10.0	D?ST4o
3.1 U_{SG} sensitivity WF = 100%																	
189	4.93	0.0059	100	0.0059	0.0000	654	4.76	-	-	654	4.76	2.0E+04	-	1.6E+03	8	-	ST2
190	9.87	0.0059	100	0.0059	0.0000	293	2.13	-	-	293	2.13	4.0E+04	-	2.1E+03	29	-	ST3
191	19.74	0.0059	100	0.0059	0.0000	127	0.93	-	-	127	0.93	7.9E+04	-	2.8E+03	117	-	ST4
192	29.60	0.0059	100	0.0059	0.0000	102	0.74	-	-	102	0.74	1.2E+05	-	3.1E+03	250	-	ST4o

Table A–12: Serie #3.1, acrylic pipe, +1 deg. upward

Exp.	U_{SG}	U_{SL}	WF	U_{SW}	U_{SO}	H_W		H_O		H_{TOT}		Re_G	Re_O	Re_W	dP/dx	T	Visual
#	m/s	m/s	%	m/s	m/s	ml	%	ml	%	ml	%	-	-	-	Pa/m	°C	
3.1 U_{SG} sensitivity WF = 0%																	
193	6.83	0.0059	0	0.0000	0.0059	-	-	1220	9.04	1220	9.04	2.8E+04	5.1E+02	-	28	22.0	ST3
194	7.50	0.0059	0	0.0000	0.0059	-	-	745	5.52	745	5.52	3.0E+04	6.1E+02	-	26	22.4	ST3
195	9.87	0.0059	0	0.0000	0.0059	-	-	330	2.45	330	2.45	4.0E+04	8.2E+02	-	35	20.7	ST3
196	19.74	0.0059	0	0.0000	0.0059	-	-	149	1.10	149	1.10	7.9E+04	1.1E+03	-	117	21.3	ST4o
197	29.60	0.0059	0	0.0000	0.0059	-	-	101	0.75	101	0.75	1.2E+05	1.2E+03	-	242	21.0	ST4o
3.1 U_{SG} sensitivity WF = 20%																	
198	7.50	0.0059	20	0.0012	0.0047	1060	7.86	555	4.11	1615	11.97	3.1E+04	4.0E+02	2.7E+02	35	22.4	SST4
199	9.87	0.0059	20	0.0012	0.0047	140	1.02	288	2.10	428	3.12	4.0E+04	6.1E+02	5.5E+02	34	17.0	SST4
200	19.74	0.0059	20	0.0012	0.0047	25	0.18	150	1.09	175	1.27	7.9E+04	8.2E+02	9.8E+02	142	17.0	DOST4o
201	29.60	0.0059	20	0.0012	0.0047	22	0.16	126	0.92	148	1.08	1.2E+05	8.7E+02	1.0E+03	325	-	D?ST4o
3.1 U_{SG} sensitivity WF = 50%																	
202	7.50	0.0059	50	0.0029	0.0029	1100	8.15	270	2.00	1370	10.15	3.1E+04	2.7E+02	6.7E+02	36	21.1	SST4
203	9.87	0.0059	50	0.0029	0.0029	143	1.04	209	1.52	352	2.56	4.0E+04	4.1E+02	1.4E+03	34	-	SST4
204	19.74	0.0059	50	0.0029	0.0029	55	0.40	117	0.85	172	1.25	7.9E+04	5.2E+02	1.9E+03	172	14.0	DOST4o
205	29.60	0.0059	50	0.0029	0.0029	35	0.25	85	0.62	120	0.87	1.2E+05	5.8E+02	2.2E+03	336	-	D?ST4o
3.1 U_{SG} sensitivity WF = 90%																	
206	7.50	0.0059	90	0.0053	0.0006	1790	13.27	55	0.41	1845	13.67	3.1E+04	5.1E+01	1.0E+03	41	21.1	SSL
207	9.87	0.0059	90	0.0053	0.0006	280	2.04	55	0.40	335	2.44	4.0E+04	8.4E+01	2.0E+03	34	14.0	SST4
208	19.74	0.0059	90	0.0053	0.0006	100	0.73	26	0.19	126	0.92	7.9E+04	1.2E+02	2.8E+03	145	9.0	DWST4o
209	29.60	0.0059	90	0.0053	0.0006	86	0.63	19	0.14	105	0.76	1.2E+05	1.2E+02	2.9E+03	288	9.0	D?ST4o

Table A–12: Serie #3.1, acrylic pipe, +1 deg. upward

Exp.	U_{SG}	U_{SL}	WF	U_{SW}	U_{SO}	H_W		H_O		H_{TOT}		Re_G	Re_O	Re_W	dP/dx	T	Visual
#	m/s	m/s	%	m/s	m/s	ml	%	ml	%	ml	%	-	-	-	Pa/m	^oC	
3.1 U_{SG} sensitivity WF = 100%																	
210	7.50	0.0059	100	0.0059	0.0000	1320	9.78	-	-	1320	9.78	3.1E+04	-	1.2E+03	37	21.1	SL
211	7.72	0.0059	100	0.0059	0.0000	1225	9.08	-	-	1225	9.08	3.2E+04	-	1.3E+03	38	20.2	ST3
212	9.87	0.0059	100	0.0059	0.0000	381	2.82	-	-	381	2.82	4.0E+04	-	1.9E+03	33	20.2	ST3
213	19.74	0.0059	100	0.0059	0.0000	134	0.99	-	-	134	0.99	7.9E+04	-	2.8E+03	121	15.1	ST4
214	29.60	0.0059	100	0.0059	0.0000	114	0.84	-	-	114	0.84	1.2E+05	-	2.9E+03	259	10.6	ST4o

Table A–13: Serie #3.1, steel pipe, horizontal

Exp.	U_{SG}	U_{SL}	WF	U_{SW}	U_{SO}	H_W		H_O		H_{TOT}		Re_G	Re_O	Re_W	dP/dx	T	Visual
#	m/s	m/s	%	m/s	m/s	ml	%	ml	%	ml	%	-	-	-	Pa/m	^oC	
3.1 U_{SG} sensitivity WF = 0%																	
215	4.93	0.0059	0	0.0000	0.0059	-	-	706	5.59	706	5.59	2.0E+04	6.1E+02	-	8	16.0	ST1
216	9.87	0.0059	0	0.0000	0.0059	-	-	236	1.87	236	1.87	4.0E+04	8.9E+02	-	30	19.0	ST3
217	19.74	0.0059	0	0.0000	0.0059	-	-	144	1.14	144	1.14	7.9E+04	1.1E+03	-	108	18.0	ST4o
218	29.60	0.0059	0	0.0000	0.0059	-	-	98	0.78	98	0.78	1.2E+05	1.2E+03	-	223	19.0	ST4o
3.1 U_{SG} sensitivity WF = 20%																	
219	4.93	0.0059	20	0.0012	0.0047	260	2.06	434	3.44	694	5.49	2.0E+04	5.0E+02	4.3E+02	8	-	SST1
220	9.87	0.0059	20	0.0012	0.0047	96	0.76	214	1.69	310	2.45	4.0E+04	6.6E+02	6.1E+02	29	-	SST3
221	19.74	0.0059	20	0.0012	0.0047	35	0.28	119	0.94	154	1.22	7.9E+04	8.3E+02	8.5E+02	121	-	SST4o
222	29.60	0.0059	20	0.0012	0.0047	32	0.25	100	0.79	132	1.04	1.2E+05	8.8E+02	8.8E+02	251	-	D?ST4o

Table A–13: Serie #3.1, steel pipe, horizontal

Exp.	U_{SG}	U_{SL}	WF	U_{SW}	U_{SO}	H_W		H_O		H_{TOT}		Re_G	Re_O	Re_W	dP/dx	T	Visual
#	m/s	m/s	%	m/s	m/s	ml	%	ml	%	ml	%	-	-	-	Pa/m	^oC	
3.1 U_{SG} sensitivity WF = 50%																	
223	4.93	0.0059	50	0.0029	0.0029	379	3.00	237	1.88	616	4.88	2.0E+04	3.3E+02	9.5E+02	8	-	SST1
224	9.87	0.0059	50	0.0029	0.0029	160	1.27	112	0.89	272	2.15	4.0E+04	4.3E+02	1.3E+03	26	-	SST3
225	19.74	0.0059	50	0.0029	0.0029	72	0.57	79	0.63	151	1.20	7.9E+04	5.3E+02	1.7E+03	132	-	SST4o
226	29.60	0.0059	50	0.0029	0.0029	58	0.46	64	0.51	122	0.97	1.2E+05	5.7E+02	1.8E+03	263	-	D?ST4o
3.1 U_{SG} sensitivity WF = 90%																	
227	4.93	0.0059	90	0.0053	0.0006	456	3.61	34	0.27	490	3.88	2.0E+04	7.3E+01	1.6E+03	7	-	SST1
228	9.87	0.0059	90	0.0053	0.0006	261	2.07	28	0.22	289	2.29	4.0E+04	8.6E+01	1.9E+03	25	-	SST3
229	19.74	0.0059	90	0.0053	0.0006	121	0.96	21	0.17	142	1.12	7.9E+04	1.1E+02	2.5E+03	115	-	DWST4o
230	29.60	0.0059	90	0.0053	0.0006	97	0.77	18	0.14	115	0.91	1.2E+05	1.2E+02	2.7E+03	238	-	D?ST4o
3.1 U_{SG} sensitivity WF = 100%																	
231	4.93	0.0059	100	0.0059	0.0000	642	5.08	-	-	642	5.08	2.0E+04	-	1.6E+03	9	-	ST2
232	9.87	0.0059	100	0.0059	0.0000	317	2.51	-	-	317	2.51	4.0E+04	-	2.0E+03	27	-	ST3
233	19.74	0.0059	100	0.0059	0.0000	130	1.03	-	-	130	1.03	7.9E+04	-	2.7E+03	106	-	ST4
234	29.60	0.0059	100	0.0059	0.0000	112	0.89	-	-	112	0.89	1.2E+05	-	2.9E+03	224	-	ST4o

Table A–14: Serie #3.1, steel pipe, +1 deg. upward

Exp.	U_{SG}	U_{SL}	WF	U_{SW}	U_{SO}	H_W		H_O		H_{TOT}		Re_G	Re_O	Re_W	dP/dx	T	Visual
#	m/s	m/s	%	m/s	m/s	ml	%	ml	%	ml	%	-	-	-	Pa/m	°C	
3.1 U_{SG} sensitivity WF = 0%																	
235	6.87	0.0059	0	0.0000	0.0059	-	-	1203	9.52	1203	9.52	2.8E+04	5.0E+02	-	27	22.4	ST4
236	7.50	0.0059	0	0.0000	0.0059	-	-	830	6.57	830	6.57	3.1E+04	5.8E+02	-	25	24.0	ST3
237	9.87	0.0059	0	0.0000	0.0059	-	-	319	2.52	319	2.52	4.0E+04	8.1E+02	-	32	22.7	ST3
238	19.74	0.0059	0	0.0000	0.0059	-	-	144	1.14	144	1.14	7.9E+04	1.1E+03	-	109	19.2	ST4o
239	29.60	0.0059	0	0.0000	0.0059	-	-	96	0.76	96	0.76	1.2E+05	1.2E+03	-	221	18.8	ST4o
3.1 U_{SG} sensitivity WF = 20%																	
240	7.50	0.0059	20	0.0012	0.0047	815	6.45	287.5	2.28	1102.5	8.73	3.1E+04	4.5E+02	2.9E+02	31	24.0	SST4
241	9.37	0.0059	20	0.0012	0.0047	394	3.12	212	1.68	606	4.80	3.8E+04	5.4E+02	3.7E+02	28	22.1	SST4
242	9.87	0.0059	20	0.0012	0.0047	132	1.04	187	1.48	319	2.52	4.0E+04	6.6E+02	5.4E+02	30	21.1	SST3
243	19.74	0.0059	20	0.0012	0.0047	38	0.30	98	0.78	136	1.08	7.9E+04	8.7E+02	8.3E+02	99	21.2	SST4
244	29.60	0.0059	20	0.0012	0.0047	24	0.19	83	0.66	107	0.85	1.2E+05	9.4E+02	9.7E+02	218	19.6	SST4o
3.1 U_{SG} sensitivity WF = 50%																	
245	7.50	0.0059	50	0.0029	0.0029	990	7.84	155	1.23	1145	9.06	3.1E+04	2.8E+02	6.8E+02	35	24.0	SST4
246	10.10	0.0059	50	0.0029	0.0029	400.5	3.17	131.5	1.04	532	4.21	4.1E+04	3.5E+02	9.3E+02	30	-	SST4
247	19.74	0.0059	50	0.0029	0.0029	72	0.57	72	0.57	144	1.14	7.9E+04	5.4E+02	1.7E+03	102	19.8	SST4o
248	29.60	0.0059	50	0.0029	0.0029	56	0.44	56	0.44	112	0.89	1.2E+05	5.8E+02	1.8E+03	256	-	SST4o
3.1 U_{SG} sensitivity WF = 90%																	
249	7.50	0.0059	90	0.0053	0.0006	1725	13.65	55	0.44	1780	14.09	3.1E+04	5.0E+01	9.9E+02	35	24.0	SSL
250	11.62	0.0059	90	0.0053	0.0006	250	1.98	18	0.14	268	2.12	4.7E+04	8.9E+01	2.0E+03	37	-	SST4
251	19.74	0.0059	90	0.0053	0.0006	131	1.04	17	0.13	148	1.17	7.9E+04	1.1E+02	2.5E+03	110	16.6	DWST4

Table A–14: Serie #3.1, steel pipe, +1 deg. upward

Exp.	U_{SG}	U_{SL}	WF	U_{SW}	U_{SO}	H_W		H_O		H_{TOT}		Re_G	Re_O	Re_W	dP/dx	T	Visual
#	m/s	m/s	%	m/s	m/s	ml	%	ml	%	ml	%	-	-	-	Pa/m	^oC	
252	29.60	0.0059	90	0.0053	0.0006	104	0.82	14	0.11	118	0.93	1.2E+05	1.2E+02	2.7E+03	234	-	D?ST4o
3.1 U_{SG} sensitivity WF = 100%																	
253	7.50	0.0059	100	0.0059	0.0000	1580	12.51	-	-	1580	12.51	3.1E+04	-	1.1E+03	32	-	ST4
254	12.20	0.0059	100	0.0059	0.0000	234	1.85	-	-	234	1.85	4.9E+04	-	2.2E+03	44	20.8	ST4
255	19.74	0.0059	100	0.0059	0.0000	135	1.07	-	-	135	1.07	7.9E+04	-	2.7E+03	107	14.2	ST4
256	29.60	0.0059	100	0.0059	0.0000	110	0.87	-	-	110	0.87	1.2E+05	-	2.9E+03	229	9.6	ST4o

Table A–15: Serie #3.1, epoxy coated steel pipe, horizontal

Exp.	U_{SG}	U_{SL}	WF	U_{SW}	U_{SO}	H_W		H_O		H_{TOT}		Re_G	Re_O	Re_W	dP/dx	T	Visual
#	m/s	m/s	%	m/s	m/s	ml	%	ml	%	ml	%	-	-	-	Pa/m	^oC	
3.1 U_{SG} sensitivity WF = 0%																	
257	4.93	0.0059	0	0.0000	0.0059	-	-	570	4.75	570	4.75	2.0E+04	6.5E+02	-	7	24	-
258	9.87	0.0059	0	0.0000	0.0059	-	-	308	2.57	308	2.57	4.0E+04	8.0E+02	-	29	25	-
259	19.74	0.0059	0	0.0000	0.0059	-	-	151	1.26	151	1.26	7.9E+04	1.0E+03	-	104	24	-
260	29.60	0.0059	0	0.0000	0.0059	-	-	88	0.73	88	0.73	1.2E+05	1.2E+03	-	230	-	-
3.1 U_{SG} sensitivity WF = 20%																	
261	4.93	0.0059	20	0.0012	0.0047	200	1.67	427	3.56	627	5.22	2.0E+04	5.1E+02	4.6E+02	7	24	-
262	9.87	0.0059	20	0.0012	0.0047	72	0.60	208	1.73	280	2.33	4.0E+04	6.7E+02	6.6E+02	27	-	-
263	19.74	0.0059	20	0.0012	0.0047	34	0.28	121	1.01	155	1.29	7.9E+04	8.2E+02	8.5E+02	114	22	-
264	29.60	0.0059	20	0.0012	0.0047	30	0.25	94	0.78	124	1.03	1.2E+05	8.8E+02	8.8E+02	238	23	-

Table A–15: Serie #3.1, epoxy coated steel pipe, horizontal

Exp.	U_{SG}	U_{SL}	WF	U_{SW}	U_{SO}	H_W		H_O		H_{TOT}		Re_G	Re_O	Re_W	dP/dx	T	Visual
#	m/s	m/s	%	m/s	m/s	ml	%	ml	%	ml	%	-	-	-	Pa/m	^oC	
3.1 U_{SG}sensitivity WF = 50%																	
265	4.93	0.0059	50	0.0029	0.0029	-	-	-	-	-	-	-	-	-	8	24	-
266	9.87	0.0059	50	0.0029	0.0029	-	-	-	-	-	-	-	-	-	24	24	-
267	19.74	0.0059	50	0.0029	0.0029	-	-	-	-	-	-	-	-	-	99	22	-
268	29.60	0.0059	50	0.0029	0.0029	-	-	-	-	-	-	-	-	-	237	23	-
3.1 U_{SG} sensitivity WF = 90%																	
269	4.93	0.0059	90	0.0053	0.0006	-	-	-	-	-	-	-	-	-	8	24	-
270	9.87	0.0059	90	0.0053	0.0006	-	-	-	-	-	-	-	-	-	23	24	-
271	19.74	0.0059	90	0.0053	0.0006	-	-	-	-	-	-	-	-	-	107	21	-
272	29.60	0.0059	90	0.0053	0.0006	-	-	-	-	-	-	-	-	-	231	14	-
3.1 U_{SG} sensitivity WF = 100%																	
273	4.93	0.0059	100	0.0059	0.0000	610	5.08	-	-	610	5.08	2.0E+04	-	1.6E+03	8	23	-
274	9.87	0.0059	100	0.0059	0.0000	280	2.33	-	-	280	2.33	4.0E+04	-	2.1E+03	26	23	-
275	19.74	0.0059	100	0.0059	0.0000	132	1.10	-	-	132	1.10	7.9E+04	-	2.7E+03	111	19	-
276	29.60	0.0059	100	0.0059	0.0000	86	0.72	-	-	86	0.72	1.2E+05	-	3.1E+03	230	13	-

Table A–16: Serie #3.2, acrylic pipe, +0.5 deg. upward

Exp.	U_{SG}	U_{SL}	WF	U_{SW}	U_{SO}	H_W		H_O		H_{TOT}		Re_G	Re_O	Re_W	dP/dx	T	Visual
#	m/s	m/s	%	m/s	m/s	ml	%	ml	%	ml	%	-	-	-	Pa/m	°C	
3.2 U_{SG} sensitivity WF = 0%																	
300	5.70	0.0400	0	0.0000	0.0400	-	-	3020	22.38	3020	22.38	2.4E+04	2.5E+03	-	38	20.6	SL
301	7.00	0.0400	0	0.0000	0.0400	-	-	1990	14.75	1990	14.75	2.9E+04	2.9E+03	-	40	20.8	ST4
302	8.00	0.0400	0	0.0000	0.0400	-	-	1520	11.27	1520	11.27	3.3E+04	3.2E+03	-	45	20.7	ST3
303	10.00	0.0400	0	0.0000	0.0400	-	-	1075	7.97	1075	7.97	4.1E+04	3.7E+03	-	61	20.7	ST3
304	15.00	0.0400	0	0.0000	0.0400	-	-	-	-	-	-	-	-	-	118	20.0	ST4
3.2 U_{SG} sensitivity WF = 20%																	
305	5.70	0.0400	20	0.0080	0.0320	1848	13.70	1673	12.40	3522	26.10	2.5E+04	2.1E+03	1.5E+03	40	20.6	SST4
306	7.00	0.0400	20	0.0080	0.0320	950	7.04	1310	9.71	2260	16.75	2.9E+04	2.4E+03	1.9E+03	42	20.8	SST3
307	8.00	0.0400	20	0.0080	0.0320	605	4.48	1160	8.60	1765	13.08	3.3E+04	2.5E+03	2.2E+03	47	20.6	SST4
308	10.00	0.0400	20	0.0080	0.0320	310	2.30	920	6.82	1230	9.12	4.1E+04	2.9E+03	2.8E+03	60	20.6	SST4
309	15.00	0.0400	20	0.0080	0.0320	-	-	-	-	-	-	-	-	-	121	17.3	SST4
3.2 U_{SG} sensitivity WF = 50%																	
310	5.70	0.0400	50	0.0200	0.0200	2465	18.27	982	7.28	3447	25.54	2.5E+04	1.4E+03	3.4E+03	44	20.6	SL
311	7.00	0.0400	50	0.0200	0.0200	1980	14.67	869	6.44	2849	21.11	3.0E+04	1.4E+03	3.6E+03	44	20.4	SST3
312	8.00	0.0400	50	0.0200	0.0200	1348	9.99	723	5.35	2070	15.34	3.3E+04	1.6E+03	4.2E+03	44	21.1	SST3
313	10.00	0.0400	50	0.0200	0.0200	710	5.26	540	4.00	1250	9.26	4.1E+04	1.8E+03	5.3E+03	56	20.8	SST3
314	15.00	0.0400	50	0.0200	0.0200	-	-	-	-	-	-	-	-	-	124	20.2	SST4
3.2 U_{SG} sensitivity WF = 90%																	
315	5.70	0.0400	90	0.0360	0.0040	2537	18.80	207	1.53	2744	20.33	2.4E+04	3.1E+02	6.0E+03	44	19.2	SL
316	7.00	0.0400	90	0.0360	0.0040	1775	13.15	147	1.09	1922	14.24	2.9E+04	3.4E+02	6.8E+03	41	19.8	SST4

Table A–16: Serie #3.2, acrylic pipe, +0.5 deg. upward

Exp.	U_{SG}	U_{SL}	WF	U_{SW}	U_{SO}	H_W		H_O		H_{TOT}		Re_G	Re_O	Re_W	dP/dx	T	Visual
#	m/s	m/s	%	m/s	m/s	ml	%	ml	%	ml	%	-	-	-	Pa/m	^oC	
317	8.00	0.0400	90	0.0360	0.0040	1460	10.82	155	1.15	1615	11.97	3.3E+04	3.5E+02	7.4E+03	42	19.9	SST4
318	10.00	0.0400	90	0.0360	0.0040	1010	7.49	125	0.93	1135	8.41	4.1E+04	3.9E+02	8.4E+03	56	20.4	SST4
319	15.00	0.0400	90	0.0360	0.0040	-	-	-	-	-	-	-	-	-	130	17.5	SST4o
3.2 U_{SG} sensitivity WF = 100%																	
320	5.70	0.0400	100	0.0400	0.0000	2903	21.52	-	-	2903	21.52	2.4E+04	-	6.3E+03	43	18.7	SL / ST4
321	7.00	0.0400	100	0.0400	0.0000	2020	14.97	-	-	2020	14.97	2.9E+04	-	7.2E+03	43	17.7	SL
322	8.00	0.0400	100	0.0400	0.0000	1775	13.15	-	-	1775	13.15	3.3E+04	-	7.6E+03	45	19.1	ST3
323	10.00	0.0400	100	0.0400	0.0000	1140	8.45	-	-	1140	8.45	4.1E+04	-	8.9E+03	58	20.1	ST4
324	15.00	0.0400	100	0.0400	0.0000	-	-	-	-	-	-	-	-	-	127	15.5	ST4

A.3 Tabulated data, transient film thinning experiments

Table A–17: Vertical air-water film thinning experiments[a]

Measurements			Computations						
time[b]	dP/dx	H	m	Re_L	We_L	f_j[c]	f_{SG}[d]	$f_{j,wallis}$	$f_{j,LF}$[c]
s	Pa/m	-	m	-	-	meas.	gas alone	-	-
100	-591	0.0249	0.000314	899.60	11.02	1.31E-02	4.4E-03	1.43E-02	5.0E-03
105	-548	0.0244	0.000307	784.11	8.57	1.22E-02	4.4E-03	1.41E-02	5.0E-03
120	-333	0.0152	0.000191	181.12	0.73	7.33E-03	4.4E-03	1.05E-02	4.9E-03
135	-3113	0.0130	0.000163	126.30	0.41	6.83E-03	4.4E-03	9.60E-03	4.9E-03
150	-301	0.0109	0.000137	88.86	0.24	6.60E-03	4.4E-03	8.76E-03	4.8E-03
160	-271	0.0109	0.000136	77.33	0.19	5.92E-03	4.4E-03	8.75E-03	4.8E-03
175	*-250*	*0.0066*	*0.000083*	*28.75*	*0.04*	*5.46E-03*	*4.4E-03*	*7.06E-03*	-
235	*-225*	*0.0040*	*0.000050*	*9.74*	*0.01*	*4.90E-03*	*4.4E-03*	*6.00E-03*	-
500	*-226*	*0.0023*	*0.000028*	*3.32*	*0.00*	*4.92E-03*	*4.4E-03*	*5.32E-03*	-
750	*-219*	*0.0011*	*0.000013*	*0.72*	*0.00*	*4.76E-03*	*4.4E-03*	*4.84E-03*	-
1000	*-195*	*0.0009*	*0.000012*	*0.50*	*0.00*	*4.20E-03*	*4.4E-03*	*4.79E-03*	-

a. lines in italic are for after film breakdown
b. liquid shut down at time equal to 100s
c. Fanning interfacial friction factor based on the superficial gas velocity, Equation [5.51]
d. Fanning friction factor at the wall based on the superficial gas velocity

Table A–18: Vertical air-Exxsol D80 film thinning experiments[a]

Measurements			Computations						
time[b]	dP/dx	H	m	Re_L	We_L	f_j[c]	f_{SG}[d]	$f_{j,wallis}$	$f_{j,LF}$[c]
s	Pa/m	-	m	-	-	meas.	gas alone	-	-
100	-551	0.0263	0.000330	289.55	9.79	1.22E-02	4.4E-03	1.49E-02	5.0E-03
105	-540	0.0237	0.000298	235.59	7.17	1.20E-02	4.4E-03	1.38E-02	5.0E-03
130	-438	0.0211	0.000265	146.99	3.14	9.69E-03	4.4E-03	1.28E-02	5.0E-03
145	-406	0.0167	0.000210	88.42	1.43	8.98E-03	4.4E-03	1.11E-02	4.9E-03
160	-379	0.0145	0.000182	63.11	0.84	8.37E-03	4.4E-03	1.02E-02	4.9E-03
190	-351	0.0136	0.000170	50.82	0.58	7.74E-03	4.4E-03	9.82E-03	4.9E-03
220	-331	0.0108	0.000135	31.13	0.27	7.29E-03	4.4E-03	8.71E-03	4.9E-03
280	-306	0.0090	0.000113	20.17	0.14	6.73E-03	4.4E-03	8.00E-03	4.9E-03
340	-291	0.0086	0.000107	17.43	0.11	6.39E-03	4.4E-03	7.83E-03	4.9E-03
400	-279	0.0073	0.000091	12.10	0.06	6.12E-03	4.4E-03	7.30E-03	4.9E-03
460	-266	0.0067	0.000084	9.84	0.04	5.82E-03	4.4E-03	7.08E-03	4.9E-03
480	-262	0.0066	0.000082	9.35	0.04	5.72E-03	4.4E-03	7.04E-03	4.9E-03
500	-257	0.0063	0.000078	8.32	0.03	5.62E-03	4.4E-03	6.91E-03	4.9E-03
520	-253	0.0060	0.000075	7.54	0.03	5.53E-03	4.4E-03	6.80E-03	4.9E-03
540	-249	0.0056	0.000069	6.40	0.02	5.44E-03	4.4E-03	6.63E-03	4.8E-03
600	-239	0.0047	0.000059	4.44	0.01	5.20E-03	4.4E-03	6.29E-03	4.8E-03

Table A–18: Vertical air-Exxsol D80 film thinning experiments[a]

Measurements			Computations						
time[b]	dP/dx	H	m	Re_L	We_L	f_j[c]	f_{SG}[d]	$f_{j,wallis}$	$f_{j,LF}$[c]
s	Pa/m	-	m	-	-	meas.	gas alone	-	-
660	*-231*	*0.0039*	*0.000049*	*2.96*	*0.01*	*5.02E-03*	*4.4E-03*	*5.96E-03*	-
1000	*-195*	*0.0017*	*0.000022*	*0.52*	*0.00*	*4.21E-03*	*4.4E-03*	*5.11E-03*	-
1500	*-191*	*0.0001*	*0.000001*	*0.00*	*0.00*	*4.12E-03*	*4.4E-03*	*4.46E-03*	-

a. lines in italic are for after film breakdown
b. liquid shut down at time equal to 100s
c. Fanning interfacial friction factor based on the superficial gas velocity, Equation [5.51]
d. Fanning friction factor at the wall based on the superficial gas velocity

A.4 Tabulated data, shear forces in two-phase flow at low liquid loading (acrylic pipe)

Table A–19: Two-phase data: measured and calculated liquid-wall shear in the acrylic pipe

Measurements							τ_L*S_L from models				
Exp	**U_{SG}**	**U_{SL}**	**WF**	**τ_G*S_G**	**τ_L*S_L**	**τ_j*S_j**	**Poiseuille**	**Blasius**	**Håland**	**Kowalski**	**Hand**
#	**m/s**	**m/s**	**%**	**N/m**	**N/m**	**N/m**					
1 U_{SL} sensitivity WF = 0%											
1	14.80	0.0400	0	0.120	0.192	0.177	0.037	0.086	0.099	0.400	0.155
2	14.80	0.0088	0	0.116	0.089	0.085	0.032	0.030	0.041	0.405	0.062
3	14.80	0.0071	0	0.116	0.082	0.079	0.031	0.025	0.035	0.381	0.051
4	14.80	0.0059	0	0.116	0.074	0.071	0.029	0.021	0.030	0.365	0.044
5	14.80	0.0047	0	0.116	0.065	0.063	0.027	0.017	0.025	0.334	0.036
6	14.80	0.0024	0	0.116	0.045	0.044	0.025	0.010	0.017	0.324	0.023
7	14.80	0.0018	0	0.116	0.039	0.038	0.024	0.008	0.014	0.302	0.018
8	14.80	0.0012	0	0.117	0.038	0.038	0.022	0.006	0.012	0.287	0.014
9	14.80	0.0006	0	0.118	0.030	0.029	0.021	0.004	0.009	0.288	0.009
10	14.80	0.0004	0	0.118	0.026	0.026	0.020	0.003	0.008	0.277	0.008
11	14.80	0.0003	0	0.119	0.028	0.027	0.021	0.002	0.008	0.310	0.008
3.1 U_{SG} sensitivity WF = 0%											
172	4.93	0.0059	0	0.016	0.006	0.005	0.005	0.003	0.004	0.022	0.004
173	9.87	0.0059	0	0.056	0.034	0.032	0.016	0.010	0.015	0.128	0.019

Table A–19: Two-phase data: measured and calculated liquid-wall shear in the acrylic pipe

Measurements							τ_L*S_L from models				
Exp	**U_{SG}**	**U_{SL}**	**WF**	**τ_G*S_G**	**τ_L*S_L**	**τ_j*S_j**	**Poiseuille**	**Blasius**	**Håland**	**Kowalski**	**Hand**
#	**m/s**	**m/s**	**%**	**N/m**	**N/m**	**N/m**					
174	14.80	0.0059	0	0.116	0.067	0.065	0.029	0.021	0.030	0.365	0.044
175	19.74	0.0059	0	0.196	0.125	0.121	0.038	0.029	0.041	0.556	0.063
176	29.60	0.0059	0	0.409	0.242	0.237	0.063	0.053	0.073	1.250	0.124
1 U_{SL} sensitivity WF = 100%											
32	14.80	0.0400	100	0.121	0.217	0.201	0.020	0.097	0.104	0.355	0.188
33	14.80	0.0088	100	0.117	0.099	0.096	0.018	0.036	0.043	0.384	0.079
34	14.80	0.0071	100	0.117	0.080	0.077	0.018	0.032	0.039	0.407	0.073
35	14.80	0.0059	100	0.117	0.071	0.069	0.020	0.031	0.038	0.459	0.072
36	14.80	0.0047	100	0.117	0.066	0.064	0.019	0.026	0.033	0.447	0.061
37	14.80	0.0029	100	0.116	0.047	0.046	0.015	0.014	0.019	0.311	0.034
38	14.80	0.0012	100	0.117	0.029	0.029	0.015	0.008	0.013	0.359	0.022
39	14.80	0.0006	100	0.118	0.022	0.022	0.014	0.005	0.009	0.359	0.014
40	14.80	0.0004	100	0.118	0.019	0.019	0.014	0.005	0.008	0.384	0.013
41	14.80	0.0002	100	0.120	0.019	0.019	0.014	0.003	0.006	0.404	0.009
3.1 U_{SG} sensitivity WF = 100% - horizontal											
189	4.93	0.0059	100	0.016	0.006	0.005	0.003	0.003	0.004	0.019	0.005
190	9.87	0.0059	100	0.055	0.026	0.024	0.008	0.011	0.014	0.108	0.022
191	19.74	0.0059	100	0.196	0.122	0.119	0.024	0.040	0.049	0.657	0.097

Table A–19: Two-phase data: measured and calculated liquid-wall shear in the acrylic pipe

Measurements							τ_L*S_L from models				
Exp	**U_{SG}**	**U_{SL}**	**WF**	**τ_G*S_G**	**τ_L*S_L**	**τ_j*S_j**	**Poiseuille**	**Blasius**	**Håland**	**Kowalski**	**Hand**
#	**m/s**	**m/s**	**%**	**N/m**	**N/m**	**N/m**					
192	29.60	0.0059	100	0.412	0.291	0.286	0.033	0.057	0.070	1.060	0.144
3.1 U_{SG} sensitivity WF = 0% - +1deg.											
193	6.83	0.0059	0	0.031	0.013	0.041	0.002	0.001	0.002	0.006	0.001
194	7.50	0.0059	0	0.035	0.017	0.034	0.005	0.002	0.004	0.018	0.004
195	9.87	0.0059	0	0.056	0.031	0.038	0.014	0.008	0.012	0.102	0.015
196	19.74	0.0059	0	0.196	0.128	0.129	0.038	0.029	0.042	0.568	0.064
197	29.60	0.0059	0	0.411	0.266	0.264	0.064	0.054	0.076	1.315	0.129
3.1 U_{SG} sensitivity WF = 100% - +1deg.											
210	7.50	0.0059	100	0.037	0.020	0.057	0.001	0.001	0.001	0.004	0.001
211	7.72	0.0059	100	0.039	0.023	0.057	0.001	0.001	0.001	0.005	0.002
212	9.87	0.0059	100	0.056	0.024	0.035	0.006	0.007	0.009	0.059	0.013
213	19.74	0.0059	100	0.197	0.136	0.138	0.022	0.036	0.044	0.564	0.085
214	29.60	0.0059	100	0.412	0.311	0.308	0.027	0.047	0.057	0.800	0.114

Table A–20: Two-phase data: measured and calculated gas-liquid interfacial shear in the acrylic pipe

Measurements							τ_j*S_j from models				
Exp	U_{SG}	U_{SL}	WF	τ_G*S_G	τ_L*S_L	τ_j*S_j	$\lambda_j = \lambda_G$	Cheremisinoff (3D waves)	Cheremisinoff (roll waves)	ARS	Andritsos
#	m/s	m/s	%	N/m	N/m	N/m					
1 U_{SL} sensitivity WF = 0%											
1	14.80	0.0400	0	0.120	0.192	0.177	0.025	0.018	0.188	0.248	0.257
2	14.80	0.0088	0	0.116	0.089	0.085	0.017	0.012	0.060	0.111	0.126
3	14.80	0.0071	0	0.116	0.082	0.079	0.016	0.012	0.052	0.100	0.116
4	14.80	0.0059	0	0.116	0.074	0.071	0.016	0.011	0.047	0.091	0.109
5	14.80	0.0047	0	0.116	0.065	0.063	0.015	0.011	0.042	0.083	0.101
6	14.80	0.0024	0	0.116	0.045	0.044	0.013	0.009	0.029	0.059	0.076
7	14.80	0.0018	0	0.116	0.039	0.038	0.012	0.009	0.026	0.052	0.068
8	14.80	0.0012	0	0.117	0.038	0.038	0.011	0.008	0.022	0.043	0.059
9	14.80	0.0006	0	0.118	0.030	0.029	0.010	0.007	0.017	0.032	0.044
10	14.80	0.0004	0	0.118	0.026	0.026	0.009	0.006	0.016	0.028	0.040
11	14.80	0.0003	0	0.119	0.028	0.027	0.008	0.006	0.014	0.024	0.033
3.1 U_{SG} sensitivity WF = 0%											
172	4.93	0.0059	0	0.016	0.006	0.005	0.004	0.002	0.007	0.019	0.003
173	9.87	0.0059	0	0.056	0.034	0.032	0.009	0.006	0.023	0.047	0.041

Table A–20: Two-phase data: measured and calculated gas-liquid interfacial shear in the acrylic pipe

Measurements							τ_j*S_j from models				
Exp	**U_{SG}**	**U_{SL}**	**WF**	**τ_G*S_G**	**τ_L*S_L**	**τ_j*S_j**	**$\lambda_j = \lambda_G$**	**Cheremisinoff (3D waves)**	**Cheremisinoff (roll waves)**	**ARS**	**Andritsos**
#	**m/s**	**m/s**	**%**	**N/m**	**N/m**	**N/m**					
174	14.80	0.0059	0	0.116	0.067	0.065	0.016	0.011	0.047	0.091	0.108
175	19.74	0.0059	0	0.196	0.125	0.121	0.025	0.019	0.081	0.159	0.231
176	29.60	0.0059	0	0.409	0.242	0.237	0.045	0.037	0.170	0.364	0.598
1 U_{SL} sensitivity WF = 100%											
32	14.80	0.0400	100	0.121	0.217	0.201	0.025	0.018	0.410	0.244	0.248
33	14.80	0.0088	100	0.117	0.099	0.096	0.017	0.012	0.108	0.110	0.119
34	14.80	0.0071	100	0.117	0.080	0.077	0.015	0.011	0.090	0.098	0.105
35	14.80	0.0059	100	0.117	0.071	0.069	0.014	0.011	0.078	0.090	0.094
36	14.80	0.0047	100	0.117	0.066	0.064	0.014	0.010	0.066	0.081	0.086
37	14.80	0.0029	100	0.116	0.047	0.046	0.013	0.010	0.049	0.065	0.078
38	14.80	0.0012	100	0.117	0.029	0.029	0.010	0.008	0.028	0.043	0.051
39	14.80	0.0006	100	0.118	0.022	0.022	0.009	0.006	0.020	0.031	0.038
40	14.80	0.0004	100	0.118	0.019	0.019	0.008	0.006	0.017	0.028	0.034
41	14.80	0.0002	100	0.120	0.019	0.019	0.007	0.005	0.013	0.021	0.025
3.1 U_{SG} sensitivity WF = 100% - horizontal											
189	4.93	0.0059	100	0.016	0.006	0.005	0.004	0.002	0.011	0.019	0.003

Table A–20: Two-phase data: measured and calculated gas-liquid interfacial shear in the acrylic pipe

Measurements							τ_j*S_j from models				
Exp	**U_{SG}**	**U_{SL}**	**WF**	**τ_G*S_G**	**τ_L*S_L**	**τ_j*S_j**	**$\lambda_j = \lambda_G$**	**Cheremisinoff (3D waves)**	**Cheremisinoff (roll waves)**	**ARS**	**Andritsos**
#	**m/s**	**m/s**	**%**	**N/m**	**N/m**	**N/m**					
190	9.87	0.0059	100	0.055	0.026	0.024	0.009	0.006	0.038	0.046	0.039
191	19.74	0.0059	100	0.196	0.122	0.119	0.023	0.018	0.137	0.159	0.202
192	29.60	0.0059	100	0.412	0.291	0.286	0.045	0.037	0.305	0.366	0.589
3.1 U_{SG} sensitivity WF = 0% - +1deg.											
193	6.83	0.0059	0	0.031	0.013	0.041	0.009	0.005	0.017	0.062	0.028
194	7.50	0.0059	0	0.035	0.017	0.034	0.008	0.005	0.017	0.048	0.029
195	9.87	0.0059	0	0.056	0.031	0.038	0.010	0.006	0.024	0.049	0.044
196	19.74	0.0059	0	0.196	0.128	0.129	0.025	0.019	0.080	0.159	0.230
197	29.60	0.0059	0	0.411	0.266	0.264	0.045	0.037	0.169	0.365	0.591
3.1 U_{SG} sensitivity WF = 100% - +1deg.											
210	7.50	0.0059	100	0.037	0.020	0.057	0.011	0.006	0.031	0.081	0.045
211	7.72	0.0059	100	0.039	0.023	0.057	0.011	0.007	0.032	0.080	0.047
212	9.87	0.0059	100	0.056	0.024	0.035	0.010	0.007	0.040	0.053	0.048
213	19.74	0.0059	100	0.197	0.136	0.138	0.024	0.018	0.138	0.159	0.214
214	29.60	0.0059	100	0.412	0.311	0.308	0.047	0.039	0.310	0.359	0.647

Appendix B Details of the flow facility

B.1 Introduction

Additional details concerning the multiphase flow loop are provided below. The flow loop is otherwise described in Chapter 4.

The additional information includes:

- The flowchart of the multiphase flow loop (Figure B–1).
- Tables of components for the fluid supply and the fluid return infrastructures: air supply (Table B–1), water supply (Table B–2), oil supply (Table B–3) and fluid return (Table B–4).

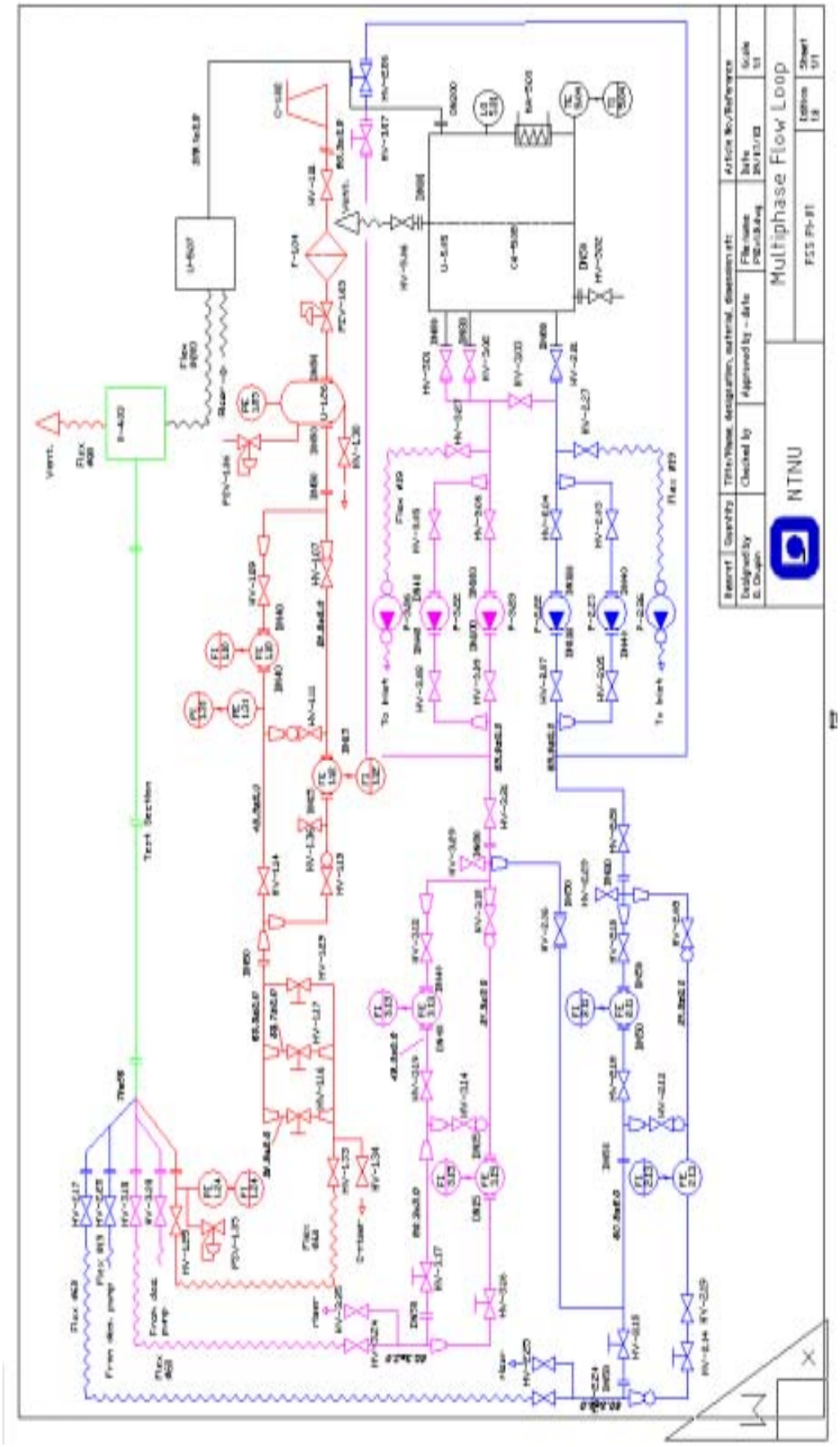

Figure B–1: Flowchart of the multiphase flow loop

Table B–1: Air supply components

ID	Description	Supplier	Type
HV 1.01	Main shut-off valve	K. Lund	BSP 2''
C 1.02	Compressor		
PZV 1.03	Pressure reduction valve	K. Lund	BSP 2''
F 1.04	Air filter	Betex	Conical - 10 µm filter
PE 1.05	Pressure gauge		BSP 1''
PSV 1.06	Pressure safety valve (2-7 bar)	K. Lund	BSP 3/4''
HV 1.07	Ball valve (brass, full bore)	K. Lund	BSP 1/2''
HV 1.09	Ball valve (brass, full bore)	K. Lund	BSP 1.1/2''
FE 1.10	Vortex flow meter sensor	JF Industrisensorer	DN40 wafer
FI 1.10	Vortex flow meter transmitter	JF Industrisensorer	
HV 1.11	Ball valve (brass, full bore)	K. Lund	BSP 1/2''
FE 1.12	Coriolis flow meter sensor	Fisher-Rosemount	DN15 flange
FI 1.12	Coriolis flow meter transmitter	Fisher-Rosemount	IFT9701
HV 1.13	Ball valve (brass, full bore)	K. Lund	BSP 1/2''
HV 1.14	Ball valve (brass, full bore)	K. Lund	BSP 1.1/2''
HV 1.16	Regulation valve, gate valve	K. Lund	BSP 1/2''
HV 1.17	Regulation valve, gate valve	K. Lund	BSP 1''
PE 1.24	Pressure sensor	Siemens	BSP 1/2''
PI 1.24	Pressure transmitter	Siemens	
HV 1.25	Ball valve (brass, full bore)	K. Lund	BSP 2''
U 1.26	Buffer tank, 200 liters	Laguna	DN50 flange
HV 1.29	Regulation valve, gate valve	K. Lund	BSP 2''
PE 1.31	Pressure sensor	Siemens	BSP 1/2''
PI 1.31	Pressure transmitter	Siemens	
HV 1.33	Ball valve (brass, full bore)	K. Lund	BSP 2''
HV 1.34	Ball valve (brass, full bore)	K. Lund	BSP 2''
PSV 1.35	Pressure safety valve (0-9 bar)	K. Lund	BSP 1/2''
HV 1.36	Ball valve (gas lift)	K. Lund	BSP 1/2''

Table B–2: Water supply components

ID	Description	Supplier	Type
HV 2.01	Butterfly valve	K. Lund	DN80 wafer
HV 2.03	Ball valve (brass, full bore)	K. Lund	BSP 2''
HV 2.04	Ball valve (brass, full bore)	K. Lund	BSP 3''
HV 2.05	Ball valve (brass, full bore)	K. Lund	BSP 2''
HV 2.06	Butterfly valve, bypass	K. Lund	DN80 wafer
HV 2.07	Ball valve (brass, full bore)	K. Lund	BSP 3''
HV 2.08	Ball valve (brass, full bore)	K. Lund	BSP 1/2''
HV 2.10	Ball valve (brass, full bore)	K. Lund	BSP 2''
FE 2.11	Electro-magnetic flow meter sensor	Fisher & Porter	DN50 flange
FI 2.11	El-mag flow meter transmitter	Fisher & Porter	
HV 2.12	Ball valve (brass, full bore)	K. Lund	BSP 1/2''
FE 2.13	Electro-magnetic flow sensor	JF Industrisensorer	1/2'' union
FI 2.13	Electro-magnetic flow sensor	JF Industrisensorer	
HV 2.14	Regulation valve, gate valve	K. Lund	BSP 2''
HV 2.15	Regulation valve, gate valve	K. Lund	BSP 1/2''
HV 2.16	Butterfly valve, oil connection	K. Lund	DN50 wafer
HV 2.17	Ball valve (brass, full bore)	K. Lund	BSP 2''
HV 2.18	Ball valve (brass, full bore)	K. Lund	BSP 2''
HV 2.19	Ball valve (brass, full bore)	K. Lund	BSP 1/2''
HV 2.20	Ball valve (brass, full bore)	K. Lund	BSP 3''
P 2.22	Large water pump	Wilo Norge AS	DN100 flange - centrifugal
P 2.23	Small water pump	Grundfos	DN40 flange - centrifugal
HV 2.24	Ball valve (brass, full bore)	K. Lund	BSP 2''
HV 2.25	Ball valve (brass, full bore)	K. Lund	BSP 2''
P 2.26	Dosage pump	Prominent	3/4'' union -SIGMA 12090 - diaphragm
HV 2.27	Ball valve	K. Lund	BSP 3/4'
HV 2.28	Ball valve	K. Lund	BSP 3/4'
HV 2.29	Ball valve	K. Lund	BSP 2''

Table B–3: Oil supply components

ID	Description	Supplier	Type
HV 3.01	Butterfly valve	K. Lund	DN80 wafer
HV 3.02	Butterfly valve	K. Lund	DN80 wafer
HV 3.03	Ball valve (brass, full bore)	K. Lund	BSP 3''
HV 3.05	Ball valve (brass, full bore)	K. Lund	BSP 2''
HV 3.06	Ball valve (brass, full bore)	K. Lund	BSP 3''
HV 3.07	Butterfly valve, bypass	K. Lund	DN80 wafer
HV 3.08	Ball valve (brass, full bore)	K. Lund	BSP 2''
HV 3.09	Ball valve (brass, full bore)	K. Lund	BSP 3''
HV 3.10	Ball valve (brass, full bore)	K. Lund	BSP 1/2''
HV 3.12	Ball valve (brass, full bore)	K. Lund	BSP 1.1/2''
FE 3.13	Coriolis flow meter sensor	Fisher- Rosemont	DN40 flange
FI 3.13	Coriolis flow meter transmitter	Fisher- Rosemont	
HV 3.14	Ball valve (brass, full bore)	K. Lund	BSP 1/2''
FE 3.15	Coriolis flow meter sensor	Fisher- Rosemont	DN15 flange
FI 3.15	Coriolis flow meter transmitter	Fisher- Rosemont	
HV 3.16	Regulation valve, gate valve	K. Lund	BSP 1/2''
HV 3.17	Regulation valve, gate valve	K. Lund	BSP 2''
HV 3.18	Ball valve (brass, full bore)	K. Lund	BSP 2''
HV 3.19	Ball valve (brass, full bore)	K. Lund	BSP 1.1/2''
HV 3.21	Ball valve (brass, full bore)	K. Lund	BSP 3''
P 3.22	Small oil pump	Grundfos Norge	DN40 flange - centrifugal
P 3.23	Large water pump	Grundfos Norge	DN100 flange - centrifugal
HV 3.24	Ball valve (brass, full bore)	K. Lund	BSP 2''
HV 3.25	Ball valve (brass, full bore)	K. Lund	BSP 2''
P 3.26	Dosage pump	Prominent	3/4'' union - SIGMA 12090 - diaphragm
HV 3.27	Ball valve	K. Lund	BSP 3/4'
HV 3.28	Ball valve	K. Lund	BSP 3/4'
HV 3.29	Ball valve	K. Lund	BSP 2''

Table B–4: Liquid return components

ID	Description	Supplier	Type
LG 5.01	Transparent monhole lid		Lexan
HV 5.02	Ball valve (brass, full bore)	K. Lund	BSP 2''
HA 5.03	Cooling, brass coil		
TE 5.04	Thermostatic valve	K. Lund	BSP 3/4''
U 5.05	Separator tank, 3000 litres	Ole Aarre Mek.	
HV 5.06	Ball valve (brass, full bore)	K. Lund	BSP 2"
U 5.07	Secondary tank		
CA 5.08	Mesh Coalescer		

Appendix C Details of the Three-Circle model

C.1 Introduction

In this appendix, computational details relative to the Three-Circle model are provided. The Three-Circle model is otherwise presented and tested in Chapter 8.

The issues dealt with in this appendix are:

- The geometric relationship between holdup, view angle and wetted half-angle for a curved (convex or concave) interface.
- The definition of "criticality".
- The calculation of the view angle for the gas-oil interface in the "critical" case.
- The calculations of the view angle in case of interfacial circle arc intersection (w_i, w_j).

C.2 Geometric relationship between holdup, view angle and wetted half-angle for a curved interface

Geometric variables are defined in Figure C–1 for curved convex and concave circular interfaces.

The interface curvature index measures the degree of curvature of the interface compared to the planar configuration. It is defined by Equation [C.1]:

$$c = \begin{cases} \dfrac{\delta - \delta^P}{\delta^P} \; for \; (0 < \delta < \delta^P) \\ \dfrac{\delta - \delta^P}{\pi - \delta^P} \; for \; (\delta^P < \delta < \pi) \end{cases} \qquad [C.1]$$

The interfacial curvature is a scalar comprised between -1 and 1. For $-1 < c < 0$, the interface is convex and for $0 < c < 1$, the interface is concave.

Reversing Equation [C.1], the following relation between δ and c is obtained:

$$\delta = \begin{cases} \delta^P(1-c) \ \ for\ (c<0) \\ \delta^P(1+c)+\pi c \ \ for\ (c>0) \end{cases} \qquad [C.2]$$

Expressions for R_i, the double circle radius, and OO_i, the distance between circle centres are obtained geometrically:

$$R_i = R\frac{\sin\delta}{\sin\delta_i} \qquad [C.3]$$

$$\begin{aligned} OO_i &= R\frac{\sin\delta}{\sin\delta_i}\cos\delta_i - \cos\delta \quad for\ (c>0) \\ OO_i &= R\frac{\sin\delta}{\sin\delta_i}\cos\delta_i + \cos\delta \quad for\ (c<0) \end{aligned} \qquad [C.4]$$

The ordinate of O_i in the cartesian axes centred in O (Oxy in Figure C–1) is defined by Equation [C.5]:

$$\begin{aligned} y_{Oi} &= OO_i \ for\ (c>0) \\ y_{Oi} &= -OO_i \ for\ (c<0) \end{aligned} \qquad [C.5]$$

It is now possible to obtain a relationship between the phase fraction of the lower phase H and the view angle δ_i for the concave and convex interface cases.

C.2.1 Concave interface

The area below the interface in Figure C–1 verifies the following equation:

$$A = 2\left[\int_{-R}^{y_{ST}} \sqrt{R^2-y^2}\,dy - \int_{(y_{Oi}-R_i)}^{y_{ST}} \sqrt{R_i^2-(y-y_{Oi})^2}\,dy\right] = H\pi R^2 \qquad [C.6]$$

Using:

$$\int \sqrt{R^2-y^2}\,dy = \frac{y^2}{2}\sqrt{R^2-y^2} + \frac{R^2}{2}\arcsin\frac{y}{R} \qquad [C.7]$$

$$\begin{cases} x_{ST} = R\sin\delta \\ y_{ST} = -R\cos\delta \end{cases} \qquad [C.8]$$

One obtains:

$$H\pi R^2 = 2\left[\frac{\pi R^2}{4} - \frac{R^2}{4}\sin 2\delta - \frac{R^2}{2}\left(\frac{\pi}{2} - \delta\right) - \frac{\pi R_i^2}{4} + \frac{R_i^2}{2}\left(\frac{\pi}{2} - \delta_i\right) + \frac{R_i^2}{4}\sin 2\delta_i\right] \quad [C.9]$$

and after re-arrangement,

$$0 = H - \frac{1}{\pi}\left[\left(\delta - \frac{\sin 2\delta}{2}\right) - \left(\frac{\sin\delta}{\sin\delta_i}\right)^2\left(\delta_i - \frac{\sin 2\delta_i}{2}\right)\right] \quad [C.10]$$

Equation [C.10] defines the circle arc characteristics (δ_i and R_i) at given holdup and wetted angle δ (or alternatively curvature index c).

C.2.2 Convex interface

From Figure C–1, the following expression is obtained for the area below the interface.

$$A = 2\left[\int_{-R}^{y_{ST}} \sqrt{R^2 - y^2}\,dy + \int_{y_{ST}}^{(y_{Oi}+R_i)} \sqrt{R_i^2 - (y - y_{Oi})^2}\,dy\right] = H\pi R^2 \quad [C.11]$$

giving after integration and re-arrangement:

$$0 = H - \frac{1}{\pi}\left[\left(\delta - \frac{\sin 2\delta}{2}\right) - \left(\frac{\sin\delta}{\sin\delta_i}\right)^2\left(\frac{\sin 2\delta_i}{2} - \delta_i\right)\right] \quad [C.12]$$

C.2.3 Use of the interfacial curvature Φ_i

An alternative variable to the view angle δ_i is the interface curvature Φ_i defined in Figure C–1.

There is the following geometrical relationship between δ_i and Φ_i:

$$\begin{cases} \delta_i = \phi_i - \pi \; for \; (c > 0) \\ \delta_i = \pi - \phi_i \; for \; (c < 0) \end{cases} \quad [C.13]$$

Replacing in Equation [C.10] and Equation [C.12], on obtains a relation between H, δ and Φ_i valid for both concave and convex interfaces:

$$0 = H - \frac{1}{\pi}\left[\delta - \frac{\sin 2\delta}{2}\right] - \left(\frac{\sin\delta}{\sin\phi_i}\right)^2 \left[\phi_i - \pi - \frac{\sin 2\phi_i}{2}\right] \qquad [C.14]$$

C.3 Definition of the critical case

When interfacial curvatures of the gas-liquid and liquid-liquid interfaces are such that interfacial circle arcs geometrically intersect, the geometry of the Three-Circle model is said to be "critical". Critical cases are defined in Figure C–2.

The geometry is critical if one of the inequalities given in Equation [C.15] is fulfilled:

$$\begin{cases} (R_j - R_i) > (y_{Oj} - y_{Oi}) \;\; for \; (c_i > 0) \; and \; (c_j > 0) \\ (R_i + R_j) > (y_{Oj} - y_{Oi}) \;\; for \; (c_i < 0) \; and \; (c_j > 0) \\ (R_i + R_j) > (y_{Oi} - y_{Oj}) \;\; for \; (c_i > 0) \; and \; (c_j < 0) \\ (R_i - R_j) > (y_{Oj} - y_{OI}) \;\; for \; (c_i < 0) \; and \; (c_j < 0) \end{cases} \qquad [C.15]$$

In the following, C_i will designate the liquid-liquid interfacial arc, C_j the gas-liquid interfacial arc and C the pipe circular section.

C.3.1 Calculation of the view angle for the gas-oil interface in the critical case

In the critical case, the view angle for the gas-liquid interface δ_j (or alternatively Φ_j) can no longer be calculated using Equation [C.14] taking for H the total liquid holdup. This would overestimate the oil holdup. Instead, a new geometrical relationship needs to be defined based on holdup conservation.

The critical value for δ_j, noted δ_j^*, is calculated based on the following exact relationship:

$$0 = L_O + I - A_L \qquad [C.16]$$

This simply states that the total area occupied by the liquid, A_L, must be the sum of the area under the gas-oil circle arc (L_O) plus the protruding portion of the area under the oil-water circle arc (I).

The new value δ_j^* is calculating by iterating on δ_j until Equation [C.16] is satisfied. The interval in which δ_j^* must be searched is given by Equation [C.17] for the critical cases identified in Figure C–2.

$$\begin{aligned} \delta_{j,\,old} < \delta_j^* < \delta_O \;\; for\ cases\ I \\ \delta_{j,\,old} < \delta_j^* < \delta_{j,\,crit} \;\; for\ cases\ II \end{aligned} \qquad [C.17]$$

where $\delta_{j,old}$ stands for the view angle calculated with Equation [C.14] and $\delta_{j,crit}$ is the view angle such that Equation [C.15] is verified (interfacial circle arcs exactly tangent). δ_O is the oil wetted half-angle.

In the rest of this section, expressions are derived for L_O, I and A_L.

- A_L is the liquid phase area and is calculated from the liquid holdup definition:

$$A_L = H_L \pi R^2 \qquad [C.18]$$

- L_O is the area of the lens between the gas-liquid interfacial arc C_j and the pipe C. It is given by

$$L_O = 2 \int_0^{x_{ST1}} |C_j - C| dx \qquad [C.19]$$

where C_j and C stand for their equations in the cartesian axes (Oxy) and ST_1 is the intersection of C_j with C.

Circle arcs C_i and C_j are defined by the following equations in the cartesian axis (Oxy):

$$\begin{aligned} y &= -\sqrt{R_{i,j}^2 - x^2} + OO_{i,j} \;\; for\ (c_{i,j} > 0) \\ y &= \sqrt{R_{i,j}^2 - x^2} - OO_{i,j} \;\; for\ (c_{i,j} < 0) \end{aligned} \qquad [C.20]$$

The lower half pipe circular shape equation in (Oxy) is:

$$y = -\sqrt{R^2 - x^2} \qquad [C.21]$$

The coordinates of C_i inter C (respectively C_j inter C) are equal to:

$$\begin{aligned} x_{ST1,\,2} &= R \sin \delta_{i,j} \\ y_{ST1,\,2} &= -R \cos \delta_{i,j} \end{aligned} \qquad [C.22]$$

The coordinates of the liquid-liquid and the gas-liquid interfacial arc intersection (C_i inter C_j) are given by Equation [C.23]:

$$x_P = \sqrt{R_i^2 - (y_P - y_{Oi})^2}$$
$$y_P = \frac{R_i^2 - R_j^2 - y_{Oi}^2 + y_{Oj}^2}{2(y_{Oj} - y_{Oi})} \quad [C.23]$$

Replacing Equation [C.20] and Equation [C.22] into Equation [C.19], L_O can be integrated using the primitive given in Equation [C.7].

• I is the area below the water circle arc and above the oil circle arc. Two cases must be distinguished:

- $\delta_O > \delta_W$: the oil phase forms two streamwise strips at the wall (cases I_A, I_B and I_C in Figure 8–6)

Then:

$$I = 2\int_0^{x_P} |C_j - C_i| dx \quad [C.24]$$

The integral is calculated by replacing C_j and C_i by their equations (Equation [C.20])

- $\delta_O < \delta_W$: the oil phase forms a lens in the cross sectional view of the phase distribution (cases II_A, II_B and II_C in Figure 8–6).

Then:

$$I = 2\Delta \quad [C.25]$$

where Δ is the area of the circular triangle PST_1ST_2. Δ and the circular triangle are defined in Figure C–3 for case II_A.

The expression for Δ is obtained by additions or subtractions of sector areas to the area of the regular triangle PST_1ST_2. The process is represented schematically in Figure C–3 for case II_A. For the other cases, Δ is defined by the relation in Equation [C.26]:

$$\Delta = A_{PST_1ST_2} - Sec_W + Sec_O + Sec_C \ \textit{for case IIA}$$
$$\Delta = A_{PST_1ST_2} - Sec_W - Sec_O + Sec_C \ \textit{for case IIB} \quad [C.26]$$
$$\Delta = A_{PST_1ST_2} + Sec_W - Sec_O + Sec_C \ \textit{for case IIC}$$

with

$$Sec_W = R_i^2 \left(\frac{\delta_i - w_i}{2} \right) - A_{OiPST_2} \qquad [C.27]$$

$$Sec_O = R_j^2 \left(\frac{\delta_j - w_j}{2} \right) - A_{OjPST_1} \qquad [C.28]$$

$$Sec_C = R^2 \left(\frac{\delta_W - \delta_O}{2} \right) - A_{OST_1ST_2} \qquad [C.29]$$

and

$$\begin{aligned} A_{ABC} &= \sqrt{a'b'c'(a'+b'+c')} \\ a' &= \frac{b+c-a}{2} \\ b' &= \frac{a+c-b}{2} \\ c' &= \frac{a+b-c}{2} \end{aligned} \qquad [C.30]$$

C.4 Calculations of w_i and w_j

W_i and w_j, are defined as the view angles of P seen for the centre of the liquid-liquid interfacial arc and gas-liquid interfacial arc respectively (Figure C–2). They are required for the exact calculation of the interfacial areas in the critical case.

Two cases must be distinguished. If the interfacial circle arc is concave, w_i (alternatively w_j) is given by the following equation:

$$\begin{cases} w_i = \left| \operatorname{atan} \left(\frac{x_P}{y_P - OO_i} \right) \right| & for\ (y_P < OO_i) \\ w_i = \pi - \left| \operatorname{atan} \left(\frac{x_P}{y_P - OO_i} \right) \right| & for\ (y_P > OO_i) \\ w_i = \frac{\pi}{2}\ for\ y_P = OO_i \end{cases} \qquad [C.31]$$

If the interfacial circle arc is convex, w_i (alternatively w_j) is given by the following equation:

$$\begin{cases} w_i = \pi - \left| \operatorname{atan}\left(\frac{x_P}{y_P + OO_i}\right) \right| \; for \; (y_P < -OO_i) \\ w_i = \left| \operatorname{atan}\left(\frac{x_P}{y_P + OO_i}\right) \right| \; for \; (y_P > -OO_i) \\ w_i = \frac{\pi}{2} \; for \; y_P = -OO_i \end{cases} \qquad [C.32]$$

Equation [C.31] and Equation [C.32] are obtained from geometrical considerations of angles in Figure C–2.

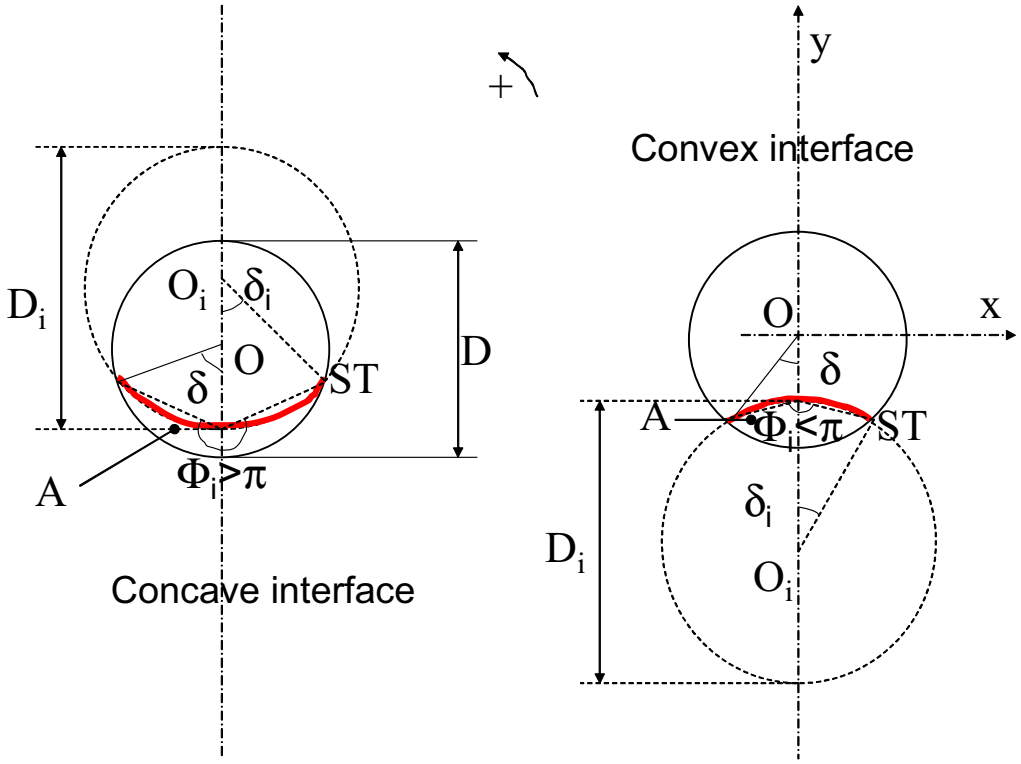

Figure C–1: Variable definitions for curved circular interface models

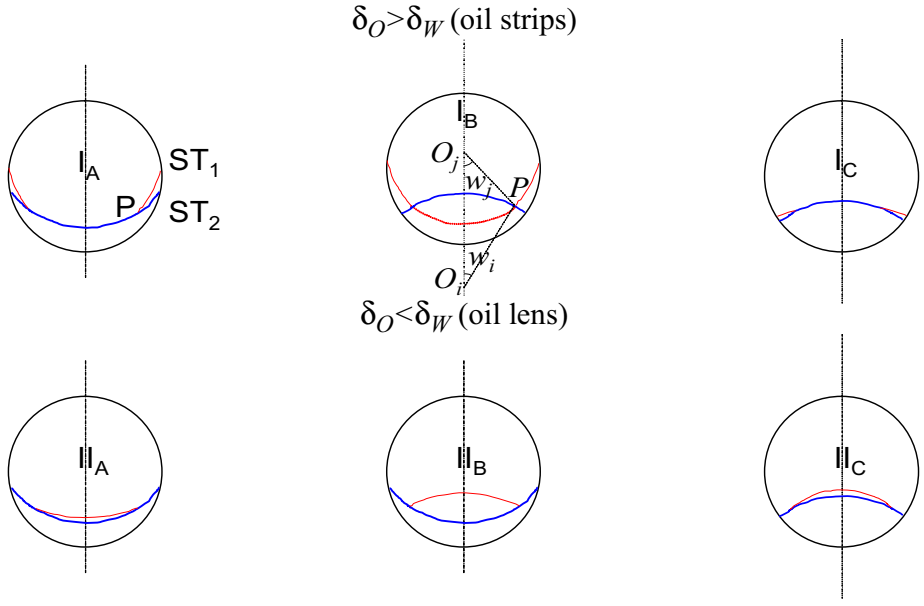

Figure C–2: Critical geometries for the Three Circle model

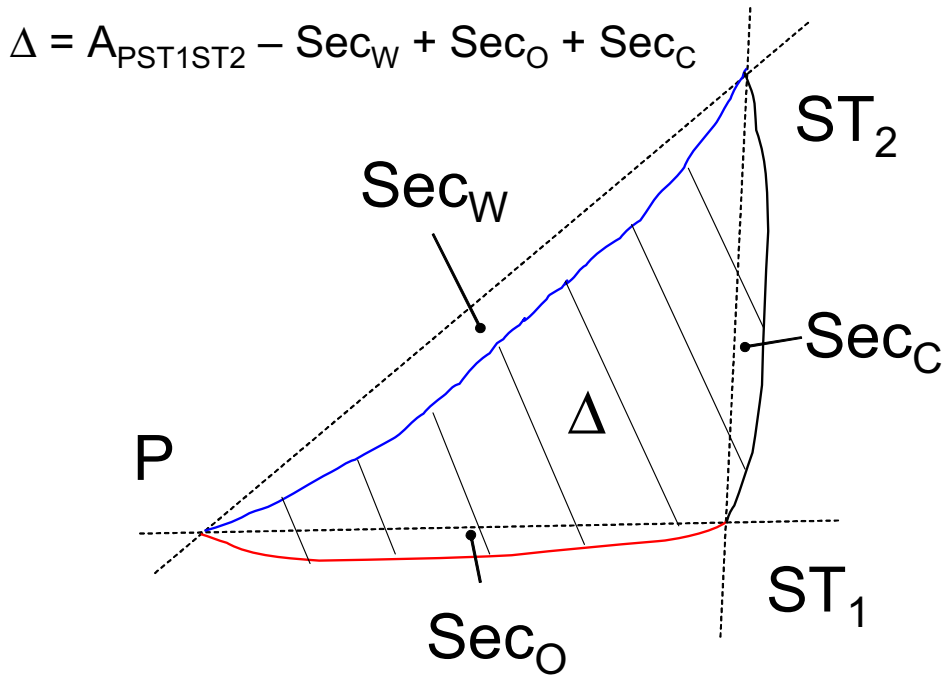

Figure C–3: Computation of the circular triangle area Δ for the case II_A defined in Figure C–2

Appendix D Terms of the pressure drop and holdup equations

D.1 Introduction

In this appendix, a method used for calculating interfacial shear stress and liquid-wall shear stress from the stratified two-phase flow momentum balance equations is presented. The methodology is applied to study an extensive data bank of low and high pressure two-phase flow data. It is also used to extract wall and interfacial friction values from holdup and pressure drop measurements in Chapter 6 and Chapter 7.

D.2 Extraction methodology

The method of analysis of two-phase stratified flow data exposed below is not new. It is, for example, used in Espedal (1998) and discussed in Newton et al. (1998). Experimental results are usually presented in form of tabulated measurements of pressure gradient, liquid holdup and fluid properties at given inlet conditions. The present analysis suggests to use this data to extract frictional and gravitational terms involved in the stratified momentum balance equations.

D.2.1 Balance equations

In Chapter 3, mass and momentum conservation equations are derived for each phase in the case of stratified steady-state gas liquid pipe flow. The combined mass and momentum balance equations can be re-written as follows:

$$-\alpha A\left(\frac{dP}{dx}\right) = F_G + F_j + G_G \qquad [D.1]$$

$$-\beta A\left(\frac{dP}{dx}\right) = F_L - F_j + G_L \qquad [D.2]$$

where frictional terms are defined by:

$$F_k = \tau_k S_k = \frac{\lambda_k}{8}\rho_k U_k |U_k| S_k \quad [D.3]$$

$$F_j = \tau_j S_j = \frac{\lambda_j}{8}\rho_j U_j |U_j| S_j \quad [D.4]$$

and hydrostatic terms are defined by:

$$G_G = \alpha A g \rho_G \sin(\theta) \quad [D.5]$$

$$G_L = H A g \rho_L \sin(\theta) \quad [D.6]$$

With these notations, the pressure drop and holdup equations (Equation [3.23] and Equation [3.26]) reduce to:

$$-A\left(\frac{dP}{dx}\right) = F_G + F_L + G_G + G_L \quad [D.7]$$

$$0 = -HF_G + \alpha F_L - F_j + (\alpha G_L - H G_G) \quad [D.8]$$

D.2.2 Expressions for the gas-wall friction

From the knowledge of pressure drop, phase fractions and fluid properties, hydrostatic terms can be easily calculated. Three remaining unknowns (friction terms) must be determined from two momentum conservation equations and one additional closure.

Measurements of gas-wall shear stresses for gas-liquid stratified flow show that gas-wall friction is traditionally accurately modelled using a friction factor correlation derived from single phase flow (Fabre et al. 1987). In this thesis, the maximum of Poiseuille equation (Equation [3.5]) for laminar flow and one of the following three gas-wall friction factor law for turbulent flow is assumed for the gas-wall friction factor:

- Blasius' equation, Equation [D.9]:

$$\lambda_G = \frac{0.184}{(Re_G)^{0.2}} \quad [D.9]$$

- Håland's equation, Equation [D.10]:

$$\lambda_G = 1.8 \log\left[\frac{6.9}{Re_G} + \left(\frac{\varepsilon}{3.7D}\right)^{1.11}\right]^{-2} \quad [D.10]$$

- Biberg's equation, Equation [D.11]:

$$\lambda_G = \left\{ -1.8\log\left[\frac{6.9}{Re_G} + \left(\frac{\varepsilon}{3.7D_G}\right)^{1.11}\right] - 2\log\left[1 + \frac{S_j}{S_G}\left(\operatorname{sgn}\frac{\tau_j}{\tau_G}\right)\sqrt{\left|\frac{\tau_j}{\tau_G}\right|} - 1\right]\right\}^{-2} \quad [D.11]$$

Another form of Equation [D.11] is given by Biberg (1998) expressed in terms of the gas-liquid interfacial friction factor:

$$\lambda_G = \left\{ -1.8\log\left[\frac{6.9}{Re_G} + \left(\frac{\varepsilon}{3.7D_G}\right)^{1.11}\right] + 2\log\left[1 + \frac{S_j}{S_G}\right] \Big/ \left[1 + 2\log\left[1 + \frac{S_j}{S_G}\right] + \frac{S_j}{S_G}\frac{U_r}{U_G}\sqrt{\lambda_j}\right]\right\}^{-2} \quad [D.12]$$

Usually, the interfacial friction factor is unknown. It must be calculated by iterating on the gas momentum equation written as an implicit equation of the interfacial friction factor:

$$0 = -\alpha A\frac{dP}{dx} - \frac{\lambda_G(\lambda_j)}{8}\rho_G U_G^2 S_G - \frac{\lambda_j}{8}\rho_G U_r^2 S_j - \alpha A\rho_L g\sin\theta \quad [D.13]$$

Hydraulic diameters, wetted and interfacial perimeters are otherwise calculated according to the expressions developed in Section 3.3 for a flat gas-liquid interface.

D.2.3 Term computation and scaling

Once gas-wall friction is known, the remaining frictional terms are readily calculated.

Liquid-wall friction is calculated from the pressure drop equation, Equation [D.7]:

$$F_L = -A\left(\frac{dP}{dx}\right) - \frac{\lambda_G}{8}\rho_G U_G|U_G|S_G - (\alpha\rho_G + H\rho_L)Ag\sin\theta \quad [D.14]$$

Interfacial friction is calculated from the holdup equation, Equation [D.8]:

$$F_j = -H\frac{\lambda_G}{8}\rho_G U_G|U_G|S_G + \alpha F_L + \alpha HA(\rho_L - \rho_G)g\sin\theta \quad [D.15]$$

If the relative magnitude of the frictional and hydrostatic terms are to be compared, it is convenient to scale the terms such that their algebraic sum is equal to one. For the pressure drop equation, terms are scaled with the total pressure drop as shown in Equation [D.16]:

$$1 = \frac{F_G}{-A\frac{dP}{dx}} + \frac{F_L}{-A\frac{dP}{dx}} + \frac{G_{dP}}{-A\frac{dP}{dx}} \quad [D.16]$$

with,

$$G_{dP} = G_G + G_L \quad [D.17]$$

For the holdup equation, terms are scaled with either the liquid-wall friction (Equation [D.18]) or the hydrostatic term (Equation [D.19]) for respectively, upward or downward flow:

$$1 = \frac{HF_G}{\alpha F_L} + \frac{F_j}{\alpha F_L} - \frac{G_{hol}}{\alpha F_L} \quad [D.18]$$

$$1 = \frac{HF_G}{G_{hol}} - \frac{\alpha F_L}{G_{hol}} + \frac{F_j}{G_{hol}} \quad [D.19]$$

with,

$$G_{hol} = \alpha G_L - HG_G \quad [D.20]$$

For comparisons, it is generally taken the absolute value of the terms composing Equation [D.16], Equation [D.18] and Equation [D.19].

D.3 Applications

D.3.1 Using Biberg's gas-wall friction factor

Biberg's gas wall friction factor has been used in this thesis in conjunction with analysis of two-phase stratified flow measurements at low liquid loading. From measured pressure drop and holdup, liquid-wall friction and interfacial friction are calculated and compared with predictions from correlations. Results are shown in Chapter 6 and Chapter 7.

D.3.2 Using Håland's gas-wall friction factor

Several sets of experimental data covering both low and high pressures have been analysed by means of the methodology presented in Section D.2. The absolute value of the

scaled contributions to the pressure drop and holdup equations are compared and their relative importance studied in function of changes of diameter, inclination, pipeline pressure and fluid properties. This work is summarized in Chupin et al. (2003b).

D.3.3 Using Blasius' gas-wall friction factor

If Blasius' equation is used for the gas-wall friction and assuming and interfacial friction factor equal to the gas-wall friction factor, Taitel et al. (1976) have shown that holdup and pressure drop are unique functions of two-dimensionless parameters given by Equation [D.21] and Equation [D.22]:

$$X = \sqrt{\frac{\left(\frac{dP}{dx}\right)_{SL}}{\left(\frac{dP}{dx}\right)_{SG}}} \qquad [D.21]$$

$$Y = \frac{(\rho_L - \rho_G) g \sin\theta}{\left|\frac{dP}{dx}\right|_{SG}} \qquad [D.22]$$

X and Y are known, respectively, as the Martinelli parameter and the angle parameter.

Using Blasius' equation to calculate gas-wall friction, the term extraction routines are run on a two-phase experimental data bank described in Table E–1. Scaled terms of the holdup and pressure drop equation are plotted against the Martinelli parameter, X. For small values of the angle parameter ($Y \ll 1$), the hydrostatic term is small compared to friction terms and the pressure drop data collapses into an X shaped pattern for which gas-wall friction dominates at low values of the Martinelli parameter ($X \ll 1$) and liquid-wall friction dominates at high values of the Martinelli parameter ($X \gg 1$). The holdup is then dominated by a balance between liquid-wall friction and interfacial friction. For high values of the angle parameter ($Y \gg 1$), gas-wall friction terms are small and hydrostatic terms dominate at small value of the Martinelli parameter and liquid-wall friction dominates at high value of the Martinelli parameter. The holdup equation is, in this case, dominated by a balance between hydrostatic terms and interfacial friction. Such plots are shown in Figure D–1 for the particular case of horizontal and positively inclined data.

For given fluid properties and pipe diameter, it is possible to draw the line corresponding to $Y = 1$ in an inclination/superficial gas velocity plane. From the definition of the angle parameter:

$$Y = \frac{(\rho_L - \rho_G) g \sin\theta}{C_G \left(\frac{D U_{SG}}{\nu_G}\right)^{-m} \frac{\rho_G U_{SG}^2}{2D}} \qquad [D.23]$$

with $C_G = 0.184$ and $m = 0.2$ (turbulent gas), the following expression is obtained for the critical superficial gas velocity in function of inclination at $Y = 1$:

$$U_{SG,crit} = \left[\frac{(\rho_L - \rho_G)g}{\frac{\rho_G}{2D} C_G \left(\frac{D}{\nu_G} \right)^{-m}} \right]^{\frac{1}{(2-m)}} \sin^{\frac{1}{(2-m)}} \theta \qquad [D.24]$$

The critical gas velocity given by Equation [D.24] i plotted against inclination as shown in Figure D–2 for the following data:

- $\rho_G = 90$ kg/m^3
- $\rho_L = 800$ kg/m^3
- $\mu_G = 1.810^{-5}$ Pa.s

The plot in Figure D–2 gives an indication on whether a given pipe is operated in a friction or gravity dominated regime. It shows that large diameter pipes are rather gravity dominated at positive inclinations while small diameter pipes are rather friction dominated. For instance at +2 deg. inclination (vertical line indicated on Figure D–2), a 1.0 m i.d. pipe is gravity dominated for superficial gas velocity below 38 m/s whereas a 0.05 m i.d. pipe is gravity dominated for superficial gas velocity below 5 m/s. In other terms, the fraction of the pressure-loss due to hydrostatic losses can be expected to be more important with a large diameter pipe than for a pipe of smaller diameter, if the pipeline route involves important variations of the pipe inclination. Pressure loss reduction technologies that solely focus on drag reduction will have less impact in large diameter pipes.

Similarly, for given fluid properties, the condition $X = 1$ leads to the definition of a critical liquid-to-gas ratio (or liquid loading) over which the flow is dominated by liquid-wall friction. From the definition of the Martinelli parameter:

$$X^2 = \frac{\frac{D}{2}\rho_L U_{SL}^2 C_L \left(\frac{D U_{SL}}{\nu_L} \right)^{-m}}{\frac{D}{2}\rho_G U_{SG}^2 C_G \left(\frac{D U_{SG}}{\nu_G} \right)^{-n}} \qquad [D.25]$$

with $C_G = C_L = 0.184$ and $m = n = 0.2$ for turbulent gas - turbulent liquid flow, the following expression is obtained for the critical LGR at $X = 1$:

$$\frac{U_{SL}}{U_{SG}} = \left(\frac{\rho_G}{\rho_L} \frac{\nu_G}{\nu_L} \right)^m \left(\frac{1}{(2-m)} \right) \qquad [D.26]$$

The critical LGR is plotted against the dimensionless group $\left(\frac{\rho_G}{\rho_L} \frac{\nu_G}{\nu_L} \right)^m$ in Figure D–3.

Figure D–3 indicates whether a friction dominated pipe i dominated by gas-wall or liquid-wall friction. For instance, at gas density equal to 90 kg/m^3 (in-field gas pipe conditions), liquid density equal to 800 kg/m^3, gas viscosity equal to 1.810^{-5} Pa.s, the critical liquid loading above which the pipe is dominated by liquid-wall friction is 20.0% whereas at gas density equal to 1.2 kg/m^3 (laboratory conditions), it is only 3.2%. This shows that high pressure pipes, when operated at conditions where friction forces are dominating, are rather dominated by gas-wall friction at low liquid loading whereas low pressure pipes at low liquid loading tend to be equally dominated by liquid-wall friction and gas-wall friction. In the friction dominated regimes, gas-wall drag reduction technologies such as internal coatings can be expected to have a larger positive impact in high pressure pipes, typically long distance trunk lines, than in lines operated at lower pressure such as production flowlines. For the latter, pressure loss reduction technologies in the friction dominated regime should also involve tackling the difficult issue of reducing liquid-wall friction.

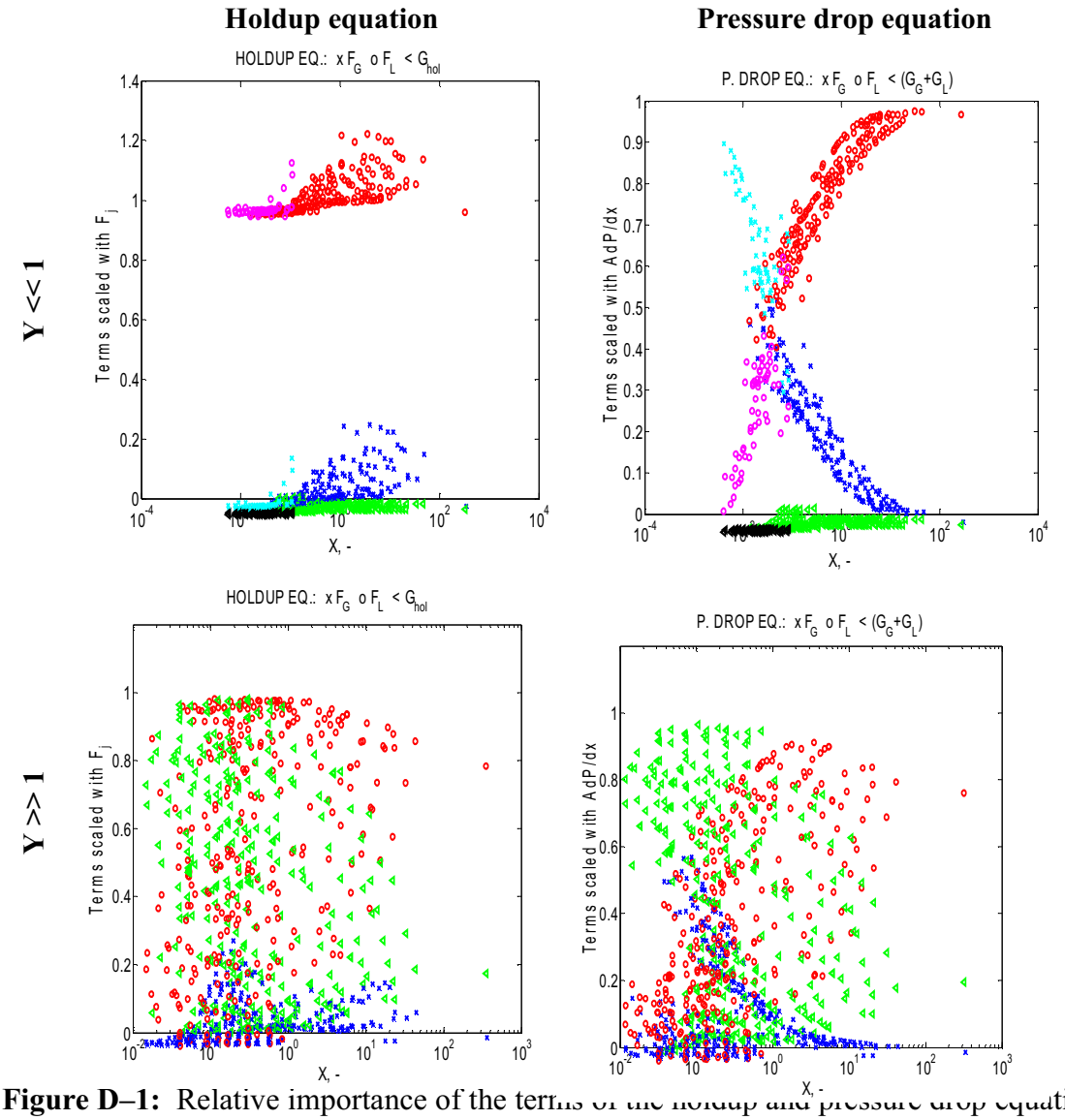

Figure D–1: Relative importance of the terms of the holdup and pressure drop equation using Blasius for the gas-wall friction factor. Only the absolute value of the scaled terms is plotted. Data is from an experimental data bank of stratified, low and high pressure, two-phase pipe flow data, at horizontal or small upward inclinations, described in Table E–1. Top: friction dominated flow (Y<<1); Bottom: gravity dominated flow (Y>>1)

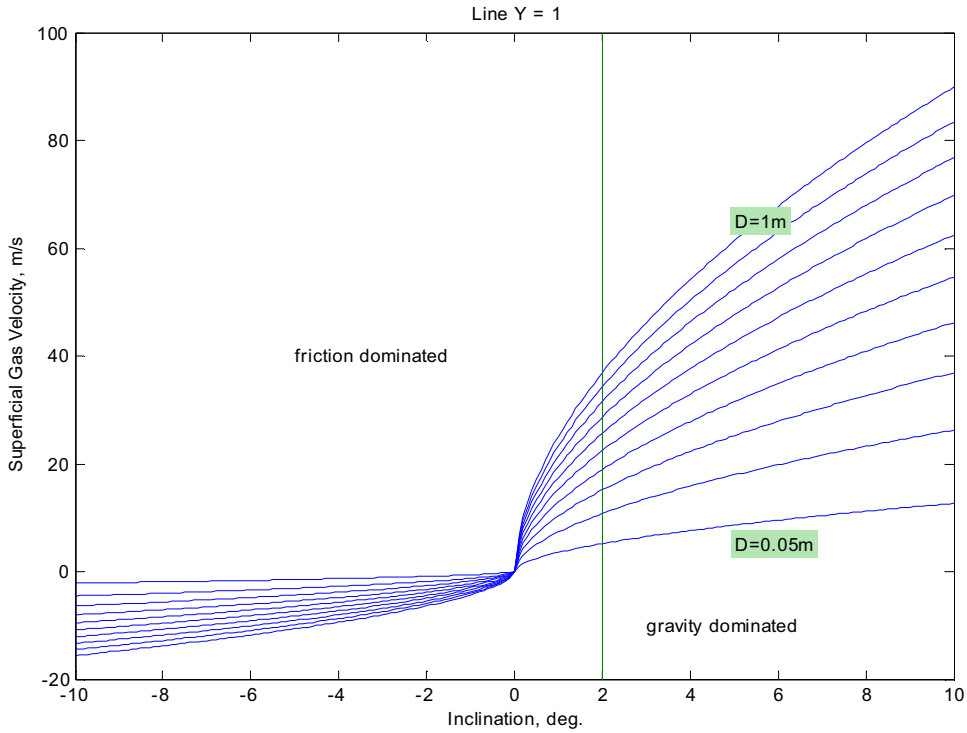

Figure D–2: Critical gas superficial velocity corresponding to Y = 1 versus pipe inclination and pipe internal diameter. Other parameters are: gas density = 90 kg/m3, liquid density = 800 kg/m3, gas viscosity = 1.810^{-5} Pa.s. Below the solid line at given internal diameter, the pipe is gravity dominated. Along the vertical line, the critical superficial velocity can be read for inclination = +2 deg.

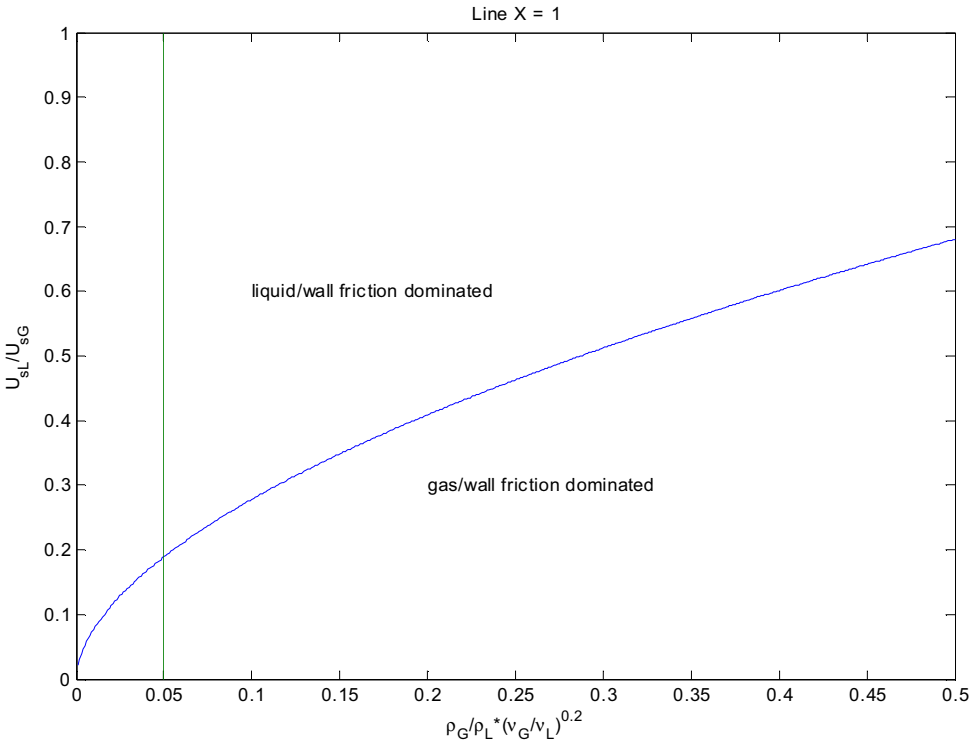

Figure D–3: Critical liquid-to-gas ratio corresponding to X = 1 versus a dimensionless group depending on fluid properties. Above the solid line for given value of the dimensionless parameter, the pipe is dominated by liquid-wall friction. The vertical line corresponds to high gas densities (gas density = 90 kg/m^3)

Appendix E Test of two-phase gas-liquid flow models at low liquid loading on an experimental data bank

E.1 Introduction

In this appendix, the performance of stratified gas-liquid flow models in predicting data at low liquid loading has been evaluated. For the purpose of designing gas-condensate pipelines, it is important to be able to predict as accurately as possible the pressure drop and the liquid content in the pipe at low liquid loading. The purpose of this testing is to identify the most appropriate models to perform this task.

E.2 Experimental data bank

In order to test the performance of model predictions at low liquid loading, a data bank has been constructed using available data from the literature. The criteria for data to qualify in the data bank were:

- Pipe flow data.
- Gas-liquid flow data.
- Stratified flow data (with or without atomization).
- Data for horizontal or slightly inclined pipes.
- Date at low liquid loading, LGR typically lower than 1%.

Generally, the available literature data is that of atmospheric two-phase flow but the present data bank has been appended with high pressure data at 20 bars and 90 bars from the Tiller Multiphase Flow Laboratory (Norway) and high density gas data (Nuland et al. 1993). For the Tiller data, the liquid loadings are higher than 1% but the data sets considered are for LGR smaller than 2% at ambient conditions. The data at low liquid loading acquired within this thesis is also included.

The content of the data bank is summarized in Table E–1. It is composed of 34 data sets. For the sake of clarity (Section E.4), data sets acquired at similar conditions (Di) are re-grouped into larger data sets (Di*). There are 13 starred data sets defined in Table E–1.

E.3 Two-phase flow models

The gas-liquid flow models tested are those described in Chapter 3. They include:

- Standard stratified flow models: Taitel et al. (1976), Espedal (1998). Biberg et al. (1998, 1999).
- Specific models at low liquid loading: Hart et al. (1989) (ARS), Grolman (1994) (MARS), Chen et al. (1997) and Meng (1999) (Double Circle model).

In addition, two simple models have been tested for their potential relevance to gas pipe flow calculations at low liquid loading. These are:

- The "single phase gas" flow model.
- The "homogeneous" flow model.

Models and characteristics and summarized in Table E–2.

The "single phase gas" flow model does not consider the presence of liquids and can only be used for calculating the pressure drop. Pressure drop is calculated from the gas momentum equation in single phase flow (Equation [3.1]) using Håland's equation (Equation [3.11]) for the gas-wall friction factor in turbulent flow.

The "homogeneous" model considers that gas-liquid flow can be seen as a single phase mist with the following properties:

$$\rho_m = (1 - H)\rho_G + H\rho_L \qquad [E.1]$$

$$\mu_m = (1 - H)\mu_G + H\mu_L \qquad [E.2]$$

with

$$H = \frac{U_{SL}}{U_{SG} + U_{SL}} \qquad [E.3]$$

This model thus assumes no slip between the gas and liquid phases. The pressure drop is calculated from the gas momentum equation for single phase flow (Equation [3.1]) together with Håland's equation (Equation [3.11]) by simply replacing gas density and visco-

sity with mixture density and Duckler equivalent viscosity (Equation [E.1] and Equation [E.2]). The liquid holdup is calculated using Equation [E.3].

The model named as "Espedal's model" is actually a construction based on Espedal's "simple" stratified flow model (Espedal 1998), using the correlation by Andritsos et al. (1987) for the interfacial friction. Espedal's "simple" model is described in Espedal (1998). It is based on the two-fluid formulation and hydraulic diameters as described in Section 3.3. It uses Håland's equation (Equation [3.11]) for the gas-wall and liquid-wall friction factors in turbulent flow.

The model by Biberg (1998, 1999) also builds on the two-fluid formulation but specific friction laws are developed for stratified flow as presented in Chapter 3. The gas-wall friction is calculated according to Equation [3.50], the liquid wall friction according to Equation [3.54] and the gas-liquid interfacial friction according to Equation [3.59]. Eventual empirical parameters are taken as recommended in Biberg (1999).

The model by Meng (1999) produces discontinuities due to the stratified/annular flow transition criterion suggested. In addition, the correlation by Ishii et al. (1989), Equation [3.78], gives sometimes unrealistic results for the entrained liquid fraction. Therefore, the model by Meng has been simplified assuming:

- Stratified flow.
- No entrained fraction ($EF = 0$).

The model by Chen et al. (1997) is in principle similar to that of Meng (1999) but it nevertheless differs from it due to:

- The correlation for the wetted half-angle (Equation [3.33] instead of Equation [3.44]).
- The correlation for the gas-liquid interfacial friction factor (Equation [3.67] instead of Equation [3.69]).
- The consideration of entrained droplets. Chen assumes $EF = 0$.

The models by Taitel et al. (1976), Hart et al. (1989) and Grolman (1994) have otherwise been implemented as proposed in the respective references without further modification. The models by Hart et al. (1989) and Chen et al. (1997) are for horizontal flow only.

E.4 Results

The models described in Section E.3 are implemented using Matlab 6.5 (Matlab 2002) and run for the data sets given in the experimental data bank. For each test case, the models M1 to M9 are run to compute the pressure drop and the liquid holdup.

Computations are further treated statistically. Calculated data and experimental measurements are compared point by point. For each data point, an algebraic error is calculated according to:

$$err_X = \frac{X_{calc} - X_{exp}}{X_{exp}} \quad [E.4]$$

where X stands for a physical variable, pressure drop or phase fraction, X_{calc} is the calculated (predicted) value and X_{exp} is the experimental (measured) value.

The error distribution is assumed to be represented by a standard unimodal gaussian probability density function (pdf) characterized by a mean value b_{err} and a standard deviation σ_{err}. The general form of the pdf is given by Equation [E.5]:

$$f(x) = \frac{1}{\sigma_{err}\sqrt{2\pi}} \exp\left[-\frac{1}{2}\left(\frac{x - \mu_{err}}{\sigma_{err}}\right)^2\right] \quad [E.5]$$

with

$$\sigma_{err} = \left[\frac{1}{n-1}\sum_{1}^{n}(err_i - \mu_{err})^2\right]^{1/2} \quad [E.6]$$

$$\mu_{err} = \frac{1}{n}\sum_{1}^{n} err_i \quad [E.7]$$

and n is the number of data points in the data set considered.

Results of the comparisons are presented as follows:

- Tables of mean error and standard deviation for models Mj on data set Di*. These are given in Table E–3 and Table E–4, for the liquid holdup and the pressure drop respectively.
- Graphs of predicted against measured holdup and pressure drop (Figure E–1 and Figure E–2).
- Graphs of pdf of error distributions for each model for the holdup and the pressure drop (Figure E–3 and Figure E–4).

E.5 Analysis

The following comments can be made of results presented in Section E.4:

• There is no model that can predict pressure drop and holdup within +/- 20% for all data sets in the data bank. Part of this spread is due to the fact that, despite the low initial liquid loadings (LGR < 2%), flow regimes can vary from slug flow to annular flow whereas models tested here are for stratified flow. In that extent, general purpose multiphase flow simulators that include a model for flow regime transitions are expected to perform statistically better than flow regime specific models.

• As expected, the actual pressure drop in gas pipe flow at low liquid loading is higher than the single phase gas pressure drop by a factor ranging from 14% to 62% in average (column M1 in Table E–4). Astonishingly, the predictions are much better for the dense gas data (Table E–4, data set D13* for model M1).

• Calculating the holdup assuming no-slip as in the "homogeneous" model (M2) severely under predicts the actual holdup by up to 97% even though predictions are better at high pressure. This is probably a consequence of the higher liquid fraction entrained as droplets.

• Standard two-fluid stratified flow models (M3, M4 and M5) do not perform very well in predicting both holdup and pressure drop but especially holdup despite the variety of closure laws involved. Those models perform better at conditions near atmospheric in small diameter pipes than for dense fluids, high pressure or large diameter pipes.

• The Taitel et al.'s model (Taitel et al. 1976), often used to compute steady state stratified flow, severely over predicts the liquid content as soon as flow conditions approach the transition to slug flow. This is a consequence of the assumption of a smooth gas-liquid interface. The pressure drop is also generally under predicted with this model.

• The "simple" two fluid model by Espedal (1998), M4, presents improvements over the Taitel et al.'s model. This illustrates the positive effect of more realistic friction closures, in particular interfacial friction. Still, deviations appear at high pressure. Biberg's model (M5) predicts pressure drop and holdup with a large spread and improves on Espedal's model only for atmospheric air-water data. This is probably a consequence of the empirical factors that are used to fit Espedal's (1998) air-water data.

• Specific models developed for dealing with stratified gas-liquid flow at low liquid loading, M6, M7, M8 and M9, perform slightly better than standard models especially for data sets at very low liquid loading (D3* to D8*) but also for high pressure, high density systems. It stresses the importance of considering pipe wall wetting and interfacial curvature for dealing with this type of flow. There are some variations, though, between the ARS/MARS approach and the Double Circle models. MARS gives better holdup predictions but poorer pressure loss predictions than the Double Circle Model, especially for the high pressure /dense gas data sets.

E.6 Summary

Liquid holdup and pressure drop predictions from gas-liquid stratified flow models have been compared with measured values from an experimental data bank made of pipe flow data at low liquid loading (LGR smaller than 1%, LGR smaller than 2% for the high pressure data). It can be concluded that:

- There is a large spread between predicted and measured values, independent of the model considered, and no model can reproduce the entire data range within +/- 20%.

- Assuming dry or homogeneous flow to simulate gas pipes at low liquid loading is not recommended and can be the source of very large errors.

- Standard stratified flow models perform almost as well as models specifically derived for dealing with low liquid loadings. Among these, the "simple" model by Espedal (1998) using a two fluid formulation, Håland's equation for wall friction laws and Andritsos et al.'s (1987) correlation for interfacial friction is to be recommended. However, there are large errors at high pressure with a spread in the holdup prediction (both over- and under estimations) and a general overestimation of the pressure drop.

- Among specific models, Grolman's MARS model (Grolman 1994) is to be preferred to Chen and Meng's Double Circle model (Chen et al. 1997, Meng 1999) for the holdup while the opposite is true for the pressure drop. Yet, there are large deviations between predictions and measurements at high pressures.

- In general, a complete two-phase flow model incorporating models for flow regime transitions is to be preferred to flow regime specific computations as it can occur a wide variety of flow regimes in wet gas pipes despite the low initial liquid content. It is expected that general purpose multiphase flow simulators will provide an overall better agreement with the experimental data.

Table E–1: Experimental data bank of gas-liquid pipe flow data at low liquid loading

Data set	D*	Ref.	Lab.	i.d., m	Material	θ, deg	P, bara	GAS			LIQUID			Comment
								Name	g_G[a], kg/m3	b_G[a], Pa.s	Name	g_L[a], kg/m3	b_L[a], Pa.s	
1	1*	Espedal (1998)	IFE	0.060	acrylic	-3	atm	air	1.2	1.810^{-5}	water	1000	10^{-3}	-
2						-1								
3						-0.5								
4						-0.104								
5	2*					0.104								
6						0.25								
7	3*	Badie et al. (2000)	Imperial College	0.078	steel	0	atm	air	1.2	1.810^{-5}	Shell Tellus oil water	865 1000	4010^{-3} 10^{-3}	holdup
8	4*													P drop
9	5*	Meng (1999)	TUFFP	0.050	acrylic	-2	1-2	air	1.2	1.810^{-5}	Lubsnap 40	877	5.710^{-3}	-
10						-1								
11	6*					0								
12						1								
13						2								
14	7*	Minami (1983)	TUFFP	0.078	PVC	0	2.7-6.2	air	1.2	1.810^{-5}	water	1000	10^{-3}	holdup
15											kerosene	800	210^{-3}	
16	8*	this thesis	NTNU	0.060	acrylic	0	atm	air	1.2	1.810^{-5}	water	1000	10^{-3}	-
17					steel						Exxsol D80	800	210^{-3}	
18	9*	-	Sintef	0.190	steel	-1	20	nitrogen	1.2	1.810^{-5}	diesel	824.2	2.3210^{-3}	confidential[b]
19						0								
20						1								

Table E–1: Experimental data bank of gas-liquid pipe flow data at low liquid loading

Data set	D*	Ref.	Lab.	i.d., m	Material	θ, deg	P, bara	GAS			LIQUID			Comment
								Name	g_G[a], kg/m3	b_G[a], Pa.s	Name	g_L[a], kg/m3	b_L[a], Pa.s	
21	10*	-	Sintef	0.190	steel	-1	90	nitrogen	1.2	1.810^{-5}	diesel	824.2	2.3210^{-3}	confidential[b]
22						0								
23						+1								
24	11*	-	Sintef	0.290	steel	5	45	naphta	-	-	diesel	824.2	2.3210^{-3}	confidential[b]
25						10								
26	12*	-	Sintef	0.29	steel	5	90	naphta	-	-	diesel	824.2	2.3210^{-3}	confidential[b]
27						10								
28	13*	Nuland et al. (1993)	IFE	0.1	pvc	2	4	freon 13B1	-	-	Exxsol D80	800	210^{-3}	-
29				0.1		10	4							
30				0.1		10	8							
31				0.065		10	8							
32				0.065		2	8							
33				0.1		2	2							
34				0.1		2	10							

a. At standard conditions of pressure and temperature
b. Confidential data

Table E–2: Models for stratified two-phase gas-liquid flow at low liquid loading

Model tag	Ref.	Gas-liquid interface	Entrain-ment	Limitations	Closures					Geometries		Holdup calc.	P drop calc.
					a_G	a_L	i_j		Υ	S_L	S_j		
							a_j	U_j					
M1	this thesis	-	-	single phase gas	Håland Equation [3.11]	-	-	-	-	-	-	-	gas mom. Equation [3.1]
M2	this thesis	-	-	no slip	Håland Equation [3.11]	-	-	-	-	-	-	no slip Equation [E.3]	gas mom. Equation [3.1]
M3	Taitel et al. (1976)	flat	no	stratified	Blasius Equation [3.7]	Blasius Equation [3.7]	$\lambda_j=\lambda_G$	0	geometric Equation [3.31]	geometric Equation [3.27]	geometric Equation [3.29]	iteration on Equation [3.26]	P drop Equation [3.23]
M4	Espedal (1998)	flat	no	stratified	Håland Equation [3.11]	Håland Equation [3.11]	Andritsos et al. Equation [3.58]	U_L	geometric Equation [3.31]	geometric Equation [3.27]	geometric Equation [3.29]	iteration on Equation [3.26]	P drop Equation [3.23]
M5	Biberg (1999)	flat	no	stratified	Biberg Equation [3.50]	Biberg Equation [3.54]	Biberg Equation [3.59]		geometric Equation [3.31]	geometric Equation [3.27]	geometric Equation [3.29]	iteration on Equation [3.26]	P drop Equation [3.23]

Table E–2: Models for stratified two-phase gas-liquid flow at low liquid loading

Model tag	Ref.	Gas-liquid interface	Entrain-ment	Limitations	Closures					Geometries		Holdup calc.	P drop calc.
					a_G	a_L	i_j		Υ	S_L	S_j		
							a_j	U_j					
M6	Grolman (1994)	concave	no	$\varepsilon_L<0.47$ $-3<\theta<6$	Eck smooth Equation [3.52]	MARS Equation [3.55]	Eck Equation [3.12]+ε_j Equation [3.65]	U_L^* U_L^* by Equation [3.66]	empirical Equation [3.36]	from δ Equation [3.27]	interpolla-tion Equation [3.40]	iteration on Equation [3.26]	P drop Equation [3.23]
M7	Meng (1999)	concave	yes Equation [3.78]	low liq. loading	Blasius Equation [3.7]	Blasius Equation [3.7]	empirical Equation [3.69]	U_L	empirical Equation [3.44]	from δ Equation [3.27]	from δ_j and D_j Equation [3.41]	iteration on Equation [3.26]	P drop Equation [3.23]
M8	Hart et al. (1989)	concave	no	$\varepsilon_L<0.06$ horizontal	Eck smooth Equation [3.52]	na	Eck Equation [3.12]+ε_j Equation [3.61]	0	energy min. Equation [3.33]	-	-	empirical Equation [3.80]	Equation [3.81]
M9	Chen et al. (1997)	concave	no	low liq. loading horizontal	Blasius Equation [3.6]	blasius Equation [3.6]	empirical Equation [3.67]	U_L	as M8	from δ Equation [3.27]	from δ_j and D_j Equation [3.41]	iteration on Equation [3.26]	P drop Equation [3.23]

Table E–3: Holdup statistics

Dataset	M2		M3		M4		M5		M6		M7		M8		M9	
	b_{err}	h_{err}	b_{err}	h_{err}	b_{err}	h_{err}	b_{err}	h_{err}	b_{err}	h_{err}	b_{err}	h_{err}	b_{err}	h_{err}	b_{err}	h_{err}
D1*	-0.93	0.03	0.07	0.15	-0.14	0.13	0.00	0.05	-0.13	0.11	0.04	0.10	-	-	-	-
D2*	-0.96	0.01	0.56	0.33	-0.06	0.38	0.12	0.16	-0.17	0.12	-0.39	0.17	-	-	-	-
D3*	-0.97	0.02	0.37	0.36	-0.47	0.51	-0.48	0.31	-0.10	0.20	-0.02	0.30	-0.12	0.16	-0.14	0.19
D5*	-0.96	0.03	0.24	0.70	-0.28	0.25	-0.33	0.58	0.42	0.57	0.03	0.52	-	-	-	-
D6*	-0.96	0.03	4.00	7.31	0.05	1.10	1.42	5.56	0.96	1.82	0.23	2.00	1.90	3.03	1.38	2.37
D7*	-0.93	0.03	0.11	0.41	-0.19	0.25	0.44	0.50	-0.24	0.19	-0.23	0.26	-0.23	0.20	-0.25	0.28
D8*	-0.97	0.01	-0.05	0.29	-0.41	0.13	0.04	0.24	0.09	0.16	-0.34	0.21	0.19	0.15	-0.13	0.14
D9*	-0.71	0.05	1.36	0.82	0.14	0.16	-0.14	0.11	-0.10	0.16	0.16	0.19	-0.15	0.08	0.48	0.17
D10*	-0.15	0.20	2.60	0.79	1.18	0.42	0.71	0.33	1.62	0.61	1.12	0.58	0.90	0.49	2.36	0.94
D11*	-0.86	0.14	11.14	16.55	9.12	12.90	3.42	3.65	0.38	1.07	0.04	0.65	-	-	-	-
D12*	-0.91	0.10	7.31	7.72	6.36	6.49	4.76	4.90	1.97	2.05	2.04	2.29	-	-	-	-
D13*	-0.79	0.12	5.84	2.99	2.18	2.27	3.25	1.89	0.91	1.37	-0.10	0.68	-	-	-	-

Table E–4: Pressure drop statistics

Dataset	M1		M2		M3		M4		M5		M6		M7		M8		M9	
	b_{err}	h_{err}	b_{err}	h_{err}	b_{err}	h_{err}	b_{err}	h_{err}	b_{err}	h_{err}	b_{err}	h_{err}	b_{err}	h_{err}	b_{err}	h_{err}	b_{err}	h_{err}
D1*	-0.35	0.17	1.26	1.01	-0.23	0.17	0.01	0.15	0.01	0.11	-0.12	0.10	0.02	0.24	-	-	-	-
D2*	-0.55	0.10	0.50	0.36	-0.17	0.26	-0.06	0.17	-0.01	0.06	-0.19	0.06	0.23	0.17	-	-	-	-
D4*	-0.43	0.29	-0.04	0.50	-0.35	0.29	0.18	0.39	1.64	1.61	0.48	0.35	-0.10	0.36	0.14	0.42	0.07	0.50
D5*	-0.46	0.19	-0.09	0.75	-0.41	0.20	-0.11	0.17	1.45	1.24	-0.08	0.22	-0.22	0.27	-	-	-	-
D6*	-0.59	0.13	-0.37	0.21	-0.06	1.10	-0.21	0.23	1.13	1.21	-0.12	0.26	-0.04	0.33	-0.04	0.30	-0.21	0.14
D8*	-0.25	0.13	-0.09	0.13	-0.22	0.12	0.02	0.07	0.11	0.10	-0.07	0.07	-0.02	0.13	0.09	0.13	0.14	0.07
D9*	-0.62	0.02	-0.40	0.06	-0.58	0.09	-0.33	0.04	0.25	0.10	-1.18	0.10	-0.07	0.32	0.63	0.06	-0.26	0.03
D10*	-0.40	0.04	-0.30	0.03	-0.55	0.02	-0.21	0.06	0.21	0.12	-4.91	1.05	0.08	0.30	1.43	0.11	-0.18	0.07
D11*	-0.51	0.26	-0.47	0.28	1.88	0.99	1.72	0.89	0.72	0.29	-0.09	0.45	0.15	0.32	-	-	-	-
D12*	-0.54	0.18	-0.51	0.19	2.15	1.10	2.01	0.99	1.46	1.09	0.54	0.61	0.85	0.72	-	-	-	-
D13*	-0.14	0.34	0.08	0.34	1.52	1.49	1.20	1.21	1.29	0.95	-0.74	1.29	0.73	0.60	-	-	-	-

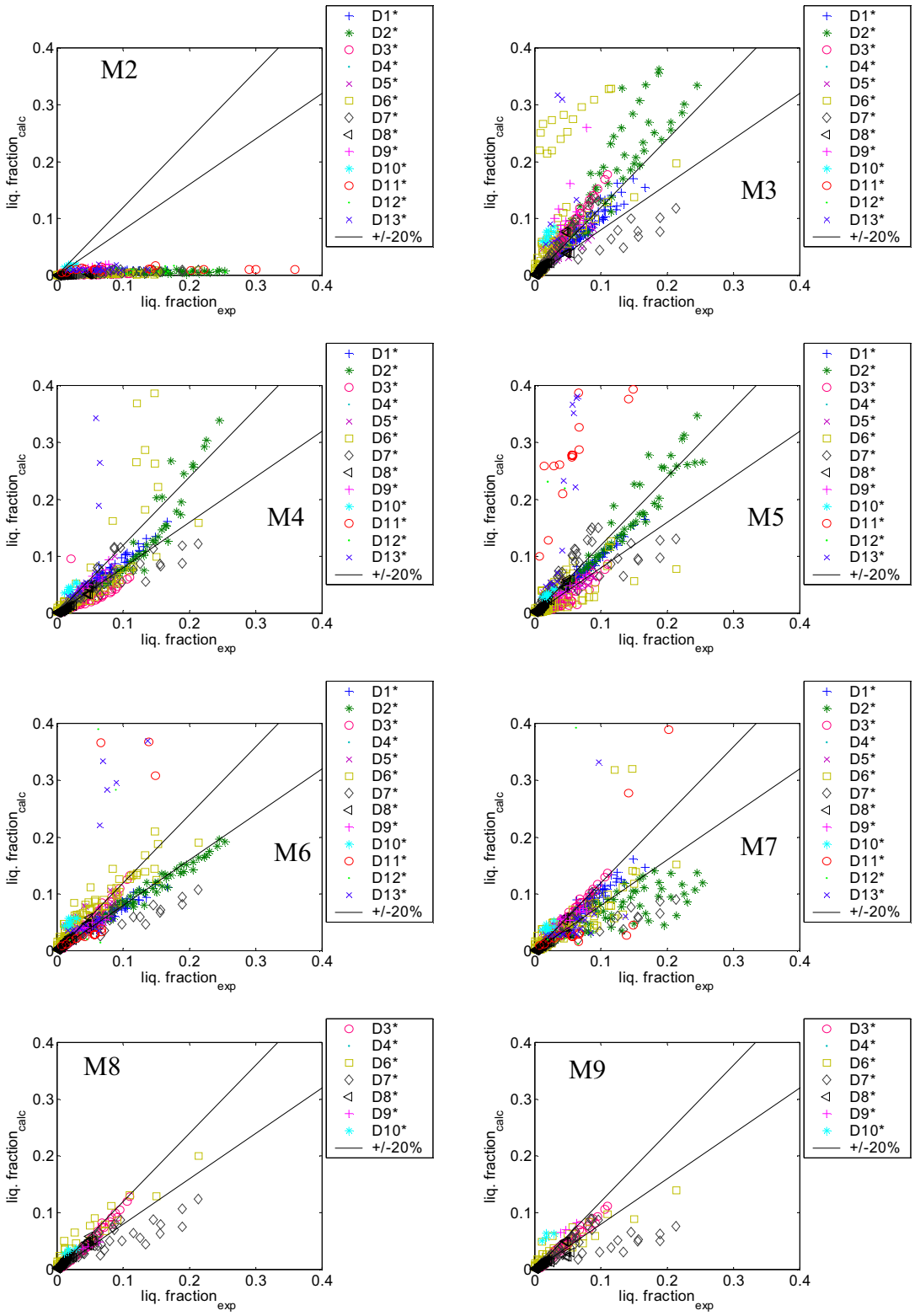

Figure E–1: Two-phase models: calculated versus measured liquid holdup

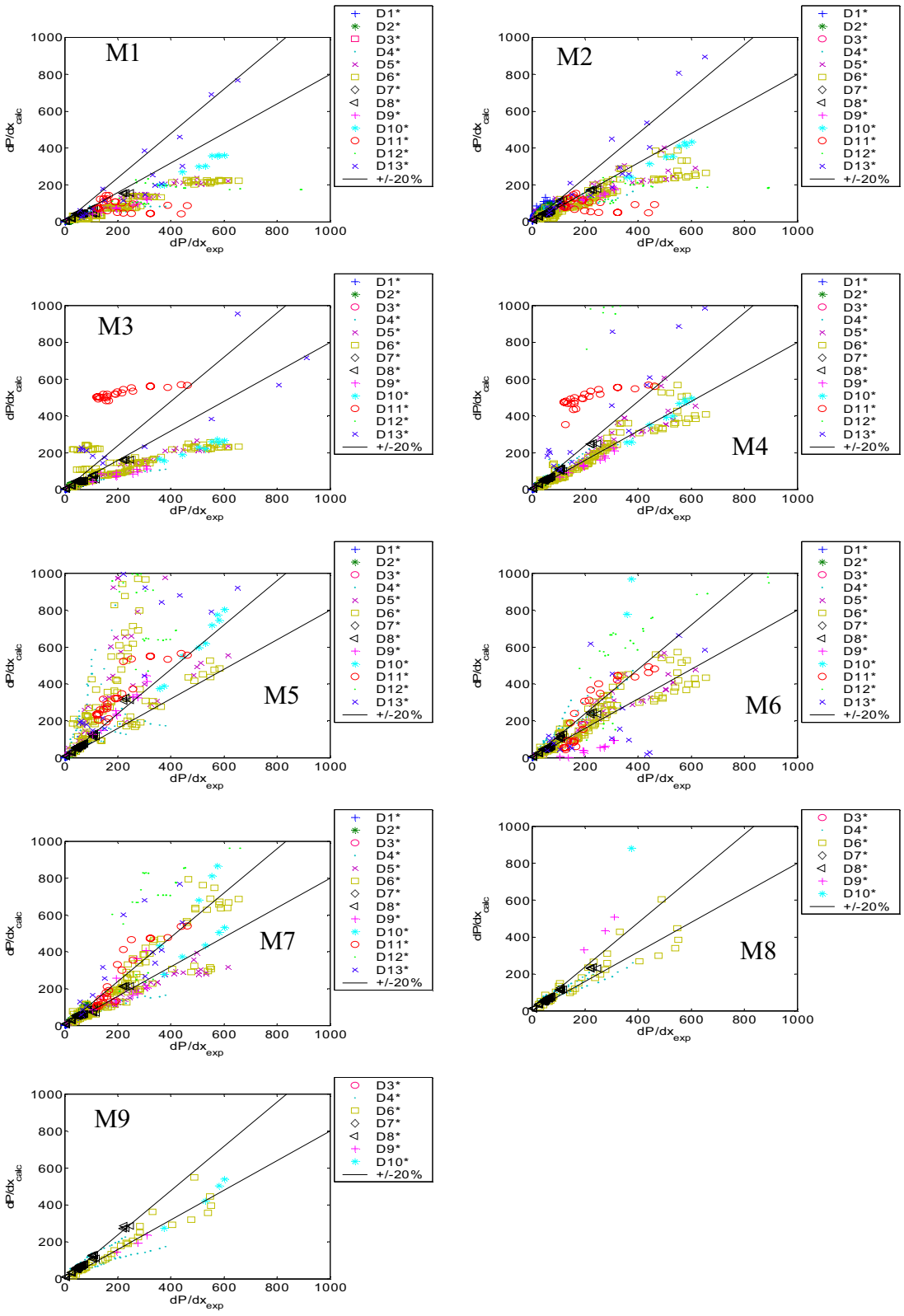

Figure E–2: Two-phase models: calculated versus measured pressure drop

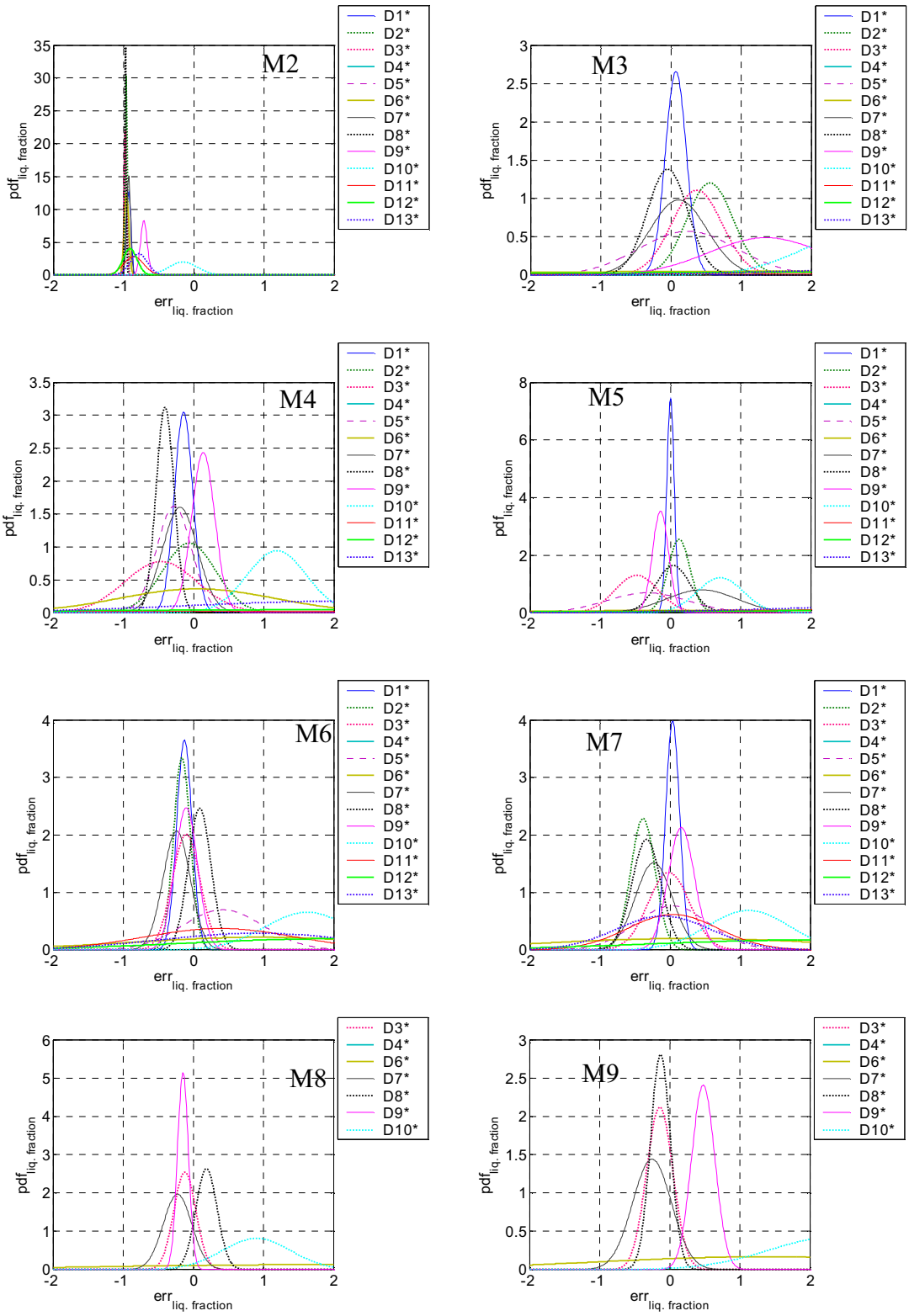

Figure E–3: pdf error on the liquid holdup

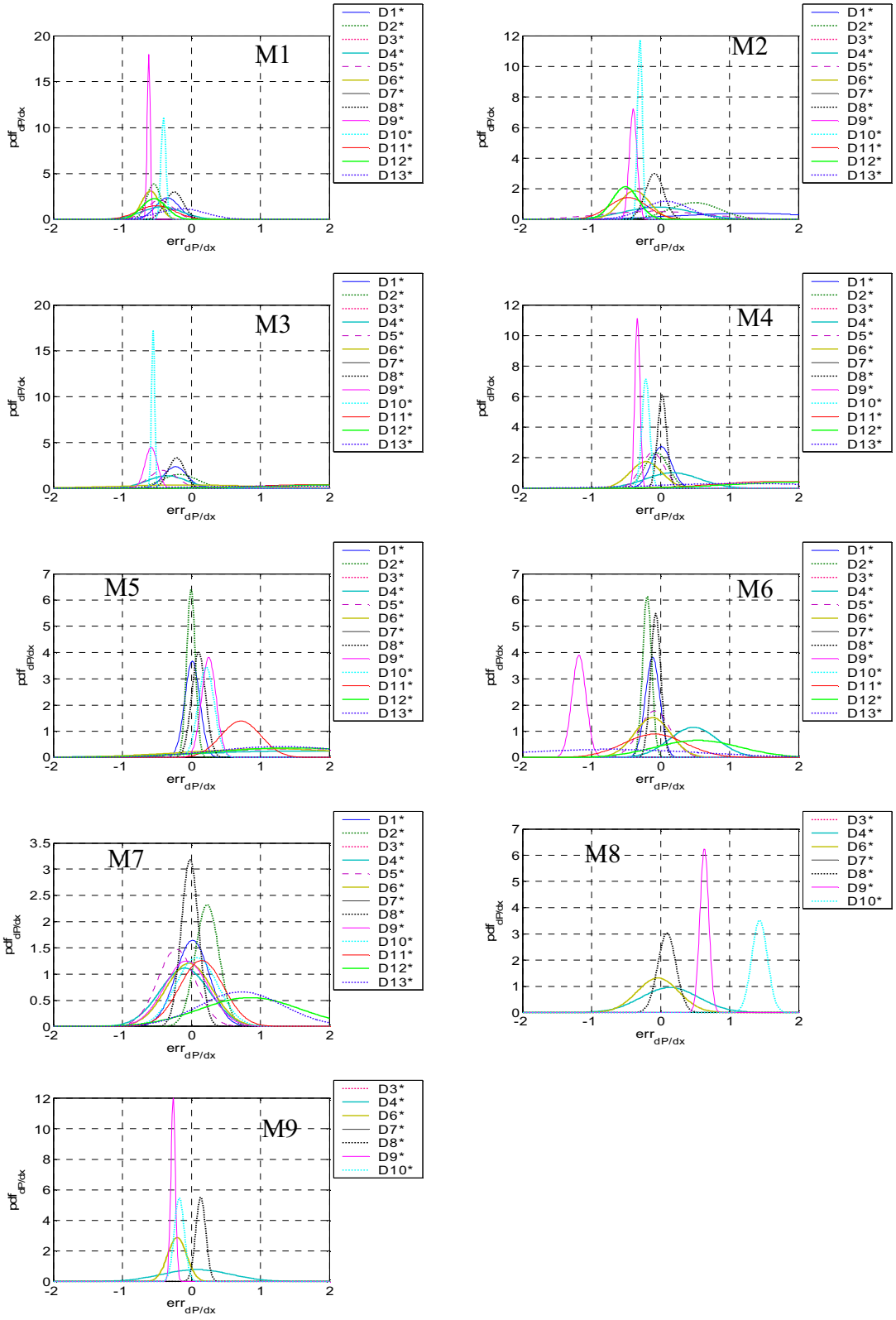

Figure E–4: pdf error on the pressure drop